REPORT DOCUMENTATION PAGE

Form Approved

AFRL-SR-BL-TR-00-

0732

1. AGENCY USE ONLY *(Leave blank)*	2. REPORT DATE	3. REPOF
	December, 1996	

4. TITLE AND SUBTITLE
1996 Summer Research Program (SRP), Summer Faculty Research Program (SFRP), Final Reports, Volume 5A, Wright Laboratory

5. FUNDING NUMBERS
F49620-93-C-0063

6. AUTHOR(S)
Gary Moore

7. PERFORMING ORGANIZATION NAME(S) AND ADDRESS(ES)
Research & Development Laboratories (RDL)
5800 Uplander Way
Culver City, CA 90230-6608

8. PERFORMING ORGANIZATION REPORT NUMBER

9. SPONSORING/MONITORING AGENCY NAME(S) AND ADDRESS(ES)
Air Force Office of Scientific Research (AFOSR)
801 N. Randolph St.
Arlington, VA 22203-1977

10. SPONSORING/MONITORING AGENCY REPORT NUMBER

11. SUPPLEMENTARY NOTES

12a. DISTRIBUTION AVAILABILITY STATEMENT
Approved for Public Release

12b. DISTRIBUTION CODE

13. ABSTRACT *(Maximum 200 words)*

The United States Air Force Summer Research Program (USAF-SRP) is designed to introduce university, college, and technical institute faculty members, graduate students, and high school students to Air Force research. This is accomplished by the faculty members (Summer Faculty Research Program, (SFRP)), graduate students (Graduate Student Research Program (GSRP)), and high school students (High School Apprenticeship Program (HSAP)) being selected on a nationally advertised competitive basis during the summer intersession period to perform research at Air Force Research Laboratory (AFRL) Technical Directorates, Air Force Air Logistics Centers (ALC), and other AF Laboratories. This volume consists of a program overview, program management statistics, and the final technical reports from the SFRP participants at the Wright Laboratory.

14. SUBJECT TERMS
Air Force Research, Air Force, Engineering, Laboratories, Reports, Summer, Universities, Faculty, Graduate Student, High School Student

15. NUMBER OF PAGES

16. PRICE CODE

17. SECURITY CLASSIFICATION OF REPORT	18. SECURITY CLASSIFICATION OF THIS PAGE	19. SECURITY CLASSIFICATION OF ABSTRACT	20. LIMITATION OF ABSTRACT
Unclassified	Unclassified	Unclassified	UL

UNITED STATES AIR FORCE

SUMMER RESEARCH PROGRAM -- 1996

SUMMER FACULTY RESEARCH PROGRAM FINAL REPORTS

VOLUME 5A

WRIGHT LABORATORY

RESEARCH & DEVELOPMENT LABORATORIES

5800 Uplander Way

Culver City, CA 90230-6608

Program Director, RDL
Gary Moore

Program Manager, AFOSR
Major Linda Steel-Goodwin

Program Manager, RDL
Scott Licoscos

Program Administrator, RDL
Johnetta Thompson

Program Administrator, RDL
Rebecca Kelly

Submitted to:

AIR FORCE OFFICE OF SCIENTIFIC RESEARCH

Bolling Air Force Base

Washington, D.C.

December 1996

PREFACE

Reports in this volume are numbered consecutively beginning with number 1. Each report is paginated with the report number followed by consecutive page numbers, e.g., 1-1, 1-2, 1-3; 2-1, 2-2, 2-3.

Due to its length, Volume 5 is bound in three parts, 5A, 5B and 5C. Volume 5A contains #1-24. Volume 5B contains reports #25-48 and 5C contains #49-70. The Table of Contents for Volume 5 is included in all parts.

This document is one of a set of 16 volumes describing the 1996 AFOSR Summer Research Program. The following volumes comprise the set:

VOLUME	TITLE
1	Program Management Report
	Summer Faculty Research Program (SFRP) Reports
2A & 2B	Armstrong Laboratory
3A & 3B	Phillips Laboratory
4	Rome Laboratory
5A , 5B & 5C	Wright Laboratory
6	Arnold Engineering Development Center, Wilford Hall Medical Center and Air Logistics Centers
	Graduate Student Research Program (GSRP) Reports
7A & 7B	Armstrong Laboratory
8	Phillips Laboratory
9	Rome Laboratory
10A & 10B	Wright Laboratory
11	Arnold Engineering Development Center, United States Air Force Academy, Wilford Hall Medical Center, and Wright Patterson Medical Center
	High School Apprenticeship Program (HSAP) Reports
12A & 12B	Armstrong Laboratory
13	Phillips Laboratory
14	Rome Laboratory
15A&15B	Wright Laboratory
16	Arnold Engineering Development Center

SFRP FINAL REPORT TABLE OF CONTENTS i-xviii

1. INTRODUCTION 1

2. PARTICIPATION IN THE SUMMER RESEARCH PROGRAM 2

3. RECRUITING AND SELECTION 3

4. SITE VISITS 4

5. HBCU/MI PARTICIPATION 4

6. SRP FUNDING SOURCES 5

7. COMPENSATION FOR PARTICIPATIONS 5

8. CONTENTS OF THE 1996 REPORT 6

APPENDICIES:

A. PROGRAM STATISTICAL SUMMARY A-1

B. SRP EVALUATION RESPONSES B-1

SFRP FINAL REPORTS

SRP Final Report Table of Contents

Author	University/Institution Report Title	Armstrong Laboratory Directorate	Vol-Page
DR Richelle M Allen-King	Washington State University , Pullman , WA Reduction Kinetics in a Batch Metallic Iron/Water System:Effect of Iron/Water Exposure	AL/EQC	2- 1
DR Anthony R Andrews	Ohio University , Athens , OH Investigation of the Electrochemiluminescent Properties of Several Natural & Synthetic Compounds	AL/EQC	2- 2
DR Deborah L Armstrong	Univ of Texas at San Antonio , San Antonio , TX Development of A primary Cell Culture Preparation for Studying Mechanisms Governi ng Circadian Rhyth	AL/CFTO	2- 3
DR Robert L Armstrong	New Mexico State University , Las Cruces , NM Microparticle Bioluminescence	AL/CFD	2- 4
DR Maureen E Bronson	Wilkes Univ School of Pharmacy , Wilkes-Barre , PA Lack of Effect of UltraWideband Radiation on Pentylenetetrazol-Induced Convulsions in Rats	AL/OER	2- 5
DR Marc L Carter, PhD, PA	University of South Florida , Tampa , FL Assessment of the Reliability of Ground-Based Observers for the Detection of Aircraft	AL/OEO	2- 6
DR Jer-Sen Chen	Wright State University , Dayton , OH A Study of Data Compression Based on Human Visual Perception	AL/CFHV	2- 7
DR Cheng Cheng	Johns Hopkins University , Baltimore , MD Sequential Optimization Algorithm for Personnel Assignmt Based on Cut-Off Profiles & Rev of Brogden	AL/HRM	2- 8
DR Elizabeth T Davis	Georgia Institute of Tech , Atlanta , GA Perceptual Issues in Virtual Environments & Other Simulated Displays	AL/CFHP	2- 9
DR Keith F Eckerman	Univ of Tennessee , Knoxville , TN	AL/OEB	2- 10
DR Paul A Edwards	Edinboro Univ of Pennsylvania , Edinboro , PA A Viartion Fuel Identification- Neural Network Analysis of the Concentration of Benzene and Naphtha	AL/EQC	2- 11

Author	University/Institution Report Title	Armstrong Laboratory Directorate	Vol-Page
DR Randolph D Glickman	Univ of Texas Health Science Center , San Antonio , TX A Study of Oxidative Reaactions Mediated by Laser-Excited Ocular Melanin	AL/OEO	2- 12
DR Ellen L Glickman-Weiss	Kent State University , Kent , OH The Effect of Short Duration Respiratory Musculature Training on Tactical Air Combat	AL/CFTF	2- 13
DR Irwin S Goldberg	St. Mary's Univ of San Antonio , San Antonio , TX Development of a Physiologically-Based Pharmacokinetic Model for the Uptake of Volatile Cheicals dur	AL/OES	2- 14
DR Robert J Hirko	University of Florida , Gainesville , FL Investigation of The Suitability of Tactile and Auditory Stimuli for use in Brain Actuated Control	AL/CFHP	2- 15
ISU VPP Acct4212313(Dooley)	Iowa State University , Ames , IA Determination of the Influence of Ultrawideband Exposure of Rts During Early Pregnancy on Pregnancy	AL/OER	2- 16
DR Andrew E Jackson	Arizona State University , Tempe , AZ A Description of Integrated Joint Use Initiatives to Satisfy Customer Reqmts Across Govt Academia	AL/HRA	2- 17
DR John E Kalns	Ohio State University , Columbus , OH	AL/AOHR	2- 18
DR Nandini Kannan	Univ of Texas at San Antonio , San Antonio , TX Modeling Decompression Sickness Using Survival Analysis Techniques	AL/CFTS	2- 19
DR Antti J Koivo	Purdue Research Foundation , West Lafayette , IN Skill Evaluation of Human Operators	AL/CFBA	2- 20
DR Suk B Kong	Incarnate Word College , San Antonio , TX Aromatic Hydrocabon Components in Diesel, Jet-A And JP-8 Fuels	AL/OEA	2- 21
DR Xuan Kong	Northern Illinois University , De Kalb , IL Mental Workload Classification via Physiological Signal Processing: EOG & EEG Analyses	AL/CFHP	2- 22

SRP Final Report Table of Contents

Author	University/Institution Report Title	Armstrong Laboratory Directorate	Vol-Page
DR Charles S Lessard	Texas A & M Univ-College Station , College Station , TX Preliminary Studies of Human Electroencephalogram (EEG) Correlates of GzAcceleration Tolerance	AL/CFTO	2- 23
DR Audrey D Levine	Utah State University , Logan , UT Biogeochemical Assessment of Natural Attenuation of JP-4 Contaminated Ground Water	AL/EQC	2- 24
DR David A Ludwig	Univ of N.C. at Greensboro , Greensboro , NC The Illusion of Control & Precision Associated w/Baseline Comparisons	AL/AOCY	2- 25
DR Robert G Main	Cal State Univ, Chico , Chico , CA Designing Instruction For Distance Learning	AL/HRT	2- 26
DR Phillip H Marshall	Texas Tech University , Lubbock , TX Time to Contact Judgments in The Presence of Static and Dynamic Objects: A Preliminary Report	AL/HRM	2- 27
MS Sandra L McAlister	Stonehill College , North Easton , MA	AL/AO	2- 28
MR Bruce V Mutter	Bluefield State College , Bluefield , WV Environmental Cost Analysis:Calculating Return on Investment for Emerging Technologies	AL/EQP	2- 29
DR Sundaram Narayanan	Wright State University , Dayton , OH Java-Based Application of the Model-View-Controller Framwork in Developing Interfaces to interactive	AL/HRT	2- 30
DR Karl A Perusich	Purdue University , South Bend , IN Examing Alternate Entry Points in a Problem Using Fuzzy Cognitive Maps	AL/CFHI	2- 31
DR Judy L Ratliff	Murray State Univ , Murray , KY A Study of The Ability of Tunicates to be used as Global Bioindicators	AL/EQC	2- 32
DR Paul D Retzlaff	Univ of Northern Colorado , Greeley , CO Computerized Neuropsychological Assessment of USAF Pilots	AL/AOCN	2- 33

Author	University/Institution Report Title	Armstrong Laboratory Directorate	Vol-Page
DR William G Rixey	University of Houston , Houston , TX The use of Solid-Phase Microextraction (SPME) for the low level Detection of BTEX and PAHs In Aqueou	AL/EQC	2- 34
DR Ali M Sadegh	CUNY-City College , New York , NY Investigation of Neck Models for Predicting Human Tolerance to Accelerations	AL/CFBE	2- 35
DR Kandasamy Selvavel	Claflin College , Orangeburg , SC Truncated Bivariate Exponential Models	AL/AOEP	2- 36
DR Barth F Smets	University of Connecticut , Storrs , CT Biodegradation of 2-4-DNTand 2,6-DNT in Mixed Culture Aerobic Fluidized Bed Reactor and Chemostat	AL/EQC	2- 37
DR Mary Alice Smith	University of Georgia , Athens , GA A Study of Apoptosis During Limb Development	AL/OET	2- 38
DR Daniel P Smith	Utah State University , Logan , UT Bioremediation & its Effect on Toxicity	AL/EQW	2- 39
MR. Joseph M Stauffer	Indiana State University , Terre Haute , IN Joint Corrections for Correlation Coefficients	AL/HRMA	2- 40
DR William B Stavinoha	Univ of Texas Health Science Center , San Antonio , TX Studies to Identify Characterisstic Changes in the Urine Following Ingestion of Poppy seed	AL/AOT	2- 41
DR William A Stock	Arizona State University , Tempe , AZ Application of Meta-Analysis to Research on Pilot Training	AL/HRA	2- 42
DR Nancy J Stone	Creighton University , Omaha , NE Engagement, Involvement, and Self-Regualted Leaarnign Construct and Measurement Development to Asses	AL/HRT	2- 43
DR Brenda M Sugrue	Univ of Northern Colorado , Greeley , CO Aptitude-Attribute Interactions in Test Performance	AL/HRTI	2- 44

SRP Final Report Table of Contents

Author	University/Institution Report Title	Armstrong Laboratory Directorate	Vol-Page
DR Stephen A Truhon	Winston-Salem State University, Winston-Salem, NC Mechanical Specialties in the U.S. Air Force: Accession Quality & Selection Test Validity	AL/HRM	2 - 45
DR Mariusz Ziejewski	North Dakota State University, Fargo, ND Validation of the Deformable Neck Model for A +Gz Acceleration	AL/CFBV	2 - 46

SRP Final Report Table of Contents

Author	University/Institution Report Title	Phillips Laboratory Directorate	Vol-Page
DR Graham R Allan	New Mexico Highlands University, Las Vegas, NM Temporal and Spatial Characterization of a Synchronously-Pumped Periodically-Poled Lithium Niobate Optical	PL/LIDN	3 - 1
DR Brian P Beecken	Bethel College, St. Paul, MN Testing of a Dual-Band Infrared Focal Plane Array & An Infrared Camera Sys	PL/VTRP	3 - 2
DR Mikhail S Belen'kii	Georgia Inst of Technology, Atlanta, GA Tilt Sensing Technique w/Small Aperture Beam & Related Physical Phenomena	PL/LIG	3 - 3
DR Asoke K Bhattacharyya	Lincoln University, Jefferson City, MO Part A: Effect of Earth's Surface & Loss on the Resonant Frequencies of Buried Objects	PL/WSQ	3 - 4
DR Joseph M Calo	Brown University, Providence, RI Transient Studies of the Effects of Fire Suppressants in a Well-Stirred Combustor	PL/GPID	3 - 5
DR James J Carroll	Youngstown State University, Youngstown, OH Examination of Critical Issues in the use of (178) hf For High Energy Density Applications	PL/WSQ	3 - 6
DR Soyoung S Cha	Univ of Illinois at Chicago, Chicago, IL A Study on Hartmann Sensor Application to Flow Aero-Optics Investigation Through Tomographic Recons	PL/LIMS	3 - 7
DR Tsuchin Chu	Southern Illinois Univ-Carbondale, Carbondale, IL	PL/RKS	3 - 8
DR Kenneth Davies	Univ of Colorado at Boulder, Boulder, CO Studies of Ionospheric Electron contents and High-Frequency Radio Propagation	PL/GPIM	3 - 9
DR Judith E Dayhoff	Univ of Maryland, College Park, MD Dynamic Neural Networks: Prediction of an Air Jet Flowfield	PL/LIMS	3 - 10
DR Ronald R DeLyser	University of Denver, Denver, CO Analysis of Complex Cavities Using the Finite Difference Time Domain Method	PL/WSTS	3 - 11
DR Andrew G Detwiler	S Dakota School of Mines/Tech, Rapid City, SD Evaluation of Engine-Related Factors Influencing Contrail Prediction	PL/GPAB	3 - 12
DR Itzhak Dotan	The Open University of Israel, Tel-Aviv Israel Studies of Ion-Molecule Reaction Rates at Very High Temperatures	PL/GPID	3 - 13

Author	University/Institution Report Title	Phillips Laboratory Directorate	Vol-Page
DR Omar S Es-Said	Loyola Marymount University, Los Angeles, CA On the Matis Selection of Durable Coatings for Cryogenic Engineer Technology	PL/RKE	3 - 14
DR Jeffrey F Friedman	University of Puerto Rico, Mayaguez, PR Testing the Frozen Screen Model of Atmospheric Turbulence	PL/LIMI	3 - 15
DR John A Guthrie	University of Central Oklahoma, Edmond, OK Ultrawide-Band Microwave Effects Testing on an Electronic System	PL/WSMA	3 - 16
DR George W Hanson	Univ of Wisconsin - Milwaukee, WI A Volumetric Eigenmode Expansion Method for Dielectric Bodies	PL/WSQ	3 - 17
DR Mayer Humi	Worcester Polytechnic Inst., Worcester, MA Wavelets and Their Applications to the Analysis of Meteorological Data	PL/GPAA	3 - 18
DR Christopher H Jenkins	S Dakota School of Mines/Tec, Rapid City, SD Shape Control of An Inflated Thin Circular Disk	PL/VT	3 - 19
DR Dikshitulu K Kalluri	University of Lowell, Lowell, MA Electromagnetic Wave Transformation in a Two-Dimensional-Space-Varying and Time-Varying Magnetoplasm	PL/GPIA	3 - 20
DR Aravinda Kar	University of Central Florida, Orlando, FL Thick Section Cutting w/Chemical Oxygen-Iodine Laser & Scaling Laws	PL/LIDB	3 - 21
DR Spencer P Kuo	Polytechnic University, Farmingdale, NY Theory of Electron Acceleration by HF-Excited Langmuir Waves	PL/GPI	3 - 23
DR Andre Y Lee	Michigan State University, East Lansing, MI Characterization Methods for Adhesion Strength Between Polymers & Ceramics	PL/RKS	3 - 24
DR Bruce W Liby	Manhattan College, Riverdale, NY Acousto-Optic Retro-Modulator	PL/VTRA	3 - 25
DR Feng-Bao Lin	Polytechnic Inst of New York, Brooklyn, NY Structural Ballistic Risk Assessment-Fracture Modeling	PL/RKEM	3 - 26
DR M Arfin K Lodhi	Texas Tech University, Lubbock, TX Theory, Modeling & Analysis of AMTEC	PL/VTP	3 - 27

Author	University/Institution Report Title	Phillips Laboratory Directorate	Vol-Page
DR Ronald A Madler	Embry-Riddle Aeronautical University, Prescott, AZ Estimating the Area of Artificial Space Debris	PL/WSAT	3 - 28
DR Carlos A Ordonez	University of North Texas, Denton, TX Boundary Conditions at A Plasma-Facing Surface	PL/WSQA	3 - 29
DR Michael J Pangia	Georgia Southwestern Coll, Americus, GA Further Analysis of Kilohertz Order Waves Associated with Electron Beam Operations on STS46	PL/GPSG	3 - 30
DR Ronald M Pickett	University of Lowell, Lowell, MA Temporal-Displacement Stereograms of the Ionosphere: An Exploration of Their Utility in the Analysis of Equatorial Emission Depletion Bands	PL/GPIA	3 - 31
DR Edgar Sanchez-Sinencio	Texas A&M Univ-College Station, College Station, TX Low Voltage Analog Circuit Design for Radiation Tolerance	PL/VTER	3 - 32
DR Joseph C Slater	Wright State University, Dayton, OH Smart Structure/Actuator Modeling 7 Design for the Integrated Ground Demonstration Lab	PL/VTI	3 - 33
DR Ashok Srivastava	Louisiana State University, Baton Rouge, LA Modeling of Total Dose Response of SOI N-MOSFETS for Low Power CMOS Circuits	PL/VTER	3 - 34
DR James M Stiles	University of Kansas, Lawrence, KS The Potential Applications of Super-Resolution & Array Processing to Space-Based Radars	PL/VTRA	3 - 35
DR Charles M Swenson	Utah State University, Logan, UT Balloon Launch Retromodulator Experiment	PL/VTRA	3 - 36
DR Miguel Velez-Reyes	University of Puerto Rico, Mayaguez, PR Regularization Methods for Linear and Nonlinear Retrieval Problems	PL/GPAS	3 - 37

SRP Final Report Table of Contents

Author	University/Institution Report Title	Rome Laboratory Directorate	Vol-Page
DR A F Anwar	University of Connecticut, Storrs, CT A Study of Quantum Wells Formed in AlxGa1-xAsySb1-y/InzGa1-zAs/AlxGa1-AsySb1-y Heterostructures	RL/ER	4 - 1
DR Ercument Arvas	Syracuse University, Syracuse, NY An Assessment of the Current State of the Art of Stap from an Electromagnetics Point of View	RL/OCSS	4 - 2
DR Ahmed E Barbour	Georgia Southern University, Statesboro, GA Formal Verification Using ORA Larch/VHDL Theorem Prover	RL/ERDD	4 - 3
DR Milica Barjaktarovic	Wilkes University, Wilkes Barre, PA Formal Specification and Verification of Missi Architecture Using Spin	RL/C3AB	4 - 4
DR Daniel C Bukofzer	Cal State Univ, Fresno, Fresno, CA Performance Analysis & Simulation Results of Delay & Spread Spectrum Modulated Flip Wave-Signal Gene	RL/C3BA	4 - 5
DR Xuesheng Chen	Wheaton College, Norton, MA Optical and Non-Destructive Methods to Determine the Composition and Thickness of an INxGA1-xAS/INP	RL/ERX	4 - 6
DR Jun Chen	Rochester Inst of Technology, Rochester, NY A Study of Optoelectronic Feedback-Sustained Pulsation of Laser Diodes at 1300 nm & 780 nm	RL/OCPA	4 - 7
DR Everett E Crisman	Brown University, Providence, RI Evaluation of Semiconductor Configurations as Sources for Optically Induced Microwave Pulses	RL/ERAC	4 - 8
DR Digendra K Das	SUNYIT, Utica, NY Techniques for Determining of the Precision of Reliability Predictions and Assessments.	RL/ERSR	4 - 9
DR Matthew E Edwards	Spelman College, Atlanta, Ga The Analysis of PROFILER for Modeling the Diffusion of Aluminum-Copper on a Silicon Substrate	RL/ERDR	4 - 10
DR Kaliappan Gopalan	Purdue University - Calumet, Hammond, IN Speaker Identification & Analysis of Stressed Speech	RL/IRAA	4 - 11
DR Joseph W Haus	Rensselaer Polytechnic Institute, Troy, NY Mode-Locked Laser Models and Simulations	RL/OCPA	4 - 12

SRP Final Report Table of Contents

Author	University/Institution Report Title	Rome Laboratory Directorate	Vol-Page
DR James P LeBlanc	New Mexico State University, Las Cruces, NM Multichannel Autoregressive Modeling & Spectral Estimation Methods for Airborne Radar Environment	RL/OCSS	4 - 13
DR David J McLaughlin	Northeastern University, Boston, MA A Review of Microwave Terrain Clutter Measurements at Bistatic	RL/ERCS	4 - 14
DR Hrushikesh N Mhaskar	Cal State Univ, Los Angeles, Los Angeles, Ca Neural Beam Steering & Direction Finding	RL/ERAA	4 - 15
DR Ronald W Noel	Rensselaer Polytechnic Institute, Troy, NY A Low Dimensional Categorization Technique for C Source Code	RL/C3CA	4 - 16
DR Jeffrey B Norman	Vassar College, Poughkeepsie, NY Frequency Response of Semiconductor Photorefractive Matls: ZnTe:Mn:V,GaAs:Cr,&CdMnTe:V	RL/OCPA	4 - 17
DR Glenn E Prescott	University of Kansas Center for Research, Lawrence, KS Rapid Prototyping of Software Radio Sys Using Field Programmable Gate Arrays & DSP Microprocessors	RL/C3BB	4 - 18
DR Mark R Purtill	Texas A&M Univ-Kingsville, Kingsville, TX A Network Flow Heuristic for Graph Mapping	RL/C3CB	4 - 19
DR Mysore R Rao	Rochester Inst. Of Technology, Rochester, NY Dectection of Concealed Objects in Images: Investigation into Wavelet Transform Based Object Isolation Techniques	RL/OCSM	4 - 20
DR Scott E Spetka	SUNY of Tech Utica, Utica, NY Integrating a Multimedia Database & WWW Indexing Tools	RL/IRD	4 - 21
DR Gang Sun	University of Massachusetts-Boston, Boston, MA Confined Optical Phonon Modes in Si/ZnS Superlattices	RL/EROC	4 - 22

SRP Final Report Table of Contents

Author	University/Institution Report Title	Wright Laboratory Directorate	Vol-Page
DR Mohammad S Alam	Purdue University, Fort Wayne, IN Fast Infrared Image Registration and High Resolution Reconstruction for Real Time Applications	WL/AAJT	5 - 1
DR Dominick Andrisani II	Purdue University, West Lafayette, IN A Fast Fourier Transform Analysis of Pilot Induced Oscillations	WL/FIGC	5 - 2
DR Pnina Ari-Gur	Western Michigan University, Kalamazoo, MI Texture and Microstructure of Hot Rolled Ti-6A1-4V	WL/MLLN	5 - 3
DR James D Baldwin	University of Oklahoma, Norman, OK Statistical Analysis of Fatigue Crack Growth Rate Data for 7075-T6 Aluminum Damaged by Prior Corrosion	WL/FIB	5 - 4
DR Armando R Barreto	Florida International Univ, Miami, FL Deconvolution of The Space-Time Radar Spectrum	WL/AAMR	5 - 5
MR Larry A Beardsley	Univ of Texas at Austin, Austin, TX The Use of Wavelets and Neural Networks in Data Compression, Data Fusion and Their Effects on Target Identification	WL/MNGA	5 - 6
DR Raj K Bhatnagar	University of Cincinnati, Cincinnati, OH Variable Width Template Construction for ATR with HRR Data	WL/AACR	5 - 7
DR Alley C Butler	University of Cincinnati, Cincinnati, OH Importance of Current Crowding and Self-Heating in a CdS/LaS Cold Cathode	WL/MLIM	5 - 9
DR Reaz A Chaudhuri	University of Utah, Salt Lake City, UT A Novel Compatibility/Equilibrium Based Iterative Post-Processing Approach for Axismmetric Brittle	WL/MLBM	5 - 11
DR Julian Cheung	New York Inst. Of Technology, New York, NY New Techniques for Non-Cooperative Target Identification	WL/AACT	5 - 12
DR Milton Cone	Embry-Riddle Aeronautical University, Prescott, AZ Of Match Maker and Metrics	WL/AACF	5 - 13
DR Robert R Criss	Randolph-Macon Woman's College, Lynchburg, VA Optical Studies of Two Novel Electro-Explosive Devices	WL/MNMF	5 - 14

SRP Final Report Table of Contents

Author	University/Institution Report Title	Wright Laboratory Directorate	Vol-Page
DR Robert J DeAngelis	Univ of Nebraska - Lincoln, Lincoln, NE Granin Size Effects in the Determination of X-Ray Pole figures and Orientation Distribution Function	WL/MNM	5 - 15
DR Yujie J Ding	Bowling Green State University, Bowling Green, OH Investigation of Photoluminescence Intensity Saturation and Decay, and Nonlinear Optical Devices in Semiconductor Structures	WL/AADP	5 - 16
DR Gregory S Elliott	Rutgers State Univ of New Jersey, Piscataway, NJ Laser Based Diagnostic Techniques for Combustion and Compressible Flows	WL/POPT	5 - 17
DR Altan M Ferendeci	University of Cincinnati, Cincinnati, OH Vertical 3-D Interconnects for Multichip Modules	WL/AADI	5 - 18
DR Dennis R Flentge	Cedarville College, Cedarville, OH Kinetic Studies of the Thermal Decomposition of Demnum and X-1P Using the System for Thermal Diagnostic Studies (STDS)	WL/POSL	5 - 19
DR Himansu M Gajiwala	Tuskegee University, Tuskegee, AL Novel Approach for the Compressive Strength Improvement of Rigid Rod Polymers	WL/MLBP	5 - 20
DR Allen G Greenwood	Mississippi State University, Mississippi State, MS A Framework for Manufacturing-Oriented, Design-Directed Cost Estimation	WL/MTI	5 - 21
DR Rita A Gregory	Georgia Inst of Technology, Atlanta, GA Affects of Int'l Quality Standards on Bare Base Waste Disposal Alternatives	WL/FIVC	5 - 22
DR Michael A Grinfeld	Rutgers University, Piscataway, Piscataway, NJ Mismatch Stresses, Lamellar Microstructure & Mech	WL/MLLM	5 - 23
DR Awatef A Hamed	University of Cincinnati, Cincinnati, OH Inlet Distortion Test Considerations for High Cycle Fatigue in Gas Turbine Engines	WL/FIM	5 - 24
DR Stewart M Harris	SUNY Stony Brook, Stony Brook, NY Compositional Modulation During Epitaxial Growth of Some III-V Heterostructures	WL/MLPO	5 - 25
DR Larry S Helmick	Cedarville College, Cedarville, OH Effect of Humidity on Wear of M-50 Steel with a Krytox Lubricant	WL/MLBT	5 - 26
DR Kenneth L Hensley	University of Oklahoma, Norman, OK Hyperbaric Oxygen Effects on the Postischemic Brain	MED/SGP	5 - 27

SRP Final Report Table of Contents

Author	University/Institution Report Title	Wright Laboratory Directorate	Vol-Page
DR Iqbal Husain	University of Akron, Akron, OH Fault Analysis & Excitation Requirements for Switched Reluctance Starter-Generators	WL/POOC	5 - 28
DR David W Johnson	University of Dayton, Dayton, OH In Situ Formation of Standards for the Determination of Wear Metals in Perfluoropolyalkylether Lubricating Oils	WL/MLBT	5 - 29
DR Marian K Kazimierczuk	Wright State University, Dayton, OH Aircraft Super Capacitor Back-Up System	WL/POOC	5 - 30
DR Edward T Knobbe	Oklahoma State University, Stillwater, OK Corrosion Resistant Sol-Gel Coatings for Aircraft Aluminum Alloys	WL/MLBT	5 - 31
DR Michael C Larson	Tulane University, New Orleans, LA Cracks at Interfaces in Brittle Matrix Composites	WL/MLLM	5 - 32
DR Douglas A Lawrence	Ohio University, Athens, OH Analysis & Design of Gain Scheduled Missile Autopilots	WL/MNAG	5 - 33
DR Junghsen Lieh	Wright State University, Dayton, OH Determination of 3D Deformations, Forces and Moments of Aircraft Tires with a Synchronized Optical and Analog System	WL/FIVM	5 - 34
DR Chun-Shin Lin	Univ of Missouri - Columbia, Columbia, MO Neural Network Technology for Pilot-Vehicle Interface & Decision Aids	WL/FIGP	5 - 35
DR Zongli Lin	SUNY Stony Brook, Stony Brook, NY Control of Linear Sys with Saturating Actuators with Applications to Flight Control Systems	WL/FI	5 - 36
DR Kuo-Chi Lin	University of Central Florida, Orlando, FL Study on Dead Reckoning Translation in High Level Architecture	WL/AASE	5 - 37
DR James S Marsh	University of West Florida, Pensacola, FL A Conceptual Model for Holographic Reconstruction & Minimizing Aberrations During Reconstruction	WL/MNSI	5 - 38
DR Paul Marshall	University of North Texas, Denton, TX Computational Studies of the Reactions of CH3I With H and OH	WL/MLBT	5 - 39

Author	University/Institution Report Title	Wright Laboratory Directorate	Vol-Page
DR Hui Meng	Kansas State University, Manhattan, KS Investigation of Holographic PIV and Holographic Visualization techniques for Fluid Flows and Flames	WL/POSC	5 - 40
DR Douglas J Miller	Cedarville College, Cedarville, OH Band Gap Calculations on Oligomers with an All-Carbon Backbone	WL/MLBP	5 - 41
DR Ravi K Nadella	Wilberforce University, Wilberforce, OH Hydrogen & Helium Ion Implantations for Obtaining High-Resistance Layers in N-Type 4H Silicon Carbide	WL/MLPO	5 - 42
DR Krishna Naishadham	Wright State University, Dayton, OH Hydrogen & Helium Ion Implantations for Obtaining High-Resistance Layers in N-Type 4H Silicon	WL/MLPO	5 - 43
DR Timothy S Newman	Univ of Alabama at Huntsville, Huntsville, All A Summer Faculty Project for Anatomical Feature Extraction for Registration of Multiple Modalities of Brain MR	WL/AACR	5 - 44
DR Mohammed Y Niamat	University of Toledo, Toledo, OH FPGA Implementation of the Xpatch Ray Tracer	WL/AAST	5 - 45
DR James L Noyes	Wittenberg University, Springfield, OH The Development of New Learning Algorithms	WL/AACF	5 - 46
DR Anthony C Okafor	University of Missouri - Rolla, Rolla, MO Assessment of Developments in Machine Tool Technology	WL/MTI	5 - 47
DR Paul D Orkwis	University of Cincinnati, Cincinnati, OH Assessing the Suitability of the CFD++Algorithm for Advanced Propulsion Concept simulations	WL/POPS	5 - 48
Dr Robert P Penno	University of Dayton, Dayton, OH Grating Lobes in Antenna Arrays	WL/AAMP	5 - 49
DR George A Petersson	Wesleyan University, Middletown, CT Absolute Rates for Chemical Reactions	WL/MLBT	5 - 50
DR Mohamed N Rahaman	University of Missouri - Rolla, Rolla, MO Effect of Solid Solution Additives on the Densification & Creep of Granular Ceramics	WL/MLLN	5 - 51

SRP Final Report Table of Contents

Author	University/Institution Report Title	Wright Laboratory Directorate	Vol-Page
DR Martin Schwartz	University of North Texas, Denton, TX AB Initio Modeling of the Enthalpies of Formation of Fluorocarbons	WL/MLBT	5 - 52
DR Thomas E Skinner	Wright State University, Dayton, OH A Method for Studying Changes in Tissue Energetics Resulting from Hyperbaric Oxygen Therapy	MED/SGP	5 - 53
DR Marek Skowronski	Carnegie Melon University, Pittsburgh, PA Investigation of Structural Defects in 4H-SiC Wafers	WL/MLPO	5 - 54
DR Grant D Smith	Univ of Missouri - Columbia, Columbia, MO Theoretical Investigation of Phthalocyanin Dimers	WL/MLPJ	5 - 55
DR James A Snide	University of Dayton, Dayton, OH Aging Aircraft: Preliminary Investigation of Various Materials and Process Issues	WL/MLLP	5 - 56
DR Yong D Song	North Carolina A & T State University, Greensboro, NC Memory-Base Control Methodology with Application to EMRAAT Missile	WL/MNAG	5 - 57
DR Raghavan Srinivasan	Wright State University, Dayton, OH Microstructural Development During Hot Deformation	WL/MLIM	5 - 58
DR Janusz A Starzyk	Ohio University, Athens, OH Feature Selection for ATR Neural Network Approach	WL/AACA	5 - 59
DR Alfred G Striz	University of Oklahoma, Norman, OK On Multiobjective Function Optimization in Engineering Design	WL/FIB	5 - 60
DR Barney E Taylor	Miami Univ - Hamilton, Hamilton, OH Optical and Electro-Optical Studies of Polymers	WL/MLBP	5 - 61
DR Joseph W Tedesco	Auburn University, Auburn, AL Effects of Airblast Characteristics on Structural Response	WL/MNSA	5 - 62
DR Scott K Thomas	Wright State University, Dayton, OH The Effects of Curvature on the Performance of a Spirally-Grooved Copper-Ethanol Heat Pipe	WL/POOS	5 - 63
DR James P Thomas	University of Notre Dame, Notre Dame, IN Subcritical Crack Growth of Ti-6Al-4V Under Ripple Loading Conditions	WL/MLLN	5 - 64
DR Karen A Tomko	Wright State University, Dayton, OH Grid Level Parallelization of an Implicit Solution of the 3D Navier-Stokes Equations	WL/FIM	5 - 65

SRP Final Report Table of Contents

Author	University/Institution Report Title	Arnold Engineering Development Center Directorate	Vol-Page
DR Saad A Ahmed	King Fahd Univ of Petroleum & Minerals, Saudi, Arabia Turbulence Statistics & Energy Budget of a Turbulent Shear Layer	AEDC	6 - 1
DR Csaba A Biegl	Vanderbilt University, Nashville, TN Turbine Engine Blade Vibration Analysis System	AEDC	6 - 2
DR Frank G Collins	Tennessee Univ Space Institute, Tullahoma, TN Laser Vapor Screen Flow Visualization Technique	AEDC	6 - 3
DR Randolph S Peterson	The University of the South, Sewanee, TN	AEDC	6 - 4
DR Robert L Roach	Tennessee Univ Space Institute, Tullahoma, TN A Process for Setting Up Computation of Swirling Flows in the AEDC H-3 Heater	AEDC	6 - 5

Author	University/Institution Report Title	U.S. Air Force Academy Directorate	Vol-Page
DR Ryoichi Kawai	Univ of Alabama at Birmingham, Birmingham, AL A Massively Parallel Ab Initio Molecular Dynamis Simulation of Polymers & Molten Salts	USAFA	6 - 6

SRP Final Report Table of Contents

Author	University/Institution Report Title	Air Logistic Centers Directorate	Vol-Page
DR Sandra A Ashford	University of Detroit Mercy, Detroit, MI Evaluation of Current Jet Engine Performance Parameters Archive, Retrieval and Diagnostic System	OCALC	6 - 7
MR Jeffrey M Bigelow	Oklahoma Christian Univ of Science & Art, Oklahoma City, OK Enhancing Tinker's Raster-to-Vector Capabilities	OCALC	6 - 8
DR K M George	Oklahoma State University, Stillwater, OK A Computer Model for Sustainability Ranking	OCALC	6 - 9
DR Jagath J Kaluarachichi	Utah State University, Logan, UT Optimal Groundwater Management Using Genetic Algorithm	OCALC	6 - 10

INTRODUCTION

The Summer Research Program (SRP), sponsored by the Air Force Office of Scientific Research (AFOSR), offers paid opportunities for university faculty, graduate students, and high school students to conduct research in U.S. Air Force research laboratories nationwide during the summer.

Introduced by AFOSR in 1978, this innovative program is based on the concept of teaming academic researchers with Air Force scientists in the same disciplines using laboratory facilities and equipment not often available at associates' institutions.

The Summer Faculty Research Program (SFRP) is open annually to approximately 150 faculty members with at least two years of teaching and/or research experience in accredited U.S. colleges, universities, or technical institutions. SFRP associates must be either U.S. citizens or permanent residents.

The Graduate Student Research Program (GSRP) is open annually to approximately 100 graduate students holding a bachelor's or a master's degree; GSRP associates must be U.S. citizens enrolled full time at an accredited institution.

The High School Apprentice Program (HSAP) annually selects about 125 high school students located within a twenty mile commuting distance of participating Air Force laboratories.

AFOSR also offers its research associates an opportunity, under the Summer Research Extension Program (SREP), to continue their AFOSR-sponsored research at their home institutions through the award of research grants. In 1994 the maximum amount of each grant was increased from $20,000 to $25,000, and the number of AFOSR-sponsored grants decreased from 75 to 60. A separate annual report is compiled on the SREP.

The numbers of projected summer research participants in each of the three categories and SREP "grants" are usually increased through direct sponsorship by participating laboratories.

AFOSR's SRP has well served its objectives of building critical links between Air Force research laboratories and the academic community, opening avenues of communications and forging new research relationships between Air Force and academic technical experts in areas of national interest, and strengthening the nation's efforts to sustain careers in science and engineering. The success of the SRP can be gauged from its growth from inception (see Table 1) and from the favorable responses the 1996 participants expressed in end-of-tour SRP evaluations (Appendix B).

AFOSR contracts for administration of the SRP by civilian contractors. The contract was first awarded to Research & Development Laboratories (RDL) in September 1990. After

completion of the 1990 contract, RDL (in 1993) won the recompetition for the basic year and four 1-year options.

2. PARTICIPATION IN THE SUMMER RESEARCH PROGRAM

The SRP began with faculty associates in 1979; graduate students were added in 1982 and high school students in 1986. The following table shows the number of associates in the program each year.

YEAR	SRP Participation, by Year			TOTAL
	SFRP	GSRP	HSAP	
1979	70			70
1980	87			87
1981	87			87
1982	91	17		108
1983	101	53		154
1984	152	84		236
1985	154	92		246
1986	158	100	42	300
1987	159	101	73	333
1988	153	107	101	361
1989	168	102	103	373
1990	165	121	132	418
1991	170	142	132	444
1992	185	121	159	464
1993	187	117	136	440
1994	192	117	133	442
1995	190	115	137	442
1996	188	109	138	435

Beginning in 1993, due to budget cuts, some of the laboratories weren't able to afford to fund as many associates as in previous years. Since then, the number of funded positions has remained fairly constant at a slightly lower level.

3. RECRUITING AND SELECTION

The SRP is conducted on a nationally advertised and competitive-selection basis. The advertising for faculty and graduate students consisted primarily of the mailing of 8,000 52-page SRP brochures to chairpersons of departments relevant to AFOSR research and to administrators of grants in accredited universities, colleges, and technical institutions. Historically Black Colleges and Universities (HBCUs) and Minority Institutions (MIs) were included. Brochures also went to all participating USAF laboratories, the previous year's participants, and numerous individual requesters (over 1000 annually).

RDL placed advertisements in the following publications: *Black Issues in Higher Education, Winds of Change,* and *IEEE Spectrum.* Because no participants list either *Physics Today* or *Chemical & Engineering News* as being their source of learning about the program for the past several years, advertisements in these magazines were dropped, and the funds were used to cover increases in brochure printing costs.

High school applicants can participate only in laboratories located no more than 20 miles from their residence. Tailored brochures on the HSAP were sent to the head counselors of 180 high schools in the vicinity of participating laboratories, with instructions for publicizing the program in their schools. High school students selected to serve at Wright Laboratory's Armament Directorate (Eglin Air Force Base, Florida) serve eleven weeks as opposed to the eight weeks normally worked by high school students at all other participating laboratories.

Each SFRP or GSRP applicant is given a first, second, and third choice of laboratory. High school students who have more than one laboratory or directorate near their homes are also given first, second, and third choices.

Laboratories make their selections and prioritize their nominees. AFOSR then determines the number to be funded at each laboratory and approves laboratories' selections.

Subsequently, laboratories use their own funds to sponsor additional candidates. Some selectees do not accept the appointment, so alternate candidates are chosen. This multi-step selection procedure results in some candidates being notified of their acceptance after scheduled deadlines. The total applicants and participants for 1996 are shown in this table.

1996 Applicants and Participants			
PARTICIPANT CATEGORY	TOTAL APPLICANTS	SELECTEES	DECLINING SELECTEES
SFRP	572	188	39
(HBCU/MI)	(119)	(27)	(5)
GSRP	235	109	7
(HBCU/MI)	(18)	(7)	(1)
HSAP	474	138	8
TOTAL	1281	435	54

4. SITE VISITS

During June and July of 1996, representatives of both AFOSR/NI and RDL visited each participating laboratory to provide briefings, answer questions, and resolve problems for both laboratory personnel and participants. The objective was to ensure that the SRP would be as constructive as possible for all participants. Both SRP participants and RDL representatives found these visits beneficial. At many of the laboratories, this was the only opportunity for all participants to meet at one time to share their experiences and exchange ideas.

5. HISTORICALLY BLACK COLLEGES AND UNIVERSITIES AND MINORITY INSTITUTIONS (HBCU/MIs)

Before 1993, an RDL program representative visited from seven to ten different HBCU/Mis annually to promote interest in the SRP among the faculty and graduate students. These efforts were marginally effective, yielding a doubling of HBCI/MI applicants. In an effort to achieve AFOSR's goal of 10% of all applicants and selectees being HBCU/MI qualified, the RDL team decided to try other avenues of approach to increase the number of qualified applicants. Through the combined efforts of the AFOSR Program Office at Bolling AFB and RDL, two very active minority groups were found, HACU (Hispanic American Colleges and Universities) and AISES (American Indian Science and Engineering Society). RDL is in communication with representatives of each of these organizations on a monthly basis to keep up with the their activities and special events. Both organizations have widely-distributed magazines/quarterlies in which RDL placed ads.

Since 1994 the number of both SFRP and GSRP HBCU/MI applicants and participants has increased ten-fold, from about two dozen SFRP applicants and a half dozen selectees to over 100 applicants and two dozen selectees, and a half-dozen GSRP applicants and two or three selectees to 18 applicants and 7 or 8 selectees. Since 1993, the SFRP had a two-fold applicant

increase and a two-fold selectee increase. Since 1993, the GSRP had a three-fold applicant increase and a three to four-fold increase in selectees.

In addition to RDL's special recruiting efforts, AFOSR attempts each year to obtain additional funding or use leftover funding from cancellations the past year to fund HBCU/MI associates. This year, 5 HBCU/MI SFRPs declined after they were selected (and there was no one qualified to replace them with). The following table records HBCU/MI participation in this program.

SRP HBCU/MI Participation, By Year				
YEAR	**SFRP**		**GSRP**	
	Applicants	**Participants**	**Applicants**	**Participants**
1985	76	23	15	11
1986	70	18	20	10
1987	82	32	32	10
1988	53	17	23	14
1989	39	15	13	4
1990	43	14	17	3
1991	42	13	8	5
1992	70	13	9	5
1993	60	13	6	2
1994	90	16	11	6
1995	90	21	20	8
1996	119	27	18	7

6. SRP FUNDING SOURCES

Funding sources for the 1996 SRP were the AFOSR-provided slots for the basic contract and laboratory funds. Funding sources by category for the 1996 SRP selected participants are shown here.

1996 SRP FUNDING CATEGORY	SFRP	GSRP	HSAP
AFOSR Basic Allocation Funds	141	85	123
USAF Laboratory Funds	37	19	15
HBCU/MI By AFOSR (Using Procured Addn'l Funds)	10	5	0
TOTAL	188	109	138

SFRP - 150 were selected, but nine canceled too late to be replaced.
GSRP - 90 were selected, but five canceled too late to be replaced (10 allocations for the ALCs were withheld by AFOSR.)
HSAP - 125 were selected, but two canceled too late to be replaced.

7. COMPENSATION FOR PARTICIPANTS

Compensation for SRP participants, per five-day work week, is shown in this table.

1996 SRP Associate Compensation

PARTICIPANT CATEGORY	1991	1992	1993	1994	1995	1996
Faculty Members	$690	$718	$740	$740	$740	$770
Graduate Student (Master's Degree)	$425	$442	$455	$455	$455	$470
Graduate Student (Bachelor's Degree)	$365	$380	$391	$391	$391	$400
High School Student (First Year)	$200	$200	$200	$200	$200	$200
High School Student (Subsequent Years)	$240	$240	$240	$240	$240	$240

The program also offered associates whose homes were more than 50 miles from the laboratory an expense allowance (seven days per week) of $50/day for faculty and $40/day for graduate students. Transportation to the laboratory at the beginning of their tour and back to their home destinations at the end was also reimbursed for these participants. Of the combined SFRP and

GSRP associates, 65 % (194 out of 297) claimed travel reimbursements at an average round-trip cost of $780.

Faculty members were encouraged to visit their laboratories before their summer tour began. All costs of these orientation visits were reimbursed. Forty-five percent (85 out of 188) of faculty associates took orientation trips at an average cost of $444. By contrast, in 1993, 58 % of SFRP associates took orientation visits at an average cost of $685; that was the highest percentage of associates opting to take an orientation trip since RDL has administered the SRP, and the highest average cost of an orientation trip. These 1993 numbers are included to show the fluctuation which can occur in these numbers for planning purposes.

Program participants submitted biweekly vouchers countersigned by their laboratory research focal point, and RDL issued paychecks so as to arrive in associates' hands two weeks later.

In 1996, RDL implemented direct deposit as a payment option for SFRP and GSRP associates. There were some growing pains. Of the 128 associates who opted for direct deposit, 17 did not check to ensure that their financial institutions could support direct deposit (and they couldn't), and eight associates never did provide RDL with their banks' ABA number (direct deposit bank routing number), so only 103 associates actually participated in the direct deposit program. The remaining associates received their stipend and expense payments via checks sent in the US mail.

HSAP program participants were considered actual RDL employees, and their respective state and federal income tax and Social Security were withheld from their paychecks. By the nature of their independent research, SFRP and GSRP program participants were considered to be consultants or independent contractors. As such, SFRP and GSRP associates were responsible for their own income taxes, Social Security, and insurance.

8. CONTENTS OF THE 1996 REPORT

The complete set of reports for the 1996 SRP includes this program management report (Volume 1) augmented by fifteen volumes of final research reports by the 1996 associates, as indicated below:

1996 SRP Final Report Volume Assignments

LABORATORY	SFRP	GSRP	HSAP
Armstrong	2	7	12
Phillips	3	8	13
Rome	4	9	14
Wright	5A, 5B	10	15
AEDC, ALCs, WHMC	6	11	16

APPENDIX A – PROGRAM STATISTICAL SUMMARY

A. Colleges/Universities Represented

Selected SFRP associates represented 169 different colleges, universities, and institutions, GSRP associates represented 95 different colleges, universities, and institutions.

B. States Represented

SFRP -Applicants came from 47 states plus Washington D.C. and Puerto Rico. Selectees represent 44 states plus Puerto Rico.

GSRP - Applicants came from 44 states and Puerto Rico. Selectees represent 32 states.

HSAP - Applicants came from thirteen states. Selectees represent nine states.

Total Number of Participants	
SFRP	188
GSRP	109
HSAP	138
TOTAL	435

Degrees Represented			
	SFRP	GSRP	TOTAL
Doctoral	184	1	185
Master's	4	48	52
Bachelor's	0	60	60
TOTAL	188	109	297

SFRP Academic Titles	
Assistant Professor	79
Associate Professor	59
Professor	42
Instructor	3
Chairman	0
Visiting Professor	1
Visiting Assoc. Prof.	0
Research Associate	4
TOTAL	188

Source of Learning About the SRP		
Category	Applicants	Selectees
Applied/participated in prior years	28%	34%
Colleague familiar with SRP	19%	16%
Brochure mailed to institution	23%	17%
Contact with Air Force laboratory	17%	23%
IEEE Spectrum	2%	1%
BIIHE	1%	1%
Other source	10%	8%
TOTAL	100%	100%

APPENDIX B – SRP EVALUATION RESPONSES

1. OVERVIEW

Evaluations were completed and returned to RDL by four groups at the completion of the SRP. The number of respondents in each group is shown below.

Table B-1. Total SRP Evaluations Received

Evaluation Group	Responses
SFRP & GSRPs	275
HSAPs	113
USAF Laboratory Focal Points	84
USAF Laboratory HSAP Mentors	6

All groups indicate unanimous enthusiasm for the SRP experience.

The summarized recommendations for program improvement from both associates and laboratory personnel are listed below:

A. Better preparation on the labs' part prior to associates' arrival (i.e., office space, computer assets, clearly defined scope of work).

B. Faculty Associates suggest higher stipends for SFRP associates.

C. Both HSAP Air Force laboratory mentors and associates would like the summer tour extended from the current 8 weeks to either 10 or 11 weeks; the groups state it takes 4-6 weeks just to get high school students up-to-speed on what's going on at laboratory. (Note: this same argument was used to raise the faculty and graduate student participation time a few years ago.)

2. 1996 USAF LABORATORY FOCAL POINT (LFP) EVALUATION RESPONSES

The summarized results listed below are from the 84 LFP evaluations received.

1. LFP evaluations received and associate preferences:

Table B-2. Air Force LFP Evaluation Responses (By Type)

Lab	Evals Recv'd	How Many Associates Would You Prefer To Get ? SFRP 0	SFRP 1	SFRP 2	SFRP 3+	GSRP (w/Univ Professor) 0	GSRP (w/Univ Professor) 1	GSRP (w/Univ Professor) 2	GSRP (w/Univ Professor) 3+	(% Response) GSRP (w/o Univ Professor) 0	GSRP (w/o Univ Professor) 1	GSRP (w/o Univ Professor) 2	GSRP (w/o Univ Professor) 3+
AEDC	0	-	-	-	-	-	-	-	-	-	-	-	-
WHMC	0	-	-	-	-	-	-	-	-	-	-	-	-
AL	7	28	28	28	14	54	14	28	0	86	0	14	0
FJSRL	1	0	100	0	0	100	0	0	0	0	100	0	0
PL	25	40	40	16	4	88	12	0	0	84	12	4	0
RL	5	60	40	0	0	80	10	0	0	100	0	0	0
WL	46	30	43	20	6	78	17	4	0	93	4	2	0
Total	**84**	**32%**	**50%**	**13%**	**5%**	**80%**	**11%**	**6%**	**0%**	**73%**	**23%**	**4%**	**0%**

LFP Evaluation Summary. The summarized responses, by laboratory, are listed on the following page. LFPs were asked to rate the following questions on a scale from 1 (below average) to 5 (above average).

2. LFPs involved in SRP associate application evaluation process:
   a. Time available for evaluation of applications:
   b. Adequacy of applications for selection process:
3. Value of orientation trips:
4. Length of research tour:
5. a. Benefits of associate's work to laboratory:
   b. Benefits of associate's work to Air Force:
6. a. Enhancement of research qualifications for LFP and staff:
   b. Enhancement of research qualifications for SFRP associate:
   c. Enhancement of research qualifications for GSRP associate:
7. a. Enhancement of knowledge for LFP and staff:
   b. Enhancement of knowledge for SFRP associate:
   c. Enhancement of knowledge for GSRP associate:
8. Value of Air Force and university links:
9. Potential for future collaboration:
10. a. Your working relationship with SFRP:
    b. Your working relationship with GSRP:
11. Expenditure of your time worthwhile:

(Continued on next page)

12. Quality of program literature for associate:
13. a. Quality of RDL's communications with you:
    b. Quality of RDL's communications with associates:
14. Overall assessment of SRP:

Table B-3. Laboratory Focal Point Reponses to above questions

	AEDC	*AL*	*FJSRL*	*PL*	*RL*	*WHMC*	*WL*
# Evals Recv'd	0	7	1	14	5	0	46
Question #							
2	-	86 %	0 %	88 %	80 %	-	85 %
2a	-	4.3	n/a	3.8	4.0	-	3.6
2b	-	4.0	n/a	3.9	4.5	-	4.1
3	-	4.5	n/a	4.3	4.3	-	3.7
4	-	4.1	4.0	4.1	4.2	-	3.9
5a	-	4.3	5.0	4.3	4.6	-	4.4
5b	-	4.5	n/a	4.2	4.6	-	4.3
6a	-	4.5	5.0	4.0	4.4	-	4.3
6b	-	4.3	n/a	4.1	5.0	-	4.4
6c	-	3.7	5.0	3.5	5.0	-	4.3
7a	-	4.7	5.0	4.0	4.4	-	4.3
7b	-	4.3	n/a	4.2	5.0	-	4.4
7c	-	4.0	5.0	3.9	5.0	-	4.3
8	-	4.6	4.0	4.5	4.6	-	4.3
9	-	4.9	5.0	4.4	4.8	-	4.2
10a	-	5.0	n/a	4.6	4.6	-	4.6
10b	-	4.7	5.0	3.9	5.0	-	4.4
11	-	4.6	5.0	4.4	4.8	-	4.4
12	-	4.0	4.0	4.0	4.2	-	3.8
13a	-	3.2	4.0	3.5	3.8	-	3.4
13b	-	3.4	4.0	3.6	4.5	-	3.6
14	-	4.4	5.0	4.4	4.8	-	4.4

3. 1996 SFRP & GSRP EVALUATION RESPONSES

The summarized results listed below are from the 257 SFRP/GSRP evaluations received.

Associates were asked to rate the following questions on a scale from 1 (below average) to 5 (above average) - by Air Force base results and over-all results of the 1996 evaluations are listed after the questions.

1. The match between the laboratories research and your field:
2. Your working relationship with your LFP:
3. Enhancement of your academic qualifications:
4. Enhancement of your research qualifications:
5. Lab readiness for you: LFP, task, plan:
6. Lab readiness for you: equipment, supplies, facilities:
7. Lab resources:
8. Lab research and administrative support:
9. Adequacy of brochure and associate handbook:
10. RDL communications with you:
11. Overall payment procedures:
12. Overall assessment of the SRP:
13. a. Would you apply again?
    b. Will you continue this or related research?
14. Was length of your tour satisfactory?
15. Percentage of associates who experienced difficulties in finding housing:
16. Where did you stay during your SRP tour?
    a. At Home:
    b. With Friend:
    c. On Local Economy:
    d. Base Quarters:
17. Value of orientation visit:
    a. Essential:
    b. Convenient:
    c. Not Worth Cost:
    d. Not Used:

SFRP and GSRP associate's responses are listed in tabular format on the following page.

Table B-4. 1996 SFRP & GSRP Associate Responses to SRP Evaluation

	Arnold	Brooks	Edwards	Eglin	Griffis	Hanscom	Kelly	Kirtland	Lackland	Robins	Tyndall	WPAFB	average
# res	6	48	6	14	31	19	3	32	1	2	10	85	257
1	4.8	4.4	4.6	4.7	4.4	4.9	4.6	4.6	5.0	5.0	4.0	4.7	4.6
2	5.0	4.6	4.1	4.9	4.7	4.7	5.0	4.7	5.0	5.0	4.6	4.8	4.7
3	4.5	4.4	4.0	4.6	4.3	4.2	4.3	4.4	5.0	5.0	4.5	4.3	4.4
4	4.3	4.5	3.8	4.6	4.4	4.4	4.3	4.6	5.0	4.0	4.4	4.5	4.5
5	4.5	4.3	3.3	4.8	4.4	4.5	4.3	4.2	5.0	5.0	3.9	4.4	4.4
6	4.3	4.3	3.7	4.7	4.4	4.5	4.0	3.8	5.0	5.0	3.8	4.2	4.2
7	4.5	4.4	4.2	4.8	4.5	4.3	4.3	4.1	5.0	5.0	4.3	4.3	4.4
8	4.5	4.6	3.0	4.9	4.4	4.3	4.3	4.5	5.0	5.0	4.7	4.5	4.5
9	4.7	4.5	4.7	4.5	4.3	4.5	4.7	4.3	5.0	5.0	4.1	4.5	4.5
10	4.2	4.4	4.7	4.4	4.1	4.1	4.0	4.2	5.0	4.5	3.6	4.4	4.3
11	3.8	4.1	4.5	4.0	3.9	4.1	4.0	4.0	3.0	4.0	3.7	4.0	4.0
12	5.7	4.7	4.3	4.9	4.5	4.9	4.7	4.6	5.0	4.5	4.6	4.5	4.6
Numbers below are percentages													
13a	83	90	83	93	87	75	100	81	100	100	100	86	87
13b	100	89	83	100	94	98	100	94	100	100	100	94	93
14	83	96	100	90	87	80	100	92	100	100	70	84	88
15	17	6	0	33	20	76	33	25	0	100	20	8	39
16a	-	26	17	9	38	23	33	4	-	-	-	30	
16b	100	33	-	40	-	8	-	-	-	-	36	2	
16c	-	41	83	40	62	69	67	96	100	100	64	68	
16d	-	-	-	-	-	-	-	-	-	-	-	0	
17a	-	33	100	17	50	14	67	39	-	50	40	31	35
17b	-	21	-	17	10	14	-	24	-	50	20	16	16
17c	-	-	-	-	10	7	-	-	-	-	-	2	3
17d	100	46	-	66	30	69	33	37	100	-	40	51	46

4. 1996 USAF LABORATORY HSAP MENTOR EVALUATION RESPONSES

Not enough evaluations received (5 total) from Mentors to do useful summary.

5. 1996 HSAP EVALUATION RESPONSES

The summarized results listed below are from the 113 HSAP evaluations received.

HSAP apprentices were asked to rate the following questions on a scale from 1 (below average) to 5 (above average)

1. Your influence on selection of topic/type of work.
2. Working relationship with mentor, other lab scientists.
3. Enhancement of your academic qualifications.
4. Technically challenging work.
5. Lab readiness for you: mentor, task, work plan, equipment.
6. Influence on your career.
7. Increased interest in math/science.
8. Lab research & administrative support.
9. Adequacy of RDL's Apprentice Handbook and administrative materials.
10. Responsiveness of RDL communications.
11. Overall payment procedures.
12. Overall assessment of SRP value to you.
13. Would you apply again next year? Yes (92 %)
14. Will you pursue future studies related to this research? Yes (68 %)
15. Was Tour length satisfactory? Yes (82 %)

	Arnold	Brooks	Edwards	Eglin	Griffiss	Hanscom	Kirtland	Tyndall	WPAFB	Totals
# resp	5	19	7	15	13	2	7	5	40	113
1	2.8	3.3	3.4	3.5	3.4	4.0	3.2	3.6	3.6	3.4
2	4.4	4.6	4.5	4.8	4.6	4.0	4.4	4.0	4.6	4.6
3	4.0	4.2	4.1	4.3	4.5	5.0	4.3	4.6	4.4	4.4
4	3.6	3.9	4.0	4.5	4.2	5.0	4.6	3.8	4.3	4.2
5	4.4	4.1	3.7	4.5	4.1	3.0	3.9	3.6	3.9	4.0
6	3.2	3.6	3.6	4.1	3.8	5.0	3.3	3.8	3.6	3.7
7	2.8	4.1	4.0	3.9	3.9	5.0	3.6	4.0	4.0	3.9
8	3.8	4.1	4.0	4.3	4.0	4.0	4.3	3.8	4.3	4.2
9	4.4	3.6	4.1	4.1	3.5	4.0	3.9	4.0	3.7	3.8
10	4.0	3.8	4.1	3.7	4.1	4.0	3.9	2.4	3.8	3.8
11	4.2	4.2	3.7	3.9	3.8	3.0	3.7	2.6	3.7	3.8
12	4.0	4.5	4.9	4.6	4.6	5.0	4.6	4.2	4.3	4.5
Numbers below are percentages										
13	60%	95%	100%	100%	85%	100%	100%	100%	90%	92%
14	20%	80%	71%	80%	54%	100%	71%	80%	65%	68%
15	100%	70%	71%	100%	100%	50%	86%	60%	80%	82%

Fast Infrared Image Registration and High Resolution Reconstruction for Real Time Applications

Mohammad S. Alam
Assistant Professor of Electrical Engineering
Purdue University, ET 327A, Fort Wayne, IN 46805-1499
(219)481-6020, alam@engr.ipfw.indiana.edu

Final Project Report:
Summer Faculty Research Program
Air Force Wright Laboratory, Dayton, Ohio

Sponsored by:
Air Force Office of Scientific Research
Bolling Air Force Base, DC
and
Wright Laboratory, Wright-Patterson Air Force Base, Ohio

August 1996

Abstract

Forward looking infrared (FLIR) detector arrays generally produce low resolution images because the FLIR arrays can not be made sufficiently dense to yield a high sampling frequency using the current technology. Microscanning is an effective technique for reducing aliasing and increasing resolution in images produced by staring infrared imaging systems, which involves recording a sequence of frames through subpixel movements of the field of view on the detector array and then interlacing them to produce a high resolution image. The FLIR system is usually mounted on a moving platform, such as an aircraft, and the normal vibrations associated with the moving platform can be used to generate shifts in the FLIR recorded sequence of frames. Since a fixed number of frames is required for a given level of microscanning, and the shifts are random, some of the acquired frames may have almost similar shifts thus making them unusable for high resolution image reconstruction. In this paper, we utilize a modified version of the algorithm reported in Ref. 1 for estimating the shifts among the acquired frames and then utilize a *k*-nearest-neighbor approach for estimating the above mentioned missing frames to form the final high resolution image. Blurring by the detector and optics of the imaging system limits the increase in image resolution when microscanning is attempted at sub-pixel movements of less than half the detector width. We resolve this difficulty by the application of Wiener filter, designed using the MTF of the imaging system, to the microscanned images. Computer simulation and experimental results are presented to verify the effectiveness of the proposed technique. This technique is significantly faster than the alternate techniques, and is found to be especially suitable for real time applications.

1 Introduction

In many Forward Looking Infrared (FLIR) imaging systems, the detector spacing in the focal plane array is not sufficiently small so as to sample a band-limited scene at the Nyquist rate, resulting in a degraded image due to aliasing artifacts. The construction of a focal plane array with smaller and more closely spaced detector elements is very difficult and prohibitively expensive due to fabrication complexity and quantum efficiency problems. Over the last four years, the Electro-Optics Branch of Wright Laboratory has been developing a microscan imaging technique to increase the spatial sampling rate of existing focal plane arrays and to alleviate the aliasing effects in infrared imagery[2]. The microscanning process uses a sequence of spatially undersampled time frames of a scene to generate the high resolution image. Each frame is subpixel shifted relative to each other frame onto a set grid pattern. The sequence of frames are then interlaced to yield the high resolution image which represents the input scene effectively sampled at a higher spatial frequency. The aforementioned process is called controlled microscanning because the subpixel shifts between the temporal image frames are controlled and therefore known *a priori*. In this paper, we consider a practical scenario where an imager is mounted on a moving and/or vibrating platform, such as an aircraft. Consequently, controlled microscanning can not be used for such applications. Uncontrolled microscanning is the process where the shifts for each frame are unknown and must be estimated before registering onto the high resolution grid pattern. The shifts for each frame are unknown because they are generated by the random motion and/or vibration of the imager platform and not by a microscan mirror. Using random shifts alone eliminates the necessity for a microscan mirror and driver system. Since a fixed number of frames is required for a given level of microscanning, and the shifts are random, some of the acquired frames may have almost similar shifts which will create empty bins in the high resolution image reconstruction. Thus, the key factors for the high resolution image reconstruction are the accurate knowledge of the subpixel translational motion of the scene relative to the FLIR array and the accurate estimation of the missing frames (a frame whose translational shifts are similar to another frame or a frame which does not exist corresponding to a desired grid pattern). In this paper, we have utilized a modified version of the algorithm reported in Ref. 1 for estimating the shifts between the acquired frames and then used a *k*-nearest-neighbor approach for estimating the aforementioned missing frames. The proposed algorithm is significantly faster than alternate techniques[3,4] and is found to be suitable for real time applications.

With the increase of microscan level (i.e., smaller and smaller subpixel movements), we expect to see a proportional increase in resolution of the final reconstructed image. However, attempts at increasing the resolution beyond the Nyquist rate produce images having the same general appearance independent of microscan level. This bottleneck in the microscanning process was found to be primarily caused by the blurring inherent to the system's modulation transfer function (MTF). The main contributors to the system MTF are the optical transfer function and the detector transfer function. Since all parameters of the imager optics and detector array are known, it is possible to accurately model the system MTF. The application of a Wiener filter[5] was found to be an effective means of removing the blurring caused by the system MTF and improving the resolution of microscanned image data. Computer simulations were performed by varying the level of microscanning along with the optical transfer function and detector transfer function. The resulting images are then compared with those images produced after using Wiener

filtering to deconvolve the optical and detector blurring functions out of the microscan images. Note that the Wiener filter restoration is done in the discrete domain on the sensor's discrete output image. However, the blurring of an image by the optics and detectors of the sensor is a continuous process. Therefore the continuous blurring function must be mapped to a discrete blurring function to be used to create a discrete Wiener filter for restoration. To avoid aliasing in the continuous to discrete conversion of the function, the continuous function must be sampled at a high enough frequency so as to meet the Nyquist rate. Microscanning increases this sampling rate and allows the continuous functions to be properly mapped and used to form the discrete Wiener filter for restoration.

A considerable understanding of the advantages and limitation of the Wiener filtering technique was acquired from the information compiled during the microscan simulation. The knowledge acquired from the simulation was applied to restoring imagery collected from a real-time FLIR imaging system. From the simulation and experimental results, it is evident that the proposed *k*-nearest-neighbor approach for estimating the missing frames significantly improves the image quality. The resolution of the final high resolution image can be improved further by the application of Wiener filtering, especially for alleviating the effects of blurring caused by system MTF.

2 The Sampling Process

2.1 Sampling in a FLIR Array

In a FLIR array, sampling is performed by a finite sized array of detectors and three main factors must be taken into consideration: the optical point spread function, the detector charge integration, and the detector array geometry. The block diagram in Fig. 1 illustrates the sampling process in a FLIR array. The object scene, denoted *o(x,y)*, is convolved with the point spread function of the optics, *psf(x,y)*, and the aperture function for the square detector[6], *d(x,y)*.

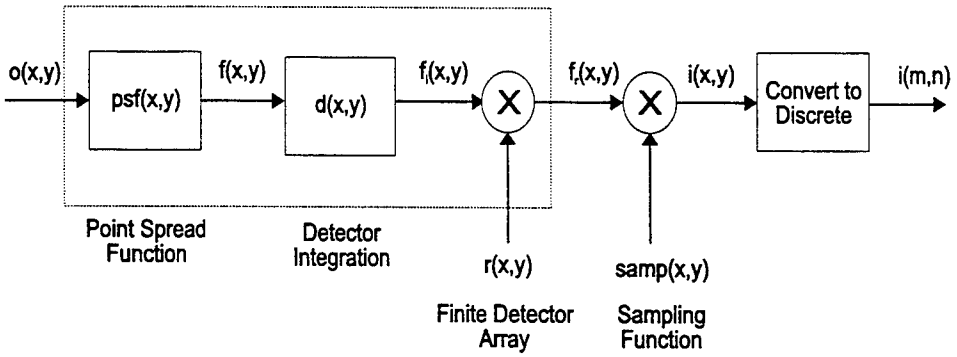

Figure 1. Block diagram of the imaging system.

For our imaging system, we assume the detector has a flat response across its active region so the detector function can be expressed as:

$$d(x,y) = \frac{1}{|ab|} rect\left(\frac{x}{a}, \frac{y}{b}\right), \tag{1}$$

where a and b are the dimensions of the individual detectors. The result is multiplied by a function representing the limited extent of the detector array, *r(x,y)*, expressed as

$$r(x,y) = rect\left(\frac{x}{X},\frac{y}{Y}\right), \tag{2}$$

where X and Y are the dimensions of the array. To apply this integration to all of the detectors, it is multiplied by the sampling lattice, $comb_{\Delta x,\Delta y}(x,y)$,

$$comb_{\Delta x\,\Delta y}(x,y) = \frac{1}{\Delta x\,\Delta y}\sum_{m=-\infty}^{\infty}\sum_{n=-\infty}^{\infty}\delta\left(\frac{x}{\Delta x}-m,\frac{y}{\Delta y}-n\right) = \sum_{m=-\infty}^{\infty}\sum_{n=-\infty}^{\infty}\delta\left(x-m\Delta x, y-n\Delta y\right) \tag{3}$$

where Δx and Δy are the center-to-center detector spacings. The resulting expression for the staring image is

$$i(x,y) = \left[o(x,y) * psf(x,y) * \frac{1}{|ab|}rect\left(\frac{x}{a},\frac{y}{b}\right)\right]\cdot rect\left(\frac{x}{X},\frac{y}{Y}\right)\cdot comb_{\Delta x,\Delta y}(x,y). \tag{4}$$

An illustration of a uniform detector array showing critical dimensions is shown in Fig. 2.

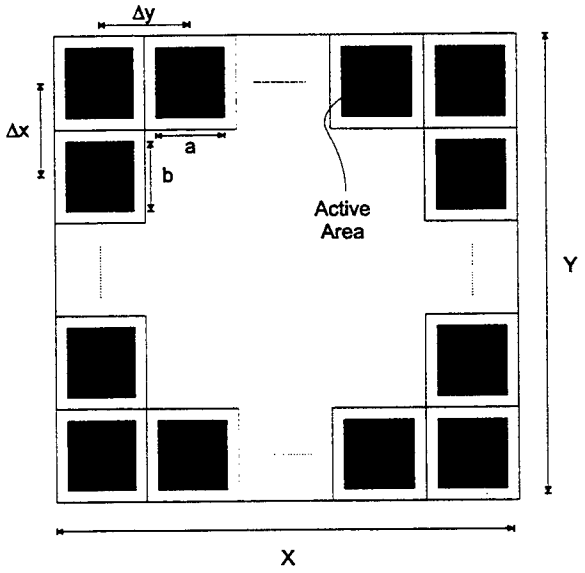

Figure 2. The detector array.

2.2 Controlled Microscanning

In controlled microscanning, the subpixel shifts between temporal image frames are controlled and therefore known in advance. A level L microscan is defined to be the case where L^2 staring frames are acquired for each high resolution frame and each staring frame has its own unique controlled subpixel shift, each shift being part of a uniform grid. Thus, each staring frame has a shift that is integer multiple of 1/L times the detector width. The staring frames are interlaced in an LxL pattern to produce a high resolution frame of size NLxNL where N is the size of the square detector array. For a level 2 or 2x2 microscanned image, the original scene is stepped one half the length of the detector in the x and y directions producing a series of four staring images. These images are then interlaced to produce the resulting microscan image of 2Nx2N pixels, as shown in Fig. 3 where the reconstructed image has 4 times the number of unique samples as any of the four frames. Thus, a level-L microscanning effectively increases the sampling frequency by L without changing the detector size or spacing. Since the effect of the finite detector array

$r(x,y)$ is small compared to the effects of the detector integration and the psf, neglecting the effect of $r(x,y)$, an LxL microscan process can be expressed as

$$i(x,y) = \left[o(x,y) * psf(x,y) * \frac{1}{|ab|} rect\left(\frac{x}{a}, \frac{y}{b}\right) \right] \frac{1}{L^2} \sum_{i=0}^{L-1} \sum_{j=0}^{L-1} comb_{\Delta x, \Delta y}\left(x - \frac{i}{L}, y - \frac{j}{L}\right) \quad (5)$$

where the factor of $1/L^2$ is used to adjust for the reduction in detector integration time at each of the L^2 microscan steps.

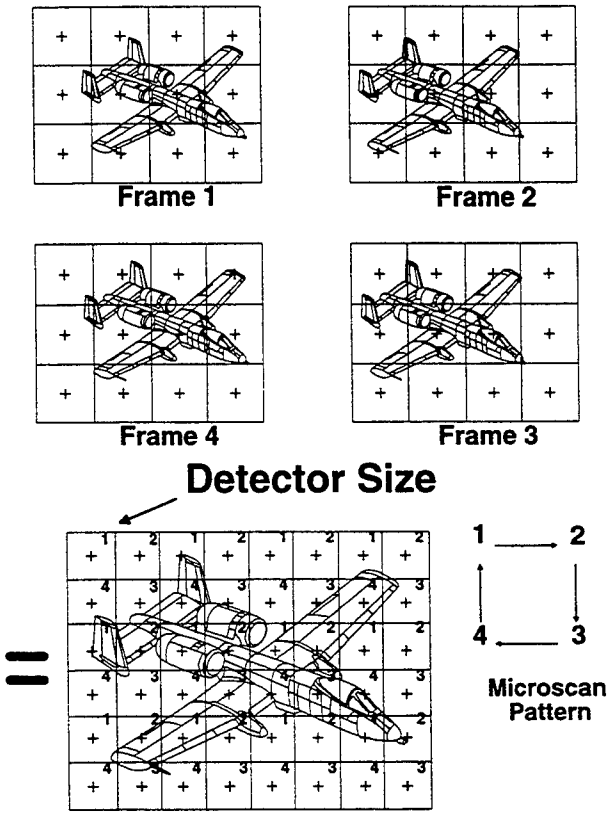

Figure 3. Illustration of a level 2 microscanning process.

2.3 Uncontrolled Microscanning

Uncontrolled microscanning results from practical applications where the imager is mounted on a moving and/or vibrating platform, such as an aircraft, and the vibrations associated with the platform can be exploited to create the shifts in the acquired frames. In uncontrolled microscanning, the shifts for each recorded frame are unknown and must be obtained before forming an estimate of the high resolution image. Because the shifts are random in uncontrolled microscanning, it eliminates the need for a microscan mirror and driver system otherwise required in controlled microscanning. Since a fixed number of frames is required for a given level of microscanning, and the shifts are random, some of the acquired frames may have almost similar shifts or unusable shifts which will generate empty bins in the high resolution image reconstruction. Thus, the key factors for the high resolution image reconstruction are the accurate knowledge of the subpixel translational motion of the scene relative to the FLIR array and the accurate estimation of the missing frames for filling the empty bins in the high resolution image.

3 Image Registration

For uncontrolled microscanning, the movement of the scene on the array is produced by random motion and/or vibration of the imager platform. Therefore the image shifts are unknown for each recoreded frame. It is necessary to develop a suitable algorithm which can accurately estimate the registration parameters i.e., in our case, the random translational shifts. Various algorithms have been reported in the literature for estimating the image registration parameters[2,7,8]. Among these techniques, the gradient based registration technique proposed in Ref. 2 appears to be particularly attractive for practical applications. However, this technique only works for small shifts. To accommodate the case where larger shift values are anticipated, we utilized the iterative technique proposed in Ref. 7 and incorporated it with the registration algorithm proposed in Ref. 1. In this algorithm, the first acquired frame is considered to be the reference frame and the shifts associated with the remaining frames are calculated with respect to the reference frame. If p represents the total number of frames acquired by the imager, and h_k and v_k represents the shifts in the horizontal and vertical directions for the kth frame, then the observed kth frame may be expressed as

$$o_k(x,y) = o_1(x+h_k, y+v_k), \tag{6}$$

where $k \in \{2, 3, 4, ..., p\}$ and for the reference frame, $h_1 = v_1 = 0$. Considering the first three terms for the Taylor series expansion, Eq. (6) may be approximated as

$$o_k(x,y) \approx o_1(x,y) + h_k \frac{\partial o_1(x,y)}{\partial x} + v_k \frac{\partial o_1(x,y)}{\partial y}. \tag{7}$$

Since Eq. (7) is an approximation itself and discrete estimates of x and y must be used, it is useful to apply the method of least squares for solving the registration parameters h_k and v_k. For the least squares solution[9] the error expression

$$E_k(h_k, v_k) \approx \frac{1}{MN} \sum_{m=1}^{M} \sum_{n=1}^{N} \left[o_k(m,n) - o_1(m,n) - h_k \frac{\partial o_1(m,n)}{\partial m} - v_k \frac{\partial o_1(m,n)}{\partial n} \right]^2 \tag{8}$$

must be minimized, where m and n are discrete variables for the x and y directions, M and N represents the total number of pixels in the x and y directions, and h_k and v_k are the translational shifts in the x and y directions between the kth frame and reference frame. Equation (8) can be minimized by differentiating $E_k(h_k, v_k)$ with respect to h_k and v_k and setting the derivatives equal to zero. This yields two equations which must be solved simultaneously and can be conveniently represented in the following matrix form:

$$\begin{bmatrix} \sum_{m=1}^{M} \sum_{n=1}^{N} \left(\frac{\partial o_1(m,n)}{\partial m} \right)^2 & \sum_{m=1}^{M} \sum_{n=1}^{N} \left(\frac{\partial o_1(m,n)}{\partial m} \frac{\partial o_1(m,n)}{\partial n} \right) \\ \sum_{m=1}^{M} \sum_{n=1}^{N} \left(\frac{\partial o_1(m,n)}{\partial m} \frac{\partial o_1(m,n)}{\partial n} \right) & \sum_{m=1}^{M} \sum_{n=1}^{N} \left(\frac{\partial o_1(m,n)}{\partial n} \right)^2 \end{bmatrix} \begin{bmatrix} h_k \\ v_k \end{bmatrix} =$$

$$\begin{bmatrix} \sum_{m=1}^{M}\sum_{n=1}^{N}\left(o_k(m,n)-o_1(m,n)\right)\dfrac{\partial o_1(m,n)}{\partial m} \\ \sum_{m=1}^{M}\sum_{n=1}^{N}\left(o_k(m,n)-o_1(m,n)\right)\dfrac{\partial o_1(m,n)}{\partial n} \end{bmatrix} \tag{9}$$

Equation (9) can be represented in a short form as

$$M \cdot S = V \tag{10}$$

where $S = [h_k \quad v_k]^T$,

$$M = \begin{bmatrix} \sum_{m=1}^{M}\sum_{n=1}^{N}\left(\dfrac{\partial o_1(m,n)}{\partial m}\right)^2 & \sum_{m=1}^{M}\sum_{n=1}^{N}\left(\dfrac{\partial o_1(m,n)}{\partial m}\dfrac{\partial o_1(m,n)}{\partial n}\right) \\ \sum_{m=1}^{M}\sum_{n=1}^{N}\left(\dfrac{\partial o_1(m,n)}{\partial m}\dfrac{\partial o_1(m,n)}{\partial n}\right) & \sum_{m=1}^{M}\sum_{n=1}^{N}\left(\dfrac{\partial o_1(m,n)}{\partial n}\right)^2 \end{bmatrix},$$

and $$V = \begin{bmatrix} \sum_{m=1}^{M}\sum_{n=1}^{N}\left(o_k(m,n)-o_1(m,n)\right)\dfrac{\partial o_1(m,n)}{\partial m} \\ \sum_{m=1}^{M}\sum_{n=1}^{N}\left(o_k(m,n)-o_1(m,n)\right)\dfrac{\partial o_1(m,n)}{\partial n} \end{bmatrix}.$$

Therefore, the estimated registration parameters can be calculated as

$$S = M^{-1}V. \tag{11}$$

To incorporate the case involving larger shift values, we follow the iterative technique of Ref. 7. At first, the initial registration parameters are estimated using Eq. (11). Using these estimated shift parameters, $o_k(m,n)$ is shifted so as to closely match $o_1(m,n)$. The resulting image is then registered to $o_1(m,n)$. Using the above mentioned procedure, $o_k(m,n)$ is continuously modified until the registration estimates become sufficiently small. The final registration estimate is obtained by summing all of these partial estimates.

4 High Resolution Image Reconstruction

4.1 Missing Frame Estimation

We define a missing frame as the frame whose translational shifts are similar to another frame or a frame which does not exist within a desired grid pattern. Since the translational shifts are random, some of the required frames for a given level of microscanning may not exist for the high resolution image reconstruction. For instance, let us assume that frame 3 of the 2×2 microscanning example shown in Fig. 3 is missing. The high resolution image reconstructed from the three available frames (1, 2 and 4) is shown in Fig. 4 where the empty spots corresponds to the missing pixels of frame 3. Therefore, such missing frames must be estimated before attempting the high resolution image reconstruction. Since the technique proposed herein is

intended for real time applications, we must devise a computationally inexpensive algorithm for estimating the missing frames. Accordingly, we have used a k-nearest-neighbor ($k = 8$) approach[9] for estimating the missing frame pixels. In this approach, a missing frame pixel (i,j) in the high resolution image f_h may be obtained as the average of its neighbors, and can be expressed as

$$f_h(i,j) = \sum_{m=-1}^{1} \sum_{n=-1}^{1} f_h(i+m, j+n) \tag{12}$$

where m and n can not be zero simultaneously.

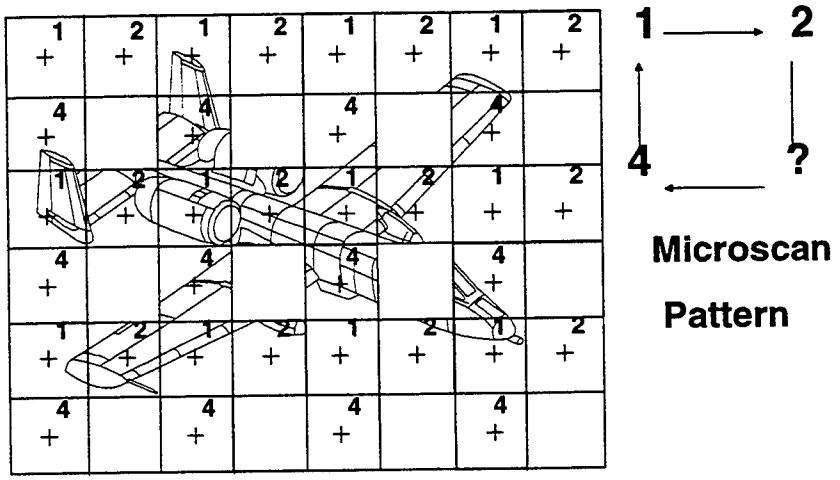

Figure 4. Level 2 microscanning process of Fig. 3 with frame 3 missing.

4.2 Blurring Effects

Let us now focus our attention towards the effect of image blurring and the use of the Wiener filter as a means of image restoration. For most FLIR imaging systems, there are two main sources of image blurring effects - the system optics and the finite detector size. Since the imager optics and detector parameters are known, one can accurately model the system MTF, which is a good representation of the overall system blurring function[10]. To deconvolve the effect of blurring, one can design a function using the system MTF which, when multiplied (convolved in the spatial domain) with the Fourier transform of the degraded image, will eliminate the system MTF and therefore the effects of blurring. This is precisely what is accomplished by the application of inverse filtering techniques such as Wiener filtering.

4.3 Wiener Filtering

It is possible to improve the image restoration with respect to the noise by incorporating some *a priori* knowledge of the statistical makeup of the noise. This is accomplished by an improved inverse filtering technique known as Wiener filtering. The Wiener filter is a linear filter which is designed to minimize the mean squared error between a given image and a desired image. Wiener filters are mathematically similar to traditional inverse filters with the addition of an

expression which attempts to minimize noise amplification by employing the power spectra of the original image $o(x,y)$, and of the noise $n(x,y)$. The continuous Wiener filter[9], $H_c^W(u,v)$ is represented by the following:

$$H_c^{\,w}(u,v) = \frac{H^*(u,v)}{|H(u,v)|^2 + \gamma\left[S_{nn}(u,v)/S_{ff}(u,v)\right]}, \tag{13}$$

where $S_{nn}(u,v)$ and $S_{ff}(u,v)$ are the power spectral densities of the noise and original image, $H(u,v)$ is the Fourier transform of the system point spread function, and γ is a statistical design constant usually set equal to 1. Since the original image is unavailable and it is difficult to characterize the noise, $S_{nn}(u,v)$ and $S_{ff}(u,v)$ are unknown, $H_c^W(u,v)$ can be approximated by

$$H_c^{\,w}(u,v) = \frac{H^*(u,v)}{|H(u,v)|^2 + nsr}, \tag{14}$$

where $nsr = S_{nn}(u,v)/S_{ff}(u,v)$ is a constant representing the noise-to-signal ratio and $nsr \in [0, 1]$[7].

The continuous optics and detector MTFs are shown Figs. 5a and 5b while the continuous system MTF is shown in Fig. 5c. From Fig 5a, it is evident that the optics cut off at 83.33cyc/mm and form Fig. 5b we observe that the first zero of the detector *sinc* occurs at 25cyc/mm. Figure 5d shows the continuous Wiener Filter obtained from Eq. (14) using the continuous system MTF shown in Fig 5c where the parameter *nsr* is set to 0.01. Notice that the optical and detector blurs are both continuous functions acting on a continuous scene. However, the output of the FLIR is a discrete image, and image restoration is done in the discrete domain. Therefore, a discrete Wiener filter that works like a continuous filter must be used to restore the image. The effective discrete filter must have the same frequency response as the continuous filter shown in Fig. 5c. To successfully map a continuous function to discrete, the continuous function must be sampled at a high enough frequency so as to avoid aliasing in the continuous to discrete conversion of the function[11]. The mapping of the continuous Wiener filter, $H_c^W(u,v)$, to a discrete Wiener filter, $H_d^W(m_1,n_1)$ is given by[12]:

$$H_d^{\,W}(m_1,n_1) = H_c^W(u,v), \text{ where } u = \frac{Lm_1}{2\pi\Delta x}, \quad v = \frac{Ln_1}{2\pi\Delta y}, \text{ and } 0 \le |m_1|, |n_1| \le \pi. \tag{15}$$

For $H_d^W(m_1,n_1)$ to operate like $H_c^W(u,v)$ as a linear system, the spatial sampling interval $\Delta x/L$ must be selected such that:

$$H_c^W(u,v) = 0, \quad \text{where} \quad |u| \ge \frac{L}{2\Delta x}, \quad |v| \ge \frac{L}{2\Delta y}. \tag{16}$$

The above condition truncates the continuous Wiener filter outside the foldover frequencies and prevents aliasing in the discrete version of the filter. The sampling interval is dictated by the detector spacing and microscan level. Increasing the microscan level will reduce the sampling interval and allow the condition of Eq. (16) to be met. If the cutoff of the continuous system MTF is known, the required microscan level can be calculated to meet this condition. In the present case where the MTF cuts off at 83.33 cycles/mm, and $\Delta x = \Delta y = 0.05$ mm, a microscan level greater than 8 will eliminate aliasing in the discrete Wiener filter. Figure 6 shows plots of the discrete system MTFs for various microscan levels. These plots show that at lower microscan levels the discrete system MTFs suffer from aliasing and are cutoff by the mapping process and therefore contain only the information in the central region of the continuous system MTF. Notice that the discrete system MTF resembles the continuous system MTF shown in Fig. 5c

only when the microscan level approaches 8. The discrete system MTFs of Fig. 6 are used in Eq. (14) to generate the discrete Wiener filters shown in Fig. 7. Microscanning at a level of 8 or higher allows us to use a discrete Wiener filter (Fig. 7c) which resembles the continuous Wiener filter shown in Fig 5d. Although lower microscan levels produce an aliased filter for restoration, the aliasing can be treated as noise and the Wiener filter *nsr* parameter can be adjusted to achieve limited deblurring.

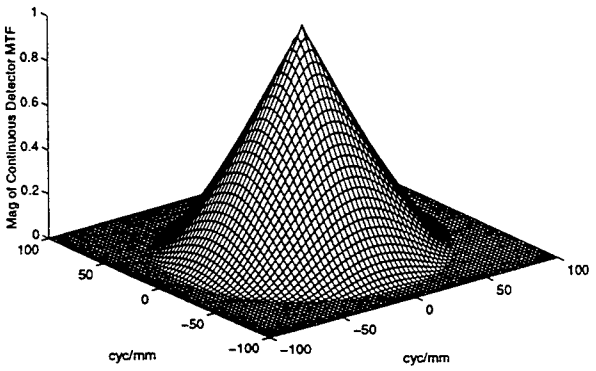

Figure 5a. Continuous Optical MTF.

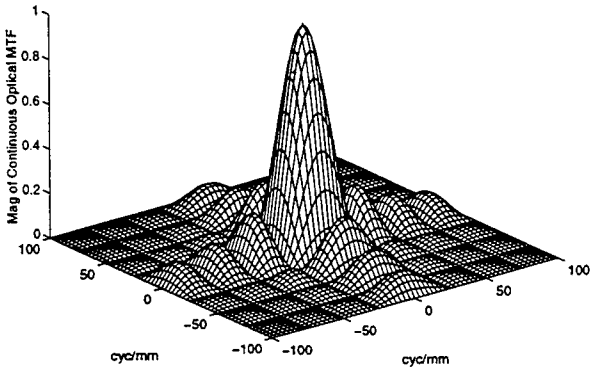

Figure 5b. Continuous Detector MTF.

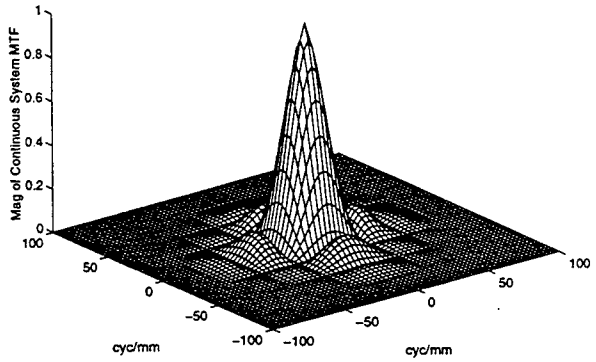

Figure 5c. Continuous System MTF.

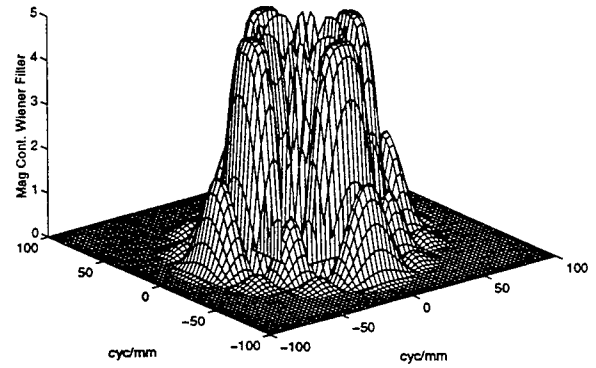

Figure 5d. Continuous Wiener Filter.

5 Computer Simulation Results

A MATLAB program was written to simulate the microscanning process under various conditions such as detector pitch, shape, and size of the active region as well as other parameters such as lens configuration. At first, we investigated the effects of aliasing at various microscan levels without using Wiener filtering. A 512×512 image taken from a digitized photograph, shown in Fig. 8a, was used as the original input scene to be blurred by the system MTF, have noise added, and be sampled by the detector array. Microscanning was then performed at various levels and under a variety of detector and lens configurations. Each detector in the array was simulated with a 8×8 kernel where each kernel returns the average of all pixels from the input

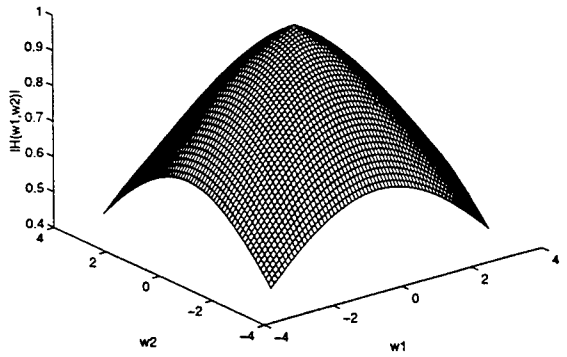

Fig 6a. Discrete System MTF. L=1.

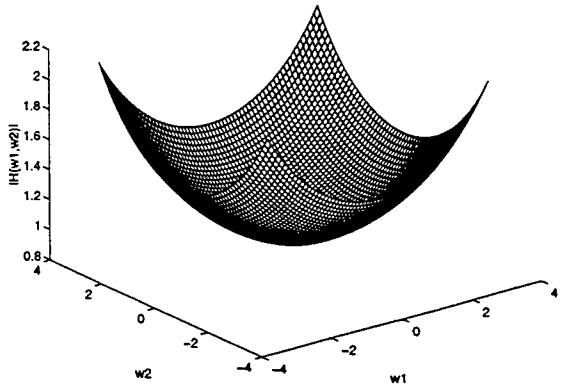

Figure 7a. Discrete Wiener Filter Model. L=1.

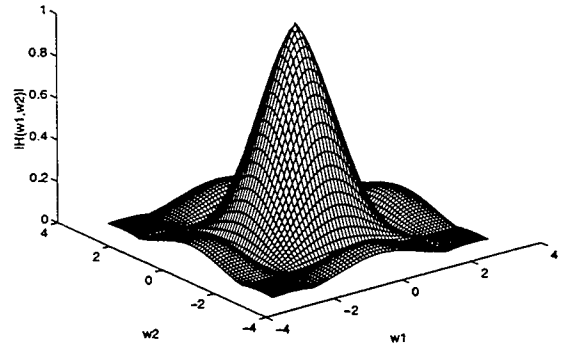

Fig 6b. Discrete System MTF. L=4.

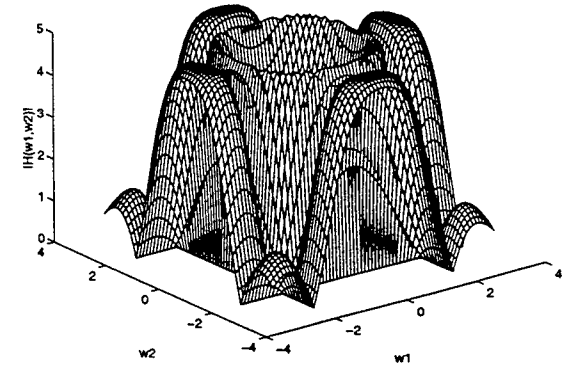

Figure 7b. Discrete WienerFilter Model. L=4.

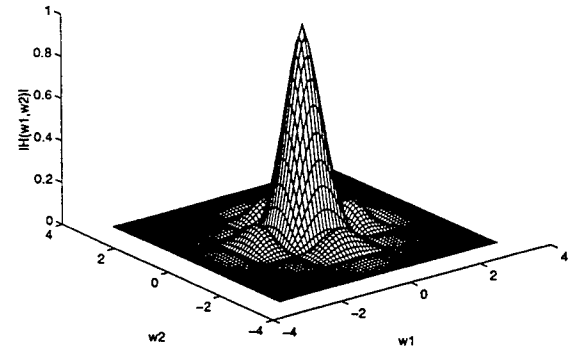

Fig 6c. Discrete System MTF. L=8.

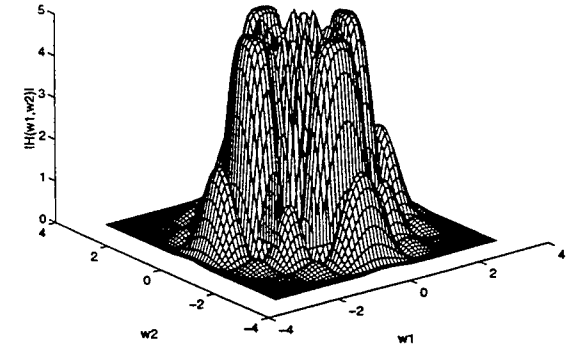

Figure 7c. Discrete Wiener Filter Model. L=8.

image which fall upon it. Figure 8b shows the highly undersampled image created by sampling in the staring mode. The translational shifts of all frames were calculated relative to the first frame (i.e., the reference frame) using the image registration algorithm discussed in Section 3. For instance, the theoretical shift values associated with each of the sixteen frames for 4×4 microscanning are shown in Fig. 9. The same shift parameters are then estimated using the registration algorithm developed in Section 3 which is also depicted in Fig. 9. It is obvious that the error between the theoretical and estimated shift values are almost negligible. The results from 2×2, 4×4, and 8×8 microscanning are shown in Fig. 10. For each case of microscanning, one out of every four frames were considered to be missing which results in the empty bins shown in Fig. 10. The missing frames were then estimated using the 8-nearest-neighbor approach discussed in Section 4.1. The estimated frames were used to fill-in the empty bins of Fig. 10 and the resulting images are shown in Fig. 11. From Fig. 11, it is obvious that there is significant improvement in the high resolution image quality after the inclusion of estimated missing frames. Furthermore, there is substantial improvement in resolution between the 2x2 microscan image and the images created using higher microscanning levels. Figure 11c shows that although aliasing may have been eliminated from the 8×8 microscanned image, this image is still blurred by the system MTF. To eliminate the blurring caused by system MTF, Wiener filtering operation

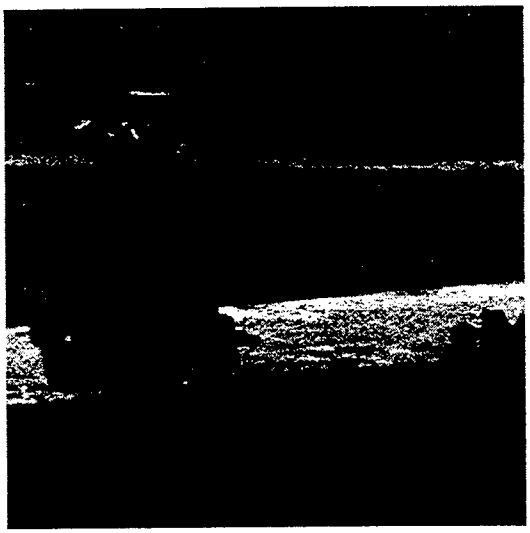

Figure 8a.

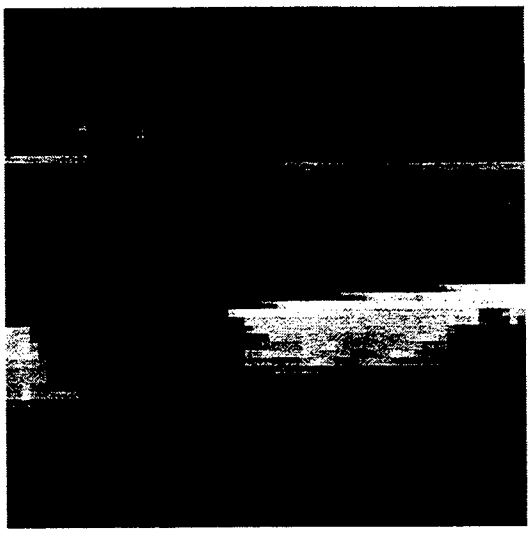

Figure 8b.

Figure 8. Microscan simulation: (a) original scene, and (b) staring frame sampled by simulated detector array.

was applied to the aforementioned microscan images. It was assumed that the power spectral density for both the original image and the noise were unknown and the Wiener filter was developed using Eq. (14). Figure 12 shows the result of applying Wiener filtering to the microscan images in Fig. 11. It is evident that with the increase in microscan levels, Wiener filtering further improves the image resolution. Comparing Figs. 11c and 8a, we observe that the Wiener filtered 8x8 microscan image is not exactly identical to the original image. This is due to the fact that the system MTF optically band-limits the scene at 8.33 cycles per milliradian and truncates all frequency information beyond that point. Frequency information from the original image beyond the cutoff can not be recovered. This explains why the Wiener filtered 8×8

microscan image is not exactly the same as the original input image. Therefore, the application of higher levels of microscanning may not yield better results.

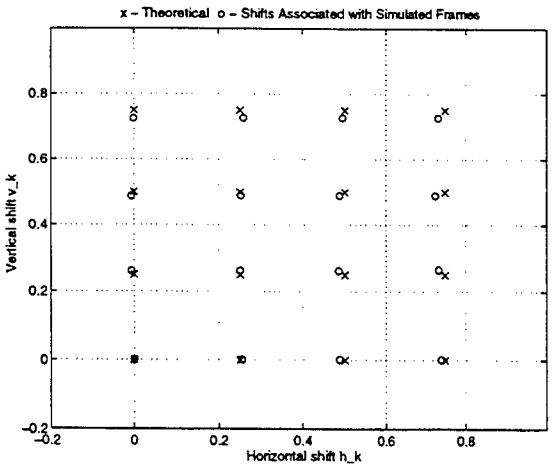

Fig. 9. Theoretical and estimated registration parameters for 16 simulated frames.

6 Experimental Results

For experimental verification of the proposed algorithm, we applied the multiframe reconstruction and Wiener filtering technique to data collected on a real-time FLIR imaging system. The FLIR camera uses a 128x128 Amber AE-4128 infrared focal plane array with a 100 millimeter focal length f/3 lens. The focal plane array uses Indium-Antimonide (InSb) detectors with a response in the 3 to 5 micron wavelength band. The 100 millimeter lens was diffraction limited producing an optical cutoff of 8.33 cycles per milliradian. The system uses square detectors of size 50 microns with an 80% fill factor, making the active detector size of 40 microns with the remaining 10 microns being inactive. The information about the detector and lens configuration was used in our estimation of the system MTF, which was used for designing the Wiener filter during the computer simulation. The FLIR image data collected at Wright Laboratory using the Amber imaging system is shown in Figure 13. Three primary targets at a range of approximately 0.9 kilometers are contained in the image: a military truck, a civilian vehicle, and an M-60 tank. Figure 13a is one of the 16 staring image frames collected for a 4×4 microscan high resolution image. The staring image was then pixel replicated to the same size as the microscan image for comparison. The 4×4 microscan image is shown in Fig. 13b where the balnk horizontal lines shows that four (frames 13, 14, 15 and 16) out of the total of sixteen frames recorded have shifts similar to other frames i.e., four frames are missing. The missing frames were estimated using the procedure discussed earlier in Sections 4.1 and 5. The empty bins of Fig. 13b were filled with these estimated frames and the resulting microscan image is shown in Fig. 13c. The 4×4 microscan image after the application of Wiener filtering is shown in Fig. 13d. Notice that the application of Wiener filtering further increased the resolution of the 4×4 microscan image. The reason for this improvement is that by using Wiener filtering one reduces the blurring of the MTF which is responsible for suppressing the increase in image resolution that should be obtained at higher microscan levels. There appears to be slight ringing in the 4×4 microscanned image after the application of Wiener filter (Fig. 13d). This ringing is most noticeable in the boundary and in regions of high contrast, and is most likely the result of

phase distortions caused by the zero crossing values present in the system MTF. Figures 13e is the same as Fig. 13a but bilinear interpolation was used for the image replication. Comparing Fig 13c with 13d and 13e, it is evident that the proposed technique yields significantly improved image resolution even without Wiener filtering.

7 Conclusion

We have developed an efficient technique for real time infrared image registration and high resolution reconstruction by using multiple frames which are randomly shifted with respect to one another (uncontrolled microscanning). Such translationally shifted image sequences may be obtained by utilizing the random motion and/or vibration of the platform, such as an aircraft, on which the imager is mounted. A registration algorithm for estimating the random translational shifts among the multiple frames has been designed which is found to be inherently suitable for real time implementation. This algorithm can be used for estimating both non-integer as well as shift values larger than the detector width. However, with uncontrolled microscanning, some of the frames acquired by the imager may have shifts similar to other frames (missing frames) which results in empty bins in the high resolution image reconstruction. This problem has been tackled by developing a *k*-nearest neighbor approach for estimating the missing frames so that it can be implemented in real time. Finally, Wiener filtering has been successfully applied as an effective means of reducing blurring in microscan images caused by the system MTF. A computer program which closely simulated the operation of the microscan system has been developed. The knowledge obtained from the microscan simulation was applied to real FLIR data collected on the microscan imaging system. The results of the application of the Wiener filter to the microscan images confirmed the results obtained from the simulation data. It was found that Wiener filtering effectively reduces the effects of blurring and increases image resolution. This especially true with the real FLIR data (compare Figs. 13c and 13d).

Future Research

Future research should address the following important issues:

1. In a practical scenario, the frames recorded by the FLIR array may be rotated as well as translated with respect to each other. Therefore, it is essential to incorporate both the rotational and translational registration parameters in the high resolution image reconstruction.
2. Investigate the effects of detector nonuniformity (gain and bias drift) which creates fixed pattern noise on an image and developing a suitable algorithm to fix this problem.
3. Investigate the effects of both additive and multiplicative noise sources and develop a suitable algorithm to mitigate their effects.
4. Improving the interpolation techniques for calculating the missing frames for real time applications.
5. Investigating the effects of temporal blurring caused by factors such as atmospheric turbulence and alleviate such problems.

Acknowledgement

The authors would like to thank the following individuals for their assistance and support: John Bognar, Russell Hardie, Ernie Armstrong, Ken Barnard, Steve Cain, Brian Yasuda, Ed Watson, Donald Tomlinson, Paul McManamon and Dennis Cupp.

References

[1] A. Schaum and M. McHugh, "Analytic Methods of Image Registration: displacement Estimation and Resampling," Naval Research Report 9298, Feb. 28, (1992).

[2] E. A. Watson, R. A. Muse and F.P. Blommel, "Aliasing and blurring in microscanned imagery," *Proc. of the SPIE*, Vol. 1689, 242-250 (1992).

[3] R. C. Hardie and S. Cain, "MAP Estimation of a High Resolution Image From a Sequence of Undersampled Translationally Shifted Images," Under review, *IEEE Transactions on Image Processing*, February (1996).

[4] S. Cain and R. C. Hardie, "Restoration of Aliased Video Sequences via a Maximum-likelyhood Approach," To appear, *Proceedings of the IRIS Symposium on Passive Sensors,* Monterey, CA, March (1996).

[5] W. K. Pratt, Digital Image Processing, John Wiley and Sons, Inc., New York (1992).

[6] J. C. Gillette, T. M. Stadmiller, and R. C. Hardie, "Reduction of Aliasing in Staring Infrared Imagers Utilizing Subpixel Techniques," *Optical Engineering*, Vol. 34, pp. 3130-3137 (1995).

[7] M. Irani and S. Peleg, "Improving Resolution by Image Registration," *CVGIP: Graphical Models and Image Processing*, Vol. 53, pp. 231-239 (1991).

[8] E. Kaltenbacher and R. C. Hardie, "Infrared Image Registration and High Resolution Reconstruction," *Proceedings of the National Aeronautics and Electronics Conference*, pp. 702-709 (1996).

[9] R. C. Gonzalez and R.E . Woods, Digital Image Processing, Addison-Wesley, New York (1992).

[10] J. W. Goodman, Introduction to Fourier Optics, McGraw-Hill, Inc., New York, (1996).

[11] A. V. Oppenheim and R. W. Schafer, Discrete Time Signal Processing, Prentice Hall, Inc., NJ, (1989).

[12] E. Armstrong, J. Bognar, B. Yasuda and R. C. Hardie, "The Appication of Wiener Filters to Microscan Imaging," To appear, *Proceedings of the IRIS Symposium on Passive Sensors,* Monterey, CA, March (1996).

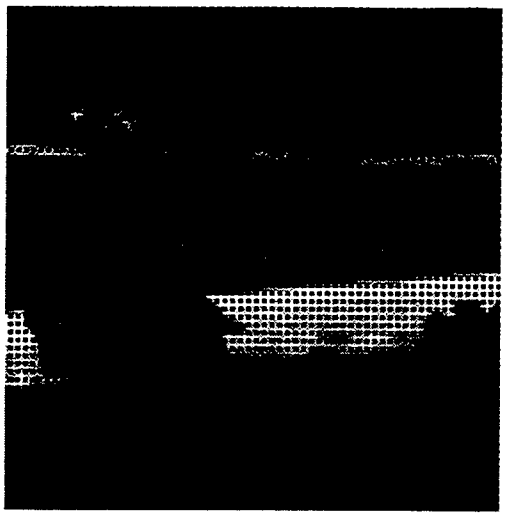

Figure 10a.

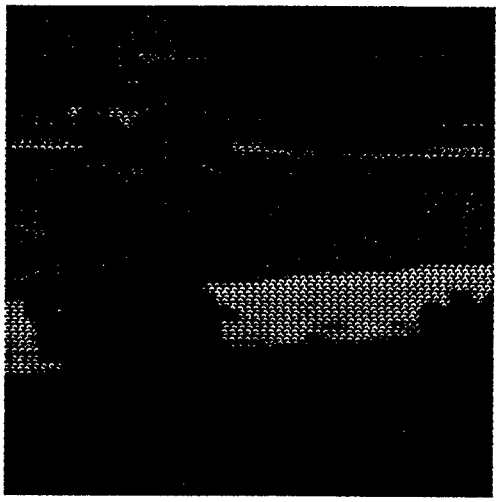

Figure 10b.

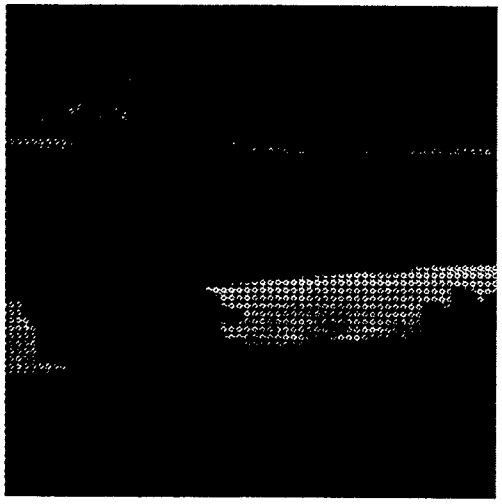

Figure 10c.

Figure 10. (a) through (c) are level 2, 4 and 8 simulated microscan images with missing frames.

Figure 11a.

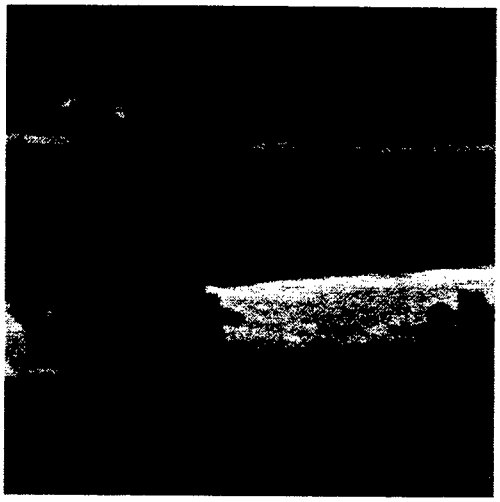

Figure 11b.

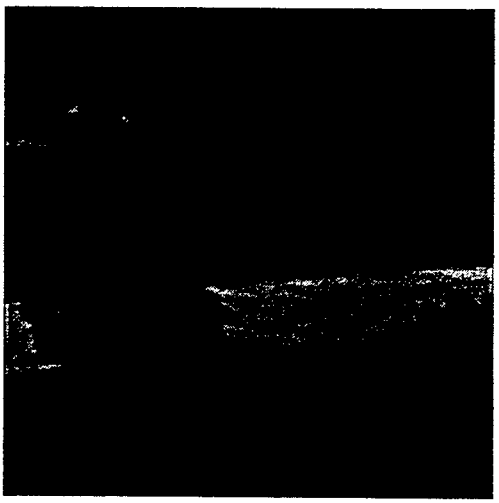

Figure 11c.

Figure 11. Restored images of Fig. 10 after estimating the missing frames.

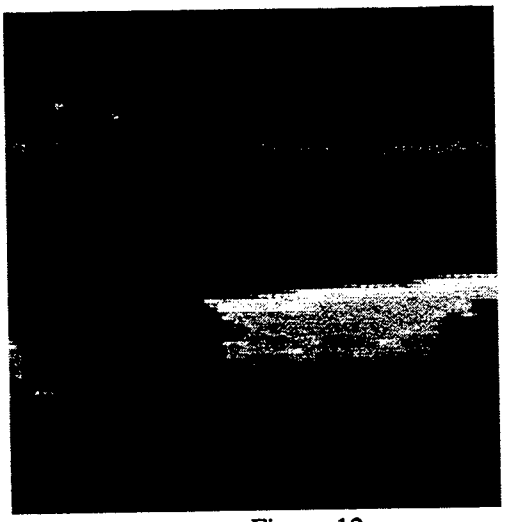

Figure 12a.

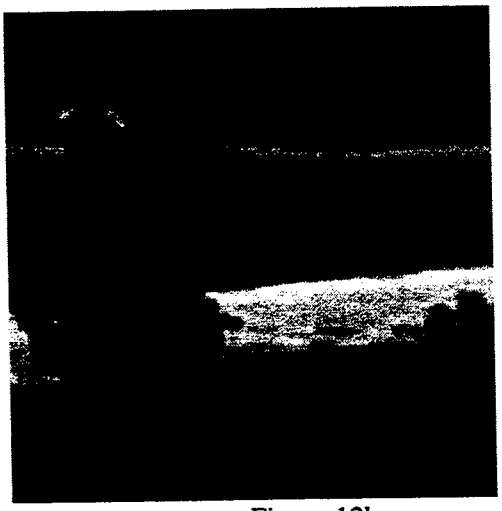

Figure 12b.

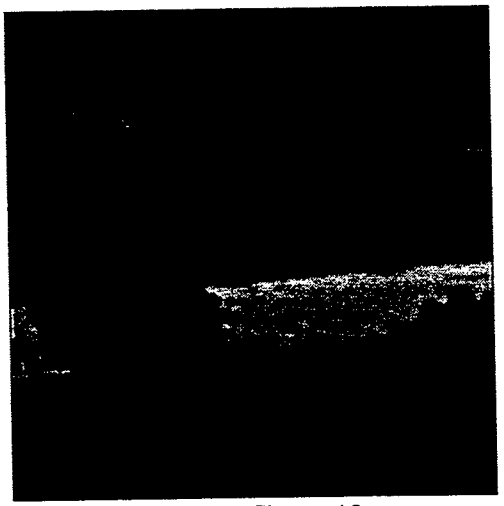

Figure 12c.

Figure 12. Wiener Filtering. Figs. 11a, b, and c are the Wiener filtered versions of Figs. 10a, b and c.

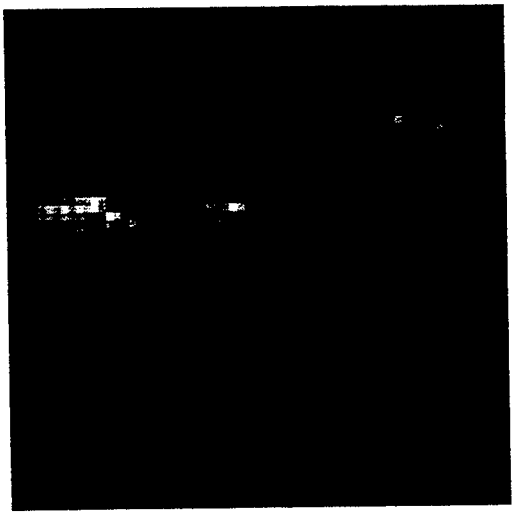

Figure 13a.

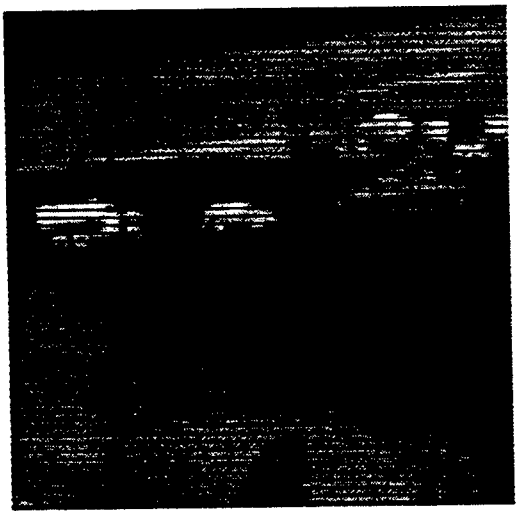

Figure 13b.

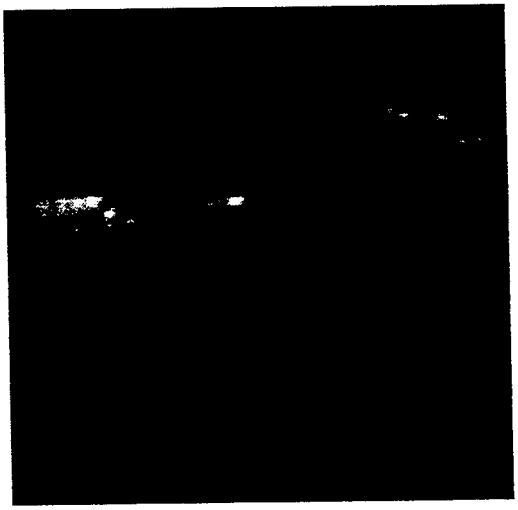

Figure 13c.

Figure 13. Real FLIR Images. (a) staring frame, (b) 4x4 microscan image. (c) restored image.

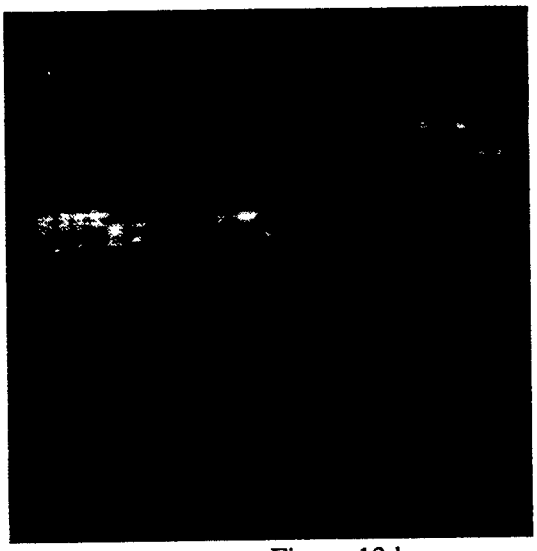

Figure 13d.

Figure 13e.

Figure 13. Real FLIR Images. (d) restored image after Wiener filtering, (e) staring frame after bilinear interpolation.

ADDENDUM

High resolution infrared images may also be reconstructed from multiple translationally shifted aliased frames using iterative techniques such as Bayesian approach via maximum *a posteriori* (MAP) algorithm[3] or maximum-likelihood approach via expectation maximization (EM) algorithm[4]. The MAP algorithm utilizes a prior statistical model for estimating the translational shifts. With this model, a maximum *a posteriori* estimator is used to estimate the high resolution image and the intraframe translational shifts. The shifts are iteratively updated along with the high resolution image using a suitable optimization technique such as gradient descent optimization. In the maximum-likelihood approach, the data are considered Poisson random variables and an EM algorithm is constructed that iteratively estimates an unaliased image compensated for the known imager system blur while simultaneously estimating the translational shifts. Both of these algorithms have been found to yield high resolution images from a sequence of randomly shifted frames. However, each of these algorithms require significant computation time and can not be implemented for real time applications using the currently available high performance microprocessors. The EM algorithm has been found to be faster than the MAP algorithm.

In this work, we have used the registration algorithm discussed earlier in Section 3 to estimate the translational shift parameters in just one step. Using this shift information, we have applied a simplified version of the EM algorithm to estimate the high resolution image from the given sequence of frames. The original EM approach recalculates the shits parameters with each iteration of the algorithm. The new image shift estimates are calulated by evaluating a cost function that compares the shifted and interlaced data frames to the corresponding values in the algorithm's latest high resolution image estimate. The cost function is the sum over all the pixels in the high resolution gird of the absolute value of the interlaced data frames divided by the high resolution image estimate. The shift parameters provided by the new registration algorithm are accurate enough to eliminate the need for iterative calculation of the translational shifts.

The proposed modified EM algorithm has been found to drastically reduce the computation burden compared to the original EM algorithm thereby making it more attractive for practical implementation. To verify the performance of the modified EM algorithm, let us consider the 16 staring FLIR real image data frames used in Section 6. One of these 16 staring FLIR image frames is shown in Fig. 13a. Using these 16 frames, the output obtained by the original EM algorithm[4] and that obtained by the modified EM algorithm after ten iterations are shown in Figures 14a and 14b respectively. Comparing Figs. 14a with 14b, we observe that the modified EM algorithm yields high quality image and can be considered as a viable alternative to the original EM algorithm. For page number limitation, the author could not discuss this approach in detail in this report.

A FAST FOURIER TRANSFORM ANALYSIS OF PILOT INDUCED OSCILLATIONS

Dominick Andrisani, II
Associate Professor

Sten E. Berge
Graduate Student

School of Aeronautics and Astronautics
Purdue University
West Lafayette, IN 47907-1282

Final Report for:
Summer Faculty Research Program and Graduate Student Research Program
Wright Laboratory
Wright-Patterson AFB, OH 45433

Sponsored by:
Air Force Office of Scientific Research
Bolling Air Force Base, DC

and

Wright Laboratory

August, 1996

A FAST FOURIER TRANSFORM ANALYSIS OF PILOT INDUCED OSCILLATIONS

Dominick Andrisani, II
Associate Professor

Sten E. Berge
Graduate Student

School of Aeronautics and Astronautics
Purdue University

Abstract

During the summer of 1996 a program was initiated by the authors to study the characteristics of pilot induced oscillations (PIOs). The long term goals are

- to develop a methodology to take time history data from flight or ground based simulation and determine if a vehicle is PIO prone,
- to determine if a PIO actually occurred in a time history record,
- to develop a non-real-time analysis tool to determine from flight simulator time history data if PIOs occurred so that simulation engineers can help insure consistency between pilot comments, Cooper-Harper ratings, PIO ratings and time history data, and
- to develop a real-time capability of detecting a PIO fast enough to take action to prevent the full development of the PIO.

Results obtained over the period 7/1/96-8/23/96 deal primarily with the first goal and are described in this report. A computer analysis tool is developed in which fast fourier transforms are used to determine

- resonant frequency and output phase angles at the resonant frequency,
- predictions of PIO susceptibility using the Smith-Geddes PIO criteria.

The following preliminary results are highly encouraging.

- 13 of 14 configurations which experienced PIOs were correctly identified.
- In 12 additional configurations 6 were correctly identified as being not PIO prone. Results for the remaining 6 configurations were complicated by multiple resonances that confuse the resonance detector. However, depending on the choice of resonant frequency the correct classification is made for each of the 6 configurations.
- The occurrence of multiple resonances is closely associated with configurations that are not PIO prone.
- continued development of the resonance detector is planned.

A FAST FOURIER TRANSFORM ANALYSIS OF PILOT INDUCED OSCILLATIONS

Dominick Andrisani, II and Sten E. Berge

Background

Pilot induced oscillations (PIOs) have received much recent attention [2-6]. Several approaches to development of a unified PIO theory are currently being pursued. A catalog of PIO events has been compiled and several existing criteria have been shown to successfully predict PIO susceptibility. Accurate analysis of the ever-growing PIO database will gather insight into the characteristics of PIOs. With this information, a PIO detector can be designed for time history data as generated in either flight or simulation.

Discretization of Time History Data

Most PIO time history data in the catalog of PIO events is in paper copy form; the original flight data having been lost or unavailable for various reasons. As a first step in this analysis, various time history records from the PIO database were digitized. Eleven classic PIOs and eighteen Bjorkman (NT-33) time histories [7] were digitized. The eleven classic PIOs were taken from the PIO catalog compiled by HAI in cooperation with STI[2]. There is one roll ratchet, several rate limited actuator cases, mode switches, and both lateral and longitudinal examples. The Bjorkman time histories are all longitudinal, but provide a consistent database encompassing nearly the entire range of the PIO tendency classification scale. The digitization was hampered by the quality of the reproductions and the scales of the plots. Sections of data were often missing because of repeated previous reproduction. Digitization noise was introduced into the data axis scaling was not well chosen. For example, the B-2 charts cover too much time, and the non-PIO Bjorkman configurations are plotted with the same scale as the large amplitude PIO histories. Conversely, there were several data sets with time scaling that covered too small a time period and which cut off the peaks of the data. The M2F2 charts are examples of this other extreme.

The following multi-step digitization process was employed.

- PIO time histories were scanned and cleaned up using OFOTO commercial software.
- PIO time histories were digitized the data using dataThief shareware.
- The resulting ASCII data file was converted to MATLAB script format.

- A MATLAB script was written to produce a second MATLAB script file with a specified uniform time increment.
- A MATLAB script was written to plot the time history data in a similar format to the original.

In all 27 longitudinal records (flight records from the T-38, Shuttle, B-2, F-8, YF-22, and X-15, 18 Bjorkman NT-33 flight records, and 3 HAVE PIO ground based simulation records) and 5 lateral records (flight records from the F/A-18(2), F-14, YF-16, and M2-F2) were digitized. These records are available at WL/FIGC-2 (Mr. David Leggett is the point of contact, 513-255-8498).

Technical Approach

A spectral analysis is performed on selected time histories to determine the quantities needed for PIO characterization. The resonance of each measurement is determined from power spectral density for that variable. The actual resonant frequency will differ from the discrete frequencies used in the power spectral density plot, unless the resonance happens to correspond to one of the harmonics of the spectral analysis. Therefore, the resonant frequency is approximated by finding the centroid of the peak and its two nearest neighbors. The cross spectrum between input and output is used to calculate a frequency response function relating input and output. The phase angle at the resonant frequency is taken from the phase angle of the frequency response function. The validity of the results is related to the coherence of the cross spectral data points used.

The Smith-Geddes criteria are then evaluated. The pilot-vehicle resonant frequency is chosen to be the resonant frequency of the variable with the most reliable time history. This is most often pitch rate. The Smith-Geddes criteria require the phase angles of both $\Theta(j\omega)/F_s(j\omega)$ and $N_z(j\omega)/Fs(j\omega)$. The phase of $\Theta(j\omega)/F_s(j\omega)$ can also be calculated by subtracting 90 degrees from the phase of $q(j\omega)/F_s(j\omega)$. The Smith-Geddes analysis is done with both the Θ and q phase angles. Susceptibility to PIO as defined in MIL-STD-1797A [8], approximate Cooper-Harper rating, and approximate PIO rating based on Ralph Smith's data method [10]are outputs of this analysis.

This procedure is not be completely automatic at this time for two reasons. First, the FFT window size must be chosen subject to several constraints: the primary (lowest) harmonic (set by the length of time (T_{window}) used in the FFT, $\Delta\omega=2\pi/T_{window}$) should be approximately 1 rad/sec, and the highest harmonic (set by the time increment (ΔT), $\omega_{max}=\pi/\Delta T$) must be at least 20 rad/sec to include the resonant frequencies of all possible types of PIOs including pitch bobbles and roll ratchets, the window not contain discrete events such as control system mode switches, and at least two similar windows are required

to compute coherence. Second, the best pilot-vehicle resonant frequency must be manually chosen when multiple resonances are present. Unless the same dominant resonant frequency appears in all measurements, the correct choice is unclear. Further research on this problem is continuing.

The spectral analysis is performed by MATLAB's spectrum function in the Signal Processing Toolbox. The procedure used is Welch's averaged periodogram method [1,9]. Each frame consists of three subframes (two consecutive and one overlapping one half of the other two). Each subframe is preprocessed by removing any bias and is windowed with a Hanning window. Use of more than one subframe helps insure valid coherence. The software steps through the time history frame by frame.

PIO susceptibility is determined by the Smith-Geddes criteria using the following steps.

- Pilot-in-the-Loop Properties

  Resonant frequency, wr,

  Amplitudes of inputs and outputs at wr from FFT data

  $\Theta(j\omega_i),\ q(j\omega_i),\ n_z(j\omega_i).$

- Pilot-Vehicle System Properties: Phase lags computed using Cross Spectral densities

$$\angle\frac{\Theta(j\omega)}{F_s(j\omega)}\bigg|_{\omega=\omega r} \quad \angle\frac{q(j\omega)}{F_s(j\omega)}\bigg|_{\omega=\omega r} \quad \angle\frac{n_z(j\omega)}{F_s(j\omega)}\bigg|_{\omega=\omega r}.$$

- Smith-Geddes PIO Metrics

  Use wr as the criterion frequency,

  Determine susceptibility to

  attitude type PIO (Type III) based on

$$\angle\frac{\Theta(j\omega)}{F_s(j\omega)}\bigg|_{\omega=\omega r} < -180 \quad \angle\frac{q(j\omega)}{F_s(j\omega)}\bigg|_{\omega=\omega r} -90 < -180,$$

  acceleration type PIO (Type I) based on

$$\Phi(\omega_r) = \angle\frac{n_z(j\omega)}{F_s(j\omega)}\bigg|_{\omega=\omega r} - 14.3\omega_r < -180 \text{ deg. when}$$

$$\angle\frac{\Theta(j\omega)}{F_s(j\omega)}\bigg|_{\omega=\omega r} < -160$$

A few comments are in order. We evaluate phase angles at the resonant frequency of the pilot-in-the-loop system, w_r. The Smith-Geddes criterion evaluates the phase angles at the criterion frequency, $w_c = 0.24S + 6$ where S is the average slope of the $|q(j\omega)/Fs(j\omega)|$ over the interval from 1-6 radians per second. wc is an approximation to the crossover frequency of the pilot-vehicle system during pitch attitude tracking. If there is a dominant resonance in a time history record our approach is reasonable since the pilot-vehicle system will resonate near the crossover frequency of the pilot-vehicle system.

Our approach is more than an open loop method because our resonant frequency is a property of the pilot-vehicle system as expressed in the time histories from the piloted system.

Problems with the Resonant Frequency Detector

Several problems were encountered with our resonant frequency detector.

• Power spectra of important traces sometimes have multiple peaks. Figure 1 shows an example of a time spectrum with two resonant peaks. Figure 2 shows the more common case where there is a single dominant resonant peak.

• Power spectra of different traces sometimes have different peaks as shown in the sketch below.

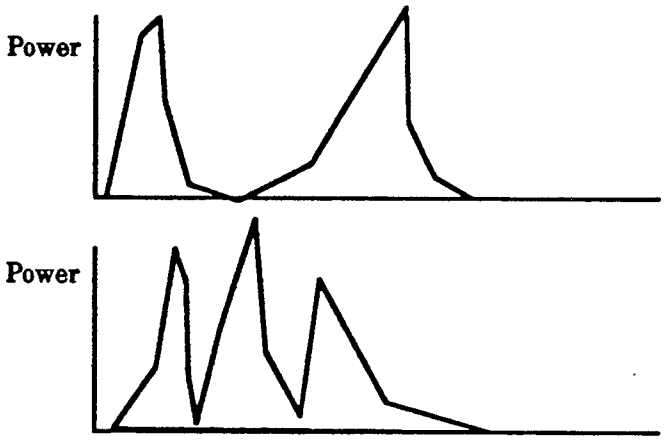

• Low frequency power sometimes confuses our resonant frequency detector. Figure 1 also illustrates this problem.

There are several possible solutions to those problems. Multiple peaks on one power spectrum and peaks that don't line up seem to correlate with the absence of PIO. Low frequency power might be removed by a different choice of windowing in computing the FFT

or by filtering the time history before the FFT is taken. We are currently using a Hanning window.

The end of the summer prevented our resolution of the problems. Development of the resonant frequency detector will continue until the end of 1996 by Professor Andrisani.

Results

The results from our analysis of longitudinal PIO data are summarized in Tables 1 and 2.

PIO amplitudes versus resonant frequency is shown in Figure 3. The longitudinal PIOs in this study occur at a wide range of amplitudes. This suggests amplitude of the resonance is not a good metric to determine if a PIO is occurring.

Angle Φ (of the Smith-Geddes criterion [10]) versus actual average PIO rating for the Bjorkman data is shown in Figure 4. The line in the figure comes from [10] and seems to underestimate the average PIO ratings. Average Cooper-Harper ratings versus angle of $\Theta(j\omega)/Fs(j\omega)$ is shown in Figure 5.

Figure 6 shows that the occurrence of a PIO seems to correlate well with a single dominant resonant frequency in the time history. This characteristic seems more helpful in determining that a PIO has occurred than output amplitude at the resonant frequency. More work is required here to determine how to effectively use this fact.

Table 1 indicates that acceleration type PIO were important in detecting PIO susceptibility in only 1 of 24 cases (B2). The need for acceleration type PIO is currently under review by the authors. These results indicate that the Smith-Geddes boundaries are reasonable.

When phase angles vary significantly during a time history nonlinear behavior is suspected. One cause of this is rate limiting, where phase lag is a function of amplitude and frequency. The Shuttle record, Figure 7, shows strong time varying phase angle of $q(j\omega)/Fs(j\omega)$. The B2 record, Figure 8, shows almost no time varying phase angle of $q(j\omega)/Fs(j\omega)$. The ability of this method to track time varying phase angles is significant because this can trigger a PIO.

Towards a Time Domain PIO Detector

The following comments summarize the status of our efforts at developing a FFT Based PIO detector.

- The existing algorithm is not set up to run in real time. A Wright Laboratory in-house effort by Mr. Phil McKeehan is anticipated in this area.

- Some operator intervention is helpful in selecting the time periods to analyze so that PIO events are not split into different time frames.
- Improvement is necessary on the resonant frequency detector.
- We still need to determine in what way amplitude at resonant frequency is helpful for PIO detection.
- We need to decide what the occurrence of multiple resonances indicates about PIO.

Conclusions

Based on recently digitized time histories of 27 longitudinal PIOs the following conclusions are drawn.

- Our FFT Based PIO Analysis Software using the Smith-Geddes criteria does an excellent job of determining PIO susceptibility.
- Preliminary results indicate that the Smith-Geddes boundaries are reasonable.
- Acceleration type PIO were important in detecting PIO proneness in only 1 of 24 cases (B2). The need for this characterization is under continuing review.
- Continued development of the resonant frequency detector is required for cases where multiple resonances occur.
- The ability of this method to track time varying phase angles is significant because this can serve as a trigger for PIOs.

Further Work

During Professor Andrisani's sabbatical at Wright Laboratories (8/19/96-12/20/96) the additional work on the following items is planned.

- resonant frequency detector,
- adequacy of the Smith-Geddes boundaries,
- need for acceleration type PIOs,
- importance of multiple resonances in PIO detection,
- automating the analysis process to achieve the third goal mentioned in the abstract.

An in-house Wright laboratory effort is anticipated to develop and implement a real time PIO detector based upon this work.

Acknowledgments

This work was conducted under the Summer Research Program supported by the Air Force Office of Scientific Research at Wright Laboratory, Wright-Patterson AFB. The focal points were Wayne Thor (513-255-8497), David Legget and Tom Cord.

References

1. Bendat, Julius S. and Allan G. Piersol, Engineering Applications of Correlations and Spectral Analysis, John Wiley & Sons, New York, 1980.

2. Mitchell, David G. and Hoh, Roger H. , *Development of a Unified Method To Predict Tendencies for Pilot-Induced Oscillations*, WL-TR-95-3049, June 1995.

3. Klyde, David H., Duane T. McRuer, and Thomas T. Myers, *Unified Pilot-Induced Oscillation Theory, Volume 1: PIO Analysis with Linear and Non linear Effective Vehicle Characteristics, Including Rate Limiting*, WL-TR-96-3028, December 1995.

4. Preston, Jeff D., Hodgkinson, John, and Buckley, Jim, *Unified Pilot-Induced Oscillation Theory, Volume II: Pilot Induced Oscillation Criteria Applied to Several McDonnell Douglas Aircraft*, WL-TR-96-3029, December 1995.

5. Anderson *Unified Pilot-Induced Oscillation Theory, Volume 1: PIO Analysis with Linear and Non linear Effective Vehicle Characteristics, Including Rate Limiting*, WL-TR-96-3028, December 1995.

6. Bailey, Randall E. and Bidlack, Timothy, J., *Unified Pilot-Induced Oscillation Theory, Volume IV: Time Domain Neal-Smith Criteria*, WL-TR-96-3031, December 1995.

7. Bjorkman, Eileen A. *Flight Test Evaluation of Techniques to Predict Longitudinal Pilot Induced Oscillations*, M.S. Thesis, Air Force Institute of Technology, AFIT/GAE/AA/86J-1, December 1986.

8. *Military Standard, Flying Qualities of Piloted Aircraft*, MIL-STD-1797A, revised 28 June 1995.

9. Welch, Peter D., The Use of Fast Fourier Transform for Estimation of Power Spectra: A Method Based on Time Averaging Over Short, Modified Periodograms, *IEEE Trans. Audio and Electroacoust.*, vol. AU-15, pp. 70-73, June 1967.

10 Smith, Ralph H., "The Smith-Geddes Handling Qualities Criterion," 1994 SAE Aerospace Atlantic Conference, Dayton, OH, April 20, 1994.

Table 1. Summary of Numerical Results for Longitudinal PIOs.

PHASE LAG ANALYSIS					
Long. PIO from Flight					
Aircraft	wr	ThetaWrdeg	qWrdeg	nzWrdeg	phi
PIO in time history					
T-38	7.49	-268	-234	-248	-355
Shuttle(t=24-30)	2.40	NaN	-153	NaN	NaN
Shuttle(t=26-32)	3.40	NaN	-171	NaN	NaN
B2 (t=25-31.7)	3.63	-165	-8	-138	-190
F8 (t=8.1-20.6)	2.79	-220	-144	-185	-225
YF-22	3.25	-213	-121	-197	-243
Bjorkman 2-5	2.57	-208	-125	-196	-232
Bjorkman 2-8	4.33	-219	-126	-174	-236
Bjorkman 3-12	1.91	-162	-72	-126	-154
Bjorkman 3-13	3.21	-184	-130	-178	-224
Bjorkman 5-9	3.51	-227	-122	-185	-235
Bjorkman 5-10	2.81	-195	-119	-176	-216
HAVE, 4/13,#21(Bj3-13)	1.32	-277	-196	-261	-279
HAVE, 4/13,#22(Bj3-13)	1.13	NaN	-195	-271	-287
HAVE, 4/13,#23(Bj3-13)	1.76	-320	-236	-322	-348
no PIO in time history					
Bjorkman 2-B	4.95	-123	-74	-137	-207
Bjorkman 2-1(wr=1.1)	1.12	-70	37	-93	-109
(wr=5.4)	5.43	-266	-97	-178	-256
Bjorkman 3-D	6.88	-180	-89	-32	-130
Bjorkman 3-1	1.78	-67	14	-67	-93
Bjorkman 3-3	3.51	-119	-47	-114	-165
Bjorkman 3-6 (wr=8.9)	8.87	-203	-108	-36	-163
(wr=3.0)	3.00	-105	-13	-50	-93
Bjorkman 4-1 (wr=6)	5.97	-174	-94	-141	-227
(wr=10)	10.00	-277	-122	-340	-483
(wr=2.5)	2.52	-120	-8	-92	-128
Bjorkman 4-2	4.83	-155	-65	-129	-198
Bjorkman 5-1	2.37	-100	-35	-100	-133
maybe PIO in time history					
Bjorkman 2-7(t=14-29)	4.29	-197	-119	-138	-200
(t=22-29, wr=4.3)	4.28	-194	-119	-144	-205
(t=22-29, wr=6.1)	6.12	-241	-149	-120	-208
Bjorkman 3-8	7.03	-246	-155	-117	-217
Bjorkman 5-11 (wr=2.5)	2.50	-202	-113	-142	-178
(wr=1.9)	1.87	-147	-56	-108	-135
(wr=3.2)	3.32	-229	-137	-145	-193

Table 1, concluded

	Overall Results					
Long. PIO from Flight	Flight Ratings		FFT Classification			
Aircraft	Act. PIOR	FQ Lev	Sus_PIO	Correct		
PIO in time history						
T-38			1	y		
Shuttle(t=24-30)			1	y		
Shuttle(t=26-32)			1	y		
B2 (t=25-31.7)			1	y		
F8 (t=8.1-20.6)			1	y		
YF-22			1	y		
Bjorkman 2-5	4.33(4,4,5)	3	1	y	single dominant freq	
Bjorkman 2-8	4(4,4,4)	3	1	y	single dominant freq	
Bjorkman 3-12	4.5(4,5)	3	0	n	clear reson., not quite, miss	
Bjorkman 3-13	4.5(4,5)	3	1	y	single dominant freq	
Bjorkman 5-9	4(4,4)	3	1	y	single dominant freq	
Bjorkman 5-10	5(5,5)	3	1	y	single dominant freq	
HAVE, 4/13,#21(Bj3-13)	5		1	y		
HAVE, 4/13,#22(Bj3-13)	5		1	y		
HAVE, 4/13,#23(Bj3-13)	5		1	y		
no PIO in time history						
Bjorkman 2-B	2(3,2,2,1)	1	0	y	multiple resonances	
Bjorkman 2-1(wr=1.1)	1(1,1,1)	1	0	y	rerun wr=6	
(wr=5.4)			1	n		
Bjorkman 3-D	1(1,1)	1	0	y	multiple resonances	
Bjorkman 3-1	2.33(3,2,2)	2	0	y	multiple reson. w/dominant	
Bjorkman 3-3	1.68(3,1,1)	1	0	y	multiple resonances	
Bjorkman 3-6 (wr=8.9)	2(2,2)	2	1	n	reurn wr=3	
(wr=3.0)			0	y		
Bjorkman 4-1 (wr=6)	1(1,1,1)	1	1	n	multip. reson., freqs no match	
(wr=10)			1	n		
(wr=2.5)			0	y	this is the 'best' wr	
Bjorkman 4-2	1.33(1,1,2)	1	0	y	single dominant freq	
Bjorkman 5-1	1(1,1)	2	0	y	multiple resonances	
maybe PIO in time history						
Bjorkman 2-7(t=14-29)	3(4,3,2)	2	1	y	reson. no mtch, rerun last 6s	
(t=22-29, wr=4.3)			1	y		
(t=22-29, wr=6.1)			1	y		
Bjorkman 3-8	3.68(4,3,4)	3	1	y	single dominant freq??	
Bjorkman 5-11 (wr=2.5)	3(2,4,3)	3	1	y	different but clear peaks	
(wr=1.9)			0			
(wr=3.2)			1			

Table 2. Summary of PIO Classification Results

Configurations	Results
14 PIO-prone Configs Bjorkmans configs with PIOR consistently >4 T-38, Shuttle, B-2, F-8, YF-22 3 HAVE PIOs (Bjorkman 3-12)	correct classification: 13 wrong classification: 1 (Bjorkman 3-12) (There was a clear single dominant frequency.)
9 not PIO-prone Configs Bjorkman Configs with PIOR consistently<4	correct classification: 6 correct by choice of wr: 3 wrong classification: 0
3 maybe PIO Configs at least 1 PIOR >=4 (Bjorkman 2-7, Bjorkman 3-8, Bjorkman 5-11)	correct by choice of wr: 3 wrong classification: 0 Config(PIOR) Bj2-7 (4,3,2) PIO-prone at 3/3 wrs Bj3-8 (4,3,4) PIO-prone at 1/1 wrs Bj5-11(2,4,3) PIO-prone at 2/3 wrs

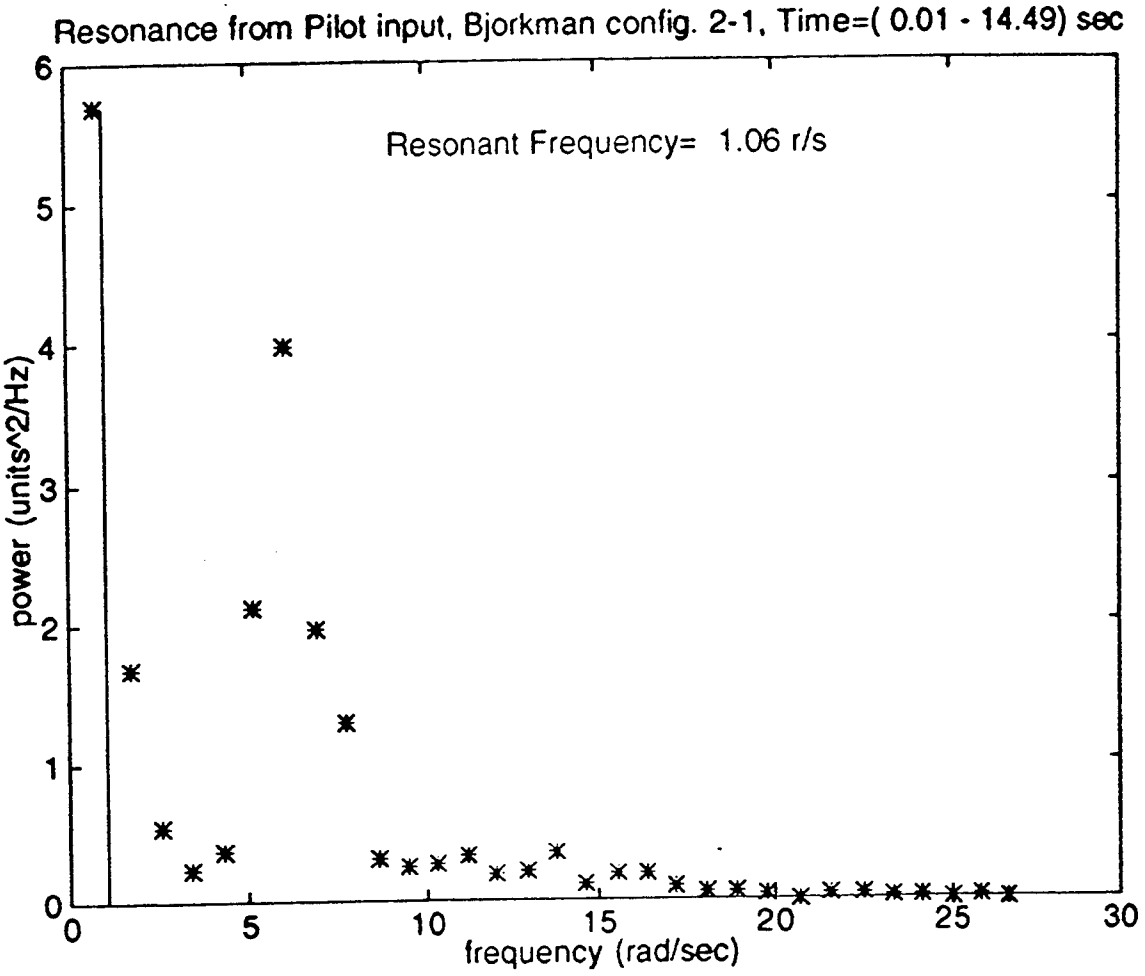

Figure 1. Power spectrum showing multiple resonances and low frequency power

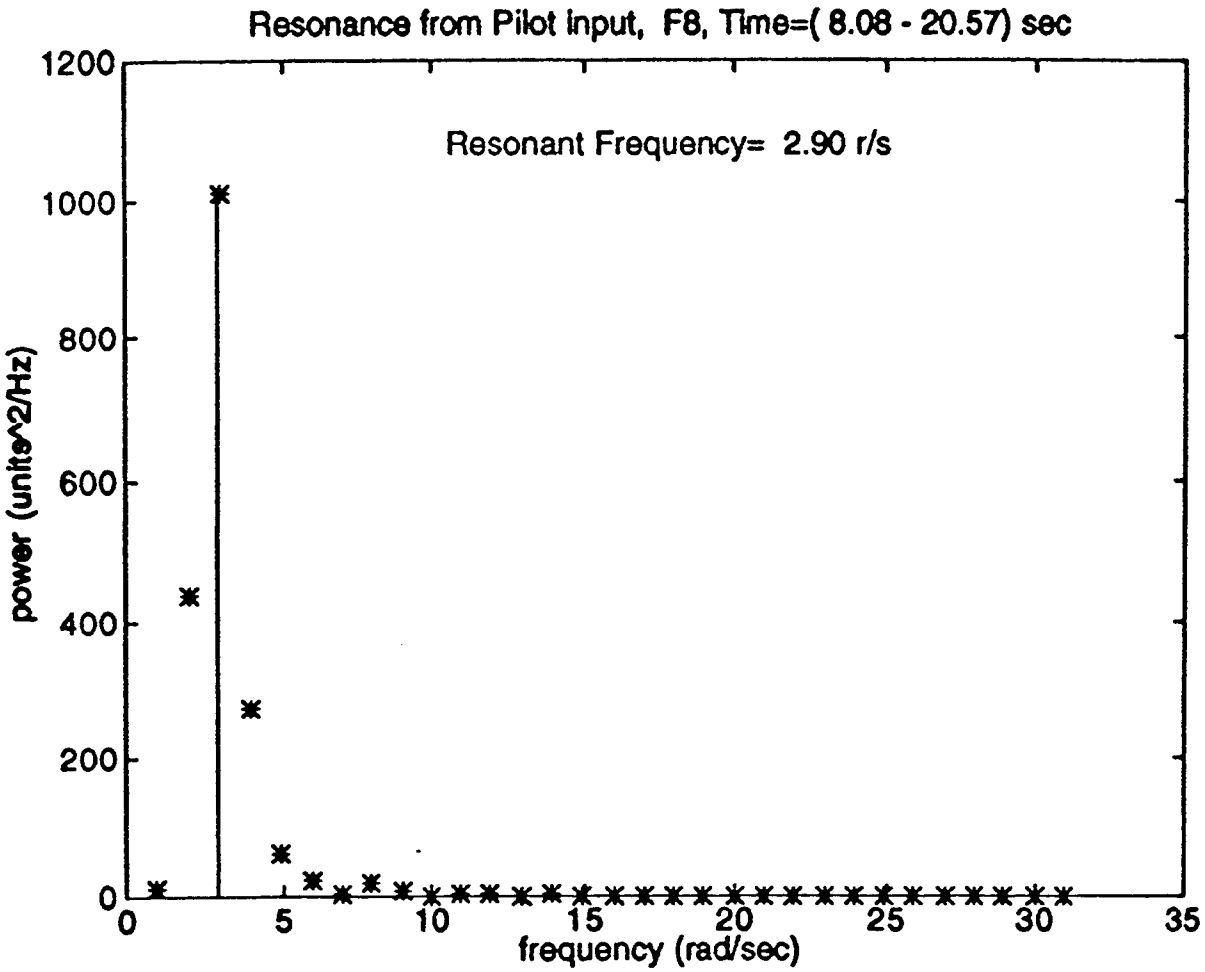

Figure 2. Power spectrum showing a single dominant frequency

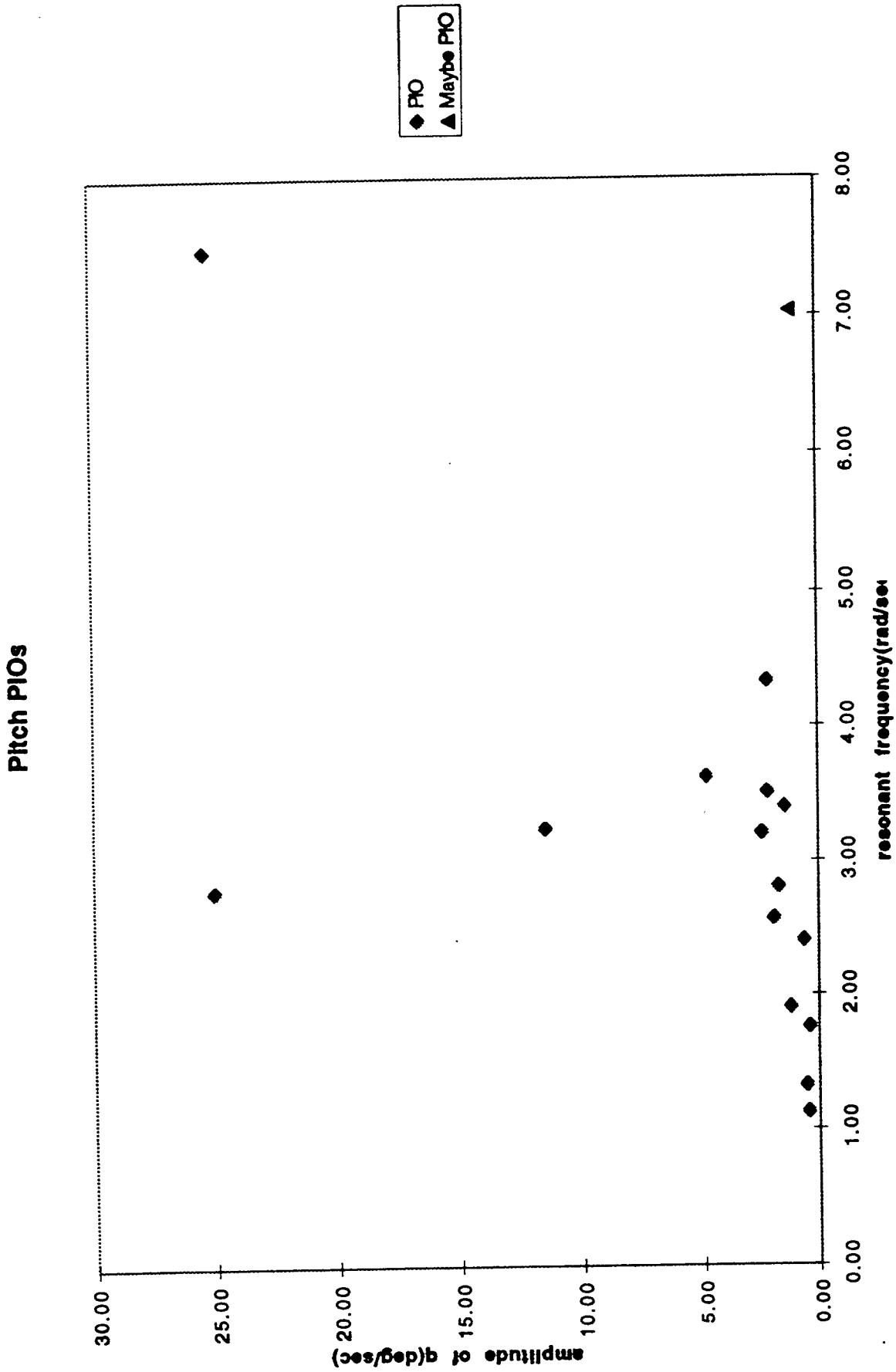

Figure 3. Properties of Longitudinal PIOs

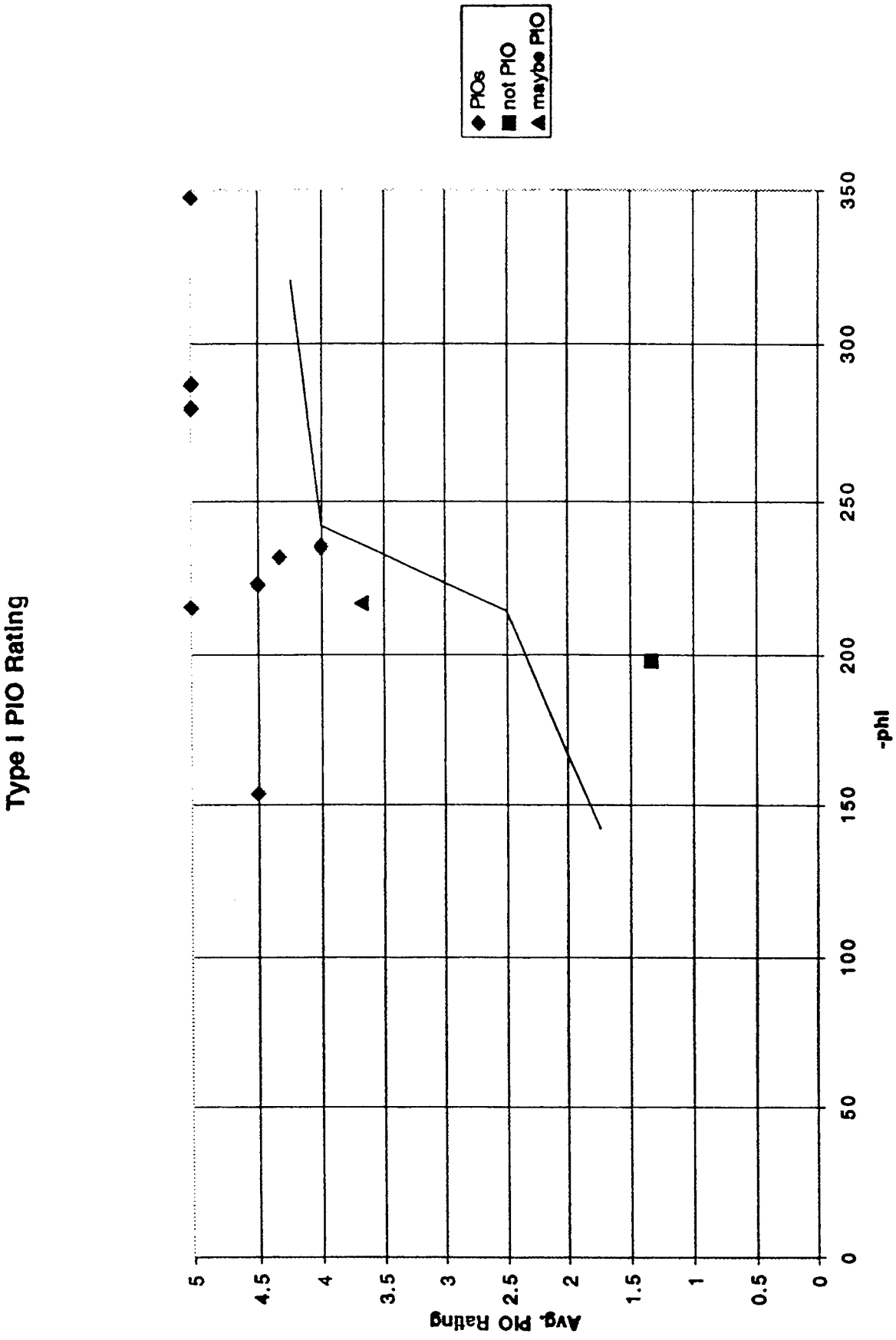

Figure 4. Actual average PIO ratings versus phi for Bjorkman records

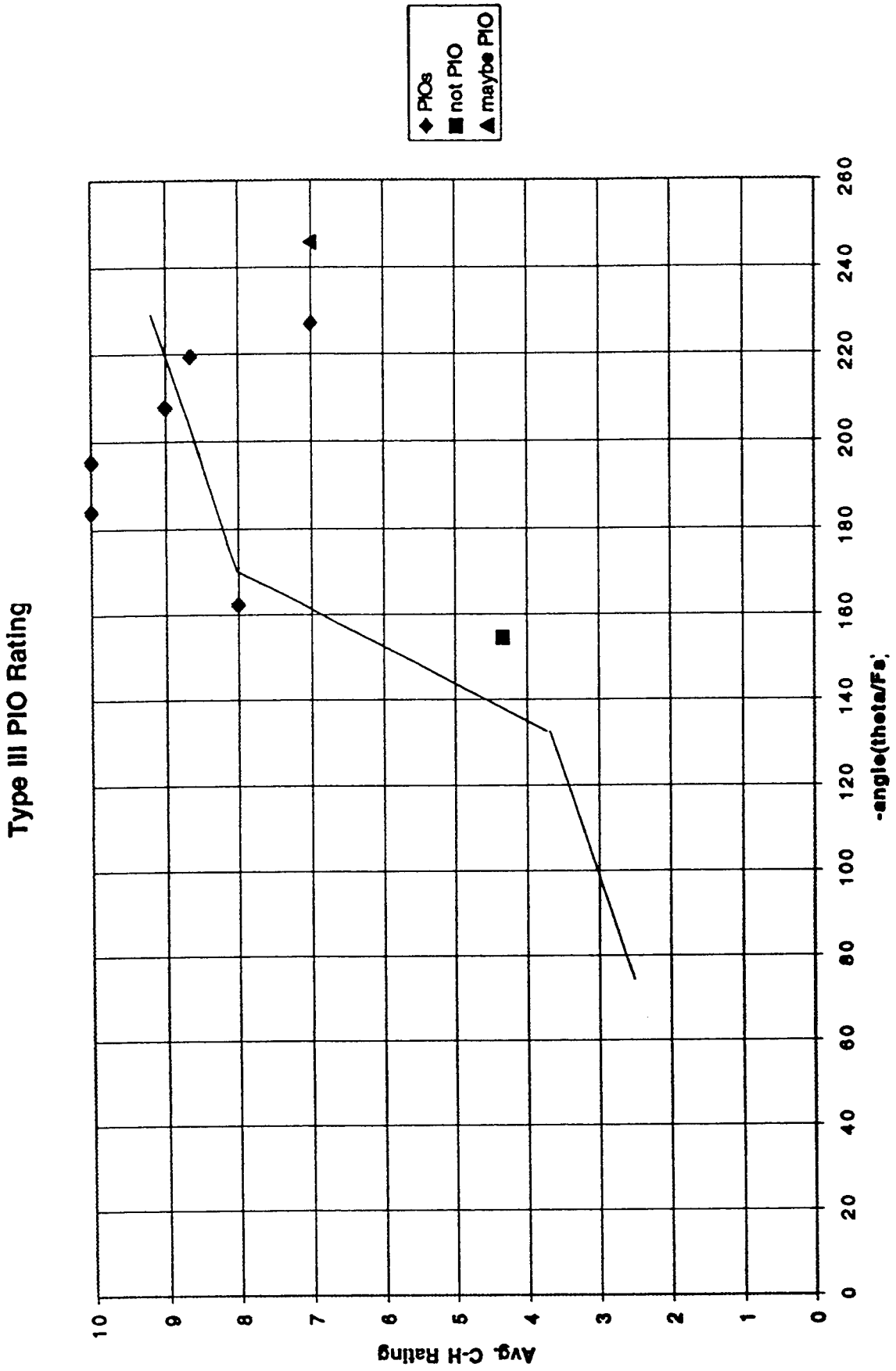

Figure 5. Actual average Cooper-Harper ratings versus phase of $\Theta(j\omega_r)/Fs(j\omega_r)$ for Bjorkman records

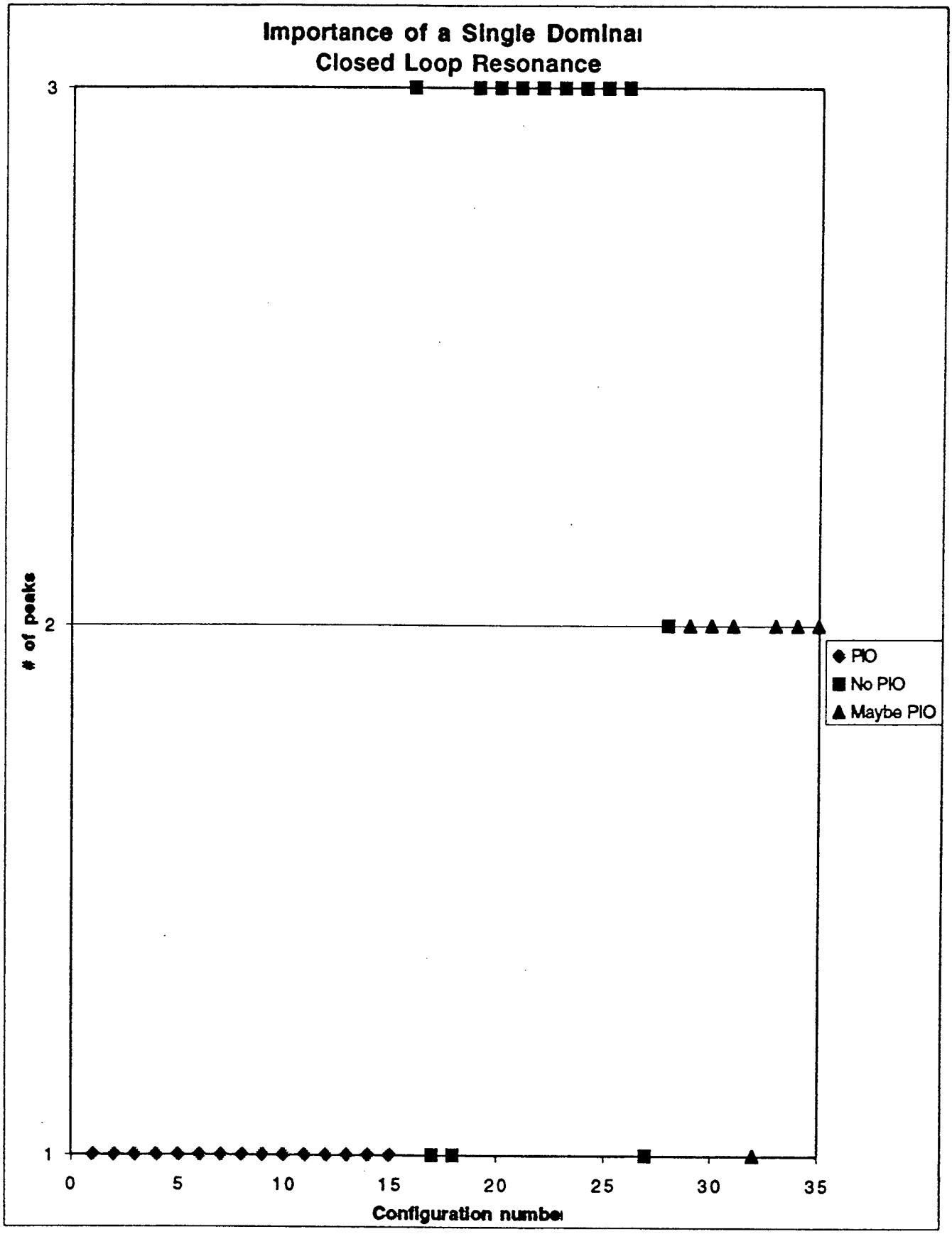

Figure 6. The importance of a single dominant frequency for PIO

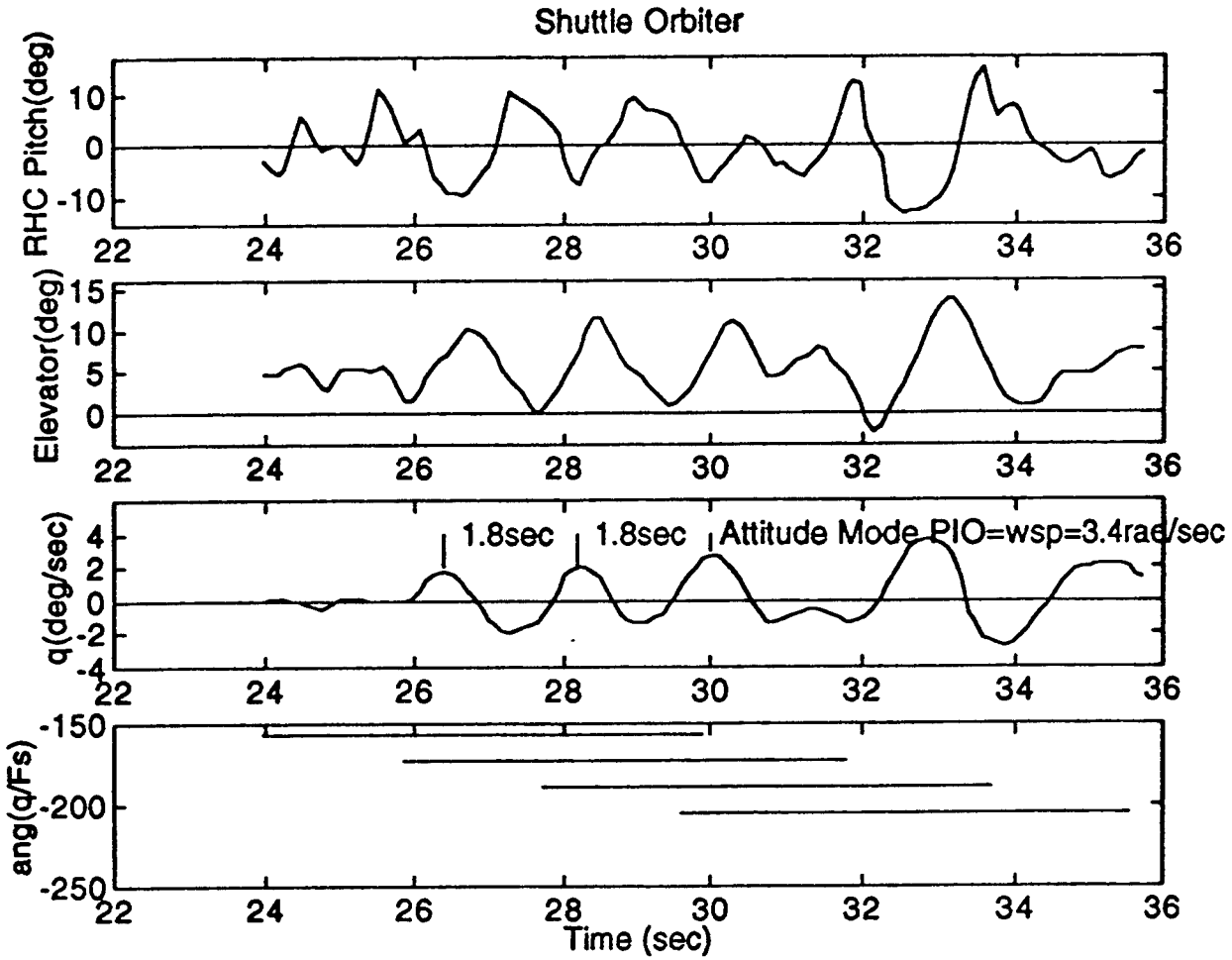

Figure 7. Shuttle record showing significant time variation of phase angle of $q(j\omega_r)/F_s(j\omega_r)$

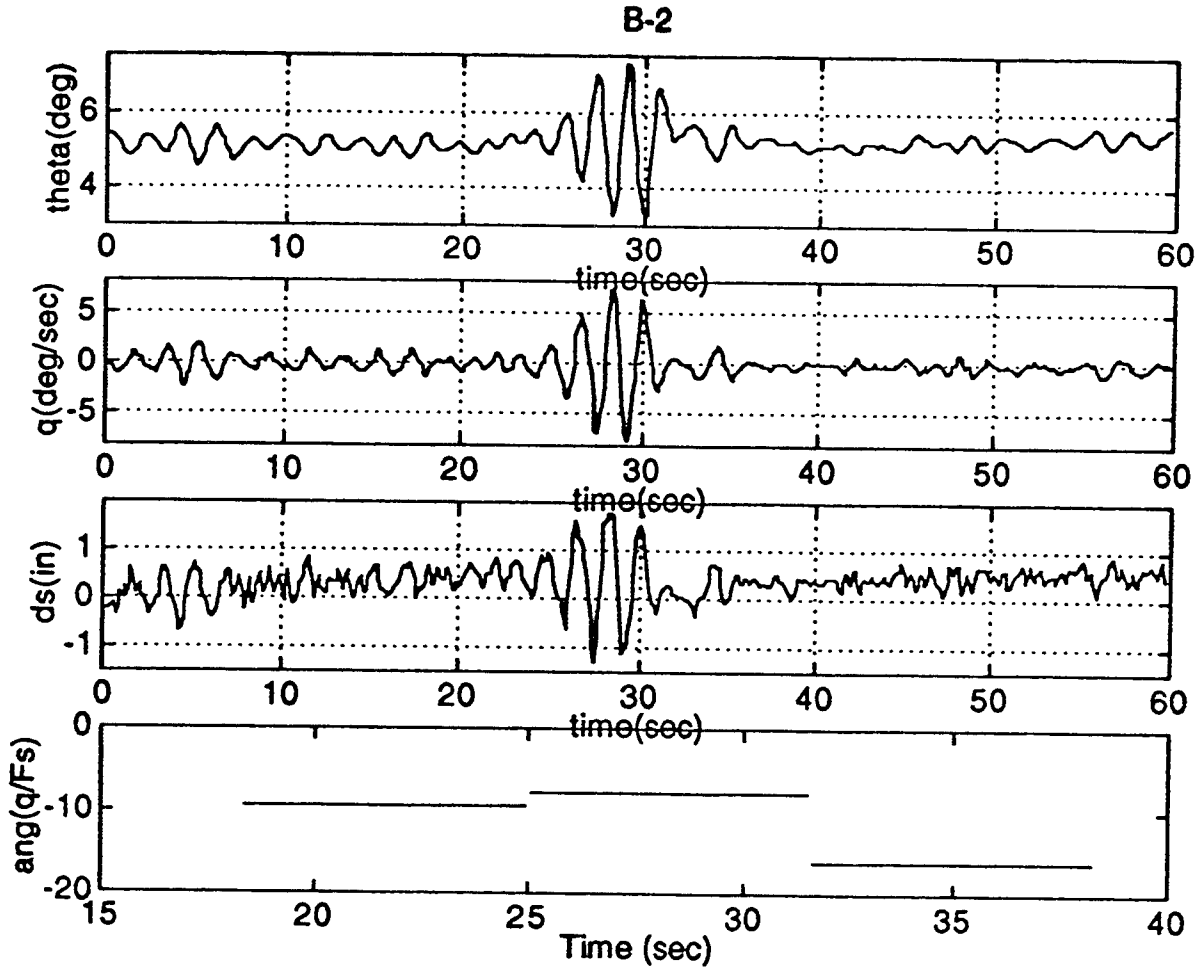

Figure 8. B2 record showing insignificant time variation of phase angle of $q(j\omega_r)/F_s(j\omega_r)$

TEXTURE AND MICROSTRUCTURE OF HOT ROLLED Ti-6Al-4V

Pnina Ari-Gur
Associate Professor
Department of Construction Engineering,
Materials Engineering & Industrial Design

Western Michigan University
Kalamazoo, MI 49008-5064

Final Report for:
Summer Faculty Research Program
Wright Laboratory

Sponsored by:
Air Force Office of Scientific Research
Bolling Air Force Base, DC

and

Wright Laboratory

September 1996

TEXTURE AND MICROSTRUCTURE OF HOT ROLLED Ti-6Al-4V

Pnina Ari-Gur
Associate Professor
Department of Construction Engineering,
Materials Engineering & Industrial Design

Abstract

The effect of initial microstructure, hot-working parameters, and post-processing heat treatments on Ti-6Al-4V were studied. Included in the studies were optical metallography, crystallographic texture measurements using back-reflection pole-figures, and micro-texture determination using orientation image microscopy. The results demonstrate strong dependency on the processing parameters, and the existence of micro-texture even in some of the cases when overall the crytallographic orientation is random.

TEXTURE AND MICROSTRUCTURE OF HOT ROLLED Ti-6Al-4V

Pnina Ari-Gur

Introduction:

Ti-6Al-4V is a high-strength light-weight material that has been in extensive use for aerospace applications. Its processing is difficult -- it is not workable at low temperatures, while at temperatures above 75% of the solidus temperature, its developing microstructure is hard to control [1].

At room temperature and up to 1815°F, Ti-6Al-4V has a dual phase ($\alpha+\beta$) structure. The α-phase (HCP), the dominant phase throughout this temperature range, is highly anisotropic in nature. The second phase (β) is BCC, and is the single phase present above the transus temperature (1815°F). Numerous studies investigated the relationship between processing and crystallographic texture development in dual-phase titanium alloys and its effect on the mechanical properties. However, failure analyses done on Ti-6Al-4V parts often reveal that even in the absence of overall preferred orientation (texture) in the part, aligned α colonies provide nucleation site for internal fatigue cracks. This phenomenon may result in a ten-fold decrease in fatigue life [2,3]. The aligned α colonies can be traced back to the original β (BCC) grain that existed above the transus temperature. Breaking the original microstructure, as well as

elimination of the micro-texture (local aligned colonies), are what thermo-mechanical processing [1] is aimed at.

The goal of this work was to study the effects of initial microstructure, assorted hot-rolling parameters, and several post-processing heat treatments on the evolution of microstructure, crystallographic texture, and micro-texture.

2. EXPERIMENTAL PROCEDURES

2.1 Processing:

The as-received plate of Ti-6Al-4V (1.17" thick) was divided to two groups, that were heat treated differently to provide different initial microstructures. Each one was heat treated in preparation for the hot rolling. These are summarized in Table 2.1.

Table 2.1 Pre-processing Heat Treatments

Group 1 (β annealed)	Temperature	1725°F	1950°F	1725°F	1500°F	Air cool
	Time	20 min	15 min	5 min	15 min	
Group 2 (β quenched)	Temperature	1725°F	1950°F	Water		
	Time	20 min	15 min	Quench		

The 1725°F and 1500°F treatments, following the 15 min at 1950°F for group 1, were intended to simulate the slow cooling of large billets.

To study the development (or breakdown) of structure during the process, specimens were hot rolled to two levels of strains:

- Light reduction (ε_T = 0.57, from 1.17" to 0.658")
- Heavy reduction (ε_T = 1.5, from 1.17" to 0.27")

Three rolling temperatures were chosen in consideration of the β transus temperature (1815°F) and the minimum temperature where Ti-6Al-4V is still workable. The rolling temperatures were:

- 1780°F
- 1700°F
- 1500°F

To guarantee temperature uniformity, specimens were placed in the furnace for 40 minutes prior to rolling. The reduction per rolling pass was 10% (except for the rolling at 1500°F that was performed at 5% reduction per pass). Between passes, the specimens were re-heated for 3 minutes.

To study the effect of dynamic versus static recrystalliztion, some of the specimens were heat treated following the hot-rolling. These heat treatments are summarized in Table 2.2. Group number four (as-hot rolled) was tested metallographically only. The heat treatment at 1300°F is for relieving stresses only and does not change the structure or texture. It was needed for the micro-texture studies, due to the sensitivity of the orientation imaging technique.

Table 2.2 Post-processing Heat Treatments

Group Number	Temperature	Time	Cooling
1	Same as rolling	2 hours	Air
2	1600°F	2 hours	Air
3	1750°F	2 hours	Air
4	As hot rolled	N/A	N/A
5	1300°F	1 hour	Air

2.2 Testing

The microstructure, crystallographic texture, and micro-texture of the hot-rolled and heat-treated samples were characterized by regular optical metallography, x-ray diffraction, and orientation imaging microscopy. For the sake of comparison, the pre-rolling, as heat treated plates were tested too.

2.2.1 Metallography

Metallographic samples were sectioned parallel to the N-R plane (perpendicular to the transverse direction), polished and etched for 15 seconds in Kroll's solution (3.5 vol% HNO_3, 1.5 vol% HF, balance H_2O). Specimens of as-hot rolled, as well as heat treated (Table 2.2) were photographed.

2.2.2 Texture

X-ray diffractometer (Cu Kα radiation) equipped with pole-figure goniometer was used for the crytallographic texture studies. Basal plane (0002) pole figures were created for samples cut and polished in the R-T plane (parallel to the rolling plane about 2.5mm below the surface). Only back reflection data were collected (maximum tilt of 80°).

2.2.3 Micro-texture

Samples were cut, mechanically polished and electro-polished parallel to the N-T plane (perpendicular to the rolling direction). The electro-polishing was necessary to remove any surface damage left after the careful mechanical polishing. Two areas of

2mm x 2mm each were scanned (1mm x 4mm for the heavily rolled samples), one close to the rolling surface, and the other -- at mid-section).

Icosahedral maps were plotted for the basal (0002) plane. They were based on 40,000 points of measurement each. Each indexed point is within 0.9° of an icosahedral face (or else the program determines that it is unable to index it and the point appears white on the map).

In addition to the icosahedral maps, pole-figures (parallel to the N-T and to the R-T plane) were drawn reflecting the average texture in each scanned area.

3. EXPERIMENTAL RESULTS AND DISCUSSION

3.1 Micro-structure

The microstructures of the pre-processing heat treated samples are shown in Figure 1. As expected, the β-annealed sample (Figure 1a) demonstrates a coarse, basket-weave (Widmanstatten) type structure, while the β– quenched sample has a lot finer microstructure (Figure 1b).

Even relatively large deformations ($\varepsilon = 1.5$) at 1500°F resulted in a non-uniform microstructure (Figure 2). Post-rolling heat treatment at 1500°F does little, if at all to change the previously deformed microstructure (Figure 3). At the higher temperatures tested , recrystalliztion occurs, and heat treatment at 1750°F following the rolling, results in equiaxed structure (Figure 4).

At the other end, rolling at 1780°F, resulted in non-uniform deformation only at small strains ($\varepsilon=0.57$, Figure 5a). Subsequent deformation to $\varepsilon=1.5$ at this temperature, resulted in a uniform microstructure (Figure 5b). Post-deformation heat treatment at 1600°F merely coarsened the microstructure of the lightly rolled specimens (Figure 6a), but resulted in basket-weave like structure for the heavily rolled specimen (Figure 6b). It seems as if the subsequent deformation has triggered an earlier transformation.

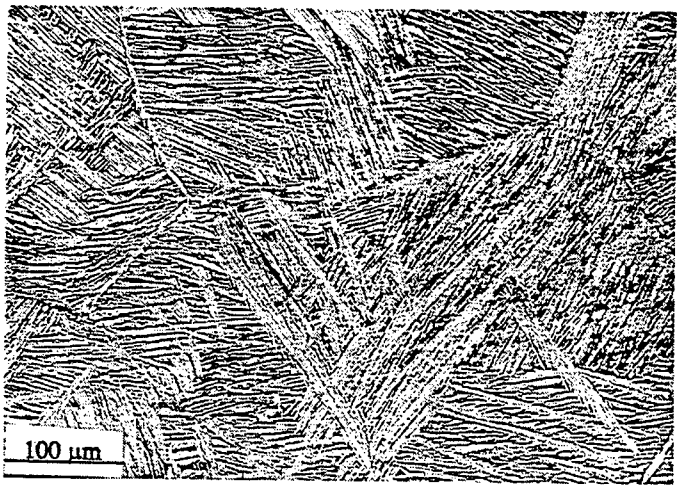

Figure 1a: Microstructure of the pre-processing β-annealed sample.

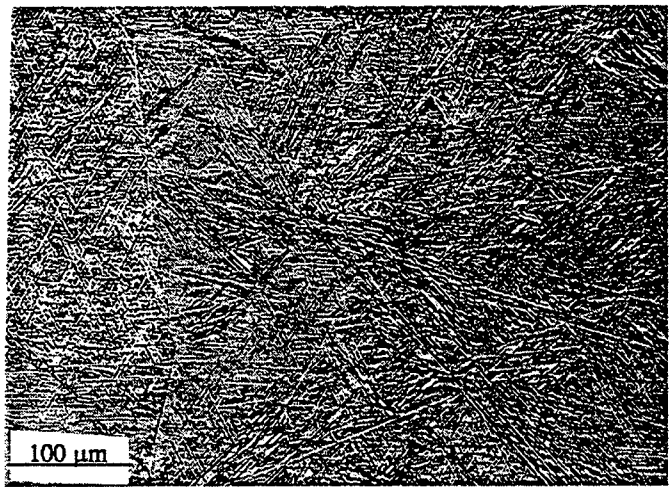

Figure 1b: Microstructure of the pre-processing β-quenched Sample.

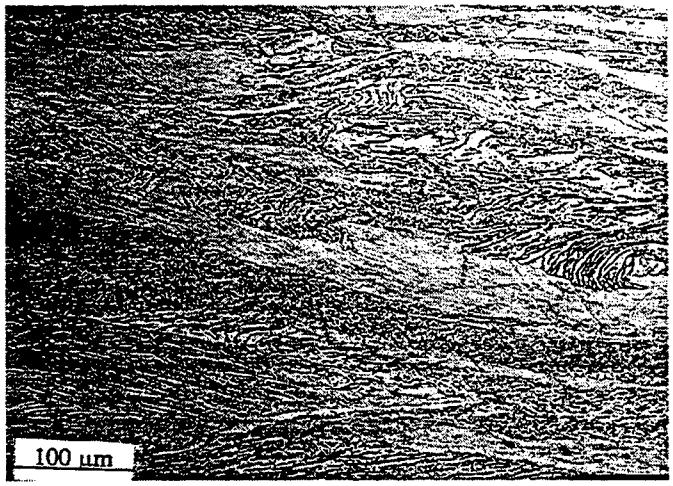

Figure 2 Microstructure of a sample that was β-annealed and hot-rolled ($\varepsilon=1.5$) at 1500°F.

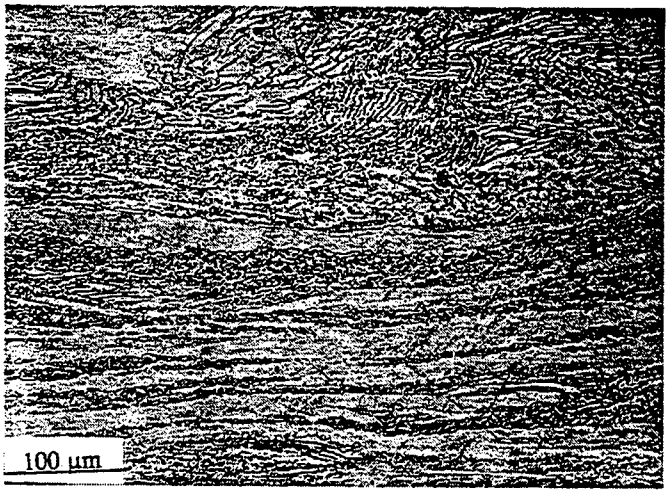

Figure 3 Microstructure of a sample that was β-annealed and hot-rolled (ε=1.5) at 1500°F and subsequently heat treated at 1500°F for two hours.

Figure 4 Microstructure of a sample that was β-annealed and hot-rolled (ε=1.5) at 1500°F and subsequently heat treated at 1750°F for two hours

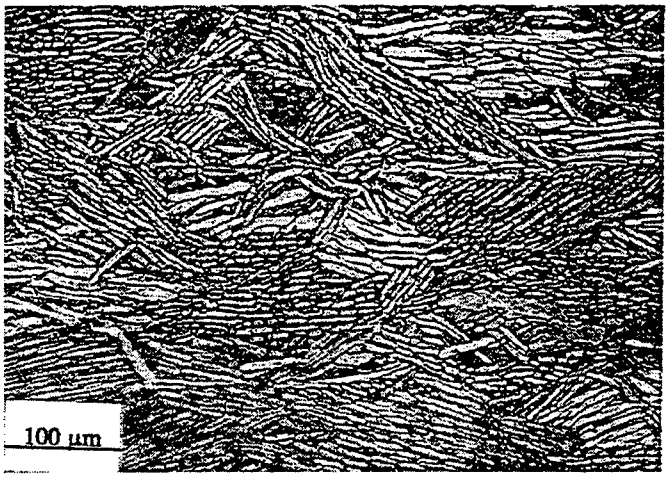

Figure 5a Microstructure of a sample that was β-annealed and lightly hot-rolled ($\varepsilon = 0.57$) at 1780°F.

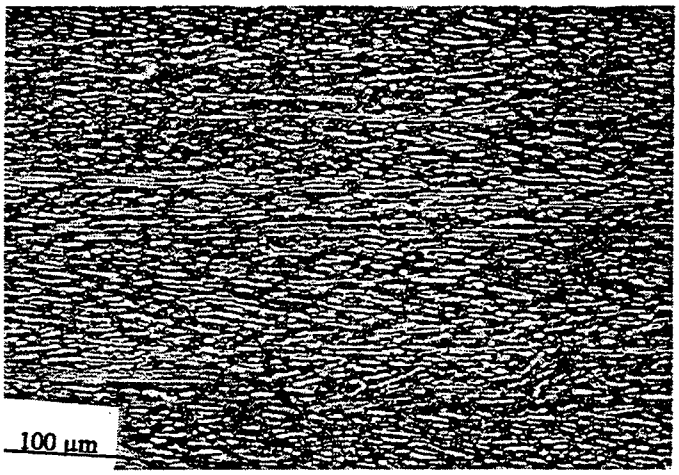

Figure 5b Microstructure of a sample that was β-annealed and heavily hot-rolled ($\varepsilon = 1.5$) at 1780°F.

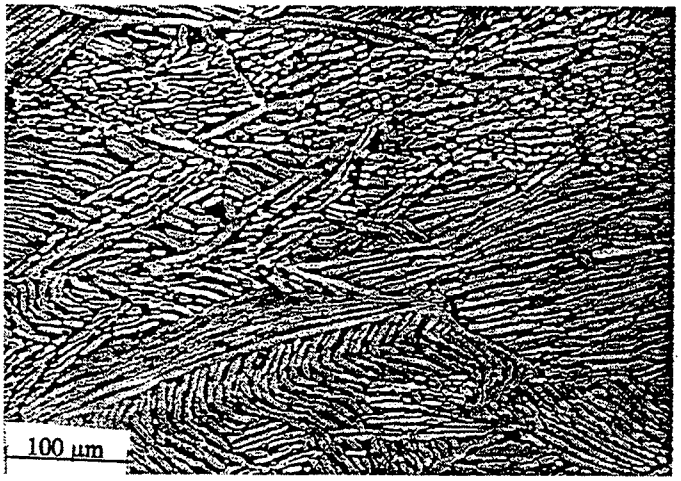

Figure 6a Microstructure of a sample that was β-annealed and lightly hot-rolled (ε=0.57) at 1780°F and subsequently heat-treated at 1600°F for two hours.

Figure 6b Microstructure of a sample that was β-annealed and heavily hot-rolled (ε=1.5) at 1780°F and subsequently heat-treated at 1600°F for two hours.

3.2 Crystallographic Texture

Pole-figures of the (0002) plane for the β-annealed β-quenched plates are presented in Figure 7. Both demonstrate preferred orientation. Although the large grain-size may make the texture appear stronger than it is, its consistency and four-fold symmetry serve as a proof of its existence. The two texture components both of them demonstrate, are in the transverse direction, and at about 45°. Rolling the plate at 1780°F (Figure 8) retained the TD texture, but eliminated the 45° and prompted an RD texture to develop. Based on the literature [4], the appearance of the RD texture was not expected for deformation below the transus. It is possible that the oxygen levels (resulting from heat treatment in air) in our samples were different than the literature and caused a shift in their location in the phase diagram.

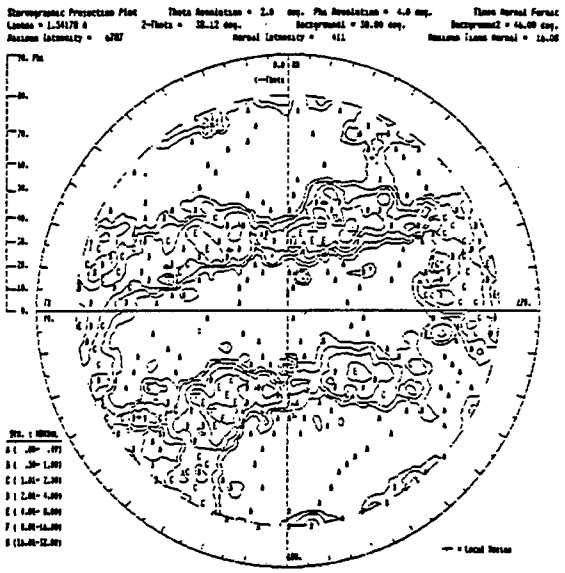

Figure 7a: Pole-figures of the (0002) plane for the β-annealed plate.

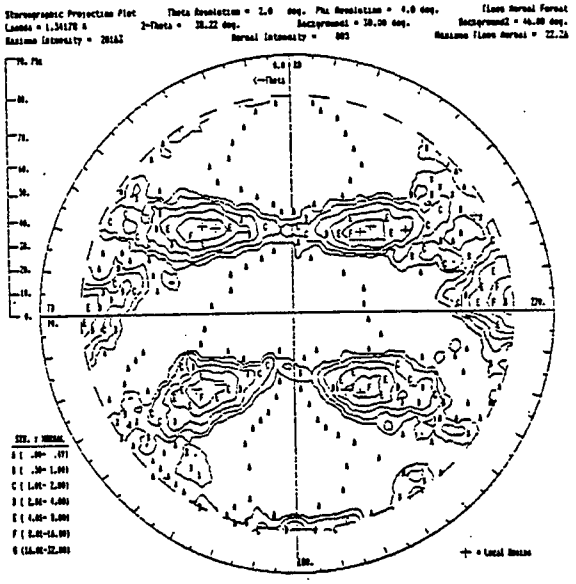

Figure 7b: Pole-figures of the (0002) plane for the β-quenched plate.

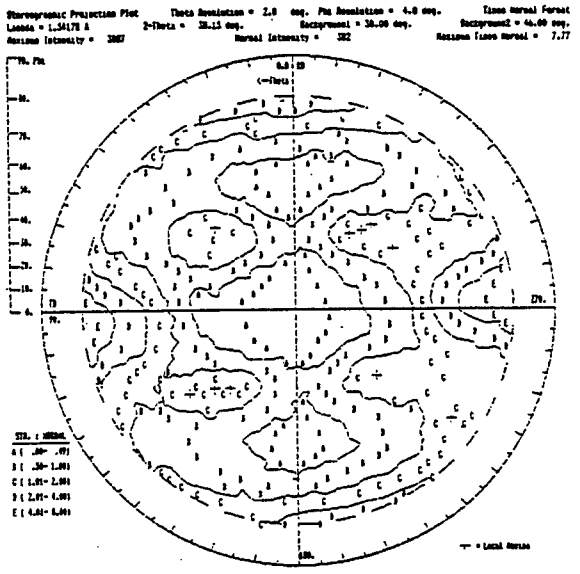

Figure 8: Pole-figures of the (0002) plane for the specimen rolled at 1780°F.

3.3 Micro-Texture

The icosahedral plots of the β-annealed sample (Figure 9a,b) reveal large clusters of similar orientation. This result is not surprising considering the large grain-size. Rolling at 1780°F reduces significantly the size of the clusters (Figure 10). Subsequent heat treatments did not increase the cluster size, but tended to foster a pancake-like structure (Figure 11) sample heat treated at 1600°F. This flattened morphology follows the original β-grains. This result is particularly interesting considering the basket-weave like microstructure of the material at this stage (see section 3.1 and Figure 6b).

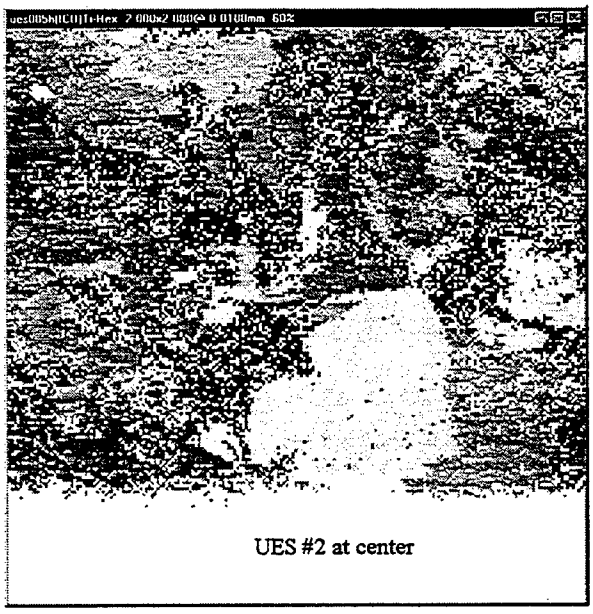

Figure (9-a) Icosahedral plots of the β-annealed sample at the center of the cross section.

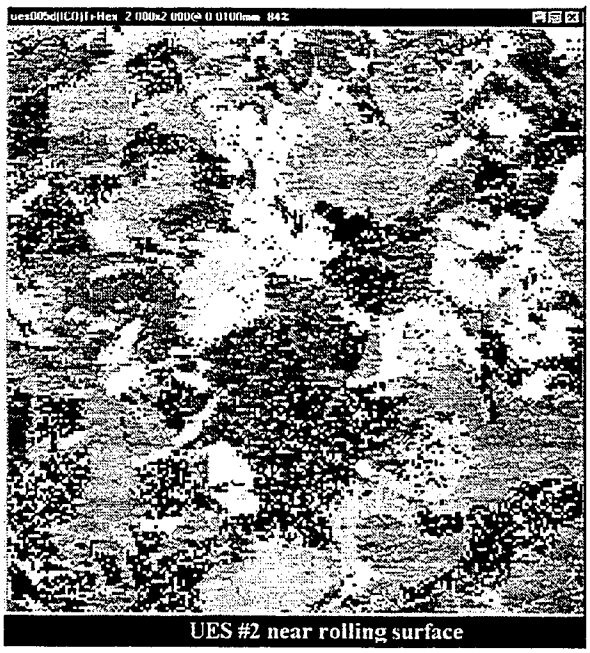

Figure (9-b) Icosahedral plots of the β-annealed sample near the rolling surface

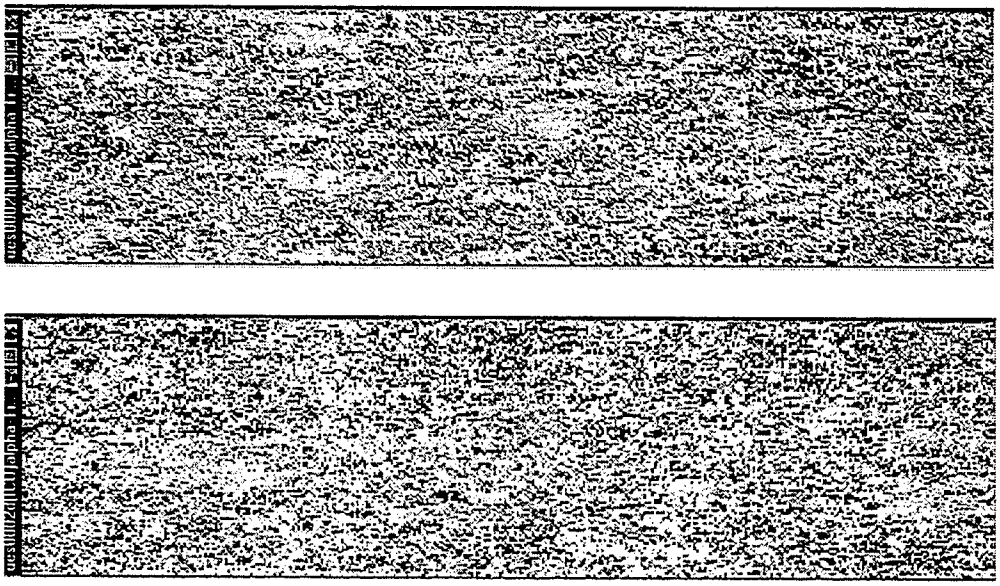

Figure 10 Icosahedral plots of a specimen rolled at 1780°F.

(a) At the center of the cross section.

(b) Near the rolling surface

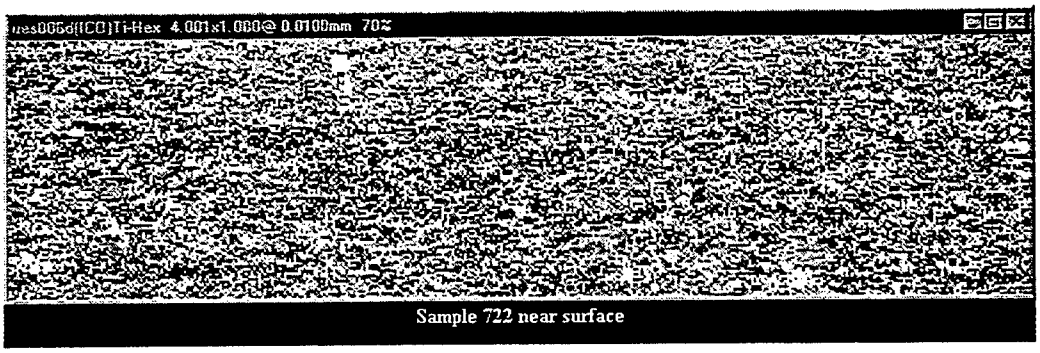

Figure 11 (a) Icosahedral plots of a specimen rolled at 1780°F then heat treated at 1600°F. Scan taken from the area near the rolling surface.

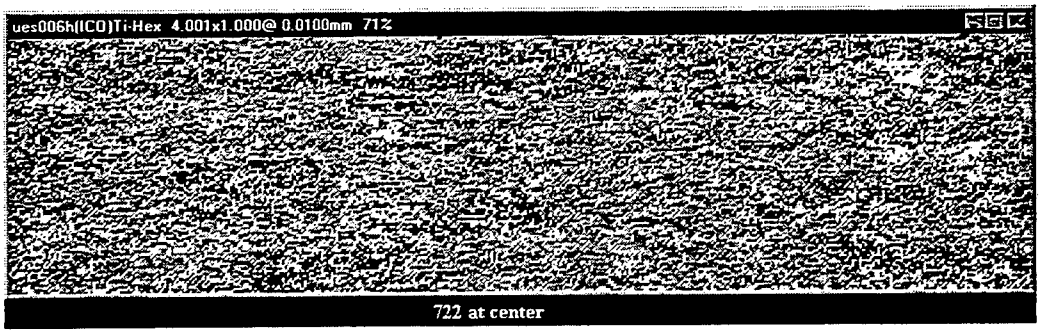

Figure 11 (b) Icosahedral plots of a specimen rolled at 1780°F then heat treated at 1600°F. Scan taken from the area near the center of the cross section

SUMMARY:

1. The samples that underwent heat treatment only, demonstrated large clusters with similar orientation. The microstructure is a typical basket-weave.
2. Light rolling the heat-treated plates resulted in a highly non-uniform deformation throughout the temperature range studied.
3. Heavy rolling close to the transus temperature resulted in a uniform deformation.
4. Heat treating the previously hot rolled samples may have fostered a pancake-like arrangement of the crystallographic orientations, that may be correlated with the original β-grains.

RECOMMENDED FUTURE STUDIES:

1. Orientation imaging microscopy studies of the evolution of micro-texture in samples that were β-quenched and subsequently hot rolled and heat treated.
2. Complete studies of samples rolled at 1725°F and 1750°F. From the results reported here, it seems as if the 1780°F temperature resulted with substantial transformation to β, testing of samples rolled at lower temperatures, will enable us to study the effect of α-phase deformation at elevated temperatures.

ACKNOWLEDGEMENTS:

Special thanks to Dr. Lee Semiatin for his contribution in numerous discussions and for his continued encouragement. Thanks also to Keith Krueger of Lambda Research for the x-ray diffraction, to John Sutliff and Scott Sitzman of General Electric for the OIM, and to Robert Lewis for his help with the metallography.

REFERENCES:

1. Semiatin, S. L., et al, "Hot Working of Titanium Alloys - an Overview", in Weiss, I., et al, eds., *Advances in the Science and Technology of Titanium Processing*, TMS, 1996.
2. Woodfield, A. P., et al, "Effect Of Microstructure On The Dwell Fatigue Behavior Of Ti-6242", in *Eighth World Titanium Conference*, Birmingham, England, October, 1995.
3. Semiatin, S. L., and Eylon, D., Private communication, 1996.
4. Williams, J. C. and Starke, E. A., "The Role of Thermomechanical Processing in Tailoring the Properties of Aluminum and Titanium Alloys", in Krauss, G., ed., *Deformation, Processing, and Structure,* (Materials Park, OH, 1984), 279-354.

STATISTICAL ANALYSIS OF FATIGUE CRACK GROWTH RATE DATA FOR 7075-T6 ALUMINUM DAMAGED BY PRIOR CORROSION

J.D. Baldwin
Assistant Professor
School of Aerospace & Mechanical Engineering

University of Oklahoma
865 Asp Avenue, Room 212
Norman, Oklahoma 73019

Final Report For
Summer Faculty Research Program
Wright Laboratory, Flight Dynamics Directorate
Wright-Patterson Air Force Base

Sponsored By:
Air Force Office of Scientific Research
Bolling Air Force Base, D.C.

August 15, 1996

ANALYSIS OF FATIGUE CRACK GROWTH RATE DATA FOR ALUMINUM ALLOYS DAMAGED BY PRIOR CORROSION

J.D. Baldwin
Assistant Professor
School of Aerospace & Mechanical Engineering
University of Oklahoma

Abstract

The differences in fatigue crack propagation behavior in 7075-T6 aluminum alloy between specimens damaged by corrosion and those in a baseline (noncorroded) condition are examined using a statistical hypothesis test. Middle tension plate specimens were corroded on one side in the laboratory and subjected to constant load amplitude (K-increasing) tests in dry and moist air environments. The results show that there is a statistically-significant increase in fatigue crack growth rates in the corroded material for stress intensity values based on nominal thickness. When the specimen thicknesses were reduced to account for corrosion material loss, the difference disappeared in most of the instances examined here. In one case, the thickness correction was found to predict fatigue crack growth rates that were *slower* in the corroded material. This anomalous result suggests that full thickness corrections may not be appropriate at higher stress intensity ranges.

INTRODUCTION

In fracture mechanics-based structural durability analysis, one of the important material response parameters is the fatigue crack growth rate (FCGR), characterized by da/dN versus ΔK data. Here a is the crack length, N is the number of load cycles and ΔK is the stress intensity factor range for the load cycle. Although the fatigue crack growth rate data for a material can be presented in the form of an empirical equation (e.g., the Paris equation), it is typically given graphically. As with other types of fatigue data, crack growth experiments display considerable scatter. Usually the variability in FCGR data is viewed as a nuisance and little account is taken of it. Attempts have been made, however, at incorporating the variability into probabilistic crack growth models. Specifically, Virkler, et al. [1979] and Ghonem and Dore [1987] developed experimental data that clearly illustrates the crack growth rate variability and scatter. Recent analyses by Yang and Manning [1996] and Maymon [1996] illustrate current developments in stochastic crack growth analysis. The data scatter also becomes of great interest, however, when one is faced with the task of comparing two sets of FCGR data to detect whether they are substantially equal or not. Such an analysis is particularly important when differences in cracking behavior are anticipated due to experimental treatments such as surface condition, environment and stress ratio.

The analysis developed here has come about within the context of the U.S. Air Force Aging Aircraft program. The USAF's fleet of cargo and tanker aircraft are being operated well beyond their original design life and structural damage mechanisms that were not considered in the design process, specifically corrosion, are becoming of increasing interest in assessing the continued durability of these aircraft. It is now well-known that the average ages of commercial and military aircraft fleets are increasing, prompting an intense examination of the tradeoffs between economic efficiency and airworthiness. As the fleets age, corrosion damage and its impact on airframe durability become of particular concern. As Schutz noted [1995], fatigue strength and corrosion parameters combine in a synergistic manner that has not yet been completely described. The technical challenges facing operators of aging aircraft came into sharp focus in April 1988 when Aloha Airlines Flight 243 experienced a catastrophic failure of the forward fuselage. Although the cause of the Aloha structural failure was formally given as multiple site damage, there was a component of corrosion damage involved. Corrosion-induced aircraft accidents have occurred

throughout the history of aviation. Campbell and Lahey [1984] reported that, since 1927, there had been over 60 accidents worldwide at least partly attributable to corrosion damage. In a more recent study, Hoeppner, et al. [1995] update Campbell's statistics, reporting that since 1975 there have been nearly 700 domestic incidents and accidents in which corrosion was at least a contributing factor.

Hendricks [1991] estimated the cost of a major commercial aircraft overhaul at $2-20 million. Compared with the approximately $50-100 million required for a new aircraft, the economic incentive for operating older planes is apparent. For operators of large fleets, however, the economic burden of keeping aging aircraft operational is becoming prohibitive. In 1994, a U.S. Air Force study showed that the maintenance costs of repairing corrosion damage alone had reached the $1-3 billion per year level [Chang, 1995]. Since the Aloha accident, the issues involved in operating aging aircraft fleets have received increased attention from agencies such as the U.S. Air Force, U.S. Navy, National Aeronautics and Space Administration and Federal Aviation Administration. It is important to realize that corrosion damage, one of the primary sources of aircraft structural degradation, is not accounted for in the design structural analysis, and thus in the inspection intervals, of any major aircraft system.

The U.S. Air Force's fleet of nearly 700 C/KC-135 tanker aircraft, first designed in the mid-1950's, now has an average age of more than 30 years with none newer than 24 years old [Chang, 1995]. By virtue of its vintage, the C/KC-135 was designed before the damage tolerant design philosophy was mandated for all USAF aircraft and therefore, does not include features such as crack arrestors commonly found in more recent designs. Corrosion of the aluminum fuselage panels and wing skins has been observed with increasing regularity, particularly in lap joints and around fastener holes. In fact, corrosion has proven to be an insidious enemy, often found only after disassembly of the structure, despite the use of nondestructive inspection systems. These tendencies are observed not only in the C/KC-135 fleet, but in other aging weapons systems as well. Because of the prohibitive cost to replace the fleet, these aircraft are considered a national asset and, as such, will be expected to serve well into the next century [Lincoln, 1995]. In fact, it is anticipated that the C/KC-135's will be one of the last of the current USAF transport platforms to be retired. Because there is no plan to replace these aircraft in the near future, the effect of corrosion on structural integrity must be quantified and incorporated into the fleet maintenance procedures.

Regarding corrosion, the relevant characteristic of the operation of such aircraft is that they

spend most of their time outdoors on the ground and only a few hundred hours per year in flight. Therefore, unlike the classical case of corrosion fatigue, where corrosion and fatigue processes evolve concurrently, to a first approximation the corrosion and fatigue damage processes can be assumed to be uncoupled in the case of military transport aircraft. Only recently have fracture mechanics-based experiments designed to quantify the fatigue response of corroded metal begun to appear. Chubb, et al. [1991a, 1991b, 1995] examined the effect of exfoliation corrosion on the fatigue crack growth rates of 2024-T351 and 7178-T6 alloys. Chubb's data shows that at low ΔK levels, the corroded material experienced crack accelerations of up to five times over noncorroded material. Scheuring and Grandt [1994, 1995] used 2024-T3, 7075-T6 and 7178-T6 materials taken from retired C/KC-135 aircraft corroded in service. Scheuring notes that the lightly corroded material shows little difference in crack growth behavior compared to noncorroded material. Their data also shows that the acceleration in crack growth tends to diminish as the stress ratio R increases. While these two research teams report valuable, although limited, results, the conclusions drawn are based on qualitative comparison of the data. Lacking a statistical analysis, it is difficult to separate the effects of the test parameters such as corrosion damage level, stress ratio and test environment.

Because of the lack of a suitable body of fatigue data on aluminum alloys damaged by prior corrosion, a material characterization program was begun by the USAF to develop some basic fatigue crack growth rate data on specimens with laboratory-grown corrosion damage. The goal of the program was to compare the crack growth behavior of corrosion-damaged material with the baseline, noncorroded material. From that data, conclusions would be drawn about the impact of corrosion damage on fatigue performance; subsequent policy decisions regarding continued airworthiness and any necessary modifications to inspection intervals and procedures would then be based on a suitably large body of experimental data.

The statistical analysis reported here was conceived to examine two issues relating to the fatigue cracking behavior of metal damaged by prior corrosion. First, the existence of any corrosion-based crack acceleration had not previously been addressed rigorously. As noted above, Chubb, et al. [1991a, 1991b, 1995] reported crack accelerations of up to five times in corroded material. On the other hand, Scheuring and Grandt [1995] observed little or no differences in the da/dN versus ΔK data for "lightly" corroded material. It is important to note that both conclusions were drawn without resorting to statistical analysis and, rather, were based on visual observation of

the data. Given the potential economic and safety ramifications of an incorrect assessment of the relative performance of baseline and corroded material, such subjective analysis is inadequate. The second issue of interest is whether or not modeling the corrosion damage as simply a thickness loss from the specimen is sufficient to describe any differences in crack growth rates; this hypothesis was initially proposed by Doerfler, et al. [1994]. If a significant difference persists after the thickness correction, one might be alerted to the presence of a secondary process effecting crack growth rates, perhaps acting on a microstructural scale. Again relying on a subjective assessment, Scheuring and Grandt reported that correcting their ΔK values for measured thickness loss did not alter the conclusion that there was no effect due to corrosion. In cases such as these, a statistical analysis of the data will allow us to address these questions in a rigorous way, avoiding the subjective nature of visual data inspection.

In this report, a statistical analysis is described that has been used to address the equality of two or more fatigue crack growth rate experiments. We begin with the body of FCGR *da/dN* vs. ΔK data segregated into two groups: the baseline group (i.e., specimens without the experimental treatment of interest) and the specimens subjected to the experimental treatment. Next, for each experiment, a curve is fit through the FCGR data using a polynomial kernel. Using the curve fits, we can then estimate the value of *da/dN* at any value of ΔK of interest for each experiment and compute the mean value of each of the two groups. A Student t-test is used to test the null hypothesis that the mean *da/dN* for each of the two groups is equal. If we are led to reject the null hypothesis, we then conclude that the experimental treatment has an effect on the fatigue cracking behavior of that material. Examples are given illustrating the analysis for aluminum alloy specimens damaged by prior corrosion compared to specimens without corrosion.

EXPERIMENTAL DATA

To motivate and illustrate the comparative statistical analysis, we will use a series of test data developed in the USAF Round-Robin Corrosion Fatigue Program. The round robin test program was carried out to explore the effect of prior corrosion on fatigue behavior of representative aircraft aluminum alloys by comparing fatigue crack growth rates in corroded and the baseline (noncorroded) specimens. *K*-increasing fatigue crack growth rate tests were conducted according to ASTM E 647 on samples of 2024-T3, 2024-T4, 7075-T6 and 7178-T6 aluminum harvested from

retired USAF KC-135 aircraft. All specimens were 1.75 inches wide and 0.062 inches thick (nominally) in the center-cracked plate configuration with EDM crack starter notches. In one half of the specimen population, corrosion was induced on one side of the specimen by exposing them to an ASTM B117 3.5% NaCl fog solution until the damage was deemed to be "severe"; no other *a priori* assessment of the corrosion damage was made. The other half of the specimen population remained in an as-delivered (i.e., baseline or noncorroded) condition. In addition to the material condition (baseline vs. corroded), the additional experimental parameters stress ratio ($R = 0.05$, $R = 0.50$) and humidity (< 15% R.H., > 85% R.H.) were considered. The test matrix illustrating the multiple replicate full factorial design used in the testing is given in Table 1; the actual test progress to date is found in Table 2. To assist future researchers in identifying data sets with common characteristics, an index to the tested specimens is compiled in Table 3. In what follows, a test series will be considered to be all of the specimens exposed to a given stress ratio-humidity combination. The round robin testing was conducted in five different laboratories, both within and outside the Air Force. Originally, the intent of the test program was to test six replicates of each test series, but organizational difficulties prevented more than four corroded specimens from being tested in any of the conditions.

In all cases, crack lengths were measured using optical microscopes on micrometer slides. The recorded a versus N data were processed into da/dN vs. ΔK using secant interpolation and the stress intensity solution for the ASTM middle tension specimen

$$\Delta K = \frac{\Delta P}{B}\sqrt{\frac{\pi\alpha}{2W}\sec\frac{\pi\alpha}{2}} \qquad (1)$$

In this expression ΔP is the cycling load range, B is the specimen thickness, W is the specimen width, and $\alpha = a/W$. Any data points that exceeded the ASTM-specified maximum plastic zone size were removed from further analysis as invalid.

Since the appearance of the Paris expression summarizing crack growth rates [Paris and Erdogan, 1960]

$$da/dN = C\Delta K^m \qquad (2)$$

it has been traditional to show these data on logarithmic coordinates. Therefore, we will use the data in log da/dN - log ΔK form. For the four experimental test series, the crack growth rate data are shown in Figure 1. All of the data here is based on using the actual specimen thicknesses making

no deduction for corrosion-induced material loss. In this program, two test conditions contributed to the relatively narrow data domain. First, the scope of the data was restricted at low ΔK levels by not being from decreasing K tests. Also, the relatively narrow test specimens could not develop long enough cracks to result in high ΔK's before reaching the plastic zone size limits of LEFM, thus data at high ΔK levels have been restricted. In Figure 1, there is certainly the *appearance* of crack acceleration due to prior corrosion, particularly at lower ΔK levels. It is interesting to note that the baseline and corroded data seem to coincide at the highest ΔK levels reached during testing. Although it has not been examined rigorously, this effect is presumably due to the overriding influence of the crack tip driving force as the crack nears instability. The question remains, however, as to whether the corroded material behavior is really different from the baseline, or are the observed differences simply due to experimental data scatter. In the analysis that follows, we develop and demonstrate a statistical hypothesis test that addresses this concern.

STATISTICAL ANALYSIS

In curve fitting equations of the form $y = mx + b$ (e.g., the Paris equation in logarithmic coordinates), the statistics of the fitting parameters m and b can be computed for each data set [Draper and Smith, 1981]. A Student t-test can then be run to identify presumably equal data sets. Such an analysis would, in this case, give only a "global" determination in that the overall equivalence throughout the relevant ΔK range is tested. Our goal was to implement a "local" analysis capable of identifying ΔK ranges where the FCGR's were equal. Thus, the polynomial-based global-local method described here, using a "global" curve fit to make "local" estimates, was found to be suitable for our purposes.

The first step in the statistical analysis is to summarize each experimental data set (the crack length versus cycles data for an individual specimen) by a curve fit of the FCGR data. By establishing a curve fit for each experiment, we can then interpolate between data points and estimate da/dN at convenient values of ΔK, rather than at the actual values that will not coincide in every experiment. There have been many different models used to describe this type of data, ranging from the simple original Paris equation, to nonlinear models such as the hyperbolic sine model [Miller and Gallagher, 1981] given by

$$\log\ da/dN = C_1\ \sinh\left[C_2\ (\log\ \Delta K + C_3)\right] + C_4 \tag{3}$$

the Weibull model [Salivar and Hoeppner, 1979]

$$da/dN = e + (\nu + e)\left[-\ln\left(1 - \frac{\Delta K}{K_b}\right)\right]^{1/k} \tag{4}$$

and a three-parameter reciprocal relationship [Saxena, et al., 1981]

$$\frac{1}{da/dN} = \frac{A_1}{(\Delta K)^{n_1}} + A_2\left[\frac{1}{(\Delta K)^{n_2}} - \frac{1}{\left(K_c(1 - R)\right)^{n2}}\right] \tag{5}$$

In this study, however, we have restricted our attention to a simple fourth-order polynomial model, given by

$$\log\ da/dN = k_0 + k_1(\log\Delta K) + k_2(\log\Delta K)^2 + k_3(\log\Delta K)^3 + k_4(\log\Delta K)^4 \tag{6}$$

This equation form does a good job of capturing the sigmoidal shape of the FCGR data (something the log-linear Paris equation cannot do) and has the computational advantage of being a linear regression calculation, as opposed to the more problematic nonlinear regression required for relationships such as Equations (3 and 5). It should be noted, that Equation (6) is not being recommended as a model for general description of FCGR data; it is used here because we have found that it does a satisfactory job of describing fatigue crack growth experimental data. Other expressions have been shown to be superior for recovering crack lengths by integration [e.g., Miller and Gallagher, 1981], but that was not the goal of this investigation. To illustrate the adequacy of the quartic polynomial for describing *da/dN* versus ΔK data, the average coefficients of determination for each of the four test series are summarized in Table 4. These values indicate that the model is a reasonable reflection of the data in the intervals where the data exist. Whereas the curve fits can be expected to provide good interpolation *between* data points, they clearly cannot be used to extrapolate beyond the domain of the data.

For this analysis, the quartic curve fits were used to estimate the *da/dN* values for each experiment (specimen) at $\Delta K = 2, 4, 6, \ldots 20$ ksi·√inch. Because the starting stress intensity range was 3-5 ksi·√inch in these experiments, the $\Delta K = 2$ ksi·√inch values were not used in the statistical analysis. Recall also, that at the higher ΔK ranges, the data was censored to remove points representing invalid plastic zone sizes according to ASTM E 647. With two experimental data sets (baseline and corroded) established at a given value of ΔK, the issue of whether the data sets can be assumed equivalent, i.e., representative of a single population, can be addressed. The following

statistical hypothesis has been posed:

H0: At the $\alpha = 0.01$ significance level, the mean baseline material *da/dN* is equal to the corroded material mean *da/dN* at a given ΔK

To explore this question, an unpaired Student *t*-test was run on each ΔK group. If the null hypothesis was rejected based on the data, we concluded that there was a statistically-significant difference between the baseline and corroded material crack growth rates. If we fail to reject the null hypothesis, we must accept the possibility that there is no difference.

ANALYSIS RESULTS

For purposes of the statistical analysis, the four 7075-T6 test series summarized in Table 2 were considered separately; no attempt was made at comparing differences due to stress ratio or relative humidity. In Table 5, the ranges of ΔK are listed where statistically-significant differences in the crack growth rates were observed. Consulting Figure 1, we can see that the regions of statistically-significant difference can be easily correlated to differences in the plotted data. Also, comparing Figure 1 and Table 5, we see that the tendency for differences in *da/dN* to disappear at higher ΔK levels is confirmed by the statistical analysis. Therefore, based on the original specimen thickness, we conclude that these data show a statistically-significant difference between baseline and corroded material, primarily at low to moderate ΔK levels.

It was noted above that a second reason for developing and implementing the current statistical analysis of FCGR data was to address the validity of modeling corrosion as mechanical damage. Doerfler, et al. [1994] originally proposed this simplification without supporting data. Scheuring and Grandt [1995], based on a subjective analysis, concluded that, for "light" corrosion, differences in FCGR were accounted for by making an appropriate thickness correction. To explore this issue further, another set of statistical analysis runs were made on the 7075-T6 data. A post fracture microscopic examination of the two shortest-life specimens revealed that, on the fracture surface, the thickness lost to corrosion was between 12% and 16% of the nominal thickness. These thickness reduction figures represent average values on the specimen cross section. More detailed analysis may be able to give more localized thickness data, thus allowing improved estimates of the

instantaneous value of ΔK at various crack positions, but it is felt that this added sophistication will not affect the engineering accuracy of the material characterization. Using the 16% thickness reduction figure as representative (and recalling that such values were not available for all the specimens), each specimen thickness was reduced by 16% and modified ΔK's were computed for each data point. The resulting *da/dN* versus ΔK are plotted in Figure 2. In this Figure, it can be seen that the corroded material data now lies on top of the baseline data throughout a much larger range of ΔK. In fact, as Table 5 shows, the regions of statistically-significant differences for the reduced thickness case effectively disappear. The exception to this trend is in the $R = 0.05$, < 15% R.H. data set, where the corroded material data are seen to lie below the baseline data. In this case, the thickness correction has resulted in corroded material FCGR's that, as shown in Table 5, are significantly slower than the baseline material. This result is unexpected and is probably not correct physically. Under no circumstances would we expect corrosion damage to retard crack growth. This test series suggests that the thickness correction should be fully applied at higher ΔK levels. In spite of this unusual occurrence, the other test series are found to confirm the assumption that thickness corrections are sufficient to explain FCGR increases in the presence of corrosion damage.

CONCLUSIONS

The statistical analysis presented here has been shown to be useful in assessing the equality of fatigue crack growth rate data. It was implemented to determine whether the experimental treatment of corrosion damage was causing significantly increased crack growth rates over a baseline (noncorroded) material. Analysis of experimental data on aluminum alloy 7075-T6 revealed that, using the nominal specimen thicknesses, the corroded material had accelerated crack growth rates, especially at low ΔK levels. At high levels, the baseline and corroded data tended to coincide. When the corroded specimens were corrected for a 16% corrosion-induced thickness loss, the crack growth rates were found to be statistically equivalent over much wider ΔK ranges. This finding represents the first objective evidence that corrosion damage can be modeled as simply a thickness loss.

REFERENCES

G.S. Campbell, and R. Lahey, 1984, "A Survey of Serious Aircraft Accidents Involving Fatigue Fracture," *International Journal of Fatigue*, 6(1), 25-30.

J.C.I. Chang, 1995, "Aging Aircraft Science and Technology Issues and Challenge and USAF Aging Aircraft Program," *Structural Integrity in Aging Aircraft*, AD-Vol. 47, American Society of Mechanical Engineers, 1-7.

J.P. Chubb, T.A. Morad, B.S. Hockenhull and J.W. Bristow, 1991a, "The Effect of Exfoliation Corrosion on the Fatigue Behavior of Structural Aluminum Alloys," *Structural Integrity of Aging Airplanes*, Atluri, Sampath and Tong, eds., 87-97.

J.P. Chubb, 1991b, "Effect of Environment and Corrosion on the Fatigue of Structural Aluminum Alloys," *Aluminum Today*, September 1991, 44-49.

J.P. Chubb, T.A. Morad, B.S. Hockenhull and J.W. Bristow, 1995, "The Effect of Exfoliation Corrosion on the Fracture and Fatigue Behavior of 7075-T6 Aluminum," *International Journal of Fatigue*, 17(1), 49-54.

M.T. Doerfler, A.F. Grandt, R.J. Bucci and M. Kulak, "A Fracture Mechanics Based Approach for Quantifying Corrosion Damage," *Proceedings of the Tri-Service Conference on Corrosion*, Orlando Florida, 433-444, 1994.

N.R. Draper and H. Smith, *Applied Regression Analysis*, 2nd edition, John Wiley & Sons, 1981.

H. Ghonem and S. Dore, 1987, "Experimental Study of the Constant-Probability Crack Growth Curves Under Constant Amplitude Loading," *Engineering Fracture Mechanics*, 27(1), 1-25.

W.R. Hendricks, 1991, "The Aloha Airlines Accident - A New Era for Aging Aircraft,", *Structural Integrity of Aging Airplanes*, Atluri, Sampath and Tong, eds., 153-165.

D.W. Hoeppner, L. Grimes, A. Hoeppner, J. Ledesma, T. Mills and A. Shah, 1995, "Corrosion and Fretting as Critical Aviation Safety Issues: Case Studies, Facts and Figures from U.S. Aircraft Accidents and Incidents," *International Committee on Aeronautical Fatigue*, 22 pages.

J. Lincoln, "The USAF Approach to Attaining Structural Integrity of Aging Aircraft," *Structural Integrity of Aging Aircraft*, AD-Vol. 47, American Society of Mechanical Engineers, 9-19.

G. Maymon, 1996, "The Problematic Nature of the Application of Stochastic Crack Growth Models

in Engineering Design," *Engineering Fracture Mechanics*, 53(6), 911-916.

M.S. Miller and J.P. Gallagher, "An Analysis of Several Fatigue Crack Growth Rate (FCGR) Descriptions," *Fatigue Crack Growth Rate Measurement and Data Analysis*, ASTM STP 738, S.J. Hudak and R.J. Bucci, eds., 1981, 205-251.

P.C. Paris and F. Erdogan, 1960, "A Critical Analysis of Crack Propagation Laws," *Journal of Basic Engineering*, 85, 528-534.

G.C. Salivar and D.W. Hoeppner, "A Weibull Analysis of Fatigue-Crack Propagation Data From a Nuclear Pressure Vessel Steel," *Engineering Fracture Mechanics*, 12, 1979, 181-184.

A. Saxena, S.J. Hudak and G.M. Jouris, "A Three Component Model for Representing Wide Range Fatigue Crack Growth Data," *Engineering Fracture Mechanics*, 12, 1979, 103-115.

Scheuring, J.N. and A.F. Grandt, 1994, "An Evaluation of Fatigue Properties of Aging Aircraft Materials," USAF Structural Integrity Program Conference, San Antonio TX.

Scheuring, J.N. and A.F. Grandt, 1995, "An Evaluation of Aging Aircraft Material Properties," *Structural Integrity of Aging Aircraft*, AD-Vol. 47, American Society of Mechanical Engineers, 99-110.

Schutz, W., 1995, "Corrosion Fatigue - The Forgotten Factor in Assessing Durability," 15th Plantema Memorial Lecture, 18th Symposium of the International Committee on Aeronautical Fatigue.

D.A. Virkler, B.M. Hillberry and P.K. Goel, 1979, "The Statistical Nature of Fatigue Crack Propagation," *Journal of Engineering Materials Technology*, 101, 148-153.

J.N. Yang and S.D. Manning, 1996, "A Simple Second Order Approximation for Stochastic Crack Growth Analysis," *Engineering Fracture Mechanics*, 53(5), 677-686.

Table 1: KC-135 Corrosion Fatigue Round Robin Planned Test Matrix

	Baseline (Non-corroded)				Corroded				
	$R = 0.05$		$R = 0.50$		$R = 0.05$		$R = 0.50$		
Material	<15%	>85%	<15%	>85%	<15%	>85%	<15%	>85%	Totals
2024-T3	6	6	6	6	6	6	6	6	48
2024-T4	6	6	6	6	6	6	6	6	48
7075-T6	6	6	6	6	6	6	6	6	48
7178-T6	6	6	6	6	6	6	6	6	48
Totals	24	24	24	24	24	24	24	24	192

Totals exclude 72 spare and 4 low frequency (0.1 Hz.) specimens

Table 2: Accomplished Test Matrix

	Baseline (Non-corroded)				Corroded				
	$R = 0.05$		$R = 0.50$		$R = 0.05$		$R = 0.50$		
Material	<15%	>85%	<15%	>85%	<15%	>85%	<15%	>85%	Totals
2024-T3	6	6	5	6	3	4	3	4	37
2024-T4	7	6	6	6	1	2	1	2	31
7075-T6	6	6	6	6	4	4	4	4	40
7178-T6	6	6	6	6	2	4	2	3	35
Totals	25	24	23	24	10	14	10	13	143

Table 3: Directory of USAF Round Robin Test Specimens by Test Series

2024-T3

Baseline
R = 0.05
< 15% R.H.
2024T3-29,34,35,37,52,58
> 85% R.H.
2024T3-33,38,39,44,48,51
R = 0.50
> 15% R.H.
2024T3-28,32,40,41,45,59
< 85% R.H.
2024T3-46,50,53,54,55,60

Corroded
R = 0.05
< 15% R.H.
2024T3-65,66,97
> 85% R.H.
2024T3-61,62,91,92
R = 0.50
< 15% R.H.
2024T3-67,98,99
> 85% R.H.
2024T3-63,64,93,94

2024-T4

Baseline
R = 0.05
< 15% R.H.
2024T4-42,48,52,61,64,68,69
> 85% R.H.
2024T4-47,53,57,62,63,67
R = 0.50
< 15% R.H.
2024T4-41,46,50,51,54,65
> 85% R.H.
2024T4-43,44,45,60,72,73

Corroded
R = 0.05
< 15% R.H.
2024T4-36
> 85% R.H.
2024T4-30,31
R = 0.50
< 15% R.H.
2024T4-37
> 85% R.H.
2024T4-32,33

7075-T6

Baseline
R = 0.05
< 15% R.H.
7075T6-15,20,24,30,32,33
> 85% R.H.
7075T6-18,23,27,28,29,31
R = 0.50
< 15% R.H.
7075T6-06,14,19,21,25,26
> 85% R.H.
7075T6-02,04,07,11,17,22

Corroded
R = 0.05
< 15% R.H.
7075T6-38,39,56,68
> 85% R.H.
7075T6-34,35,66,70
R = 0.50
< 15% R.H.
7075T6-40,41,69,73
> 85% R.H.
7075T6-37,44,67,71

7178-T6

Baseline
R = 0.05
< 15% R.H.
7178T6-01,02,28,29,65,74
> 85% R.H.
7178T6-05,06,32,33,67,76
R = 0.50
< 15% R.H.
7178T6-03,04,30,31,66,75
> 85% R.H.
7178T6-07,08,35,36,68,77

Corroded
R = 0.05
< 15% R.H.
7178T6-60,62
> 85% R.H.
7178T6-24,47,57,61
R = 0.50
< 15% R.H.
7178T6-63,64
> 85% R.H.
7178T6-48,58,59

Table 4: Mean Coefficients of Determination From Quartic Curve Fits of *da/dN* vs. ΔK Data

	Mean Coefficient of Determination, r^2		
Test Series	Baseline	No Thickness Corr.	16% Thickness Corr.
$R = 0.05$, < 15% R.H.	0.9900	0.9355	0.9355
$R = 0.05$, > 85% R.H.	0.9781	0.9637	0.9637
$R = 0.50$, < 15% R.H.	0.9772	0.9714	0.9719
$R = 0.50$, > 85% R.H.	0.9806	0.9620	0.9612

Table 5: Range of Statistically-Significant Differences in *da/dN* vs. ΔK

	ΔK Range of Statistically-Significant Difference		
Experiment	No Thickness Corr.	16% Thickness Corr. regression derivative	16% Thickness Corr. local derivative
R = 0.05, < 15% R.H.	6-8	14-18	14-16
R = 0.05, > 85% R.H.	6-12	6	6*
R = 0.50, < 15% R.H.	4-12	--	--
R = 0.50, > 85% R.H.	4-8	--	--

* At $\Delta K = 6$ ksi·√in, significance was found when *t*-test was run with at failed equal variance test (p=0.0465)

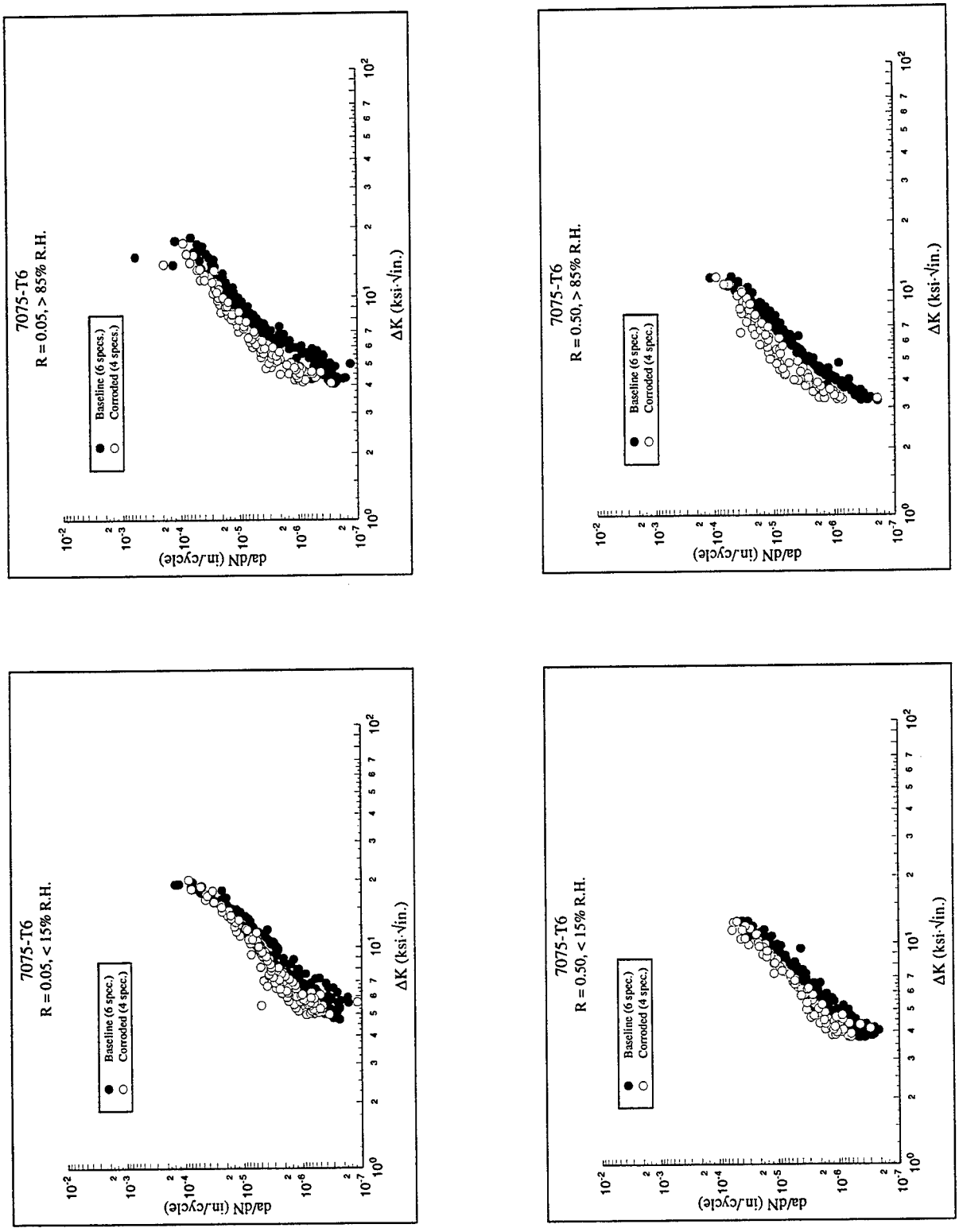

Figure 1: Fatigue Crack Growth Rate Comparison - Nominal Thickness

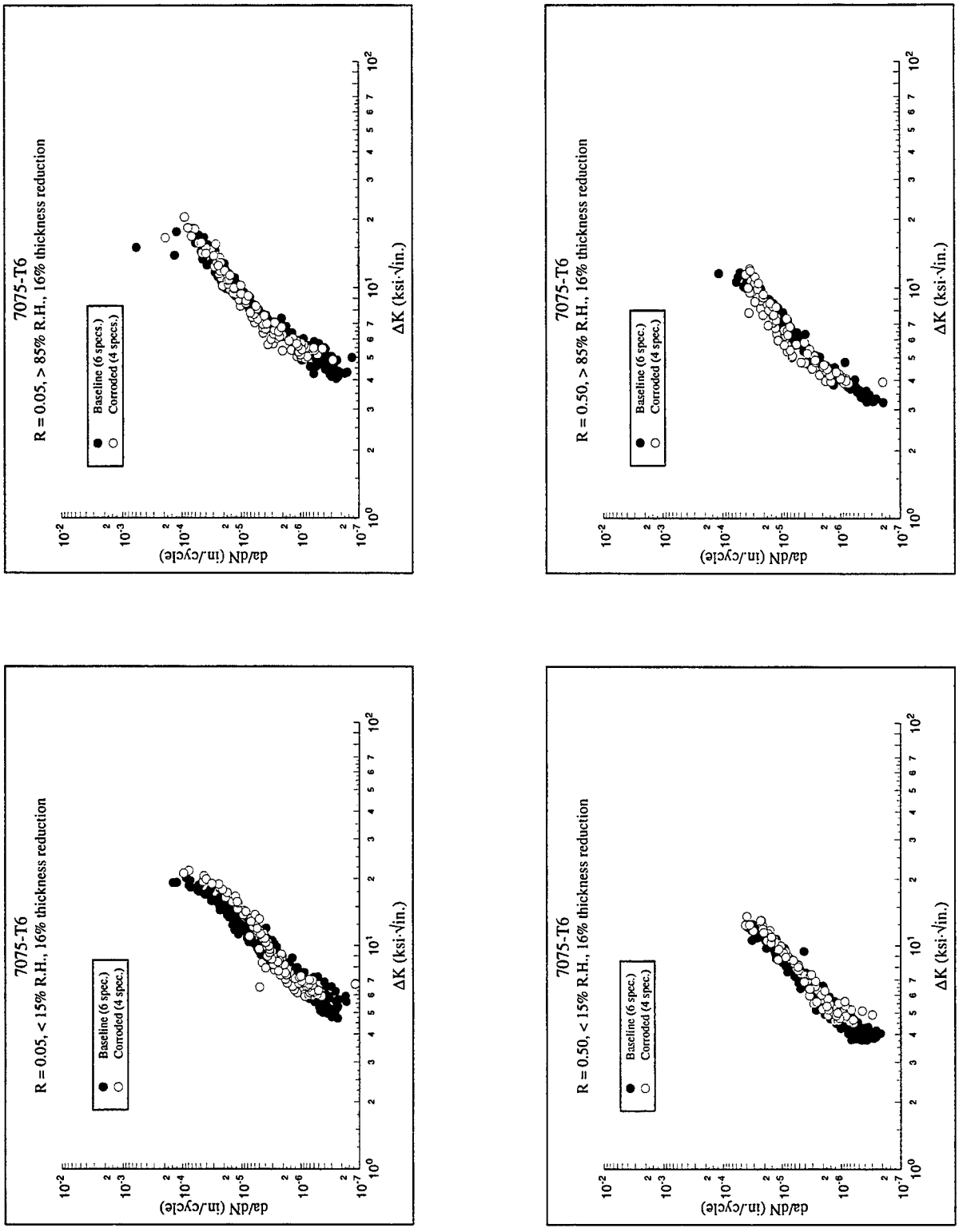

Figure 2: Fatigue Crack Growth Rate Comparison - Damage Corrected Thickness

DECONVOLUTION OF THE SPACE-TIME RADAR SPECTRUM

Armando B. Barreto
Assistant Professor
Department of Electrical and Computer Engineering

Florida International University
University Park - EAS 3942
Miami, Florida, 33199

Final Report for:
Summer Faculty Research Program
Wright Laboratory

Sponsored by:
Air Force Office of Scientific Research
Bolling Air Force Base, DC

and

Radar Branch
Radio Frequency Division
Avionics Directorate
Wright Laboratory
Wright-Patterson Air Force Base, OH.

September 1996

DECONVOLUTION OF THE SPACE-TIME RADAR SPECTRUM

Armando B. Barreto
Assistant Professor
Department of Electrical and Computer Engineering
Florida International University

Abstract

Modern processing of radar data collected through an antenna array comprising a number of elements takes advantage of the structure of the data in both space and time. In order to exploit that spatio-temporal structure, data are arranged in a three-dimensional "Datacube", where each of the dimensions corresponds to the different antenna elements, the consecutive radar pulses in a Coherent Pulse Interval (CPI) and to different range gates . The two-dimensional FFT of data collected for a single range gate (i.e., *a space-time snapshot*), reveals the presence of scatterers of interest, i.e., targets, in terms of their relative velocity with respect to the radar system (Doppler frequency) and the azimuth angle with respect to the array normal. This Space-Time Radar Spectrum may, on the other hand, incorporate the representations of unwanted phenomena, such as the radar return due to scatterers that are not relevant to the detection process, or "clutter", and the presence of jamming signals designed to obscure the existence of relevant targets. Due to the operational principles of the radar system the manifestation of a target in the space-time spectrum will have a structure that depends on the number of elements in the antenna array, N, and the number of pulses in each CPI, M. This report explores the possibility of using the advanced knowledge of the structure of the spectral configurations caused by valid targets to simplify the presentation of the velocity / angle characteristics of the targets, by the process of ***deconvolution***. Since some unwanted components of the radar signal, such as clutter, do not necessarily have the same structure in their spectral manifestation as valid targets, this report also explores the possibility of using the deconvolution process to aid in the filtering of those unwanted components. The discussion is developed around examples involving both simulated and real radar data.

DECONVOLUTION OF
THE SPACE-TIME RADAR SPECTRUM

Armando B. Barreto

Introduction

The availability of continuously increasing computational power has enabled the enhancement of state-of-the-art radar systems which are now capable of processing the radar signals in both the domains of space and time. The radar data collected through a modern radar system incorporating an antenna array with N elements and using M pulses in each Coherent Pulse Interval (CPI) are typically arranged in a data structure known as the "CPI Datacube" {1} . Figure 1 shows such arrangement. This figure also shows a simplified summary of the rationale behind radar processing algorithms. The data from each M by N set of samples associated with a given range gate, or "Space-Time Snapshot" are processed by a certain transformation to give an indication of the likelihood of the presence of a valid target. If the estimate of the likelihood of a target being present at a given range fulfills certain criteria the radar system will indicate the presence of a target at that range.

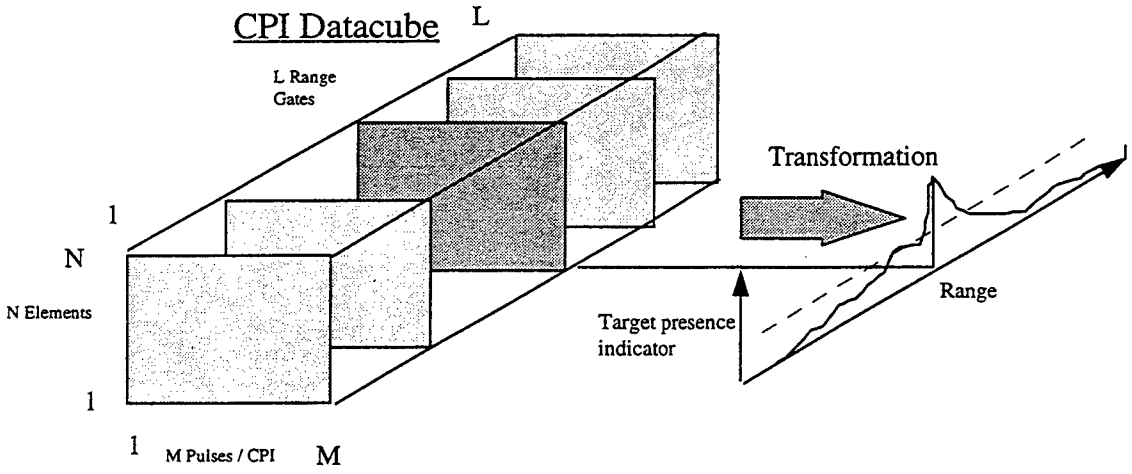

Figure 1. The CPI Datacube and the target detection process

In the absence of unwanted components of the radar signal, the power spectral density, or space-time spectrum of a space-time snapshot, obtained as the two-dimensional FFT transformation of the space-time

snapshot, would provide a good indication of the presence, relative velocity and angle of a valid target at the range under study.

In a realistic operational scenario, however, there will be a number of unwanted components in the data contained in the Datacube, which will also have an expression in the result of the two-dimensional FFT and can potentially disrupt the target detection process. The predominant types of those unwanted components are returns form irrelevant backgrounds, or *clutter*, and *jamming* signals purposely radiated to overwhelm and obscure the returns from valid targets {5}.

There are three important characteristics of the process by which the presence of targets, clutter and jamming express themselves in the space-time spectrum:

1) The space-time spectral manifestation of an elementary target (a target that exists at *one azimuth angle* and has *one relative velocity with respect to the radar system*) has a predictable format, which depends on the operational specifications of the radar system: The number of antenna elements in the array, N, and the number of radar pulses per CPI.

2) The space-time spectral manifestation of unwanted components in the radar signal do not necessarily follow the same format as for an elementary target.

3) The expressions for targets, clutter and jamming in the pace-time spectrum for a given range gate appear combined in a *additive* fashion.

To enhance the capabilities of the radar system to identify valid targets exclusively several approaches can be taken. The current Space-Time Adaptive Processing (STAP) techniques aim at the elimination of the interference components in the space-time spectrum by the application of two-dimensional filters to the space-time snapshot to place nulls in the areas of space-time spectrum where the interferences express themselves. Given the variability of the interference these two-dimensional filters need to be recalculated periodically, in a data-adaptive manner that requires the repeated estimation of the characteristics of the interference. The alternative approach to the identification of valid targets proposed in this report is the reversion of the process that transforms the information (velocity, azimuth and power) of a clearly specified

target into its expression in the space-time spectrum. This process of ***deconvolution*** of spectral expression of valid targets will be beneficial to the detection process in that it will result in a sharper and more identifiable representation for each one of the valid targets contained in the space-time snapshot. Furthermore, since the deconvolution process is based on the spectral representation of a valid target only, forms of interference not conforming to this model will not be represented in the deconvolved result, providing some partial or total elimination of those unwanted components.

Methodology

The process of deconvolution of the space-time spectrum proposed here is based on the abstraction of the whole process leading to the space-time spectrum of a snapshot containing one or several targets as a linear, shift-invariant, two dimensional transformation, $H_{NM}\{t(\phi, \omega_d)\}$, applied to an abstract "Target Field", $t(\phi, \omega_d)$. This "Target Field", $t(\phi, \omega_d)$ is the discrete representation of the presence / absence and power of elementary targets at any given azimuth ϕ and normalized Doppler frequency ω_d, within the ranges (same as ranges covered by the ordinary space-time spectrum):

$$-1 \leq \sin(\phi) \leq 1$$

$$-0.5 \leq \omega_d \leq 0.5$$

It should be noted that this "Target Field" is an abstract model synthesized from two physical quantities: The relative velocity of any targets represented in the space-time snapshot (as indicated by the corresponding Doppler frequency) and the azimuth of the targets. Thus, if a single target of unit power exists in the space-time snapshot for a given range, at an azimuth ϕ_1, moving at a velocity represented by a Doppler ω_{d1}, then the only non-zero value in the whole Target Field will be an impulse located at (ϕ_1, ω_{d1}), i.e., $t(\phi, \omega_d) = \delta(\phi_1, \omega_{d1})$.

The proposed linear, shift-invariant transformation, $H_{NM}\{t(\phi, \omega_d)\}$ models the complete process involved in the operation of the multi-element radar system (which defines the data contained in the space-time snapshot under analysis from the abstract Target Field), and the generation of the corresponding

space-time spectrum in terms of the Power Spectral Density for any given Doppler and azimuth, PSD((ϕ, ω_d):

$$PSD(\phi, \omega_d) = H_{NM}\{\ t(\phi, \omega_d)\ \}$$

Under the assumption of linearity and shift-invariance of $H_{NM}\{\}$, $PSD(\phi, \omega_d)$ can be obtained as the circular convolution of the Target Filed and the impulse response associated with $H_{NM}\{\}$, $h(\phi, \omega_d)$:

$$PSD(\phi, \omega_d) = t(\phi, \omega_d) \otimes h(\phi, \omega_d)$$

Figure 2 shows this whole process for a Target Filed with a single elementary target and the impulse response of a system with 6 antenna elements and 6 pulses per CPI (N=6, M=6).

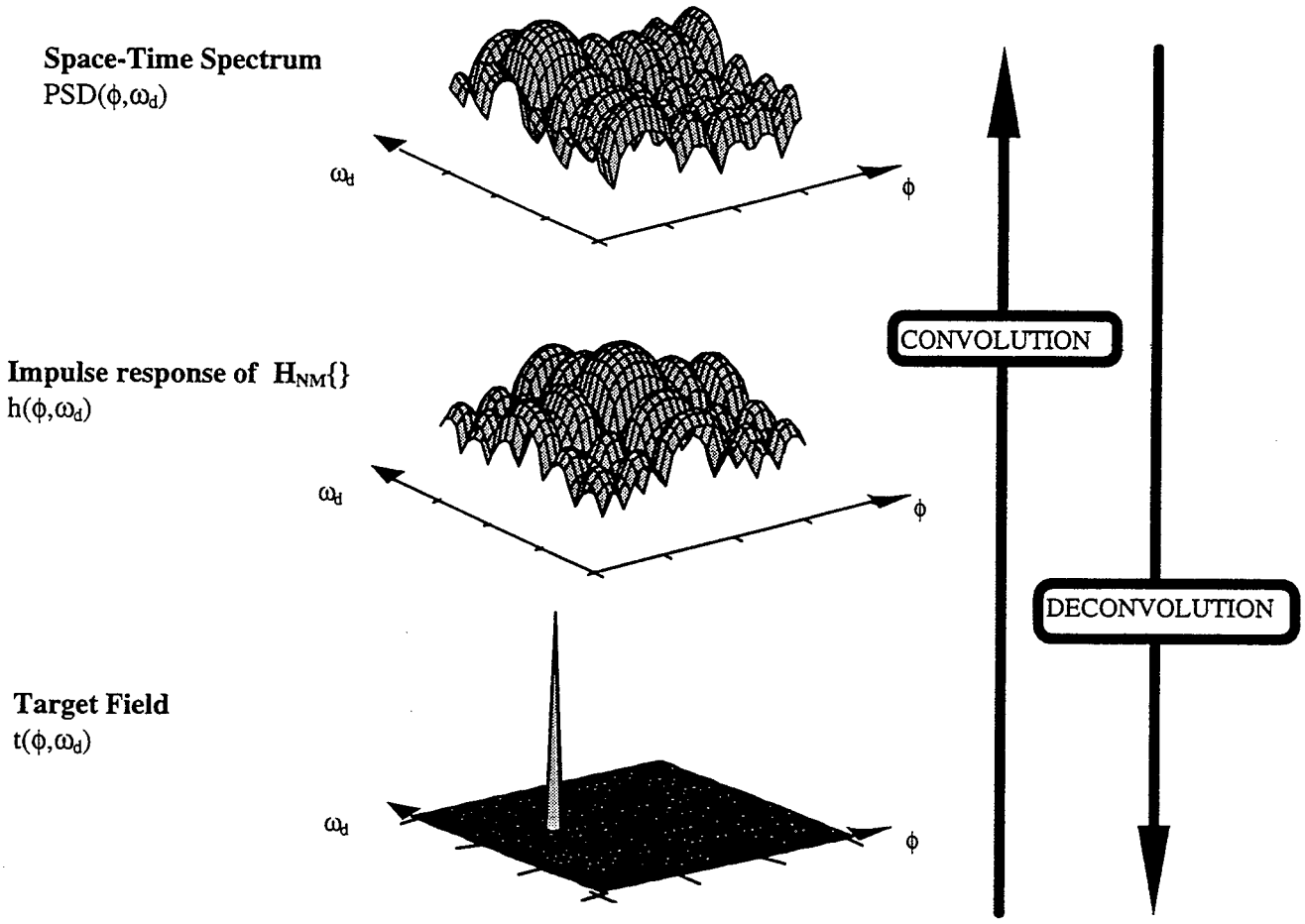

Figure 2. Relationship between the Target Field, The $H_{NM}\{\}$ transformation and the space-time spectrum under the convolution model.

Furthermore, in the context of discrete Target Fields and discrete space-time spectra, both of them with finite support , the circular convolution operation representing the application of $H_{NM}\{\}$ to $t(\phi,\omega_d)$ can be put in terms of a matrix product of the row-scanned target filed, pre-multiplied by an appropriate matrix **H**[i,j] to result in a vector representing the row-scanned time-space:

$$\mathbf{H}_{(K^2)x(K^2)}\ \mathbf{t}_{(K^2x1)} = \mathbf{PSD}_{(K^2x1)}$$

In this equation K is the assumed number of discrete values for both dimensions of the Target Field and the space-time spectrum. The [i,j] entries of the matrices involved in the above equation represent the following:

t[p(N-1) +q,1]: the q^{th} element of the p^{th} row of the original N by M target field matrix

PSD[p(N-1) +q,1]: the q^{th} element of the p^{th} row of the original N by M space-time matrix

H[i,j]: the contribution to the PSD in the Doppler, azimuth combination represented by the [i,1] element of the vector **PSD**, due to an assumed elementary target of unit power located at the Doppler / azimuth combination represented by the [j,1] element of the vector **t**.

The functional definitions of the elements in the matrix formulation of the convolution process that yields the space-time spectrum from the Target Field is particularly useful in the context of the problem at hand. This is because the **H** matrix can be generated by a numerical process that starts with the simulation of the space-time spectrum for an elementary target at zero Doppler and zero azimuth :

$$H_{NM}^{0} = H\{\delta(\phi,\omega_d)\}$$

H_{NM}^{0} can be obtained as a K by K matrix, simulating that target configuration, without any interference, using the MATLAB functions developed by Y. Seliktar, from the Georgia Institute of Technology, assuming N antenna elements and M pulses per CPI {2}. Then an augmented matrix can be formed by placing 9 replicas of H_{NM}^{0} in a 3 by 3 arrangement and each i^{th} row of the required transformation matrix **H** can be found by selecting a K by K submatrix from the augmented matrix, chosen such that the origin of the central replica of H_{NM}^{0} matches the position of the element represented by the [i,1] element of the vector **t** and then row-scanning it into a single row.

Casting the circular convolution process in the form of a matrix product has the specific advantage that it provides an immediate representation for the ***deconvolution*** process, i.e. the process that regenerates the Target Filed from knowledge of the space-time spectrum and the transformation H{ } that links them.

An immediate approach to the numerical implementation of the deconvolution process would be, assuming that the original transformation matrix H is non-singular:

$$\mathbf{H^{-1}\ PSD = t}$$

This implementation of deconvolution would also be very computationally efficient, since the bulk of the computation would be required for the one-time calculation of $\mathbf{H^{-1}}$, given the fact that H is only a function of the known characteristics of the radar system (N array elements, M pulses per CPI). Thus, H^{-1} could be calculated in advance and the prospective real-time implementation of the deconvolution would only require the product of a K^2 by K^2 matrix, times a K^2 by 1 vector (the PSD from the space-time snapshot). Unfortunately, this is an unconstrained solution that will commonly model PSD components that should be attributed to single positive targets as caused by configurations of multiples targets, some of them negative, that can also explain the PSD features in question. Figure 3 shows the example of a target field obtained by H^{-1} deconvolution from a PSD calculated for a simulated Target Filed with only one target at zero Doppler and zero azimuth. The presence of excess components, some of them negative is evident.

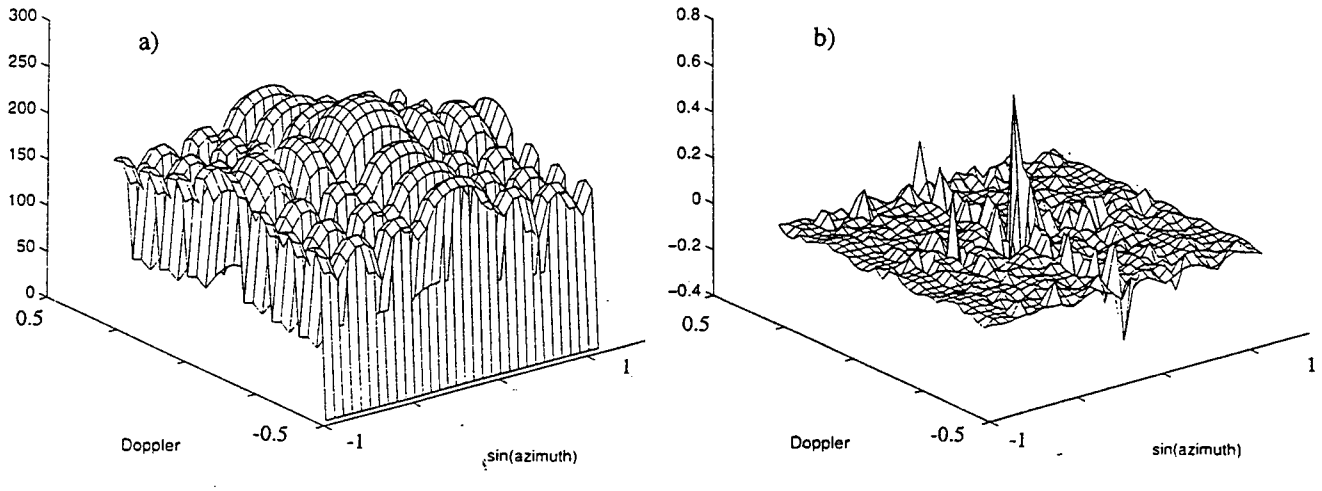

Figure 3. Example of results obtained through H^{-1} Deconvolution. a) PSD, b) Target Field

According to the initial formulation of the abstract Target Field, its values can only represent the presence ($t(\phi,\omega_d) > 0$) or absence ($t(\phi,\omega_d) = 0$) of a target at the specified Doppler frequency and azimuth. Therefore, a deconvolution result which implies a target field with negative components does not adjust to the modeling of the problem. This, in turn, indicates that we should look for a solution mechanism in which the positivity constraint can be imposed over the solution. The initially proposed solution to the system

$$\mathbf{H\ t = PSD}$$

Requires that the following be strictly verified:

$$\| \mathbf{H\ t - PSD} \| = 0$$

Alternatively, the implementation of the deconvolution of the space-time spectrum can be approached as the ***constrained minimization of*** $\| \mathbf{H\ t - PSD} \|$, subject to the condition that ***all the elements of the resulting solution PSD be positive or zero***. Numerical methods for such type of constrained minimization have been developed for the solution of problems in diverse fields. Specifically, Lawson and Hanson {6} have developed a solution to the "Non-Negative Least Squares" (NNLS) problems that carries out this constrained minimization. Their text demonstrates that the convergence of the minimization process is guaranteed, although both the time required and the accuracy of the solution may vary, according to the specifics of the matrix and vector involved.

Figure 4 shows the results of constrained minimization deconvolution of a space-time spectrum calculated for a single simulated target at 30° azimuth and 150 Hz Doppler. The simulation of the single target and the definition of the H matrix assumed the use of six antenna elements (N = 6) and six pulses per CPI (M = 6). In this case the space-time spectrum obtained from the Georgia Tech MATLAB ® routines had to be decimated from 256 by 256 values to 32 by 32, so that matrix sizes and computational time were practical. It should be noted that even after this reduction in the accuracy of the representation for the target its velocity and azimuth are indicated clearly in the deconvolved Target Field.

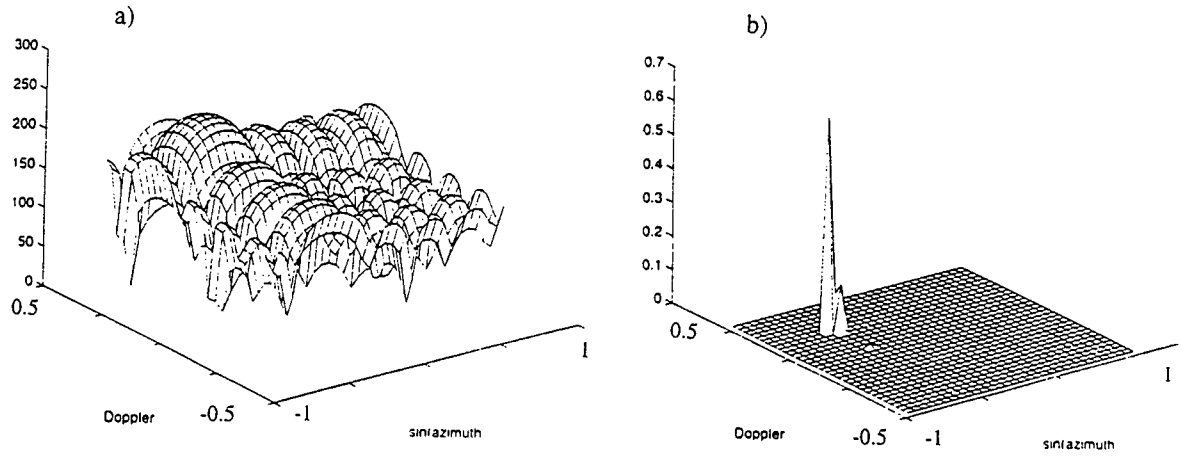

Figure 4. Example of constrained minimization deconvolution on simulated target data.

a) Original PSD, b)Deconvolved Target Field

Results

In this section of the report results of the deconvolution process as applied to space-time radar data will be shown, as evidence of the feasibility of this new approach to the enhancement of signal processing systems to retrieve information about valid targets. Initially, the results for sets of ***synthetic*** data will be shown. These data were simulated using the "simit" MATLAB ® utility developed by Y. Seliktar of Georgia Tech {2}. In reach case the synthesis of data was carried out under controlled conditions (Target, clutter and jamming information known and M and N values pre-specified). In each case, the space time spectrum was also obtained using a customized version of "dispit" MATLAB ® utility by Y. Seliktar, saving the magnitude of the space-time spectrum as a 256 by 256 matrix of real values . After decimation to 32 by 32 for ease and speed of implementation, the spectrum matrix was row-scanned into the column vector **PSD**, used in the constrained optimization. Next, results are shown of the application of space-time spectral deconvolution to ***real*** space-time data from the **C**ommon **R**esearch **E**nvironment for STAP **T**echnology (**CREST**) Data Library, collected under the Mountain Top Program {7}. The author thanks and acknowledges the assistance and access provided by the CREST office at the Maui High-Performance Computer Center.

* Results from synthetic data:

In all the results from synthetic data the general settings for the simulation were as follows:

- A single target with a power of 30 dB was simulated at -30° Azimuth and 150 Hz Doppler
- The Doppler Range was from -300 Hz to 300 Hz.
- The orientation of the "clutter ridge" was determined by a platform speed of 100 m/s
- When a jamming source was used, it was simulated at 0° azimuth
- The parameters N = 6 and M = 6 were used. The spectrum was downsampled to 32 by 32 (K = 32)

Target and low clutter and jamming: Figure 5 shows two views of the space-time spectrum for a scenario in which the power of both clutter and jamming were simulated at 10 dB.

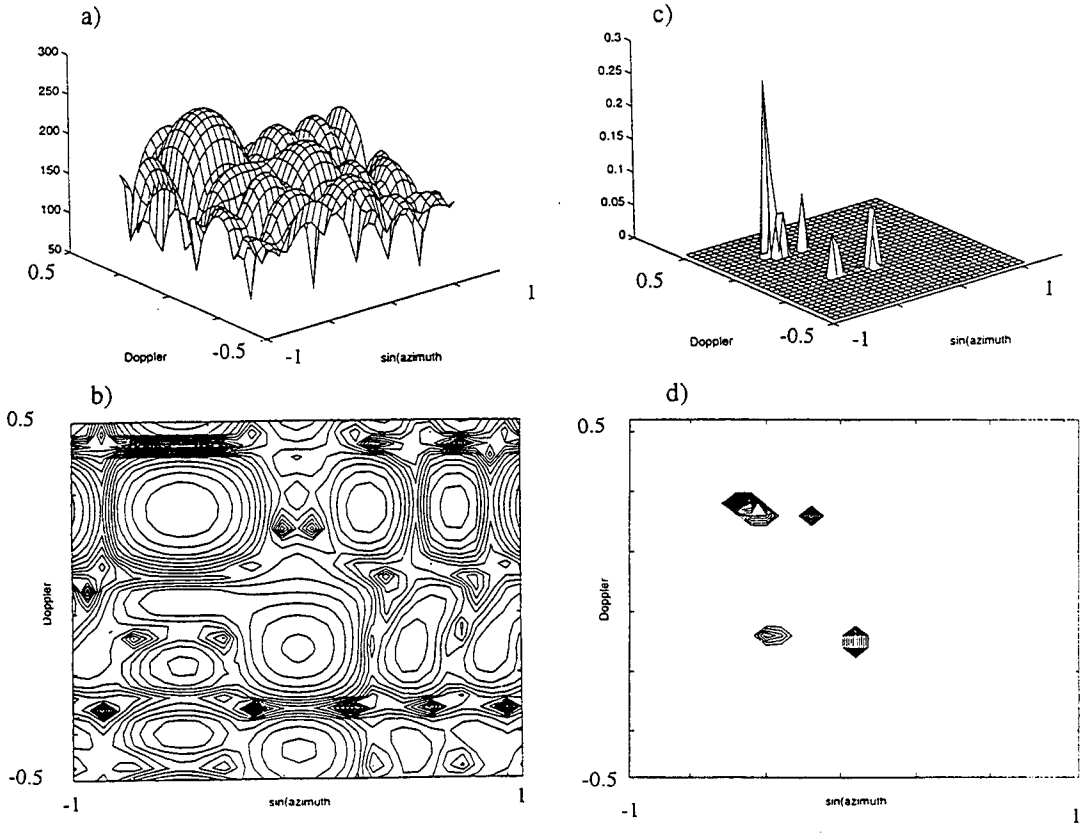

Figure 5. Deconvolution of PSD including a target and low-power clutter and jamming. a), b) 3-D and contour plots of original spectrum. c) d): 3-D and contour plots of deconvolved Target Field.

Figure 5 also shows two views of the resulting Target Field obtained by constrained minimization. It should be noted that, under these conditions of relatively low clutter and jamming, the deconvolution correctly represents the velocity and azimuth of the single target simulated and minimizes the representation of clutter and jamming. These unwanted components, in fact, are only barely modeled in Doppler, azimuth combinations were their spectra intersect, resembling the spectrum of a small valid target.

Target and strong clutter: Figure 6 shows the results of deconvolution when the power of the simulated clutter was increased to 60 dB and no jamming was included. This experiment exemplifies the capability of deconvolution to minimize the representation of clutter in the Target Filed, given the fact that it typically has a spectral manifestation with a structure different to that of a valid target.

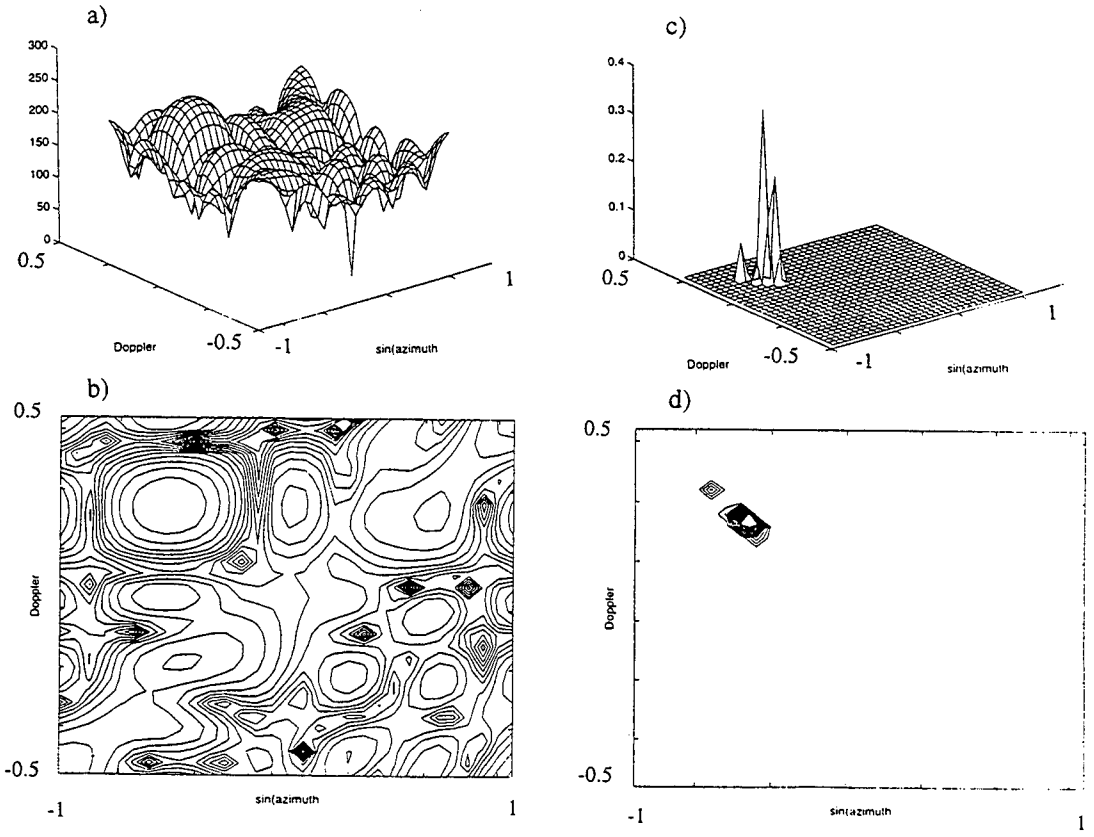

Figure 6. Deconvolution of PSD including a target and clutter. a), b) 3-D and contour plots of original spectrum. c) d): 3-D and contour plots of deconvolved Target Field.

Target and Jamming and low-power clutter: Figure 7 shows the results of space-time spectrum deconvolution when clutter with a power level of 10dB and jamming interference with a power level of 30dB were simulated along with the target. The overwhelming presence of the jammer is evident in both views of the space-time spectrum. In this case, the spectral expression of the jamming resembles a succession of the typical spectral patterns of valid targets, arranged along a line of constant azimuth (0°). Accordingly, the deconvolution process modeled the jammer as a series of targets at 0° azimuth, obscuring the retrieval of the true valid target in the simulation.

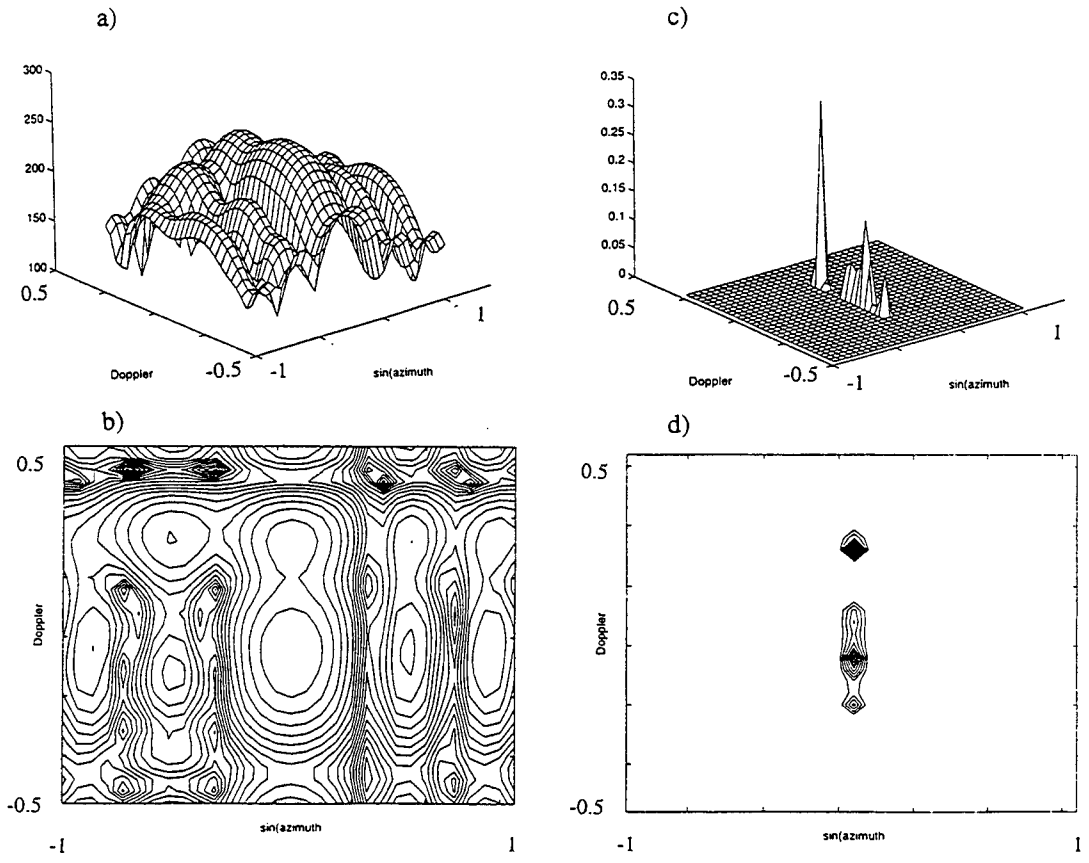

Figure 7. Deconvolution of PSD including a target , jamming and low-power clutter. a), b) 3-D and contour plots of original spectrum. c) d): 3-D and contour plots of deconvolved Target Field.

* Results from real radar data: In order to verify the validity of the deconvolution method to retrieve an accurate representation of the Doppler and azimuth of targets sensed through a real radar system, some files from CREST Data Library have been processed. Real data were also used to confirm the observations regarding the decreased sensitivity of the deconvolution process to clutter components of the space-time spectrum.

Radar Data including a moving target simulator and IDPCA clutter: The following two experiments show the results of constrained minimization deconvolution on space-time spectra of data collected through the Radar Surveillance Technology Experimental Radar (RSTER) using the Inverse Displacement Phase Center Array (IDPCA) at WSMR, New Mexico. Although the Array is physically at a fixed location, the sequencing of the transmitted pulses in the IDPCA produces clutter returns equivalent to those sensed by a moving antenna array. The Internal Test Target Generator in the RSTER was used to generate a target signal in the record.

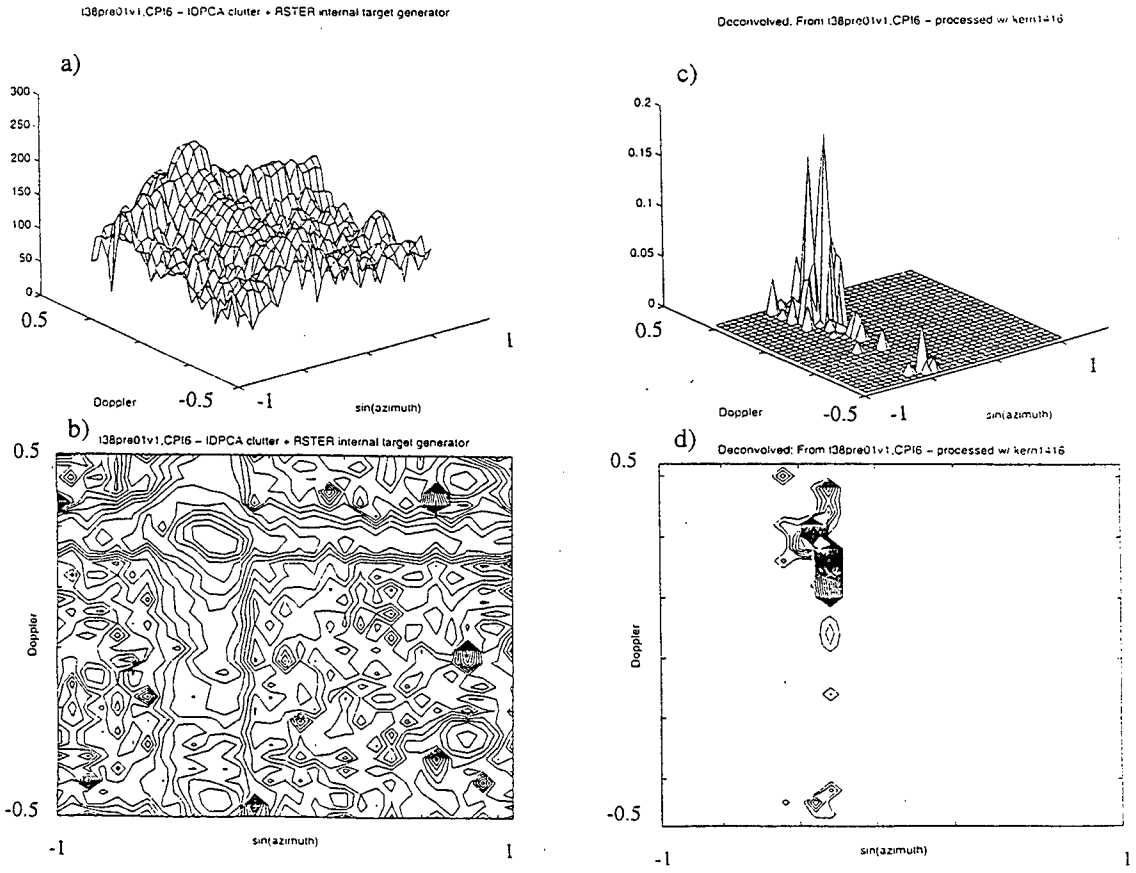

Figure 8. Deconvolution of file t38pre01v.cpi6.mat. a), b) Original spectrum. c) d): Target Field.

Figure 8 shows the original space-time spectrum and the deconvolved Target Field for data file t38pre01v1.cpi6.mat . Here again, the original 256 by 256 space-time spectrum had to be downsampled to 32 by 32 to reduce the computational load of the solution. The spectral manifestation of the target is discernible in the original space-time spectrum, but it is much more clear and localizable in the deconvolved Target Field. There is virtually no evidence of a "clutter ridge" in the deconvolved Target Field. Figure 9 shows the results for a similar data file: t38-04v1.cpi1.mat. Here the deconvolved Target Field is almost exclusively defined by a non-zero target element, corresponding to the identifiable Doppler and azimuth of the discernible target in the original space-time spectrum, with no representation of clutter.

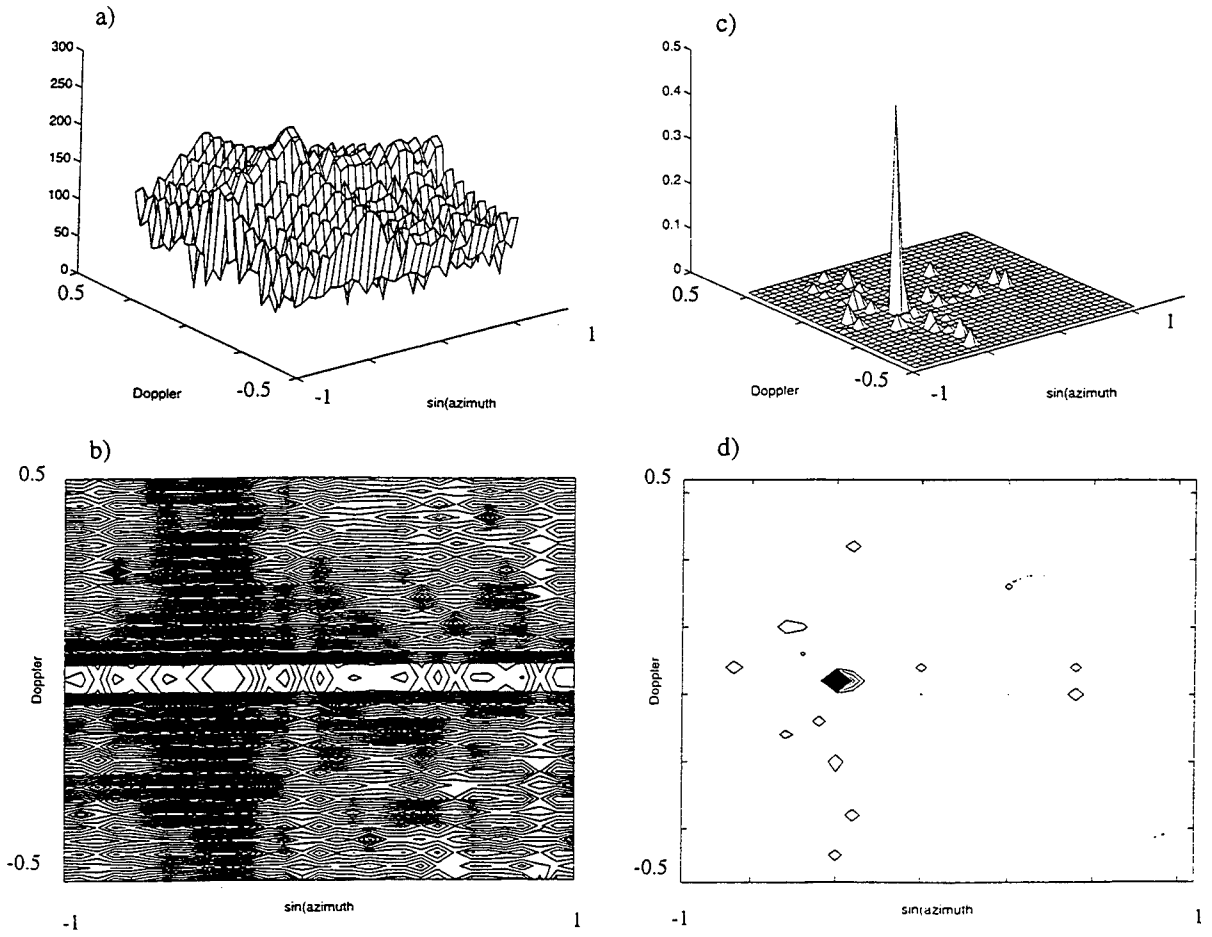

Figure 9. Deconvolution of file t38-04v1.cpi1.mat. a), b) Original spectrum. c) d): Target Field.

The final example of deconvolution results from real data, shown in Figure 10, illustrates the level of resistance of the deconvolution process to represent unwanted spectral components that do not conform to the pattern of valid targets. The file, mmit003v1.cpi1.mat, does not contain targets. It only contains "Hot clutter" and light effects of a jammer, which have already been mitigated in the original space-time spectrum. The results of constrained minimization deconvolution show a Target Field comprised of several disorganized and very low-power components (the heights of the elements in the 3-D Target Field plot are much smaller than those of targets in Figures 8 and 9.)

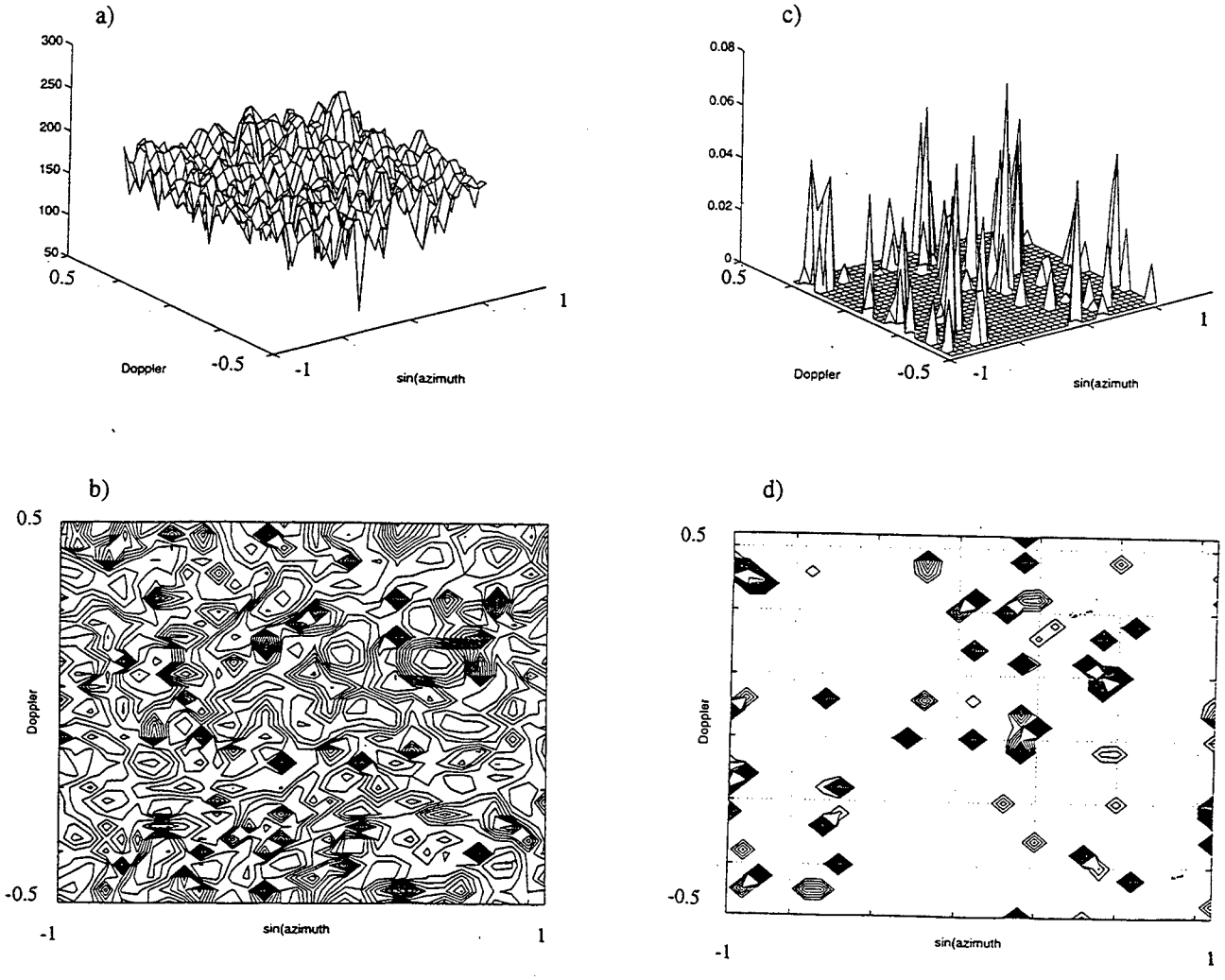

Figure 10. Deconvolution of file mmit003v1.cpi1.mat. a), b) Original spectrum. c) d): Target Field.

Discussion

The results of constrained minimization deconvolution shown in the previous section confirm the potential of this technique to:

a) Accurately model the presence of valid targets in the Target Field, clearly defining their azimuth and their velocity, as represented by their Doppler frequency.

b) Provide only a limited representation of space-time spectrum components that do not conform to the spectral patterns of valid targets, such as clutter.

It should be noted that the above experiments were carried out on space-time spectra downsampled from their original 256 by 256 size to a reduced size of 32 by 32. This was done to bring the amounts of storage and processing cycles involved to levels manageable by the system used for this project. The impact of this simplification was less pronounced in the synthetic data experiments, where the number of antenna elements, N, and the number of pulses per CPI, M, were both set at a value of six. It is interesting to note that, for the purpose of deconvolution, the wider sidelobes in Doppler and azimuth that result from these low values of N and M actually contribute to a good definition of the target spectral pattern in a downsampled spectrum (K = 32). In contrast, spectra of real space-time snapshots obtained from the CREST Data Library, recorded using N = 14 and M=16, experienced significant loss of detail through downsampling, relative to the size of the lobes of the target spectral pattern. These limitations in both the spectra under analysis and the impulse response used to form the **H** matrix required for the deconvolution influenced the appearance of spurious non-zero values around the main components of the recovered Target Fields.

The capability of the constrained minimization deconvolution to partially avoid the representation of clutter was evidenced with both synthetic and real (IDPCA) clutter. This feature of the process is attributed to the fact that the spectral manifestation of clutter is, in general, different from that of a valid target, which is the one model that is being used for the reconstruction of the Target Field. On the other hand, experiments involving synthetic jamming showed that the characteristic spectral pattern of *barrage*

jamming, spanning all frequencies along a single azimuth line, is interpreted by the deconvolution process as the superposition of a series of targets with different velocities but lined up in a single angle.

While the deconvolution process does not appear to be able to discard jamming interference in the reconstruction of the Target Field, its ability to accentuate the presence of valid targets and significantly reduce the representation of clutter makes it suitable for its integration to partial adaptive algorithms that excel in removing uni-directional jamming interference {8}. Specifically, spectral deconvolution could be proposed as post-processing to follow standard beamforming techniques (adaptation in space only).

In considering the merits and potential of this new form of space-time radar data, it must be kept in mind that this approach attempts to make an efficient use of the combined ***features in space and time of data samples captured in a single space-time snapshot.*** This is in sharp contrast with most fully- or partially-adaptive space-time processing methods for airborne radar {1}, {3}, {4}. In most of those approaches the required knowledge about the interference and the target is made accessible by resorting to the processing of augmented sets of data. For example, the estimation of the interference covariance matrix $\boldsymbol{R}_u$, used for the definition of the STAP weight vector that is appropriate for a single space-time snapshot requires the processing of a number of snapshots "surrounding" the snapshot under study. This "Sample Support" around the snapshot of interest may involve 2MN to 5MN auxiliary snapshots, each containing MN space-time samples, under the assumption that the interference is effectively stationary. So, calculation of a single weight vector, optimized for a specific combination of range, expected target Doppler frequency and expected azimuth may require manipulation of a matrix $\boldsymbol{R}_u$ of size $(MN)^3$ by $(MN)^3$, in the fully adaptive case {1}. Additionally, in the absence of *a priori* knowledge about the expected velocity and azimuth of the target or targets, a number of different weight vectors need to be calculated and applied to each space-time snapshot under study, to explore the possibility of finding a target in each Doppler / azimuth cell of interest within the whole space-time spectrum.

In the context described above, it may be suggested that this new approach to the detection of relevant targets in space-time radar data may be used, after standard adaptive beamforming to minimize the effects

of *barrage* jamming, to indicate the Doppler / azimuth combinations that may contain a target, if any. Since the process of deconvolution may be carried simultaneously with any of the other fully- or partially-adaptive STAP methods, this form of *preselection* of Doppler / Azimuth cells to study could expedite the determination of presence or absence of a target in a given space-time snapshot.

Conclusions

This report has presented an exploration into the proposition of an alternative approach to the definition of targets from space-time radar data. Most of the current space-time adaptive processing methods concentrate in the development of multidimensional filters aimed at establishing nulls in the areas of the space-time spectrum where the interferences lie. In order to achieve this goal extensive *knowledge about the interference type is needed*, which is ordinarily estimated from additional data. In contrast, the proposed deconvolution approach is based on the knowledge available about the space-time spectral manifestation *of a valid target*, minimizing the representation of some forms of interference, such as clutter, precisely because their spectral manifestation does not conform to the model sought (the spectral pattern associated with a valid target). The shift of the focus in this alternative approach, from finding out and de-emphasizing the interference, to finding out and emphasizing the target prompts to the potential application of space-time spectral deconvolution as a parallel method to other STAP algorithms, within a comprehensive detection system.

In this project an implementation for the deconvolution of discrete space-time radar spectra was proposed. This implementation is developed as the constrained minimization of the norm of the difference between the two sides of the equality relating the abstract "Target Field" and the space-time spectrum of radar data contained in a single snapshot. The proposed implementation was used to prove the feasibility and potential of the deconvolution concept with both synthetic and real data. In both cases the method showed the ability to properly represent valid targets while significantly de-emphasizing clutter. On the other hand, the method was only able to de-emphasize the representation of jamming interference of low power. Accordingly, it was suggested that for a realistic scenario an adaptive beamforming pre-processing

block aimed at canceling jamming would greatly benefit the performance of the deconvolution approach. It is important to note, however, that while jamming interference may be very powerful and overwhelm a target detection system, it is still a "one-dimensional" interference (single azimuth). On the other hand, space-time deconvolution appears to be useful against some forms of interference that are truly two-dimensional in nature, such as the clutter ridges that appear in spectral configurations (e.g. diagonals) that effectively span a full range of Doppler frequencies and azimuth values.

References:

1. Ward, "Space-Time Adaptive Processing for Airborne Radar", Technical Report # 1015, Lincoln Laboratory, MIT, Lexington Massachusetts, December 1994.
2. Y. Seliktar, D. Williams and J. McClellan, "Evaluation of Partially Adaptive STAP Algorithms on the Mountain Top Data Set", ICASSP 96 (pre-print).
3. Wang and L. Cai, "On adaptive Spatio-Temporal Processing for Airborne Surveillance Radar Systems", IEEE Transactions on Aerospace and Electronic Systems, Vol. 30, No. 3, July, 1994, pp. 660 - 669.
4. C. Barile, T. P. Guella and D. Lamensdorf, " Adaptive Antenna Space-Time Processing Techniques to Suppress Platform Scattered Clutter for Airborne Radar", IEEE Transactions on Aerospace and Electronic Systems, Vol. 31, No. 1, January 1995, pp. 382 - 389.
5. Skolnik (ed.) , "Radar Handbook, 2nd. Edition", McGraw-Hill Publishing Co., 1990.
6. Lawson and R. Hanson, " Solving Least Squares Problems", Prentice-Hall Series in Automatic Computation, 1974.
7. Titi, "An overview of the ARPA/NAVY Mountaintop Program," 1994 IEEE Long Island Section Adaptive Antenna Systems Symposium, Melville, New York, November 7-8, 1994.
8. Compton, Jr., "Adaptive Antennas, Concepts and Performance", Prentice-Hall, 1988

THE USE OF WAVELETS AND NEURAL NETWORKS IN DATA COMPRESSION, DATA FUSION AND THEIR EFFECTS ON TARGET IDENTIFICATION

LARRY A. BEARDSLEY
INSTRUCTOR OF MATHEMATICS
DEPARTMENT OF MATHEMATICS

UNIVERSITY OF TEXAS
26th & SPEEDWAY
AUSTIN, TX

Final Report for:
Summer Faculy Research Program
Wright Laboratory
Armament Directorate
Eglin Air Force Base, Florida

Sponsored by:
Air Force Office of Scientific Research
Bolling Air Force Base, DC

and

Wright Laboratory

September 1996

THE USE OF WAVELETS AND NEURAL NETWORKS IN DATA COMPRESSION AND FUSION WITH RESPECT TO TARGET IDENTIFICATION

Larry A. Beardsley
Instructor of Mathematics
Department of Mathematics
University of Texas

Abstract

The usefulness of wavelets in digital and signal processing has been widely accepted and appreciated for the past several years. Also, the need for data compression as well as the ability to train networks via radial basis functions has been known for the past decade. This research was conducted for the purpose to ascertain the benefits of using wavelets for data compression followed by the use of a radial basis function to determine if data fusion in the context of infared and passive millimeter wave imaging can benefit the identificatiion of potential targets as well as discriminate between a non-target. The study showed that data compression can be attained while retaining a high percentage of image characteristics of a target. Also, it is conjectured that data fusion most likely enhances target identification. However, further study needs to be udertaken to determine under what conditions data fusion is most successful. Finally, further investigation needs to be done to determine how well a non-target can be discriminated from a non-target using neural networks.

THE USE OF WAVELETS AND NEURAL NETWORKS IN DATA COMPRESSION AND DATA FUSION WITH RESPECT TO TARGET IDENTIFICATION

LARRY A. BEARDSLEY

Introduction

In the recent past, the need for data compression has been recognized in many different applications. One of the most well-known uses of data compression is in its value to fingerprinting. As of June, 1994, the FBI had about 30 million sets of fingerprints [5]. This number has substantially increased. These need to be digitized. For example, when a thief is apprehended, fingerprints are recorded electronically. A central computer looks for a match. Until the early 1990's, this process was time consuming and this would be costly to the chances of apprehending of the criminal in time that could be valuable. In the beginning, it was expected that older Fourier methods would succeed here. However, with a compression ratio of 20:1, the fingerprint ridges could not be easily followed due to the fact that lines were broken between one eight-by-eight square and the next. Also, the short-timed Fourier transform introduced too much blocking. With the used of wavelets, the image can be compressed at the given ratio of 20:1 with little loss of information.

With the above applications and even earlier ones, it was conjectured by prominent individuals in academia, industry, and the defense agencies, that there may be widespread advantages to military applications. Since time is of the essence when imaging a military target with either passive millimeter wave or infared or both, the less the amount of data to be processed to obtain virtually the same target, the better. Since the advent of the Coiflet and Daubechie wavelet, great work has been accomplished in many applications, and data compression is one of these.

For the past year, the effect of using wavelets in military applications has been studied. This study was undertaken to determine if wavelets were beneficial in target identification with less data. Also, later in the research period, the study of neural nets and radial basis functions was underaken to see how it benefited in target recognition using the two methods of imaging, passive milliter wave and infared. No strong results are presented in this paper with respect to this last venture due to time constraints. However, the value of the use of neural nets to train for target and non-target is not to be minimized. A detailed summary report of results of compression of images and the effects of data fusion on the given images using PCNN is to be presented to the laboratory along with this final report. Due to the classification of the images and the number of them, they are not included in this report. Also, more detailed suggestions are included in that follow-up report.

Methodology

Several military targets were provided by the laboratory. These targets were in the form of what is commonly called "raw format" or "tif format". The "tif" formatted files could be opened using microsoft word. However, the wavelet analysis could not be performed in this format. Yet, the raw format could be manipulated using matlab and a wavelet

toolbox to perform both imaging and data compression. Also, results could be derived using matlab programming to determine the percentage of the image retained as well as generating histograms of the wavelet coifficients which in turn gave useful information. Also, programming was done to decompress the data. The results of data compression were very positive yielding high compression ratios while retaining the "energy" of the given picture; that is, the image was virtually the same after data compression.

The last aspect of the study took place with only a few weeks of the researcher's tenure at the laboratory. So, conclusive results were not found. However, using a method called PCCN, "pulse-coupled neural networks", to segment the data, it is conjectured that PCCN can be used in the fusion of the two methods of imaging yielding enhanced results in particular cases. Under what conditions, fusion is favorable needs to be studied as well as the accuracy that target and non-target can be discriminated.

The Experiment

Original infared and mmw images were compressed using both the Daubechie2 and Daubechie6 wavelet to compress the entire images. Then, PCNN was run on the entire image. Outlines of the regions of interest (ROI) of possible targets were generated. Then a wavelet histogram routine was used to find the 50 (or 25, or other depending on what was called for) on the largest coefficients. A window was created around the region of interest. Then, an RBF algorithm "was to be used" to train a radial basis function using the given coefficients or the the wavelet histograms. The next step was to do this for all N-1 histograms for training. Then, results were to be kept track of based on probably of hit P(Hit) and P(miss).

THE USE OF WAVELETS AND NEURAL NETWORKS IN DATA COMPRESSION AND DATA FUSION WITH RESPECT TO TARGET IDENTIFICATION

The appearance of wavelets in mathematics is not so recent in mathematics but it is fairly recent in its application to engineering, in particular to digital signal processing. The word wavelet or "*ondelette*" was first known to have been used by the French researchers, Morlet [1}and Grossman [2], [3], in the early 1980's. However, the existence of wavelet-like functions has been known since the early part of the 20th century, the first examples being the Haar wavelet and the Littlewood-Payley wavelet. Many of the ideas formulated using wavelets have their origins in work in subband coding in engineering, coherent states and renormalization group theory in physics and the study of Calderon-Zygmund operators in mathematics. However, it was not until recently that the unifying concepts necessary for a general understanding of wavelets were provided by researchers such as [5] Stromberg, Meyer, Mallat, Daubechies, and Lemarie. Since that time, the growth of applications of wavelets has been colossal with numerous authors contributing significantly to the research.

To give the reader an appreciation for how wavelets play a role in data compression, it seems appropriate that a short introduction to wavelets be given in this paper.

The wavelet transform is a tool that cuts up data, functions or operators into different frequency components, and studies each component with a resolution matched to its scale. For example, in signal analysis, the wavelet transform yields a time history in terms of its frequency components. In this one respect, the wavelet transofrm performs in much the same way as the Fourier transform. The Fourier transform extracts from the signal details of the frequency content, but loses all information on the location of a particular frequency within the signal. A partial solution is attempted by windowing the signal and then taking its Fourier transform. The problem with windowing is that the slice of the signal that is extracted is always the same length. As a result, the slice or number of data points used to resolve a high-frequency component is the same as the number used to resolve a low-frequency component. The wavelet transform's solution to this is that it adapts the width of its time slice according to the frequency components being extracted. For example, for a windowed Fourier transform expressed as

$$(T^{win}f)(w,t) = \int f(s)g(s-t)e^{-i\omega t}ds\,,$$

then the corresponding wavelet transform is

$$(T^{wav}f)(a,b) = \int f(t)\varphi\left(\frac{t-b}{a}\right)dt$$

where the position of the slice of the signal that the wavelet samples in time is controlled by *'b'* and the extent of the slice by the parameter '*a*". Wavelets are being used in signal processing to develop *best basis* methods for signal compression and signal characterization.

THE CONSTRUCTION OF WAVELETS AND THE RELATION TO DATA COMPRESSION

The construction of wavelets begins with vectors. We begin with the concept that every two-dimensional vector (x,y) is a combination of the basis vectors (1,0) and (0,1). For example, the vector (4,3) can be obtained by multiplying the first basis vector, (1,0) by 4 and the second basis vector, (0,1), by 3. In a like manner, all possible vectors can be obtained by using the same two basis vectors. The basis vectors are not unique, but the number of basis vectors for a given dimension, "n", must be also be "n". The best bases have another valuable property, orthogonality. For example, the standard basis for R^2 includes the vectors (0,1) and (1,0) , and of course their dot product is 0.

Considering four dimensions where we take the four components (x_1 , x_2 , x_3 , x_4) as the strengths of the signal, if the signal is x = (1,1,1,1), the tone is steady whereas if x = (1,2,4,8), the volume is increasing. An easy way to send a signal *x* is to give its four components. You are then using the basis for R^4 with basis vectors (1,0,0,0), (0,1,0,0), (0,0,1,0), and (0,0,0,1) , and the numbers x_1 , x_2 , x_3 and x_4 are sent. You may question how this could be less than optimal. The answer depends on the signal being transmitted.

Compression discards basis vectors that are absent or barely present in a signal. When the vectors represent different frequencies, the Fourier basis, high frequencies can often be discarded. With the standard basis, the vector (0,0,0,1) can be discarded, for example when the fourth vector is not used. It was novel in the early 1900's to devise a basis that included the constant, or scaling vector, (1,1,1,1) and the second basis vector (1,1,-1,-1), up once and down once. Alfred Haar, the German mathematician, completed a perpendicular baisis in 1910 by dilation and translatilon (ie. squeezing and shifting). He squeezed the vector (1,1,-1,-1) to produce the third vector (1,-1,0,0). Then, he shifted the third vector by two time intervals to produce the fourth vector (0,0,1,-1). These basis vectors are the columns of the Haar matrix.

$$H_4 = \begin{bmatrix} 1 & 1 & 1 & 0 \\ 1 & 1 & -1 & 0 \\ 1 & -1 & 0 & 1 \\ 1 & -1 & 0 & 1 \end{bmatrix}$$

To find the amplitudes for longer signals, averages and differences are used. The averages move up in a pyramid to be averaged again. The differences give the fine details at each level. Compression works by ignoring what the eye cannot see and the ear cannot hear. So, for example, when a signal changes quickly, it is considered unimportant; when a signal is almost steady, the signal may not be transmitted. The concept being developed here is that of what is called multiresolution. We see a signal at multiple scales, fine, medium, and coarse. The signals are resolved at each scale by details and averages.

HOW MULTIRESOLUTIONAL ANALYSIS WORKS?

Before undertaking how multiresolutional analysis works, it may be helpful to first look at how to develop a multilevel representation of a function. The goal of multiresolution analysis is to develop representations of a function f(x) at various levels of resolution. We achieve this by expanding the given function in terms of basis functions $\phi(x)$ which can be scaled to give multiple resolutions of the original function. In order to develop a multilevel representation of a function in $\mathbf{L}^2(\mathbf{R})$ we seek a sequence of embedded subspaces $\mathbf{V}_i$ such that

$$\{0\} \ldots \subset V_{-1} \subset V_0 \subset V_1 \subset V_2 \ldots \subset \mathbf{L}^2(\mathbf{R})$$

with the following properties:

(a) $\bigcup_{j \in Z} V_j$ is dense in $\mathbf{L}^2(\mathbf{R})$. (where Z is the set of integers.)

(b) $\bigcap_{j \in Z} V_j = \{0\}$

(c) The embedded subspaces are related by a scaling law

$$g(x) \in \mathbf{V}_i \Leftrightarrow g(2x) \in V_{j+1}$$

(d) Each subspace is spanned by integer translates of a single function g(x) such that

$$g(x) \in \mathbf{V}_0 \Leftrightarrow g(x+1) \in \mathbf{V}_0$$

We also seek a scaling function $\phi(x) \in V_0$ such that its integer translatges $\{ \phi(x - k) , k \in Z\}$ from a Riesz basis for the space $\mathbf{V}_0$. Then $\phi(2x - k)$ form a basis for $\mathbf{V}_1$. (Scaling by powers other than two is possible but is not discussed here.) Therefore,

$\mathbf{V}_0 = \text{span}\{ \phi(x - k) , k \in Z\}$
$\mathbf{V}_1 = \text{span}\{ \phi(2x - k) , k \in Z\}$

Since the space $\mathbf{V}_0$ lies within the space $\mathbf{V}_1$, we can express any function in $\mathbf{V}_0$ in terms of the basis functions of $\mathbf{V}_1$. In particular, $\phi(x) = \sum_{k=-\infty}^{k=\infty} a_k \quad \Phi(2x-k)$ in which a_k, $k \in Z$ is a square summable sequence. (*)

We will refer to equation (*) as the dilation equation. The dilation equation is often referred to as the refinement equation or the scaling relation.

If we now define $\phi_{m,k}(x) = 2^{m/2} \ \phi(2^m x - k)$, then $\phi_{m,k}(x)$, $k \in Z$ forms a Riesz basis for the space $\mathbf{V}_m$. The dilation parameter *m* will bae called the scale.

An example using the box function as a basis (commonly know as the Haar basis).

This example will be used to demonstrate the validity of our assumptions. Refer to figure 1 (a). .

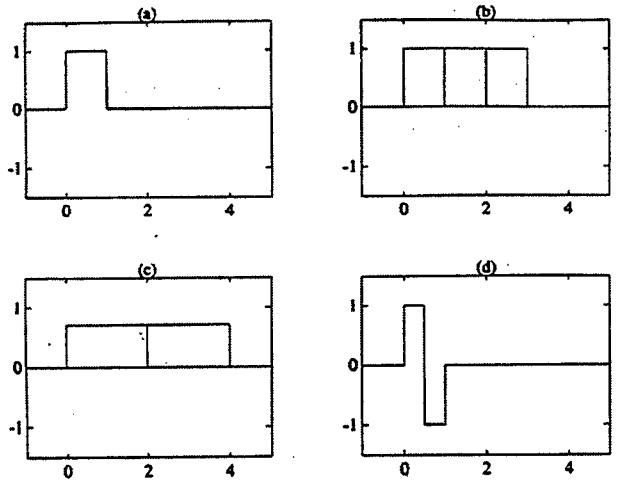

Figure 1. (a) The Haar scaling function $\phi(x) \equiv \phi_{0,0}$. (b) Translations of the Haar scaling function $\phi_{0,0}$, $\phi_{0,1}$ and $\phi_{0,2}$. (c) Dilations of the Haar scaling function $\phi_{-1,0}$ and $\phi_{-1,1}$. (d) The Haar wavelet $\psi(x) \equiv \psi_{0,0}$

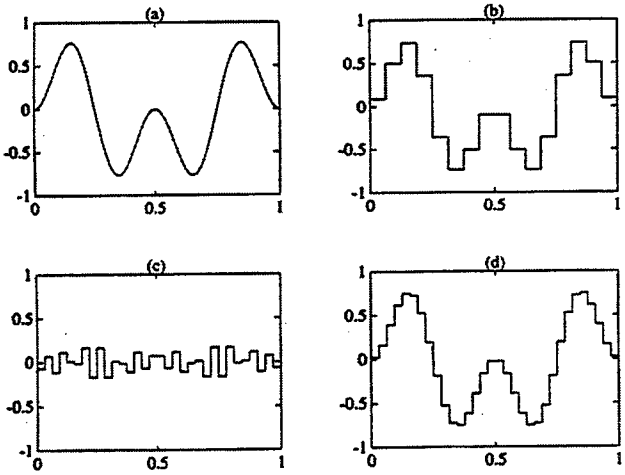

Figure 2. Successive approximations to a function. (a) $f = \sin(2\pi x)\sin(4\pi x)$. (b) Approximation at scale 4, $P_4 f$. (c) Detail at scale 4, $Q_4 f$. (d) Approximation at scale 5, $P_5 f$

$$\text{Let } \phi(x) = \begin{cases} 1, & 0 \le x \le 1 \\ 0, & \textit{otherwise} \end{cases}$$

From the figure, it is evident that $\{\phi(x - k), k \in Z\}$ is an orthonormal set. We can now approximate a function $f \in L^2(\mathbf{R})$ by its projection $P_0 f$ onto the space $\mathbf{V}_0$:

$$P_0 f = \sum_{k=-\infty}^{k=\infty} c_{0,k} \quad \Phi(x-k)$$

In general, a function may be approximated by its *projection* $P_m f$ onto the space $\mathbf{V}_m$:

$$P_m f = P_0 f = \sum_{k=-\infty}^{k=\infty} c_{m,k} \quad \Phi_{m,k}(x)$$

In fact $P_m f$ approaches f as $m \rightarrow \infty$

Figures 2 on p. 7 and Figure 3 below show two approximations to a function at consecutive scales. Note that the box function satisfies the dilation equation with coefficients $a_0 = a_1 = 1$, and $\phi(x) = \phi(2x) + \phi(2x - 1)$, and from this we can see that

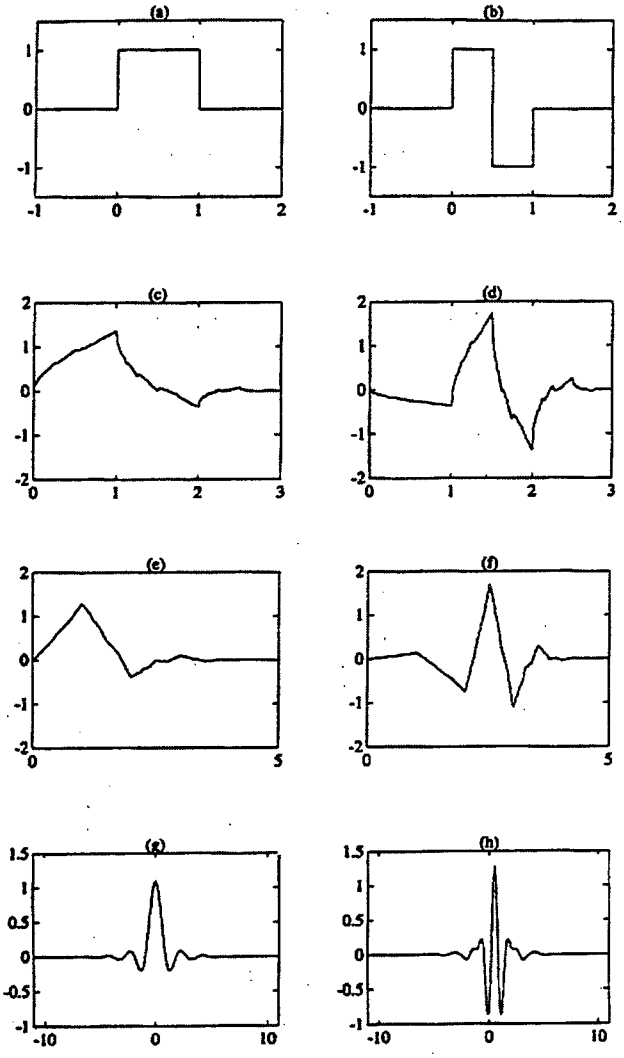

Figure 3. (a) Haar scaling function, (b) Haar wavelet, (c) Daubechies D4 scaling function, (d) Daubechies D4 wavelet, (e) Daubechies D6 scaling function, (f) Daubechies D6 wavelet, (g) Battle–Lemarié scaling function, (h) Battle–Lemarié wavelet

$V_0 \subset V_1 \subset V_2 \ldots$

This example shows that the box function can be used to develop a sequence of embedded spaces with each space spanned by the translates of the box function at that scale.

Now , multiresolution decomposition takes the expansion coefficients $c_{m,k}$ of an approximation $P_m f$, to a function at scale *m* and decomposes them into

(1) the expansion coefficients, $c_{m-1,k}$, of the approximation $P_{m-1} f$ at the next coarser scale *m* -1,

(2) the expansion coefficients, $d_{m-1,k}$ of the detail component $Q_{m-1}f = P_m f - P_{m-1} f$.

For details of the algorithm for this decomposition refer to Mallat [6]. Basically, the above process is repeated with respect to the expansion coefficients $c_{m-1,k}$ of the approximation $P_{m-1}f$ to find the coefficients $c_{m-2,k}$ and $d_{m-2,k}$, and so on. The effect of multiresolution decomposition is therefore the breaking down of the L^2 space into a series of orthogonal subspaces at different resolutions.

WHAT DO WAVELETS HAVE TO DO WITH DATA COMPRESSION?

The discrete wavelet transform (DWT) and the fast Fourier transform (FFT) have similitaries that have practical application. The DWT and the FFT are both linear operations that generate a data structure containing $\log_2 n$ segments of various lengths, usually filling and transforming it into a different data vector of length 2^n. The mathematical properties of the two transforms are also similar. For example, the inverse transform matrix for both the FFT and the DWT is the transpose of the original. As a result, both transforms can be viewed as a rotation in function space to a different domain. Concerning the FFT, the new domain contains basis functions that are sines and cosines, whereas for the wavelet transform, the new domain contains more complicated basis functions called wavelets, mother wavelets, or analyzing wavelets. Another similarity that both transforms have is that the basis functions are localized in frequency, making mathematical tools such as power spectra and scalegrams useful at picking out frequencies and calculating power distributions.

It is the most interesting dissimilarity between the wavelet transform and the fast Fourier transform that lends itself to usefulness in data compression, feature detection in images, and noise removal from time series. Individual wavelet functions are localized in space; fourier sine and cosine functions are not . This localization feature and the wavelets' localization of frequency makes many functions and operators using wavelets "sparse" when transformed into the wavelet domain. It is this sparseness, in turn, which makes wavelets viable for the aforementioned applications.

An advantage of wavelet transforms is that the windows vary. One would like to have some very short basis functions in order to isolate signal discontinuities. Also, at the same time, in order to obtain detailed frequency analysis, one would like to have some very long basis functions. A way to achieve this is to have short high-frequency basis functions and long low-frequency basis functions. This is exactly the happy medium that wavelet transforms affords us. The main point here is that wavelet transforms do not have a single set of basis functions like the Fourier transform, consisting of sine and cosine functions, but rather an infinite set of possible basis functions. Therefore, wavelet analysis offers us immediate access to information that can be obscured by other time-frequency methods such as Fourier analysis.

In the next section, a brief review of the mathematics behind wavelets will be given, but I deemed it appropriate to offer a brief description of what wavelets look like and their characteristics. Wavelet transforms

comprise an infinite set, and different wavelet families yield different trade-offs between how compactly the basis functions are localized in space and how smooth they are. Many of the wavelet bases have fractal structure of which the Daubechies wavelet family is an example. Within each family of wavelets are wavelet subclasses distinguished by the number of coefficients and by the level of iteration. This is an extra set of mathematical relationships which the coefficients must satisfy and is directly related to the number of coefficients. [7]

The key to the wavelet analysis procedure is to adopt a wavelet prototype function, called a mother wavelet. Temporal analysis is performed with a contracted, high-frequency version of the protype wavelet, while frequency analysis is performed with a dilated, low-frequency version of the same wavelet. Since the original signal or function can be represented in terms of a wavelet expansion (using coefficients in a linear combination of the wavelet functions, data operations can be performed using just the corresponding wavelet coefficients. If you desire further to choose the wavelets best adapted to your data or truncate the coefficients below a threshold, your data are sparsely represented. It is this sparse coding that makes wavelets an excellent tool in the field of data compression.

HOW ARE FILTER COEFFICIENTS DERIVED FROM GENERALIZED SCALING FUNCTIONS AND WAVELETS?

From a heuristic standpoint to aid in a pedagogical environment, the Haar scaling function and Haar wavelet previously described are very useful. However, from an applied standpoint, particularly to digital signal processing, the Haar wavelet is not very useful. Their graphs are made from flat pieces consisting of 1's, 0's, and -1's, and approximation to most signals is poor at best. Many flat pieces are needed to represent even a sloping line to decent accuracy. The Haar basis will not give compression ratios desired such as 20:1 minimally or 100:1. The key to the problem is a better basis.

Actually, the Haar basis and scaling function described earlier are special cases of a more general class of functions. In general, a scaling function, Φ (x), is the solution to a dilation equation of the form

$$\Phi(x) = \sum_{k=-\infty}^{k=\infty} a_k \quad \Phi(Sx-k) \tag{1}$$

A good choice of the dilation factor is S = 2, in which case the equation becomes

$$\Phi(x) = \sum_{k=-\infty}^{k=\infty} a_k \quad \Phi(2x-k) \tag{2}$$

The constant coefficients a_k are called filter coefficients and it is often the case that only a finite number of these are non-zero. The filter coefficients are derived by imposing conditions on the scaling function, $\Phi(x)$. One condition is that the scaling function and its translates should form an orthonormal set; that is,

$$\int_{-\infty}^{\infty} \Phi(x)\Phi(x+l)dx = \delta_{0,\ell}, \quad \ell \in \mathbf{Z} \tag{3}$$

where $$\delta_{0,\ell} = \begin{cases} 1, & l = 0 \\ 0, & otherwise \end{cases}$$

A wavelet, Ψ (x), is orthogonal to the scaling function and is defined by

$$\Psi(x) = \sum_{k=-\infty}^{k=\infty} (-1)^k a_{N-1-K} \quad \Phi(2x-k) \tag{4}$$

where N is an even integer. This definition satisfies orthogonality since

$$\langle \Phi(x), \Psi(x) \rangle = \int_{-\infty}^{\infty} \sum_{k=-\infty}^{k=\infty} a_k \ \Phi(2x-k) \sum_{k=-\infty}^{k=\infty} (-1)^{\ell} a_{N-1-\ell} \quad \Phi(2x-l)\, dx$$

$$= 0.$$

The set of coefficients $\{a_k\}$ and $\{(-1)^k a_{N-1-K}\}$ are said to form a pair of quadrature mirror filters.

Figure 3 depicts the Haar scaling function and Haar wavelet, Daubechies 4 scaling function and Daubechies 4 wavelet, Daubechies 6 scaling function and Daubechies 6 wavelet, and the Coiflet 2 scaling function and Coiflet 2 wavelet respectively. These were obtained by using different sets of filter coefficients to solve equations 3 and 4 above.

Now for the derivation of the coifficients. In order for the scaling function to provide a useful basis for functional analysis, it should satisfy useful properties which lead to corresponding conditions on the filter coefficients. These properties are:

(I) To uniquely define all scaling functions of a given shape, the area under the scaling function is normalized to unity; that is,

$$\int_{-\infty}^{\infty} \Phi(x)dx = 1. \tag{4'}$$

Also, the fact that the scaling function has a non-vanishing integral forces the sum of the filter coefficients to be equal to 2; that is, $\sum_{k=-\infty}^{k=\infty} a_k = 0$. (If this is not obvious, employ the "trick" of multiplying the scaling function $\Phi(x)$ by 2 and integrating by 2 to obtain

$$2\int_{-\infty}^{\infty}\Phi(x)dx = 2\int_{-\infty}^{\infty}\sum_{k=-\infty}^{k=\infty}a_k\ \Phi(2x-k)$$

$$= \sum_{k=-\infty}^{k=\infty}a_k\int_{-\infty}^{\infty}\Phi(2x-k)d(2x-k)$$

$$\Rightarrow \sum_{k=-\infty}^{k=\infty}a_k = 2. \qquad (5)$$

The uniqueness of $\Phi(x)$ is guaranteed by $\sum_{k=-\infty}^{k=\infty}a_k = 2$. However, a *smooth* solution does not necessarily follow.

As an example, let $c_0 = 2$ with $\Phi(x) = \delta(x)$. Then $\delta(x) = 2\delta(2x)$, and yet the delta function *is not smooth.*

For a scaling function to be orthogonal to its integer translates, the filter coefficients must satisfy the additional requirement that $\int_{-\infty}^{\infty}\Phi(x)\Phi(x+\ell)dx = \delta_{0,\ell},\ \ell \in \mathbf{Z}$

This forces the condition $\sum_{k=-\infty}^{k=\infty}a_k a_{k+2\ell} = 2\delta_{0,\ell},\ \ell \in \mathbf{Z}$ (6)

To determine a unique set of filter coefficients, one more condition other than (5) and (6) needs to be satisfied. In an *N* coefficient system, the two equations yield a total of N/2 + 1 equations. For a unique solution, another N/2 - 1 equations are necessary. To obtain the remaining equations, it was discovered by Daubechies [4] that we can require the scaling function to be able to exactly represent polymonials of order up to, but not greater than *p*. Enforcement of this requirement results in the compactly supported wavelets developed by Daubechies. This requirement for approximation of order *p* is that any function of the form

$f(x) = a_0 + a_1x + a_2x^2 + a_3x^3 + \cdots + a_{p-1}$ (7)

can be exactly represented by an expansion of the form $f(x) = \sum_{k=-\infty}^{k=\infty}a_k\Phi(x-k)$. (8)

Another way of saying this is that the polynomials 1,x, . . ., x^{p-1} are linear combinations of the translates, $\Phi(x-k)$. This now may be translated as a condition on the wavelet. Taking the inner product of the equation in (8) with $\psi(x)$ yields

$$\langle f(x), \Psi(x)\rangle = \sum_{k=-\infty}^{k=\infty}a_k\langle\Phi(x-k), \Psi(x)\rangle \equiv 0.$$

Using this result with (7) and (8), we arrive at

$$a_0\int_{-\infty}^{\infty}\Psi(x)dx + a_1\int_{-\infty}^{\infty}\Psi(x)xdx + a_2 + \cdots + a_{p-1}\int_{-\infty}^{\infty}\Psi(x)\,x^{p-1}dx.$$

Since this identity is valid for all a_j (j = 0,1,2,..., p-1), choosing $a_j = 1$ and letting all other $a_j = 0$

yields $\int_{-\infty}^{\infty} \Psi(x)\, x^{\ell}\, dx \equiv 0, \quad \ell = 0,1,2,\ldots, p\text{-}1$ (9)

So, the first *p* moments of the wavelet must be zero.. To determine the constraints this places on the filter coefficients, substitute equation (4) into (9). From this, it can be shown that

$$\sum_{k=-\infty}^{k=\infty} (-1)^k a_k k^{\ell} = 0, \; l = 0,1,2,\ldots, p-1 \tag{10}$$

It was shown earlier that equation (10) must yield n/2 - 1 new equations. Now, the equation obtained by letting l = 0 is redundant since it may be obtained from

$$\sqrt{2[equaion(6)]_{l=0} + 4[equation(6)]_{l>0} - [equation(5)]^2} \tag{11}$$

Equation (11) yields p-1 new equations which implies from (9) that p = N/2. So, the final conditions on the filter coefficients is

$$\sum_{k=-\infty}^{k=\infty} (-1)^k a_k k^{\ell} = 0, \quad \ell = 0,1,2,\ldots,N/2 - 1 \tag{12}$$

Thus, the filter coefficients $\{a_k \; k = 1,\ldots, N - 1\}$ for an N coefficient system are uniquely defined by (5), (6), and (12). The table below gives the coefficients for the Daubechies D$, D6, and D8 wavelet systems. The final problem that has to be constructed is the actual scaling function $\Phi(x)$ from the fillter coefficients.

Table I. Filters coefficients for Daubechies DN filter where N = 4, 6, and 8 (rounded to nearest ten thousandth).

k	D4	D6	D8
0	0.6830	0.4704	0.3258
1	1.11830	1.4144	1.0109
2	0.3170	0.6504	0.8922
3	-0.1830	-0.1909	-0.0396
4		-0.0450	0.2645
5		0.0498	0.0436
6			0.0465
7			-0.0150

How are the scaling functions constructed?

Generally, scaling functions do not have a closed form solution; rather, they have to be generated recursively from the dilation equation (2). This equation may be explicitly written as

$$\Phi(x) = a_0\Phi(2x) + a_1\Phi(2x-1)+\ldots+a_{N-1}\Phi(2x-N+1)$$

Writing this relationship for all integer values x = j, the following set of equations can be generated.

$$\Phi(0) = a_0\Phi(0)$$

$$\Phi(1) = a_0\Phi(2) + a_1\Phi(1) + a_2\Phi(0)$$

$$\Phi(2) = a_0\Phi(4) + a_1\Phi(3) + a_2\Phi(2) + a_3\Phi(1) + a_4\Phi(0)$$

$$\vdots$$

$$\Phi(N-2) = a_{N-3}\Phi(N-1) + a_{N-2}\Phi(N-2) + a_{N-1}\Phi(N-3)$$

$$\Phi(N-1) = a_{N-1}\Phi(N-1)$$

The matrix form of the above can be generated and may be written as $M\Phi = \Phi$.

So, the vector of integer values of the scaling function, Φ, is the eigenvector of M corresponding to the eigenvalue 1. As in all eigenvalue problems, the solution of the equation

$$(M - I)\Phi = 0. \tag{13}$$

is not unique, and therefore a normalizing condition is needed in order to determine a unique eigenvector. In this case the normalizing condition arises from equation 4'. After some calculation, we obtain

$$\sum_{k=-\infty}^{k=\infty} \Phi(i) = 1, \; i \in \mathbf{Z} \tag{14}$$

Therefore, the values of the scaling function at the integers are given bhy the solution to equation (13) and normalized by equation (14). So, we have how to find the integer values of 'x'; the values of $\Phi(x)$ of the half integers can be found by equation (2). That is,

$$\Phi(x/2) = \sum_{k=-\infty}^{k=\infty} a_k \Phi(x-k), \tag{15}$$

So, this process is repeated as many times as necessary to find the values of $\Phi(x)$ at all dydadic points $\{i/2^n \;, n \in Z\}$

How to Calculate the Wavelet Coefficients for a particular Example.

An example: The Daubechies 4 coefficient wavelet system

We will demonstrate how to use the previous results to construct the D4 (Daubechies 4 coefficient) scaling function and wavelet.

(1) First construct the filter coefficients.

So, we want to solve equations (5), (6), and (12). The easiest way todo tihis is to include the redundant equation for $\ell = 0$ in equation (6), which we know is linear, and to exclude the non-linear equation for $\ell = 1$in equation (12). Therefore, we have

$$a_0 + a_1 + a_2 + a_3 = 2$$
$$a_0^{\,2} + a_1^{\,2} + a_2^{\,2} a_3^{\,3} = 2$$
$$a_0 - a_1 + a_2 - a_3 = 0$$
$$-a_0 + a_1 + 2a_2 - 3a_3 = 0$$

Now, from the above linear equations, we have:

$a_0 = a_1 - 1/2$, $a_2 = 3/2 - a_1$, $a_3 = 1 - a_1$

Substituting for a_0, a_2, and a_3 in the quadratic equation and solving gives

$$a_1 = \frac{3 \pm \sqrt{3}}{4}, \text{ and from this we find that}$$

$$a_1 = \frac{1 \pm \sqrt{3}}{4}, a_2 = \frac{3 \mp \sqrt{3}}{4}, a_3 = \frac{1 \mp \sqrt{3}}{4}$$

It is obvious that one set of solutions is the antithesis of the other. That is, if one leads to the scaling function $\Phi(x)$, then the other will lead to $\Phi(-x)$. Yet, both equations satisfy the condition of normality, orthonormality and exact representation of a linear function. The solution that will be adopted is the one with the upper of "plus-minus or minus-plus" in the above notation.

The values of the scaling function at the integer points are given by equation (13):

$$\begin{bmatrix} a_{0-1} & 0 & 0 & 0 \\ a_2 & a_{0-1} & a_0 & 0 \\ 0 & a_3 & a_{0-1} & a_1 \\ 0 & 0 & 0 & a_{0-1} \end{bmatrix} \begin{bmatrix} \Phi(0) \\ \Phi(1) \\ \Phi(2) \\ \Phi(3) \end{bmatrix} = \begin{bmatrix} 0 \\ 0 \\ 0 \\ 0 \end{bmatrix}$$

From this, we find that $\Phi(0) = 0$, $\Phi(3) = 0$, $\Phi(2) = \frac{1-\sqrt{3}}{1+\sqrt{3}} \Phi(1)$

Substituting this into equation (14) yields

$$\Phi(1) = \frac{1+\sqrt{3}}{2} \text{ and } \Phi(2) = \frac{1-\sqrt{3}}{2}$$

Equation (15) then gives us the values of $\Phi(x)$ at the half-integers.

$$\Phi\left(\frac{1}{2}\right) = a_0 \Phi(1) = \frac{2+\sqrt{3}}{4}$$

$$\Phi\left(\frac{3}{2}\right) = a_3 \Phi(2) + a_2 \Phi(1) = 0$$

$$\Phi\left(\frac{5}{2}\right) = a_3 \Phi(2) + \frac{2-\sqrt{3}}{4}$$

Now, the Mallat [6] transform decomposition algorithm or another can be used to operate on the coefficients for data compression.

REFERENCES

1. J. Morlet, G. Arens, I. Fourgeau and D. Giard, Wave propagation and sampling theory', Geophys., **47,** 203-236 (1982).

2. J. Morlet, Sampling theory and wave propagation', in Chen (ed.) NATO ASI Series, Issues in Acoustic Signal/Image Processing and Recognition, Vol. I, Springer, Berlin, 1983, pp. 233-261.

3. A. Grossman and J. Morlet, 'Decomposition of Hardy fuctions into square integrable wavelets of constant shape', SIAM J. Math, Anal., **15.** 723-736 (1984).

4. J.O. Stromberg,' A modified Franklin system and higher order spline systems on R^n as unconditional bases for Hardy spaces', *Conf. in Honour of A. Zygmund, Vol. II , Wadsworth Math. Ser., 1982, pp. 465-493.*

5. G. Strang, "Wavelets", American Scientist, 82, 250-255, (1994).

6.. S.G. Mallat, " A theory for multiresolution signal decomposition: the wavelet decomposition", IEEE waveletdecomposition",IEEE Transactions on Pattern Analysis and Machine Intelligence, **2**(7), 674-693 (1989).

7. I. Daubechies, *Ten Lectures on Wavelets,* CBMS-NSF Regional Conference Series, SIAM, Philadelphia, 1992.

Variable-Width Template Construction for ATR with HRR Data

Raj Bhatnagar
Associate professor
ECECS Department

University of Cincinnati
Cincinnati, OH 45221

Final Report for:
Summer Faculty Research program
Wright Laboratory

Sponsored By:
Air Force office of Scientific Research
Bolling Air Force Base, DC

and

Wright Laboratory

September 1996

1 Introduction

The research described in this report was conducted with the objective of studying and suggesting ways to improve the performance of Air-to-Ground Target Recognition systems that use High Resolution Radar (HRR) data. Specifically, we worked with the HRR data for five target vehicles.

During the first phase of research we performed a number of investigations with the objective of learning about the nature and characteristics of the HRR data. Our perspective during these studies was to determine the suitability of various types of features for the classification of target vehicles.

The insights provided by these studies led us to hypothesize that ATR performance can potentially be improved if instead of uniform-width templates, sets of variable-width templates are constructed from data. We developed a heuristic search based algorithm for constructing variable-width templates and demonstrated the potential improvement.

In the following sections we first list the results of the studies performed with the data and then outline our algorithm and results for constructing variable-width templates. We also describe a hierarchical attributes based recognition system for which only some preliminary work was initiated during this study.

2 Nature of Data

Our studies were performed using synthetic data generated by the XPATCH system. A brief description of the data is as follows. A transmitted signal containing 100 different frequencies is beamed at the target vehicle and the reflected energy is collected. This reflected energy depends on the shape of the reflection characteristics of the area from which it is reflected. A plot of the reflected energy for the 100 pulses, the (*signature*), contains information about the characteristics of the reflecting area. The data consists of signatures obtained from every 0.04 degree of each target vehicle. This gives us a 100 x 9000 matrix of complex numbers for each target vehicle and for a fixed elevation angle. We worked with the data for 5 target vehicles. These vehicles were: M1 tank, T-72 tank, School Bus, Fire Truck, and Scud Missile.

3 General Approach

The three phases of the ATR process are: (i) Pre-processing of data; (ii) Data Reduction and Representation; and (iii) Pattern Recognition. In the following, we discuss the prevalent methods, details of studies performed by us and the results of modifications implemented by us.

3.1 Pre-Processing of Data

Most prevalent methods transform the signatures from frequency domain into time domain using Fourier Transform methods and work with the resulting Range-Profile data. In our studies we used the magnitude part of such Range-Profile data. We also performed a power transform of the data before using it so as to restore the normal distribution of the values that gets altered during the process of computing magnitude of complex numbers. A plot of one range profile is shown in Figure-1. Figure-2 shows the intensity plot for the 9000 range profiles of one target.

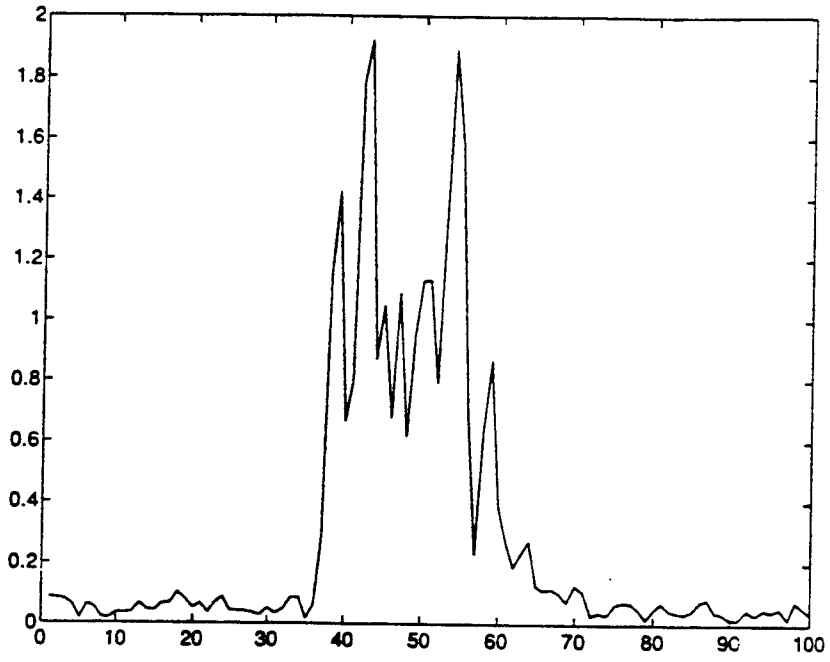

Figure 1: An Example Range Profile

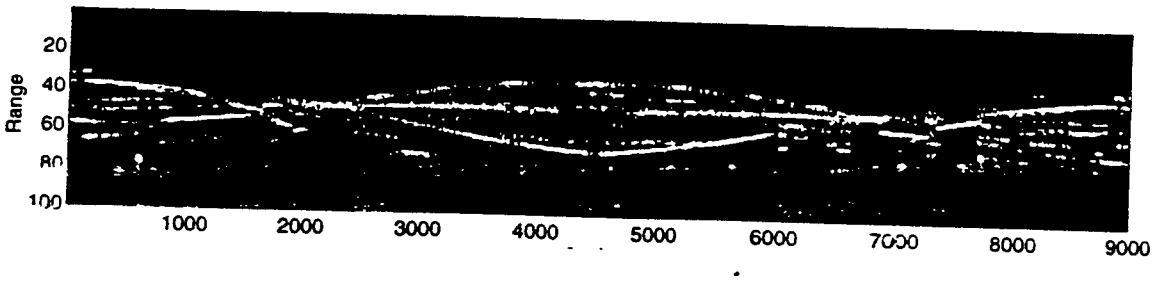

Figure 2: Intensity Plot of 9000 Range Profiles for Fire-Truck

3.2 Data Reduction and Representation

The data that needs to be stored for each target consists of one array of 100 x 9000 complex numbers for each target, and for each angle of elevation. This is an enormous amount of data. There is a large amount of redundancy in this data which arises due to the fact that signature of a vehicle varies only gradually as we change the rotational and/or the elevation angle.

In current ATR methods, this redundancy is exploited by constructing templates of fixed-sized angular regions around a vehicle. Typically, 180 templates of 2-degree angular width each may be constructed for a vehicle. Within each such template fifty contiguous range-profiles are averaged to obtain the representative *template* signature. During the recognition stage, a signature is matched to these templates to find the closest template. Figure-3 shows the intensity plot of range profiles for T-72 (for 90-180 degrees region) and also a similar plot for 3-degree templates in this region. Representation of 9000 range profiles for a target by 120 or 180 template signals is significant reduction in the amount of data to be stored.

3.3 Recognition

The Prevalent Method is to determine the distance between the sample (to be classified) range-profile and each of the template signals and find the closest template. Sample is then classified as belonging to the target of the closest template.

4 Preliminary Investigations

We performed a number of investigations for determining the characteristics of the HRR data for the targets. Most of these investigations employed measurement of various information-theoretic quantities for the data sets. A brief description of the investigations and their results is mentioned below.

- **Task 1:** We computed informational entropy for each range profile for the HRR data for each target. The calculation for the entropy was performed as follows. Take range profiles $p_m, pm+1$, and p_{m+2} for a target. Each of these profiles is of the type shown in Figure-1 and consists of 100 real values. Determine the maximum Max and the minimum Min of these three hundred values. Partition the Max-to-Min range in 25 equal intervals and determine the number of data points (out of 300) lying within each interval. Compute the entropy

$$E_m = \sum_{i=1}^{25} -P_i log(P_i) \tag{1}$$

  where P_i is the probability of a data point belonging to the i^{th} of the 25 intervals. This value is shown as the entropy for the m^{th} point and the step is repeated for all the 9000 profiles of a target data. An example of such a plot for target M-1 is shown in Figure-4.

  - These investigations showed areas of each target that are rich/deficient in informational entropy. Interestingly, each target's data showed very low entropy value around 0, 90, 180, and 270 degree regions. Intuitively, it is easier to distinguish targets in regions where they possess high informational entropy.

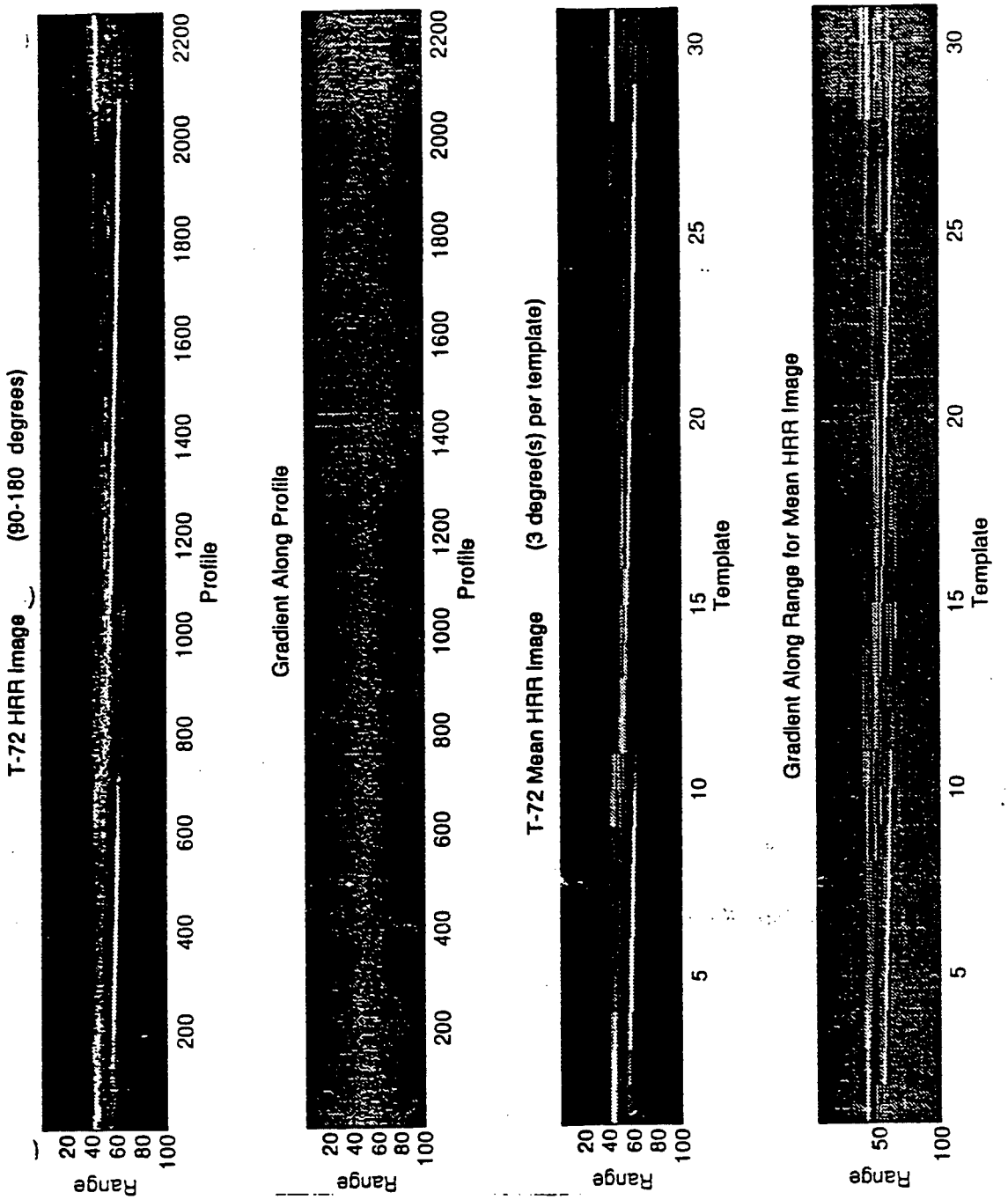

Figure 3: Templates for T-72 Target (90-180 degrees)

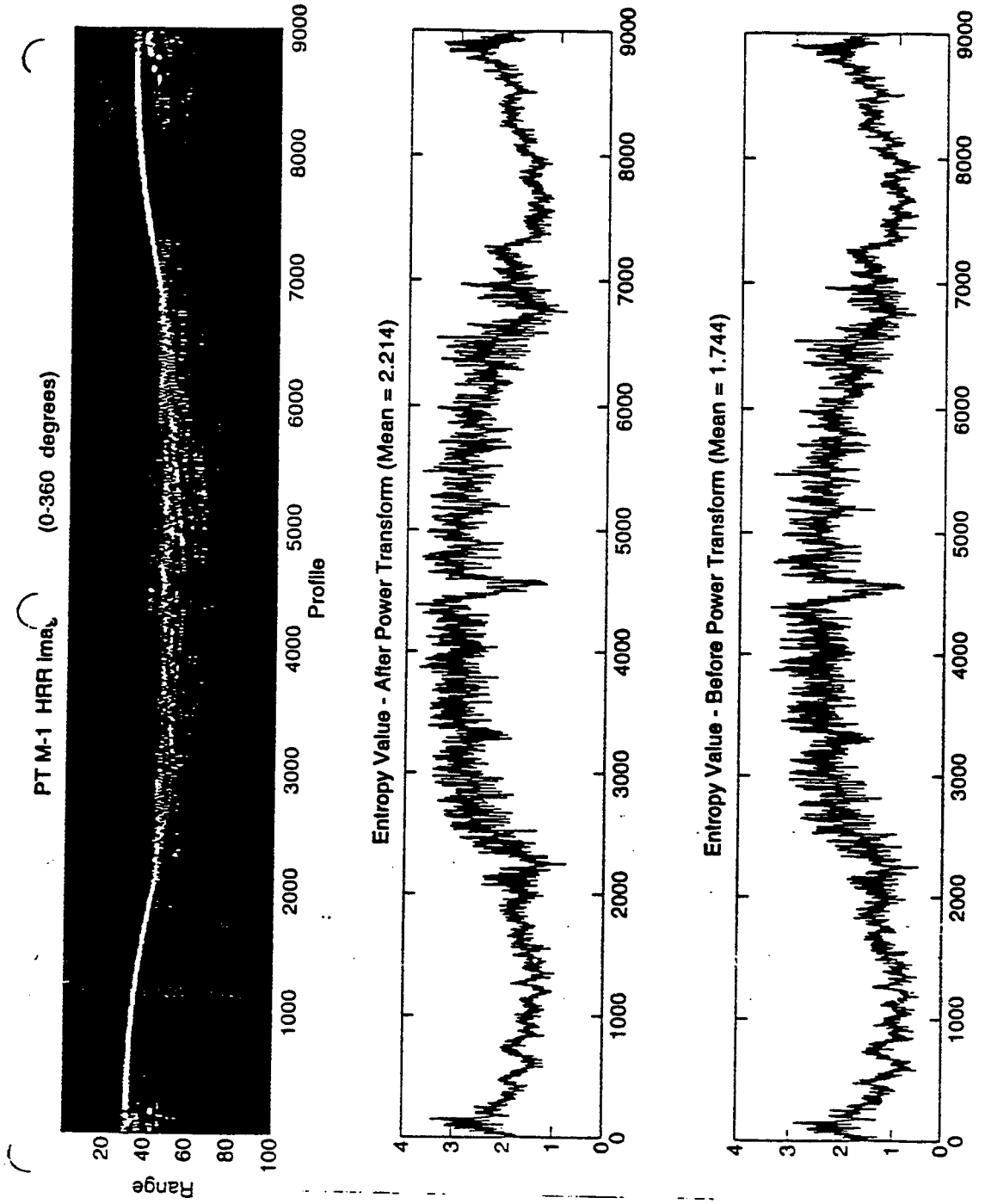

Figure-4: Entropy Values for the HRR Data of M-1 Tank

7-06

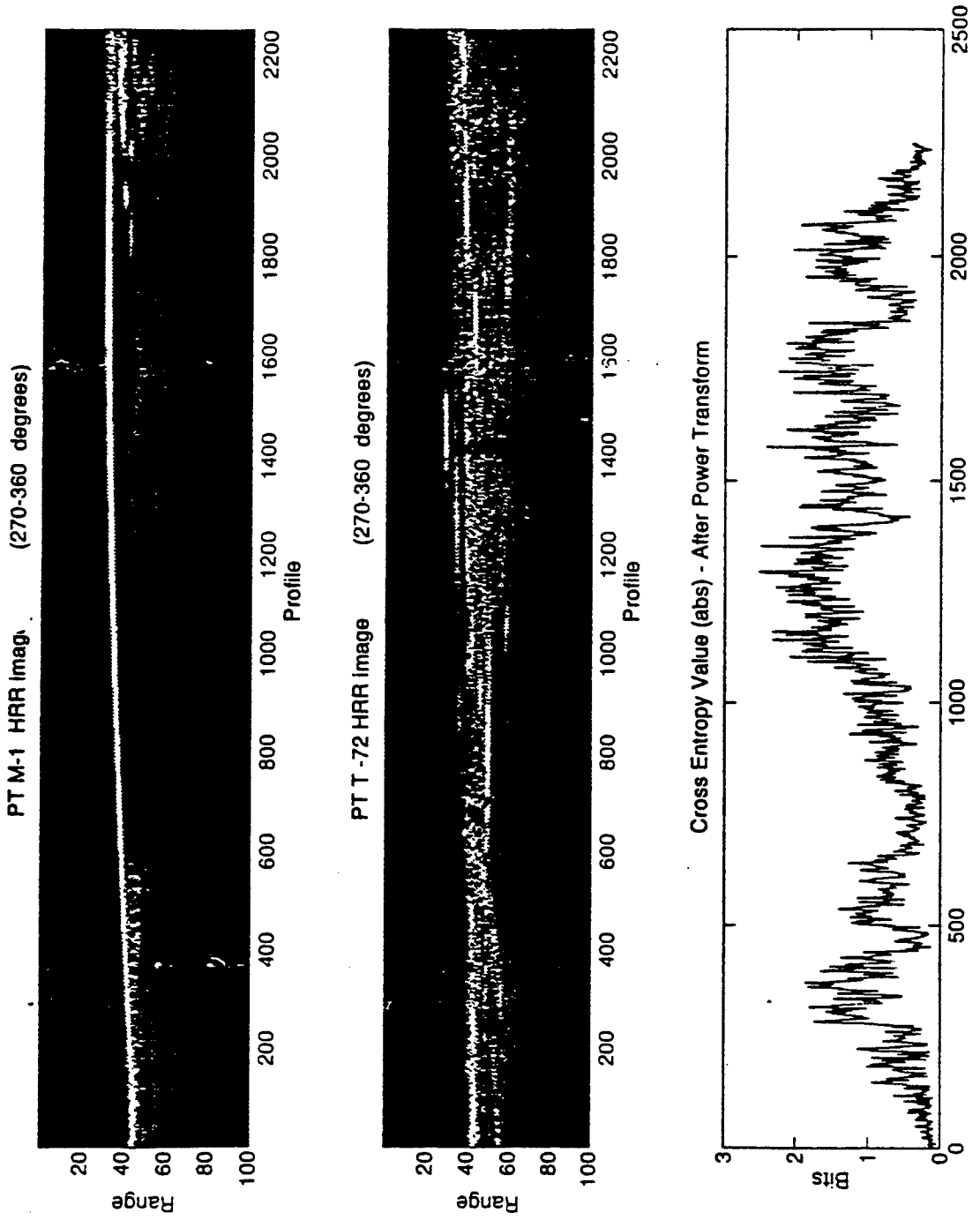

Figure 5: Mutual Information between Pairs of Targets

7-07

- **Task 2:** We compared the informational entropy of range profiles, the same quantity as described above, for all targets before and after applying the power transform. Figure-4 shows the plots for the entropy values in the two cases.
  - It is evident from these plots that throughout the target's 360 degrees the entropy value increases by an almost constant amount as a result of applying the power transform. However, the relative amount of information in various regions of a target remains the same.
- **Task 3:** Computed Mutual information for all pairs of targets. This study compared regions of targets and showed which regions were similar/different to each other from the perspective of informational entropy. A sample output is shown in Figure-5.

5 Seeking Good Features

Based on the insight provided by the above studies we designed a set of hierarchical features to be extracted for the HRR Data set of each target. An overview of these features can be summarized by the three-level binary tree shown in the following diagram.

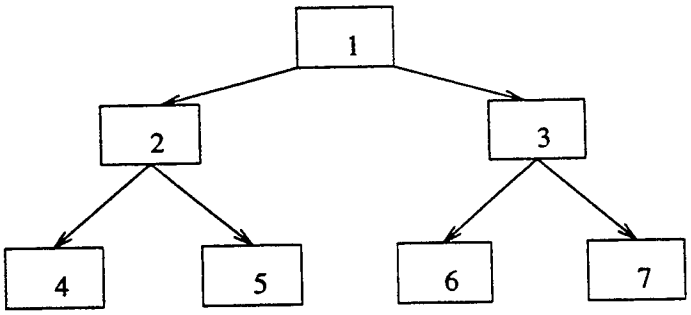

One such binary tree corresponds to one range-profile signal similar to the one shown in Figure-1. Each such signal is 100-points wide. we examine all 10-point wide regions and determine the region with maximum amount "Energy" in it. An estimated measure of energy is obtained by the product of informational entropy in the 10-point wide region and the average value of the signal in the region. The center of this 10-point wide region is called the location of the corresponding energy amount.

For a signal we determine the location of the maximum energy and assign it to the node number 1 of the binary tree. The signal is then partitioned at this point into two parts. The *Left Part* contains the signal that lies to the left of the 10-point region of maximum energy and the *Right Part* contains the signal that lies to the right of the maximum energy region. Determination of regions of maximum energy and partitioning is recursively continued until the seven nodes of the above tree have been filled. It is possible that many nodes of this tree may remain unfilled due to the nature of a particular signal.

This system was fine-tuned and binary trees determined for the 180 2-degree templates of each target. That is, data for each target was reduced to 180 template signals by summing over 2-degree regions and then a binary tree was generated for each resulting template signal. Figure-6 shows a plot of these binary trees for a target. This plot only shows the locations where regions of high energy are found in the consecutive template signals. Solid line shows the locus of the location stored at node number 1 of the tree. Loci for the locations stored at node numbers 2 and 3 of the tree are shown by dashed line; and those for node numbers 4 and 7 by the dotted lines. The plot shown in Figure-6 presents a very good presentation of the main scatter centers for the target. This is a validation of the fact that the features capture good physical properties of the target from the HRR data. There is much noise, however, in the plot in Figure-6 and the definitions of features need to be further refined before a recognition system is finally constructed.

The binary tree representation stores at its nodes information about the locations and amounts of energy at the various energy-centers of a signal. This information can be used to synthesize new attributes at each node. For example, a *moment-of-energy* can be computed at each node based upon the *moments-of-energy* at the children nodes. A number of encouraging results were obtained in this direction but they also pointed towards an anomaly having its origins in the data-reduction stage.

5.1 A Problem with Template-Making

Each range-profile is a signal consisting of 100 values. In our HRR dataset a signal is obtained after every 0.04 degree movement around a target, and from a fixed elevation. This results in 9000 range-profiles being collected for a target, for an elevation. Templates are made by Averaging contiguous sets of 50 profiles each, assuming that the shapes of signals change only gradually.

The assumption that the shapes of signals change only gradually is largely true but there are numerous points where the transitions in signals' characteristics are sharper than the usual. When the sharper transitions are included within a templates and the signals averaged, the resulting templates have larger variation from the individual signals contained in the template. More formally, let us define i^{th} range-profile as $P_i(k)$ where k takes the values from 1 to 100. The m^{th} template t_m is formed by averaging 50 contiguous range profiles as follows:

$$t_m(k) = \sum_{l=(m-1)*50+1}^{m*50} P_l(k) \quad for \;\; k = 1....100. \tag{2}$$

The *averaged* template signals differs from each of the 50 individual signals of which it is an average. One way to define this error for the i^{th} range profile is by determining the *Square-Error* as follows:

$$E_i(k) = (abs(P_i(k) - t_m(k)))^2 \quad for \;\; k = 1....100. \tag{3}$$

The average of the *Square-Error* vector for a template can be computed as follows:

$$MSE_m(k) = \sum_{l=(m-1)*50+1}^{m*50} E_l(k) \quad for \;\; k = 1....100. \tag{4}$$

Figure-7 shows a template signal and its corresponding MSE signal. A measure of how much, on the average, a template varies from its constituent signals can be obtained by computing the area

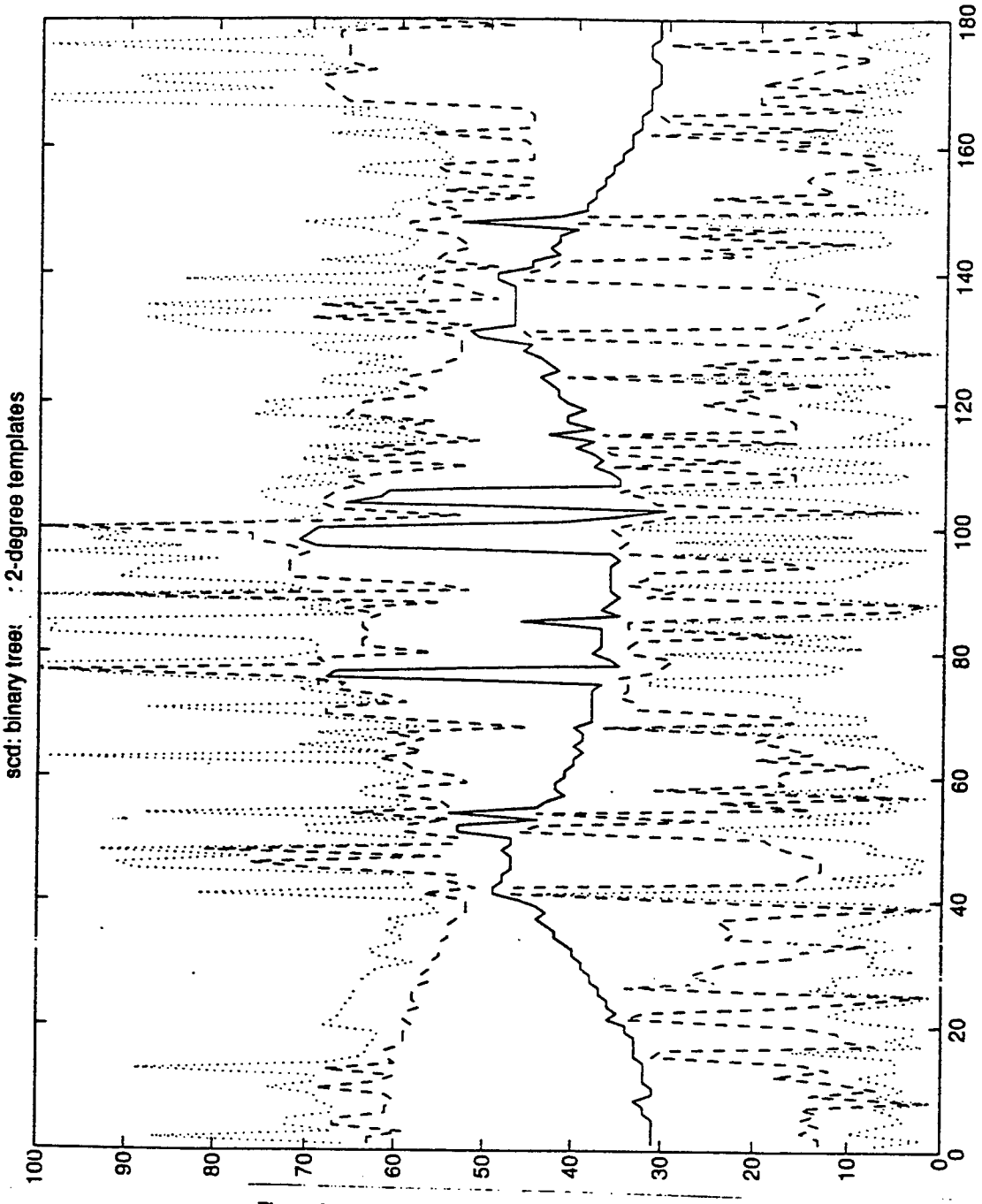

Figure 6: A Plot of Binary Tree-structured Attribute Values

7-10

under the MSE curve shown in Figure-7. This area can be computed as:

$$ERROR_m = \sum_{l=1}^{100} MSE_m(l). \tag{5}$$

5.2 Uniform-Width Templates

The prevalent method for making templates is to partition the entire angular region around a target into equal-sized angular regions and then average the range-profiles falling within the region of each template. For our dataset, if we want to make 2-degree templates then contiguous sets of 50 profiles would be taken to form template signals. The starting points of these templates would be at profile numbers: 1, 51, 101, 151 ...8951. The average error resulting from forming 180 uniform-width templates in this way can be determined as:

$$Avg - MSE = 1/180(\sum_{n=1}^{180} ERROR_m. \tag{6}$$

5.3 Variable-Width Templates

Our insights into the HRR data for target vehicles suggested that the ERROR resulting from averaging within a fixed-width template is high because signatures of significantly different characteristics get averaged together. That is, the angular regions around a target where the transition in signal shapes is sharper than the average gradual rate of change, the resulting template signals have higher value for ERROR. The ERROR-value can be decreased if the boundaries of the 180 templates are moved around and readjusted in such a way that the points of sharper transitions form the boundaries between templates. The problem now is to determine the placements for the boundaries such that the ERROR is minimized.

5.4 Heuristic Search for Template Boundaries

The problem of finding the template boundaries so as to minimize the value of ERROR is an optimization problem and can possibly be formulated in a number of different ways. After our initial attempts at formulating it in terms of some relaxation algorithms did not show much promise, we formulated it as a heuristic search problem. Main steps of this algorithm are as follows:

1. Take a Window of 5-degree width and slide it, by changing one range profile at a time, across the entire dataset for the target. Determine the value of MSE for each 5-degree template as the window slides across the target. Figure-8 shows a plot of the MSE value for one target.
2. Rearrange the points according to increasing values of their corresponding MSE values.
3. Select a subset of 50 template-starting points from the above list such that:
   (a) Every range profile gets included in one or the other template. (By a template we refer to all those contiguous range profiles that will be averaged to obtain a representative template signal.)

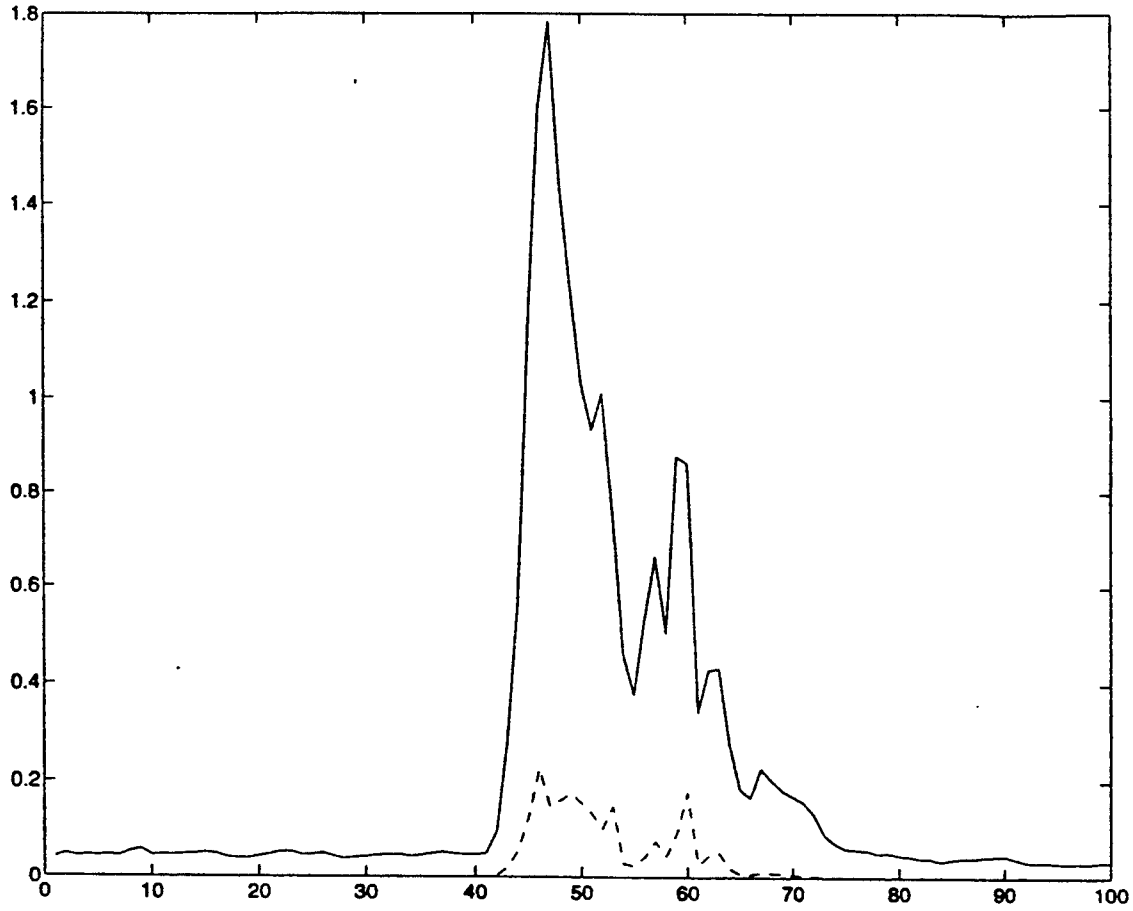

Figure7: A Template Signal and corresponding MSE signal

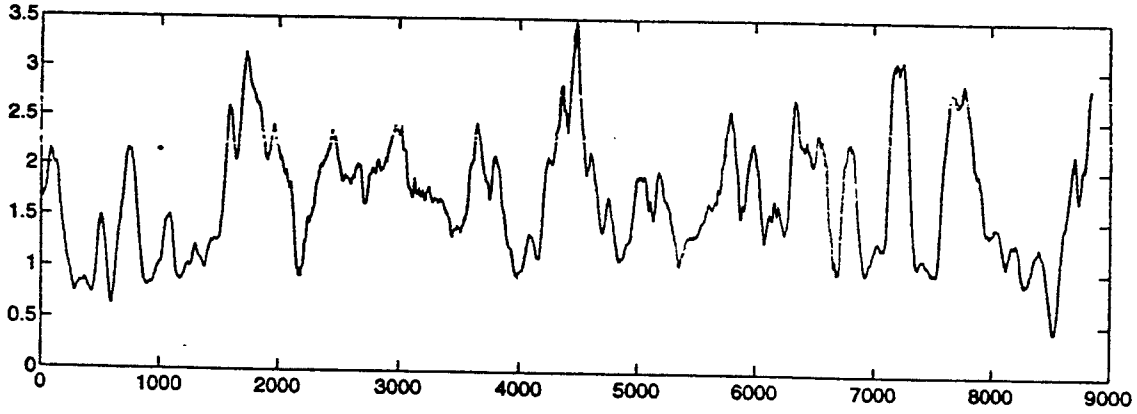

Figure 8: Mean Square Error for a sliding window of 2-degree width (Fire Truck)

(b) No two templates overlap.

(c) Starting points are chosen as much as possible towards the beginning of the list created in step-2.

A set of points generated as above constitutes one hypothesis about the template starting points. It is possible to generate a number of such hypotheses. After generating these hypotheses we have to find the best solution by suitable refining the most promising hypotheses by operators that change the staring points of templates. This is achieved by the following step that performs a heuristic search.

4. Run a heuristic algorithm (modeled after A^* search algorithm) with the following search operators:

   (a) Expand a template to include more range profiles.

   (b) Partition a template into two templates in such a way that their weighted MSE is minimized. The weightings are provided by the width of each partition.

   (c) Merge two adjoining templates into one.

   At each step of this algorithm a heuristic function is used to determine the hypothesis that should be selected for modification by one of the above steps.

5. The algorithm terminates when the number of templates has reached 180.

For the case of uniform-width templates the value *Avg-MSE* as defined above gives an indication of "Goodness" of the templates. The same function can be employed to determine the similar "Goodness" for the variable-width templates generated by our search algorithm. However, there is one difference that we must account for. When the templates are of different widths their contribution to the average error for all the templates should be in proportion to their individual widths. That is,

$$Avg - MSE = (1/9000)(\sum_{n=1}^{180}(ERROR_m * Width_m) \quad where \tag{7}$$

$Width_m$ is the width of the m_{th} template. The heuristic functions chosen by us for the above described search algorithm were designed to minimize this error function. It is also possible to alter these heuristic functions and minimize some other measure of error, such as,

$$Avg - MSE = (Max_{n=1}^{180}(ERROR_m * Width_m). \tag{8}$$

5.5 Results of Search Algorithm

We plotted the values of *Avg-MSE* for an equal number of uniform-width and variable-width templates constructed from the same regions of all targets. The plot for the fire-truck target is shown in Figure-9. It can be seen from this plot that for the case of 180 templates the average value of error for variable-width templates is about 12% less than the error for the same number of uniform-width templates. Or alternatively, about 30% fewer templates of variable-width need to be constructed for maintaining the same error rate. Figure-10 shows the distribution of error-values for individual templates for the two types of template construction procedures.

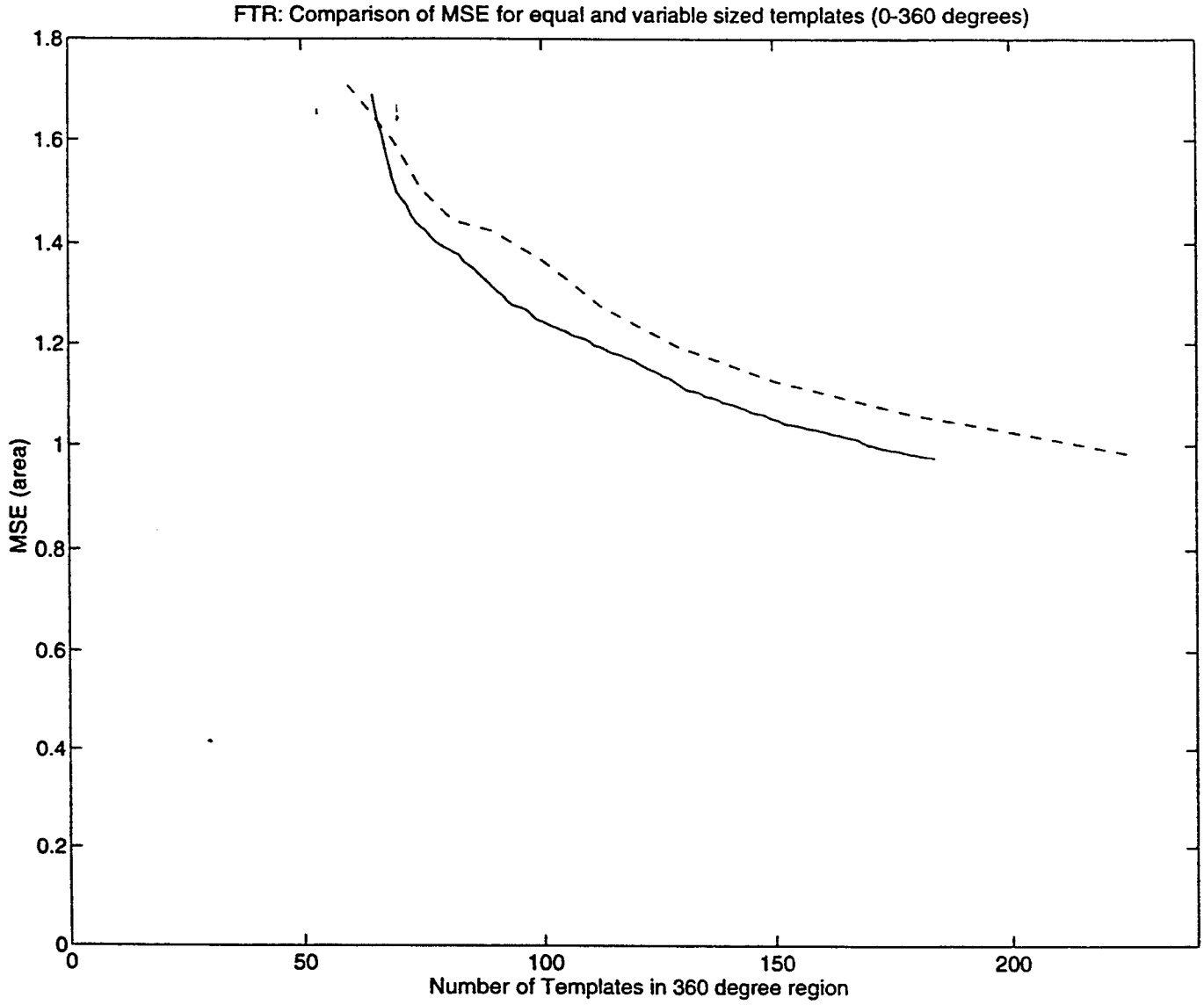

Figure-9: Mean Square Error for Equal Number of Uniform and Variable Width Templates

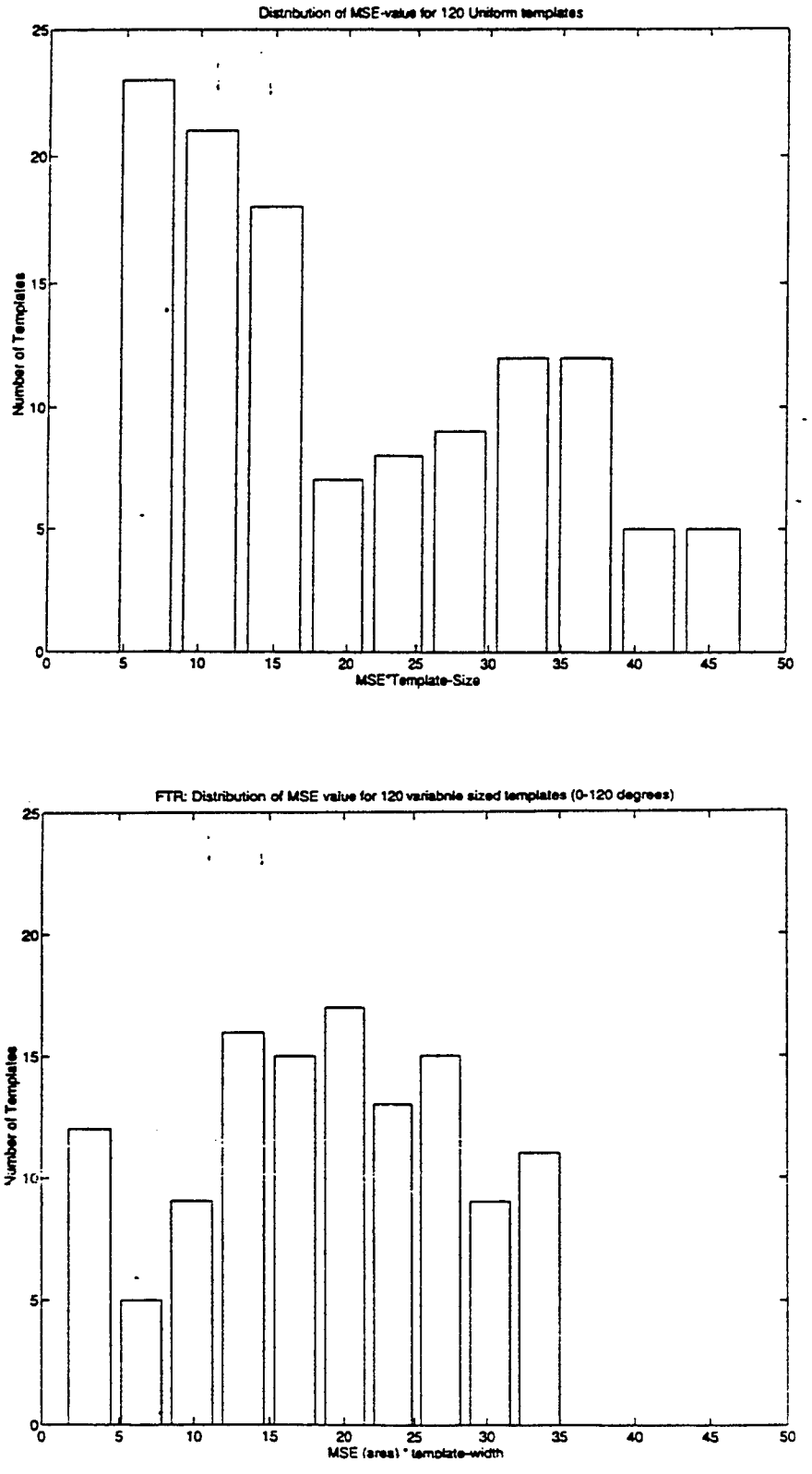

Figure 10: Distribution of Error among Uniform and Variable Width Templates

This result is significant in that is demonstrates that by adjusting the boundaries of templates it is possible to significantly reduce the Mean-Square Error within each template. This should result in enhanced performance for those implementations of ATR algorithms that use variable-width templates instead of uniform-width templates.

The comparison between uniform-width and variable-width templates was performed for each of the five targets. It is evident from these tests that the weighted average of the MSEs can be reduced by approximately 10-15 percent, or alternatively, the same MSE level can be maintained by constructing 30-40 percent fewer variable-width templates.

The above results have been possible with the help of a very crude heuristic implemented only for demonstrating the correctness of the approach. The intuitive explanation for the improvement is that the structural features of the target vehicles are aligned at the boundaries of variable-width templates. It is possible to improve these heuristics and obtain better reduction in the MSE values by constructing variable-width templates.

6 Conclusion

The main contribution of this research has been the demonstration of an algorithm for efficiently constructing variable-width templates. These variable-width templates result in template signals for ATR that have significantly smaller data-compression error. This can help increase the performance of ATR systems. The scope of this study was limited and the actual ATR tests could not be carried out to ascertain the extent to which the performance of ATR can be improved.

Other contributions of this study are the insights that have been obtained into the characteristics of the HRR data for ground vehicles.

ROBOT PATH PLANNING

into

CAVITIES DEFINED BY SPLINES

Alley C. Butler, Ph.D., P.E.
Associate Professor
Mechanical & Industrial Engineering Dept.

Louisiana Tech University
P.O. Box 10348
Ruston, LA 71272-0046

Final Report for:
Summer Faculty Research Program
U. S. Air Force Materials Direcotrate
(WL/MLIM) Wright Patterson AFB

Sponsored by:
Air Force Office of Scientific Research
Bolling AFB, Washington, DC.

and

Air Force Materials Directorate

October 1996

ABSTRACT

This report describes the development of a robot path planning system in which computational geometry is used to generate an optimal robot path. The architecture of this system makes extensive use of B-splines. The system is designed to support non-destructive testing of jet engine parts which contain multiple cavities. These cavities are modeled by B-splines, and a Voronoi tree is developed by finding the intersection points for offset curves or hodographs from the B-splines. In a manner similar to the Voronoi diagram, the Voronoi tree is maximally distant from adjacent obstacles. This Voronoi tree, therefore, represents the path with greatest clearance. For this reason, the Voronoi tree is used to guide path development for a single robot manipulator which is inserted into the cavities. The addition of potential field methods allow development of complete path information for the robot manipulator, based on attaching the potential field to the robot arm. In this report, a literature survey is provided, and the techniques for finding a Voronoi tree are described. Next, the adaptation of these techniques to develop manipulator paths using a potential field is discussed. Further evolution of the methodology is outlined, and conclusions with recommendations are provided.

TABLE OF CONTENTS

Abstract 8-2

Table of Contents 8-3

Introduction 8-4

Literature Survey 8-5

Development of a Spline Based Model
- Finding the Voronoi Tree 8-9
- Adding Linkages 8-10

Evolution of the Methodology 8-12

Conclusions and Recommendations 8-13

Acknowledgment 8-14

References 8-14

INTRODUCTION

Reliability of high performance jet aircraft engines is important to the combat survival of the pilot and the aircraft. This reliability is ensured by periodic non-destructive inspection of the jet engines. For the Pratt and Whitney F100-PW-229 engine, the inspection is done on a partly automated basis. Further automation of non-destructive inspection has the potential for dramatically reducing engine inspection costs, thereby allowing the Air Force to improve affordability. Figure 1 shows a cut-away view of the F100-PW-229 jet engine (Pratt & Whitney, 1996).

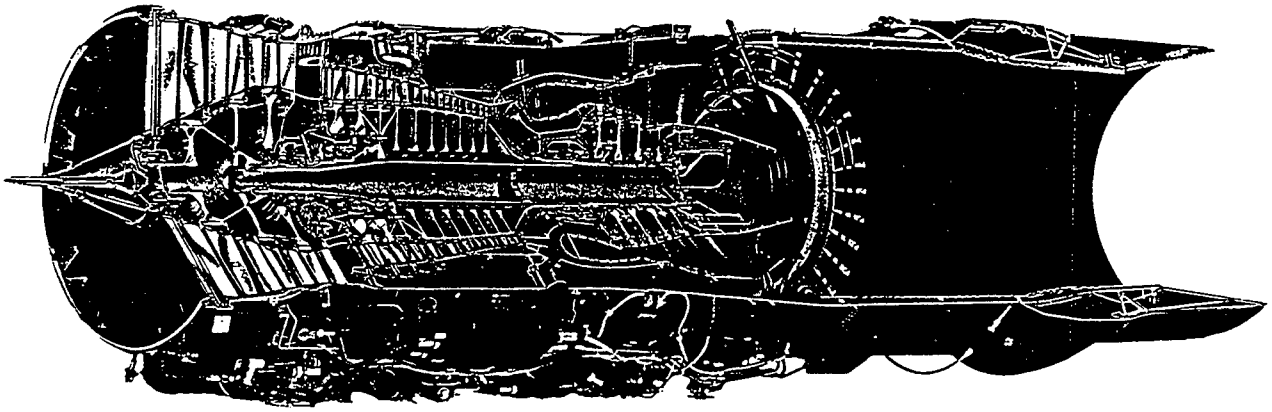

Figure 1 - Cutaway View of F100-PW-229 Engine (Pratt & Whitney, 1996)

Present methods involve eddy current inspection of engine parts using a Cartesian robot system. The path planning process for these Cartesian systems takes approximately 25 hours of work for manual path planning through conventional teach pennant technology. Recent advances in the development of algorithms for automated robot path planning have reduced this tedious and manpower intensive process, significantly to a matter of minutes. However, the present techniques are not optimal in nature, and the occurrence of undetected collisions requires additional computational steps.

One of the more challenging inspection processes, involves inspection of engine internals which form a set of cavities, presently inspected by a Cartesian robot with a probe for flaw detection using eddy currents. These cavities must be entered by a robot manipulator without collision with the part that is being inspected. This involves developing a path which describes the motion of the robotic arm as it moves the probe into position for inspection. The beginning point is called the home position by those involved in operating the robot, but the terminology in the literature typically discusses movement from a start position, S, to a goal position, G. Figure 2 shows a sectional view of this process for the eddy current inspection of engine internals.

The sectional view represents a three dimensional engine part in two dimensions. This is appropriate, since the engine is symmetric about its central axis. For the purpose of path planning, two dimensional analysis can be undertaken as a simplification of the more complex three dimensional problem, because of symmetry about the central axis. This approach, in which the path plan is developed in two dimensions and subsequently checked in three dimensions, is the currently used method. It is also the approach employed in this study.

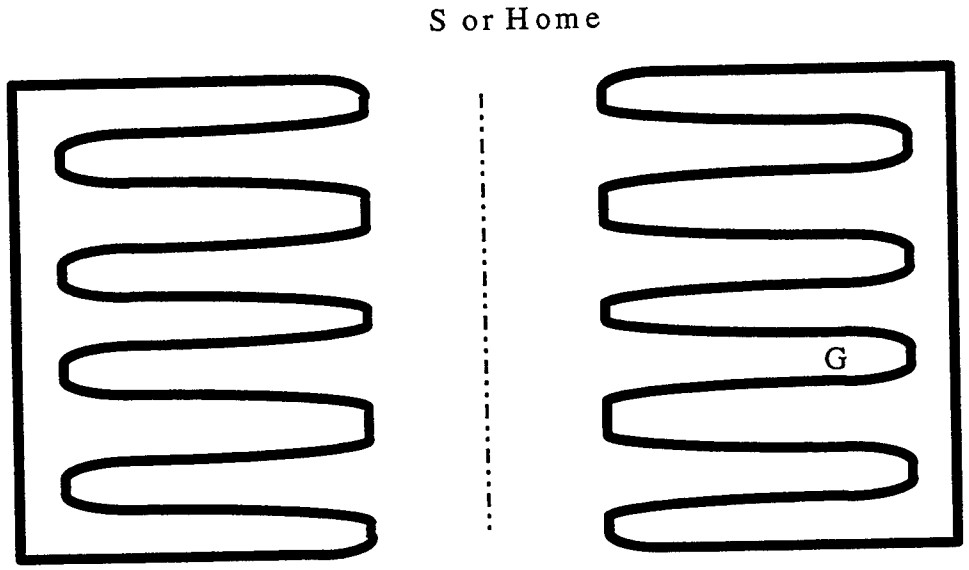

Figure 2 - Sectional View for Robot Path Planning

The presently employed path planning method includes a number of steps which provide a path without collision from S to G (Chemaly, 1996). The planning process begins with the development of a straight line from S to G. If this does not intersect a boundary, then no adjustments must be made. However, this is unlikely. Adjustments are made for those parts of the line between S and G which interfere (intersect) with the engine part. The adjustments are developed by replacing the portions of the straight line path which interfere, with a path which follows the surface of the engine part. This is distinctly similar to the method used by Lumelsky's (1991) Bug-2 algorithm. Once collisions are eliminated by replacing intersecting paths with paths following the part's boundary, a limited technique for improving the path can be employed. This limited technique finds shorter paths by finding straight line motions which eliminate segments of the path. The result from this sequence of steps is a path which is similar in principle to the visibility methods described by Lozano-Perez and Taylor (1989), and identical to the "string tightened path" discussed by DuPont and Derby (1988).

In the visibility methods, the path is very close to collision, similar to a string which is stretched tight against all obstacles. This is done to shorten the distance traveled. Unfortunately, this similarity to visibility techniques has important drawbacks in the present application. Because the present technique shortens the path in a manner identical to the visibility methods, the path is close to collision for some portions of the planned path.

When the two dimensional plan is translated into a three dimensional plan, collisions may be detected in 3D which are not found in 2D. These collisions in 3D must then be corrected, causing additional time and computational expense.

As an alternate approach, this study advocates the development of a Voronoi tree which is by nature maximally distant from all surfaces of the part. The Voronoi tree is similar to the Voronoi diagram used in Computational Geometry, which is also maximally distant from all obstacles. Hence, the name Voronoi tree is descriptive. The Voronoi tree is generated through the use of offset curves or hodographs to the B-splines which model the engine part. It should be noted that the development ov the Voronoi tree as a technique was created through discussion of hodograph technology with Dr. LeClair (WL/MLIM) and subsequent application as described in this study.

In addition to the Voronoi tree, offset curves are used to define an artificial potential field which repels the robot arm from all surfaces. The result is a path for the robot arm which is maximally distant from all potential collisions. The optimal path developed by using the potential field, therefore, has the greatest chance of avoiding collision with boundaries. This has distinct advantages when the path is converted from 2D to a 3D path.

The techniques outlined here form the basis of a set of new methods for planning robot paths into cavities defined by splines. These methods are purposefully constructed to cause the robot arm to be maximally distant from all boundaries as it traverses from S to G. This allows solution of the path planning problem in two dimensions which is both convenient and computationally efficient. However, it also minimizes the possibility for collision when the path is converted to 3D. For these reasons, it is believed that the techniques advocated by this study represent a significant improvement over presently employed methods.

The remainder of this report will review the literature which is relevant to these methods. Then, additional details will be provided on the construction of paths into cavities which are defined by splines. This includes a discussion of the development of the Voronoi tree and addition of a potential field to allow robot arm motion. Next, additional work which is evolutionary to this method is described, and conclusions with recommendations are made.

LITERATURE SURVEY

The literature describes many methods for robot motion planning. Schwartz and Sharir (1988) classify robot motion planning into three types: 1) optimal motion planning, 2) exploratory motion planning, and 3) planning with moving obstacles. The optimal motion planning problem includes use of complete knowledge about

the robot's environment, and typically, the only moving object is the robot. For the problem considered here, optimal motion planning is required.

Most approaches to motion planning approximate the obstacles as polytopes which are polygons in 2D and polyhedra in 3D (Mitchell, 1988). However, there are exceptions to this rule. For example, Gasmi and Reboulet (1988) model obstacles as ellipses, and Rohnert (1991) models the robot as a disk traveling between polygons. Although Souvaine (1986) considers obstacles as "splinelegons," the author is unaware of any methods which uses B-splines to model obstacles in the form of cavities.

Surveys of robot motion planning exist which classify the optimal motion planning problem. For example, Hwang and Ahuja (1992) provide an extensive taxonomy of the motion planning process. They list current approaches as cell decomposition, skeleton, potential field, and mathematical programming, with the skeleton methods including visibility graph, Voronoi diagram, silhouette, and subgoal network. Yap (1987) defines motion planning in terms of physical space, geometry of placement, boundaries, objectives, optimality criteria, local planning, and the decision problem. In a survey by Whitesides (1985), a strong connection between motion planning and computational geometry is drawn. Surveys on computational geometry, which are relevant to this work, also allude to the use of computational geometry as a key tool in robot path planning and related sciences (Lee & Preparata, 1984; Bohm et al. 1984).

Often, the use of computational geometry and motion planning methods involve conversion of a problems into a more manageable form. Lozano-Perez (1982) describes this conversion as finding the "free space." In another approach, he discusses configuration space which is used to make the motion planning problem more tractable. In the configuration space, all obstacles are expanded by the dimensions of the robot, thus allowing the robot to be reduced to a point (Lozano-Perez, 1983). The SHARPS system also involves search through configuration space (Laugier, 1988). Brooks (1983) searches free space, which is similar in function to configuration space, as regions of overlapping cones. In one system, development of a path in configuration space is managed through a division of the space into unoccupied cells, and A* search is used to plan motion among the cells (Brooks & Lozano-Perez, 1985). In a related approach, a connectivity graph is developed from cells and adjacency relationships (Sharir & Ariel-Sheffi, 1984). Another technique which employs graph search for acceptable paths, develops the graph from the vertices of forbidden regions (Lozano-Perez & Wesley, 1979). In each of these methods, the path planning problem is convolved into a more manageable representation, and there is a search for a solution.

The process of changing the problem representation to allow an efficient search for solution is present in potential field methods as well. Hwang (1992) describes his technique as using "a potential function similar to the electrostatic potential assigned to each obstacle." Based on tests of his system, Hwang states that his method is fast

and reaches solutions on all but a small set of problems involving tight free space. Koren (1991) discusses implementation of the potential field with a mobile robot. He focuses on the problems experienced in potential field applications. In another study, a snake configuration is employed with potential energy, kinetic energy, and dissipative terms to cause the snake to find a goal location (McLean & Cameron, 1993). The use of artificial terms with physical analogies appears to be common with potential field methods.

By seeking a position of lowest potential, an optimization process occurs. Optimal path approaches in the literature, include terms which consider the dynamics of the robot manipulator and the desire for traversing a path in minimal time (Wapenhans et al., 1994; Bessonnet & Lallemand, 1993). This is accomplished using dynamic programming for some systems (Sandgren & Venkataraman, 1989; Leu & Singh, 1988). Other optimization methods are also employed to achieve results, including simulated annealing (Carriker et al., 1990; Sandgren & Venkataraman, 1989) and recursive quadratic programming (Leu & Singh, 1988). As a general rule, these optimization techniques use relatively complex cost functions which allow inclusion of manipulator dynamics.

Most studies of optimal path planning have considered only manipulator movement in an environment modeled by polytopes rather than into cavities. For the present application, cavities have been the obstacles. These cavities were recognized as natural candidates for the use of splines. The use of NURBS (non-uniform, rational b-splines) has become the predominant spline format. NURBS were advocated by Forrest (1980), Tiller (1983), and by Piegl and Tiller (1987). Piegl (1991) has provided a survey of NURBS properties.

For the construction of the Voronoi tree, the intersection of splines must be found, and for the potential field technique described here, line-spline intersections are needed. Earlier work on intersections of splines includes the development of an array of techniques. For example, recursive subdivision is used to find intersections (Dokken et al., 1989; Dokken, 1985). Sederberg and Parry (1986) compared techniques for Bezier curves, one of which was based on recursive subdivision. Others have worked on the intersection of patches as a three dimensional implementation of splines (Barnhill et al., 1987; Barnhill, 1989; Sederberg & Meyers, 1988; Kaufmann & Klass, 1988). Intersections of lines and splines have been studied by Pantelic and Janevski (1989). Of course, in this study the important problems revolve around intersection with offset curves or hodographs.

A number of researchers have focused on offset curves or hodographs. Klass (1983) developed a method for offset curves which follows the Hermite form (Foley et al., 1990). A technique for uniform B-splines was studied by Pham (1988). Tiller and Hansen (1984) and Coquillart (1987) worked on the development of offsets for NURBS. Others have focused on rational or Pythagorean hodographs (Farouki & Sakkalis, 1990; Sederberg & Wang, 1987). Farouki (1985 & 1986) also worked on offset surfaces. In one paper the authors wrote that finding offsets for splines is a complex process, and they further add that the offset of a spline is not necessarily a spline

(Tiller & Hansen, 1984). Despite the complexity, detecting intersections with offset curves is a key process in computational geometry, for path planning using splines.

In addition to path planning using splines, the use of spline architectures is useful in another way. The path planning process outlined here develops an ordered sequence of points in 2D for the robot and its joints to traverse. This ordered sequence must be translated into a continuous path with smooth and continuous motion. This means that the C^0, C^1, and C^2 properties of B-splines can be used to avoid abrupt changes in velocity and acceleration. Development of splines from a sequence of points has been studied by Papamichael and Soares (1987) and by others. The use of these splines for the control of robot manipulators has also been demonstrated (Patel & Lin, 1988; and others). From these this prior work, it is apparent that development of robot path plans using splines is easily feasible.

DEVELOPMENT OF A SPLINE BASED MODEL

Finding the Voronoi Tree

The name Voronoi tree has been chosen to describe the technique outlined here, because of the similarity to the Voronoi diagram which is maximally distant from all objects in a two dimensional space (Lozano-Perez & Taylor, 1989). Both the Voronoi diagram and the Voronoi tree described here, provide paths for robot motion which avoid collisions to the greatest extent allowed by the geometry, and this should permit solution of the path planning problem in two dimensions without difficulties when the plan is checked in 3D.

The cavities found in the jet engine part, as shown in Figure 2, represent parts which should be described by splines in a CAD system. The Voronoi tree is developed directly from the spline geometry. Therefore, this spline based approach is both natural and efficient for path planning.

Offset curves from splines can be found for the cavity geometry. The utility of these curves or hodographs was originally recognized by Air Force personnel (Dr. LeClair) with subsequent application here. These offset curves or hodographs follow the contour of the spline, but they exist at an offset distance, d, from the spline. The equations which describe the offset curves are parametric in t in a manner similar to the spline curves (Hoschek, 1985):

$$x'(t) = x(t) \mp d(\vec{n}_x) \quad (1)$$

$$y'(t) = y(t) \pm d(\vec{n}_y) \quad (2)$$

where x', y' describe the offset curve, x, y describes the spline, d is the offset distance, and $\vec{n}$ represents the normal to the spline curve. Offset curves can be developed for different values of d.

If offset curves from two surfaces described by splines intersect, the point of intersection is a distance d from each spline curve. So, the points of intersection for offset curves (having identical values of d) are equidistant from both surfaces. By intersecting multiple offset curves with different values of d, points which are equally distant from both surfaces can be found. By connecting these points, a Voronoi tree is developed in which points on the tree are equally distant to adjacent surfaces. This is a key technique advocated by this study, and it is illustrated in Figure 3 for one cavity.

Adding Robot Linkages

Although the Voronoi tree represents a path which is equally distant to all bounding splines, it does not provide information on how a robot's linkages should be controlled to enter a cavity. For this reason, additional computation is required to find the robot's optimal configuration as it traverses the Voronoi tree from S to G. To accomplish this portion of the path planning problem, offset curves are again required. These offset curves are configured to provide a measure of the potential for intersection. As such, the approach is similar to potential field methods (Hwang, 1992). The principle behind the potential field method rests with the development of an artificial field which is used to surround all obstacles. Although this artificial potential field is based on simply adding terms to the path planning algorithm, these added terms provide a means of "repelling" the robot away from any obstacle in an optimal manner. So, a potential field keeps the robot manipulator from coming into contact with obstacles.

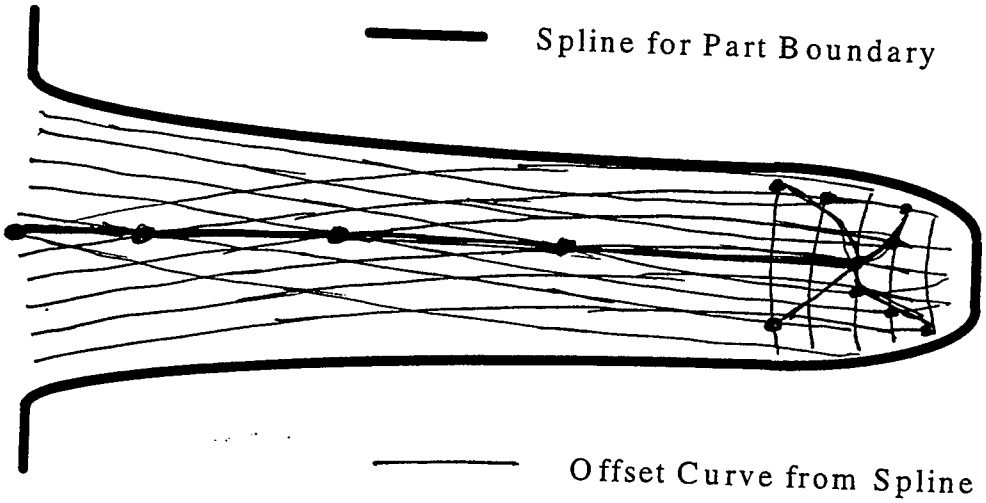

Figure 3 - Developing Points on the Voronoi Tree with Intersecting Offset Curves

In the technique advocated here, there is one difference to other potential field methods. Most potential fields are associated with obstacles. However, if that approach is used here there will be multiple offset curves, and

the offset curves will require significant computational time. Additionally, the intersections between the offset curves and the polygonal boundaries of the robot must be found. This is a relatively complex computational task.

To limit these difficulties, an equivalent approach is used. The potential field is attached to the robot arm. This allows offsets to be constructed as simple lines which are parallel to the polygon which represents the robot's arm. These lines are intersected with the splines which form the cavity. This represents a very efficient way to represent and compute potential, since the lines all intersect with a spline which has known control points. (The control points of the offset curve would have to be determined as added computational burden.) These control points form a convex hull around portions of the curve, and this permits checking of line intersections with the convex hull. The checking of intersection with the convex hull is a local property of the spline curve, and line-spline intersections can, therefore, be rapidly and easily found. This is a significant innovation directly inspierd by close collaboration with an Air Force research enginer (again, Dr. LeClair).

As presently implemented in C language code, the intersection of a line and spline is found by a hierarchical method which rapidly excludes trivial cases in the computational hierarchy. This process of descending down the hierarchy is developed to maximize computational speed. It involves excluding line spline intersection first by a bounding box. Then, exclusion of line-spline intersection is accomplished by checking for intersection with the convex hull for the spline. If the convex hull is intersected, then Newton-Raphson procedures are employed to determine the point of intersection (Mortonson, 1985; Mortonson, 1990) using data from the earlier computations on the convex hull. This provides line-spline intersection data rapidly and avoids expensive computation for non-intersecting cases.

Once line-spline intersections are determined, the level of potential field interference with the cavity boundaries as obstacles can be determined. This potential field is based on the length of the offset lines which intersect the splines. Equation (3) below shows how the potential function should be constructed. The first term involves the development of a measure for the Euclidean distance between the manipulator tip at x_t, y_t and a point on the Voronoi tree as x*, y*. This term is multiplied by a factor K which is adjusted to obtain a good balance between robot arm position and motion of the manipulator tip relative to the Voronoi tree. The second term sums the product of the weight associated with an offset curve as w_i and the length of intersection as L_i between the offset curve and the spline describing the cavity. The value of L_i should reflect the severity of interference between the obstacle and the offset line. Of course, offset lines at greater distance from the robot arm would have lesser weight as w_i, since the probability of collision is less. The result is a measure as Φ of how close the robot arm is to a collision.

$$\Phi(\bar{x}, \bar{y}) = K\sqrt{(x^* - x_t)^2 + (y^* - y_t)^2} + \sum L_i w_i \qquad (3)$$

With this measure available, an optimal position for the robot arm can be found to avoid collision. This technique is illustrated in Figure 4 for three linkages and a portion of the part.

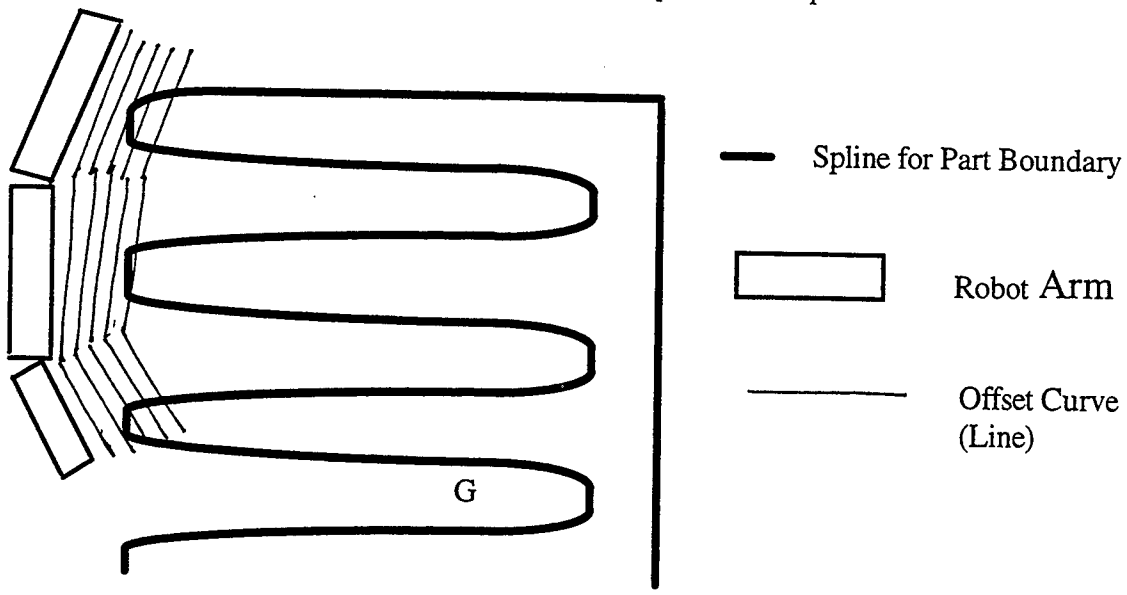

Figure 4 - Developing a Potential Field Attached to the Robot Arm

EVOLUTION OF THE METHODOLOGY

Time allocated to the research has been finite, and choices regarding which veins of research to pursue aggressively had to be made. Despite limitations in time and resources, several key steps have been completed which represent an important beginning. The steps which were completed include an orientation to the problem, an in depth literature review (which is only partially represented in this report), development of key research concepts and approaches, and commencement of programming for a prototype system. The programming was conducted in the C language in a Unix and X Windows environment.

Due to limited time, some processes are deferred. These include the choice of offset curve architecture, and the optimization of hodograph-hodograph intersection algorithms. Present methods require human computer interaction which necessitates limited user involvement.

Additionally, programming is continuing on the development of the potential field technique. Code for representation and rendering of splines as non-uniform, non-rational b-splines is presently in place. Intersection algorithms for line-spline intersection have been developed using methods outlined by Prasad (1991) as improved by Shafer and Fuestel (1992) for intersections with the convex hull. These methods are hierarchical and represent an approach designed for fast computation. The development of other functions and routines for the path planning system are continuing, with the development of algorithms to determine Φ in equation (3) as the next priority.

After development and testing of this code, a simulated annealing approach is planned for the optimization of Φ. This will demonstrate the feasibility and utility of the overall Voronoi tree and potential field methods.

CONCLUSIONS AND RECOMMENDATIONS

As a result of this investigation, there are a number of conclusions which can be drawn from this work. These conclusions are represent in the following:

1. Most of the literature discusses path planning in an environment with obstacles described by polytopes (polygons in 2D and polyhedra in 3D). A few other papers discuss path planning using other regular geometric shapes like the ellipse, circle, or cone. The author is unaware of any work which investigates path planning into cavities defined by splines.

2. Computational speed is a key issue in the benchmarking of path planning systems. There is a trade-off between using faster methods which require extensive checking and rework due to collisions in 3D, and a method which may take longer to avoid the extensive checking and rework. Therefore, computational speed continues to be an important item on the research agenda.

3. It is anticipated that solutions will be sensitive to the values of d in the offset curves or hodographs (equations 1 and 2), and to the values of K and w_i in equation (3). Experience with the method should be the best guide to generate proper solutions.

4. The algorithms described here for Robot path planning have no proof of convergence. The result is that the algorithms may fail under certain conditions. It is expected that the outcome should, however, be similar to Hwang's (1992) results in which failure occurs over a very limited subset of problems.

There is one key recommendation: The work which was begun through this study should continue. This involves additional programming and program testing which can be accomplished in the coming months. As secondary recommendations, robot dynamics/kinematics should be considered more fully in future approaches (Seereeram & Wen, 1995; Xue & Sheu, 1989), and a migration to a continuous path approach should also be considered (Brady, 1982).

The research outlined here uses a novel approach to accomplish path planning for robot arms which travel into cavities. It is believe that the methods will prove superior to existing techniques, and improvements will drive down inspection costs. This will make greater levels of reliability needed by the Air Force more affordable.

REFERENCES

Barnhill, R. E., G. Farin, M. Jordan, and B. R. Piper, 1987, "Surface/Surface Intersection," *Computer-Aided Geometric Design*, vol. 4, pp. 3-16.

Barnhill, Robert E., 1989, "Geometry Processing: Curvature Analysis and Surface-Surface Intersection," in *Mathematical Methods in Computer Aided Geometric Design*, (edited by) Tom Lyche and Larry L. Schumaker, Academic Press, Boston, pp. 51-60.

Bessonnet, G. and J. P. Lallemand, May 2-6, 1993, "Planning of Optimal Free Paths of Robotic Manipulators with Bounds on Dynamic Forces," *Proceedings of the IEEE International Conference on Robotics and Automation*, Atlanta, GA, pp. 270-275.

Bohm, Wolfgang, Gerald Farin, and Jurgen Kahmann, 1984, "A Survey of Curve and Surface Methods in CAGD," *Computer Aided Geometric Design*, vol. 1, pp. 1-60.

Brady, Michael, 1982, "Trajectory Planning," as chapter 4 *in Robot Motion: Planning and Control*, (edited by) Michael Brady, John M. Hollerback, Timothy L. Johnson, Tomas Lozano-Perez, and Matthew T. Mason, The MIT Press, Cambridge, MA, pp. 221-243.

Brooks, Rodney A., March/April 1983, "Solving the Find-Path Problem by Good Representation of Free Space," *IEEE Transactions on Systems, Man, and Cybernetics*, vol. SMC-13, no. 3, pp. 190-197.

Brooks, Rodney A. and Tomas Lozano-Perez, March/April 1985, "A Subdivision Algorithm in Configuration Space for Findpath with Rotation," *IEEE Transactions on Systems, Man, and Cybewrnetics*, vol. SMC-15, no. 2, pp. 224-233.

Carriker, Wayne F., Pradeep K. Khosla, and Bruce H. Krogh, May 13-18, 1990, "The Use of Simulated Annealing to Solve the Mobile Manipulator Path Planning Problem," *Proceedings of the 1990 IEEE International Conference on Robotics and Automation*, Cincinnati, OH, pp. 204-209.

Chemaly, Adel, July 26, 1996, private communication with Alley Butler, Technosoft, Inc., Cincinatti, OH,

Coquillart, Sabine, July/August 1987, "Computing Offsets of B-Spline Curves," *Computer Aided Design*, vol. 19, no. 6, pp. 305-309.

Dokken, Tor, 1985, "Finding Intersections of B-Spline Represented Geometries using Recursive Subdivision Techniques," *Computer-Aided Geometric Design*, vol. 2, pp. 189-195.

Dokken, Tor, Vibeke Skytt, and Anne-Marie Ytrehus, 1989, "Recursive Subdivision and Iteration in Intersections and Related Problems," in *Mathematical Methods in Computer Aided Geometric Design*, (edited by) Tom Lyche and Larry L. Schumaker, 207-214.

DuPont, Pierre E. and Stephen Derby, Oct. 16-22, 1988, "An Algorithm for CAD-Based Generation of Collision-Free Robot Paths," *Proceedings of the NATO Advanced Research Workshop on Sensory Robotics for Limp Materials*, Ciocco, Italy, pp. 433-465.

Farouki, R. T., 1985, "Exact Offset Procedures for Simple Solids," *Computer Aided Geometric Design*, vol. 2, pp. 257-279.

Farouki, R. T., 1986, "The Approximation of Non-degenerate Offset Surfaces," *Computer-Aided Geometric Design*, vol. 3, pp. 15-43.

Farouki, R. T. and T. Sakkalis, September 1990, "Pythagorean Hodographs," *IBM Journal of Research and Development*, vol. 34, no. 5, pp. 736-752.

Foley, James D., Andries van Dam, Steven K. Feiner, and John F. Hughes, 1990, *Computer Graphics, Principles and Practice*, Second Edition, Addison Wesley, Reading, MA, pp. 471-530.

Forrest, A. R., July 1980, "The Twisted Cubic Curve: A Computer-Aided Geometric Design Approach," *Computer Aided Design*, vol. 12, no. 4, pp. 165-172.

Gasmi, Bernadette, and Claude Reboulet, Oct. 16-22, 1988, "Trajectory Planning and Obstacle Avoidance," *Proceedings of the NATO Advanced Research Workshop on Sensory Robotics for Limp Materials*, Ciocco, Italy, pp. 244-261.

Hoschek, Josef, March 1985, "Offset Curves in the Plane," *Computer Aided Design*, vol. 17, no. 2, pp. 77-82.

Hoschek, Josef, 1988, "Spline Approximation of Offset Curves," *Computer Aided Geometric Design*, vol. 5, pp. 33-40.

Hwang, Yong K. and Narendra Ahuja, February 1992, "A Potential Field Approach to Path Planning," *IEEE Transactions on Robotics and Automation*, vol. 8, no. 1, pp. 23-32.

Klass, Reinhold, September 1983, "An Offset Spline Approximation for Plane Cubic Splines," *Computer Aided Design*, vol. 15, no. 5, pp. 297-299.

Kaufmann, E. and R. Klass, 1988, "Smoothing Surfaces using Reflection Lines for Families of Splines," *Computer Aided Design*, vol. 20, no. 6, pp. 312-316.

Koren, Yoram, April 9-11, 1991, "Potential Field Methods and Their Inherent Limitations for Robot Navigation," *Proceedings of the 1991 IEEE International Conference on Robotics and Automation*, Sacramento, CA, pp. 1398-1404.

Laugier, Christian, Oct. 16-22, 1988, "Planning Robot Motions in the SHARP System," *Proceedings of the NATO Advanced Research Workshop on Sensory Robotics for Limp Materials*, Ciocco, Italy, pp. 151-187.

Lee, D. T. and Franco P. Preparata, December 1984, "Computational Geometry - A Survey," *IEEE Transactions on Computers*, vol. C-33, no. 12, pp. 1072-1101.

Leu, M. C. and S. K. Singh, July 4-6, 1988, "Optimal Planning of Trajectories for Robots," *Proceedings of the NATO Advanced Research Workshop on CAD Based Programming for Sensory Robots*, Ciocco, Italy, pp. 467-477.

Lozano-Perez, Tomas, and Michael A. Wesley,1979, "An Algorithm for Planning Collision-Free Paths Among Polyhedral Obstacles," *Communications of the ACM*, vol. 22, no. 10, pp. 560-570.

Lozano-Perez, Tomas, 1982, "Task Planning," as chapter 6 in *Robot Motion: Planning and Control*, edited by Michael Brady, John M. Hollerback, Timothy Johnson, Tomas Lozano-Perez, and Matthew T. Mason, MIT Press, Cambridge, MA, pp. 485-585.

Lozano-Perez, Tomas, February 1983, "Spatial Planning: A Configuration Space Approach," *IEEE Transactions on Computers*, vol. C-32, on. 2, as reprinted in Autonomous Mobile Robots: Perception, Mapping, and Navigation, edited by S. S. Iyengar and Alberto Elfes, pp.395-407.

Lozano-Perez, Tomas and Russell H. Taylor, 1989, "Geometric Issues in Planning Robot Tasks," as Chapter 6 in, *Robotics Science*, edited by Michael Brady, MIT Press, Cambridge, MA, pp. 227-261.

Lumelsky, V. J., 1991, "A Comparative Study on the Path Length Performance of Maze-Searching and Robot Motion Planning Algorithms," *IEEE Transactions on Robotics and Automation*, vol. 7, no. 1, pp. 57-66.

McLean, Alistair and Stephen Cameron, May 2-6, 1993, "Snake-Based Path Planning for Redundant Manipulators," *Proceedings of the IEEE International Conference on Robotics and Automation*, Atlanta, GA, pp. 275-282.

Mitchell, Joseph J. B., December 1988, "An Algorithmic Approach to Some Problems in Terrain Navigation," *Artificial Intelligence*, vol. 37, no. 1-3, pp. 171-201.

Mortenson, Michael E., 1990, *Computer Graphics Handbook, Geometry and Mathematics*, Industrial Press, New York, pp. 138-145 & 197-199.

Mortenson, Michael E., 1985, *Geometric Modeling*, John Wiley and Sons, New York.

Papamichael, N. and M. J. Soares, 1987, "Cubic and Quintic Spline-on-Spline Interpolation," *Journal of Computational and Applied Mathematics*, vol. 20, pp. 359-366.

Patel, R. V. and Z. Lin, August 8-12, 1988, "Collision Free Trajectory Planning for Robot Manipulators," *Proceedings of the 1988 IEEE International Conference on Systems, Man, and Cybernetics*, Bejing and Shenyang, China, vol. 2, pp. 787-790.

Pantelic, Dejan V. and Zoran D. Janevski, 1989, "A New Kind of Splines and Their Use for Fast Ray-Tracing in Reflective Cavities," *Computer Physics Communications*, vol. 55, pp. 5-11.

Papamichael, N. and M. J. Soares, 1987, "Cubic and Quintic Spline-on-Spline Interpolation," *Journal of Computational and Applied Mathematics*, vol. 20, pp. 359-366.

Pham, B., 1988, "Offset Approximations of Uniform B-Splines," *Computer Aided Design*, vol. 20, no. 8, pp. 471-474.

Piegl, Les and Tiller, Wayne, November 1987, "Curve and Surface Constructions using Rational b-Splines," *Computer-Aided Design*, vol. 19, no. 9, pp. 485-493.

Piegl, Les A., 1991, "Rational B-Spline Curves and Surfaces for CAD and Graphics," *in State of the Art in Computer Graphics, Visualization and Modeling*, (edited by) David F. Rogers and Rae A. Earnshaw, Springer-Verlag, New York, pp. 225-269.

Prasad, Mukesh, 1991, "Intersection of Line Segments," *Graphics Gems II*, edited by James Arvo, Academic Press, Boston, pp. 7-9 & 473-476.

Pratt & Whitney, United Technologies Corp., 1996, "F100-PW-229 Increased Performance Engine," brochure 1991-10M, PO Box 109600, W. Palm Beach, FL 33410-9600.

Rohnert, Hans, 1991, "Moving a Disc Between Polygons," *Algorithmica*, vol. 6, pp. 182-191.

Sandgren, E. and S. Venkataraman, Sept. 17-21, 1989, "Robot Path Planning via Simulated Annealing: A Near Real Time Approach," *Proceedings of the ASME Design Automation Conference*, pp. 345-351.

Schwartz, J. T. and M. Sharir, December 1988, "A survey of Motion Planning and Related Geometric Algorithms," *Artificial Intelligence*, vol. 37, no. 1-3, pp. 157-169.

Sederberg, Thomas W. and Scott R. Parry, 1986, "Comparison of Three Curve Intersection Algorithms," *Computer Aided Design*, vol. 18, no. 1, pp. 58-63.

Sederberg, Thomas W. and Xuguang Wang, 1987, "Rational Hodographs," *Computer Aided Geometric Design*, vol. 4, pp. 33-335.

Sederberg, Thomas W. and Ray J. Meyers, 1988, "Loop Detection in Surface Patch Intersections," *Computer Aided Geometric Design*, vol. 5, pp. 161-171.

Seereeram, Sanjeev and John T. Wen, February 1995, "A Global Approach to Path Planning for Redundant Manipulators," *IEEE Transactions on Robotics and Automation*, vol. 11, no. 1, pp. 152-160.

Shafer, Clifford A. and Charles D. Feustel, 1992, "Exact Computation of 2-D Intersections," *Graphics Gems III*, edited by David Kirk, Academic Press, Boston, pp. 188-192 & 491-495.

Sharir, Micha, and Elka Ariel-Sheffi, July 1984, "On the Piano Mover's Problem: Various Decomposable Two Dimensional Motion-Planning Problems," *Communications on Pure and Applied Mathematics*, vol. 37, no. 4, pp. 479-493.

Souvaine, D. L., 1986, *Computational Geometry in a Curved World*, Ph.D. Dissertation, Department of Computer Science, Princeton University, Princeton, NJ.

Tiller, Wayne, September 1983, "Rational B-splines for Curve and Surface Representation," *IEEE Computer Graphics and Applications*, vol. 3, no. 6, pp. 61-69.
Discusses NURBS and they are needed.

Tiller, Wayne and Eric G. Hanson, 1984, "Offsets of Two Dimensional Profiles," *IEEE Computer Graphics and Applications*, vol. 4, no. 9, pp. 36-46.

Wapenhans, H., J. Holzl, J. Steinle, and F. Pfeiffer, 1994, "Optimal Trajectory Planning with Application to Industrial Robots," *International Journal of Advanced Manufacturing Technology*, vol. 9, pp. 49-55.

Whitsides, S. H., 1985, "Computational Geometry and Motion Planning," in *Computational Geometry*, (edited by) Godfried T. Toussaint, North-Holland, New York, pp. 377-427.

Xue, Quing and P. C-Y. Sheu, 1989, "Path Planning for Two Cooperating Robot Manipulators," *IEEE Proceedings*, pp. 649-657.

Yap, Chee-Keng, 1987, "Algorithmic Motion Planning," as chapter 3 in, *Algorithmic and Geometric Aspects of Robotics*, Volume 1, (edited by) Jacob T. Schwartz and Chee-Keng Yap, Lawrence Erlbaum Associates, Hillsdale, NJ., pp. 95-141.

Hwang, Yong K., and Narendra Ahuja, September 1992, "Gross Motion Planning - A Survey," *ACM Computing Surveys*, vol. 24, no. 3, pp. 219-291.

Importance of Current Crowding and Self-heating Effects in a CdS/LaS Cold Cathode

M.Cahay
Associate Professor
Department of Electrical Engineering

University of Cincinnati
832 Rhodes Hall
Cincinnati, Ohio 45221

Final Report for:
Summer Faculty Research Program
Wright Laboratory

Sponsored by:
Air Force Office Of Scientific Research
Bolling Air Force Base, DC

and

Wright laboratory

November 1996

Modeling and Design of New Cold Cathode Emitters Using Wide Bandgap Semiconductors

M.Cahay
Associate Professor
Department of Electrical Engineeering
University of Cincinnati

ABSTRACT

We analyze the importance of current crowding in a new cold cathode emitter which consists of a thin wide bandgap semiconductor material sandwiched between a metallic or heavily doped semiconductor and a low work function semimetallic thin film. Potential material candidates are suggested to achieve low-voltage (< 10 V), room-temperature cold cathode operation with emission currents of several tens of A/ cm^2. We calculate the lateral potential drop which occurs across the emission window of cold cathodes with circular geometry and describe its effects on the emitted current density profile. The power dissipation in the cold cathode is calculated as a function of a dimensionless parameter characterizing the importance of current crowding. We determine the range of dc bias over which cold cathodes of different radii must be operated to minimize current crowding and self-heating effects.

I. INTRODUCTION

Recently, there has been renewed interest into cold cathode emitters for applications to a variety of electronic devices, including microwave vacuum transistors and tubes, pressure sensors, thin panel displays, high temperature and radiation tolerant sensors, among others [1, 2]. Introduction of such emitters would permit an unprecedented compactness and weight reduction in device and equipment design. Low temperature operation in nonthermionic electron emitters is very desirable for keeping the statistical energy distribution of emitted electrons as narrow as possible, to minimize thermal drift of solid state device characteristics, and to avoid accelerated thermal aging or destruction by internal mechanical stress and fatigue. To keep the emitter temperature rise small appears easy if the emitters are built as thin epitaxial films using vertical layering technology due to the extremely short heatpaths and excellent heatsinking possibilities offered with this architecture. For an electron emitter to be useful in microwave tube applications it should be capable of delivering current densities in excess of 10 A/ cm^2 and to sustain emission during operational lifetimes over periods of 10^5 hrs. To satisfy this requirement, the structural and chemical composition must be stable. This rules out the historically practiced use of alkali metal films on emitter surfaces for the lowering of electronic work functions. These films sublimate, evaporate or surface migrate over time and end up on various surfaces inside the vacuum envelop.

Several cold cathode emitters have been proposed since their first successful demonstration by Williams and Simon [3] using a cesiated p-type GaP structure. A review and criticism of the different cold cathode approaches was given recently by Akinwande et al. [4]. In this work, we propose a new cold cathode emitter concept and use a simple model to show that the new emitter is capable of achieving low voltage (< 10 V) room temperature operation with emission current approaching 100 A/cm^2 and large efficiencies. A preliminary report of this work has been published earlier [5]. The architecture of the structure is shown in Fig. 1. The main elements in the design and functioning of such an emitter are : (1) a wide bandgap semiconductor slab equipped on one side with a metallic contact [6] or a heavily doped semiconductor ($n^{++} - InP$) on one side of an undoped CdS region that supplies electrons at a sufficient rate into the conduction band and (2) on the opposite side, a thin semimetallic film that facilitates the coherent transport (tunneling) of electrons from the semiconductor conduction band into vacuum. Of importance is the mutual alignment of the crystalline energy levels at the semiconductor-semimetal film junction. This requires the use of new materials and development of their epitaxial growth technologies. For that

reason, the choice of InP as a substrate is particularly attractive since the lattice constant of InP (5.86 Å) closely matches the lattice constant of the zincblende cubic CdS (5.83 Å). Furthermore, there have been recent reports on the deposition of crystalline layers of CdS on InP by molecular beam epitaxy [7], chemical bath deposition [8], and pulsed laser deposition [9]. The proposed cold cathode should therefore be realizable with present day technology.

As shown in Fig. 1(a), a thick metal grid is defined on the surface of the LaS thin film to bias the structure. There are openings in the grid structure to expose the thin LaS film which forms the active emission area of the cold cathode. Cathodes with rectangular (Fig.1(b)) emission windows were studied previously [5]. Current crowding and self-heating effects in cathodes with circular geometry (Fig.1(c)) emission windows will be considered hereafter. The bias is applied between the back metallic contact and the metal grid with emission occuring from the exposed LaS surface. If the applied voltage is equal or larger than the semiconductor bandgap energy and the quotient of the applied voltage divided by the semiconductor thickness approaches $0.1eV/\mathring{A}$, then electrons are tunnel injected into the conduction band and ascend during their travel across the semiconductor film to levels of increasing energy. Referring to Fig. 2, the conduction band of the wide bandgap semiconductor provides the launching site for electrons where they are - through a thin film - injected into vacuum. This injection of electrons into vacuum becomes possible and is effective as long as the semimetallic film is very thin and has a work function small enough so that its vacuum edge is located energetically below the conduction band edge of the semiconductor. This situation is referred to as negative electron affinity (NEA) for the semiconductor material [10]. Depending on the particular materials choices, this implies that the semimetal work function ϕ_M in relation to the semiconductor energy bandgap E_G must obey one of the inequalities $\phi_M < 0.5E_G$ or $\phi_M < E_G$ if an intrinsic or p-type doped wide bandgap semiconductor is used, respectively. A negative ϕ_M implies according to Fig.2 that the vacuum level would be located below the lower conduction band edge. In that case, electrons in the conduction band with momenta pointing toward the surface have a good chance to get emitted unless deflected by collision or trapped by impurities or defects.

This paper is organized as follows. In section II, we derive the basic equations describing the forward bias operation of the cold cathode emitter described above. We then calculate the current density-voltage characteristics of the newly proposed cold cathode for specific sets of materials and device parameters. In section III, we investigate the importance of current crowding effects in various cold cathodes with circular geometry. Our analysis includes a

self-consistent modeling of current crowding effects and an analysis of power dissipation in the cold cathode active area. The influence of power dissipation on self-heating effects in the active area of the cathode is also described. Finally, Sec. IV contains our conclusions.

II. THE MODEL

Hereafter, we analyze the cold cathode whose energy band diagram is shown in Fig. 2 [5]. Under the influence of a large electric field in the wide bandgap semiconductor, electrons will eventually tunnel from the left contact through the barrier at the metal-semiconductor interface. A portion of the current emitted at the metal or heavily doped semiconductor -CdS contact (which we model assuming Fowler-Nordheim injection) is transmitted at the boundary of the LaS as well as the vacuum boundary. However, a fraction of the current is lost in the thin LaS quantum well gives rise to the dynamic shift of the effective material work function (Fig. 2). For a cathode operated at room temperature, we model this internal field emission at the injection junction using a Fowler-Nordheim (FN) type expression for the injected current (in A/cm^2) [11]

$$J_{FN} = C_1(E^2/\Delta)e^{C_2\Delta^{3/2}/E}, \tag{1}$$

where C_1 and C_2 are constants which depend on the wide bandgap semiconductor. In our numerical simulations, we chose $C_1 = 1.5X10^6$ A/V and $C_2 = 6.9X10^7(V^{1/2}cm)^{-1}$ which are of the same order of magnitude as the constants appearing in the FN expression [11]. In Eq.(1), Δ is the barrier height (in eV) at the metal-semiconductor junction and E is the electric field (in V/cm) in the wide bandgap semiconductor [12]. We assume that the semiconductor layer thickness is such that the transport of injected electrons is close to being ballistic up to the interface between the semiconductor and the thin semimetallic film. In so doing, we also neglect carrier ionization processes in the semiconductor slab which could be the main antagonist to ballistic transport in that region.

Because of the finite probabilities for the injected current to be transmitted at the semiconductor-semimetal (probability T_1) and semimetal-vacuum interfaces (probability T_2), the contributions to the total emitted current can be calculated as the sum of the contributions resulting from the mutiple reflections of electrons in the semimetallic layer (See Fig. 2). The magnitudes of the emitted current components decreases with the number of multiple reflections in the semimetallic layer. Rather than trying to calculate these contributions exactly, we assume that the current amplitude is decreased by a factor $\epsilon = exp(-L_2/\lambda_{LaS})$

for each traversal of the semimetallic layer, where λ_{LaS} is the collisional mean free path in the semimetallic layer and L_2 is the length of the semimetallic layer. Adding the contributions resulting from multiple crossings of the semimetallic layers, the total emitted current is found to be

$$J_{em} = \epsilon T_1 T_2 J_0 (1 + x + x^2 + ...), \tag{2}$$

where $x = \epsilon^2 (1 - T_1)(1 - T_2)$. In calculating J_{em} we limited the number of traversals of the semimetallic slab to five to include the fact that electrons loose energy in each crossing and eventually do not have enough energy to surmount the barrier at the semimetal-vacuum interface. According to Eq.(2), the contributions from the multiple reflections decrease rapidly since, in general, the quantity x will be much smaller than unity [13]. Once the emitted current is found, the total current contributing to the increase in the sheet carrier concentration in the thin semimetallic film can easily be written as $J_{capt} = J_{FN} - J_{em}$. The total trapped current is then given by

$$i_T = A J_{capt} = A R J_{FN} \tag{3}$$

where A is the area of each LaS emission window which in practice can be either rectangular or circular (See Fig. 1b and 1c). In Eq.(3), R is the trapping coefficient of the well

$$R = 1 - \epsilon T_1 T_2 \, (1 + x + x^2). \tag{4}$$

The semimetallic thin film can be modeled as a quantum well (Q.W) which will loose the trapped electrons essentially at its lateral boundaries. In reality, Fig. 1(a) indicates that not all electrons will move to the three-dimensional contact regions surrounding the thin semimetallic layer but many of them will get reflected at the lateral thin film layer with an average probability r (calculated for electrons with the Fermi velocity in the thin film). The exiting number of electrons will depend on the thickness of the semimetallic layer and could be adjusted by intentional passivation so that reflection at the boundaries of the thin semimetallic film could be tuned from almost zero to nearly unity. Taking into account the finite reflection amplitude at the thin film boundaries, the leakage current of the Q.W can be rewritten

$$\frac{dQ_T}{dt} = 2eLN_{2D}v_F(1 - r), \tag{5}$$

for the case of a rectangular emission window and

$$\frac{dQ_T}{dt} = 2\pi eaN_{2D}v_F(1 - r), \tag{6}$$

for the case of a circular emission window.

In Eqns.(5) and (6), Q_T is the total charge captured by the well, e is the magnitude of the electronic charge, N_{2D} is the excess sheet carrier concentration in the thin film due to the captured electrons, and v_F is the Fermi electron velocity in the semimetallic thin film. Under steady state operation of the cold cathode, the excess charge in the two-dimensional semimetallic film is found using Eq.(3) and imposing the current balance requirement $\frac{dQ_T}{dt} = i_T = AJ_{capt}$. This leads to

$$N_{2D} = WJ_{capt}/2e(1-r)v_F, \tag{7}$$

for the case of a rectangular geometry and

$$N_{2D} = aJ_{capt}/2e(1-r)v_F, \tag{8}$$

for the case of a circular geometry.

Simultaneously, the change N_{2D} in the excess sheet carrier concentration in the Q.W due to trapped electrons leads to the occupation of the boundstate energy levels according to the energy density of states up to an energy level which will establish the dynamic Fermi level ${E_F}^1$. The Fermi velocity v_F entering Eqns.(5) and (6) must be calculated self-consistently because of the dynamic work function shift $|\Delta\chi|$ illustrated in Fig. 2. This dynamical shift $|\Delta\chi|$ is equal to $|{E_F}^1 - {E_F}^0|$, where ${E_F}^0$ is the Fermi level in the thin semimetallic layer under zero bias. For simplicity, we assume that the electrons in the conduction band of the semimetallic films can be described using the Sommerfeld theory of metals while assuming s-band conduction in the semimetallic thin film and while modeling the thin film using the particle in a box model for the quantum well [14]. The set of equations (1-8) is then solved self-consistently to calculate the work function shift $|\Delta\chi|$ as a junction of the externally applied bias. Once the dynamic shift has been determined self-consistently, Eq.(2) can then be used to determine the emitted current.

RESULTS

We consider a specific structure with the material and structural parameters listed in Table I and II, respectively. Both Au and Ag are known to form contacts to thin films of semiconducting (n-type) CdS. In that case, the barrier height Δ shown in Fig. 2 is quite small and is equal to 0.78 eV and 0.56 eV for the case of Au and Ag contacts, respectively [11]. The lattice constant of CdS (5.83$\mathring{A}$) is very close to the lattice constant of the thin semimetallic surface layer LaS (5.85 $\mathring{A}$) which in its cubic crystalline structure will therefore

be lattice matched to the semiconducting material. Additionally, LaS is expected to have quite a low room temperature work function (1.14 eV) [15], a feature when combined with the large energy gap (2.5 eV) of CdS leads to NEA of the semiconductor material. In the following numerical simulations, the thicknesses of the CdS (L_1) and LaS (L_2) layers are set equal to 500 $\AA$ and 24.6 $\AA$ (4 monolayers), respectively. We model a cathode with a square (W = L) emission window with a 1 cm^2 area.

Figure 3 is a plot of the dynamic work function shift as a function of applied bias for the cold cathode emitter with both Au and Ag injecting contacts. The following parameters were used: $\lambda_{LaS} = 300\AA$, $T_1 = T_2 = 0.5$, and $v_F = 1.36X10^8 cm/s$. Figure 3 indicates that the dynamic shift of the LaS work function is sensitive to the quality of the interface between the two-dimensional semimetallic layer and the three-dimensional contacts which we model by varying the reflection coefficient r between the two-dimensional semimetallic thin film and the three-dimensional contact regions (See Fig. 1(a)). It should be noticed that the LaS work function shift can approach the LaS workfunction even for the case of a *leaky* interface between the thin semimetallic layer and the 3D contact regions. The dynamic shift $|\Delta\chi|$ is comparable to the work function of LaS for a smaller value of the applied bias in the case of Ag contact because of the lower barrier at the Ag/CdS interface.

Figure 4 compares the emitted current densities J_{em} for the structure with Au and Ag contacts calculated while including or neglecting the effects of the dynamic shift of the LaS work function. The current density versus bias plots are stopped at the values of V_{bias} at which $|\Delta\chi| = \phi_M(LaS) = 1.14eV$. Beyond that point, the theory exposed here is no longer valid since we would need to include the spill over of the excess trapped carriers into vacuum. As can be seen in Fig. 4, the emitted current densities can be more than a factor two larger when the effects of the dynamic shift of the work function of the semimetal are included. The effects could be made more drastic if a set of materials and device parameters could be found for which the dynamic shift of the work function could be made comparable to the work function itself at fairly low value of the applied bias ($< 5V$).

Sensitivity of Dynamic Work Function Shift on Design Parameters

The previous numerical examples have shown that, under forward bias operation, the electrons captured in the low work function material are responsible for an effective reduction of the semimetallic film work function together with a substantial increase of the cathode emitted current. This dynamic work function shift was shown to increase with the amount of

injected current. Hereafter, we perform a more extensive study of the dynamic work function shift which includes variations of the length of the CdS region (L_1), the electron mean free path in the LaS region (λ_{LaS}), the emission window size (W), the transmission coefficients at the CdS/LaS (T_1) and LaS/Vacuum interfaces (T_2), and the reflection at the 2D/3D interface region in the LaS quantum well (r).

Figure 3 indicates that the dynamic work function shift $|\Delta\chi|$ rises exponentially above a threshold voltage of several volts and reaches rapidly (within a few volts range) a value comparable to the LaS work function. For a structure with the parameters listed in Table I and with the structural and physical parameters ($L_1 = 500$ $\mathring{A}$, $L_2 = 24.6\mathring{A}$, W = 1cm, $\lambda_{LaS} = 300\mathring{A}$, $T_1 = T_2 = 0.5$, $\Delta(A_g) = 0.56eV$), Fig. 5(a) shows that the dynamic work function shift rises exponentially at a lower bias as the reflection coefficient at the 2D/3D interface in the LaS region approaches unity. Figure 5(b) also shows that the difference between the current densities calculated with and without including the dynamic work function shift are more pronounced for smaller values of the applied bias when the reflection coefficient between the 2D and 3D LaS regions is approaching unity. This results from the fact that any mechanism (like r being closer to unity) which increases the amount of charge being trapped in the LaS quantum well leads to an enhancement of the dynamic work function shift at a given bias. For instance, all other cathode parameters being equal, the dynamic work function rises much faster as a function of applied bias in structures with thinner CdS regions (Fig. 6), with smaller values of the transmission coefficients T_1 and T_2 (Fig. 7), or with smaller mean free path (λ_{LaS}) in the semimetallic thin film (Fig. 8). As shown in Fig. 8(a), the dynamic work function shift occurs at a lower bias as λ_{LaS} is decreased. On the other hand, the emitted current density is lesser at a given bias in a cathode whose LaS thin film has a lower electron mean free path (Fig. 8(b)). We have found this trend to be valid for all values of the reflection coefficient at the LaS 2D/3D interface. However, there is a larger spread in the family of curves representing the bias dependence of the dynamic work function and emitted current densities as a function of the mean free path in the LaS thin film for smaller values of the reflection coefficient r. Finally, even though not shown here, the exponential rise of the dynamic work function shift and emitted current density has been shown to occur at lower value of the bias by either reducing the thickness of the CdS layer or by lowering the barrier height Δ at the metal/CdS interface.

Before leaving this section, we make two additional remarks on the bias dependence of the emitted current density and the dynamic work function shift which we have checked

numerically on all the cold cathodes modelled in this work. First, since the emission of electrons at the metal(or heavily semiconductor)/CdS interface is assumed to be of the Fowler-Nordheim type, the emission current is expected to have a bias dependence of the form

$$J_{FN} = A{V_{bias}}^2 exp(-B/V_{bias}). \tag{9}$$

This was checked numerically for all the cold cathodes modelled here. A typical example is given in Fig.9(a), with the values of the parameters A and B listed in the inset. Most of the quantities of interest to be determined hereafter (power dissipation, lateral variation of emitted current and lateral potential drop,...) can be calculated exactly analytically if the following approximation is used

$$J_{FN} = J_0 e^{\alpha V_{bias}}. \tag{10}$$

For all the cold cathodes simulated here, we have shown that Eq.(10) gives a fairly accurate fit to the plot of the emitted current density versus applied bias if the range of the fit is restricted to current densities between 1 and 1000 A/cm^2 . A typical fit for the one of the cold cathode studied here is shown in Fig.9(b) with the values of the parameters J_0 and α in Eq.(8) shown in the inset. Table III gives a summary of the parameters J_0 and α for cold cathodes of different width and with the physical parameters listed in the caption of Fig.5. We have found that the bias dependence of the dynamic work function shift is also of the Fowler-Nordheim type, i.e,

$$\Delta\chi = \Delta_0 {V_{bias}}^2 exp(-V_0/V_{bias}). \tag{11}$$

This is illustrated in Fig.10 for the cold cathode with the same parameters as in Fig.9. The values of Δ_0 and V_0 are indicated in the inset of Fig.10. We point out that the values of the parameters B and V_0 in Eqns.(9) and (10) are nearly identical.

Temperature Rise in the Cold Cathode

Hereafter, we derive an upper estimate of the temperature rise in the LaS thin film as a result of the power dissipation mechanisms discussed above. We focuss on a cold cathode where the CdS thin film is deposited on a InP substrate as shown in Fig.1(a). The successful growth of cubic CdS thin films with good crystalline quality on InP substrates has been reported recently by Shen and Kwok [9]. For the case of a InP/CdS interface, there has not been any report of the conduction band discontinuity ΔE_c at the interface between the two

materials, to the best of our knowledge. For that reason, ΔE_c was assumed to be given by Anderson's rule, i.e, Δ in Fig. 2 is assumed to be given by $|\chi(InP) - \chi(CdS)| = 0.2$ eV [16]. This estimate was based on the measured electron affinities of InP (4.4 eV) and CdS (4.2 eV) reported in refs. [17] and [18], respectively. The back contact to the substrate is assumed to be perfectly ohmic and to act as a perfect heat sink (300K). Since the device area (heat source formed of the LaS thin fim) is much thinner than the substrate, it is necessary to consider the effect of heat spreading laterally in the substrate. Furthermore, we assume that the temperature of the CdS layer will be the same as the LaS top layer. The active area of the cathode (CdS and LaS layers) is therefore assumed to be acting as a heat source with the power density calculated in the previous section. Because of the finite thermal conductivity of the substrate, we expect self-heating effects to affect the operation of the cold cathode if the power level dissipated in the active area of the cathode becomes too important. Hereafter, we model the thermal conductivity of the InP substrate as follows

$$\kappa(T) = \kappa_0 (T/T_0)^{-b}, \tag{12}$$

where κ_0 is the thermal conductivity at T_0 (300K), $\kappa_0 = 0.74$ W/Kcm is the room temperature thermal conductivity of InP and b=1.45. Starting with Fick's law and making use of a Kirchoff transformation to take into account the temperature dependence of the thermal conductivity of the InP substrate given by Eq.(12), it can be shown that the active area of the cold cathode will be operated at a temperature given by

$$T = \left[\frac{1}{T_0^{b-1}} - (b-1) \frac{R_{th,0} P_{diss}}{T_0^{b}} \right]^{\frac{-1}{(b-1)}}, \tag{13}$$

where T_0 is the ambient room temperature (assumed to be 300 K hereafter), P_{diss} is the total power dissipated per finger as calculated in the previous section, and

$$R_{th,0} = \frac{1}{\kappa_0} \int_0^{zs} \frac{dz}{A(z)}, \tag{14}$$

where Z_S is the thickness of the InP substrate. Our estimate of the temperature rise in the active cold cathode area will give an upper estimate of the temperature of operation since we neglected heat conduction to the top Au contacts in the thick portion of the LaS thin film.

III. Current Crowding Effects in Proposed Cold Cathode with a Circular Geometry

In this section, we study the effects of current crowding in the case of an emission window with circular geometry (see Fig.1(c)). The lateral potential drop in the circular LaS window satisfies the following differential equation [19]

$$\frac{dV}{dr} = \frac{\rho_s}{t} i(r), \tag{15}$$

where i(r) is the total lateral current per unit length flowing outward across a circle of radius r, whose center coincide with the center of the emission window. The lateral current satisfies the following equation

$$2\pi r i(r) = 2\pi R \int_0^r dr' r' j(r'). \tag{16}$$

If we further assume that the Fowler-Nordheim emitted current j(r) can be approximated by Eq.(10) over the range of dc bias considered here, the following second-order differential equation must be satisfied by the lateral potential drop:

$$\frac{d^2V}{dr^2} + \frac{1}{r}\frac{dV}{dr} = \frac{\rho_S R J_0}{t} e^{V(r)/V_T}. \tag{17}$$

This differential equation must be solved subject to the following boundary conditions valid for the circular geometry

$$\frac{dV}{dr} = 0, \tag{18}$$

at r = 0, and

$$V(r = a) = V_{bias}, \tag{19}$$

at the edge of the circular window. Introducing the reduced variable $r' = r/a$ and the quantity

$$Y = \frac{V - V_{bias}}{V_T}, \tag{20}$$

Eq.(17) can be recast as follows

$$\frac{d^2Y}{dr'^2} + \frac{1}{r'}\frac{dY}{dr'} = 2\gamma^2 e^Y, \tag{21}$$

where $\gamma^2 = \frac{\beta^2 a^2}{2}$ and the parameter β is identical to the one defined for the planar problem [20].

The general solution of Eq.(21) can be found analytically and is given by

$$e^Y = (c\delta^2/\gamma^2)[r'^{\delta-2}/(1-cr'^{\delta})^2], \tag{22}$$

where δ and c are constants to be determined so the boundary conditions (18) and (19) are satisfied. Using the new system of variables, Eq.(18) becomes

$$\frac{dY}{dr'}|_0 = 0, \tag{23}$$

while Eq.(19) now reads

$$Y(1) = 0. \tag{24}$$

Equation (23) leads to

$$\delta = 2. \tag{25}$$

and Equation (24) becomes

$$\delta^2 = (1-c)^2\gamma^2/c. \tag{26}$$

Combining these last two equations, we obtain the following result

$$\gamma^2 = \frac{4c}{[1-c]^2}, \tag{27}$$

Equation (27) can be solved exactly for the parameter c

$$c = [\gamma^2 + 2 - 2\sqrt{\gamma^2+1}]/\gamma^2 \tag{28}$$

in terms of which we can write various quantities of interest, including the ratio

$$J(0)/J(a) = [1-c]^2, \tag{29}$$

characterizing the importance of current crowding in the circular geometry. Using Eqn.(22), the radial dependence of the lateral potential drop if found to be

$$V(r) = V_{bias} - 2V_T ln[\frac{a^2 - cr^2}{a^2(1-c)}], \tag{30}$$

from which the maximum value of the in plane electric field is found to be

$$E_r(r=a) = \frac{4c}{c-1}\frac{V_T}{a}. \tag{31}$$

As in the case of the rectangular geometry, the total power dissipated in the LaS thin film is given by the sum of the following four contributions [20]. The power dissipated by the electrons being trapped in the LaS circular thin film is given by

$$P_1 = 2\pi R \int_0^a dr j(r)V(r). \tag{32}$$

The power dissipated by Joule heating as trapped electrons move to the edge of the LaS window is given by

$$P_2 = \frac{2\pi\rho_s R^2}{t}\int_0^a \frac{dr}{r}[\int_0^r r' j(r')dr']^2. \tag{33}$$

The third contribution to power dissipation comes from from Joule heating linked to the current making it from the LaS thin film to the Au contacts on top of the thick LaS regions.

$$P_3 = R_c(2\pi a i(a))^2. \tag{34}$$

where R_c is the resistance of the LaS region between the edge of the LaS thin film and the top Au layer. This resistance can be estimated as follows [21]

$$R_c = \frac{\rho_S H}{t2\pi a}\frac{lnk}{k-1}, \tag{35}$$

where $k = b/t$, a is the radius of the circular window, and H is the height of the thick LaS region.

Finally, there is also a contribution to power dissipation due to the blocking effect on the Folwer-Nordheim emission current emitted under the wide LaS contacts:

$$P_4 = \pi b(b+2a)J_0 e^{\alpha V_{bias}}. \tag{36}$$

Starting with Eqns.(10) and (30), the different contributions to the power dissipation can be calculated exactly and are found to be

$$P_1 = \pi a^2 J_0 R e^{\alpha V_{bias}} V_{bias}(1-c) - \pi a^2 J_0 R e^{\alpha V_{bias}} V_T[2(1-c) + \frac{(1-c)^2}{c} ln(1-c)^2], \tag{37}$$

$$P_2 = R(\pi a^2 J_0 e^{\alpha V_{bias}}) V_T[2(1-c) + \frac{(1-c)^2}{c} ln(1-c)^2], \tag{38}$$

P_3 is given by Eq.(34) and P_4 is found to be

$$P_4 = \frac{R_c R^2}{2(1-R)^2} {I_{em}}^2, \tag{39}$$

where I_{em} is the total emitted current through the circular window

$$I_{em} = 2\pi(1-R)\int_0^a rj(r)dr. \tag{40}$$

The latter can be calculated explicitely and is found to be

$$I_{em} = (1-R)[\pi a^2 J_0 e^{\alpha V_{bias}}](1-c). \tag{41}$$

The input power (per emission window) delivered by the power supply biasing the cold cathode is given by

$$P_{input} = \int_0^{a+b} 2\pi r j(r) V(r) dr, \tag{42}$$

which can readily be shown to be given by

$$P_{input} = P_1/R + P_4. \tag{43}$$

The power efficiency of the cold cathode can be calcualted as follows

$$\eta_P = \frac{P_{input} - P_{diss}}{P_{input}}. \tag{44}$$

and the temperature rise in the cathode is given by Eq.(13). where the thermal resistance $R_{th,0}$ must be calculated for the case of power dissipation through the substrate from a heat source with circular geometry. In this case, we find

$$R_{th,0} = \frac{1}{\kappa_0} \frac{z_s}{a} \frac{1}{[a + z_s tan\theta]}, \tag{45}$$

in which the heat spreading angle θ is set equal to 45° in the numerical examples below, for simplicity.

Numerical Examples

Figure 11 shows the variation of the parameter c in Eq.(28) as a function of applied bias for cold cathodes with circular emission window of different radii. For all cathodes, the physical parameters are the same as listed in the caption of Fig.5. As in the case of a rectangular window, we use the criterion that current crowding is negligible if the lateral potential drop between the center and the edge of the LaS circular window, $V(r = 0) - V_{bias}$, is kept less than $0.1V_T$. Using Eqns.(28) and (30), we find that this criterion requires the parameter c to be less than 0.05. This limit is indicated as a vertical line in Fig. 11. The family of curves in Fig.11 is parametrized with the radius of the emission window. Figure 11 shows that the range of dc bias over which current crowding can be neglected in a circular window is comparable to the range of dc bias over which current crowding is negligible in a rectangular window whose width is equal to the radius of the circular emission window [20].

Figure 12 illustrates the importance of current crowding on the lateral potential drop in emitter windows of different radii. The left frames show the radial dependence of the electrostatic potential for four different values (1,10,100,1000 A/cm^2) of the current density at

the rim of the circular LaS window. The right frames in Fig.12 show the corresponding radial dependence of the emitted current density. From Fig.12, it can be seen that current crowding is negligible in emitter windows with radius less than 50 μm if the emitted current density is kept under 10 A/cm^2. As in the case of LaS windows with rectangular geometry, Figure 12 shows that the current density profiles are much more sensitive to the finite resistivity of the LaS thin film than the lateral potential drop.

Figure 13 is a plot of the four contributions to the total power dissipated in cold cathodes with different radii plotted as a function of the parameter c. For all cathodes, the power dissipation due to Joule heating in the LaS thin film and the thick LaS regions is negligible compare to the power released by electrons being trapped in the LaS thin film and by electrons blocked in the thick LaS regions. The latter is always about one of magnitude higher than the former. Figure 13 shows that substantial power dissipation occurs in the cathode with radius under $50\mu m$ while the cathode is still operating without any substantial current crowding effects (i.e, c $<$ 0.05). The power efficiency η_P of cathodes of different width is plotted as a function of V_{bias} and the emitted current density J_{em} in Figs. 14(a) and 14(b), respectively. For all window size, the efficiency decreases with V_{bias} and J_{em} as a result of current crowding. The efficiency is more or less constant over a wider range of V_{bias} for window with smaller radius because current crowding is less important in that case, as illustrated in Fig. 12. The overall lower efficiency for window with smaller radius illustrated in Fig. 14 comes from the fact that the width of the thick LaS regions was set equal to $100\mu m$ for all cathodes. The efficiency of cathodes could be increased by making the ratio b/a in Fig.1(b) closer to unity.

Figure 15 shows the temperature of the active area of a cold cathode with the parameters listed in Table I as a function of V_{bias} for emitter window with different radii. The thickness of the LaS contacts and InP substrate was set equal to $100\mathring{A}$ and $100\mu m$, respectively. As in case of cold cathodes whose emission window as a rectangular geometry [20], Fig. 15 indicates that to limit the temperature rise in any cathode to less than 200 K, the dc bias must be limited to a smaller range for emitters with smaller window radius. For instance, according to Figures 11 and 15, a cathode with a $20\mu m$ diameter can be operated up to 8.3 V with negligible self-heating effects (ΔT around 100 K). For that bias, Figure 12 indicates that current crowding would be negligible in the cathode and the emitted current density would be around 100 A/cm^2 (See Fig. 16). On the other hand, Figure 11 indicates that a $100\mu m$ diameter window can be operated up to 6.8 V before current crowding becomes

non negligible. At this bias, the emitted current density would be around 15 A/cm^2 (Fig. 16) while the temperature rise in the device would be only about 15 K as shown in Fig. 15.

IV. CONCLUSIONS

We have proposed a new cold cathode emitter which consists of a thin wide bandgap semiconductor material sandwiched between a metallic material or heavily doped semiconductor, and a low work function semimetallic thin film. We have shown that the capture of electrons by thin semimetallic layers grown on the escape surface of wide bandgap semiconductors can lead to a dynamical shift of the work function of the semimetallic layers together with an increase of the cathode emission current. While varying the device and physical parameters of the structure, our studies suggest that any mechanism which promotes additional charge deposit in the well enhances the dynamic work function shift phenomenon thereby increasing the emitted current. Potential material candidates were proposed for cold cathode operation with applied bias under 10 V, with current densities approaching several tens of A/cm^2, and with large power efficiencies (η_P approaching 15 %).

The results of our analysis show that a cold cathode with either a rectangular or circular emission window and with the parameters listed in Tables I and II would emit a uniform current density of about $15A/cm^2$ at a dc biasing voltage of about 8V. For that bias, the effects of current crowding would be negligible and the temperature rise in the active area of the cathode (CdS/LaS layers) as a result of self-heating effects would be negligible.

Further improvements to the theory should include a more realistic model for the emission current and transport through the wide bandgap material. Also, the semimetallic film energy density of states (to account for the d-band character of the conduction band in the chosen rare-earth semimetallic samples [14]), the finite probability for electron wavefunctions in the thin semimetallic films to extend in the semiconductor material [22], a more accurate description of the energy loss mechanisms [23] and screening effects (including the lateral ohmic voltage drop) in thin semimetallic layers [24]. Finally, our study of self-heating effects should include partial cooling of the cathode due to heat conduction through the thick LaS layers which was neglected in this study. The latter would allow to extend slightly the dc biasing operating range of the cathode beyond the estimate reported here. Furthermore, the thermal and electrical models of the cathode described here should be solved self-consistently. Once all these effects are taken into account, we believe the quantitative operation of the cold cathode exposed here will stay essentially correct predicting a dynamical shift of the

work function of the thin semimetallic film of the same order of magnitude than the one reported here.

Our analysis provides the basic design rules to fabricate a new cold cathode with emission windows with a rectanguler or circular geometry. The growth of the structure would require the epitaxial growth of the structure shown in Fig.1. As discussed above, the epitaxial growth of InP/CdS heterostructures has been reported in the literature in the past [9]. The deposition of epitaxial LaS thin films has not been reported, to the best of our knowledge. We believe, however, that the figures of merits of the various cold cathodes analyzed in this work are a strong incentive towards the experimental investigation of these devices. If successful, such an experimental effort would lead to big pay-offs with the design of highly efficient cold cathodes for large panel displays, IR image convertors and sensors, and active power devices in mobile and airborne electronic equipment for military, commercial, and private use.

ACKNOWLEDGMENT

This work was sponsored by the Air Force Office of Scientific Research, Boiling AFB, D.C and by Wrigth laboratory.

References

[1] S. Iannazzo, Solid State Electronics, Vol. 36(3), 301 (1993).

[2] I. Brodie and C. A. Spindt, Advances in Electronics and Electron Physics, Vol. 83, p.2 (1992).

[3] B. K. Williams and R. E. Simon, Physical Review Letters, Vol. 18(13), 485 (1967).

[4] A. I. Akinwande, P. P. Ruden, B. L. Goldenberg, D. K. Arch, and John King, Proceedings of 1994 Tri-Service (NASA) Cathode Workshop, Cleveland, Ohio, March 1994, p. 105.

[5] A preliminary account of this work has been published in: P. D. Mumford and M. Cahay, Journal of Applied Physics, Vol. 79(5), 2176 (1996). This work follows suggestions which are documented in two in-house reports by W. Friz, Final Technical Report, Task ELM-

9, June 1992, and Technical Note, Task ELM-6, January 1995 (Wright-Patterson Air Force Base).

[6] The most desirable form of electron injection is accomplished by an ohmic contact because it puts minimal electrical stress on the material and, at the same time, provides the highest current densities.

[7] Deposition of crystalline layers of CdS on InP by MBE are presented by W. G. Wilke, R. Seedorf, and K. Horn, J. Vac. Sci. Technology. B, Vol.7, p.807 (1989).

[8] Chemical bath deposition (CBD) of crystalline layers of CdS on InP are discussed by D. Lincot, R. Ortega-Borges, and M. Froment, Appl. Phys. Letters, Vol. 64, p.569 (1994).

[9] W. P. Shen and H. S. Kwok, Appl. Phys. Letters, Vol. 65(17), p.2162 (1994). In this article, the authors report the epitaxial growth of various II-VI compound semiconductors ($ZnS, ZnSe, CdS, CdSe$, and $CdTe$) on (111) and (1000) InP and $GaAs$ substrates by excimer laser ablation. All the films have good crystalline quality (fully in-plane) and mirror-like surface morphology. They found that, on (111)-oriented substrates, CdS and $CdSe$ films were in the hexagonal phase with the c axis perpendicular to the surface, while ZnS and $ZnSe$ flms were in the cubic phase. The films grwon on (100)-oriented substrates were all cubic. See also W. P. Shen and H. S. Kwok in *Compound Semiconductor Epitaxy*, edited by C. W. Tu, L. A. Kolodziejski, and V. R. McCrary, [Mater. Res. Soc. Symp. Proc. **340**, 1994].

[10] P. R. Bell, Negative Electron Affinity Devices, Oxford: Claredon Press, 1973

[11] Sze, Physics of Semiconductor Devices, 2nd Edition, Wiley, p. 291 (1981).

[12] Assuming that the most part of the wide bandgap semiconductor is an intrinsic material (See Fig. 1), accumulation and depletion effects can be ignored. Referring to Fig. 1, the resulting uniform electric field across the wide bandgap semiconductor is then given by

$$E = \frac{1}{L_1}[V_{bias} + \Delta - (\frac{E_G}{2} - |\Delta\chi|)]. \tag{46}$$

[13] Both T_1 and T_2 should actually be function of the number of reflections in the semimetallic slab since the electrons loose energy during each traversal. This is however just a refinement to the general theory exposed in this paper.

[14] N. W. Aschcroft and N. D. Mermin, Solid State Physics, Saunders College, Philadelphia, 1976.

[15] The room temperature work function for LaS was calculated by extrapolating measured work function values at high temperature as reported by S. Fomenko in *Handbook of Thermionic properties* (Plenum, New York, 1966). Within the range of temperature investigated by Fomenko, the LaS work function increases with temperature at a rate of $2meV/K$.

[16] There are other reports for the electron affinity of CdS, including $\Delta\Xi_{CdS} = 4.5$ eV in [11]. In this case, Anderson's rule would allow electrons to spill over from the InP to the CdS region, an injection mechanism hard to control. The problem of the InP/CdS interface deserves more attention [9].

[17] Shyh Wang, Fundamental of Semiconductor Theory and Device Physics, Prentice Hall Series in Electrical and Computer Engineering, Leon O. Chua, Series Editor (1989).

[18] There are conflicting reports for the measured electron affinity of CdS. The affinity is known to vary with the surface orientation and the phase of the semiconductor material. Here, we use the electron affinity $\chi_{CdS} = 4.2$ eV reported in O. Madelung, "Semiconductors other than Group IV elements and III-V compounds ", Springer (1992).

[19] E. S. Kohn, Journal of Applied Physics, Vol. 42(6), 2493 (1971).

[20] M. Cahay, Final report, Summer Faculty Research Program, AFOSR, September 1996.

[21] J. A. Edminister, Electromagnetics, Schaum's Outline Series, McGraw-Hill Book Company (1979).

[22] M. L. Huberman and J. Maserjian, Physical Review B, Vol. 37(15), 9065 (1988).

[23] R. C. Jaklevic and J. Lambe, Phys. Rev. B, Vol. 12, 4146 (1975).

[24] Y. Silberberg and T. Sands, IEEE Journal of Quantum Electronics, Vol. 28 (7), 1663 (1992).

Associate did not participate in program.

A NOVEL COMPATIBILITY/EQUILIBRIUM BASED ITERATIVE POST-PROCESSING APPROACH FOR AXISYMMETRIC BRITTLE MATRIX COMPOSITES

Reaz A. Chaudhuri, Associate Professor

Department of Materials Science & Engineering,

304 EMRO Building

University of Utah

Salt Lake City, UT 84112

Final Report for:

Summer Faculty Research Program

Wright Laboratory

Sponsored by:

Air Force Office of Scientific Research

Bolling Air Force Base, DC

and

Wright Laboratory

Wright -Patterson Air Force Base, Ohio

October, 1996

A NOVEL COMPATIBILITY/EQUILIBRIUM BASED ITERATIVE POST-PROCESSING APPROACH FOR AXISYMMETRIC BRITTLE MATRIX COMPOSITES

Reaz A. Chaudhuri, Associate Professor

Department of Materials Science & Engineering, University of Utah

Abstract

A semi-analytical iterative approach for enhancing the existing two-dimensional quasi-continuous axisymmetric stress field for a brittle matrix micro-composite (i. e., a single fiber surrounded by a concentric matrix cylinder), is presented. The existing solution employs Reissner's variational theorem in conjunction with an equilibrium stress field in which the radial (r-) dependence is assumed *a priori.*

In the present approach, the stress distribution in the radial direction obtained from the afore-cited variational model is improved *a posteriori* through an iterative approach that involves successive substitution of the previously computed strains (or stresses) into the equations of compatibility and equilibrium. The boundary/interface conditions at r = constant surfaces are satisfied in the pointwise sense. However, this process leaves the end boundary conditions in the axial direction (i.e., at surfaces z = constant) undefined thus rendering the boundary-value formulation ill-posed. This ill-posedness is removed by introducing appropriate boundary error terms that help satisfy the end boundary conditions at surfaces z = constant. As a first step, an approximate plane strain version of the present solution is implemented in a FORTRAN code. An illustrative thermal stress problem is solved and used to compare with the existing variational solution .

A NOVEL COMPATIBILITY/EQUILIBRIUM BASED ITERATIVE POST-PROCESSING APPROACH FOR AXISYMMETRIC BRITTLE MATRIX COMPOSITES

Reaz A. Chaudhuri, Associate Professor
Department of Materials Science & Engineering, University of Utah

1. Introduction:

Studies of the behavior of unidirectional and laminated composites made from stiff elastic matrix materials which may develop imperfect interfaces with the fibers have enjoyed a revival after the early classical work of Aveston, Cooper, and Kelly (1971). Pagano (1991) refers to these materials as brittle matrix composites (BMC). The aforementioned ACK modeling, as well as the more recent development proposed by Budiansky, Hutchinson, and Evans (1986), are based upon primitive approximations of the stress field developed within a concentric cylinder, i.e., a circular cylindrical body of one material surrounded by a concentric annulus or ring of a second material. There exists a considerable body of literature associated with the elasticity problem of a concentric cylinder, where modern interest is focused on its use as a representative volume element (RVE) of a unidirectional composite (Hashin and Rosen, 1964; Pagano and Tandon, 1988). Additionally, a significant segment of the composite literature is based upon the one-dimensional shear lag analysis, which was apparently originated by Cox (1952). The results obtained using this kind of analysis are too inaccurate to merit further attention in this report.

Sternberg (1970) solved several axisymmetric load diffusion problems within a concentric cylindrical domain, in which the elasticity formulations are simplified by the assumption that the core material (fiber) can be modeled as a one-dimensional bar while the annular region (matrix) in all cases extends to infinity. An exact solution was derived for the case in which the bar was circular in cross-section, and was fully immersed within the unbounded matrix. A similar approach, with the difference of the fiber being assumed rigid, was employed by Luk and Keer (1979). This assumption is more appropriate for resin matrix composites, where the fiber to

matrix modulus ratio is very high. The axisymmetric elasticity problem of a broken fiber embedded in an infinite matrix was treated by Pickett and Johnson (1967). In that work, the fiber is represented as a three-dimensional elastic medium; however, the report contained no numerical results for the stress field. Smith and Spencer (1970) also formulated an axisymmetric elasticity solution by a semi-inverse method for a class of boundary value problems in which the radius and length of the concentric cylinder are both finite. The solution is expressed in the form of a series of non-orthogonal functions which satisfy the field equations exactly. Homogeneous boundary conditions on the radial surface of the body are satisfied exactly while realistic end conditions can be approximated. The singularities predicted by Zak (1964) are smoothed out in this approach. A very formidable study, which includes correlation with experimental observations, is that by Atkinson et al (1982). In this work, the pullout of a single fiber from a matrix cylinder is treated. The fiber extends only partially along its length into the matrix. Results are provided for a perfectly bonded fiber-matrix interface as well as for states in which lateral (curved) surface debonding or fiber end plane debonding take place. The problem is solved by "patching" the asymptotic singular stress field to that given by finite elements, although this method is not always reliable. An interesting conclusion is reached that, at least in a qualitative sense, the interface failure response can be anticipated from the stress field within the uncracked rod. In a model similar to Pagano's (1991), McCartney (1990) treated a class of concentric cylinder problems in which matrix cracking or debonding with or without friction are present. In that work, the functional r-dependence of the stress components is assumed which leads to a system of ordinary differential equations in z. All appropriate field equations are satisfied with the exception of two of the constitutive relations while some of the boundary/interface conditions could only be satisfied in an average sense. The ease and potential effectiveness of this model for composite analysis will demand its careful consideration in comparison with exact solutions and solutions given by competitive approaches. For example, Kurtz and Pagano (1991) formulated an infinite series solution of the axisymmetric elasticity problem in which a fiber is being pulled from the matrix. The length of the body as well as the outer radius are finite. Although the singularity is not explicit in the solution, Cesaro summation has been employed to improve the convergence of the stress field within the singular region.

The solution for the stated problem has been obtained by employing a modified version of the variational model (Pagano, 1991) of an axisymmetric concentric cylinder, which was successfully implemented earlier in the case of a flat laminate by Pagano (1978). The model is generated by subdividing the body into regions consisting of a core and a number of shells of constant thickness and length and satisfying the Reissner variational equation (1950) with an assumed stress field in each region. The number of regions, in particular in the r direction, can be increased in order to improve solution accuracy. The regions are selected such that the thermoelastic properties are constant and the boundary conditions do not change character on any of the bounding surfaces within each region. Pagano (1991) has sought to predict the influence of various kinds of damage (see Figure 1) and their interactions by accurately modeling the micro-mechanical stress field in their presence by using the afore-cited variational approach.

Strengths and Weaknesses of the Existing Approach (Pagano, 1991)

Strengths:

1. This assumed stress based approach insures satisfaction of the axisymmetric equilibrium equations;

2. The existing method utilizes a reasonably accurate non-singular axial (z-direction) variation of the computed stress field that also satisfies the end (z = const.) boundary conditions (i. e., no artificial discontinuity due to sectioning).

Weaknesses:

1. Layering in the radial direction, that introduces artificial discontinuities in some stress components at a layer interface within the same material;

2. As the number of layer increases, the computed eigenvalues become numerically very large, thus limiting the number of layers required for accurate stress field in the vicinity of a stress singularity point.

Objectives of the Current Research:

The present method seeks to alleviate the afore-mentioned weaknesses of the existing approach, while preserving its inherent strengths. The specific goals of the present investigation includes

- Improvement of the radial (r-) variation of the stresses so that subdivision into very thin layers and the associated blow-up of the computed eigenvalues can be avoided,

- Artificial discontinuities of some stress components, such as σ_θ at a layer interface within the same material can be avoided.

2. Method of Analysis

Starting point of the present research is Pagano's (1991) layerwise axisymmetric solution for fiber-matrix concentric cylinder model, based on Reissner's variational theorem (1950) in conjunction with an equilibrium stress field, in which the radial (r-) dependence is assumed *a priori*. An approximate model was formulated to define the thermoelastic response of a concentric fiber-matrix cylindrical body under axisymmetric boundary conditions. The interfaces between continguous cylinders may be either continuous or subjected to mixed traction and displacement boundary conditions. The external surfaces may be subjected to mixed boundary conditions that are consistent with the model assumptions but otherwise arbitrary.

In this paper, an improved stress field within a layer is derived starting from Pagano's layerwise axisymmetric fiber-matrix concentric cylinder solution. The stress distribution in the radial direction obtained from the afore-cited layerwise fiber-matrix concentric cylinder model is improved *a posteriori* through an iterative approach that involves successive substitution of the previously computed strains (or stresses) into the equations of compatibility and equilibrium. A similar procedure was implemented in the post-processing part of a layerwise finite element code for analysis of quasi-three-dimensional laminated plates/shells to obtain a more accurate through-thickness distribution of interlaminar shear stresses (see Chaudhuri and Seide, 1987a; and Chaudhuri, 1990). The boundary/interface conditions at r = constant surfaces are satisfied in the pointwise sense, thus eliminating artificial discontinuity in computed $\sigma_\theta(r,z)$ and $\sigma_z(r,z)$ across a layer-interface within the same material. In what follows, the axisymmetric fiber-matrix concentric cylinder is assumed, for the purpose of illustrating the potential of the new method, to be divided into two layers — the core or fiber layer and the annulus or matrix layer. First, the method of deriving the improved stress field is illustrated for the fiber layer, which is then followed by the same for the matrix layer.

Improved Stress Field in the Core (Fiber Layer)

Pagano (1991) in his axisymmetric fiber-matrix concentric cylinder model has assumed a linear variation of axial stress, $\sigma_z(r,z)$ and hoop stress, $\sigma_\theta(r,z)$, with respect to r within a fiber or matrix layer. This is consistent with the assumption of Love-Kirchhoff's thin shell theory. However, he derived the interlaminar shear stress, $\tau_{rz}(r,z)$, and the radial stress, $\sigma_r(r,z)$, using the equations of equilibrium in line with his earlier work (see Pagano, 1969) before substituting these stresses into Reissner's (1950) variational principle. Pagano (1969) had shown that these stresses are improved to the extent that they are reasonably close to their elasticity theory based counterparts. Chaudhuri (1986), and Chaudhuri and Seide (1987a) successfully implemented this method in a finite element based post-processing approach for computing interlaminar shear stress distribution through the thickness of a symmetric laminate. Pagano's (1991) stress field for the fiber layer (core) is as shown below:

$$\bar{\sigma}_z^f(r,z) = p_{11}^f(z)\frac{r_2 - r}{r_2} + p_{12}^f(z)\frac{r}{r_2} \tag{1a}$$

$$\bar{\tau}_{rz}^f(r,z) = p_{52}^f(z)\frac{r}{r_2} + p_{53}^f(z)(r - r_2)r \tag{1b}$$

$$\bar{\sigma}_r^f(r,z) = p_{31}^f(z)(\frac{r_2 - r}{r_2}) + p_{32}^f(z)\frac{r}{r_2} + p_{33}^f(z)(r^2 - r_2^2)r + p_{34}^f(z)(r - r_2)r \tag{1c}$$

A bar on the stresses indicates that these are computed using the axisymmetric variational model due to Pagano (1991). The general form of Pagano's (1991) solution for any of the dependent variables P(z) is expressed by

$$P(z) = \sum_i A_i e^{\lambda_i z} + P_p(z) \tag{2}$$

within each constituent where A_i are constants, λ_i are eigenvalues of a determinant, and $P_p(z)$ is a particular solution, which in the present case is a simple polynomial. Further details of the solution procedure including the method for determining the higher order eigenvector and higher order particular solution are discussed by Brown (1992).

It is worthwhile to point out here that although the barred stresses satisfy the equations of equilibrium for an axisymmetric elastic body, the corresponding strains fail to satisfy the equations

of compatibility in the pointwise sense. It is noteworthy that although both the plane strain and axisymmetric deformations represent two-dimensional states, the latter case requires four compatibility equations to be satisfied by the strains computed using Pagano's (1991) axisymmetric variational model. This is in contrast to the case of plane strain, wherein only one compatibility equation out of the six is not an identity. However, if the hoop stress, σ_θ, is derived using the exact axisymmetric elasticity based kinematic relations and Hooke's law, then three of the four compatibility equations required by the axisymmetric elasticity theory become identities. The combined kinematic and stress-strain relations for axisymmetric elasticity theory are given as follows (Timoshenko and Goodier, 1959):

$$u(r,z) = r\varepsilon_\theta(r,z) = \frac{1}{E}\{\sigma_\theta - \nu(\overline{\sigma}_r + \overline{\sigma}_z)\} \tag{3a}$$

$$\frac{\partial u(r,z)}{\partial r} = \varepsilon_r(r,z) = \frac{1}{E}\{\overline{\sigma}_r - \nu(\sigma_\theta + \overline{\sigma}_z)\} \tag{3b}$$

Elimination of u(r,z) from eqns (3), followed by integration with respect to r, yields

$$\tilde{\sigma}_\theta(r,z) = r^{-(1+\nu)}\left[\int\left\{(1+\nu)r^\nu\overline{\sigma}_r(r,z) + \nu r^{(1+\nu)}\frac{\partial\overline{\sigma}_r(r,z)}{\partial r} + \nu r^{(1+\nu)}\frac{\partial\overline{\sigma}_z(r,z)}{\partial r}\right\}dr + F_0(z)\right] \tag{4}$$

where $F_0(z)$ is an arbitrary function of z. Substitution of $\overline{\sigma}_r^f(r,z)$ and $\overline{\sigma}_z^f(r,z)$ from eqns (1a,b) into the right side of eqn (4) yields

$$\tilde{\sigma}_\theta^f(r,z) = \sigma_\theta^f{}^*(r,z) + \frac{1}{r^{1+\nu_f}}D_0(z) \tag{5a}$$

where

$$\sigma_\theta^f{}^*(r,z) = (1+\nu_f)[p_{31}^f(z)(\frac{1}{\nu_f+1} - \frac{r}{r_2(\nu_f+2)}) + p_{32}^f(z)\frac{r}{r_2(\nu_f+2)} + p_{33}^f(z)(\frac{r^3}{\nu_f+4} - \frac{rr_2^2}{\nu_f+2})$$
$$+p_{34}^f(z)(\frac{r^2}{\nu_f+3} - \frac{r_2 r}{\nu_f+2})] + \nu_f[-p_{31}^f(z)\frac{r}{(\nu_f+2)r_2} + p_{32}^f(z)\frac{r}{r_2(\nu_f+2)} + p_{33}^f(z)(\frac{3r^3}{\nu_f+4}$$
$$-\frac{rr_2^2}{\nu_f+2}) + p_{34}^f(z)(\frac{2r^2}{\nu_f+3} - \frac{rr_2}{\nu_f+2}) - p_{11}^f(z)\frac{r}{r_2(\nu_f+2)} + p_{12}^f(z)\frac{r}{\nu_f+2}] \tag{5b}$$

The corresponding strains, $\bar{\varepsilon}_r$ and $\bar{\gamma}_{rz}$, can now be obtained by substitution of the above stresses into Hooke's law:

$$\bar{\varepsilon}_r = \frac{1}{E}[\bar{\sigma}_r - \nu(\tilde{\sigma}_\theta + \bar{\sigma}_z)]; \qquad \bar{\gamma}_{rz} = \frac{1}{G}\bar{\tau}_{rz} \tag{6a,b}$$

It may be noted that the above two strains, $\bar{\varepsilon}_r$ and $\bar{\gamma}_{rz}$, are not compatible with the axial strain, $\bar{\varepsilon}_z$, computed using Hooke's law

$$\bar{\varepsilon}_z = \frac{1}{E}[\bar{\sigma}_z - \nu(\tilde{\sigma}_\theta + \bar{\sigma}_r)] \tag{6c}$$

because the remaining compatibility equation

$$\frac{\partial^2 \varepsilon_z}{\partial r^2} + \frac{\partial^2 \varepsilon_r}{\partial z^2} = \frac{\partial^2 \gamma_{rz}}{\partial r \partial z} \tag{7}$$

is not satisfied. The axial strain is, therefore, obtained by substituting $\bar{\varepsilon}_r$ and $\bar{\gamma}_{rz}$ given by eqns (5a,b) into the integrated (twice with respect to r) version of the compatibility equation (7)

$$\varepsilon_z(r,z) = -\iint \frac{\partial^2 \varepsilon_r}{\partial z^2} ds dr + \int \frac{\partial \gamma_{rz}}{\partial z} dr + rF_1(z) + F_2(z) \tag{8}$$

which yields

$$\tilde{\varepsilon}_z^f(r,z) = \varepsilon_z^f{}^*(r,z) - \frac{\nu_f{}^2}{E_f} D_0''(z)(\log r - 1) + \frac{1}{G_f}\{rD_1(z) + D_2(z)\} \tag{9a}$$

where

$$\varepsilon_z^f{}^*(r,z) = -\frac{1}{E_f}[p_{31}''(z)\frac{r^2(3r_2 - r)}{6r_2} + p_{32}''(z)\frac{r^3}{6r_2} + p_{33}''(z)\frac{r^3}{2}(\frac{r^2}{10} - \frac{r_2^2}{3}) + p_{34}''(z)\frac{r^3}{6}(\frac{r}{2} - r_2)]$$

$$-\nu_f(1+\nu_f)[p_{31}''(z)\{\frac{r^2}{2(\nu_f+1)} - \frac{r^3}{6(\nu_f+2)r_2}\} + p_{32}''(z)\frac{r^3}{6(\nu_f+2)r_2} + p_{33}''(z)\{\frac{r^5}{20(\nu_f+4)}$$

$$-\frac{r_2^2 r^3}{6(\nu_f+2)}\} + p_{34}''(z)(\frac{r^4}{12(\nu_f+3)} - \frac{r_2 r^3}{6(\nu_f+2)})] - \nu_f^2[-p_{31}''(z)\frac{r^3}{6(\nu_f+2)r_2} + p_{32}''(z)\frac{r^3}{6(\nu_f+2)r_2}$$

$$+p''_{33}(z)\left(\frac{3r^5}{20(\nu_f+4)}-\frac{r_2^2r^3}{6(\nu_f+2)}\right)+p''_{34}(z)\left(\frac{r^4}{6(3+\nu_f)}-\frac{r_2r^3}{6(2+\nu_f)}\right)-p''_{11}(z)\frac{r^3}{6r_2(2+\nu_f)}$$

$$+p''_{12}(z)\frac{r^3}{6(2+\nu_f)}]+D''_0(z)\frac{1}{r^{\nu}}\}+\frac{1}{G_f}[p'_{52}(z)\frac{r^3}{6r_2}+p'_{53}(z)(\frac{r^4}{12}-r_2\frac{r^3}{6})] \qquad (9b)$$

It may be noted that the superscript f on p_{ij} is dropped, in the interest of notational convenience, in eqn (9b) and in those that follow. The corresponding normal stress, $\tilde{\sigma}_z^f$, can be obtained by using Hooke's law as follows:

$$\tilde{\sigma}_z^f(r,z)=E_f\tilde{\varepsilon}_z^f(r,z)+\nu_f\{\tilde{\sigma}_r^f(r,z)+\tilde{\sigma}_\theta^f(r,z)\} \qquad (10)$$

It is noteworthy that although the axial strain or its stress counterpart, $\tilde{\sigma}_z$, satisfies the compatibility eqn (7), it is no longer in equilibrium (in the pointwise sense) with the stresses, $\tilde{\tau}_{rz}$ and $\tilde{\sigma}_r$. These stresses are, therefore, rederived from the following two equilibrium equations:

$$\frac{\partial\tau_{rz}}{\partial r}+\frac{\tau_{rz}}{r}+\frac{\partial\sigma_z}{\partial z}=0 \qquad (11a)$$

$$\frac{\partial\sigma_r}{\partial r}+\frac{\sigma_r-\sigma_\theta}{r}+\frac{\partial\tau_{rz}}{\partial z}=0 \qquad (11b)$$

$\tilde{\tau}_{rz}$ and $\tilde{\sigma}_r$ can now be obtained from eqns (11) upon integration as follows:

$$\tilde{\tau}_{rz}(r,z)=\frac{1}{r}[-\int r\frac{\partial\tilde{\sigma}_z}{\partial z}dr+F_3(z)] \qquad (12a)$$

$$\tilde{\sigma}_r(r,z)=\frac{1}{r}[\int\tilde{\sigma}_\theta dr-\int r\frac{\partial\tilde{\tau}_{rz}}{\partial z}dr+F_4(z)] \qquad (12b)$$

Substitution of $\tilde{\sigma}_z^f(r,z)$, given by eqn (10) into the integrated equilibrium equation (12a) yields

$$\tilde{\tau}_{rz}^f(r,z)=\tau_{rz}^f{}^*(r,z)+D'''_0\frac{r^{1-\nu_f}}{2-\nu_f}\}+D'_0(z)\frac{1}{(1-\nu_f)r^{\nu_f}}+\frac{r}{2G_f}\{D'_1(z)+D'_2(z)\}+\frac{D_3(z)}{r} \qquad (13a)$$

where

$$\tau_{rz}^{f}*(r,z)=p_{31}'''(z)\left(\frac{15r_2r^3-4r^4}{120r_2}\right)+p_{32}'''(z)\frac{r^4}{30r_2}+p_{33}'''(z)\left(\frac{r^6}{140}-\frac{r_2^2r^4}{30}\right)+p_{34}'''(z)\left(\frac{r^5}{72}-\frac{r_2r^4}{30}\right)$$

$$-E_f\nu_f(1+\nu_f)\left[p_{31}'''(z)\left\{\frac{r^3}{8(\nu_f+1)}-\frac{r^4}{30(\nu_f+2)r_2}\right\}+p_{32}'''(z)\frac{r^4}{30(\nu_f+2)r_2}+p_{33}'''(z)\left\{\frac{r^6}{140(\nu_f+4)}\right.\right.$$

$$\left.\left.-\frac{r_2^2r^4}{30(\nu_f+2)}\right\}+p_{34}'''(z)\left\{\frac{r^5}{72(\nu_f+3)}-\frac{r_2r^4}{30(\nu_f+2)}\right\}\right]-E_f\nu_f^2\left[-p_{31}'''(z)\frac{r^4}{30(\nu_f+2)r_2}\right.$$

$$+p_{32}'''(z)\frac{r^4}{30(\nu_f+2)r_2}+p_{33}'''(z)\left\{\frac{3r^6}{140(\nu_f+4)}-\frac{r_2^2r^4}{30(\nu_f+2)}\right\}+p_{34}'''(z)\left\{\frac{r^5}{36(\nu_f+3)}-\frac{r_2r^4}{30(\nu_f+2)}\right\}$$

$$\left.-p_{11}'''(z)\frac{r^4}{30(\nu_f+2)r_2}+p_{12}'''(z)\frac{r^4}{30(\nu_f+2)}\right]+\frac{E_f}{G_f}\left[p_{52}''(z)\frac{r^4}{30r_2}+p_{53}''(z)\left(\frac{r^5}{72}-\frac{r_2r^4}{30}\right)\right]$$

$$+\nu_f\left[p_{31}'(z)\left(\frac{3rr_2-2r^2}{18}\right)+p_{32}'(z)\left(\frac{r^2}{3r_2}\right)+p_{33}'(z)\left(\frac{r^4}{5}-\frac{r_2^2r^2}{3}\right)+p_{34}'(z)\left(\frac{r^3}{4}-\frac{r^2r_2}{3}\right)\right]$$

$$+\nu_f(1+\nu_f)\left[p_{31}'(z)\left\{\frac{r}{2(\nu_f+1)}-\frac{r^2}{3(\nu_f+2)r_2}\right\}+p_{32}'(z)\frac{r^2}{3(\nu_f+2)r_2}+p_{33}'(z)\left\{\frac{r^4}{\nu_f+4}-\frac{r_2^2r^2}{\nu_f+2}\right\}\right.$$

$$\left.+p_{34}'(z)\left\{\frac{r^3}{4(\nu_f+3)}-\frac{r_2r^2}{3(\nu_f+2)}\right\}\right]+\nu_f^2\left[-p_{31}'(z)\frac{r^2}{3(\nu_f+2)r_2}+p_{32}'(z)\frac{r^2}{3(\nu_f+2)r_2}\right.$$

$$+p_{33}'(z)\left\{\frac{3r^4}{5(\nu_f+4)}-\frac{r_2^2r^2}{3(\nu_f+3)}\right\}+p_{34}'(z)\left\{\frac{r^3}{2(\nu_f+3))}-\frac{r_2r^2}{3(\nu_f+2)}\right\}-p_{11}'(z)\frac{r^2}{3(\nu_f+2)r_2}$$

$$\left.+p_{12}'(z)\frac{r^2}{3(\nu_f+2)}\right] \qquad (13b)$$

Substitution of $\tilde{\sigma}_\theta^f(r,z)$ and $\tilde{\tau}_{rz}^f(r,z)$ given by eqns (5) and (13) into the second integrated equilibrium equation (12b) yields

$$\tilde{\sigma}_r^f(r,z)=\sigma_r^{f}*(r,z)-(1+\nu_f)D_0(z)\nu_f r^{1-\nu_f}+D_0''(z)\frac{r^{1-\nu_f}}{(1-\nu_f)(2-\nu_f)}$$
$$+D_0''''(z)\frac{r^{2-\nu_f}}{(2-\nu_f)(3-\nu_f)}\Big\}+\frac{r^2}{6G_f}\{D_1''(z)+D_2''(z)\}-D_3'(z)+\frac{D_4(z)}{r} \qquad (14a)$$

where

$$\sigma_r^f{}^*(r,z) = (1+\nu_f)[p_{31}(z)\{\frac{1}{(\nu_f+1)} - \frac{r}{2(\nu_f+2)r_2}\} + p_{32}(z)\frac{r}{2(\nu_f+2)r_2}$$

$$+p_{33}(z)\{\frac{r^3}{4(\nu_f+4)} - \frac{rr_2^2}{2(\nu_f+2)}\} + p_{34}(z)\{\frac{r^2}{3(\nu_f+3)} - \frac{r_2 r}{2(\nu_f+2)}\}] + \nu_f[-p_{31}(z)\frac{r}{2(\nu_f+2)r_2}$$

$$+p_{32}(z)\frac{r}{2(\nu_f+2)r_2} + p_{33}(z)\{\frac{3r^3}{4(\nu_f+4)} - rr_2^2\frac{1}{2(\nu_f+2)}\} + p_{34}(z)\{\frac{2r^2}{3(\nu_f+3)} - \frac{r_2 r}{2(\nu_f+2)}\}$$

$$-p_{11}(z)\frac{r}{2(\nu_f+2)r_2} + p_{12}(z)\frac{r}{2(\nu_f+2)}] - [p_{31}''''(z)(\frac{r_2 r^4}{40} - \frac{r^5}{180})\frac{1}{r_2} + p_{32}''''(z)\frac{r^5}{180r_2}$$

$$+p_{33}''''(z)(\frac{r^7}{1120} - \frac{r_2^2 r^5}{180}) + p_{34}''''(z)(\frac{r^6}{504} - \frac{r_2 r^5}{180}) - E_f\nu_f(1+\nu_f)[p_{31}''''(z)\{\frac{r^4}{40(\nu_f+1)} - \frac{r^5}{180(\nu_f+2)r_2}\}$$

$$+p_{32}''''(z)\frac{r^5}{180(\nu_f+2)r_2} + p_{33}''''(z)\{\frac{r^7}{960(\nu_f+4)} - \frac{r_2^2 r^5}{180(\nu_f+2)}\} + p_{34}''''\{\frac{r^6}{504(\nu_f+3)}$$

$$-\frac{r_2 r^5}{180(\nu_f+2)}\}] - E_f\nu_f^2[-p_{31}''''(z)\frac{r^5}{180(\nu_f+2)r_2} + p_{32}''''(z)\frac{r^5}{180(\nu_f+2)r_2}$$

$$+p_{33}''''(z)\{\frac{3r^7}{1120(\nu_f+4)} - \frac{r_2^2 r^5}{180(\nu_f+2)}\} + p_{34}''''(z)\{\frac{r^6}{252(\nu_f+3)} - \frac{r_2 r^5}{180(\nu_f+2)}\}$$

$$-p_{11}''''(z)\frac{r^5}{180(\nu_f+2)r_2} + p_{12}''''(z)\frac{r^5}{180(\nu_f+2)r_2}] + \frac{E_f}{G_f}[p_{52}''''(z)\frac{r^5}{180r_2} + p_{53}''''(z)(\frac{r^6}{504} - \frac{r_2 r^5}{180})]$$

$$+\nu_f\{p_{31}''(z)(\frac{r^2 r_2}{6} - \frac{r^3}{12}) + p_{32}''(z)\frac{r^3}{12r_2} + p_{33}''(z)(\frac{r^5}{30} - \frac{r_2^2 r^3}{12}) + p_{34}''(z)(\frac{r^4}{20} - \frac{r^3 r_2}{12})\}$$

$$-\frac{r_2^2 r^3}{4(\nu_f+2)}\} + p_{34}''(z)\{\frac{r^4}{20(\nu_f+3)} - \frac{r_2 r^3}{12(\nu_f+2)}\}] + \nu_f^2[-p_{31}''(z)\frac{r^3}{12(\nu_f+2)r_2}$$

$$+p_{32}''(z)\frac{r^3}{12(\nu_f+2)r_2} + p_{33}''(z)\{\frac{3r^5}{30(\nu_f+4)} - \frac{r_2^2 r^3}{12(\nu_f+3)}\} + p_{34}''(z)\{\frac{r^4}{10(\nu_f+3)}$$

$$-\frac{r_2 r^3}{12(\nu_f+2)}\}-p_{11}''(z)\frac{r^3}{12(\nu_f+2)r_2}+p_{12}''(z)\frac{r^3}{12(\nu_f+2)}] \tag{14b}$$

Improved Stress Field in the Annular Region (Matrix Layer)

The procedure illustrated above for the fiber layer can easily be repeated for the matrix layer. Pagano's stress field for the matrix layer (annular region) is as shown below:

$$\bar{\sigma}_z^{(m)} = p_{11}(z)\left(\frac{r_2-r}{r_2-r_1}\right)+p_{12}(z)\left(\frac{r-r_1}{r_2-r_1}\right) \tag{15a}$$

$$\bar{\tau}_{rz}^{m} = p_{51}(z)\frac{r(r_2-r)}{r_1(r_2-r_1)}+p_{52}(z)\frac{r(r-r_1)}{r_2(r_2-r_1)}+p_{53}(z)\left(\frac{(r_1+r_2)r^2-(r_1^2+r_1r_2+r_2^2)r}{r_1^2r_2^2}+\frac{1}{r}\right) \tag{15b}$$

$$\bar{\sigma}_r^{(m)}.= p_{31}(z)\left(\frac{r_2-r}{r_2-r_1}\right)+p_{32}(z)\left(\frac{r-r_1}{r_2-r_1}\right)+p_{33}(z)\left(r^3-(r_1^2+r_1r_2+r_2^2)r+r_1r_2(r_1+r_2)\right)$$

$$+p_{34}(z)\left(r^2-(r_1+r_2)r+r_1r_2\right)+p_{35}(z)\left(r^2-(r_1+r_2)r+r_1r_2\right)\frac{1}{rr_1r_2} \tag{15c}$$

Following the procedure illustrated above, the improved hoop stress, $\tilde{\sigma}_\theta^m(r,z)$, axial strain, $\tilde{\varepsilon}_z^m(r,z)$, interlaminar shear stress, $\tilde{\tau}_{rz}^m(r,z)$, and the radial stress, $\tilde{\sigma}_r^m(r,z)$, are obtained as follows:

$$\tilde{\sigma}_\theta^m(r,z) = \sigma_\theta^m{}^*(r,z)+\frac{C_1(z)}{r} \tag{16a}$$

$$\sigma_\theta^m{}^*(r,z) = (1+\nu_m)[p_{31}(z)\frac{1}{r_2-r_1}(\frac{r_2}{\nu_m+1}-\frac{r}{\nu_m+2})+p_{32}(z)(\frac{r}{\nu_m+2}-\frac{r_1}{\nu_m+1})$$

$$+p_{33}(z)\{\frac{r^3}{\nu_m+4}-(r_1^2+r_1r_2+r_2^2)\frac{r}{\nu_m+2}r_1r_2(r_1+r_2)\frac{1}{\nu_m+1}\}+p_{34}(z)\{\frac{r^2}{\nu_m+3}$$

$$-(r_1+r_2)\frac{r}{\nu_m+2}+\frac{r_1r_2}{\nu_m+1}\}+p_{34}(z)\frac{1}{r_1r_2}\{\frac{r}{\nu_m+2}-(r_1+r_2)\frac{1}{\nu_m+1}+\frac{1}{r\nu_m}r_1r_2\}]$$

$$+\nu_m[-p_{31}(z)\frac{r}{(r_2-r_1)(\nu_m+2)}+p_{32}(z)\frac{r}{(r_2-r_1)(\nu_m+2)}+p_{33}(z)\{\frac{3r^3}{(\nu_m+4)}$$

$$-(r_1^2+r_1r_2+r_2^2)\frac{r}{(\nu_m+2)}\}++p_{34}(z)\{\frac{2r^2}{(\nu_m+3)}-(r_1+r_2)\frac{r}{(\nu_m+2)}\}$$

$$+p_{35}(z)\{\frac{1}{r_1r_2(\nu_m+1)}-\frac{1}{r\nu_m}\}-p_{11}(z)\frac{r}{(r_2-r_1)(\nu_m+2)}+p_{12}(z)\frac{r}{(r_2-r_1)(\nu_m+2)}] \tag{16b}$$

The axial strain is now obtained by substituting into the compatibility equation:

$$\tilde{\varepsilon}_z^m(r,z)=\varepsilon_z^m*(r,z)-\frac{\nu_m^{\,2}}{E_m}C_0''(z)(\log r-1)+\frac{1}{G_m}\{rC_1(z)+C_2(z)\} \tag{17a}$$

where

$$\varepsilon_z^m*(r,z)=-\frac{1}{E_m}[p_{31}''(z)\frac{(3r_2r^2-r^3)}{6(r_2-r_1)}+p_{32}''(z)\frac{(r^3-3r_1r^2)}{6(r_2-r_1)}+p_{33}''(z)\{\frac{r^5}{20}$$

$$-(r_1^2+r_1r_2+r_2^2)\frac{r^3}{6}+r_1r_2(r_1+r_2)\frac{r^2}{2}\}+p_{34}''(z)\{\frac{r^4}{12}-(r_1+r_2)\frac{r^3}{6}+r_1r_2\frac{r^2}{2}\}$$

$$+p_{35}''(z)\{\frac{r^3}{6r_1r_2}-\frac{(r_1+r_2)r^2}{2r_1r_2}+r(\log r-1)\}]+\frac{\nu_m(1+\nu_m)}{E_m}[\frac{p_{31}''(z)}{(r_2-r_1)}\{\frac{r_2r^2}{2(\nu_m+1)}$$

$$-\frac{r^3}{6(\nu_m+2)}\}+p_{32}''(z)\frac{1}{(r_2-r_1)}\{\frac{r^3}{6(\nu_m+2)}-\frac{r_1r^2}{2(\nu_m+1)}\}+p_{33}''(z)\{\frac{r^5}{20(\nu_m+4)}$$

$$-(r_1^2+r_1r_2+r_2^2)\frac{r^3}{6(\nu_m+2)}+\frac{(r_1+r_2)r_1r_2r^2}{2(\nu_m+1)}\}+p_{34}''(z)\{\frac{r^4}{12(\nu_m+3)}-\frac{(r_1+r_2)r^3}{(\nu_m+2)6}$$

$$+\frac{r_1r_2r^2}{2(\nu_m+1)}\}+p_{35}''(z)\{\frac{r^3}{6(\nu_m+2)}-\frac{(r_1+r_2)r^2}{2(\nu_m+1)}+\frac{r_1r_2r\log(r-1)}{\nu_m}\}]$$

$$-\frac{\nu_m^{\,2}}{E_m}[-p_{31}''(z)\frac{r^3}{6(r_2-r_1)(\nu_m+2)}+p_{32}''(z)\frac{r^3}{6(\nu_m+2)(r_2-r_1)}+p_{33}''(z)\{\frac{3r^5}{20(\nu_m+4)}$$

$$-(r_1^2+r_1r_2+r_2^2)\frac{r^3}{6(\nu_m+2)}\}+p_{34}''(z)\{\frac{r^4}{6(\nu_m+3)}-\frac{(r_1+r_2)r^3}{6(\nu_m+2)}\}+p_{35}''(z)\{\frac{r^2}{2r_1r_2(\nu_m+1)}$$

$$-(\log r-1)\}-p_{11}''(z)\frac{r^3}{6(r_2-r_1)(\nu_m+2)}+p_{12}''(z)\frac{r^3}{6(r_2-r_1)(\nu_m+2)}]$$

$$-\frac{\nu_m}{E_m}[p_{11}''(z)\frac{(3r_2r^2-r^3)}{6(r_2-r_1)}+p_{12}''(z)\frac{(r^3-3r_1r^2)}{6(r_2-r_1)}]+\frac{1}{G_m}[p_{51}'(z)\frac{(3r^2r_2-r^3)}{6r_1(r_2-r_{1)}}$$

$$+p'_{52}(z)\frac{(r^3-3r_1r^2)}{6r_2(r_2-r_1)}+p'_{53}(z)\{\frac{2(r_1+r_2)r^3-3(r_1^2+r_1r_2+r_2^2)r^2}{6r_1^2r_2^2}+\log r\}] \quad (17b)$$

$$\tilde{\sigma}_z^m(r,z)=E_m\tilde{\varepsilon}_z^m(r,z)+\nu_m\{\bar{\sigma}_r^m(r,z)+\tilde{\sigma}_\theta^m(r,z)\} \quad (18)$$

$$\tilde{\tau}_{rz}^m(r,z)=\tau_{rz}^m{}^*(r,z)+C_0'''\frac{r^{1-\nu_m}}{2-\nu_m}\}+C_0'(z)\frac{1}{(1-\nu_m)r^{\nu_m}}+\frac{r}{2G_m}\{C_1'(z)+C_2'(z)\}+\frac{C_3(z)}{r} \quad (19a)$$

where

$$\tau_{rz}^m{}^*(r,z)=-[p'''_{31}(z)\frac{(15r_2r^3-4r^4)}{120(r_2-r_1)}+p'''_{32}(z)\frac{(4r^4-15r_1r^3)}{120(r_2-r_1)}+p'''_{33}(z)\{\frac{r^6}{140}$$

$$-(r_1^2+r_1r_2+r_2^2)\frac{r^4}{30}+r_1r_2(r_1+r_2)\frac{r^3}{8}\}+p'''_{34}(z)\{\frac{r^5}{72}-(r_1+r_2)\frac{r^4}{30}+r_1r_2r^3\frac{1}{8}\}$$

$$+p'''_{35}(z)(\frac{r^4}{30r_1r_2}-\frac{(r_1+r_2)r^3}{8r_1r_2}+\frac{r^2}{3}(\log r-1)]-\frac{\nu_m(\nu_m+1)}{E_m}[p'''_{31}(z)\frac{1}{r_2-r_1}\{\frac{r_2r^3}{8(\nu_m+1)}$$

$$-\frac{r^4}{30(\nu_m+2)}\}+p'''_{32}(z)\frac{1}{r_2-r_1}\{\frac{r^4}{30(\nu_m+2)}-\frac{r_1r^3}{8(\nu_m+1)}\}+p'''_{33}(z)\{\frac{r^6}{120(\nu_m+4)}$$

$$+(r_1^2+r_1r_2+r_2^2)\frac{r^4}{30(\nu_m+2)}+\frac{r_1r_2(r_1+r_2)r^3}{8(\nu_m+1)}\}+p'''_{34}(z)(\frac{r^5}{72(\nu_m+3)}-\frac{(r_1+r_2)r^4}{30(\nu_m+2)}$$

$$+\frac{r_1r_2r^3}{8(\nu_m+1)}\}+p'''_{35}(z)\{\frac{r^4}{30(\nu_m+2)}-\frac{(r_1+r_2)r^3}{8(\nu_m+1)}+\frac{r_1r_2r^2}{3\nu_m}(\log r-1/3)\}]$$

$$-\frac{\nu_m{}^2}{E_m}[-p'''_{31}(z)\frac{r^4}{30(r_2-r_1)(\nu_m+2)}+p'''_{32}(z)\frac{r^4}{30(\nu_m+2)(r_2-r_1)}+p'''_{33}(z)\{\frac{r^6}{40(\nu_m+4)}$$

$$-\frac{(r_1^2+r_1r_2+r_2^2)r^4}{30(\nu_m+2)}\}+p'''_{34}(z)\{\frac{r^5}{36(\nu_m+3)}-\frac{(r_1+r_2)r^4}{30(\nu_m+2)}\}+p'''_{35}(z)\{\frac{r^3}{8r_1r_2(\nu_m+1)}$$

$$-\frac{r\log r}{2}+\frac{3r}{4}\}-p'''_{11}(z)\frac{r^4}{30(r_2-r_1)(\nu_m+2)}+p'''_{12}(z)\frac{r^4}{30(r_2-r_1)(\nu_m+2)}]$$

$$-\frac{\nu_m}{E_m}[p'''_{11}(z)\frac{(15r_2r^3-4r^4)}{120(r_2-r_1)}+p'''_{12}(z)\frac{(4r^4-15r_1r^3)}{120(r_2-r_1)}]+\frac{1}{G_m}[p''_{51}(z)\frac{(15r^3r_2-4r^4)}{120r_1(r_2-r_1)}$$

$$+p''_{52}(z)\frac{(4r^4-15r_1r^3)}{120r_2(r_2-r_1)}+p''_{53}(z)\{\frac{(r_1+r_2)4r^4-15(r_1^2+r_1r_2+r_2^2)r^3}{120r_1^2r_2^2}+\log r-1\}]$$

$$-\nu_m[p'_{31}(z)\frac{(3r_2r-2r^2)}{6(r_2-r_1)}+p'_{32}(z)\frac{(2r^2-3r_1r)}{6(r_2-r_1)}+p'_{33}(z)\{\frac{r^4}{5}-(r_1^2+r_1r_2+r_2^2)\frac{r^2}{3}$$

$$+r_1r_2(r_1+r_2)\frac{r}{2}\}+p'_{34}(z)\{\frac{r^3}{4}-(r_1+r_2)\frac{r^2}{3}+r_1r_2\frac{r}{2}\}+p'_{35}(z)\{\frac{r^2}{3}-(r_1+r_2)\frac{r}{2}+\frac{r_1r_2}{r}\}]$$

$$-\nu_m(1+\nu_m)[p'_{31}(z)\frac{1}{(r_2-r_1)}\{\frac{r_2r}{2(1+\nu_m)}-\frac{r^2}{3(\nu_m+2)}\}+p'_{32}(z)\frac{1}{(r_2-r_1)}\{\frac{r^2}{3(\nu_m+2)}$$

$$-\frac{rr_1}{2(\nu_m+1)}\}+p'_{33}(z)\{\frac{r^4}{5(\nu_m+2)}-(r_1^2+r_1r_2+r_2^2)\frac{r^2}{3(\nu_m+2)}+\frac{rr_1r_2(r_1+r_2)}{2(\nu_m+1)}\}$$

$$+p'_{34}(z)\{\frac{r^3}{\nu_m+3}-(r_1+r_2)\frac{r^2}{3(\nu_m+2)}+r_1r_2\frac{r}{2(\nu_m+1)}\}+p'_{35}(z)\frac{1}{r_1r_2}\{\frac{r^2}{3(\nu_m+2)}$$

$$-\frac{(r_1+r_2)r}{2(\nu+1)}+\frac{r_1r_2}{\nu_m}\}]-\nu_m{}^2[-p'_{31}(z)\frac{r^2}{3(\nu_m+2)(r_2-r_1)}+p'_{32}(z)\frac{r^2}{3(\nu_m+2)(r_2-r_1)}$$

$$+p'_{33}(z)\{\frac{3r^4}{5(\nu_m+4)}-(r_1^2+r_1r_2+r_2^2)\frac{r^2}{3(\nu_m+2)}\}+p'_{34}(z)\{\frac{r^3}{2(\nu_m+3)}-\frac{(r_1+r_2)r^2}{3(\nu_m+2)}\}$$

$$+p'_{35}(z)\{\frac{r}{2(\nu_m+1)r_1r_2}-\frac{1}{\nu_m}\}-p'_{11}(z)\frac{r^2}{3(\nu_m+2)(r_2-r_1)})+p'_{12}(z)\frac{r^2}{3(\nu_m+2)(r_2-r_1)}] \tag{19b}$$

$$\tilde{\sigma}_r^m(r,z)=\sigma_r^m{}^*(r,z)-(1+\nu_m)C_0(z)\nu_m r^{1-\nu_m}+C''_0(z)\frac{r^{1-\nu_m}}{(1-\nu_m)(2-\nu_m)}$$

$$+C''''_0(z)\frac{r^{2-\nu_m}}{(2-\nu_m)(3-\nu_m)}\}+\frac{r^2}{6G_m}\{C''_1(z)+C''_2(z)\}-C'_3(z)+\frac{C_4(z)}{r} \tag{20}$$

The expression for $\sigma_r^m{}^*(r,z)$ is too long to be incorporated in this brief report.

The above procedure introduces 10 "constants" of integration — 5 per layer— which are functions of z. These are determined by using appropriate boundary/interface conditions including those at the axis of symmetry. In the present two-layer fiber-matrix concentric cylinder model, the continuity of the radial and shear stresses, and also of the radial and axial displacement components, is enforced at the fiber-matrix interface. Additionally, the radial displacement component and the shear stress vanish at the axis of symmetry. On the outer free surface, the radial and shear stresses vanish. The details are available in Chaudhuri et al. (to be published), and are omitted here because of space limitation.

Ill-posedness and Its Remediation Through Regularization

The above procedure loses the end boundary conditions in the axial direction (i.e., at surfaces z = constant) , a kind of mathematical Alzheimer's, thus rendering the boundary-value formulation ill-posed. This is due to the fact that the boundary-value problem has now been transformed into an initial value problem, which is analogous to Hadamard's treatment of the Cauchy problem (see Tikhonov and Arsenin, 1979). This ill-posedness is removed by introducing appropriate boundary constraint terms that help satisfy the end boundary conditions at surfaces z = constant. The details are available in Chaudhuri et al. (to be published), and are omitted here because of space limitation.

3. Example Problem — Preliminary Results

As an illustration of the present approach and to examine the fidelity of its predictive capability, we consider the body depicted in Figure 2 and compare our result to the respective Pagano's (1991) variational model solution. We assume that all the boundaries are traction-free and that the body is subjected to a 1°C temperature rise. The fiber is represented as a single solid cylinder or the core, while the matrix is represented as a single annular ring (Pagano's N=1). Both materials are assumed to be isotropic with the following properties

$$E_f = 413\text{GPa} \qquad \nu_f = 0.2 \qquad \alpha_f = 3.25\mu/^\circ\text{C}$$
$$E_m = 63\text{GPa} \qquad \nu_m = 0.2 \qquad \alpha_m = 3.50\mu/^\circ\text{C}$$

where the subscripts f and m stand for fiber and matrix, respectively, and the geometric parameters are taken as

$$\frac{l}{a} = 10 \qquad \frac{b}{a} = 2$$

As a first step, the present solution is further simplified by assuming two-dimensional "plane strain" condition, and dropping 1/r terms in the equilibrium equations. Additionally, the constitutive relations used are those due to plane strain. Although the preliminary results thus obtained demonstrate that the present approach can be implemented in the existing FORTRAN code, the accuracy of the results are far from encouraging. We are currently in the process of implementing the exact axisymmetric analysis in the FORTRAN code. The results will be reported in Chaudhuri et al. (to be published.

4. Summary and Conclusions

A semi-analytical iterative approach for enhancing the existing two-dimensional quasi-continuous axisymmetric stress field for a brittle matrix micro-composite (i. e., a single fiber surrounded by a concentric matrix cylinder), is presented. In the present approach, the stress distribution in the radial direction obtained from the afore-cited variational model is improved *a posteriori* through an iterative approach that involves successive substitution of the previously computed strains (or stresses) into the equations of compatibility and equilibrium. The boundary/interface conditions at r = constant surfaces are satisfied in the pointwise sense. However, this process leaves the end boundary conditions in the axial direction (i.e., at surfaces z = constant) undefined thus rendering the boundary-value formulation ill-posed. This ill-posedness is removed by introducing appropriate boundary error terms that help satisfy the end boundary conditions at surfaces z = constant. As a first step, an approximate plane strain version of the present solution is implemented in a FORTRAN code. An illustrative thermal stress problem is solved using the plane strain version and used to compare with the existing variational solution.

We are currently in the process of implementing the exact axisymmetric analysis in the existing software. The results will be reported in Chaudhuri et al. (to be published.

The ongoing/future work is concerned with the determination of the "stress intensity factor" by way of matching the local asymptotic stress field due to Zak (1964) with the improved solution at an arbitrarily close distance from the point of stress singularity (i. e., fiber-matrix

interface located at a free edge). The model is designed to analyze experiments such as pullout tests, and also to represent the concentric cylinder model of a composite representative volume element and it contains the capability to enhance the accuracy of a given numerical solution. When completed, this research will represent a novel semi-analytical approach to improve solution accuracy and numerical efficiency of existing variational solutions for micro-composites.

Acknowledgment

This work was performed during the author's stay at the WL/MLBM, Wright-Patterson AFB as an AFOSR summer faculty research associate in 1996. The author wishes to thank Dr. N. J. Pagano for his technical discussions as well as mentoral support. Thanks are also due to Dr. G. P. Tandon of Ad Tech. for his computing and other assistance.

References

C. Atkinson, J. Avila, E. Betz, and R. E. Smelser, "The Rod Pull Out Problem, Theory and Experiment," *J. Mech. Phys. Solids* , **30** (1982).

J. Aveston, G. A. Cooper, and A. Kelly, "Single and Multiple Fracture," *The Properties of Fibre Composites Conference Proceedings*, National Physical Laboratory, pp. 15-26. IPC Science and Technology Press Ltd, Guildford, UK (1971).

H. W. Brown III, "Analysis of Axisymmetric Micromechanical Concentric Cylinder Model," *Seventeenth Annual Mechanics of Composites Review, Air Force 86145/09-10-92-150,* Dayton, OH (1992).

B. Budiansky, J. W. Hutchinson, and A. G. Evans, "Matrix Fracture in Fiber-Reinforced Ceramics," *J. Mech. Phys. Solids*, **34**, 167 - 189 (1986).

R. A. Chaudhuri, "An Equilibrium Method for Prediction of Transverse Shear Stresses in a Thick Laminated Plate," *Computers and Structures*, **23**,139 - 146 (1986).

R. A. Chaudhuri and P. Seide, "An Approximate Method for Prediction of Transverse Shear Stresses in a Laminated Shell," *Int. J. Solids and Structures*, **23**, 1145 - 1161 (1987a).

R. A. Chaudhuri and P. Seide, "An Approximate Semi-Analytical Method for Prediction of Interlaminar Shear Stresses in an Arbitrarily Laminated Anisotropic Plate," *Computers and Structures*, **25**, 627 - 636 (1987b).

R. A. Chaudhuri, "A Semi-Analytical Approach for Prediction of Interlaminar Shear Stresses in Laminated General Shells," *Int. J. Solids and Structures,* **26**, 499 - 510 (1990).

R. A. Chaudhuri, N. J. Pagano, G. P. Tandon and A. H. Khan, "Interfacing of Local Asymptotic Singular and Global Axisymmetric Micromechanical Stress Fields in Brittle Matrix Composites," to be published.

H. L. Cox, "The Elasticity and Strength of Paper and Other Fibrous Materials," *British J. Appl. Phys.* , **3** (1952).

Z. Hashin and B. W. Rosen, "The Elastic Moduli of Fiber Reinforced Materials," *J. Appl. Mech.* **31** (1964).

R. D. Kurtz and N. J. Pagano, "Analysis of the Deformation of a Symmetrically Loaded Fiber Embedded in a Matrix Material," *Engr Composites* , **1** (1991).

V. K. Luk and L. M. Keer, "Stress Analysis for an Elastic Half Space Containing an Axially-Loaded Rigid Cylindrical Rod," *Int. J. Solids Structures* , **15** (1979).

L. N. McCartney, "New Theoretical Model of Stress Transfer Between Fibre and Matrix in a Uniaxially Fibre-Reinforced Composite," *Proc. R. Soc. London* **A 425**, 215 - 244 (1990).

N. J. Pagano, "Exact Solution for Composite Laminates in Cylindrical Bending", *J. Compos. Mater.* , **3**, 398 - 411 (1969).

N. J. Pagano, "Stress Fields in Composite Laminates," *Int. J. Solids Structures*, **14** (1978).

N. J. Pagano, "Axisymmetric micromechanical stress fields in composites," *Proceedings 1991 IUTAM Symposium on Local Mechanics Concepts for Composite Materials Systems*, p 1. Springer Verlag (1991).

N. J. Pagano and G. P. Tandon, "Elastic Response of Multi-directional Coated-Fiber Composites," *Comp. Sci. Tech..*, **31** (1988).

G. Pickett and M. W. Johnson, "Analytical Procedures for Predicting the Mechanical Properties of Fiber Reinforced Composites," *Technical Report AFML-TR-65-220* (1967).

E. Reissner, "On a Variational Theorem in Elasticity," *J. Math. Phys.*, **29** (1950).

G. E. Smith and A. J. M. Spencer, "Interfacial Tractions in a Fibre-Reinforced Elastic Composite Material," *J. Mech. Phys. Solids* , **18** (1970).

E. Sternberg, "Load-Transfer and Load-Diffusion in Elastostatics," *Proceedings of the Sixth U.S. National Congress of Applied Mechanics*, The American Society of Mechanical Engineers, New York (1970).

A. N. Tikhonov and V. Y. Arsenin, *Solutions of Ill-Posed Problems*, John Wiley & Sons, New York (1977).

S. P. Timoshenko and J. N. Goodier, *Theory of Elasticity*, 2nd edn., McGraw-Hill, New York (1959).

A. R. Zak, "Stresses in the Vicinity of Boundary Discontinuities in Bodies of Revolution," *J. Appl. Mech.*, **31**, 150 - 152 (1964).

NEW TECHNIQUES FOR

NON-COOPERATIVE

TARGET IDENTIFICATION

Julian Cheung
Associate Professor

Department of Electrical Engineering

New York Institute of Technology
1855 Broadway
New York, NY 10023

Final Report for:
Summer Faculty Research Program
Wright Laboratory

Sponsored by:
Air Force Office of Scientific Research
Bolling Air Force Base, DC

and

Wright Laboratory

September 1996

NEW TECHNIQUES FOR NON-COOPERATIVE TARGET IDENTIFICATION

Julian Cheung
Associate Professor
Department of Electrical Engineering
New York Institute of Technology

ABSTRACT

A new methodology for identifying aircraft using radar range profiles through application of the generalized likelihood ratio test is developed. The new identifier maximizes the probability of target identification, at a prespecified Type I error, in dependent Gaussian noise, and it identifies the target without the compromise of making forced decisions. When subjected to more restrictive conditions, it reduces to other classes of identifiers, including the maximal cross-correlation identifier and, after power transformation, the shortest Euclidean distance identifier. All system parameters necessary for implementation are estimated, and the procedure does not require any prior information about the statistical properties of the measured data. The results of experiments with an extensive real high range resolution (HRR) data set demonstrate that the proposed identifier attains reasonable probability of detection and is amenable to real time processing. It also suggests the feasibility of target identification using synthetic signatures, and the implementation, except for minor modifications, parallels its counterpart using measured signatures.

NEW TECHNIQUES FOR NON-COOPERATIVE TARGET IDENTIFICATION

Julian Cheung

I. INTRODUCTION

The application of radar to target detection has been an important problems almost since its invention. The crucial issue that has been overlooked is to identify what the radar has detected, without which proper action cannot be initiated. This urgency is evident by the downing of two US helicopters by two US F15's over the Kurdish region in Iraq. In its own right, target identification is an important topic in pattern recognition. Motivated by these needs, there is a tremendous effort to advance the problem of target identification using radar. A promising approach is to use the range profile, which is the 1-dimensional (D) scattering distribution of a target along the meradial distance, for data representation. Besides providing information pertinent to the location and scattering strength of the target's scattering centers at a particular aspect, the shape of the range profile is essentially preserved for minor changes in aspect angles. This should be compared to the target's radar cross-section which, due to its dependency on frequency and aspect angles, is preventing it from use in direct applications.

Most of these algorithms are designed based on maximizing the correlation of the testing profile with the target signatures in the data base [1-4]. The pre-stored target signature correlating most strongly with the testing profile is declared to belong in the latter's target class. The maximal correlation technique is simple, fast and, after normalization, it is not susceptible to the variability of the underlying profile's power resulting from the ever-changing radial distance between the target and the radar. However, it does not maximize the probability of target identification and, therefore, it is a suboptimal identifier. Neither does the procedure accommodate the intra-bin dependence of noise processes due to the high sampling rate afforded by modern radar. At best, all these algorithms only make forced decisions: they decide the testing profile to be a target class *trained* in the library set, even if the underlying profile belongs to a target class *not* in the library set. These difficulties are addressed in this paper, by developing a new methodology for identifying an aircraft using radar range profiles and an algorithm for computing them. A detailed discussion of this methodology can be

found in [5]. For purpose of brevity, only the basic concepts are presented in this technical report, which is organized as follows.

Section II is devoted to the derivation of optimal target identifiers based on the generalized likelihood test with unknown target signatures and dependent Gaussian noise processes. Section III considers the problem of estimation of system parameters. Section IV concentrates on some practical problems, including the variability of view of aspect, power, and signature location that plague a parametric system, by suggesting appropriate remedies to circumvent these difficulties. The compensation of synthetic target signatures in place of corresponding measured signatures is also considered. In Section V identification experiments using real radar range profiles are undertaken to demonstrate the efficacy of the new target identifiers. Further discussions and suggestions are presented in Section VI.

II. OPTIMAL TARGET IDENTIFICATION

In this section the target identification problem for binary classes is formulated. The resulting identifier requires only the noise covariance matrix and the average target-signature vectors. This is generalized to the M-ary identification problem.

(a) Binary Classifier: Consider the radar scatterer returns $\boldsymbol{x}=[x_1 \cdots x_B]'$ from B range bins. According to [6-7] the return from bin b, x_b, is a complex scalar that entails in-phase and quadrature components $x_{b;R}$, $x_{b;I}$, respectively, $b=1,\cdots,B$.

When target class ω_1 is present, i.e., hypothesis H_1, each real part of x_b is due to target plus noise, implying that $x_{b;R}=v_{b;R}+s_{(1)b;R}$ and $x_{b;I}=v_{b;I}+s_{(1)b;I}$. In each bin the noise components are normally distributed with zero mean and variance $\frac{1}{2}\sigma_b^2$, so $v_{b;R}$, $v_{b;I} \sim N(0, \frac{1}{2}\sigma_b^2)$. Introduce a 2-tuple variate $\boldsymbol{y}_b=[x_{b;R}\ x_{b;I}]'$. The B-tuple *complex* scatter returns $\boldsymbol{x}$ are converted to a $2B$-tuple *real* scatter returns $\boldsymbol{y}$, $\boldsymbol{y}=[\boldsymbol{y}_1' \cdots \boldsymbol{y}_B']'$, whose pdf is, for $\boldsymbol{s}_{(1)}=[s_{(1)1;R}\ s_{(1)1;I} \cdots s_{(1)B;R}\ s_{(1)B;I}]'$,

$$f(\boldsymbol{y}|H_1) = (2\pi)^{-2B}|\boldsymbol{\Sigma}_y|^{-\frac{1}{2}} \exp\left(-\tfrac{1}{2}(\boldsymbol{y}-\boldsymbol{s}_{(1)})'\boldsymbol{\Sigma}_y^{-1}(\boldsymbol{y}-\boldsymbol{s}_{(1)})\right). \tag{2.1}$$

The covariance matrix $\boldsymbol{\Sigma}_y$, $\boldsymbol{\Sigma}_y = cov(\boldsymbol{y} \mid H_1) = cov(\boldsymbol{y} \mid H_2) = \{\boldsymbol{\alpha}_{jk}\}$, contains $B \times B$ submatrices $\boldsymbol{\alpha}_{jk}$:

$$\boldsymbol{\alpha}_{jk} = cov(\boldsymbol{y}_j, \boldsymbol{y}_k) = \begin{bmatrix} cov(x_{j;R}, x_{k;R}) & cov(x_{j;R}, x_{k;I}) \\ cov(x_{j;I}, x_{k;R}) & cov(x_{j;I}, x_{k;I}) \end{bmatrix} = \begin{bmatrix} cov(v_{j;R}, v_{k;R}) & cov(v_{j;R}, v_{k;I}) \\ cov(v_{j;I}, v_{k;R}) & cov(v_{j;I}, v_{k;I}) \end{bmatrix}. \quad (2.2)$$

In this paper bold case letters represents vectors/matrices; $|.|$, $\|.\|$, prime denote determinant, norm, and transposition, respectively.

Under hypothesis H_2 target class ω_2 is present, we have $x_b = (v_{b;R}+s_{(2)b;R}) + i\,(v_{b;I}+s_{(2)b;I})$. The pair $s_{(2)b;R}, s_{(2)b;I}$ represents the in-phase, quadrature returns to the target ω_2 at range bin b. The corresponding multivariate pdf is

$$f(\boldsymbol{y}|H_2) = (2\pi)^{-2B}|\boldsymbol{\Sigma}_y|^{-½} \exp\left(-½(\boldsymbol{y}-\boldsymbol{s}_{(2)})'\boldsymbol{\Sigma}_y^{-1}(\boldsymbol{y}-\boldsymbol{s}_{(2)})\right). \quad (2.3)$$

The identification of a target embedded in noise, based on HRR radar returns, is thus formulated as a dual hypothesis testing problem

$$\begin{aligned} H_1&: \quad \boldsymbol{y} = [\, v_{1;R}+s_{(1)1;R} \;\; v_{1;I}+s_{(1)1;I} \;\cdots\; v_{B;R}+s_{(1)B;R} \;\; v_{B;I}+s_{(1)B;I}\,]' \\ H_2&: \quad \boldsymbol{y} = [\, v_{1;R}+s_{(2)1;R} \;\; v_{1;I}+s_{(2)1;I} \;\cdots\; v_{B;R}+s_{(2)B;R} \;\; v_{B;I}+s_{(2)B;I}\,]'. \end{aligned} \quad (2.4)$$

Taking the natural logarithm of the ratio of (2.1) to (2.3) and simplifying, we have

$$Q_2(\boldsymbol{y}) - Q_1(\boldsymbol{y}) \underset{H_2}{\overset{H_1}{\gtrless}} \tau_{21}. \quad (2.5)$$

The quadratic terms are $Q_m(\boldsymbol{y}) = (\boldsymbol{y}-\boldsymbol{s}_{(m)})'\boldsymbol{\Sigma}_y^{-1}(\boldsymbol{y}-\boldsymbol{s}_{(m)})$, m=1,2. The threshold τ_{21} is chosen for a prespecified Type I error α, with subscripts 2, 1 indicating it is set for the pair (hypothesis, alternative) = (H_2, H_1).

The decision rule is: if $Q_1(\boldsymbol{y})$ that is designed on the basis of the presence of target class ω_1 is less than $Q_2(\boldsymbol{y})$, the latter designed on the basis of target class ω_2, by τ_{21} then class ω_1 *matches* better to the observable $\boldsymbol{y}$ and so H_1 is accepted; if $Q_1(\boldsymbol{y})$ exceeds $Q_2(\boldsymbol{y})$ then H_2 is accepted.

Under H_1 the quadratic term $Q_1(y)$ is close to zero while $Q_2(y)$ is a large positive number. This is because, recalling (2.1),(2.3) and the principle of the likelihood ratio test [8], $f(y|H_1)$ is designed to be maximum that is attained when $Q_1(y)$ is minimum; $f(y|H_2)$ is not designed to be a maximum and so $Q_2(y)$ is not a minimum. As expected, $Q_2(y) - Q_1(y)$ is a large positive value, yielding the correct decision H_1. By the same argument for H_2 to be true $Q_1(y)$ is a large positive value while $Q_2(y)$ is nearly zero. Therefore, $Q_2(y) - Q_1(y)$ is small, leading to the correct decision that H_2 is true. Consequently, the above classifier is effective in emphasizing a valid target and suppressing the invalid target and noise. In fact, the quadratic classifier is a sufficient statistic of the likelihood ratio test and it is the most powerful classifier.

(b) Unforced M-ary Classifier: The binary classifier can be generalized to generate the M-ary classification, for instance, by picking target class ω_l such that $Q_l(y) \le Q_m(y)$, $m \in \{1, \cdots, M\} \wedge m \neq l$ [8]. This approach does not consider the situations: i) y may be noise only, ii) the underlying target may belong to an *unknown* class. The italized word signifies that the corresponding class is untrained and hence not in the library set. An M-ary classifier can be implemented via a two-step process: i_a) place all $Q_m(y)$ satisfying $Q_0(y) - Q_m(y) \ge \tau_{0m}(\alpha/M)$ into the set C, $m \in \{1, \cdots, M\}$; i_b) decide on H_0 if C is an empty set, otherwise decide on H_l corresponding to the *smallest* element $Q_l(y)$ in the set. The threshold $\tau_{0m}(\alpha/M)$ is determined in the learning period pertinent to class ω_m at Type I error α/M (for each subsystem); and $Q_0(y) = y' \Sigma_y^{-1} y$ presupposes a null feature vector (no target).

Still i_a) does not cater to the situation ii) (unknown class of targets). This is because the feature vector for an unknown target class is not available and, therefore, its threshold cannot be set. This dilemma is bypassed on recognizing that the distribution of $Q_m(y)$ is known from the learning period. To see this, denote $\underline{Q_m}, \overline{Q_m}$ the minimum, maximum of $Q_m(y)$ computed in the learning interval. An M-ary classifier with unforced decision thus may be implemented by:

Place all triplets $\{m, Q_m(y), Q_{jm}(y)\}$, $m \in \{1, \cdots, M\}$, satisfying the condition $Q_{jm}(y) \equiv (Q_j(y) - Q_m(y)) / \tau_{jm}(\alpha/M) \geq 1$ in a set D.
If D is not an empty set, order the elements in the set from the smallest to the largest. Decide on H_l for the smallest possible element $Q_{jl}(y)$ (since it belongs to D it naturally satisfies the normalized thresholding condition) such that its second component $Q_l(y) \in [\underline{Q_l}, \overline{Q_l})$. Otherwise decide on $H_{\hat{0}}$.

(2.6)

Here $H_{\hat{0}}$ is the composite hypothesis pertaining to no target or a target of unknown class. By normalizing $Q_j(y) - Q_m(y)$ with respect to the corresponding threshold, $Q_j(y) - Q_m(y)$ can now be quantified with other members of the class. Direct comparison in the ordinary M-ary testing is impossible, owing to the incompatible thresholds for different pairs in simple hypothesis testing.

We remark that an unforced classifier is desirable because it avoids making a decision contingent on the known target classes when there is no target or the target does not belong to the known classes. Nevertheless, a larger number of target classes lowers the false alarm rate for each of the subsystems, thereby increasing their thresholds and decreasing the identification power. These drawbacks are inherent in both the unforced and forced M-ary systems.

III. SYSTEM PARAMETER ESTIMATION

In this section the estimation of parameters, necessary for the implementation of the identifier, is considered.

(a) Target Signature Estimation: Suppose N statistically independent samples $\boldsymbol{y}_{\lceil 1 \rceil}, \cdots, \boldsymbol{y}_{\lceil N \rceil}$ are collected during the learning period and target class ω_m is present *a priori* throughout the duration. The *posteriori* pdf is evaluated from (2.1) as

$$f(\boldsymbol{y}_{\lceil 1 \rceil}, \cdots, \boldsymbol{y}_{\lceil N \rceil} | H_m) = \prod_{n=1}^{N} f(\boldsymbol{y}_{\lceil n \rceil} | H_m) = (2\pi)^{-2BN} |\boldsymbol{\Sigma}_y|^{-\frac{1}{2}N} \exp\left(-\tfrac{1}{2} \sum_{n=1}^{N} (\boldsymbol{y}_{\lceil n \rceil} - \boldsymbol{s}_{(m)})' \boldsymbol{\Sigma}_y^{-1} (\boldsymbol{y}_{\lceil n \rceil} - \boldsymbol{s}_{(m)})\right).$$

Taking the natural logarithm and, because of the identity $\boldsymbol{A}^{1\times J}\boldsymbol{B}^{J\times 1} = trace\,(\boldsymbol{B}\boldsymbol{A})$, we obtain

$$\ln f(\boldsymbol{y}_{\lceil 1 \rceil}, \cdots, \boldsymbol{y}_{\lceil N \rceil} | H_m) = c - \tfrac{1}{2} N \ln |\boldsymbol{\Sigma}_y| - \tfrac{1}{2} \sum_{n=1}^{N} \mathit{trace} \left(\boldsymbol{\Sigma}_y^{-1} (\boldsymbol{y}_{\lceil n \rceil} - \boldsymbol{s}_{(m)}) (\boldsymbol{y}_{\lceil n \rceil} - \boldsymbol{s}_{(m)})' \right), \quad (3.1)$$

and c is a constant.

Utilizing the identity $(d/dA)\, \mathit{trace}\,(A'B) = B$, the derivative with respect to $\boldsymbol{s}_{(m)}$ is $(d/d\boldsymbol{s}_{(m)}) \ln f(\boldsymbol{y}_{\lceil 1 \rceil}, \cdots, \boldsymbol{y}_{\lceil N \rceil} | H_m) = -2 \sum_{n=1}^{N} \boldsymbol{\Sigma}_y^{-1} (\boldsymbol{y}_{\lceil n \rceil} - \boldsymbol{s}_{(m)})$. Setting the derivative to zero and, because $\boldsymbol{\Sigma}_y^{-1}$ is invertible, the maximum likelihood estimate (MLE) of $\boldsymbol{s}_{(m)}$ is

$$\hat{\boldsymbol{s}}_{(m)} = N^{-1} \sum_{n=1}^{N} \boldsymbol{y}_{\lceil n \rceil}. \quad (3.2)$$

Taking the derivative with respect to $\boldsymbol{s}_{(m)}$ once more to get $(d^2/d\boldsymbol{s}_{(m)}^2) \ln f(\boldsymbol{y}_{\lceil 1 \rceil}, \cdots, \boldsymbol{y}_{\lceil N \rceil} | H_m) = -N \boldsymbol{\Sigma}_y^{-1}$; it is a negative-definite matrix, implying that $\hat{\boldsymbol{s}}_{(m)}$ is a necessary and sufficient estimator of $\boldsymbol{s}_{(m)}$.

(b) Noise Covariance Matrix Estimation: Since the covariance matrix $\boldsymbol{\Sigma}_y$ is the same for all target classes, it suffice to estimate the covariance matrix under H_1. Upon taking the derivative of (3.1) ($\boldsymbol{s}_{(m)}$ replaced by its estimate) with respect to $\boldsymbol{\Sigma}_y$ and invoking the identities $(d/dA) \ln |A| = A^{-1}$, $(d/dA)\, \mathit{trace}\,(A^{-1}B) = -A^{-1}BA^{-1}$, then

$$(d/d\boldsymbol{\Sigma}_y) \ln f(\boldsymbol{y}_{\lceil 1 \rceil}, \cdots, \boldsymbol{y}_{\lceil N \rceil} | H_1) = -\tfrac{1}{2} N \boldsymbol{\Sigma}_y^{-1} + \tfrac{1}{2} \sum_{n=1}^{N} \boldsymbol{\Sigma}_y^{-1} (\boldsymbol{y}_{\lceil n \rceil} - \hat{\boldsymbol{s}}_{(1)}) (\boldsymbol{y}_{\lceil n \rceil} - \hat{\boldsymbol{s}}_{(1)})' \boldsymbol{\Sigma}_y^{-1}. \quad (3.3)$$

Setting it to zero, the MLE is

$$\hat{\boldsymbol{\Sigma}}_y = N^{-1} \sum_{n=1}^{N} (\boldsymbol{y}_{\lceil n \rceil} - \hat{\boldsymbol{s}}_{(1)}) (\boldsymbol{y}_{\lceil n \rceil} - \hat{\boldsymbol{s}}_{(1)})'. \quad (3.4)$$

Thus $\boldsymbol{\Sigma}_y$ is estimated by (3.4) in conjunction with (3.2). Furthermore, making use of data samples from all *a posteriori* target classes the estimate can be improved, in the context of convergence rate, as

$$\hat{\boldsymbol{\Sigma}}_y = (MN)^{-1} \sum_{m=1}^{M} \sum_{n=1}^{N} (\boldsymbol{y}_{\lceil n \rceil} - \hat{\boldsymbol{s}}_{(m)}) (\boldsymbol{y}_{\lceil n \rceil} - \hat{\boldsymbol{s}}_{(m)})'. \quad (3.5)$$

Because $y_{\lceil n \rceil}$, $n=1, \cdots, N$, is Gaussian distributed, all MLE estimators developed hitherto are also the minimum variance unbiased estimators [9].

IV. UNCERTAINTY CONSIDERATIONS

In this section some practical problems confronting a parametric HRR classifier are considered. These introduce additional layers of complexity into the system thereby degrading its performance. Some solutions are suggested below.

(a) Variability of View of Aspect: Until now, the view of aspect (ϕ, θ)[1] of a target is assumed constant. In reality this is not so, either because of the imperfection in estimation or the high maneuverability of modern aircrafts. This makes the target identification problem difficult. To see this, consider an aircraft of length L (nose to tail), width W (farthest distance between the wings), height H, and view of aspect (ϕ_0, θ_0). Suppose the aircraft is nose-on to the radar. In this case, radar returns from the front side on both wings appear in the same set of bins. The same can be said for any subgroup of scatterers equidistant to the radar line of sight. Suppose now the view of aspect is switched to (ϕ_1, θ_0), $\phi_1 \neq \phi_0$, then returns from the front side of both wings may no longer be in the same bins. The same phenomenology occurs when the angle of elevation changes. Apparently, a target at different views of aspect casts different range profiles.

The variability of the range profile of a target (after alignment) as affected by the view of aspect often confuses a parametric classifier; it assumes that the embedded signature of the same target stays the same from one profile to the next. However, the shape of the range profile does not vary much if the aspect angle changes are sufficiently small. This condition is assured if the maximal

---

[1]Imagine an aircraft parked on the equatorial plane of a sphere in such a way that its nose points to the South, the wings to the East-West, the intersection of the wings and the fuselage coincides with the sphere's center, and the radar is along the South and noise-on to the aircraft. Suppose the aircraft rotates with respect to the center. The angle of azimuth ϕ, $-180^\circ \leq \phi \leq 180^\circ$, is the angle between the South axis and the projection of the fuselage onto the equatorial plane. The angle of elevation θ, $-90^\circ \leq \theta \leq 90^\circ$, defines the angle between the aircraft fuselage and its projection on the equatorial plane. The pair (ϕ, θ) constitutes the view of aspect of the aircraft with respect to the radar. A segment of the sphere's surface forms an aspect window.

time difference among all scatter returns caused by the aspect change is less than the radar sampling interval. This is equivalent to the situation that the maximal distance difference among all compatible scatters, due to aspect angle changes $(\Delta\phi, \Delta\theta)$, is less than the radar resolution r_{resol} and it is satisfied, for $\Delta\phi,\Delta\theta>0$, by[2]

$$L\,\Delta\phi < \tfrac{1}{2} r_{resol},\quad W\,\Delta\phi < \tfrac{1}{2} r_{resol},\quad H\,\Delta\phi < \tfrac{1}{2} r_{resol}. \tag{4.1}$$

Given the radar resolution and the target dimension, it becomes feasible to find the pair $(\Delta\phi, \Delta\theta)$ satisfying (4.1). One thus can be assured that the profile of a target at the nominal view of aspect (ϕ_0, θ_0) is essentially the same as any profiles of the same target in the aspect window $[\phi_0-\tfrac{1}{2}\Delta\phi, \phi_0+\tfrac{1}{2}\Delta\phi) \times [\theta_0-\tfrac{1}{2}\Delta\theta, \theta_0+\tfrac{1}{2}\Delta\theta)$.

Suppose $[\underline{\phi}, \overline{\phi}]$, $[\underline{\theta}, \overline{\theta}]$ denote the closed intervals of azimuth and elevation angle, respectively; the underbar, overbar represent the minimum, maximum of the associated parameter. In the $R\times R$ space, the domain underlying the variability of ϕ, θ is divided into $N_\phi N_\theta$ subregions commonly called aspect windows $\{a_{n_\phi n_\theta} \mid n_\phi=1,\cdots,N_\phi;\ n_\theta=1,\cdots,N_\theta\}$, where $N_\xi = \lfloor (\overline{\xi}-\underline{\xi})/\Delta\xi \rfloor, \xi=\phi,\theta$. Aspect window $a_{n_\phi n_\theta}$ is a 2-D region in the space of view of aspect, and $a_{n_\phi n_\theta} = [(n_\phi-1)\Delta\phi, n_\phi\Delta\phi) \times [(n_\theta-1)\Delta\theta, n_\theta\Delta\theta)$.

With this in mind, an unrestricted binary identifier that compensates for the variability of view of aspect is thus a restricted binary identifier that assumes exact view of aspect accommodating all the $N_\phi N_\theta$ aspect windows. It is modified from (2.5) as

$$Q_2(y; n_\phi n_\theta) - Q_1(y; n_\phi n_\theta) \underset{H_2}{\overset{H_1}{\gtrless}} \tau_{21},\quad N_\phi \ge n_\phi \ge 1; N_\theta \ge n_\theta \ge 1. \tag{4.2}$$

---

[2]Suppose the aircraft is nose-on to the radar. At $\phi=0$ the wings are perpendicular to the radar line of sight (RLOS). For $\phi=\phi_0$ the projection of the wings to the RLOS is $W\,Cos\,(90+\phi_0)$. When $\phi=\phi_0+\Delta\phi$ the projection of the wings to the RLOS is $W\,Cos\,(90+\phi_0+\Delta\phi)$. The difference is thus $\mid WSin(\phi_0) - WSin(\phi_0+\Delta\phi)\mid \simeq W\,\Delta\phi$. If it is less than $\tfrac{1}{2} r_{resol}$ then both wings' returns will fall on same set of bins. The factor $\tfrac{1}{2}$ accounts for round-trip travel. Other incidences are derived in a similar fashion.

Correspondingly, the quadratic term becomes $Q_m(y; n_\phi n_\theta) = (y - s_{(m)}^{(n_\phi n_\theta)})' \Sigma_y^{-1} (y - s_{(m)}^{(n_\phi n_\theta)})$, m=1,2.

The unrestricted M-ary identifier, either forced or unforced, is developed in an analogous way.

(b) Discrepancy between Synthetic and Measured Data: In the same spirit as SPICE that simulates the response of an electronic circuitry, there exists some sophisticated electromagnetic codes capable of predicting the range bin returns of an aircraft, given its geometrical and physical structures. The government proprietary XPATCH is a good example [10]. The output from these codes are called synthetic data; and the data collected from a real scenario form measured data.

The importance of synthetic data cannot be overstated. For example, normal access to foreign aircrafts is denied. The only option is to feed in structural information about the unknown aircraft (as obtained from *Jane's Aircraft*, for example) to the degree possible from the predictive code, in the hope that the resulting synthetic data resembles the measured data. Also, signature estimation of an aircraft in a particular aspect window demands a large quantity of profiles of a very fine (possibly granular) view of aspect which may be too costly or impractical for generation.

As Fig.1 indicates, although the synthetic data resembles reasonably well the measured data (after aligning bin 252 of the former with bin 316 of the latter), such agreement is qualitative and not quantitative. To compensate for the inequality of the synthetic data $\ddot{s}_{(m)}^{(n_\phi n_\theta)}$ as compared to the measured data $s_{(m)}^{(n_\phi n_\theta)}$, of aircraft class m at aspect window $a_{n_\phi n_\theta}$, a constant vector $c_{(m)}^{(n_\phi n_\theta)}$ is added to the synthetic data. The problem reduces to finding $c_{(m)}^{(n_\phi n_\theta)}$ such that $s_{(m)}^{(n_\phi n_\theta)} \simeq \ddot{s}_{(m)}^{(n_\phi n_\theta)} + c_{(m)}^{(n_\phi n_\theta)}$. The mean-square error is $\epsilon = E\{ (s_{(m)}^{(n_\phi n_\theta)} - \ddot{s}_{(m)}^{(n_\phi n_\theta)} - c_{(m)}^{(n_\phi n_\theta)})' (s_{(m)}^{(n_\phi n_\theta)} - \ddot{s}_{(m)}^{(n_\phi n_\theta)} - c_{(m)}^{(n_\phi n_\theta)}) \}$, and the expectation is taken over all samples in the aspect window $a_{n_\phi n_\theta}$. Taking the derivative of ϵ with respect to $c_{(m)}^{(n_\phi n_\theta)}$ and setting it to zero, the estimate is

Here $s_{(m)[j]}^{(n_\phi n_\theta)}$ (or $\hat{s}_{(m)[j]}^{(n_\phi n_\theta)}$) denotes the j_th measured (or synthetic) data set of target class ω_m in aspect window $a_{n_\phi n_\theta}$.

(c) Nonstationarity of Power: In general, the power of the observation y may not equal to the power of the training data set $y_{[1]}, \cdots, y_{[N]}$ that were used to estimate target signatures. Also, the power may vary from observation to observation. This may be caused by several factors. Firstly, the distance between a radar and its target may be changing. Because the radar transmitting power is inversely proportional to the square of the meradial distance [6], on the receiver side the power of the back-scattered signal after a two-way trip is inversely proportional to the fourth power of the distance. Secondly, radar returns may be attenuated either by the transmitting media or other natural or man-made sources. Lastly, the radar hardware in the field may be different from that used for training; or the radar may be aging. Consequently, the embedded target signature may not be equal to any member of the library set thereby degrading the identifier. To resolve this difficulty the incoming data y is multiplied by ρ for power equalization between the data and the training set, that is, $(\rho y)'(\rho y) = N^{-1} \sum_{n=1}^{N} y'_{[n]} y_{[n]}$. The power equalizing factor is

$$\rho = \sqrt{\frac{N^{-1} \sum_{n=1}^{N} y'_{[n]} y_{[n]}}{y'y}} \quad . \tag{4.4}$$

Of course, both the observation and the training set are associated with the same target at a specified aspect window.

(d) Non-constant Target Signature Location: In each measurement embedded target signatures may not belong in the same bins. Alignment of the observation is thus in demand because of two reasons. Firstly, during training a target feature at a particular bin it is estimated by the mean of the observables at the same bin (after noise compensation, ct. eq.(3.2)). A large number of observables results in an efficient estimate of target signatures. The estimate is meaningless if the target features embedded in the observation are misaligned. Secondly, the optimal parametric identification is

results in an efficient estimate of target signatures. The estimate is meaningless if the target features embedded in the observation are misaligned. Secondly, the optimal parametric identification is designed on the basis that when the observation contains a target feature $s_{(m)}$ the quadratic term $Q_m(y) = (y - s_{(m)})'(y - s_{(m)})$ attains a minimum, while other quadratic terms $Q_j(y)$, $j \neq m$, do not (refer to (eq.2.5)).[3] This is because $Q_m(y) = (v_m + s_{(m)} - s_{(m)})'(v_m + s_{(m)} - s_{(m)})$ would be noise only, but will not behave so when target features embedded in y are not aligned with respect to the feature vector in the library set.

One way to align the observation vector is to correlate y with $\hat{s}_{(m)}$

$$\mathcal{L}(\upsilon) = \sum_{j=1}^{B} \hat{s}_{(m)2j} y_{2j-2\upsilon} + \hat{s}_{(m)2j+1} y_{2j+1-2\upsilon}, \qquad \upsilon = 1,\cdots,B \tag{4.5}$$

and y is zero-padded for out-of-bound elements. The υ^* that delivers the largest value among all $\mathcal{L}(\upsilon)$ is the order of bin the data profile needs *to shift to the left* for proper alignment. The summand underneath the summation sign contains two terms because each bin consists of two components.

The alignment algorithm (4.5) requires $4B^2$ multiplication operations ($B > 600$) and is time consuming. A more efficient computationally method is to choose L largest features among $\hat{s}_{(m)}$ that belong to the target *a priori*, and the corresponding bin numbers in set D (see (2.6)). The L pair of entries are subsequently copied onto $\acute{s}_{(m)}$ (same indexing), all other elements of $\acute{s}_{(m)}$ are assigned null. A counterpart of (4.5) is

$$\acute{\mathcal{L}}(\upsilon) = \sum_{j \in D} \acute{s}_{(m)2j} y_{2j-2\upsilon} + \acute{s}_{(m)2j+1} y_{2j+1-2\upsilon}, \qquad \upsilon = 1,\cdots,B;\ D \subset \{1,\cdots,B\}. \tag{4.6}$$

Besides require only $4BL$ multiplication operations ($L \leq 50$), a subtle advantage is that because major target features are more immune to noise effect (higher signal-to-noise ratio), $\acute{\mathcal{L}}(\upsilon)$ may be less susceptible to noise as well as the generation and destruction of features arising from minor changes in the view of aspect. Moreover, the nonlinear filtering approach (4.6) may perform

---

[3] For simplicity, throughout this section y is assumed statistically independent. In dependent processes y, $s_{(m)}$ are replaced by $\tilde{y}$, $\tilde{s}_{(m)}$, respectively.

V. EXPERIMENTAL RESULTS

The operation of the foregoing identifier is summarized in Fig.2. A C-based software package was coded to implement the identification process. Using a Sun Sparc-10 workstation, it takes about 120 minutes for: i) system parameters estimation using 9906 profiles entailing three target classes and 18 aspect windows, and ii) identification using a second set of 9876 profiles. Most of the computer time is spent on target training. If identification only is carried out, i.e., the lower portion in Fig.2, the time is about 60 minutes. In other words, unforced target identification, when supplied with pre-estimated system parameters, takes about $60\times60/9876 = 0.3645$ seconds per profile.

In particular, Fig.3 shows the performance of the proposed identifier in 18 various aspect windows using measured target signatures. The superior performance of the new identifier speaks for itself. Some aspect windows encounter low probability of identification. We offer three reasons. Firstly, signatures of different targets (at least two) exhibit sufficient similarity in the affected windows as to confuse the identification system. Secondly, in the affected windows a very low number of profiles is available for training (less than 5). System parameters cannot be estimated and, consequently, any parametric identifiers simply break down. Lastly, during the course of evaluation it was discovered that algorithm (4.5) misaligns at a rate of about 1 per 20. Alignment is critical both to signature estimation and target identification (Section IV). A single incidence of misalignment may cause the process to break down, regardless of how efficient it may be.

The same diagram also presents the results when synthetic signatures are used. The performance is satisfactory.

In Fig.4 we also compare the performance of the new identifier when alignment is carried out either by the regular correlation algorithm (4.5) or by the magnitude correlation:

$$\tilde{\mathcal{L}}(\upsilon) = \sum_{j=1}^{B} \sqrt{\hat{s}^2_{(m)2j} + \hat{s}^2_{(m)2j+1}}\sqrt{y^2_{2j-2\upsilon} + y^2_{2j+1-2\upsilon}}, \qquad \upsilon=1,\cdots,B.$$

The inferiority of the magnitude approach in both aspect windows implies that misalignment occurs even more frequently. This is expected. It is well known in basic communication theory that a detector under-utilizing data information performs worse than its counterpart that uses the full knowledge about the data [8]. A good example is incoherent (envelope) detection versus coherent detection. Regrettably, target identification using the envelope (magnitude) version of (2.6) has not

a detector under-utilizing data information performs worse than its counterpart that uses the full knowledge about the data [8]. A good example is incoherent (envelope) detection versus coherent detection. Regrettably, target identification using the envelope (magnitude) version of (2.6) has not been coded in our software package and hence direct comparison cannot be made. Based on the above results, we may infer loosely that the magnitude profile approach, including the power transformation, performs worse than the new detector.

VI. CONCLUSIONS

We have developed a new methodology for identifying an aircraft using radar range profiles through application of the generalized likelihood ratio test. The new identifier maximizes the probability of target identification, at a prespecified Type I error, in dependent Gaussian processes, and it identifies the target without the degradation associated with making forced decisions. If the new identifier is subjected to more restrictive conditions, it reduces to other classes of identifiers, including the maximal cross-correlation identifier and, after power transformation, the shortest Euclidean distance identifier. All system parameters necessary for the implementation of the identifier are estimated, and the process does not require any prior information about the statistical properties of the measured data.

The results of experiments with an extensive real HRR data set demonstrate that the proposed identifier attains a reasonable probability of detection (see Fig.3) and, moreover, it is amenable to real time processing. It also delivers satisfactory results upon the replacement of measured target signatures by a superposition of synthetic target signatures and compensation vectors. This is not surprising. The identifier (2.6) processes an HRR profile based on the Euclidean distance (after decorrelation). The norm of a profile that is effected from a target signature remains distinguishable to the data processor from the norm of the same profile that is subtracted from other target signatures, provided the associated target signatures are separable from each other; this is true irrespective of whether the signatures are of measured or synthetic target type. It also suggests that target identification based on magnitude or its variants (power transformation technique, for example), is not recommended (see Fig.4).

These experiments, coupled with the theoretical analyzes, justifies the proposed technology

for reliable aircraft identification. Further, target identification using synthetic signatures is feasible and its implementation procedure, except for minor modifications, parallels its counterpart using measured signatures.

REFERENCES

[1] H.J. Li and S.H. Yang, "Using range profiles as feature vectors to identify aerospace objects," *IEEE Trans. Antennas Propagat.*, vol.41, no.3, pp.261-268, March 1993.

[2] S. Hudson and D. Psaltis, "Correlation filters for aircraft identification from radar range profiles," *IEEE Trans. Aero. Elect. Syst.*, vol.29, no.3, pp.741-748, July 1993.

[3] L.H. Wang and H.J. Li, "Using range profiles for data association in multiple-target tracking," *IEEE Trans. Aero. Elect. Syst.*, vol.32, no.1, pp.445-450, Jan. 1996.

[4] I. Jouny, F.D. Garber, and R.L. Moses, "Radar target identification using the bispectrum: a comparative study," *IEEE Trans. Aero. Elect. Syst.*, vol.31, no.1, pp.69-77, Jan. 1995.

[5] J. Cheung, J. Hughes and L. Kurz, "A class of target identifiers using a high range resolution radar," *IEEE Trans. Aero. Elect. Syst.*, (submitted for publication).

[6] J.L. Eaves and E.K. Reedy, Eds., *Principles of modern radar*, Van Nostrand-Reinhold, New York, 1987.

[7] N. Levanon, *Radar principles*, John Wiley, New York, 1988.

[8] H.L. Van Trees, *Detection, estimation, and modulation theory*, part I, John Wiley, New York, 1968.

[9] D. Behar, J. Cheung and L. Kurz, "Contrast techniques for line detection in a correlated noise environment," *IEEE Trans. Image Process.*, (to appear in 1997).

[10] D.J. Andersh, M. Hazlett, S.W. Lee, D.D. Reeves, D.P. Sullivan and Y. Chu, "XPATCH: A high frequency electromagnetic scattering prediction code and environment for complex 3-dimensional objects," *IEEE Antennas Propagat. Magazine*, 36, pp.65-69, Feb. 1994.

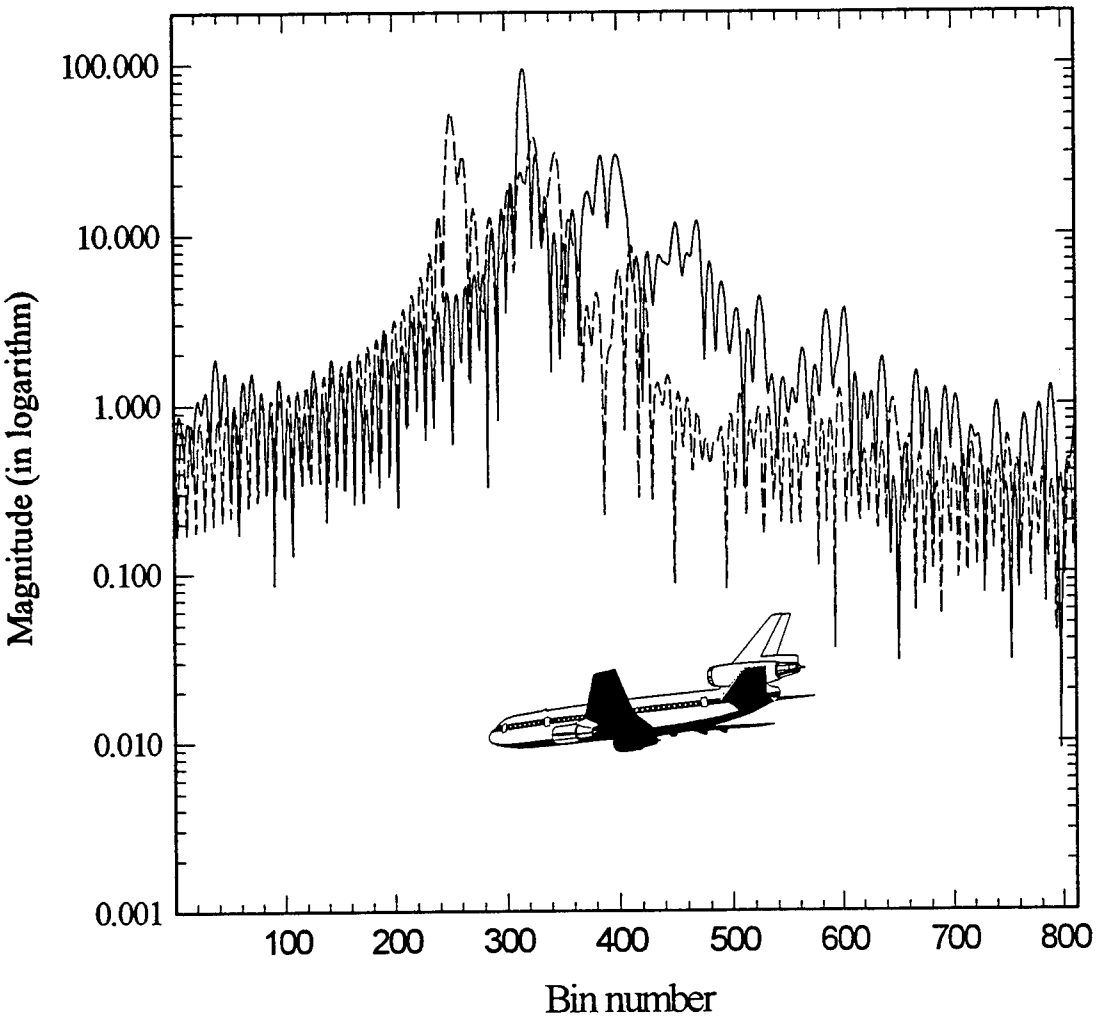

Fig.1 Magnitude plot of target signature *A* at azimuth=25°, elevation=-5° using measured data (solid line) or synthetic data (dotted line)
Note: they are unaligned with respect to each other

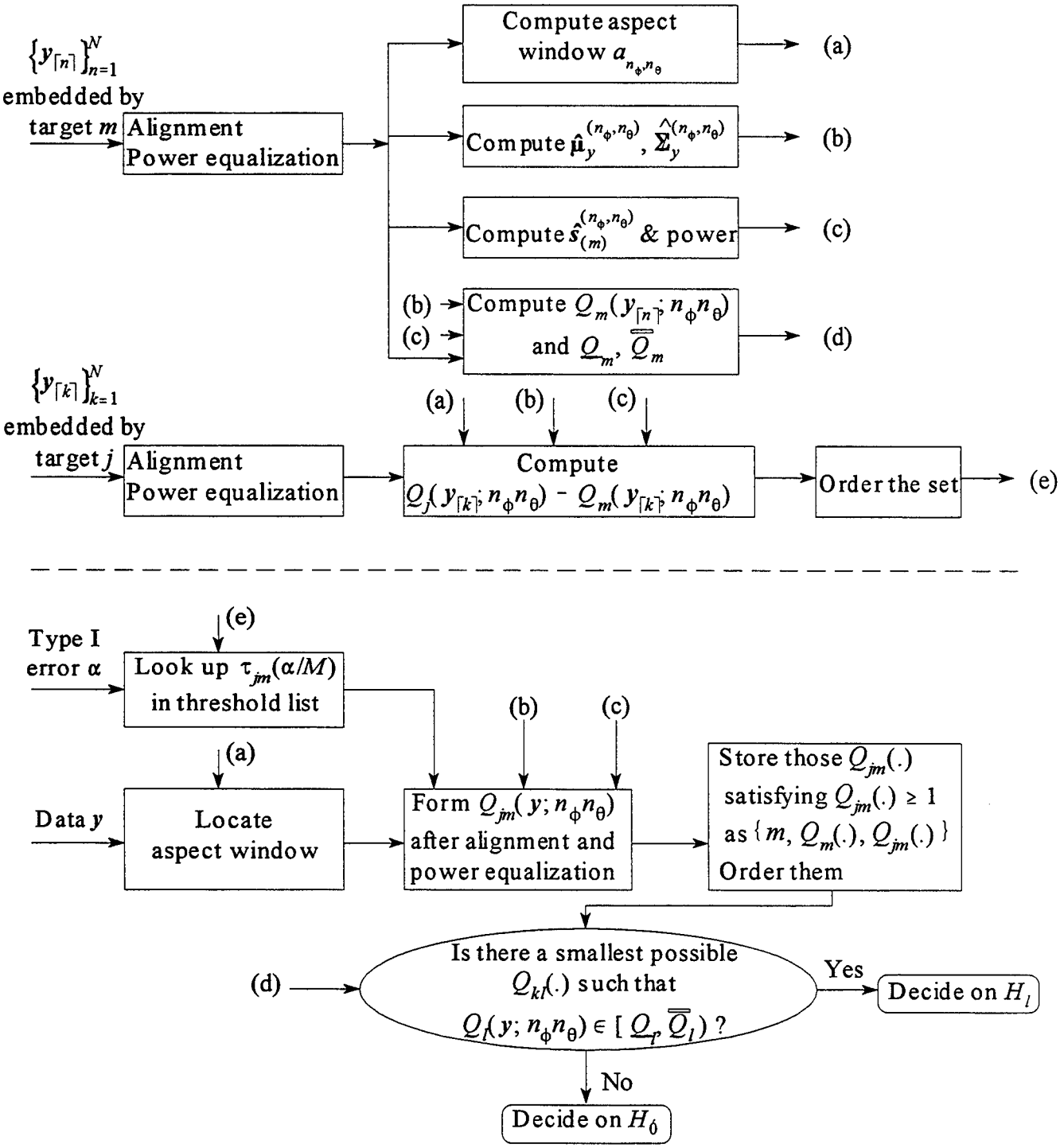

Fig.2 Schematic diagram of unforced M-ary target identification using measured HRR target signatures

Note: The upper, lower half denote training, detection period, respectively

j, m=1,…,M; j≠m; ∀ n_ϕ, n_θ

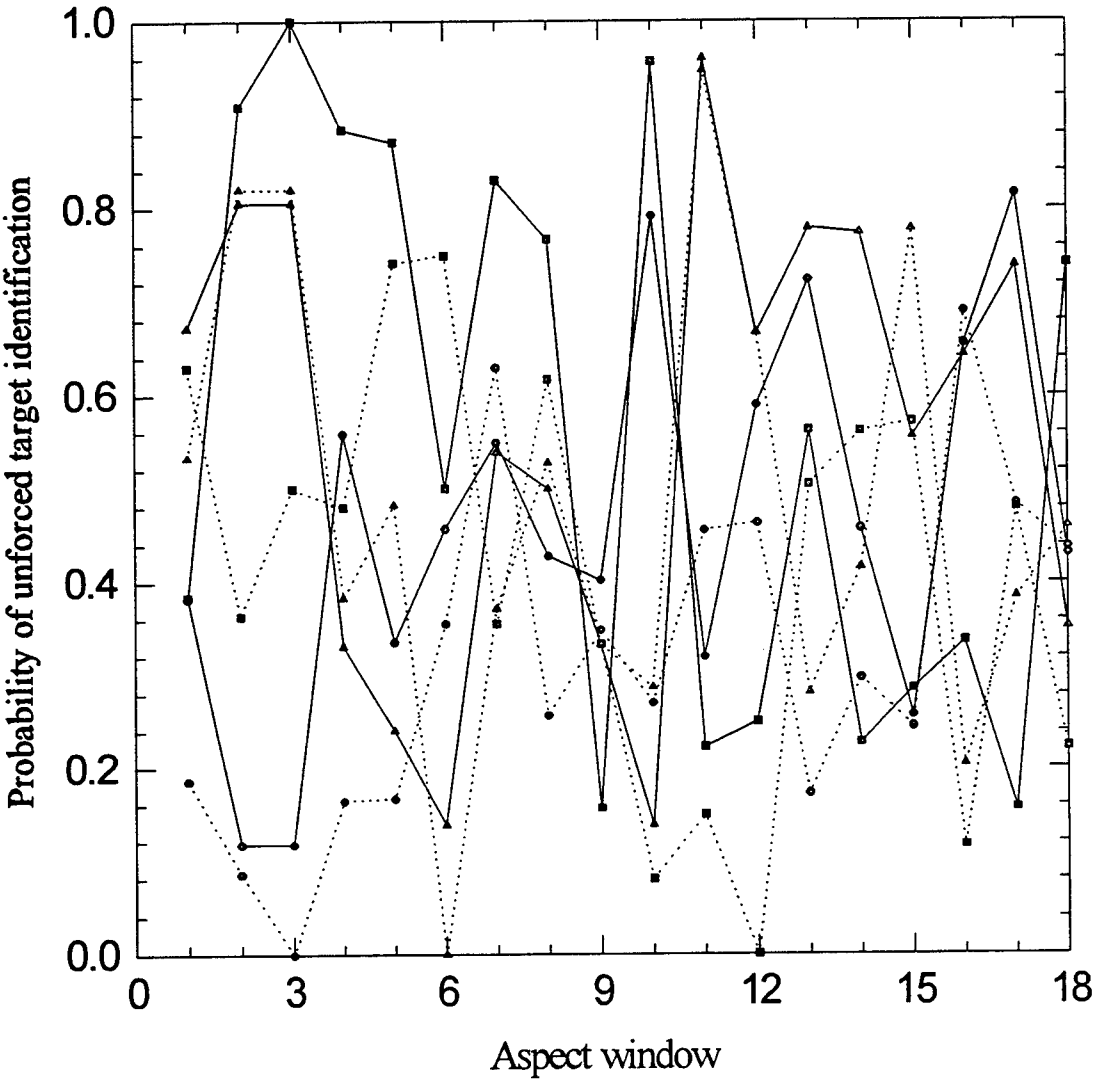

Fig.3 Probability of unforced identification of target j, $j=A$ (●), B (■), C (▲), that is embedded in data and in aspect window A_n, $n=1,\cdots,18$, using measured (solid line) or synthetic (dotted line) data signature

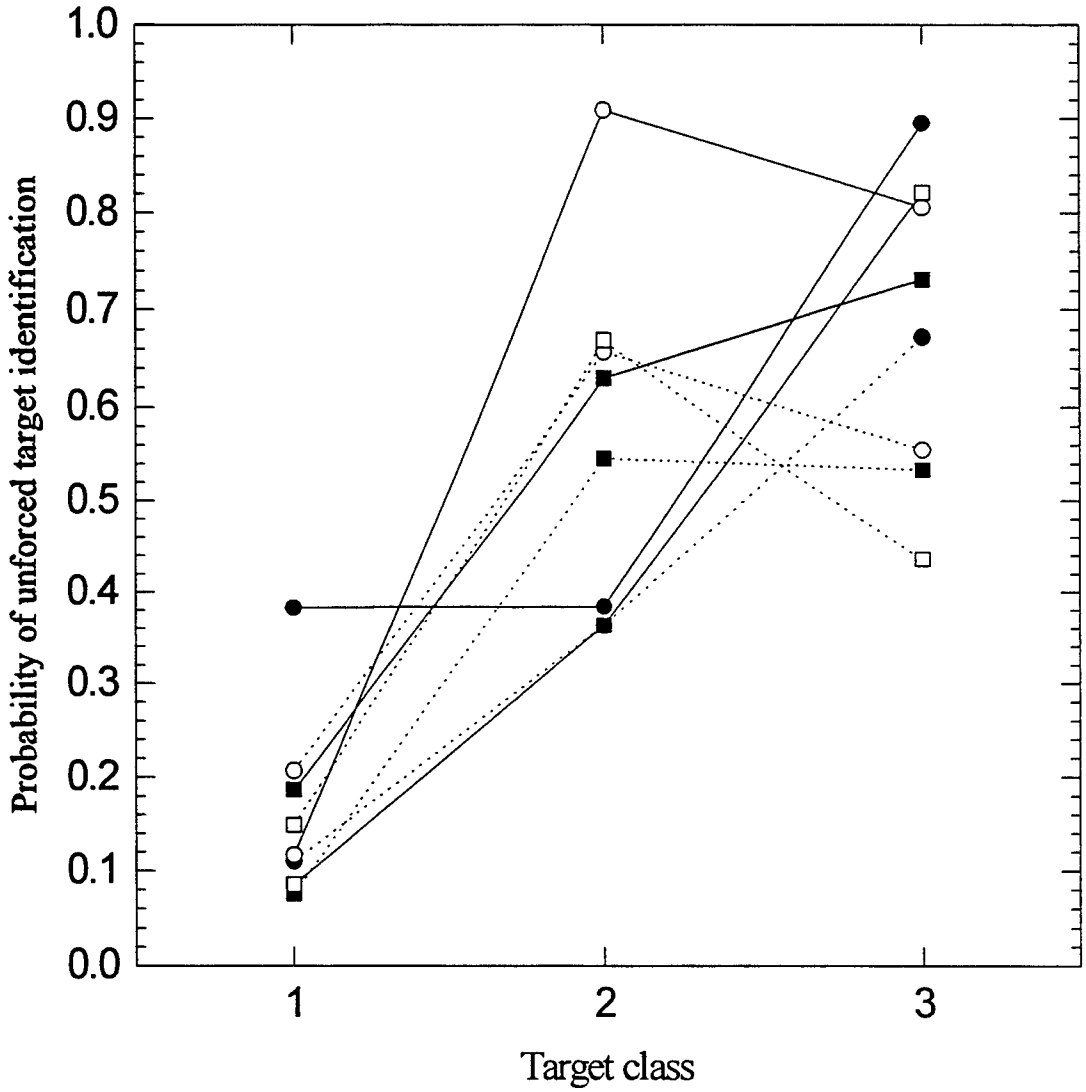

Fig.4 Probability of unforced target identification with the HRR data profiles aligned by in-phase and quadrature correlation (solid line) or magnitude correlation method (dotted line) using measured (circles) or synthetic (rectangles) target signatures
Note: solid, hollow symbols (circles, rectangles) represent aspect window A_1, A_2; 1,2,3 on x-axis represent target class A, B, C, respectively

OF MATCH MAKER AND METRICS

Milton L. Cone
Assistant Professor
Department of Computer Science/Electrical Engineering

Embry-Riddle Aeronautical University
3200 Willow Creek Road
Prescott, Az 86301-3720

Final Report for:
Summer Faculty Research Program
Wright Laboratory

Sponsored by:
Air Force Office of Scientific Research
Bolling Air Force Base, DC

and

Wright Laboratory

August 1996

OF MATCH MAKER AND METRICS

Milton L. Cone
Assistant Professor
Department of Computer Science/Electrical Engineering
Embry-Riddle Aeronautical University

Abstract

The task of a sensor manager is to improve the performance of the individual avionics sensors by coordinating their activities based on the sensor manager's best estimate of the future. This report continues the study of scheduling algorithms for the sensor manager. It is composed of two individual reports, Match Maker and Metrics. Match Maker offers a modification to the crossover algorithm of genetic algorithms that shows promise of speeding convergence of the genetic search. Metrics is a discussion of the role the choice of the evaluation function has on the performance of scheduling algorithms.

OF MATCH MAKER AND METRICS

Milton L. Cone

Introduction

The task of a sensor manager is to improve the performance of the individual avionics sensors by coordinating their activities based on the sensor manager's best estimate of the future. One way to improve that performance is develop schedules that make better use of the limited resources onboard the aircraft. This report continues the study of scheduling algorithms for the sensor manager. It is composed of two individual reports, Match Maker and Metrics.

Match Maker offers a modification to the crossover operator of genetic algorithms that might speed convergence of the genetic search. The summer afforded limited time to test Match Maker. On a six machine/six job job shop scheduling problem Match Maker showed statistically significant improvement in the average number of schedules the genetic algorithm needed to find the known optimal solution for the minimum time to process all tasks. Experience on a wide variety of problems is needed to test the robustness of Match Maker.

Metrics is a discussion of the role the choice of the evaluation function has on the performance of scheduling algorithms. The paper concludes that a combination of classical metrics, while not maximizing the performance of any one metric, leads to schedules that produce a balanced result between schedules that meet deadlines and those that maximize processor utilization.

Match Maker

1. Introduction

The strength of genetic search is that it can integrate many different dispatch techniques into its algorithm by using different dispatch rules to generate some of the schedules for the initial population that starts the genetic algorithm (GA) search. By returning the best schedule found during the search, the GA guarantees that the final schedule is no worse than the best schedule produced by the dispatch rules that helped build the initial population. GA seems unique among scheduling approaches in its ability to unify different scheduling algorithms. Unfortunately even with good starting locations, the search can take a long time to converge since the search space, even for simple problems, is huge.

Another strength of genetic search is that, by comparison with other search techniques [Grefenstette, et. al., 1991], the genetic algorithm can rapidly (comparatively) search large spaces. Grefenstette reports that genetic search outperforms gradient search techniques in realistic problems where the constraints of the gradient search are not completely met and random search in common problems that involve discontinuous, noisy, high dimensional, and multimodal functions. The problem for this application is that for a real-time application, genetic search may still be too slow. Ways to speed the search are needed.

2. Background

The final report from the 1995 AFOSR extension program [Cone, 1995] looked at genetic search's ability to solve one of the standard job shop problems, the 6x6 JSSP. In this problem there are 6 machines to be scheduled with 6 jobs. Each job passes through each machine but not in the same order and each job may take different times to execute on the various machines. This problem is similar to the one expected in the sensor manager.

Attempts to improve the performance of the genetic search were reported in [Cone, 1995]. These included staticly varying the crossover and mutation rates as well as trying to optimize them dynamically during execution of the search. The parametric study of the mutation and crossover rates showed certain combinations of rates performed better than others. Starting with a seed of (123456789) for the random number generator, the trial, τ, in which the optimal makespan result of 55 was first found was recorded for 25 experiments consisting of 120 generations with 50 schedules (trials) in each generation. The average number of trials needed to find the optimal schedule was averaged over the 25 experiments and that single number reported as $\overline{\tau}$. $\overline{\tau}$ measures, on average, how fast the GA finds the optimal solution for makespan. The assumption is that better performing GA's for this problem will also be better performing for more

complex problems. The smallest $\bar{\tau}$ was found at a crossover rate of 0.4 and mutation rate 0.1. $\bar{\tau}$ for various mutation and crossover rates varied from 892 to 5762. Recent investigation found a better $\bar{\tau}$ of 735 with a crossover rate of 0.4 and a mutation rate of 0.14 for this random seed. Finding the correct mutation and crossover rates is an important step to improving the performance of the GA.

An alternate random number seed was also studied by Cone to see if a different random number string would make a difference. The alternate seed is (987654321) and is generally referred to as the reverse seed. The best result for starting the process with the reverse seed was 593 but that result was discounted since there was no crossover in that particular study. Presumably the sequence of random numbers happened to find the optimal solution early in the search an unusual number of times. With random seed (123456789) the metric jumps to 1223 supporting the contention that the 593 was atypical. The next two best results for the reverse seed were 816 and 866.

The dynamic adjustment of mutation and crossover rates did not show any improvement in the metric. In fact, none of the techniques tried were able to beat 892 although the moving window, which limits the number of genes over which crossover can occur, performed nearly as well. This lead Cone to try a new approach, match maker, to accelerate convergence.

3. Match Maker

Match maker is inspired by the characteristic of a species to match the better suited of a species together. In normal genetic search, chromosomes are randomly mated together to produce off-spring. In match maker the chromosomes are matched before mating. This is accomplished by rank ordering the chromosomes based on their evaluation. Crossover is then performed between the best chromosome and the second best. Then third and fourth are matched and so on.

4. Early Results

Match maker was first tried on the same problem studied in [Cone, 1995]. Each study consisted of 25 experiments where each experiment produced 6000 schedules (trials). Table 1. shows a comparison of average trial number, $\bar{\tau}$. R indicates the process started with the reverse seed.

While match maker didn't always improve the standard GA, where it did the effect is dramatic. For crossover equal to 0.4 and mutation equal to 0.1 which was mean trial 892, match maker was able to find the optimal makespan on average in 564 trials. Further tuning of the mutation rate got the average trial down to 405. While the data may not always be statistically significant, the data suggests that there is

Crossover	Mutation Rate	Standard GA	Match Maker
0.2	0.1	816R	349R
0.4	0.01	1470	3682
	0.08	1203	532
	0.1	892	564
	0.1	1106R	450R
	0.13	889	524
	0.14	735	411
	0.15	1053	405
	0.17	1014	412
	0.2	1023	431
	0.25	1215	586
	0.4	1549	748
0.6	0.1	866R	472R
	0.15	1046	669
0.8	0.15	1307	490

Table 1. $\bar{\tau}$ for optimal makespan for 6x6 JSSP.

something positive happening. By comparison, none of the dynamic optimization techniques tried before really showed much improvement.

The data in Table 1. is based on 25 experiments. Another study was conducted with more experiments to establish the statistical significance of the data. The next section reports the results of this study.

4. Study of Statistical Significance

In statistical decision theory, [Spiegel, 1988], a hypothesis is created for the purpose of rejecting or nullifying it. The hypothesis is denoted by H_0 and is often called the null hypothesis. An alternative hypothesis is any one that differs from the null hypothesis. This hypothesis is generally noted by H_1. If a random sample is drawn from a population but the results of the sample differ significantly from the results expected under the null hypothesis, then the hypothesis can generally be rejected or at least not accepted. The procedures that enable one to determine whether observed samples differ significantly from the expected results are called statistical decision rules.

There are two types of errors associated with decision rules. A Type I error occurs when the null hypothesis is rejected when it should be accepted. In testing a given hypothesis the maximum probability with which a Type I error is allowed is called the level of significance and designated α. Usually an α of 0.05 or 0.01 is used. An $\alpha = 0.05$ means that there are about 5 chances in 100 of rejecting a hypothesis when it should be accepted. A Type II error occurs when the H_0 hypothesis is accepted when it should be rejected. The probability of making a Type II error is usually denoted by β. Type I errors are more important if the goal is to reject the null hypothesis, while Type II errors are more important when H_0 is to be accepted. There is a tradeoff between α and β. Increasing the likelihood of making a Type I error reduces the likelihood of a Type II error.

In order to develop a more complete statistical picture of the effectiveness of match maker, 331 (331 is just a convenient number) experiments were run to determine the mean trial number in which 55 was found. In case 55 was not found in 6000 trials then the total number of trials was set at 6000. This has minimal effect on the statistics as 99.9% of the experiments reach 55 in less than 6000 trials. Three combinations of crossover and mutation rates were compared. The forward seed (F) to start the random process was (123456789) and the reverse seed (R) was (987654321). Means and standard deviations were recorded for both the standard genetic search and the genetic search with match maker. Table 2. records the results.

Crossover	Mutation	Seed	Standard GA		Match Maker	
			μ	σ	μ	σ
0.2	0.1	F	952	793	618	719
0.2	0.1	R	943	803	558	641
0.4	0.1	F	1029	909	541	526
0.4	0.1	R	1083	974	507	503
0.6	0.1	F	1105	954	522	490
0.6	0.1	R	1224	1163	508	457

Table 2. Mean and standard deviation of sampling distributions.

If the null hypothesis, H_0, is accepted then the two studies being compared come from the same population and the difference in means is due to the random nature of the sampling process. If H_0 is rejected then there is a difference presumably due to match maker. If the random process has stabilized then forward and reverse samplings at the same crossover and mutation rates should be the same. The next section presents the results of the analysis of this data.

6. Analysis of the Statistical Data

The following paragraphs give results of the analysis of the data collected in section 5. The data was tested at the 0.05 significance level which means that H_0 is not rejected if the normalized variable z is $|z| \leq 1.96$ and is rejected if $|z| > 1.96$ for a two-tailed test. To preview the results, each sample collected with the same crossover and mutation rates tested from the same distribution regardless of forward or reverse seed. This indicates that the 331 samples is enough to make the process independent of the starting seed. A comparison of samples under identical conditions, except for match maker, shows that the samples come from very different populations and that the results are highly significant.

Crossover 0.2 Mutation 0.1

Comparison of forward and reverse seeds without match maker.

$z = 0.14$ Samples from same distribution, process independent of seed. Because the means are so close the chance of accepting the null hypothesis when the means come from different populations is quite high. β for $z = 0.14$ is 0.9434 when α is 0.05. If α is relaxed then β can be reduced.

Comparison of forward and reverse seeds with match maker.

$z = 1.15$ Samples from same distribution, process independent of seed but the conclusion is not as clear cut as above. β is 0.79. Because the separation of the means is greater than above the chance of accepting the null hypothesis when it should be rejected is less.

Comparison of forward seeds with and without match maker.

$z = 7.38$ Samples clearly from different distributions. At this level of significance there is very little chance of error.

Comparison of reverse seeds with and without match maker.

$z = 6.83$ Samples clearly from different distributions.

Crossover 0.4 Mutation 0.1

Comparison of forward and reverse seeds without match maker.

$z = 0.734$ Accept H_0. The samples probably come from the same distribution. β is 0.8715.

Comparison of forward and reverse seeds with match maker.

$z = 0.865$ Samples from same distribution, process independent of seed. β is 0.8619.

Comparison of forward seeds with and without match maker.

$z = 8.44$ Samples clearly from different distributions. At this level of significance there is very little chance of error.

Comparison of reverse seeds with and without match maker.

$z = 9.56$ Samples clearly from different distributions.

Crossover 0.6 Mutation 0.1

Comparison of forward and reverse seeds without match maker.

$z = 1.44$ Accept H_0. The samples probably come from the same distribution . β is 0.699.

Comparison of forward and reverse seeds with match maker.

$z = 0.372$ Samples from same distribution, process independent of seed. β is 0.9342.

Comparison of forward seeds with and without match maker.

$z = 9.89$ Samples clearly from different distributions.

Comparison of reverse seeds with and without match maker.

$z = 10.4$ Samples clearly from different distributions.

7. Conclusions

It is concluded that match maker has an effect, that the results are not statistical variations of the sampling process and that match maker favorably impacts the process. Thus match maker makes an important improvement in the convergence rate for this problem. Match maker should undergo further testing to see if it can also improve the convergence rate in other, more difficult problems. If it can, then, match maker can be an important contribution to genetic algorithms.

References

M. L. Cone (1995). A genetic algorithm scheduler for the sensor manager. In *USAF Summer Research Extension Program.* RDL: Culver City, CA.

J. J. Grefenstette, L. Davis, & D. Cerys (1991). *GENSIS and OOGA: Two Genetic Algorithm Systems.* TSP, Melrose, MA.

M. R. Spiegel (1988). *Schaum's Statistics.* McGraw-Hill, New York

Metrics

1. Introduction

The purpose of this paper is to look at classic metrics to see which are appropriate for evaluating the sensor manager's schedule. The metric dictates to some extent the kind of scheduler that is appropriate since for some metrics there are optimal dispatch rules that can be used and for others a heuristic scheduling approach may be known only for certain metrics. The paper starts with an overview of the sensor manager scheduling problem. Next several classic metrics that have been used to develop schedules are summarized. An evaluation of some of the metrics versus the sensor manager's scheduling problem follows. Finally, examples showing the impact of different metrics on the similar job shop scheduling problem are given, followed by conclusions.

2. The sensor manager's scheduling problem

Aspects of the scheduling problem have been summarized by [Popoli, 1992]. He lists the following problems that the sensor manager might have to deal with:

- There are hard deadline tasks that have to be completed in a narrow window if they are to be of any value.
- There are tasks without deadlines that have earliest start times before which they can't begin execution.
- There are differences in task priorities. Some tasks are very important, others routine. A task's priority generally reflects the urgency of its start time.
- Some tasks may be interruptable, others not.
- Tasks may vary greatly in length.
- Tasks can become necessary or unnecessary very suddenly.
- There may be some uncertainty in the requirements for the task. For example, the duration of the task may not be known when the task begins execution.

Other problems not mentioned by Popoli include:

- Sensors may need to operate in parallel. At times one of the parallel tasks may be a no-op effectively keeping one sensor from interfering with the operation of another sensor.
- Sensors may need to operate in series so that one sensor can cross queue another. This task requires sequential operation of two or more sensors with possibly slack time between operations to allow data to be transferred between sensors.
- The plant may change while the scheduler is operating. Some sensors may become inoperable requiring an emergency rescheduling.

- Workload can be heavy requiring efficient use of all resources.

3. Classic Metrics

Unless noted these metrics come from [Penedo, 1995]. Generally the goal of the scheduler is to minimize the value of these metrics (also called objective functions).

Makespan (C_{max}). Makespan is the maximum of the completion times of the jobs in the system. It is the time when the last job finishes. By minimizing the makespan jobs get through the system faster which leads to better utilization of the machines.

Total weighted completion time ($\Sigma w_j C_j$). Completion time is taken as the time when a job finishes. It is not referenced to when the job starts. Total weighted completion time measures how long it takes to process the *n* jobs that the sum runs over. A longer weighted completion time means that there is more work-in-process (WIP) in the plant. The weights account for different inventory costs while the material to produce the products is in the plant. The sum of the completion times is also known as the flow time and this metric may also be called the weighted flow time. A variation of this metric involves squaring the completion time and adding a weight leading to the weighted sum of squared completion time metric.

Maximum lateness (L_{max}). Lateness is the difference in time between the time when the job actually completes and the due date for the completion of a job. Positive lateness means the job finished late and negative lateness means the job finished early. The goal is to minimize the lateness of the worst job. Lateness relates to customer satisfaction and is not appropriate when the jobs do not have deadlines. If all jobs in the problem have a common deadline, then minimizing maximum lateness is the same as minimizing makespan. Two variants of lateness are total lateness, the sum of the lateness for each job, and total weighted lateness which applies a weight to each job's lateness.

Total weighted tardiness ($\Sigma w_j T_j$). Tardiness is the maximum of lateness or 0. It recognizes that in some cases there are penalties for being late but no benefits for being early. The total weighted tardiness sums the tardiness for each job in the *n* jobs being considered in this planning cycle. Jobs must have deadlines for this metric to be useful. Other variations on this same theme include letting all of the weights equal 1, only considering the maximum tardiness or summing the weighted tardiness squared ($\Sigma w_j T_j^2$).

Weighted number of tardy jobs ($\Sigma w_j U_j$). U_j is either one or zero. If the weights are all one then the weighted number of tardy jobs is just the number of tardy jobs. This measure is simple to collect and

understand so is frequently used in practice. It is a measure of total customer satisfaction but is not sensitive to how mad customers might be if their jobs are very late.

Sequence dependent setup times (Σs_{ijk}). s_{ijk} is the sequence dependent setup time between job j and job k for machine i. Minimizing this measure increases throughput and decreases slack time between jobs.

Idleness (ΣI_j). Idleness is the time between the finish and the start of a job that is not devoted to processing. It includes the dead time when the jobs are waiting to get on a machine and the sequence dependent setup times. It is computed by taking the completion time of a job and subtracting the start time and all of the time devoted to processing. Idleness is also known as slack time.

Economic makespan ($\Sigma R_k(C_k-a_k)$). The economic makespan metric [Morton and Pentico, 1993] builds schedules that reflect the cost of machine utilization. A price, R_k, is estimated for running the machine. This price is multiplied times the completion time, C_k, of the last job on that machine minus the earliest time, a_k, that the machine is available. This objective function is good in a heavily loaded shop where new jobs are always coming in so that the idle time at the end of the current planning horizon for a particular machine can be filled by the new jobs. It is generally equivalent to minimizing the internal slack in the system.

Discounted total weighted completion time ($\Sigma w_j(1-e^{-rC_j})$). In the discounted total weighted completion time the jobs that take longer to complete contribute a larger percentage of their weight, w_j, to the metric. As a measure, it favors finishing the longer jobs at the cost of taking longer to do the shorter jobs.

Total weighted earliness ($\Sigma \beta_i E_i^2$). [Czerwinski and Luh, 1994] estimate the theoretical part start date by backtracking along the critical path from the due date. Earliness is defined as the time ahead of the theoretical part start date that the part actually starts production. There is no penalty for starting after the theoretical start date. Squaring the earliness function causes the penalty to increase faster the larger earliness becomes.

Number of processors (n). If there are more machines available then jobs then this schedule tries to minimize n, the number of machines used. This objective function is usually associated with a shop that has several identical machines operating in parallel.

4. Discussion of individual metrics

Makespan is probably the most frequently used metric for schedule generation. [Kober, 1994] has suggested that some metric other than makespan may have some value for the sensor manager scheduler. [Stankovic, et. al., 1995] believes that makespan is important in that it minimizes required system resources but since it does not directly address deadlines it can't be a primary metric. Stankovic maintains that for real-time systems the sum of completion times is not important because it doesn't have a direct assessment of timing properties like deadlines and periods. He sees value in the weighted sum of completion times since it recognizes that some jobs have more value than others. He also feels that value and deadlines are both important and that many real-time scheduling systems concentrate only on deadlines.

Minimizing maximum lateness doesn't prevent tasks from being late. It is possible to construct an example that minimizes the maximum lateness yet has all tasks miss their deadlines, [Stankovic, et. al., 1995]. Optimizing the total lateness or total weighted lateness may help but it also might cause more tasks to miss their deadlines while trying to reduce the lateness of a very tardy task. Tardiness has the same problem as lateness. By itself it isn't sensitive to the number of late jobs. For a real-time operation, being on time is the most important measure of the effectiveness of a schedule. Minimizing the number of tardy jobs or the weighted number of tardy jobs helps correct this. However, since the sensor manager is dealing with a task set that may contain many jobs without deadlines, in cases where processor utilization is equally important, objective functions that are only sensitive to deadlines are not totally adequate.

Minimizing either sequence dependent setup times or idleness is a direct measure of throughput through the system. While these metrics increase efficiency they do not directly assess a schedule's ability to meet deadlines.

The total weighted earliness metric penalizes a job for starting early. The presumption here is that jobs that start too early end up staying in the plant too long which increases the work-in-process (WIP) costs. This metric is generally used in conjunction with a metric that senses completion time so that the job has a window of opportunity in which to move through the plant.

The economic makespan is similar to idleness except that idleness is based on how long jobs set idle whereas economic makespan is based on how long machines are idle. Like several of the other metrics, it has no sense of which jobs need to be completed to meet deadlines. Plant efficiency may have to be sacrificed in order to complete certain jobs on time. This metric has the distinction of including a weight measuring the importance of each machine. For example, the IR system may be favored over the radar in low emission modes so the weight of the IR sensor may be high in certain periods of the mission.

The discounted total weighted completion time evaluation function produces schedules that improves plant efficiency by scheduling longer and more important jobs first. Schedules generated from this metric are similar to those using the longest processing time first dispatch rule. The difference is that the discounted total weighted completion time metric includes slack time. This metric is useful to the sensor manager only if another metric is included which measures the ability of the schedule to meet deadlines.

The last metric, number of processors, is not particularly useful for the sensor manager. It is appropriate when there are several jobs and several machines available to choose from, and the jobs can run in parallel. As this is not the usual sensor manager architecture the number of processors metric would not be appropriate.

For a dynamic scheduling algorithm (one that schedules tasks when they arrive and the arrival times are unknown in advance to the scheduler) the choice usually goes to a metric for which an optimal dispatch rule is known. These rules generally exist only for standard plant models which the sensor manager architecture will probably not match. For example there are dispatch rules such as "weighted shortest processing time first" when all release dates and due dates are 0 or "earliest due date first" when all due dates are sufficiently loose and spread out, that optimize the weighted tardiness under certain very restrictive conditions. While these dispatch rules may not be appropriate for the configuration the sensor manager finds itself in, they can still be used to make schedules for the initial population.

The next section considers the effect of combining individual metrics to improve the performance of the schedules.

5. Evaluation of combined metrics

Metrics generally fall into two classes. The first deals with a schedule's ability to meet its deadlines. Lateness, tardiness, number of tardy jobs and their variants belong to this class. The second group of objective functions measures some aspect of processor utilization. Makespan, economic makespan, completion time, sequence dependent setup times, earliness, number of processors and their variants are examples. A good metric should have a measure from each class if it is to address the needs of real-time scheduling.

Penedo suggests that one particular combination of objectives used in the process industry is the minimization of total weighted tardiness and the sum of sequence-dependent setup times. Weighted tardiness measures a company's ability to maintain the quality of its service while the sum of sequence-dependent setup times indirectly measures the plant's efficiency (throughput). The relative importance of

the two may change over time. When the workload is light, tardiness may be more important, but when the workload is heavy, plant efficiency may be more important.

[Czerwinski and Luh, 1994] also use a combined objective function in their Lagrangian relaxation technique. This one combines an earliness with a tardiness penalty. These penalties together define a time interval in which an operation can be scheduled with zero penalty. The objective of this penalty function is to ensure on-time part completion and low work-in-process inventory. By penalizing schedules that start early, machine utilization is improved and slack time is reduced.

The next two subsections evaluate the Pinedo and Czerwinski/Luh combined metrics ability to handle the sensor manager's scheduling problem.

5.1 Pinedo pair discussion

Schedules produced by the Pinedo pair, total weighted tardiness and the sum of sequence-dependent setup times will be evaluated as to its ability to solve the sensor manager's scheduling problems of Section 2. Hard deadlines that have earliest start times use both metrics to define an operating window in which they can operate. The weighting factor takes care of any differences in the tasks' priorities. While the metrics do not directly address whether the tasks are interruptable, any task that is can be tested against the metric to see if it produces a better schedule. Varying task length does not directly impact the metric evaluation. Sudden changes in a task's priority require a separate mechanism in the scheduler which is not a function of the metric. For example, a pop-up job may be handled by a separate reactive scheduler [Morton & Pentico, 1993]. The reactive scheduler tries to produce a feasible schedule that has a minimal impact on the current working schedule. It may not use a metric at all and may be as simple as trying to fit the task into a space in the existing schedule or delaying tasks on a machine by enough to fit in the pop-up job. Reactive schedulers have to be fast. If a new schedule can be built in time to handle the pop-up task using the usual scheduling cycle, then there is no need for a reactive scheduler. The Pinedo pair, while not taking much longer than any other metric, probably takes too long to be considered for reactive use.

Uncertainty in task requirements means that there is some information that is needed for scheduling that is not precisely known. Whatever uncertainty there is gets mapped into uncertainty in the objective function. It then becomes a matter for the scheduling algorithm to manage that uncertainty. Under some conditions there are some NP-hard problems for deterministic models that have known optimal solutions for stochastic models. One of these results is for the single machine problem when all deadlines are equal and the metric is the sum of the weighted tardiness. This may be useful information to the scheduling algorithm whenever the Pinedo pair is chosen.

The next two bullets from Section 2. concern sensor architecture, the modeling of the sensors in series or parallel or a combination of both (job or flow shops). Sensor architecture only affects the Pinedo pair in that there are limited configurations and conditions for which optimal scheduling algorithms are known. In particular, one metric of the Pinedo pair, the sum of weighted tardiness, is NP-hard in the strong sense even for one machine. This means that it is unlikely that a general algorithm can be found that gives an optimal schedule in polynomial time and suggests that a heuristic scheduling technique like genetic search or Lagrangian relaxation is required to develop good schedules.

The next problem, plant change, really doesn't affect the Pinedo pair. For example, if one sensor goes off-line while the schedule is operating, the scheduler may have to go into a short rescheduling sequence using a less demanding metric. This is the same as letting the reactive scheduler take over for the short term before transitioning back into the long range scheduler.

Heavy workload presents its own problems. The ideal schedule is one that has the plant working at peak efficiency. The weighted sum of tardiness is appropriate under heavy workload conditions since it allows the most important jobs to be scheduled first and less important jobs to be left to later. Minimizing the setup times reduces sensor idle time which helps throughput when the workload is heavy. The setup times metric may not be as appropriate as makespan or economic makespan which more directly address processor utilization.

5.2 Czerwinski and Luh discussion

The Czerwinski and Luh metric combines tardiness and earliness penalties for operations. They use the following formula summed over all jobs:

$$\Sigma(w_j T_j^2 + \beta_j E_j^2)$$

In their formulation, the squaring of the tardiness and earliness metric penalizes the later or earlier jobs more. This metric seems to be superior to the Pinedo pair against the first criteria, hard deadlines. While it forces jobs into a window of opportunity which is what the first bullet requires, it also works directly on the second bullet which requires jobs to start after a certain time. This metric is superior to Pinedo on this point as Pinedo addresses the start time only as a second order effect. A possible problem with the Czerwinski/Luh metric is that if some of the start times can't be violated, this objective function penalizes but does not prevent jobs from starting early. As with Pinedo, weighting takes care of differing task priorities.

The Czerwinski and Luh metric has no known optimal dispatch rule for any interruptable system (or for any system for that matter). This means that a heuristic is required to develop schedules. Varying length schedules pose no problem for the metric. Pop-up jobs have to be handled by a reactive scheduler as was done for Pinedo. Uncertainty in the knowledge of start times for due dates is reflected in uncertainty in the evaluation of a schedule. The Pinedo pair may have an advantage here since the setup times should be determined in advance and the type of job to be scheduled has to be known as a minimum. Thus it is likely there are less unknowns in the Pinedo pair.

The other problems that the scheduler may have to handle are similar for both metric combinations with the exception of the last bullet which is heavy workload. By squaring the tardiness and earliness penalties, Czerwinski and Luh get a tighter control of throughput and should be able to develop schedules that make more efficient use of the sensors.

5.3 Recommendation

Inclusion of both classes of metrics is needed to produce a balanced result and so the recommendation is to choose one metric from each class and build schedules using the combined metric. Which metrics to use depend on the details of the avionics architecture used for the sensor suites and may vary with the intended mission. Of the two combined metrics considered, the Czerwinski and Luh combination seems a better choice.

6. Comparison of Example Schedules Generated by Different Metrics

As a simple demonstration of the impact of metrics on schedules, consider the 6x6 job shop scheduling problem (JSSP), [Muth & Thompson, 1963]. In the 6x6 JSSP there are 6 machines and 6 jobs. Each job is processed on all six machines but each in a different order. Three schedules were generated using different evaluation functions. The three metrics used were makespan, sum of squared completion times and a combination of makespan and sum of squared completion times. An evaluation of 55 is the known optimal solution for makespan and is easily found by the genetic algorithm (GA). One of the many schedules with a makespan of 55 was chosen to evaluate the sum of squared completion times. The sum of squared completion times takes the time when each of the six jobs in the 6x6 JSSP completes, squares the completion times and adds them. If the due date for each job is 0 then the completion date is the same as the tardiness and the sum of squared completion times is the same as the sum of squared tardiness. Table 1. lists the makespan and sum of squared completion times for all three schedules. The schedules in Table 1. are individual schedules arbitrarily chosen from the list of those schedules minimizing their performance metric.

Measure of Performance	Schedule Evaluation Function		
	Makespan	Squared Completion	Combined
Makespan	55	64	60
Squared Completion	15607	13191	13298
End Time			
Job 1	48	26	26
Job 2	52	64	60
Job 3	55	56	56
Job 4	54	59	58
Job 5	53	29	29
Job 6	43	31	41
Idle Time	108	68	73

Table 1. Comparison of schedules produced by three different metrics.

The makespan schedule found the optimal value of makespan but at the expense of the sum of completion times squared. Looking at the end times of the jobs, the makespan metric tends to balance the completion times of all jobs. There is no premium for completing jobs early. On the other hand, the sum of squared completion times tries to complete jobs as soon as possible. If the environment is such that machines set idle after a job is done waiting for the next surge, then makespan is a better metric since the last of the jobs completes earlier and the next sequence can start sooner. If there are jobs coming in that could be scheduled on a machine when it is available then the sum of squared completion times finishes some jobs early and frees the machines for new jobs. For example, job 1 finishes at 48 for the makespan schedule, but at 26 for the sum of squared completion times. If there are new jobs that could use machine 1 but are not in the original schedule, then they could start at 26 with the squared completion times schedule. Job 5 shows similar results.

The third metric combines makespan and squared completion times. The makespan is squared in order to get the units of makespan the same as squared completion times. The result is a compromise between the makespan and squared completion time schedules. Compared to the previous schedules, the makespan is about half-way between and the sum of squared completion times is nearly as good as the sum of squared completion time schedule.

Another way to compare schedules is on the basis of idle or slack time (defined as the completion time minus the actual total time on all machines required for a job). For example, job 1 on the makespan

schedule completes at 48. If it is scheduled without any other jobs it would take 26 units to complete by going directly from one processor to another. Thus job 1 sets idle for 22 units sometime during its processing. Table 1. shows the idle time for each schedule. For these schedules the sum of squared completion times produces a schedule that has the machines setting idle for the least time, although the combined metric does almost as well.

As another example, consider the schedules produced by the dispatch rules, shortest processing time (SPT) first and longest processing time first (LPT). In SPT the job with shortest execution time which has an open machine and has its previous task completed is run next. LPT is the same as SPT except the job with the longest processing time is considered first. The SPT rule is optimal for a flow shop where each of m machines are in series, every job must be processed on every machine, each machine takes the same amount of time to process job j, and the criteria is to minimize makespan. LPT optimizes makespan on m parallel machines by assigning the m longest jobs to the m machines. After that, whenever a machine is freed, the longest unscheduled job is put on that machine. Table 2. shows the results of the SPT and LPT rules applied to the JSSP.

Measure of Performance	Schedule Evaluation Function	
	SPT	LPT
Makespan	84	76
Squared Completion	19507	21506
End Time		
Job 1	38	70
Job 2	84	53
Job 3	50	49
Job 4	41	52
Job 5	51	54
Job 6	65	76
Idle Time	132	158

Table 2. Schedules produced by dispatch rules.

SPT doesn't produce a particularly good schedule for either of the two metrics considered here. The LPT rule does even worse. Jobs take longer and set idle more than with any of the previous schedules. This example illustrates the trouble with most dispatch rules when used in situations different than those in which they were designed to operate. Performance is generally poor.

7. Conclusions

This paper has examined the impact of metrics on schedules. The sensor manager's scheduling problem was described. Several classic metrics were listed along with the intended performance goal of the metric. It was suggested that metrics generally fall into two classes and that a good schedule could be built by taking a metric out of each class. Two combined metrics were evaluated as to their suitability for the sensor manager problem. Examples of schedules built by three different metrics: makespan, sum of squared completion times and a combination of both metrics were presented. They were evaluated based on the makespan and sum of squared completion times metrics and also by a third metric, idleness, that none of the schedules were designed to optimize. Finally two common dispatch rules, SPT and LPT, were used to produce schedules that were based on the three previous metrics.

As expected, a schedule that is tuned to one metric generally performs poorly in a different metric. Thus the sensor manager problem needs to be carefully analyzed so that the right metric is chosen. The schedule generated by the combined makespan and sum of squared completion times was a compromise between the schedules produced by the individual metrics. If the due dates of all jobs are considered to be the beginning of the scheduling period, then the sum of squared completion times is the same as squared tardiness and the combined metric example is an example of a metric taken from each class. The result is a schedule that combines features of each of the individual metrics to produce a good schedule but not one that maximizes the performance of any one individual metric.

References

C. S. Czerwinski & P. B. Luh (1994). Scheduling products with bills of materials using an improved lagrangian relaxation technique. *IEEE Trans on Robotics and Automation*, Apr.

W. Kober (1994). Personal communication.

T. E. Morton & D. W. Pentico (1993). *Heuristic Scheduling Systems*. John Wiley and Sons, Inc, New York.

J. F. Muth & G. L. Thompson (1963). *Industrial Scheduling*. Prentice Hall, Englewood Cliffs, NJ.

M. Pinedo (1995). *Scheduling Theory, Algorithms, and Systems*. Prentice Hall, Englewood Cliffs, NJ.

R. Popoli (1992). The sensor management imperative. In Yaakov Bar-Shalom, editor, *Multitarget-Multisensor Tracking: Applications and Advances Volume II*. Artec House, Norwood, MA.

J. A. Stankovic, M. Spuri, M. Di Natale, & G. C. Buttazzo (1995). Implications of classical scheduling results for real-time systems. *Computer*, Jun.

OPTICAL STUDIES OF TWO NOVEL ELECTRO-EXPLOSIVE DEVICES

Robert R. Criss
Assistant Professor
Department of Physics

Randolph-Macon Woman's College
2500 Rivermont Avenue
Lynchburg, VA 24503-1526

Final Report for:
Summer Faculty Research Program
Wright Laboratory, Eglin AFB, FL

Sponsored by:
Air Force Office of Scientific Research
Bolling Air Force Base, DC

and

Wright Laboratory, Eglin AFB, FL

July 1996

OPTICAL STUDIES OF TWO NOVEL ELECTRO-EXPLOSIVE DEVICES

Robert R. Criss
Assistant Professor
Department of Physics
Randolph-Macon Woman's College

Abstract

High speed streak photography and time integrated spectroscopy were used to characterize optical emissions from plasmas formed by two novel electro-explosive devices; a semiconductor bridge (SCB), and a semiconductor junction igniter (SJI). The spatial extent and expansion velocity of each plasma were determined as a function of time. An estimation of ion/neutral temperature was made by assuming that the identity of the ion/neutral was known and that the plasma was expanding freely in the plane parallel to the plane of the device. Time integrated spectra of the plasmas were complex and analysis is not complete at this time.

OPTICAL STUDIES OF TWO NOVEL ELECTRO-EXPLOSIVE DEVICES

Robert R. Criss

Introduction

Semiconductor bridges (SCB's) and semiconductor junction igniter's (SJI's) are electro-explosive devices used to provide ignition of energetic compounds such as pyrotechnics and propellants. They can be used in products ranging from automotive airbags to ordinance systems. The detailed structure of these devices has been published elsewhere and will not be discussed in this report.[1-2] A current pulse applied to the SCB/SJI quickly heats the device, producing an ionized plasma which is used to ignite an energetic compound. Though the exact mechanisms responsible for ignition are unknown, one might reasonably expect them to be related to plasma properties such as the identity of species, temperature, density, expansion velocity, and amount of ionization. A study of optical emissions from the plasma, taken in conjunction with current-voltage measurements, offers the promise of determining all of the aforementioned plasma properties. Our optical studies consisted of high speed streak photography and time integrated, multichannel emission spectroscopy. A preliminary analysis of the results is presented in this report.

Methodology

The procedures used to collect data were the same for both SCB and SJI devices. All of the devices were fired with a current pulse from a 0.2μF capacitor charged to 1kV. Multiple SCB's (and SJI's) were necessary to collect a complete data set. Since the I-V measurements from all of the SCB's were nearly identical, it has been assumed that the plasma properties were reproducible from shot to shot. This was also the case for the SJI's.

A bi-convex lens was used to focus an image of the device onto the entrance slit of the streak camera. Streak pictures (covering a 2μs time interval) of the luminous plasma were taken with the plane of the device parallel to the plane of the camera entrance slit (front view) and with the plane of the device perpendicular to the plane of the camera entrance slit (side view). Intensity contours from pictures taken with the device in each orientation determine the location of the luminous plasma as a function of time. An intensity contour from the front view pictures was used to determine the extent of the luminous plasma in the plane parallel to the plane of the device as a function of time. When this location is plotted against the time, the slope of the curve yields the parallel expansion

velocity (this is the velocity of the plasma in the plane parallel to the plane of the device). Likewise, pictures taken from the side view yield, as a function of time, the extent of the luminous plasma in the plane perpendicular to the device and the perpendicular expansion velocity.

Spectra were collected with a 1-dimensional, computer interfaced diode array coupled to the exit of a grating spectrometer. Each device was aligned with the plane of the device parallel to the plane of the spectrometer entrance slit. Spectra were collected from 200nm to 700nm in intervals of approximately 100nm.

Results

Typical front and side view streak pictures of the plasma formed by an SCB are shown in figure 1. A contour was traced along the edge of each picture and, from this contour, data points were taken for the plots of the spatial extent of the SCB plasma as a function of time, shown in figure 2. Sixth order polynomials were fit to each curve. The derivatives were then used to generate plots of the instantaneous expansion velocities as a function of time, shown in figure 3. If the expansion of the plasma is assumed to be a free expansion, and if the identity of the plasma species is known, the equipartition of energy theorem can be used to estimate the plasma ion/neutral temperature. Under these conditions, the temperature can be written as

$$T \approx mv^2 / 3k \quad . \qquad (1)$$

where T is the temperature, m is the mass of the plasma species, k is Boltzmann's constant, and v is the velocity. Aluminum and silicon are the species present in the plasma (this conclusion can be drawn from knowledge of device construction and confirmed spectroscopically). The condition of 'free expansion' would most likely be met for plasma expansion in the plane parallel to the plane of the device and at some time after the initial burst of plasma formation. Using the parallel expansion velocity of the SCB plasma at a time 0.2 μs after the initial burst yields a temperature of 693 K for an aluminum plasma and 720 K for a silicon plasma. A volume of 0.09 mm^3 was calculated for the plasma at this time(0.2 μs) by using the equation for the volume of a right circular cone and dimensions taken from figure 2.

Typical front and side view streak pictures of the plasma formed by an SJI are shown in figure 4. Plots of the spatial extent of the SJI plasma and the instantaneous expansion velocities, generated by the procedure outlined above, are shown in figures 5 and 6. Substituting the parallel expansion velocity of the SJI plasma at a time 0.2 μs after the initial burst into equation (1) yields a temperature of 1309 K for an aluminum plasma and 1362 K for a

silicon plasma. A volume of 0.19 mm^3 was calculated for the plasma at this time(0.2 μs) by using the equation for the volume of a right circular cone and dimensions taken from figure 5.

Spectra collected from both devices should confirm the identification of species in the plasma and might be suitable for determination of the plasma electron temperature. The analysis has not been completed at this time but will be presented for publication at a later date. Values for the resistivity, calculated from the current-voltage traces, might also be used in conjunction with this temperature to determine the fractional ionization of the plasma.

Summary & Conclusions

Streak photography has been used to determine the location and expansion velocity of luminous plasmas from SCB and SJI devices. Expansion velocities were measured both parallel and perpendicular to the plane of the device. In each case, the velocity started at a maximum and decreased most sharply in the first 0.1μs of the plasma discharge. For both devices, the initial parallel expansion velocity was slightly larger than the initial perpendicular expansion velocity. This may be due to shock effects or errors in alignment of the device with the streak camera slit. The effect of contrast enhancement of the streak pictures on the results of the image analysis also needs to be considered. Further data analysis, which includes the consideration of shock effects, should resolve questions about the validity of the temperature measurement discussed in this report.

Though not presented in this report, analysis of the spectral data is ongoing. A tentative summary of those results is presented in this report. Spectral emissions from aluminum and silicon have been identified. It seems possible that at least some of the features appearing in the spectra are from the air surrounding the plasma discharge. Calculations of the plasma density as a function of time should suggest at what stage of the discharge features from the surrounding air would be expected to appear. Spectra collected when the device is in a vacuum could also assist in the identification of spectral peaks. It should be noted that all of the spectra collected were integrated, in time, over the full duration of the plasma discharge.

We are still at too early a stage of data analysis to compare the results from the measurements on SCB plasmas to those on SJI plasmas. Indeed, most of the analysis not yet complete. An ion/neutral temperature and an estimation of plasma density should be possible from the streak pictures, used in conjunction with knowledge of device geometry and some reasonable assumptions. The spectra have already confirmed the presence of aluminum and silicon in the plasma. It might be possible to calculate a temperature, approximating the electron temperature,

from the spectra. If so, this temperature could be used in conjunction with the plasma resistivity (taken from the I-V curves) to estimate the fractional ionization of the plasma. The complete analysis will be submitted for publication in professional journals at a later date.

References

1. D. A. Benson, M. E. Larsen, A. M. Renlund, W. M. Trott, and R. W. Bickes, Jr. , *J. Appl. Phy.* **62**(5), 1622 (1987).

2. Thomas A. Baginski, *IEEE Trans. Ind. App.* **29**(2), 412 (1993).

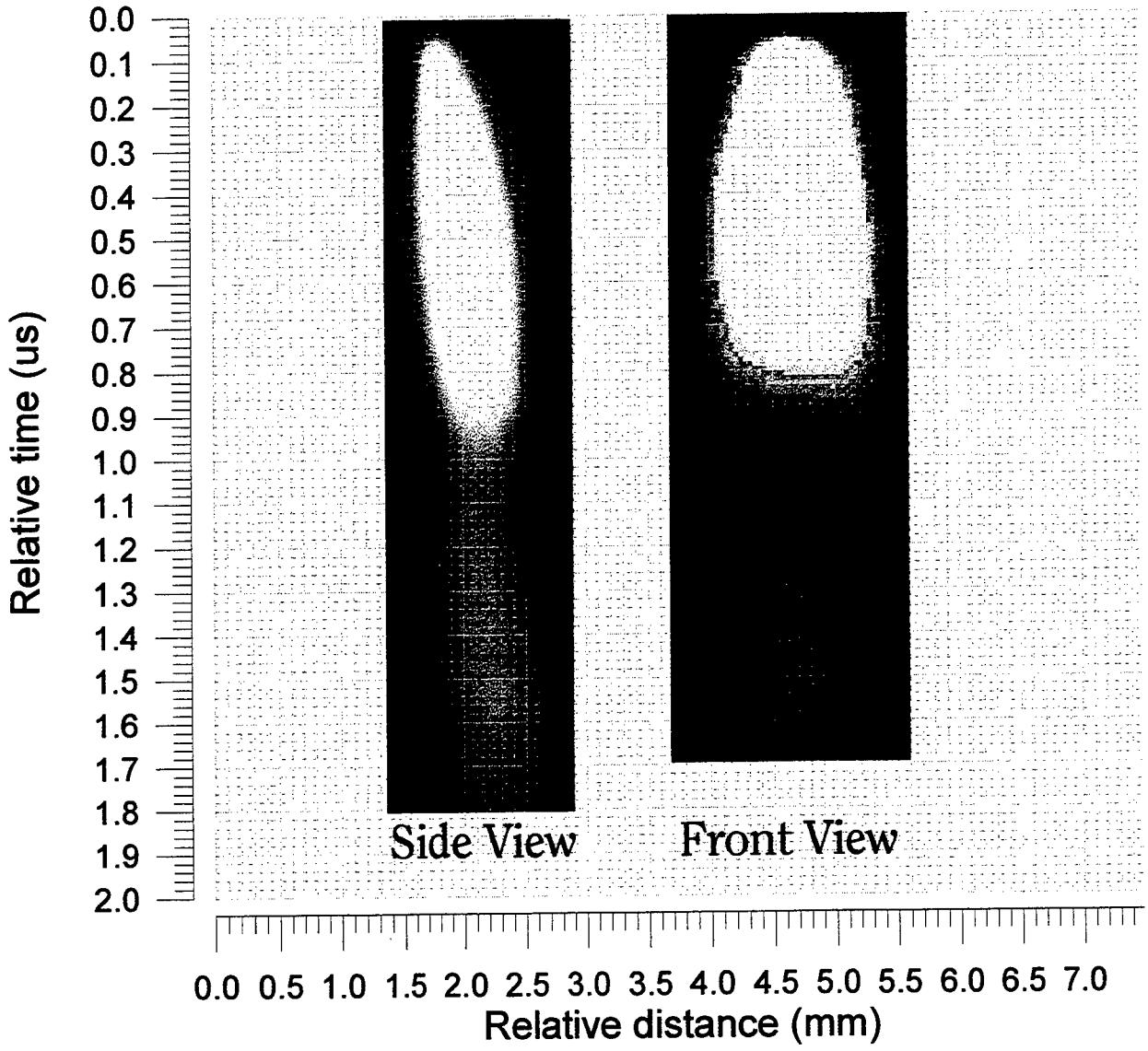
SCB Streak Pictures
Relative time (us)
0.0
0.1
0.2
0.3
0.4
0.5
0.6
0.7
0.8
0.9
1.0
1.1
1.2
1.3
1.4
1.5
1.6
1.7
1.8
1.9
2.0
Side View
Front View
0.0 0.5 1.0 1.5 2.0 2.5 3.0 3.5 4.0 4.5 5.0 5.5 6.0 6.5 7.0
Relative distance (mm)

Figure 1.

SCB : Position of Luminous Perpendicular Expansion Front

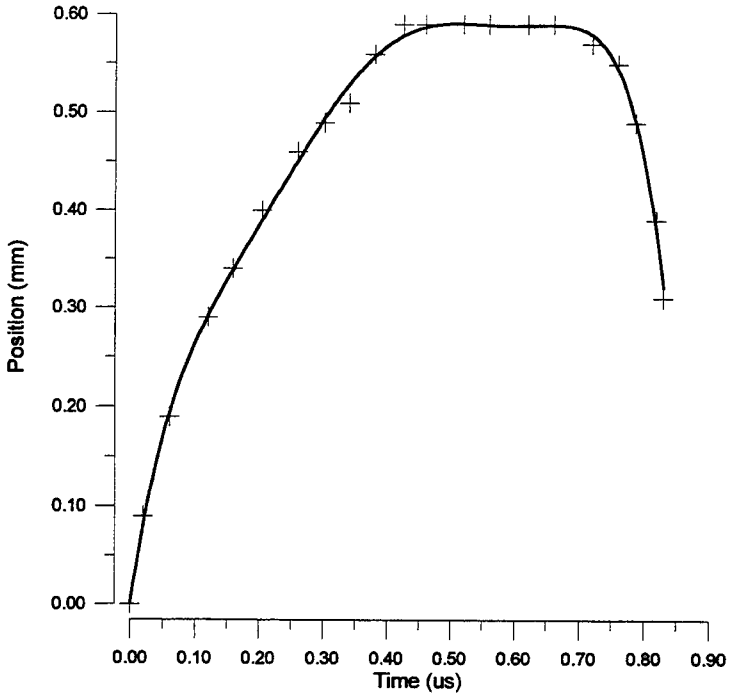

SCB : Position of Luminous Parallel Expansion Front

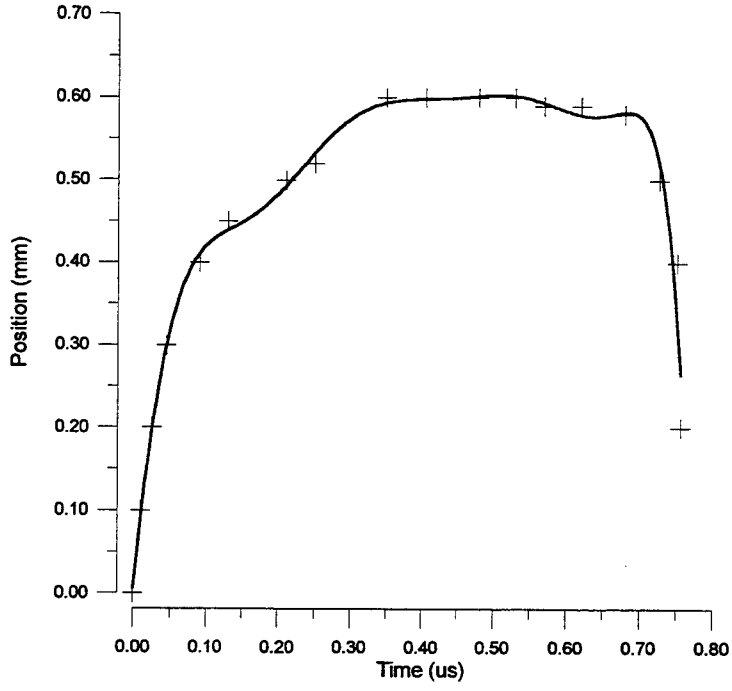

Figure 2.

SCB : Perpendicular Velocity

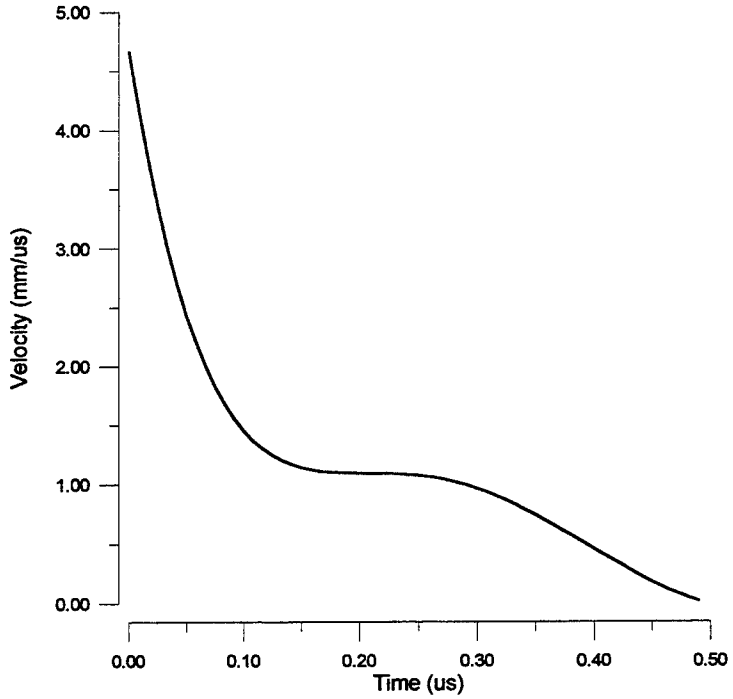

SCB : Parallel Velocity

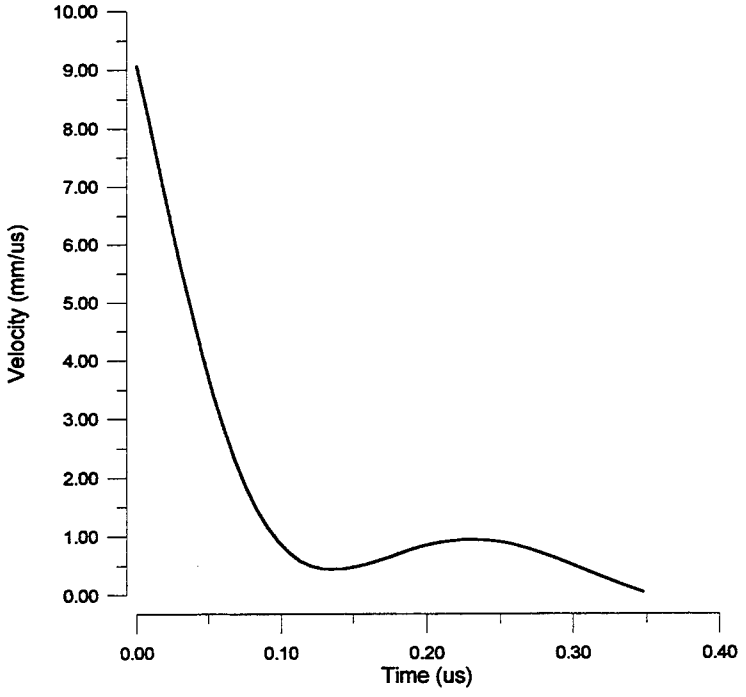

Figure 3.

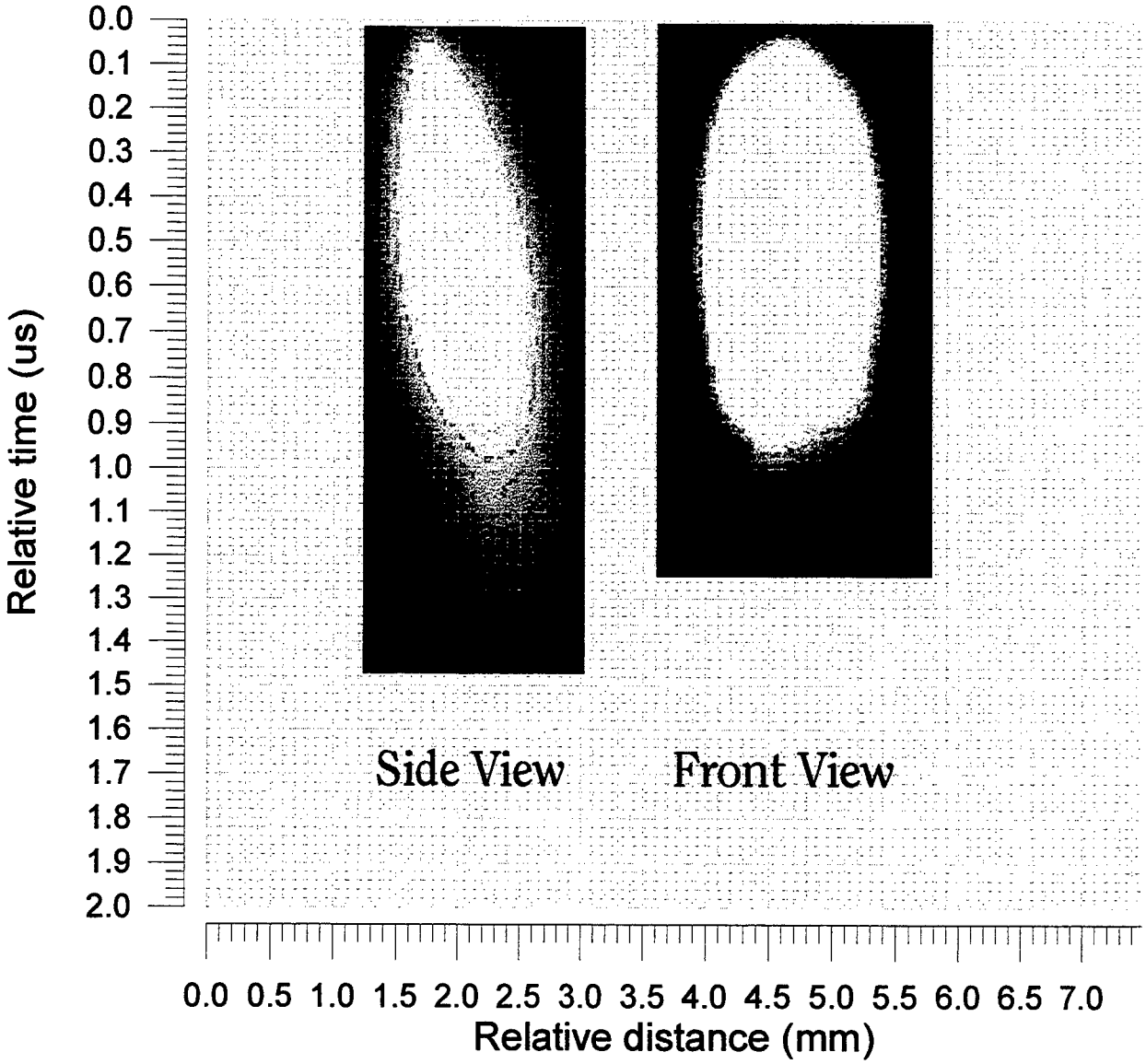
SJI Streak Pictures
Relative time (us)
0.0
0.1
0.2
0.3
0.4
0.5
0.6
0.7
0.8
0.9
1.0
1.1
1.2
1.3
1.4
1.5
1.6
1.7
1.8
1.9
2.0
Side View
Front View
0.0 0.5 1.0 1.5 2.0 2.5 3.0 3.5 4.0 4.5 5.0 5.5 6.0 6.5 7.0
Relative distance (mm)

Figure 4.

SJI : Position of Luminous Perpendicular Expansion Front

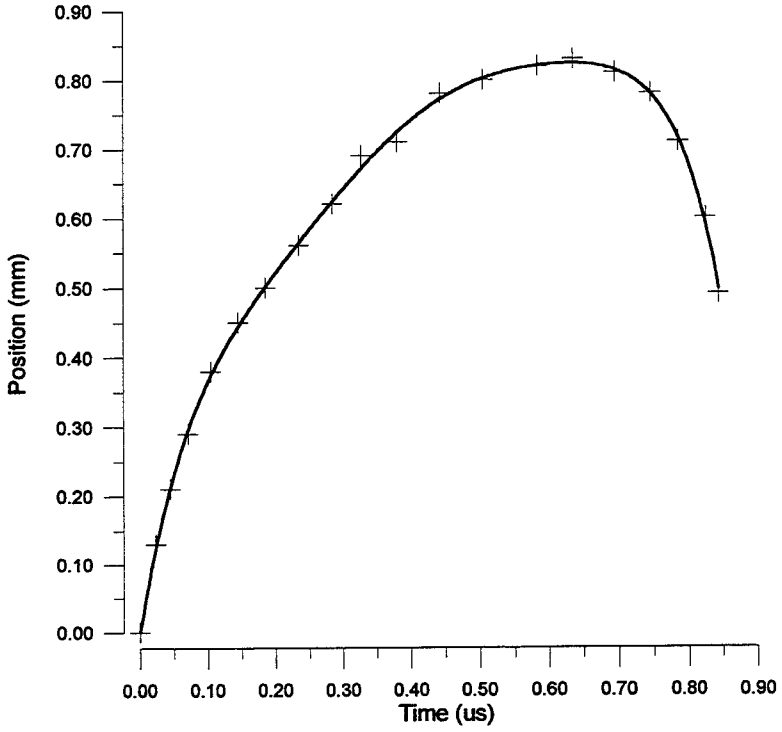

SJI : Position of Luminous Parallel Expansion Front

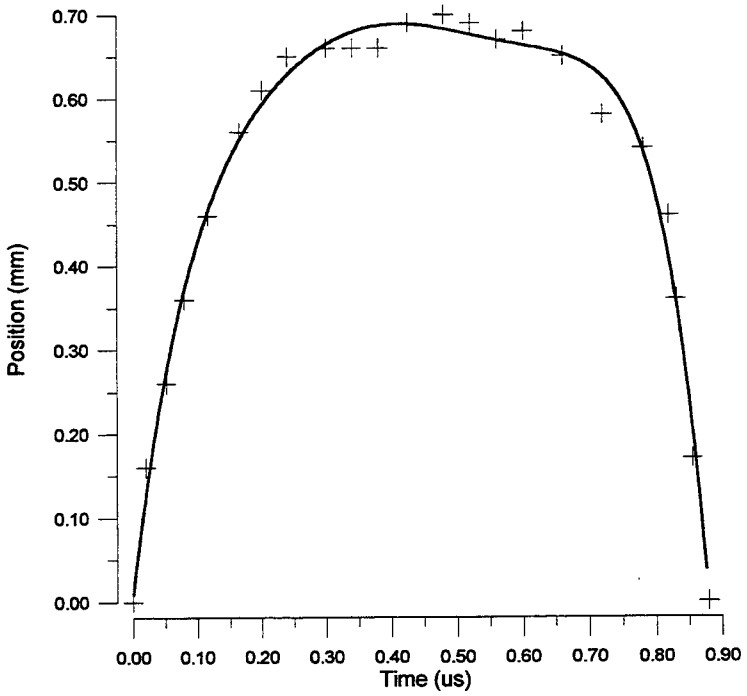

Figure 5.

SJI : Perpendicular Velocity

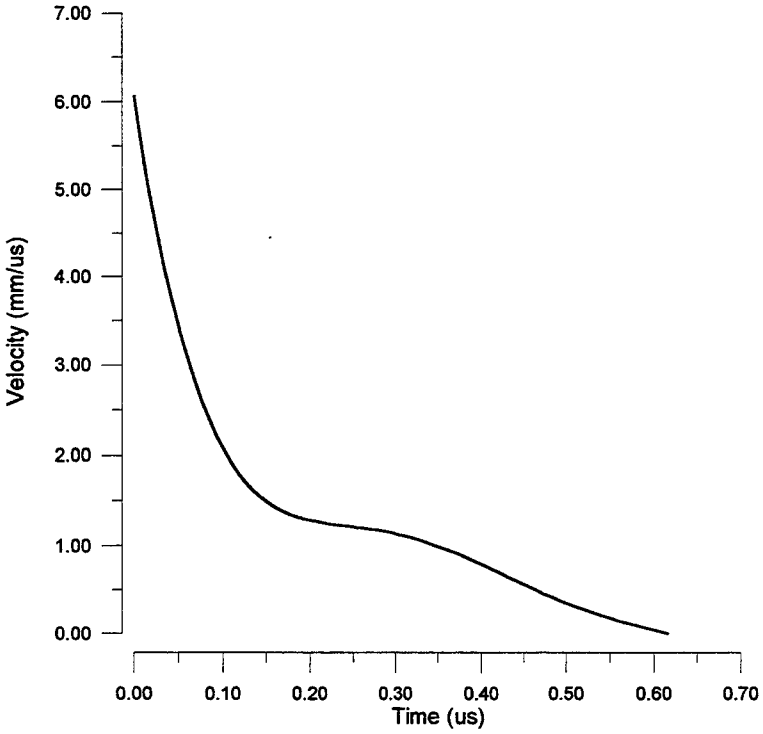

SJI : Parallel Velocity

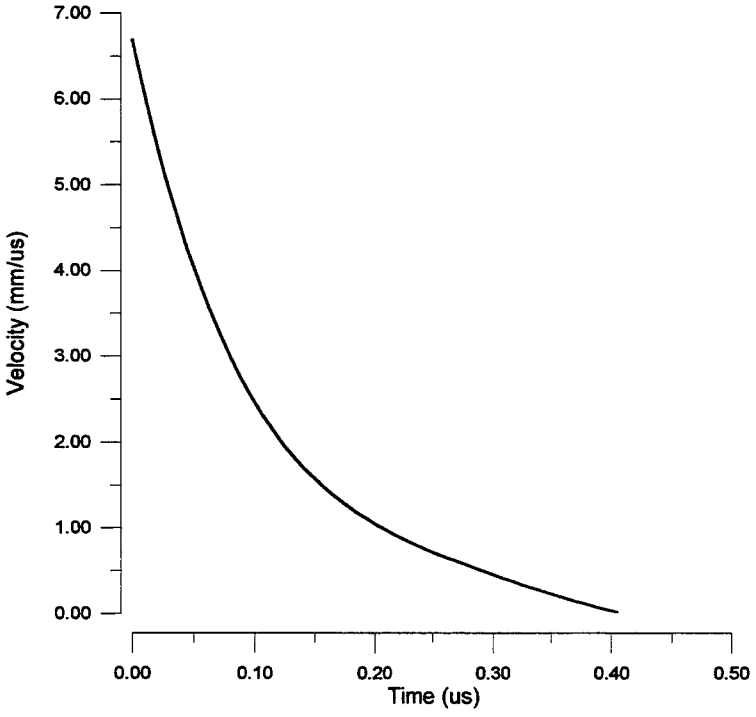

Figure 6.

GRAIN SIZE EFFECTS IN THE DETERMINATION OF X-RAY POLE FIGURES AND ORIENTATION DISTRIBUTION FUNCTIONS

Robert J. De Angelis
Professor
Department of Mechanical Engineering

University of Nebraska-Lincoln
255 Walter Scott Engineering Center
Lincoln, Nebraska 68588-0656

Final Report for:
Summer Faculty Research Program
Wright Laboratory
Eglin Air Force Base, FL 32542

Sponsored by:
Air Force Office of Scientific Research
Bolling Air Force Base, DC

and

Wright Laboratory
Eglin Air Force Base, FL

August 1996

GRAIN SIZE EFFECTS IN THE DETERMINATION OF X-RAY POLE FIGURES AND ORIENTATION DISTRIBUTION FUNCTIONS

by:
Robert J. De Angelis
Department of Mechanical Engineering
University of Nebraska-Lincoln
Lincoln, Nebraska 68588-0656

Abstract

The production of metallic materials with controlled degrees of anisotropy is important because the controlled texture provides significant assurance that subsequent plastic deformation can be performed successfully and reproducibly. To proceed to this condition, the degree of anisotropy must be quantified by the experimental determination of x-ray pole figures and the orientation distribution functions (ODF) calculated from the pole figure data. To insure the intensity data collected is reliable the grain size of the specimen must be suitably small. The objective of this research was to determine the grain size error in measurement of pole figures on the x-ray diffractometer at Eglin AFB.

GRAIN SIZE EFFECTS IN THE DETERMINATION OF X-RAY POLE FIGURES AND ORIENTATION DISTRIBUTION FUNCTIONS

Robert J. De Angelis

Introduction

Since the 1980's the description of material textures or crystal orientations in polycrystalline wires and sheets started to move beyond the x-ray determined pole figures, the norm since the 1930's. The orientation distribution function (ODF) has recently become the method of choice for presenting the description of material textures. This change was driven by the need for a more complete method of describing and quantifying textures in the tailor making of materials and was made possible by the advances in computer speed and capacity. The ODF is computed from pole density data usually represented on pole figure plots which give the density of poles (normals to a crystallographic plane) of a specific {hkl} plane in units of multiples of the random pole density for that particular {hkl} pole. Pole figures are usually

represented on two dimensional polar coordinate plots where the center of the pole figure is the normal to the sheet surface and the direction to the right is parallel to the rolling direction. Therefore it is clear that the pole figure gives the position of the orientation of the specified {hkl} poles relative to and axial system based on the sample; e.g. rolling plane and rolling direction in the case of sheet textures or wire axis direction in the case of wire textures. The ODF gives the statistical distribution of crystallites in a small range of orientations plotted on an angular axial system related to the crystallographic axis. A great advantage to the ODF method of texture representation is that the coefficients of the harmonic equations employed to describe the function provide weighing factors for the determination of the anisotropic elastic and plastic properties of the material. These coefficients also are sensitive to orientation changes that occur during certain solid state processes, such as; phase transformations, plastic deformation and recrystallization.

However there has been little concern over the errors in measurement when determining pole figures. There exist two contributors which determine the statistical relevance of pole figure measurements; the number of grains irradiated in the diffraction experiment and the photon detection. The main objective of this work is to determine the grain size error in pole figure determinations.

Problem Description:

There is a statistical error based on the number of grain diffracting associated with the determination of a texture pole figure. In a fixed geometry x-ray experiment the number of grains in the beam will decrease inversely with the grain size of the diffracting material. The error due to the number of grains diffracting is very similar to the statistical error in counting

the number of pulses arriving at a photon detector. Obviously the determination of pole densities is a statistical process. Initially let us consider the statistical error due to photon counting.

If many measurements of the number of photons, n, arriving at a fixed position in a defined period of time are made. The number n will fluctuate about an average value of counts, $<n>$. For a great enough number of counts ($n > 100$) the distribution of counts observed follow a Gaussian distribution with a standard deviation of $(n)^{1/2}$. Therefore the counting error for one standard deviation is given by $(n)^{1/2}/n$ or $(n)^{-1/2}$. For example: If $<n>$ is 100 counts the one standard deviation error is 0.1 or 10 counts. That is, 68% of the time the counts observed will be between 90 and 110 counts. In practice the statistical counting error is estimated from only one count.

Now turning to the error associated with the number of grains diffracting these same concepts are directly applicable; i.e. the one standard deviation error in measurement is $(N_g)^{-1/2}$, where N_g is the number of grains diffracting at a fixed position. Except for a ideal random sample the value of N_g varies depending on measurement position due to type and strength of the texture existing in the material. The most direct method to account for these variations and evaluate the grain number error is by considering the reciprocal lattice geometry of the powder diffraction process.

Consider the total irradiated volume of the specimen having a total of N randomly oriented crystallites with an average volume of dv. Consider a set of (hkl) planes oriented for diffraction. The reciprocal lattice is a sphere of radius r, where the magnitude of r is $1/d_{(hkl)}$. The sphere is the locus of all normals to the (hkl) planes from all the crystallites in the

irradiated volume. The Ewald sphere intersects the reciprocal lattice sphere along a circular line of radius (r cos ($\pi/2$ - θ), where θ is the perfect Bragg angle for the planes (hkl) (see Fig. 1). Very few normals, if any, that fall on the line will produce crystallites oriented for Bragg diffraction. In a horizontal diffraction experiment the incident beam has a vertical divergence of α. This divergence increases the contact area of the Ewald sphere and the reciprocal lattice sphere from a line to a band of width $d\alpha$, as shown in Fig. 2. This immensely increases the number of crystallites diffracting (i.e. having normals in the band on the reciprocal lattice sphere). The fraction of crystallites diffracting at any position is given by the ratio of the area of the band on the reciprocal lattice sphere to area of the total sphere; or:

$$\frac{N_g}{N} = \frac{2\pi r^2 \cos(\theta - \alpha)}{4\pi r^2} d\alpha = \frac{1}{2}\cos\theta d\alpha \qquad (1)$$

Introducing the multiplicity, m, of the (hkl) plane gives:

$$\frac{N_g}{N} = \frac{m}{2}\cos\theta d\alpha \qquad (2)$$

In most metallic materials the diffraction process takes place in a specimen depth of dimension much less than the grain size. Therefore it is very reasonable to employ an area rather than a volume consideration in arriving at the number of grains available for diffraction. If a Pisson-Voronoi mosaic basis is assumed for describing the grain size

distribution with a mean diameter d, then the average area, A_d, of a spherical grain exposed to the beam on a flat surface is:

$$A_d = d^2/3.0988 \tag{3}$$

Now:

$$N = A_{l_o}/A_d \tag{4}$$

where A_{l_o}, is the area of the specimen covered by the incident beam. Then the number of crystallites diffracting is given by:

$$N_g = \frac{mA_{l_o} \cos\theta \, d\alpha}{A_d} \tag{5}$$

The diffraction spots from these grains are spread over a cone of diffraction with an apex angle of 4θ and having a length of R, the distance from the specimen to the detector. The perimeter of the circle containing these diffraction spots is $2\pi R \sin 2\theta$ at the position of the detector.

The fraction of the diffraction cone intercepted by the detector of length ℓ is:

$$\ell/4\pi R\sin\theta \tag{6}$$

Giving the number of grains diffracting at a given position of:

$$N_g' = \frac{m\ell A_{I_o} d\alpha}{4\pi A_d R \sin\theta} \qquad (7)$$

Results:

To determine the number of grains diffracting in a typical pole figure determination experiment on a Siemens 5000 diffractometer, the following values for the quantities in Eq(7) were employed:

$$d\alpha = \frac{\text{height of } I_o \text{ at the specimen}}{R} = \frac{0.1\ cm}{30\ cm} = .003$$

$\theta = 22.8°$

m = multiplicity = 12

ℓ = 1 cm

$A_{I_o} = 1\ cm \times 0.2\ cm = 0.2\ cm^2$

$A_d = d^2/3.0988$

R = 30 cm

Inserting these quantities gives:

$$N_g' = \frac{1.69 \times 10^{-4}\ cm}{d^2} = \frac{1.69 \times 10^{-4} (\mu m)^2}{d^2} \qquad (8)$$

This result is shown graphically in Fig. 3 for grain sizes up to 100 microns. As can be determined from Fig. 3 a grain size of 50 μm has a statistical error of 0.39, meaning there is a 68% probability that any measurement from this specimen where; N is 24.8 x 10^3 grains, N_g is 914 grains and N_g' is 6.25 grains, will be from grains ranging in number from 8.95 to 3.81. Another way to look at this is, this specimen could have pole densities of between 1.39 to 0.69 times random.

REFERENCES:

H. J. Bunge, Texture Analysis in Materials Science, Butterworth, London 1982

Siemens Analytical X-ray Instruments, Inc., 6300 Enterprise Lane, Madison, WI 83719

Leonid V. Azaroff, Elements of X-ray Crystallography, McGraw Hill Book Co., New York, 1968

FIGURE CAPTIONS:

Figure 1. X-ray Powder Diffraction Geometry in Reciprocal Space.

Figure 2. The Area Sweep Out on the Reciprocal Lattice Sphere Due to Incident Beam Divergence.

Figure 3. One Standard Deviation Error in Measurement as a Function of Grian Size.

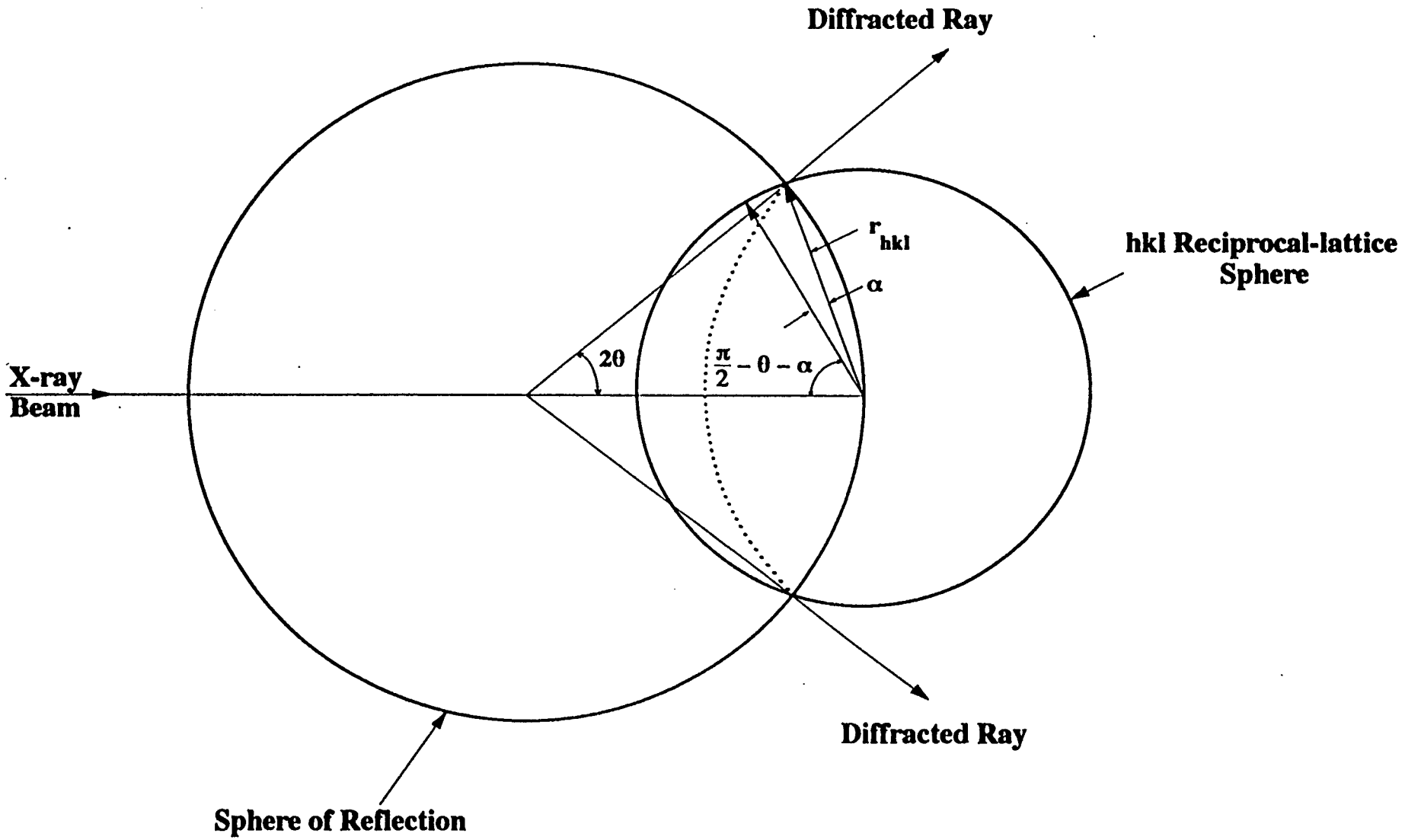
Diffracted Ray
r_{hkl}
hkl Reciprocal-lattice Sphere
α
X-ray Beam
2θ
$\frac{\pi}{2} - \theta - \alpha$
Diffracted Ray
Sphere of Reflection

Figure 1

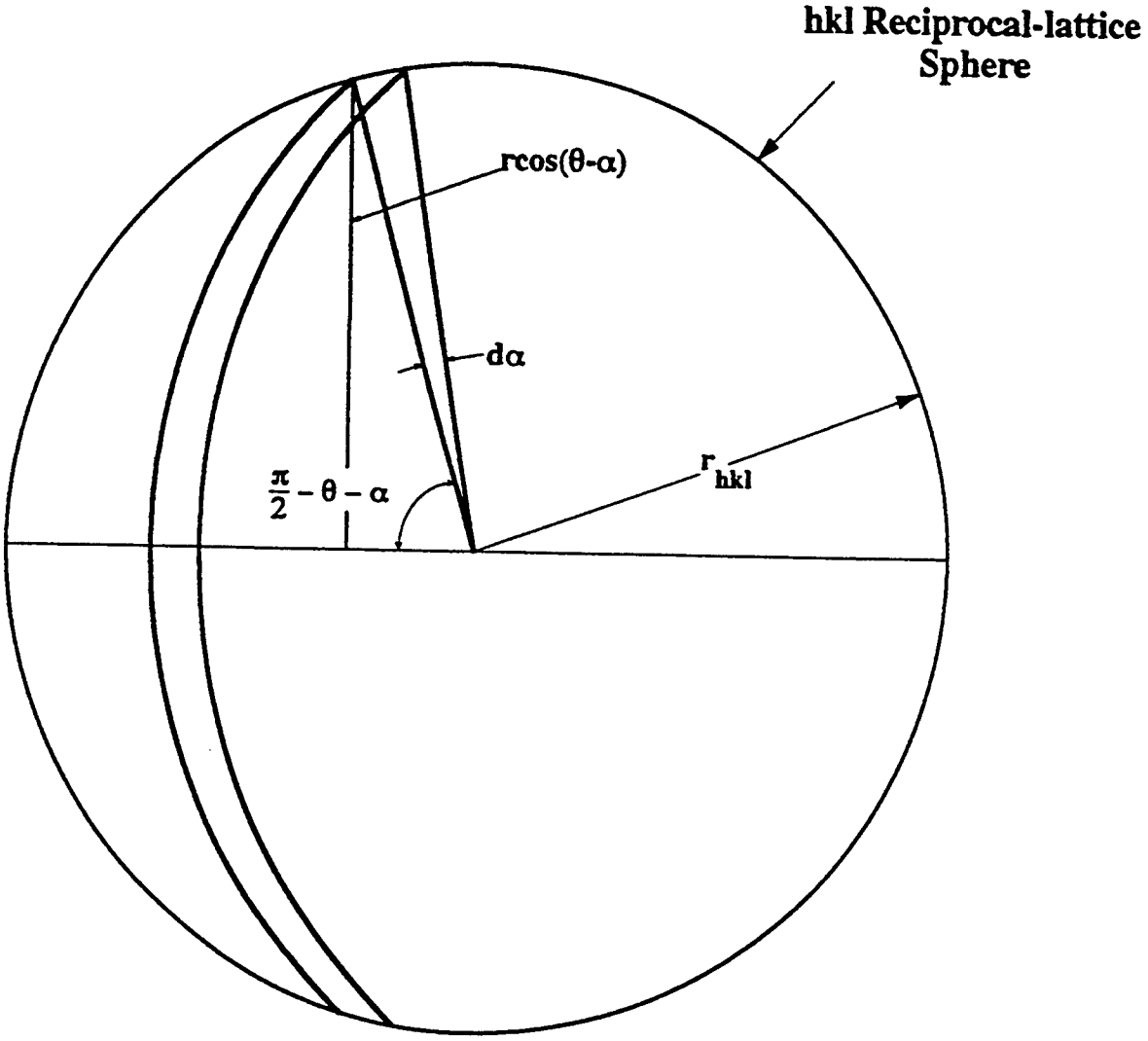
hkl Reciprocal-lattice Sphere
rcos(θ-α)
dα
$\frac{\pi}{2} - \theta - \alpha$
r_{hkl}

Figure 2

GRAIN SIZE ERROR

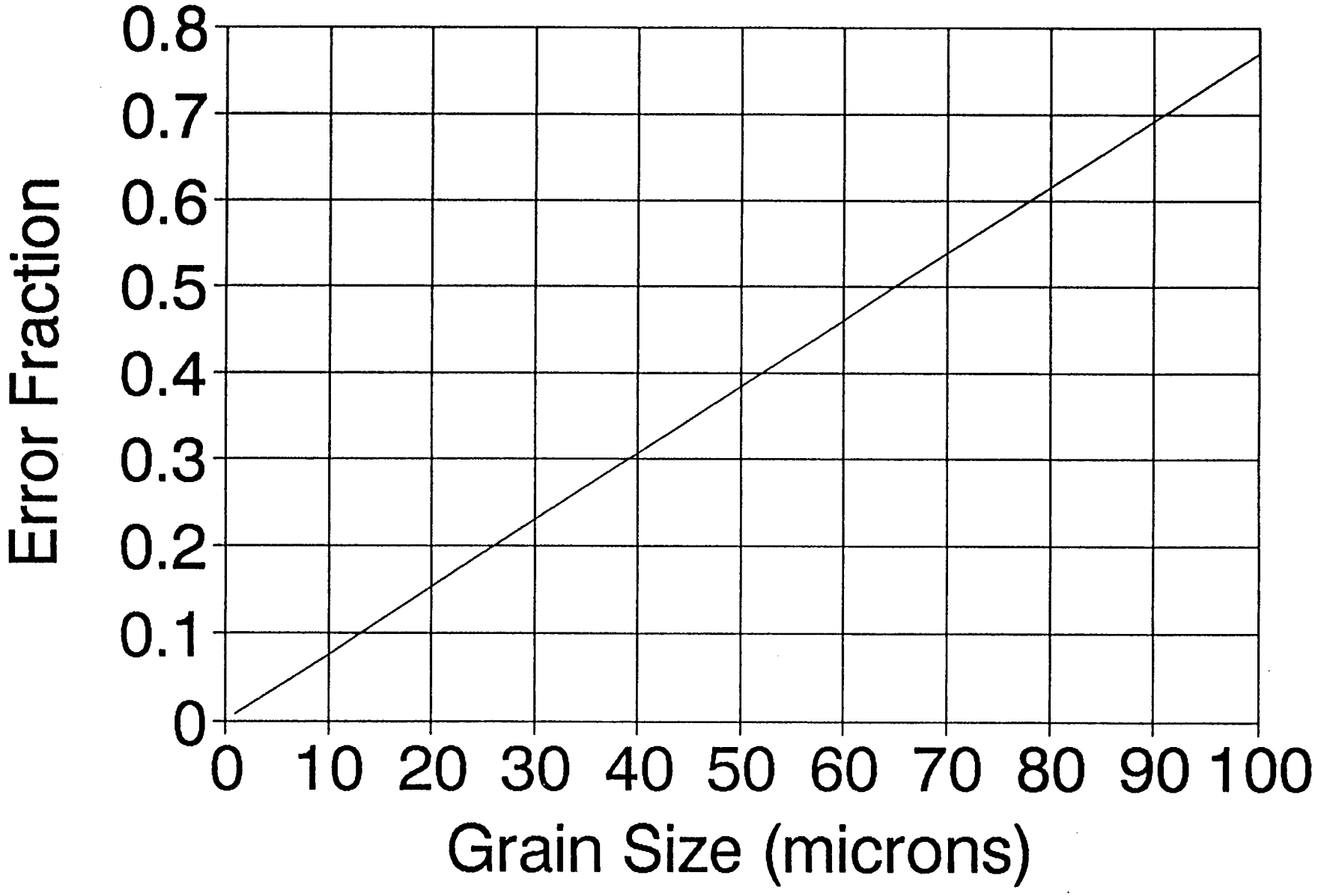

Investigation of Photoluminescence Intensity Saturation, Decay, and Nonlinear Optical Devices in Semiconductor Structures

Yujie J. Ding
Assistant Professor
Department of Physics and Astronomy

Bowling Green State University
Bowling Green, OH 43403

Final Report for:
Summer Research Program
Wright Laboratory

Sponsored by:
Air Force Office of Scientific Research
Bolling Air Force Base, Washington DC

and

Wright Laboratory

October 1996

INVESTIGATION OF PHOTOLUMINESCENCE INTENSITY SATURATION AND DECAY, AND NONLINEAR OPTICAL DEVICES IN SEMICONDUCTOR STRUCTURES

Yujie J. Ding
Assistant Professor
Department of Physics and Astronomy
Bowling Green State University

Abstract

We have observed saturation of photoluminescence peak at low pump intensities in growth-interrupted asymmetric-coupled quantum-well structure. We believe the saturation is due to filling of the exciton states localized at the interface islands. We have observed increase of the photoluminescence decay time as pump intensity increases in the same structure.

Based on our design, a new multilayer structure was grown for demonstrating transversely-pumped counter-propagating optical parametric oscillation and amplification, and achieving surface-emitting sum-frequency generation in a vertical cavity.

We have attempted to mode-lock Ti:Sapphire laser pumped by an Argon laser. We conclude that stability of the Argon laser is crucial for achieving stable mode-locking.

INVESTIGATION OF PHOTOLUMINESCENCE INTENSITY SATURATION AND DECAY, AND NONLINEAR OPTICAL DEVICES IN SEMICONDUCTOR STRUCTURES

Yujie J. Ding

1. Introduction

Recently, it has been shown that by interrupting sample growth at every interface, one can obtain multiple photoluminescence (PL) peaks with separate emission energies that correspond to the excitonic emissions at interface islands of different sizes [1-4]. Because of the formation of these interface islands, the well widths at these islands generally differ by one monolayer with respect to the designed width in high quality samples [5]. However, the area ratios among all these islands of different well widths are random, which cannot be controlled in growth process. (Without the growth interruption, the recombination of the carriers in the wells with different widths results in the inhomogeneous broadening in the PL spectrum.) At low temperatures, all the carriers generated by the pump will be eventually relaxed down to the lowest energy levels and localized in the islands, resulting in very large carrier densities. If the total area of the islands is small, it would be possible to completely fill exciton states in these islands at relatively low intensities that may manifest as the saturation of the PL peaks. It is worth noting that in growth-interrupted samples, Band-filling effects are spatially-localized effects, due to additional confinement along the interface, similar to situation in quantum dots (i.e. all the islands are spatially isolated).

Recently, surface-emitting green light was obtained [6] by frequency-doubling infrared laser beam (1.06 μm) in the waveguide based on periodically modulated second-order susceptibility in alternating $Al_xGa_{1-x}As$ and $Al_yGa_{1-y}As$ ($x \neq y$) layers. When the multilayers are sandwiched between two quarter-wave stacks, large increase in the conversion efficiency was observed [7] though quasi phase-matching was not established. Following Ref. [8], second-order susceptibility of asymmetric-coupled quantum-well (QW) domain structures were measured in the surface-emitting geometry [9]. The maximum conversion efficiency so far is still less than 1%/W. Recently, we proposed a novel practical scheme for implementation of the cascaded nonlinearity using surface-emitting second-harmonic generation (SHG) in the Fabry-Perot cavity. We have shown that such scheme can be efficiently used for optical power limiting and optical phase conjugation at low input power [10]. Most recently [11], we propose to achieve nearly 100% conversion efficiency of SHG for the low input power, by combining quasi phase-matching and cavity enhancements in semiconductor multilayers or

asymmetric QW domain structures. Thus, our investigation leads to the implementation of *practical* frequency doublers which can cover the range from blue to infrared. More importantly, we proposed to implement tunable optical parametric oscillators (OPOs) and amplifiers [12] based on a novel configuration. Frequency doublers, optical parametric oscillators and amplifiers, and the nonlinear optical devices based on the cascaded second-order nonlinearities have potential applications in generation of blue light, generation and amplification of tunable mid-IR light, optical communication, ultrafast detection, sensor protection, real-time holography, or optical lithography.

2. Discussion of Problem

a. Saturation of photoluminescence peak

Previously, we observed [13] saturation of photoluminescence peaks. We believe that it is due to band-filling effects at the interface islands as a result of the growth interruption. The intensities required to observe the saturation reflect the total area of the interface islands, thus the interface roughness.

b. Photoluminescence decay

To determine the characteristic carrier density for completely filling the interface islands, one needs to measure the carrier recombination times. Furthermore, the dependence of the recombination time on the excitation intensity may provide information about nature of the recombination processes.

The sample for studying Sections a and b above was grown by MBE on a semi-insulating GaAs substrate at the temperature of 600 C in collaboration with Naval Research Labs. The epitaxial layers consist of 20 periods, each of which is composed of two narrow asymmetric coupled GaAs quantum wells with the designed thicknesses of 50 Å and 65Å, coupled by 35Å-$Al_{0.35}Ga_{0.65}As$ barriers, see Fig. 1. The thicknesses of the barriers between the adjacent periods are 150 Å. During the sample growth there is an interruption for 60 seconds at every interface. Because of this growth interruption, interface islands with sizes larger than the average exciton radius are formed, allowing excitons being spatially-localized within these islands with separate optical transition energies from that of free-excitons [1]. As a result, in each designed well the absorption and/or emission peaks are separated from each other corresponding to one monolayer thickness (2.8 Å) difference.

c. Growth of a new structure

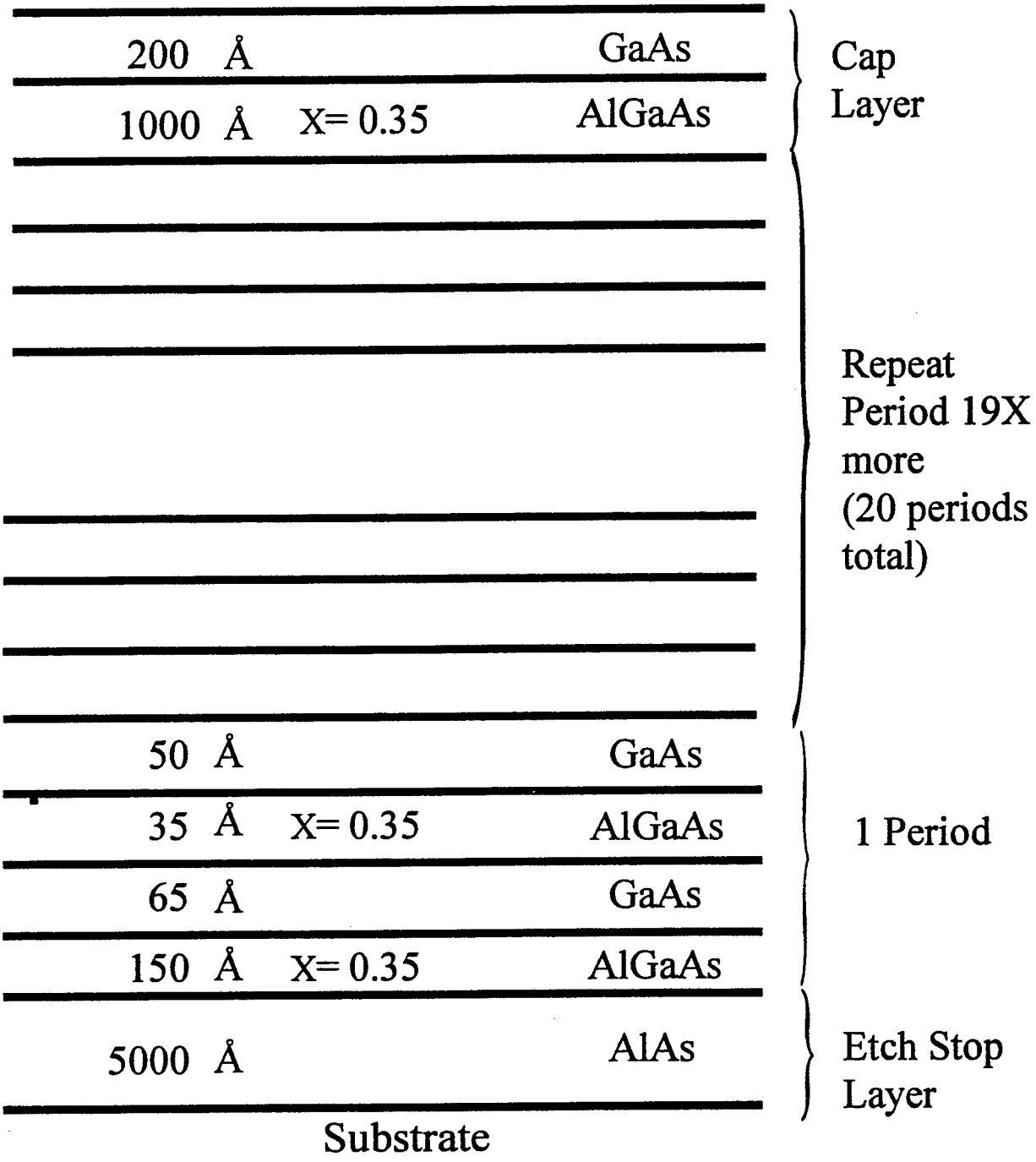
200 Å GaAs
1000 Å X= 0.35 AlGaAs
Cap Layer
Repeat Period 19X more (20 periods total)
50 Å GaAs
35 Å X= 0.35 AlGaAs
65 Å GaAs
150 Å X= 0.35 AlGaAs
1 Period
5000 Å AlAs
Etch Stop Layer
Substrate

Fig. 1

Previously, we proposed to use semiconductor multilayers to generate surface-emitting second-harmonic radiation [11] to implement transversely-pumped counter-propagating OPOs [11]. Recently, we designed the first structure. The epitaxial layers consist of two Bragg reflectors and alternating layers for achieving quasi-phase matching.

d. Attempt to mode-lock Ti:Sapphire laser

To characterize semiconductor lasers in time-resolved domain, an ultrafast laser source (i.e. mode-locked Ti:Sapphire laser) is required to excite the carriers to the high-energy sub-bands. The relaxation processes can be then probed via different techniques.

3. Methodology

a. Photoluminescence spectrum

Our asymmetric-coupled quantum-well structure is pumped by a CW Argon laser at the wavelength of 5145 Å. The photoluminescence was collected by a monochromator via a lens.

b. Photoluminescence decay

For the measurement of the PL decay, we used a mode-locked Ar^+ laser as our excitation pulse with the pulse duration of 150 ps and output wavelength of 5145 Å. The temporal traces of the PL signal were taken via a streak camera with a time resolution of 20 ps. Fig. 2 shows our schematic set-up.

c. Design of a new structure

Our optimized design of the multilayer structure is based on our vigorous consideration of surface-emitting frequency doublers [Fig. 3(a)] and transversely-pumped counter-propagating OPOs and OPAs [Fig. 3(b)], see Refs. [11,12].

d. Attempt to mode-lock Ti:Sapphire laser

The schematic set-up for Argon-laser-pumped mode-locked Ti:Sapphire laser and the Ti:Sapphire laser cavity are shown in Fig. 4. We have followed the manual for Ti:Sapphire provided by Clark-MXR Inc. The mode structure and stability were determined by eyes after expanding the laser beam. The output laser pulse from mode-locked Ti:Sapphire laser can be sent to Coumarin 460 for generating two-photon fluorescence.

4. Results

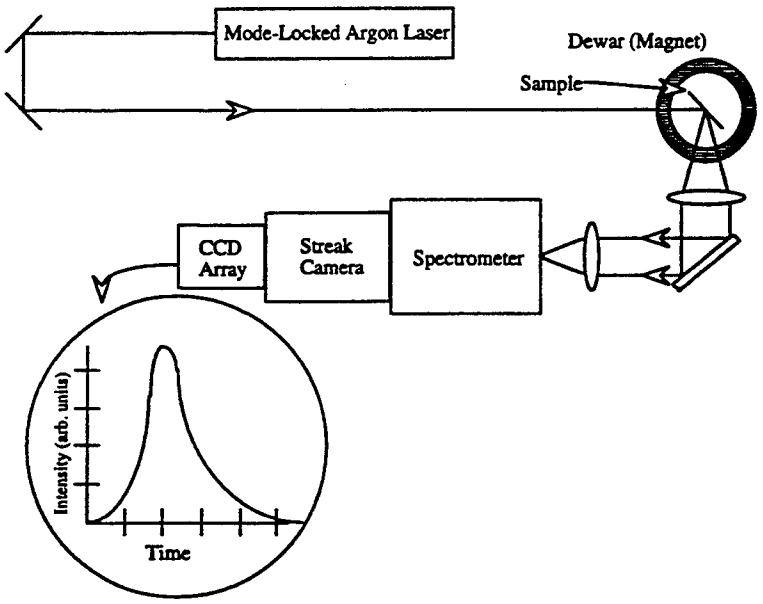
Mode-Locked Argon Laser
Dewar (Magnet)
Sample
CCD Array
Streak Camera
Spectrometer
Intensity (arb. units)
Time

Figure 2

(a)

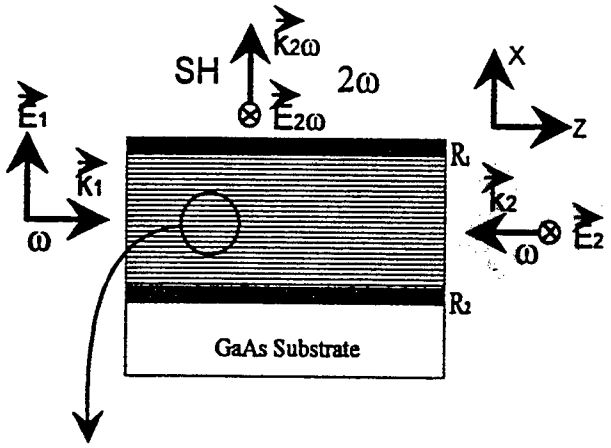

(b)

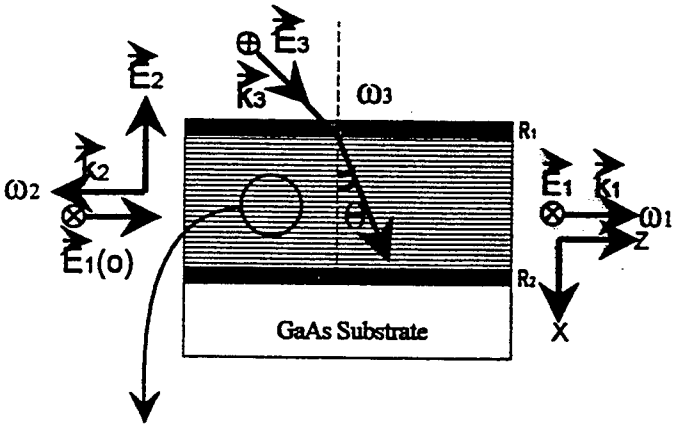

500 Å	GaAs	
550 Å	$Al_{0.5}Ga_{0.5}As$	x 15
620 Å	AlAs	
1080Å	$Al_{0.4}Ga_{0.6}As$	
1240Å	AlAs	x 4
550 Å	$Al_{0.5}Ga_{0.5}As$	
620 Å	AlAs	x 15

(100) GaAs Substrate

(c)

Figure 3

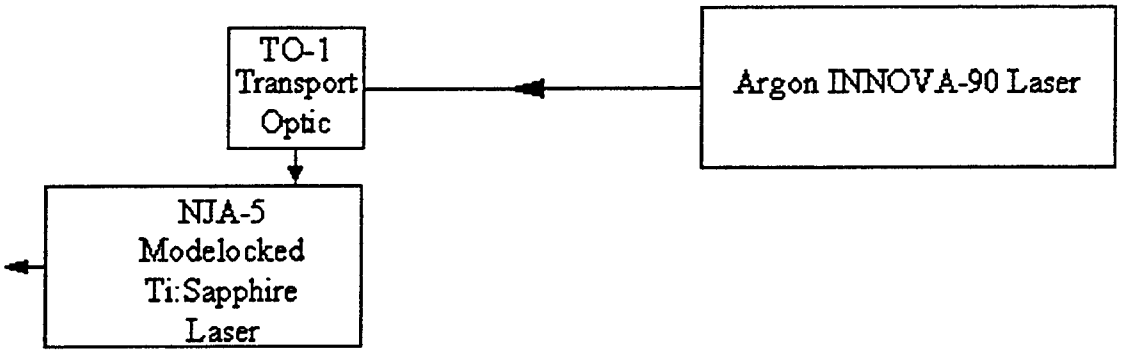

(a)

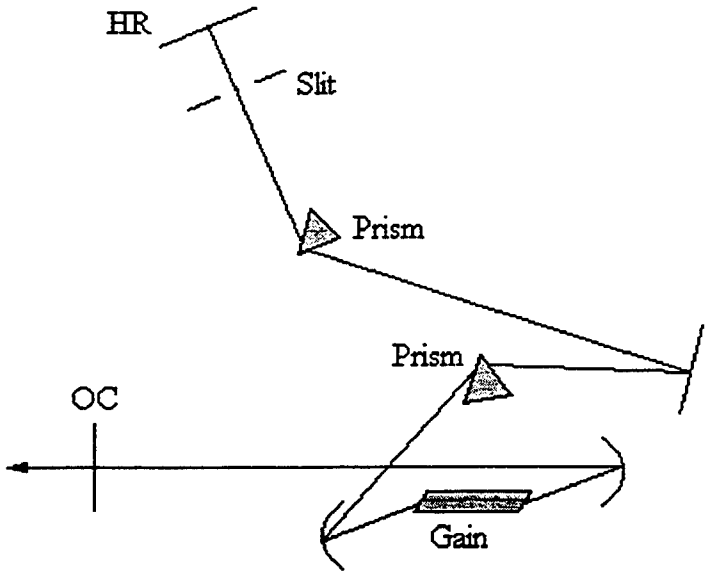

(b) Ti:Sapphire Laser Cavity

Figure 4

a. Saturation of photoluminescence peak

The PL spectra for several pump intensities are shown in Fig. 5. At laser intensity of 9.7 mW/cm^2 there are two emission peaks: the one on the long wavelength side (~7780 Å) corresponds to the emission of excitons at the interface islands while the other one (~7773 Å) corresponds to the free excitons. When we change the laser intensity from 9.7 mW/cm^2 to 1.4 W/cm^2 at 4 K, we can see that the emission peak for the localized excitons loses its relative strength.

Due to growth interruption, a single PL peak breaks into two because of the formation of interface islands with the size larger than the exciton radius. At low temperatures, all the carriers generated by the pump laser will be eventually relaxed down to the lowest energy levels and localized in the islands, resulting in large carrier densities. If the total area of the islands is small, it would be possible to completely fill exciton states in these islands at relatively low intensities, which manifests as the saturation of the PL peaks. This type of the band-filling effect only occurs at the spatially-localized islands. The laser intensity required to almost completely fill the localized exciton states is more than two orders of magnitude lower than that obtained before [13].

b. Photoluminescence decay

We have made the time-resolved PL measurements in our sample. Fig. 6 shows the typical temporal PL traces detected at the center wavelength of e_1hh_1 emission peak (the excitonic emission peak) as a result of the carrier recombination at the interface islands. At the low excitation intensity (207 W/cm^2), the PL signal at the e_1hh_1 (II) emission peak has a decay time of about 269 ps. As the intensity increases, the decay time increases. As shown in Fig. 6, when the laser intensity is 414, 621, and 828 W/cm^2, the decay time is about 326, 537, and 666 ps.

In the quasi-CW regime, the density of excitons can be determined as

$$N_{ex} = \tau \frac{I_{laser}\alpha}{\hbar\omega_{laser}} \qquad (1)$$

where I_{laser} is the laser intensity, α is the absorption coefficient, and $\hbar\omega_{laser}$ is the energy of a single photon. The intensity required to completely fill the e_1hh_1 exciton states is about 1.4 W/cm^2. Assuming $\alpha \approx 10000\,cm^{-1}$ at the pumping wavelength in our experiments, the exciton density is then estimated to be $9.75\times10^{12}\,cm^{-3}$. The corresponding area density is $1.46\times10^{7}\,cm^{-2}$. This carrier density is more than two orders of magnitude lower than that in Ref. [13].

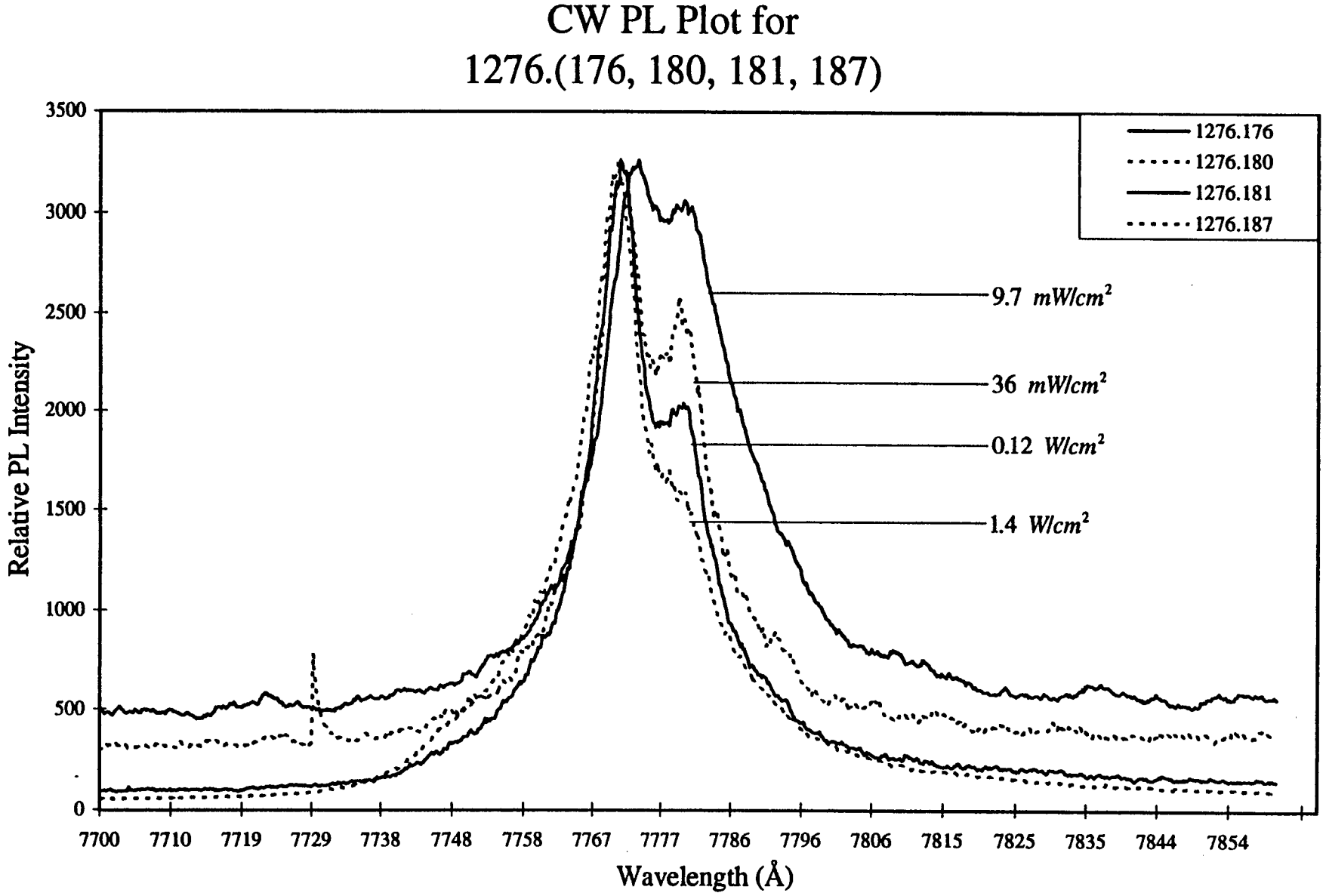
CW PL Plot for
1276.(176, 180, 181, 187)
Relative PL Intensity
Wavelength (Å)
1276.176
1276.180
1276.181
1276.187
9.7 mW/cm²
36 mW/cm²
0.12 W/cm²
1.4 W/cm²
3500
3000
2500
2000
1500
1000
500
0
7700
7710
7719
7729
7738
7748
7758
7767
7777
7786
7796
7806
7815
7825
7835
7844
7854

Figure 5

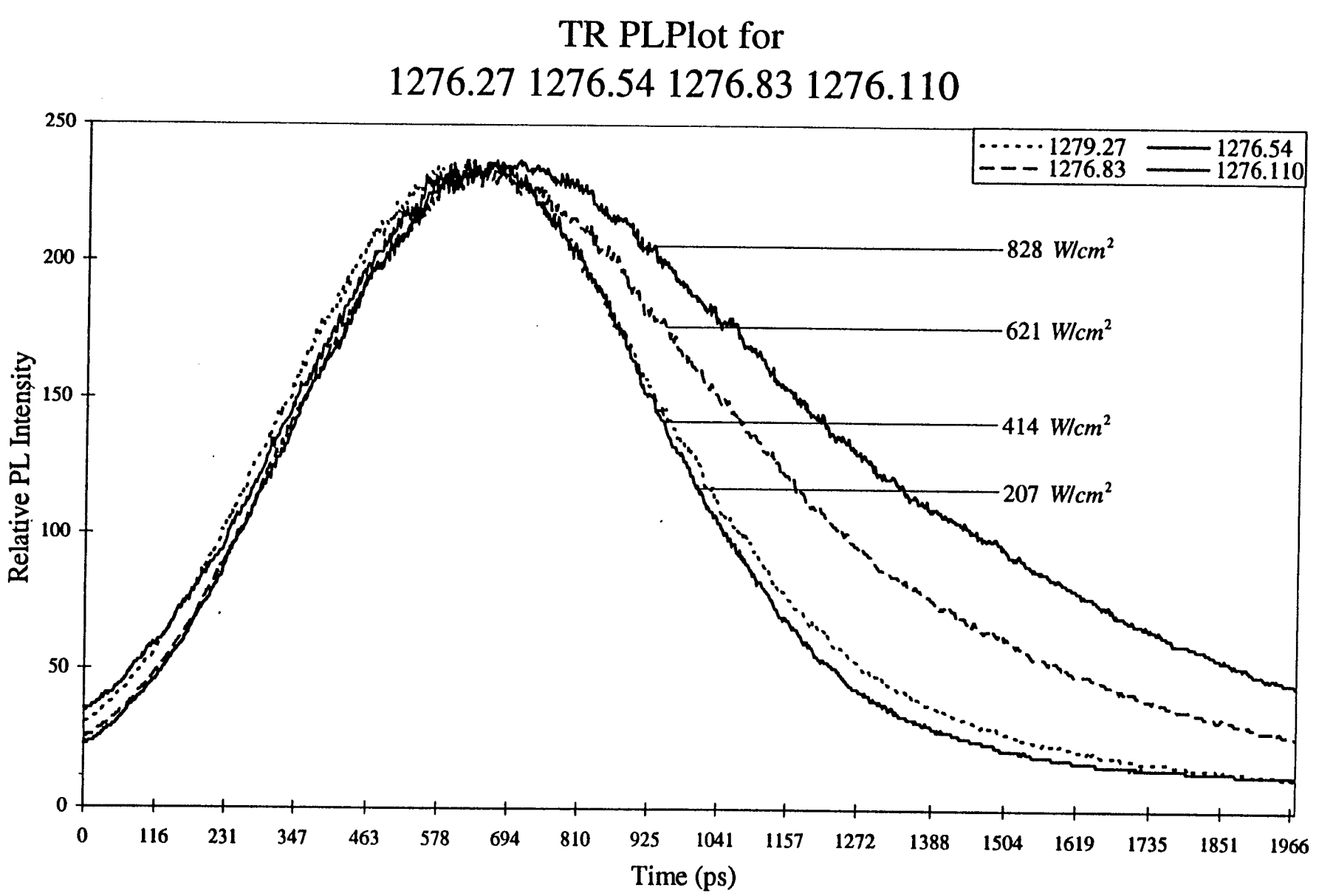
TR PLPlot for
1276.27 1276.54 1276.83 1276.110
1279.27
1276.54
1276.83
1276.110
828 W/cm²
621 W/cm²
414 W/cm²
207 W/cm²
Relative PL Intensity
Time (ps)
0
50
100
150
200
250
0
116
231
347
463
578
694
810
925
1041
1157
1272
1388
1504
1619
1735
1851
1966

Figure 6

c. Growth of a multilayer structure

Based on Refs. [11,12], we had already designed an optimized structure [see Fig. 3(c)]. We had grown this structure in collaboration with Drs. J. L. Loehr and J. Ehret at Wright Labs. We will test the performance of this structure as an efficient frequency doubler and optical parametric oscillator and amplifier at Bowling Green State University. The pump, input and output wavelengths are designed to be 1.06 μm, 1.58 μm, and 3.23 μm. By changing the incident angle, one can tune the output wavelengths [12].

d. Attempt to mode-lock Ti:Sapphire laser

The Ti:Sapphire laser is pumped by a re-furnished Argon laser (Coherent Innova 90), see Fig. 4. For 4-watt pump power of a multi-line Argon laser, conversion efficiency as high as 20% was achieved in CW regime. We had tried our best to mode-lock Ti:Sapphire laser. We observed two-photon fluorescence in Coumarin 460, however, was not able to stablize the mode-locked laser output. We believe that mode structure and pointing stability could be the problems for mode-locking the Ti:Sapphire laser. When there is no aperture for the Argon laser, high-order modes other than TEM_{00} exist in the Argon output beam profile. In addition, we have crudely estimated the pointing stability as ~ 100 μrad, which is an order of magnitude larger than that required for stable mode-locking.

5. Conclusion

We have observed saturation of photoluminescence peak. We have measured time-resolved photoluminescence decay in growth-interrupted asymmetric-coupled quantum wells. We have subsequently determined decay times and characteristic carrier densities for the observed photoluminescence intensity saturation. We have grown a multilayer structure that can be used to implement an optical parametric oscillator and amplifier and frequency doubler in a novel configuration. Finally, we have tried to mode-lock Ti:Sapphire laser and summarized potential problems causing unstable mode-locked output.

Two journal papers based on our results will be submitted for publication.

6. Acknowledgement

We are indebted to Drs. J. P. Loehr, R. E. Sherriff, J. Ehret, J. Hoelscher, and D. C. Reynolds for their expertise in the areas above, that had made it possible for us to work on four different projects during ten-week period.

7. References

[1] D. Bimberg, D. Mars, J. N. Miller, R. Bauer, O. Oertel, and J. Christen, Supperlatt. Microstruc. 3, 79 (1987).

[2] M. Kohl, D. Heitmann, S. Tarucha, K. Leo, and K. Ploog, Phys. Rev. B39, 7736 (1989).

[3] D. C. Reynolds, K. K. Bajaj, C. W. Litton, P. W. Yu, J. Singh, W. T. Masselink, R. Fischer, and H. Morkoc, Appl. Phys. Lett. 46, 51 (1985).

[4] K. Fujiwara, K. Kanamoto, and N. Tsukada, Phys. Rev. B40, 9698 (1989).

[5] B. Devcaud, A. Chomctte, N. Roy, B. Scrmagc, and D. S. Katzer, Sur. Sci. 267, 199 (1992); D. Gammon, B. V. Shanabrook, and D. S. Katzer, Appl. Phys. Lett. 57, 2710 (1990).

[6] R. Normandin, R. L. Williams, and F. Chatenoud, Electr. Lett. 26, 2088 (1990); R. Normandin, H. Dai, S. Janz, A. Delage, J. Brown, and F. Chatenoud, Appl. Phys. Lett. 62, 118 (1993); D. Vakhshoori, R. J. Fischer, M. Hong, D. L. Sivco, G. J. Zydzik, G. N. S. Chu, and A. Y. Cho, Appl. Phys. Lett. 59, 896 (1991).

[7] R. Lodenkamper, M. L. Bortz, M. M. Fejer, K. Bacher, and J. S. Harris, Jr., Opt. lett. 18, 1798 (1993).

[8] J. Khurgin, Appl. Phys. Lett. 21, 2100 (1987); Phys. Rev. B38, 4056 (1988); J. Appl. Phys. 64, 5026 (1988); J. Opt. Soc. Amer. B 6, 1673 (1989).

[9] S. Janz, F. Chatenoud, and R. Normandin, Opt. Lett. 19, 622 (1994).

[10] J. B. Khurgin and Y. J. Ding, Opt. Lett. 19, 1066 (1994).

[11] Y. J. Ding, S. J. Lee, and J. B. Khurgin, J. Opt. Soc. Am. B 12, 1586 (1995).

[12] Y. J. Ding, S. J. Lee, and J. B. Khurgin, Phys. Rev. Lett. 75, 429 (1995); Y. J. Ding, S. J. Lee, and J. B. Khurgin, IEEE J. Quant. Electr. 31, 1648 (1995).

[13] A. G. Cui, Y. J. Ding, S. J. Lee, J. V. D. Veliadis, J. B. Khurgin, S. Li, D. C. Reynolds, and J. Grata, J. Opt. Soc. Am. B 13, 536 (1996).

LASER BASED DIAGNOSTIC TECHNIQUES FOR COMBUSTION AND COMPRESSIBLE FLOWS

Gregory S. Elliott
Assistant Professor
Department of Mechanical and Aerospace Engineering

Rutgers University
P.O. Box 909
Piscataway, NJ 08855-0909

Final Report for:
Summer Faculty Research Program
Wright-Patterson Air Force Base

Sponsored by:
Air Force Office of Scientific Research
Bolling Air Force Base, DC

and

Wright-Patterson Air Force Base

September 1996

LASER BASED DIAGNOSTIC TECHNIQUES FOR COMBUSTION AND COMPRESSIBLE FLOWS

Gregory S. Elliott
Assistant Professor
Department of Mechanical and Aerospace Engineering
Rutgers University

Abstract

Laser based diagnostic techniques were used and developed in the study of combustion and compressible flows. Laser diagnostic techniques based on using molecular filters to discriminate the Rayleigh scattering from molecules or particles in a flow field were investigated. The first technique termed filtered Rayleigh scattering was used to measure the instantaneous temperature field in hydrogen-air and methane-air flames. Uncertainties in these measurements were explored and found to be from 4 to 7% for the product region of the flame, but slightly higher (approximately 16%) in the reaction region of the flames studied. This uncertainty was primarily associated with the unknown species concentration and possible solutions to this problem will be investigated. A second molecular filter based technique called filter planar velocimetry (FPV) allows the measurement of the instantaneous velocity in a two dimensional plane. FPV was used to investigate axisymmetric and elliptic jets in a M = 2 cross flow. To date preliminary average measurements have been analyzed and are presented here. Lastly, flow visualizations were taken of underexpanded square jets to investigate the flow structure and use as a possible mixing enhancement configuration.

LASER BASED DIAGNOSTIC TECHNIQUES FOR COMBUSTION AND COMPRESSIBLE FLOWS

Gregory S. Elliott

I. THE USE OF FILTERED RAYLEIGH SCATTERING FOR PLANAR TEMPERATURE MEASUREMENTS IN COMBUSTION

I.A. Introduction

Techniques employing molecular filters to modify the light scattered from particles or molecules in a flow offer the possibility of measuring single or multiple properties simultaneously. The molecular filter is simply a cylindrical optical cell containing a molecule which has absorption transitions within the frequency of the laser interrogating the flow field. The molecular filter is placed in front of the receiving optics to modify the frequency spectrum of the scattering. Miles et al.[1992] first demonstrated filtered Rayleigh scattering (FRS) employing molecular iodine filters in conjunction with injection seeded, frequency-doubled Nd:YAG laser (λ = 532 nm). With injection seeding the linewidth is narrow (100 MHz) and the laser frequency can be tuned to match the transitions of iodine. In addition to qualitative flow visualizations, Miles et al. [1992] showed that average properties of the flow at each point in the illuminated plane can be obtained if the scattered signal is collected from molecules. Recently Schrami et al. [1996] demonstrated that FRS could also be used to obtain temperature measurements in lightly sooting flames, but there is still a need for more comprehensive treatment of the uncertainties of the measurement technique.

I.B. Experimental Arrangement

Figure 1 gives a schematic of the burner and optical arrangement for the preliminary measurements given here. Three different burners were used in this study. At Wright-Patterson Air Force Base a hydrogen-air flame was studied using a Hencken burner with a 25 mm square combustion region. The ability of FRS to record temperatures near the burner surface were investigated in a methane/air flame created above a sintered bronze McKenna burner which is water cooled to 283 K. The third burner is copper burner with an array of 64 1 mm diameter holes within an area of 169 mm^2.

The interrogation laser beam was formed into a sheet with a combination of cylindrical and spherical lenses. Two different frequency doubled Nd:YAG laser were used in the present experiments a Spectra Physics GCR-150 (Henken and McKenen burner experiments at Wright Paterson) with approximately 400 mJ per pulse and a Spectra Physics GCR-230 (copper burner

experiment at Rutgers) with 650 mJ per pulse. Both lasers have an injection seeder to provide a narrow line width (~ 100 MHz) which can be tuned through the absorption lines of iodine around 532 nm. The Nd:YAG lasers used in these experiments have a pulse width of approximately 10 ns with a repetition rate of 10 Hz. Two photodiodes were used to monitor the laser energy and frequency fluctuations, using a second iodine filter. The Rayleigh scattering signal is collected using a Princeton Instruments 14-bit intensified CCD camera. The images are stored on a Pentium 100 MHZ personal computer which provided camera control, laser synchronization, and frequency tuning control of the laser.

A major component of the FRS system is the iodine filter. The iodine filter is basically a glass cylinder 9 cm in diameter and 24 cm in length with flat optical windows on both ends. Iodine vapor is formed in the cell by inserting a small amount of iodine crystals and evacuating the cell. The cell temperature (T_{cell}) is raised above the ambient temperature with electrical heat tape so that no iodine crystallizes on the windows. The coldest point in the cell is set in the side arm (T_{I2}), which is housed in a water jacket and maintained at a constant temperature by a circulation water bath. The temperature of the side arm controls the vapor pressure (number density) of the iodine in the absorption cell. The Nd:YAG laser has a narrow line width and at $\lambda = 532$ nm it can be tuned across the absorption bands of iodine. Figure 2 presents the absorption spectra with the two optically thick absorption lines which were used in the present experiments at wave numbers of 18788.44 and 18789.28. The profile was taken with the cell operated at $T_{cell} = 358$ K and $T_{I2} = 318$ K.

I.C. Theoretical Description

Rayleigh scattering has been used to investigate combustion and flow fields for many years and much of the theoretical analysis is well known. When interrogating a flow with a laser and collecting the Rayleigh scattering signal from molecules, there are many important parameters governing the scattered intensity (intensity of the illuminating light, polarization, frequency of the illuminated light, etc.). In the current use of the FRS technique in combustion environments, the intensity and spectral profile of the scattering are needed to deduce the temperature. Since the flames studied here are at atmospheric pressure the Rayleigh scattering can be in the kinetic regime and contain Brillouin scattering effects. Many different models exist for calculating the Rayleigh scattering spectral profile [Yip and Nelkin, 1964 and Tenti et al.,1972] and have been confirmed by experimental measurements [Lao et al., 1976]. The shape of the scattered spectrum is typically parameterized by the dimensionless frequency X and the y parameter. The dimensionless frequency is nondimensionalized by the thermal broadening and is given by

$$X = \frac{\lambda |\nu - \nu_0|}{2 \sin(\theta/2)} \sqrt{\frac{M}{2kT}} \qquad (1)$$

where λ is the wavelength of the incident light, $(\nu - \nu_0)$ is the frequency difference from line center, θ is the angle between the incident and scattered wave vectors, k is the Boltzmann's constant, T is the temperature of the gas, and M is the molecular mass. The y parameter (which is the ratio of the collisional frequency to the acoustic spatial frequency) describes the shape of the Rayleigh scattering spectrum and is given by

$$y = \frac{\lambda P}{4\mu \sin(\theta/2)} \sqrt{\frac{M}{2kT}} \qquad (2)$$

where P is the pressure, and μ is the viscosity. For y of the order of unity, the kinetic regime, Brillouin components become important and kinetic models must be used. For $y \ll 1$ (low pressures or high temperatures) the scattering spectrum is Gaussian and the Brillouin components can be neglected. The total spectral intensity is given by the intensity of the scattering of the ith gas species weighted with its mole fraction x_i and Rayleigh cross section σ_{Ri} and is given by

$$I(\nu) = C\, I_0\, N \sum_i x_i\, \sigma_{Ri}\, r_i(T,P,M_i,\theta,\nu) \qquad (3)$$

where C is the optical calibration constant, I_0 is the incident laser light intensity, N is the total number density, and r_i is the scattering distribution of the ith gas species determined by the kinetic model (ie. S6 model used by Tenti et al., 1972).

The intensity collected by the camera is a convolution of the total spectral intensity $[I(\nu)]$and the transmission profile $[A(\nu)]$ as shown schematically in Figure 3. As illustrated in Figure 3 the scattering from particles and surfaces has a narrow linewidth and is attenuated by the iodine filter. Since the Rayleigh scattering from molecules is thermally broadened much of the scattered intensity passes outside the absorption profile (as illustrated by the shaded region of Figure 3). This is a significant characteristic of FRS since molecular Rayleigh scattering is weak relative to surface and particle scattering.

In order to eliminate the dependence on the optical calibration constant and on the incident laser irradiance distribution, images with the flame on were normalized by scattering collected from the air at ambient conditions. For the present experiments only premixed flames are considered and the dominate species is nitrogen, and therefore the scattering will be assumed to be from a single species. Also the velocity component with the current arrangement leads to little change in frequency due to Doppler shift and so it will be ignored in the present analysis. With these assumptions and since the flames are all at atmospheric pressure the intensity is a function only of temperature for a given optical arrangement and the ratio is given by

$$\frac{S(\nu)}{S_{air}(\nu)} = \frac{N_{N_2} \int \sigma_{N_2} r(T,P,M_{N_2},\theta,\nu) A(\nu - \nu') d\nu'}{N_{air} \int \sigma_{air} r(T_{STP},P_{STP},M_{air},\theta,\nu) A(\nu - \nu') d\nu'} \quad (4)$$

The local gas temperature influences the collected intensity through the gas number density (N) and the thermal broadening which increases the portion of the scattering which is not absorbed by the filter. Thus if the normalized intensity ratio is known [$S(\nu)/S_{air}(\nu)$] the temperature can be determined.

I.D. Hydrogen-Air Flame Results

Figure 4 gives the two dimensional temperature field (x-y view) for a hydrogen-air flame (Φ = 0.25) 2 cm above the Henken burner with a plot of the temperature profile in the center of the image given below the appropriate image. It should be noted that no particular care was taken to physically eliminate particles in the flame or in the surroundings. Scattering from particles generally will dominate the Rayleigh scattering, however, in the present experiment the particle scattering is strongly absorbed since it is not thermally broadened. The adiabatic flame temperature in this case is 1065 K. The first case (Fig. 4a) shows a single shot instantaneous temperature field with the average temperature away from the edges of the flame being 1062 K. The instantaneous temperature profile has a high degree of fluctuation in what should be a relatively flat profile as shown by CARS measurements. Most likely this fluctuation is due to the photon statistics. Thus the signal to noise ratio can be improved by either increasing the number of photons collected (more laser energy per pulse), low pass filtering, or binning multiple pixels together. Figure 4b shows the effect of binning 3 adjacent pixels together (Fig. 4c) and as expected the random temperature fluctuations decrease, but at the cost of decreased spatial resolution (from 0.1 mm^2 to 1 mm^2). Figure 4c is the two-dimensional temperature field made by averaging 40 instantaneous images together. As expected this shows the least amount of temperature fluctuation, but of course the instantaneous information is lost.

Figure 5a and 5b give the average temperature and standard deviation of the temperature in the flat portion of the hydrogen-air flame for various equivalence ratios. The temperatures measured with FRS are in excellent agreement with the adiabatic flame temperature. The maximum deviation is at the highest temperatures with the FRS measurements always slightly lower as expected. The standard deviation of the temperature across the flat portion of the flame is given in Figure 5b for the instantaneous, bin by 3, and average temperature fields for various equivalence ratios. As expected binning the pixels of the instantaneous image by three increases the signal to noise ratio by approximately three for all cases which would be the case if the fluctuations were a result of

photon statistics. The percent of temperature fluctuation for the average, instantaneous, and instantaneous bin by three temperature fields were found to be approximately 2%, 8%, 3% respectively.

I.E. Methane-Air Flame Results

One advantage of FRS is that it can be used to make measurements close to surfaces without being affected strongly by surface scattering, since surface scattering like particle scattering is at the laser frequency and is not Doppler shifted or broadened outside of the absorption profile. Figure 6a and b are the respective average two-dimensional temperature fields of a methane-air flame lifted from the surface of a McKenna burner. The burner is water cooled and has a surface temperature of approximately 283 K with the edge located at x = 0 slightly off the left side of the image. For the lifted flame (Fig. 6a) the temperature before the flame front is slightly low (262 K) which is due primarily to the fact that the Rayleigh scattering cross section of the mixture is slightly higher than that of pure nitrogen. For the attached flame (Fig. 6b) the temperature gradient can be seen on the left side of the image due to the greater heat transfer at the burner edge. The adiabatic flame temperature for the lifted and attached flames was 1623 K and 1690 K, respectively, while the measured temperatures were 1522 K and 1537 K respectively. Note that the measured values are expected to be lower due to the heat transfer to the much cooler burner surface. At the current resolution, measurements were made within 300 μm of the burner surface, limited mostly by the focal length of the camera lens.

One of the greatest advantages of FRS for two dimensional temperature measurements is in its ability to capture instantaneous fluctuations of unsteady flames. Figure 7 is the average (Figure 7a) and instantaneous temperature fields (Figs. 7b-h) of the premixed methane-nitrogen-oxygen flame ($\Phi = 1.21$, adiabatic flame temperature of 2510K). Using FRS the average flame temperature was measured at 2265 K. Again this lower temperature is due in part to unsteadiness in conjunction with the averaging process. Almost all the instantaneous images show buoyantly driven vortices rolling up on the edge of the flame and the associated temperature variation within them.

I.F. Uncertainty Analysis

A simple uncertainty analysis has been performed to estimate the uncertainty associated with the temperature field measurements using FRS. The uncertainties for the hydrogen-air flame are approximately 8.5% on average which seems high when compared with the agreement obtained between the FRS measured temperatures and the adiabatic flame temperature. This is due mainly to the fact that for these flames the uncertainty due to the molecular weight and Rayleigh scattering cross section are added when in actuality they cancel each other out (ie. the molecular weight is lower than nitrogen which results in more of the scattering broadened outside of the absorption filter

and the Rayleigh scattering cross section is lower than nitrogen resulting in less signal). Taking this fact into consideration reduces the uncertainty to approximately 5% which is more in line with the measurements.

The highest uncertainties (above 10%) were found to be within the reactant region of the methane flame particularly for the flame with the equivalence ratio of 1.2. The predominance of methane with a Rayleigh scattering cross section twice that of nitrogen causes the temperatures to be under estimated as is seen in the FRS measurements presented in Figure 6 and 7. The product region of the flame, however, shows a lower uncertainty of approximately 4% for these methane flames since the molecular weight and Rayleigh scattering cross section is much closer to nitrogen. The uncertainties for the instantaneous images are higher (due to higher noise in the recorded intensity) being approximately 20% for the reactant region and 7% for the product region of the flame. It should also be noted here that the values for the uncertainty of the independent variables were generally over estimated resulting in very conservative estimates of the total uncertainty in the temperature measured with FRS.

II. FILTER PLANAR VELOCIMETRY MEASUREMENTS OF A JET IN A M = 2 CROSS FLOW

II.A. Introduction

Although filtered Rayleigh scattering relies on scattering from molecules for the temperature measurements described above, other techniques use scattering off of particles natural present or seeded into the flow. These molecular filter Based velocity techniques have been developed to measure the average velocity (Doppler Global Velocimetry, DGV, [Meyers and Komine, 1991]) or instantaneous velocity (Filtered Planar Velocimetry, FPV, [Elliott et al., 1994]). FPV utilizes two cameras. One camera has a pressure broadened iodine filter in front of it which produces gradual slopes (Figure 8) in the absorption profile instead of the sharp temperature broadened filter used by Miles et al. [1992]. A second camera with no filter (similar to DGV) is used to normalize the image from the filtered camera, accounting for variations in laser intensity, and particle size and density in the measurements. When the laser frequency is tuned to the edge of the sloping region, the Doppler shift will move the scattered intensity into the sloping region of the absorption profile resulting in a deviation in the transmission ratio (Figure 8). The Doppler shift is given by

$$\Delta f_D = \frac{1}{\lambda}(\underline{k}_s - \underline{k}_0)\cdot\underline{V} \qquad (5)$$

where $\underline{k}_s$ and $\underline{k}_0$ are the observed and incident unit light wave vectors, respectively, and $\underline{V}$ is the flow

velocity vector. Thus when the transmission ratio is calculated from the two cameras the frequency shift can be obtained and the velocity is calculated from Equation 6. Instantaneous velocities have been measured in compressible mixing layers [Elliott et al., 1994] and multiple velocity components in boundary layers [Arnette et al., 1995] using FPV.

II.B. Experimental Arrangement

The flow field studied using FPV was a jet in a Mach 2 cross flow which utilized the supersonic research facility at Wright-Paterson Air Force Base. Details of this facility are presented elsewhere [Gruber et al. 1996]. Figure 9 gives a schematic of the tunnel, laser, and camera geomtry. The test section for these experiments has a constant area test section with a cross section of 131mm by 152 mm. The tunnel can be run continuously with a stagnation temperature and pressure of 300 K and 317 kPa respectively resulting in an average free stream velocity of 516 m/s. Two different injector geometries, circular (6.35 mm diameter) and elliptic (6.2 mm major axis and 1.63 minor axis, effective diameter of 6.35 mm) were incorporated into removable test inserts housed within the bottom wall of the test section. The exit pressures of both jets were regulated to 476 kPa resulting in a jet to free stream momentum flux ratio of 2.93. Particles were seeded into the freestream by the combustion of silane which produces silicone dioxide particles in the range of 0.2 μm diameter.

The laser and camera system used here was the same as in the FRS experiments with the exception of an additional camera which recorded the normalized image for each instantaneous filtered image. Another difference between the FRS and FPV system is in the absorption properties of the iodine filters used with each system. Figure 10 shows the difference between the two filter profiles used in this study. The filter profile used in the FRS measurements was dominated by thermal broadening resulting in relatively sharp slopes on either side of the profile. The absorption profile used for FPV has a much more gradual profile which is made by introducing a nonabsorbing gas (nitrogen with a partial pressure of 15 torr) into the iodine filter. This results in the absorption profile being dominated by pressure broadening effects which can be used to adjust the slope for the expected frequency range encountered in the flow studied.

In the past when making velocity measurements using molecular filter based techniques a problem is encountered in measuring a velocity component which is "natural" to the flow being studied is difficult without using more than one camera pair or viewing the flow at oblique angles. To circumvent this problem we chose to use the laser optical arrangement of Figure 9 and reflect the laser sheet back on itself. From Equation 6 it can be shown that for the present arrangement this results in a sensitivity to the velocity vector essentially in the streamwise direction and instantaneous streamwise velocities can be obtained. In order to find information about the spanwise velocity a single laser pass was used resulting in a velocity vector 40 degrees from the streamwise direction. Although the spanwise velocity component can not be decoupled from the streamwise velocity

component for the instantaneous measurements, for the average velocity field both optical arrangements can be combined to calculate the spanwise velocity component.

II.C. Preliminary results

Measurements were taken at several streamwise locations for the circular and elliptic jet injection geometries both with and without the laser sheet reflecting back on itself. At the present time only the average velocity images have been reduced. Figure 11 gives of the unfiltered image and streamwise velocity image for the circular jet, and the spanwise velocity image for the elliptic jet. For these preliminary results the freestream velocity was used to calibrate the measurements which will not be necessary when the instantaneous images are fully analyzed. As expected the streamwise velocity image shows the velocity decrease after the bow shock consistent with the shock angle which the flow has passed through. The streamwise velocity decreases further as the jet core and boundary layer are approached. It should be kept in mind, however, that the jet was not seeded and therefore the measurements in the core region are biased by the free stream velocity resulting in a higher value than is really the case. The spanwise velocity image shows essentially zero spanwise velocity outside the bow shock and in the core of the jet. There are however positive and negative spanwise velocity components inside the bow shock to the left and right of the jet respectively. This is most likely due to the streamwise vortices which are formed around the jet. It should be emphasized that these results are very preliminary and further conclusions will be drawn as the instantaneous images are calculated.

III. FLOW VISUALIZATIONS OF AN UNDEREXPANDED SQUARE JET

III.A. Introduction

In recent years much effort has been devoted into investigating non-circular (ie. square, rectangular, elliptical) jets and the possibilities of their use to enhance mixing particularly in the compressible flow regime [Grinstein, 1996 and Glawe, 1995]. These non-circular geometries find applications in thrust vectoring, enhancing entrainment for combustion, and heat signature reduction. Square jets have shown 45 degrees of axis rotation in the near field caused by the vortex dynamics in the corners of the jet. Although these observations have been made there is still a need to better understand the fluid mechanisms which govern these observations. As a first step toward this goal, flow visualizations and FPV images have been taken in an under expanded square jet. Preliminary images are given here with the majority of the data still to be processed.

III. B. Experimental Arrangement

The laser and camera system were the same as described previously for the FRS and FPV experiments, allowing instantaneous (pulse width of 10 ns) images to be taken. The square jet studied has a 25.4mm by 24.5mm cross section and can be operated continuously with the supply air at the Wright-Patterson Air Force Base supersonic research facility. Stagnation pressures from 240 to 517 kPa were studied which resulted in an underexpanded jet for all conditions. Two different laser sheet orientations were investigated one aligned parallel to the jet axis (streamwise view) and one with the sheet aligned perpendicular to the jet axis (spanwise view). The scattering was collected from ice particles formed from the moisture in the supply air as the temperature decreases through the nozzle (marking the core of the jet), and as the moist ambient air mixes with the colder supersonic air (marking the mixing region of the jet). These ice particles have been used by other investigators to study various flow fields using similar techniques [Elliott et al., 1992].

III. C. Preliminary Results and Discussion

Average streamwise images are given in Figure 12 for the square jet operated at $P_0 = 240$ to 517 kPa. Each average image is calculated from 120 instantaneous images and normalized to remove the Gaussian intensity distribution in the laser sheet. Oblique shock and expansion waves are clearly visible above a stagnation pressure of 310 kPa. What appears to be a Mach disk occurs for stagnation pressures above 380 kPa at an $x/s \approx 1.5$ (where s is the height of the jet). Instantaneous streamwise images are given in Figure 13. For $P_0 = 240$ and 345 kPa large scale structures are apparent with alternate spacing above and below the jet centerline similar to what is seen in axisymmetric jets when a helical mode is present. Also the instantaneous shock/expansion wave pattern is much different than the average images for the $P_0 = 345$ kPa case. Spanwise images were taken for each operating pressure at various downstream locations. Average spanwise images for the square jet operating at $P_0 = 276$ and 517 kPa are given in Figure 14. For the lower stagnation pressure case evidence of streamwise vorticity in the corners of the jet is visible, but there appears to be no axis rotation as the shear layers on the sides of the jet develop down stream. For the higher stagnation pressure case ($P_0 = 517$ kPa), however, axis rotation of 45 degrees is observed as the complex shock and expansion wave patterns develop downstream.

IV. ACKNOWLEDGMENT

I would like to acknowledge Dr. C. Carter, Mr. J. Donbar, Dr. D. Glawe, Dr. M. Gruber, and Dr. A. Nejad for running these experiments (sometimes late at night) and building the facility to allow the research to take place. Also, I would like to acknowledge the support of AFOSR for funding this work and the National Science Foundation for providing funding for part of the equipment used here under grant number NSF-9622108 with Dr. R. Arndt.

IV. REFERENCES

Arnette, S.A., Samimy, M., and Elliott, G.S., "Two-Component filtered Planar Velocimetry in the Compressible Turbulent Boundary Layer" Submitted to the AIAA 34th Aerospace Sciences Meeting, 1996.

Elliott, G.S., Samimy, M., and Arnette, S.A., "Study of Compressible Mixing Layers Using Filtered Rayleigh Scattering Based Visualizations," *AIAA Journal*, Vol. 30, No. 10, 1992.

Elliott, G.S., Samimy, M., and Arnette, S.A., "A Molecular Filter Based Velocimetry Technique for High Speed Flows," *Experiments in Fluids*, Vol. 18, pp. 107-118, 1994.

Glawe, D.D. "Parallel Injection from the Base of an extended Strut Into Supersonic Flow," Ph.D. Dissertation, The Ohio State University, 1995.

Grinstein, F.F. "Dynamics of Coherent Structures and Transition to Turbulence in Free Jets," AIAA Paper 96-0781, 1996.

Gruber M.R., Nejad, A.S., Chen, T.H., and Dutton, J.C., "Large Structure Convection Velocity Measurements in Compressible Transverse Injection Flowfields," AIAA Paper 96-0203, 1996.

Lao, Q.H. Schoen, P.E., and Chu, B., "Rayleigh-Brillouin Scattering of Gases with Internal Relaxation," *The Journal of Chemical Physics*, Vol. 64. No. 9, pp. 3547-3555, 1976.

Meyers, J.F., and Komine, H., "Doppler Global Velocimetry: A New Way to Look at Velocity," *Laser Anemometry*, Vol. 1, 1991.

Miles, R.B., Forkey, J.N., and Lempert, W.R., "Filtered Rayleigh Scattering Measurements in Supersonic/Hypersonic Facilities," AIAA Paper 92-3894, 1992.

Schrami, S., Will, S., Hofmann, D. Munch, K.U., and Leipertz, A., "Two-Dimensional Laser Diagnostics for Sooting Flames," 8th International Symposium on Applications of Laser Techniques to Fluid Mechanics, 1996.

Tenti, G., Boley C., and Desai, R., "On the Kinetic Model Description of Rayleigh-Brillouin Scattering from Molecular Gases," *Canadian Journal of Physics*, Vol. 52, pp. 285-290, 1974.

Yip, S. and Nelkin, M., "Application of a Kinetic Model to Time-Dependent Density Correlations in Fluids," *Physical Review*, Vol. 135, 1964, pp. A1241-A1245.

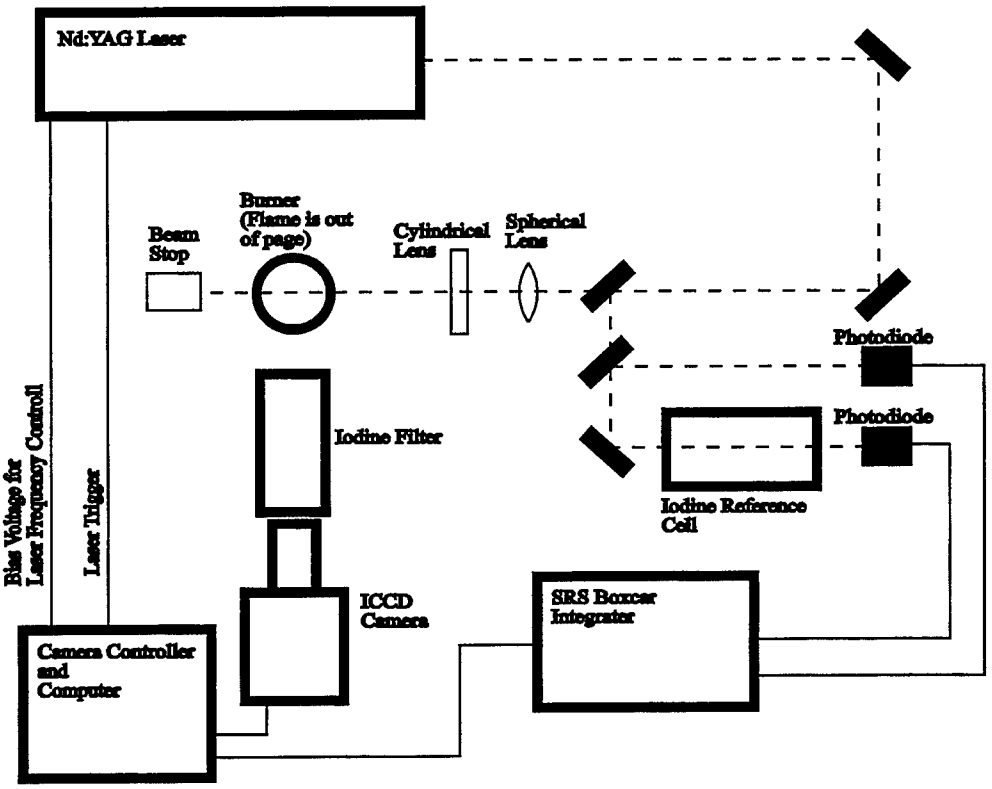

Figure 1. Schematic of laser and optical arrangement for FRS temperature measurements.

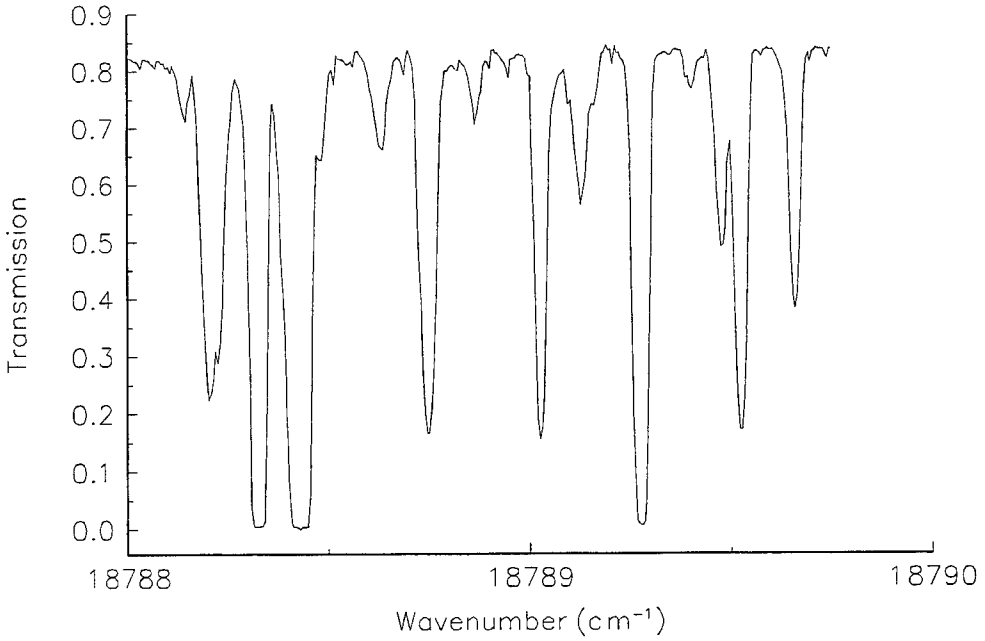

Figure 2. Absorption lines of iodine in the frequency tuning range of the Nd:YAG laser.

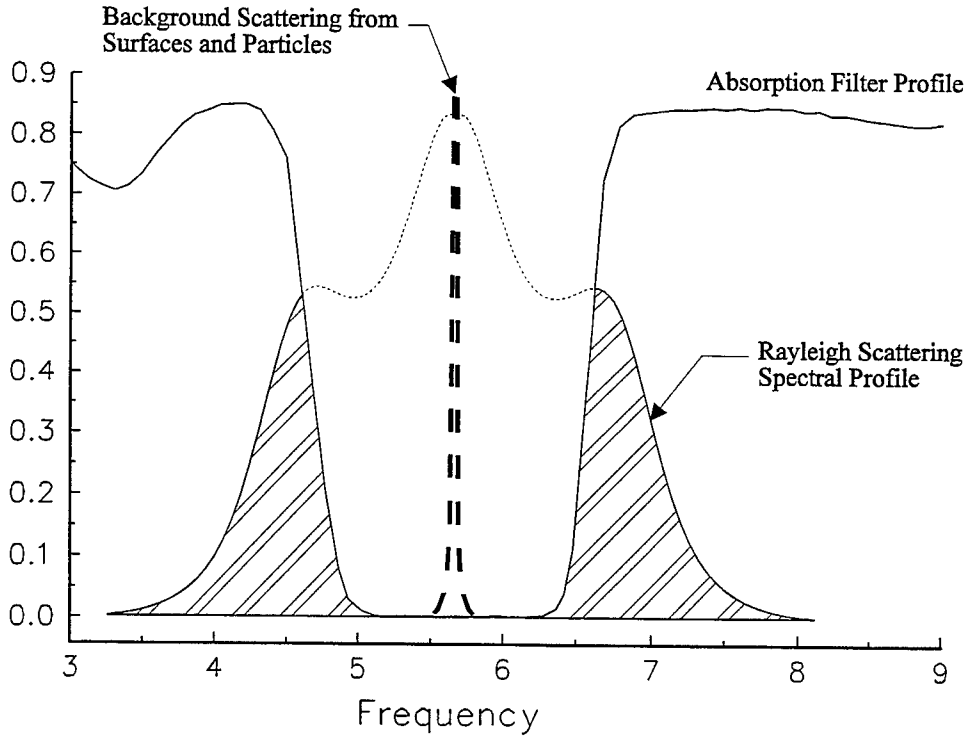

Figure 3. Schematic of absorption profile convoluted with molecular Rayleigh scattering.

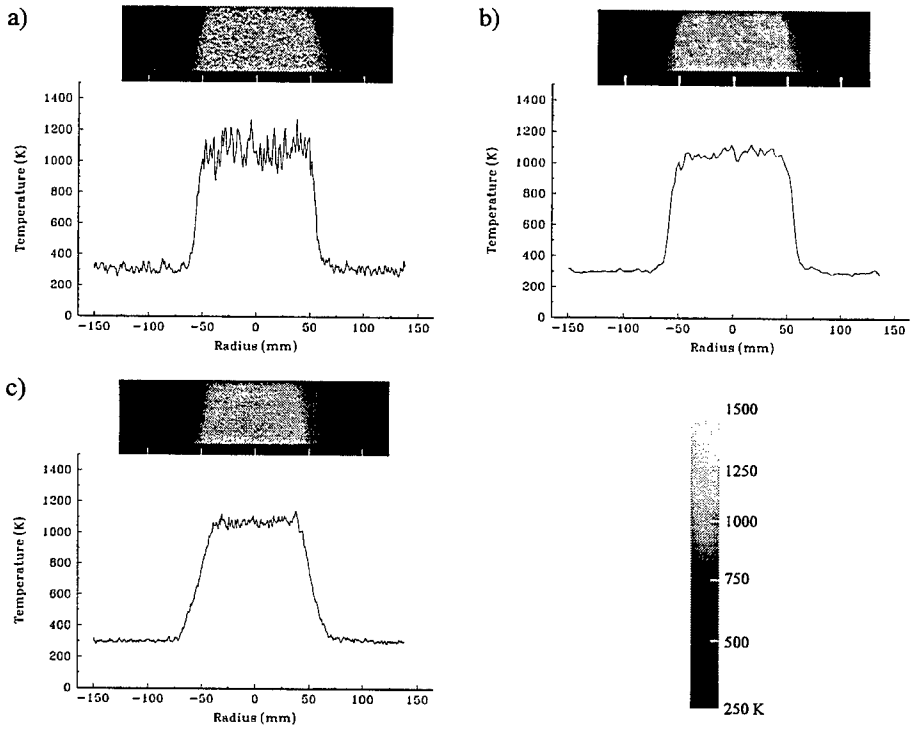

Figure 4. Instantaneous (a) bin by 3 (b) and average (c) images and temperature profiles taken using FRS above a hydrogen-air flame.

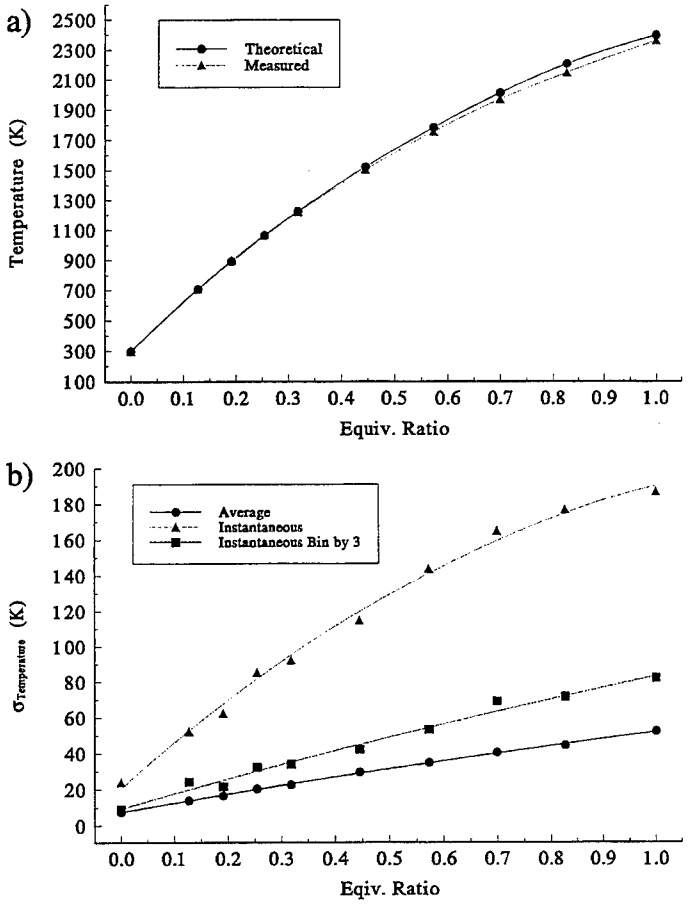

Figure 5. Average temperature (a) and standard deviation (b) of the temperatures for a hydrogen-air flame operated at various equivalence ratios.

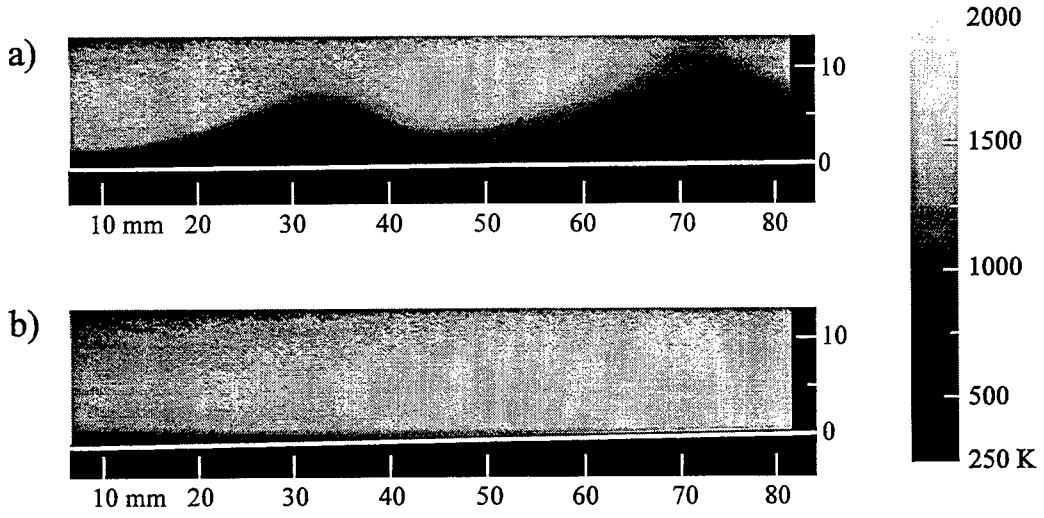

Figure 6. Average two-dimensional temperature fields of a methane-air flame lifted (a) and attached (b) to the burner surface.

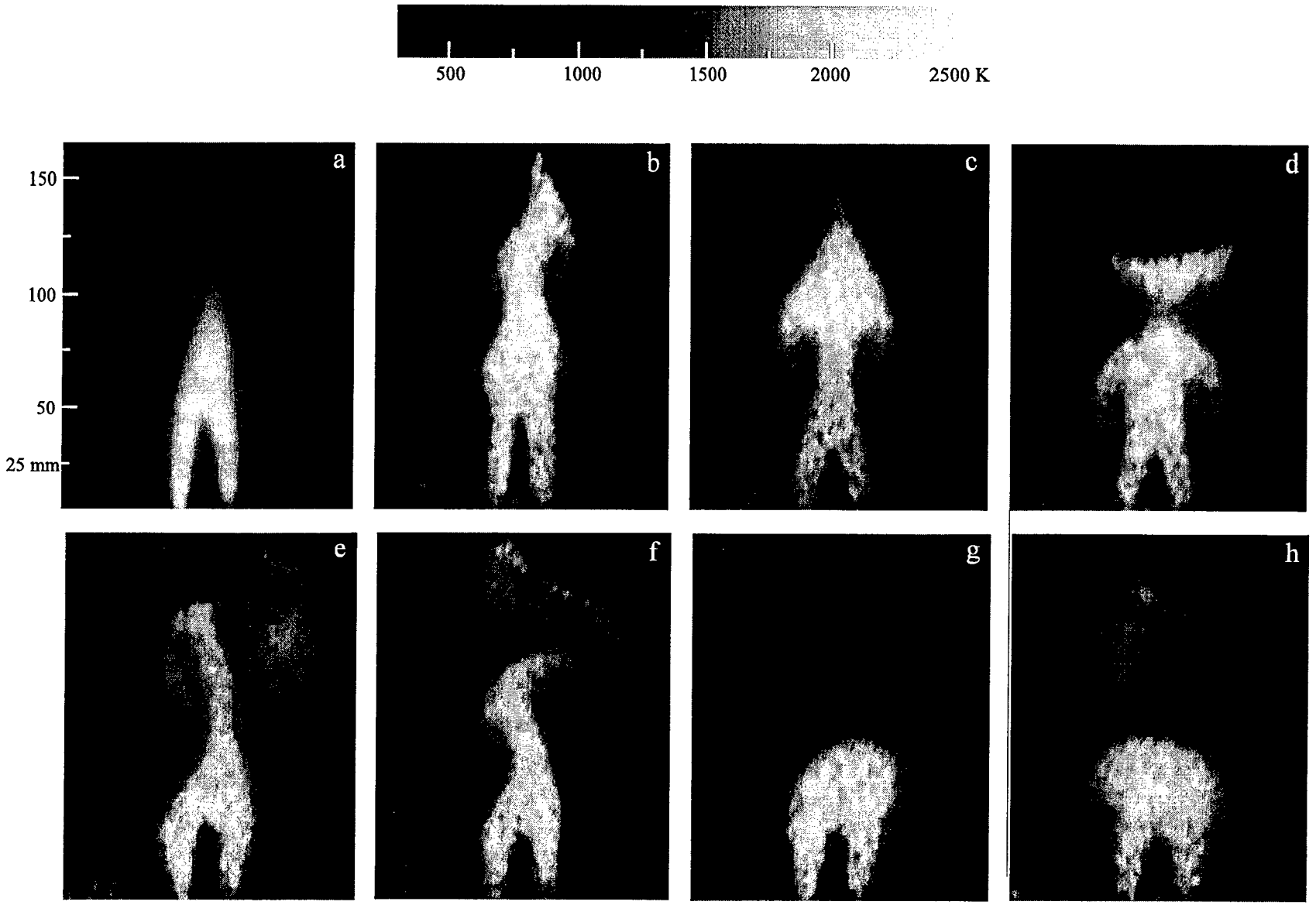

Figure 7. Average and instantaneous temperature fields of an unsteady premixed methane flame taken using FRS.

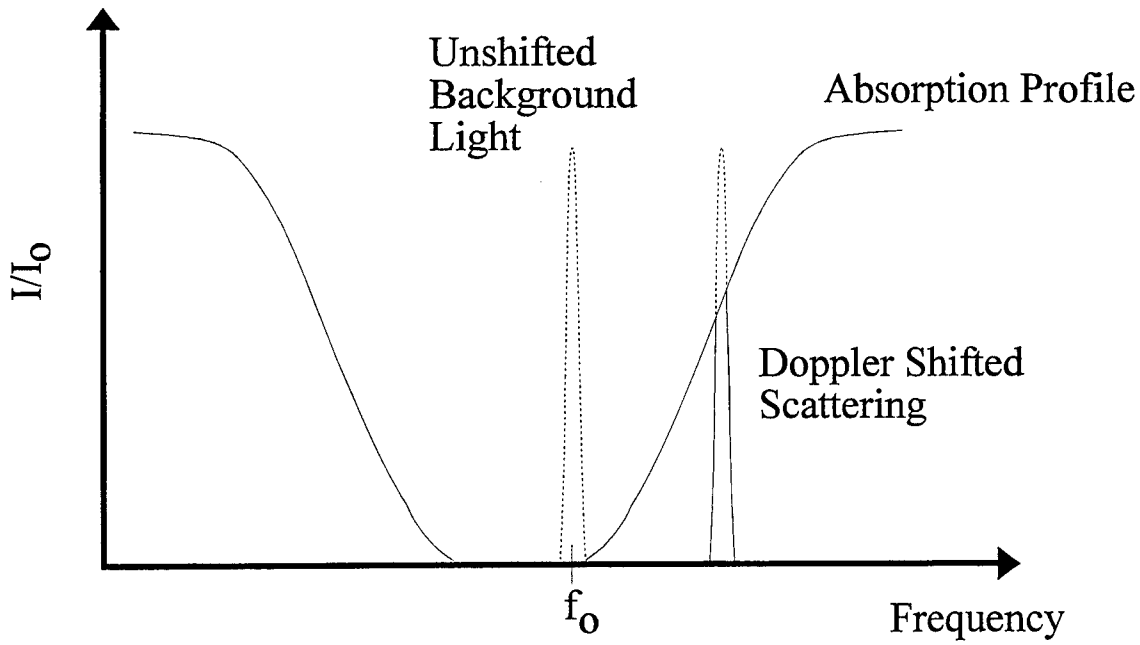

Figure 8. Schematic illustrating Filtered Planar Velocimetry.

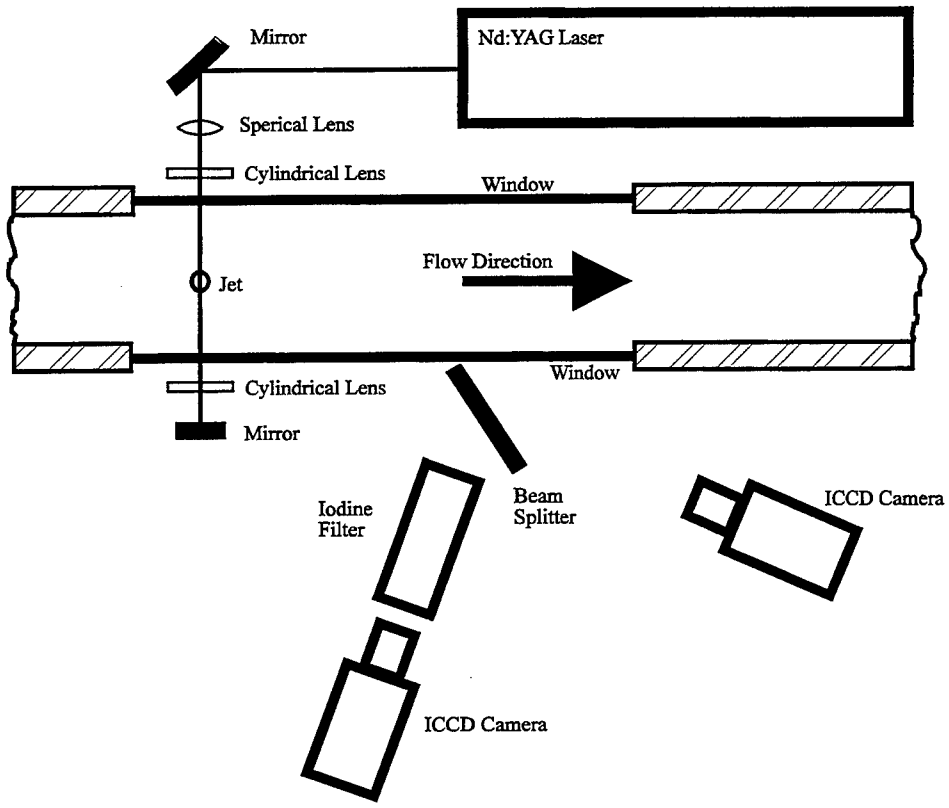

Figure 9. Plan view of the tunnel and optical arrangement for FPV measurements of a jet in a supersonic cross flow.

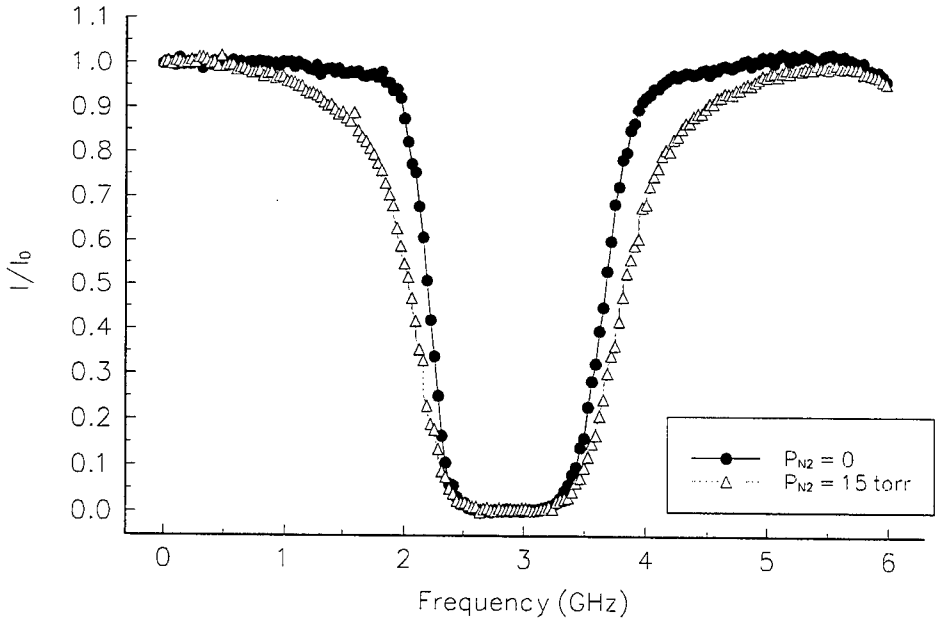

Figure 10. Iodine absorption filter profiles with and without pressure broadening from nitrogen.

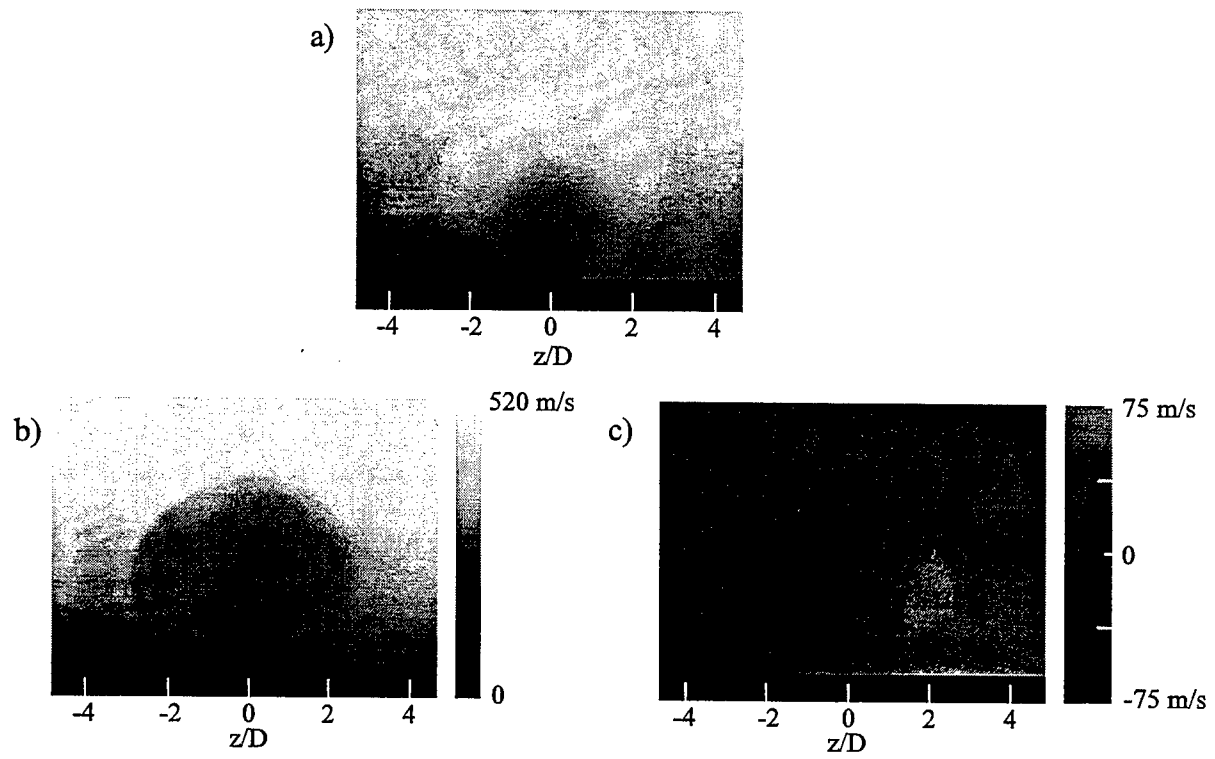

Figure 11. Reference (a), streamwise velocity (b), and spanwise velocity (c) average images of a jet in a Mach 2 cross flow taken using FPV.

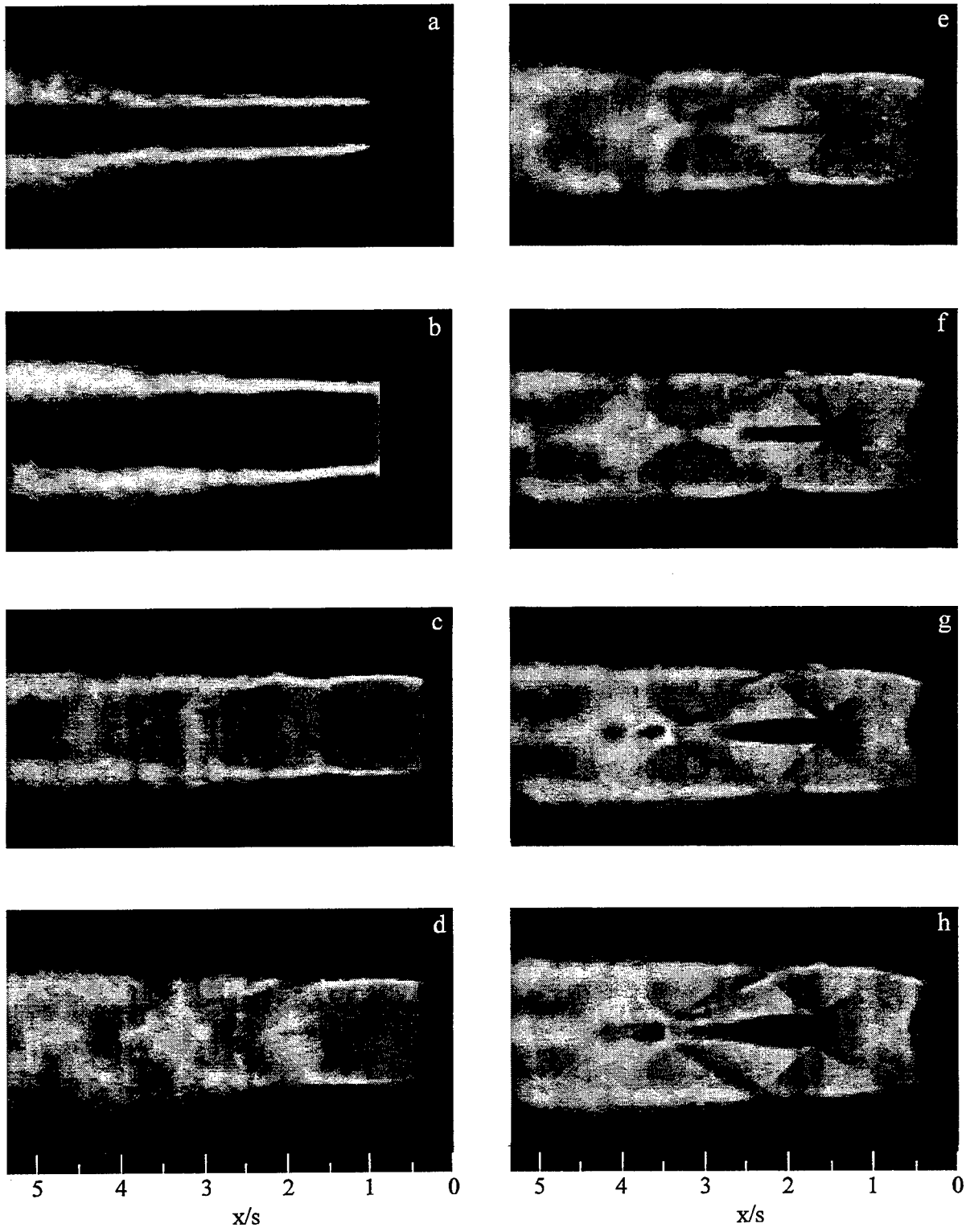

Figure 12. Average streamwise flow visualizations of underexpanded square jets operated at stagnation pressures (kPa) of 240 (a), 276 (b), 310 (c), 345 (d), 380 kPa (e), 414 (f), 450 (g), and 517 (h).

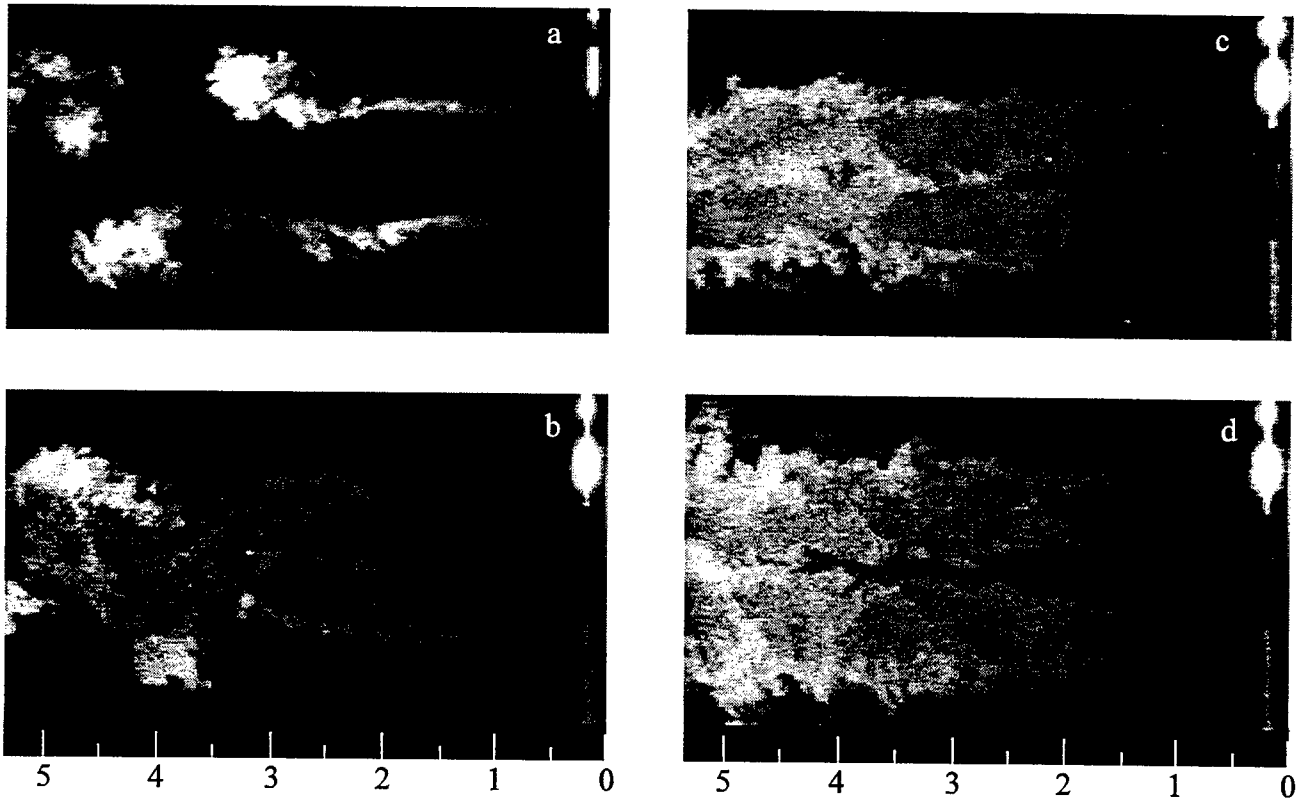

Figure 13. Instantaneous streamwise flow visualizations of underexpanded square jets operated at stagnation pressures (kPa) of 276 (a), 345 (b), 414 (c), and 517 (d).

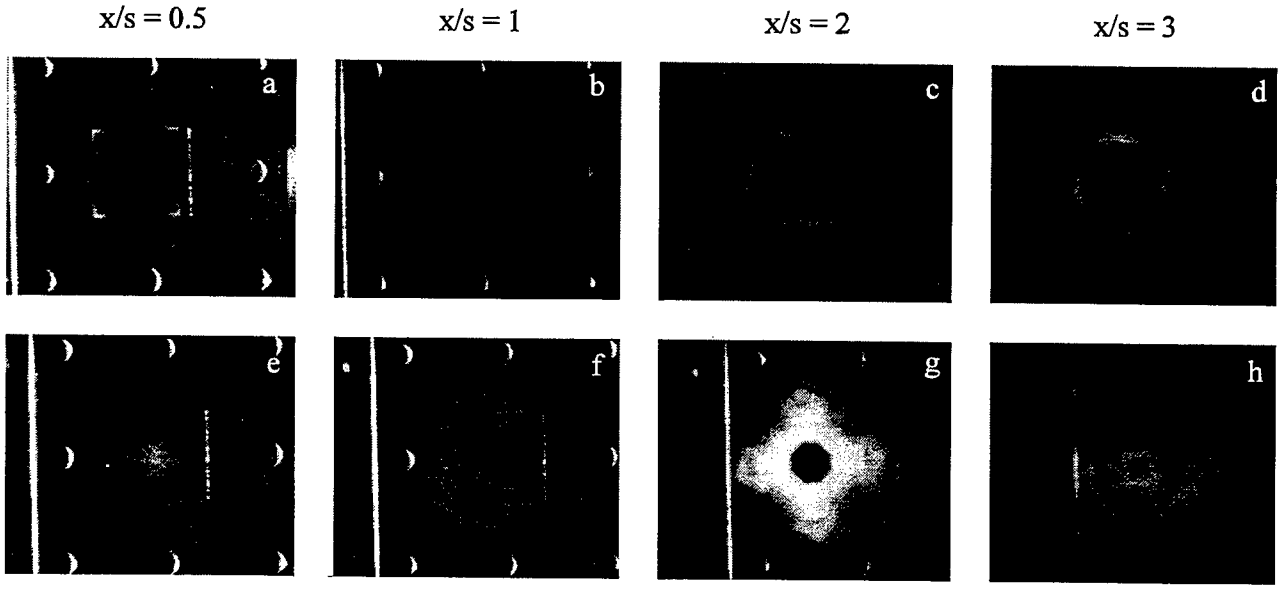

Figure 14. Average sspanwise flow visualizations of underexpanded square jets operated at stagnation pressures (kPa) of 276 (a-d), and 517 (e-h).

VERTICAL 3-D INTERCONNECTS FOR MULTICHIP MODULES

Altan M. Ferendeci
Associate Professor
Department of Electrical and Computer Engineering
and Computer Science Department
University of Cincinnati
Rhodes Hall 823, ML-30
Cincinnati, Ohio 45221-0030

Final Report for :
Summer Faculty Research Program
Wright Laboratories

Sponsored by

Air Force Office of Scientific Research
Bolling Air Force Base, DC
and
Wright Laboratory

August 1996

VERTICAL 3-D INTERCONNECTS FOR MULTICHIP MODULES

Altan M. Ferendeci
Associate Professor
Department of Electrical and Computer Engineering
and Computer Science Department
University of Cincinnati

Abstract

In this report, a vertically-connected 3D T/R module for a conformal phased array antenna systems is investigated. Active and passive elements and circuits suitable for the proposed 3/D modules are analyzed. The module involves the use of thermally shunted HBT for power amplifier, various distributed circuit elements realized by coplanar waveguides (CPW), and vertical posts interconnecting the various circuit layers. Coplanar waveguides completely immersed in a dielectric medium and surrounded by an upper and a lower ground plane is analyzed using conformal mapping. It is shown that if the separation distance between the side ground planes of the CPW is small compared to the vertical distances to the upper and lower ground planes, the impedance of the line becomes independent of the dielectric layer thickness. Sycar is chosen as the dielectric material. Uniformity and thickness control during the processing of sycar will lead to reliable low loss vertical interconnects. The goal of the project is to implement a 3D T/R module and demonstrate the feasibility of 3D vertical interconnects by incorporating these modules in a 2x2 phased array antenna system.

VERTICAL 3-D INTERCONNECTS FOR MULTICHIP MODULES

Altan M. Ferendeci

Introduction

At present, solid state power sources can not replace the high power slow-wave microwave tubes. But by incorporating novel power combining techniques, the overall combined power of the solid state sources may approach that of a single tube output. This is especially true for phased array antenna systems where each radiator has its own power amplifier and the total radiated power is the combined power of all the radiators. In a phased array antenna system, the transmit/receive (T/R) modules are placed on a line (linear array), on a plane (planar array) or on a circular area (circular array). To eliminate the main side lobes, the separation distance between the antennas should be less than half the free space wavelength of the radiated signal.

At microwave and millimeter wave frequencies, planar antennas are replacing the conventional antenna structures. The dimensions of the patch antennas are generally less than the required free space half-wavelength. They can be configured to be used in any array configuration. Unfortunately, if a compact module including all the electronics is to be integrated with the patch antenna, it is impossible to place all the individual circuit modules on the same substrate and at the same time satisfy the antenna spacing requirements. This becomes more important especially at millimeter wavelengths. Even though most of the system components are in the form of monolithic integrated circuits, they still occupy a large surface area of a substrate. Even if the complete circuit can be laid out on the same GaAs or InP substrate, it will too expensive to use this type of large area substrates behind each of the radiator . The complete transmit/receive (T/R) module also contains a high power amplifier. Unless precautions are taken to remove the generated heat, placing this circuit on the same substrate with other temperature sensitive circuits such as low noise preamplifiers may not be desirable. Even if lumped elements are replaced by distributed elements at higher frequencies, the overall T/R module may still require a large substrate area.

At present, all circuit modules are placed an enclosed casing. The power is coupled to the antenna through one end of the casing. Unfortunately, this increases the overall depth of the T/R module relative to the lateral dimensions of the antenna. These modular units have the distinct disadvantage of having a surface area to depth ratio very small. Even with these limitations, they can still be utilized in a linear or a planar array. They can not be distributed over a general curved surface. For a module to be universally conformal to any surface, the depth of the module should be negligibly small compared to the maximum lateral dimensions of the modular unit.

It is possible to place the circuit modules vertically one over the other so that the final T/R module will occupy less space. 3D module configuration dictates the development of a new packaging technology so that various circuit modules at various levels can be vertically interconnected with each other with little or no loss in signal amplitude, with no cross coupling between the elements and with manageable processing steps.

There is already considerable research and development effort being extended to incorporate vertical interconnects in the implementation of monolithic microwave integrated circuits (MMIC)[1,2]. There are two major concentrated research areas that utilize 3D vertical interconnects. First area is the use of vertical interconnects for compacting the size of an integrated circuit module [3]. In this scheme, thin multiple dielectric layers (2.5 μm) are used for connecting the various elements of the circuit together. The second major concentrated effort is to stack various circuit modules of the overall T/R module one over the other using vertical interconnects. Actually both of these concepts complement each other since the final T/R module may contain various vertically interconnected MMICs.

In either case, coupling of microwave or millimeter wave signals between the layers become a major area of research. Already, there is considerable research work going on related to the coupling mechanisms between transmission lines of the various layers [4]. Novel transmission lines are also proposed and analyzed [5-9].

In this report, a complete 3D vertically interconnected 3D T/R module for a conformal phased array antenna system is proposed. Details of the proposed configuration including an integral patch antennas will be given. The major components of the T/R module and the specific areas that have to be developed will be discussed.

Phased Array Antenna Module

Typical front end of a T/R module for a radar system is shown Figure 1. Figure 2 shows a 2x2 modular phased array antenna system. The control and processing electronics are not shown in these figures. The lowest substrate layer contains the power amplifier. Heat can be easily transferred from the substrate by placing the overall module on a highly heat conducting metallic surface.

Various layers of the T/R module are processed by deposition of multiple dielectric materials of known thickness followed by metal depositions immersed between the dielectric layers. As the module is processed, necessary interconnecting posts (or vias) are electro-deposited and the circuit for that layer is finally processed.

The upper layer of the module has a patch antenna which could be either in rectangular, circular or ring shape [10]. The thickness of the upper dielectric layer below the patch can be adjusted to provide the maximum radiation condition for a specific antenna [11].

Typical dimensions for patch antennas operating at 10 GHz and with a dielectric material of $\varepsilon_r=2.5$ are given in Table I. The overall dimensions of these patches are smaller than $\lambda_o/2=15$ mm and thus can be used in phased array antenna systems since they easily satisfy the phased array antenna spacing requirements .

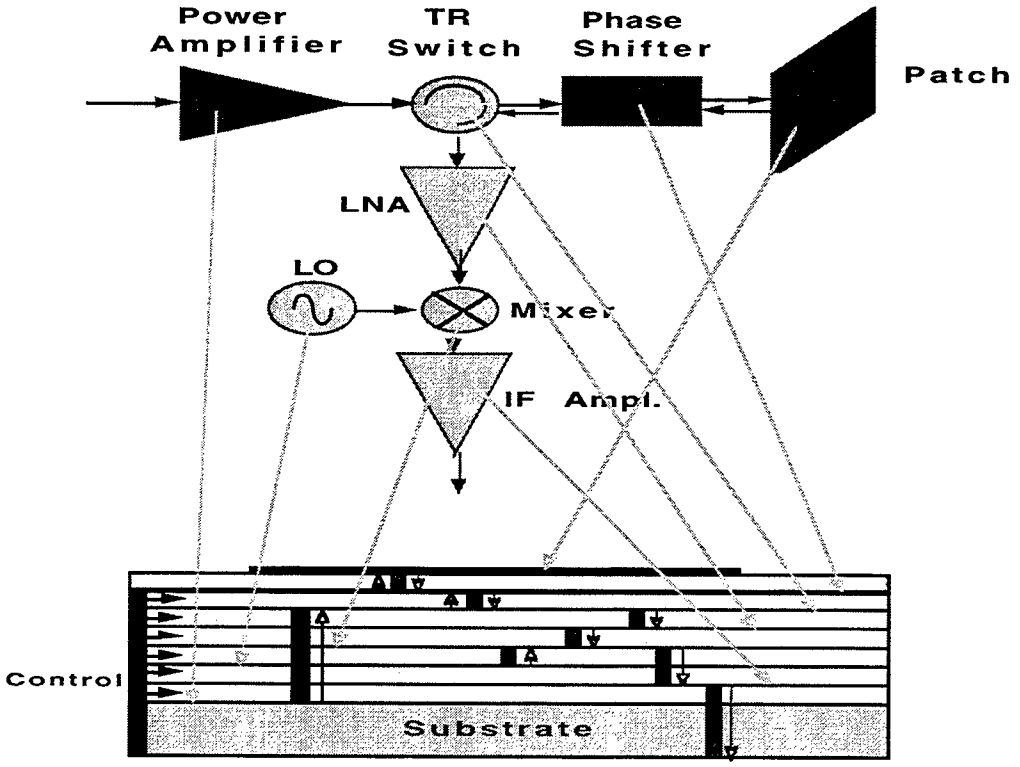

Figure 1. Major components of a T/R module.

Figure 3 shows possible distribution of vertically interconnected 3D T/R modules over various surface configurations. These surface can actually be of any shape provided the radius of curvature of the surface is not too small compared the lateral dimensions of the T/R module. Since the overall thickness of the proposed vertically interconnected 3D T/R module is expected to be a few millimeters, they can easily be distributed over any conformal surface topology. These properties may lead to vast number of applications in communication and radar systems.

Table I. *Dimensions of a patch antennas*

(f=10 GHz, $\lambda_g/2$ = 15 mm, ε_r=2.5)

Patch	*Dimensions (mm)*	*Directivity (dB)*
Rectangular	*w=11.3, L=10.8*	*6.9*
Circular	*D = 10.8*	*7.1*
Ring	*b=4.1, a=2.6*	*< 7.0*

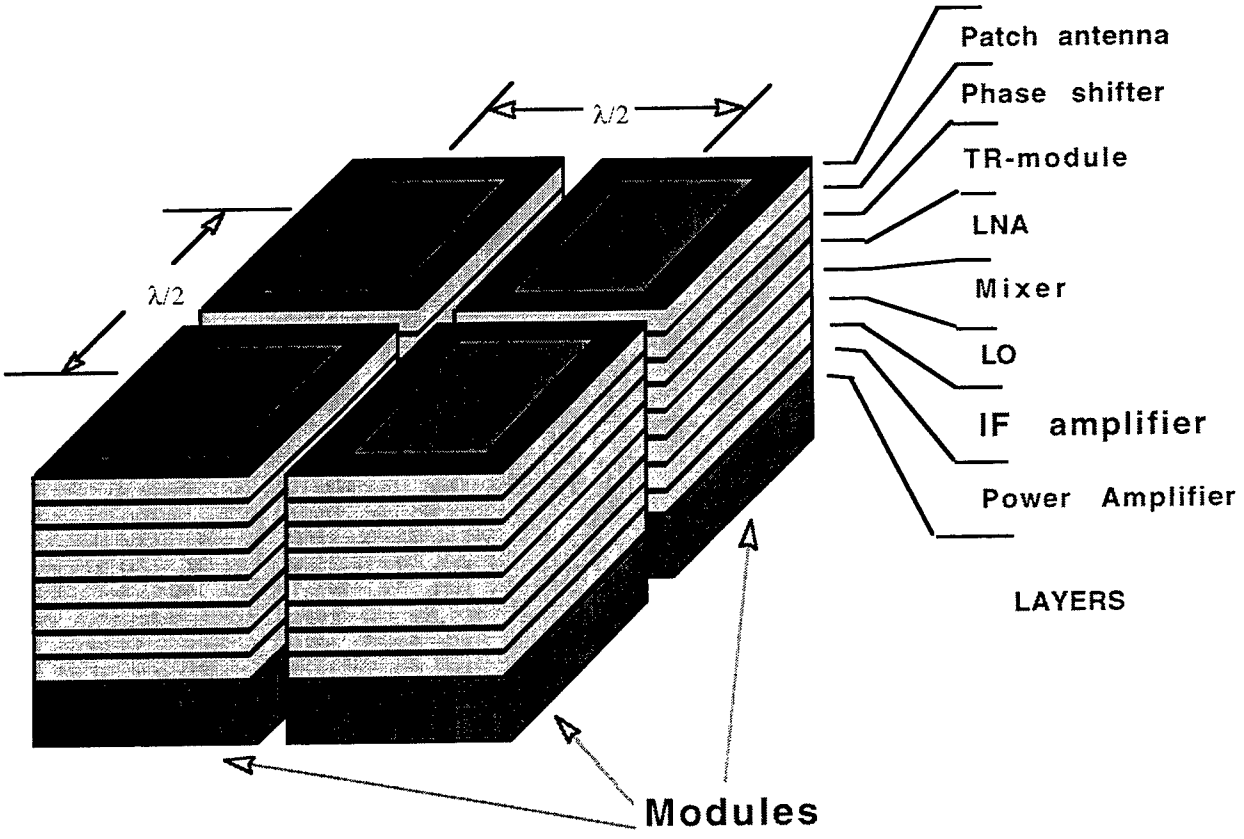

Figure 2. 4 element phased array antenna system with 3D T/R modules.

Figure 4 shows the essential components of a typical representative vertically interconnected 3D T/R module. A substrate (preferably a SI-Silicon or Alumina) is the base of the building block. Since the substrate can be attached to another heat conducting material such as a metal, the power amplifier circuitry is processed on this substrate. The power amplifier chip is attached to the Si-substrate by micromachining an opening on the Silicon surface and flip bonding

of the chip into the opening [12,13]. Since the dielectric thickness of the vertical layers are relatively thin and their thickness may be comparable to the overall height of a thermally shunted HBT, it is recommended that the micromachining depth should be as deep as the transistor height so that the ensuing dielectric layers can be deposited uniformly over the substrate material.

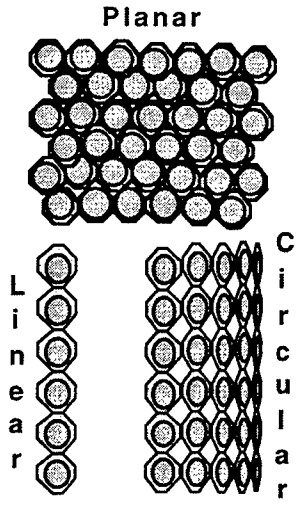

Figure 3. Distribution of patch antennas over a line, plane or a cylinder.

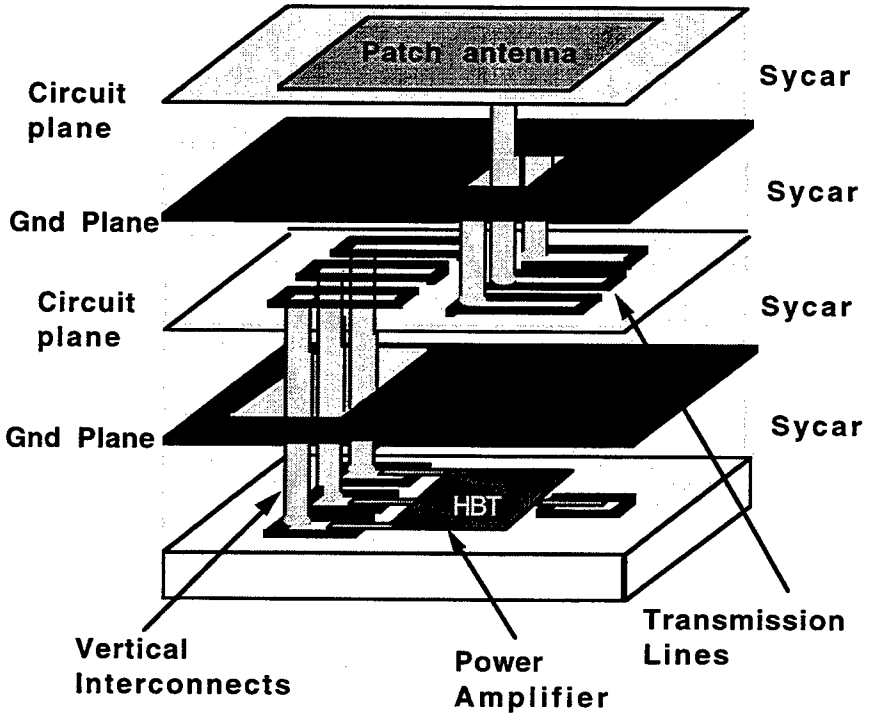

Figure 4. Representative components of a 3D module.

There are four major areas that have to be developed in implementing a vertically interconnected 3D T/R module. These are:

a) Power amplifier

b) Transmission lines and passive circuit components

c) Deposition and processing of dielectric layers

d) Low loss vertical interconnects.

Power Amplifier.

There are many possibilities for the implementation of the power amplifier. The complete power amplifier can be processed as a monolithic integrated circuit using either HBTs or FETs, Since there is a very successful development program on thermally shunted HBT power devices (Figure 5) at the Devices Branch of the Electronics Division of the Avionics Laboratory (AADD) of the Wright Laboratory [14], it will be an excellent opportunity to incorporate these devices in the proposed 3D T/R modules. This will also allow close collaboration between the various branches of the Electronics Division. The combined expertise of the various branches will lead to the development of the best circuit topology for maximum operational efficiency.

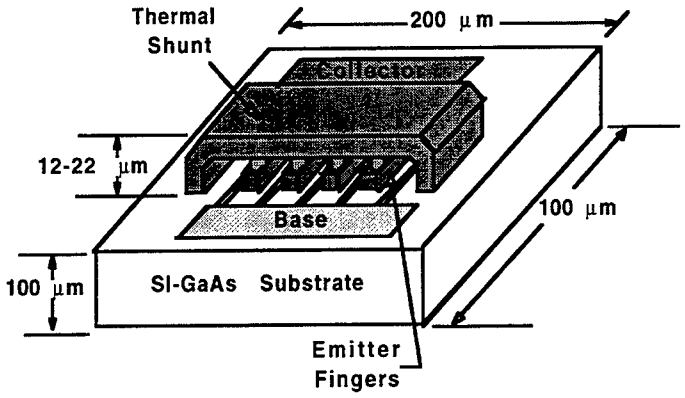

Figure 5. Thermally shunted power HBT developed at AADD of Avionics Laboratory (Ref.14).

Transmission Lines

There are many transmission line configurations that can be used in the implementation of the vertically interconnected 3D T/R modules [15,16]. Microstrip lines, strip lines, slot lines and coplanar waveguides are the best possible candidates that can be used with these modules. Because of the unsymmetric nature of the slot line, it has limited applicability and in general is used for line

couplings between various layers. In many cases, circuit planes will be sandwiched between two conducting ground planes. Therefore microstrip lines are replaced by stripline type transmission lines. If the upper dielectric layer of a circuit plane is relatively thick compared to the lower dielectric layer, microstrip like transmission lines can still be implemented with a slight modification to the line characteristic. In this case, the strip is now embedded completely in a dielectric material of ε_r.

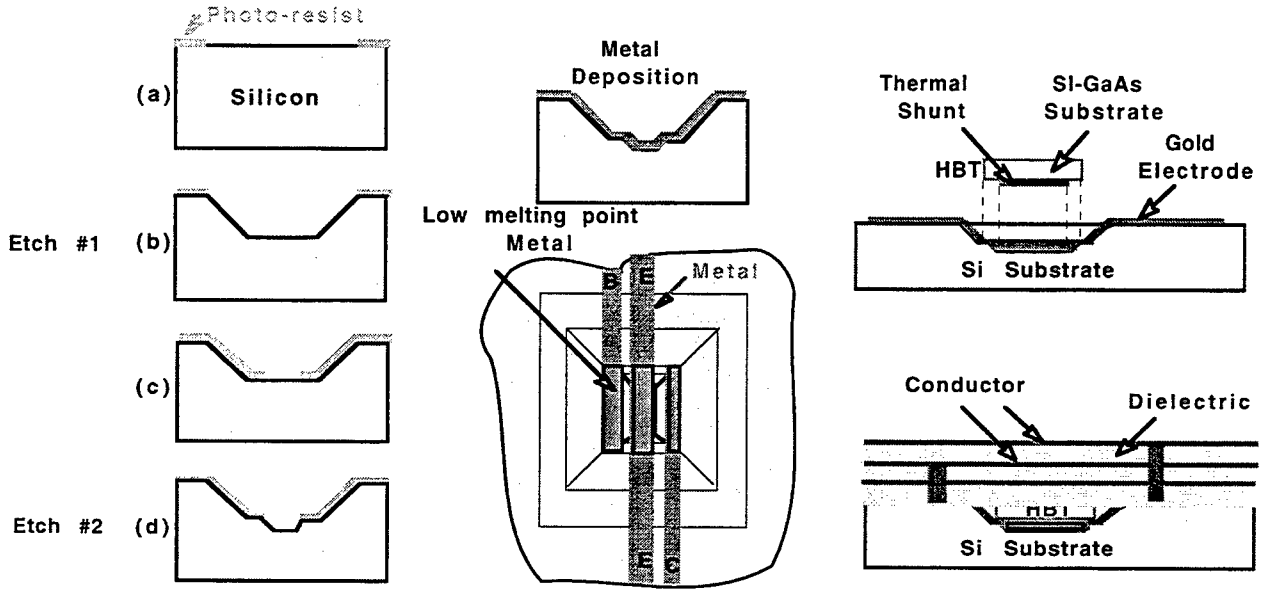

Figure 6.3 Micromachining steps in Silicon for attaching the HBT chip. The transistor shunt metal makes direct contact with Si-substrate.

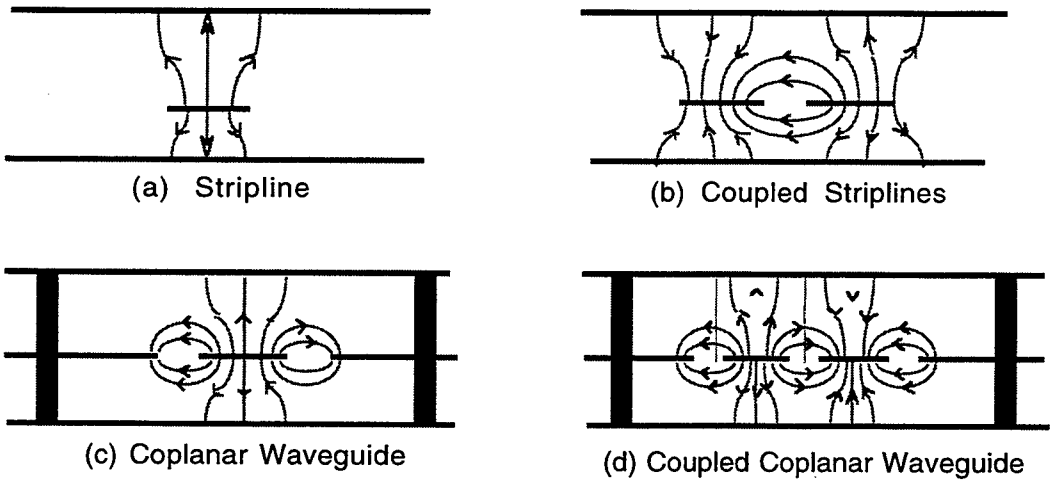

Figure 7. Transmission line suitable for 3D interconnects.

In selecting transmission line structures best suited for the proposed 3D T/R module, the lines should have low loss, easy to process and above of all they should be less sensitive to the thickness of the processed dielectric layers. If the thickness of the dielectric layer can be controlled accurately, the choice of the transmission line structure will not be critical.

For a circuit plane sandwiched between two ground planes, striplines (SL) and coplanar waveguides (CPW) are the two best transmission line configurations that can be used in implementing the passive elements of a vertically interconnected 3D module.

Figure 7 shows the stripline and the coplanar waveguide in the presence of both upper and lower conducting planes. If the upper conducting ground plane is not present, the stripline becomes a modified microstrip transmission lines imbedded in a dielectric material. Already successful power coupling configurations from one layer to the other are implemented when the lines are embedded within multiple dielectric layers [2].

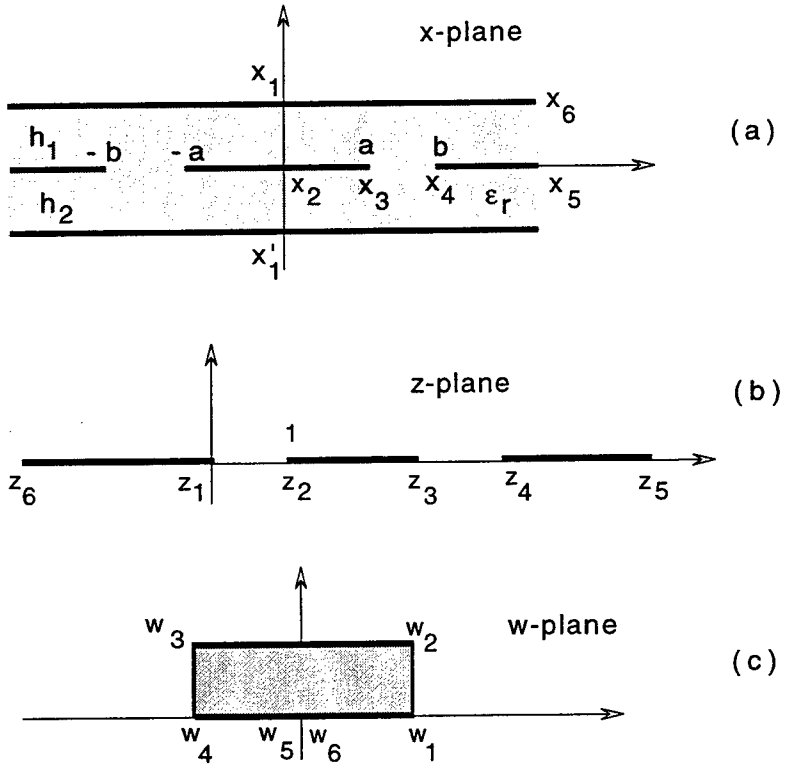

Figure 8. Conformal mapping of the CPW with top and bottom ground planes immersed completely in a dielectric material.

In order to verify the suitability of CPW for the proposed 3D modules, the effect of the upper and lower ground planes on the impedance characteristic of the coplanar waveguide is investigated. The geometry given in Figure 8a represents a typical coplanar waveguide imbedded in a dielectric material sandwiched between two conducting planes separated by distances h_1 and h_2. A quasi-electrostatic solution for the CPW can be found by using conformal transformations [17-19]. The geometry given in Figure 8.a is treated as two separate problems, one for the upper and one for lower parts of the transmission line. Both parts can be transformed into the z-plane through the transformation

$$z = \tanh(\frac{\pi x}{2h})$$

The transformed z-plane coordinates are shown in Figure 8b. The z-plane is then transformed into the w-plane using elliptic transformations (Figure 8c). The resulting characteristic impedance can be written as

$$Z_o = 60\ \pi \frac{1}{\sqrt{\varepsilon_{eff}}\ (\frac{K(k_2)}{K(k'_2)} + \frac{K(k_3)}{K(k'_3)})}\ (\Omega) \qquad (1)$$

Here

$$k_3 = \tanh(\pi a / 2h_1) / \tanh(\pi b / 2h_1)$$

$$k_2 = \tanh(\pi a / 2h_2) / \tanh(\pi b / 2h_2)$$

and $K(k)$ is the Complete Elliptic Integral of the First Kind with argument k and $k' = \sqrt{1 - k^2}$. Since the whole line is imbedded in a dielectric material, the $\varepsilon_{eff}=\varepsilon_r$.

A FORTRAN program is written and the thickness of the dielectric layers between the upper and lower ground planes are taken to be equal. For a gap of 2 μm and width of 20 μm, the variation of the line impedance as a function of the dielectric thickness h is plotted as shown in Figure 9. The impedance is not effected as the dielectric thickness becomes greater than twice the overall separation distance of the two side ground planes. Therefore, for dielectric layer thickness grater than $2(W+2S)$, the CPW parameters will not be critically dependent on the small differences in the thickness of the deposited dielectric layers.

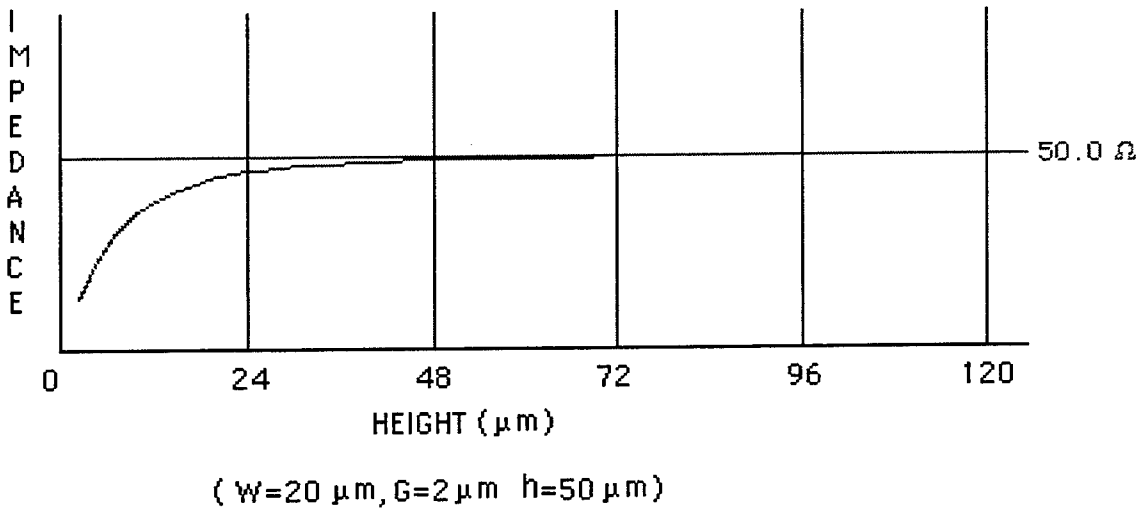

Figure 9. Impedance variation as a function of ground plane to CPW distance h for ε_r=2.5.

In order to show the feasibility of utilizing CPWs as distributed circuit elements, a 3 section equal ripple coupled-line filter is designed and simulated. The line parameters for the odd and even mode impedance of the coupled CPW are calculated beginning from a low pass filter prototype using the insertion loss method. The physical dimensions of the coupled CPW lines are then found from the Line_Calc program of Libra simulation software. These are tabulated in Table II for h=50 μm and ε_r=2.5. The layout of the filter is shown in Figure 9a.

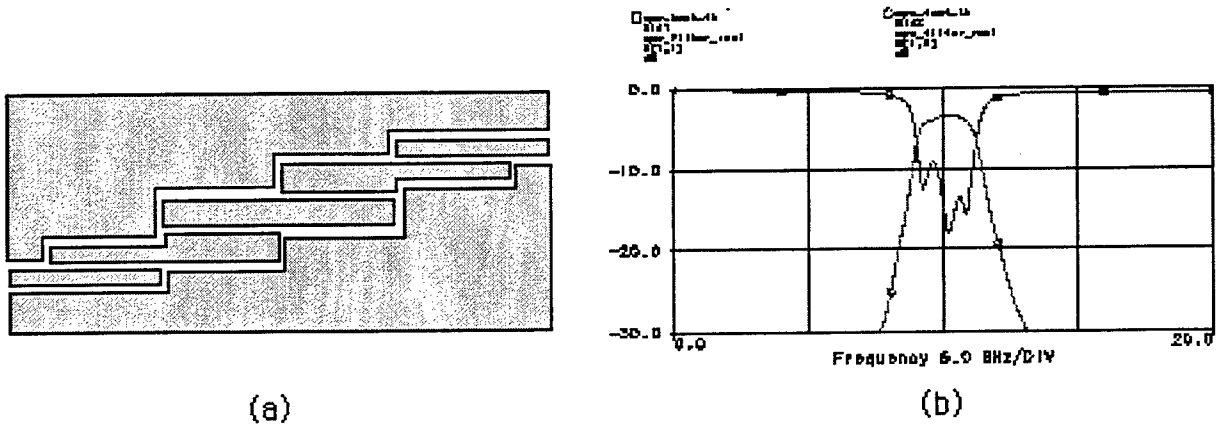

Figure 9. (a) Layout and (b) simulated S parameters of a CPW 3-section coupled equal ripple filter.

Table II. *Parameters of the coupled coplanar waveguide filter*

Section	Z_{odd}	Z_{even}	Gap (C-C)	Width	S (C-G)
1	40.2	88.9	10	292.2	24.6
2	47.3	74.2	10	506.6	118.5
3	47.3	74.2	10	506.6	118.5
4	40.2	88.9	10	292.2	24.6

Using Libra, the circuit is simulated and the resulting $|S_{21}|$ and $|S_{11}|$ are plotted in Figure 9b. It should be noted that coupled CPW line parameters used in the Libra simulations are for a CPW with the upper layer in air.

Dielectric Deposition.

One of the crucial components of a vertically interconnected 3D system is the choice, deposition and processing of the dielectric material. There are many different dielectric materials that are used in the processing of semiconductor devices. Table III lists the properties of some of the dielectric materials used in the implementation of 3D interconnects. The parameters in this table are for a 50 Ω microstrip transmission line. Gold metal is used to calculate the conductor losses.

. Dielectric materials to be used in vertically interconnected microwave and millimeter wave modules should have some stringent mechanical, chemical and electrical properties. These can be summarized as:

a) deposition of uniform and controlled thickness layers

b) adhesion to metal (gold) surface

c) adhesion of metal (gold) on the dielectric

d) low shrinkage during curing

e) compatibility with photoresists

f) prossesable with wet and dry etching techniques

g) maintain its properties over wide range of temperature operation.

Polyimide is one of the widely used dielectric materials in 3D interconnect circuitry. In this work a new dielectric material referred to as 'Sycar' developed by Hercules Inc. Sycar will be used

due to its excellent moisture resistance, electrical properties, ionic purity and ease of handling. It is applied by spin coating and curing at 200° C [17].

Table II. *Properties of dielectric materials used in 3D interconnected modules.*

	BBC	Si)2	Sycar	Polyimide
Deposition Process	Spin coat and bake	CVD	spin coat and bake	spin coat and bake
Dielectric Constant	2.7	4.0	2.6	3.1-3.6
Tan d	0.004	0.03	0.003	0.001
Possible thickness (μm)	26	9	25	2.5-25
Loss/λ_g (dB) dielectric	0.093	0.712	0.070	0.023
Loss/λ_g (dB) conductive	0.812	2.307	0.838	7.327-0.876

It is very important that during the deposition process, the thickness of the dielectric layers should be controlled to provide the desired thickness uniformity. Any variations in the thickness of the layers will prevent successful implementation of the circuit elements especially those of the distributed line elements whose parameters are likely to depend on the dielectric thickness. As has been discussed above, distributed line elements such as CPW are recommended for the implementation of the transmission lines since they are less dependent on the dielectric thickness provided their lateral dimensions are small compared to the thickness of the dielectric material

Mechanical properties of the dielectric material also plays a very important role in the implementation of the 3D interconnects. Shrinkage during processing, stability of the material, adhesion to metals as well as adhesion of metal on the dielectric, pealing strength of the metal on the dielectric are some of the properties that have to thoroughly investigated.

Compatibility of photoresists with the dielectric material and the type of etching process such as wet or dry etching are also major steps in the successful implementation of the 3D

interconnects. It is possible that there may be a need for mechanical surface removal and polishing. Thus the dielectric material should also be robust enough to allow this type of abuse.

Vertical Interconnects

Another major component of a 3D T/R module is signal routing a microwave or millimeter waves from one level to another. In some of the 3D interconnects used in MMIC processing novel coupling schemes between various layers are already used. If a complete T/R module as shown in Figure 1 is to be implemented, several ground planes will separate various circuit levels from each other. Therefore, it will be necessary to couple signal from one layer to the other by means of vertical posts (vias). IF CPWs are used, it is possible that parallel transmission line TEM modes may be also excited in addition to CPW TEM modes. To prevent these unwanted modes, shorting connections between the top and lower ground planes and the side ground planes of the CPW have to be made. These will also require additional vertical posts.

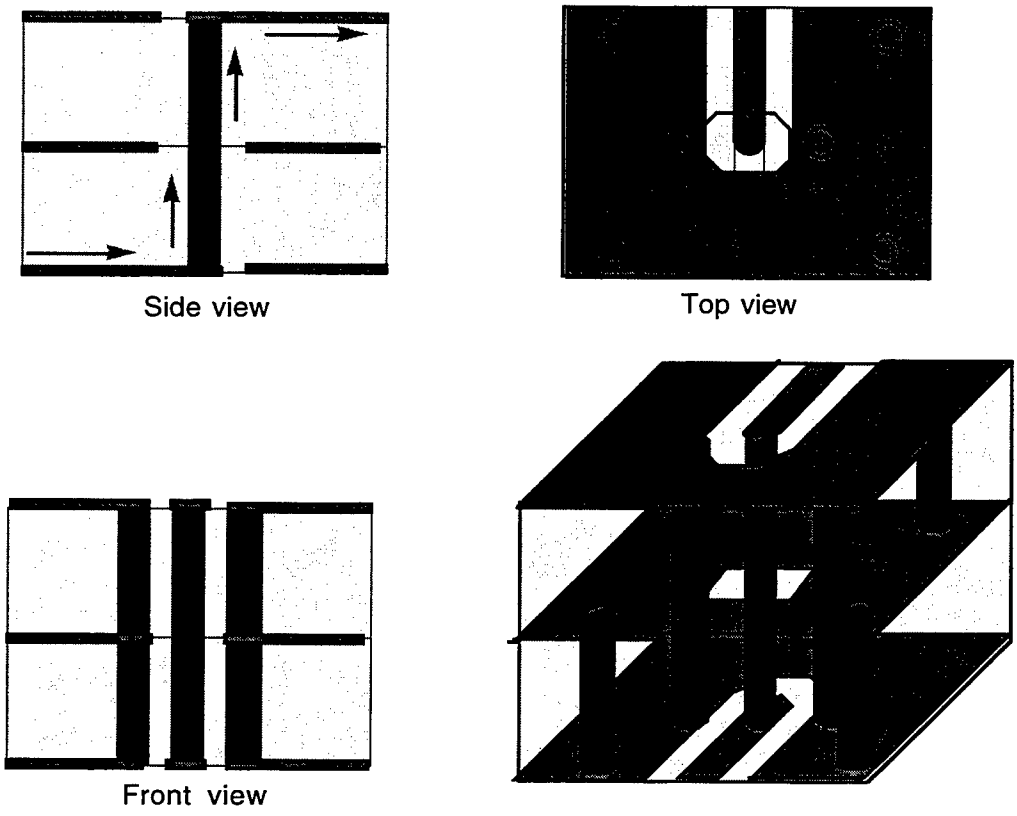

Figure 10. Vertical Interconnecting posts between layers. Additional posts to prevent possible parallel plate TEM modes are also shown.

Figure 10 shows the connecting posts (vias) from one layer to the next. Even though the posts are shown as solid uniform cylinders, their shape may be intentionally modified to decrease the return loss. The cross section of the posts may not be uniform vertically as a result of the processing steps in the electrodeposition of the posts. In either case, extensive simulations and refined processing steps will be necessary to find the best possible coupling configuration. In Figure 10, additional posts connecting the ground planes and the side ground electrodes of the CPWs are also shown.

There are two possible processing procedures in realizing the vertical interconnects. The first one is to initially spin coat and cure the dielectric material to the required thickness. Photoresist is then used to locate the post locations. Through a chemical or wet etching process, the dielectric material is removed from these openings. Then gold metal is electro-deposited in these holes to the height of the dielectric layer. Necessary circuit or ground metal plane is then deposited. The second process involves first the deposition of a ground plane over the dielectric. Using photoresist, the post locations and sizes are exposed. Metal posts are then electrodeposited to the required height. The photo resist is then removed and the dielectric layer is spin coated and cured. This process will form mesas over the posts. Thus mechanical lapping may be required to planarize the upper surface of the dielectric material to the depth of the metal posts. Even though this process seems to be attractive in the overall implementation of the 3D interconnects, required mechanical lapping may not be desirable.

Modeling and Simulations

In order to implement an optimum vertically interconnected 3D T/R module, extensive component and circuit simulations are necessary.

Even though circuit simulation software such as Libra, MDS and Compact are available, they do not include some of the modified circuit topology that will be used with the 3D T/R modules. For example, the CPW model used in Libra is for a CPW with the upper surface exposed to air. In the CPWs that will be used in the 3D modules, the electrodes will be completely immersed in a dielectric material and there will also be the upper and lower ground planes. In the quasistatic solution given in Equation 1 for the CPW, both the dielectric and the presence of the upper and the lower ground planes are included. Since Libra does not have this type of circuit element in the Library, either a new library element has to be added to the simulator, or a new simulation procedure has to be developed. This is also true for the coupled CPWs. The filter

simulations presented in Figure 9 are made using the conventional CPW models that are available in Libra. The response of the filter will be modified by the presence of the upper ground plane as well as complete immersion of the CPW in the dielectric medium. The lack of these elements will generate large errors in the simulation results especially when resonant circuit elements are used in a circuit.

Some of the simulation software also lacks detailed device modeling especially for the power devices [19,20]. Since temperature effects modify the operating characteristics of power devices such as HBTs, new nonlinear models has to be introduced into the software or new device files have to generated and used with SPICE like programs.

There are also many electromagnetic simulators available. Among these, Microwave Lab and Sonnet are the two software which are exclusively dedicated to modeling planar circuit elements. CPWs and the vertical interconnects will be simulated using these software. Even though these programs require large computer memory to run complicated geometry, they provide both electric and magnetic field distributions, current distributions in the conductors as wells the S parameter data at a given frequency. These are essential in the successful implementation of various circuit components especially in finalizing the shapes and locations of the interconnects for minimum return loss.

It can be concluded that successful implementation of 3D T/R modules will require extensive and careful device and circuit modeling and simulations in addition to developing novel processing techniques.

Short Term Goals

The short term goals of this research project is to implement a microwave transmitter with and integral power amplifier, a bandpass filter and a patch antenna similar to the layer structure given in Figure 4. The major emphasis in this phase of the project is to develop a reliable and controllable dielectric deposition process so that necessary number of dielectric layers can be deposited. The power amplifier will be designed to operate either in class B or class AB configuration and will be processed on a SI Si-substrate. The first dielectric layer will be deposited over the substrate followed by the first ground plane. Between the second and third dielectric layers, a 3 section bandpass coupled CPW filter with equal ripple transmission characteristic will be processed. In addition to demonstrating the feasibility of using CPWs, the filter circuitry will prevent the higher harmonics of the amplified signal to reach the patch antenna. Over the fourth dielectric layer, a patch antenna will be processed. In order to optimized the patch antenna radiation

characteristics, the thickness of this final layer may be thickener than the pervious three layers. Vertical interconnects between the power amplifier and the filter and between filter and the patch antenna will be processed and optimized for minimum transmission loss. This circuit essentially includes all the major components and processing steps necessary in implementing the final 3D T/R module. The transmitter will be experimentally tested in detail to verify the various parameters predicted by various modeling and simulations.

The initial phase of the program will be concentrated in the deposition of the dielectric layers. The uniformity as well as the reproducibility of these layers are very important. Thickness control is also a major part of the development program. If a successful dielectric deposition process is developed and the thickness of the deposited layers can be controlled to within a micrometer, the ensuing circuit designs will be relatively simplified.

Long Term Goals

Long term goals of the project will be to implement complete T/R modules and test them in a 2x2 array for their applicability in a conformal phased array antenna system. This challenging task will be achieved through extensive theoretical analysis, simulations and experimental testing of various components and circuit modules.

Conclusion

In this report, a novel vertically interconnected 3D transmit-receive module using an integral patch antenna is proposed for a conformal phased array antenna system. Deposition of uniform dielectric material and vertical interconnects between various circuit modules are a major part of the development program. The feasibility of the proposed program will be demonstrated by a microwave transmitter using a four dielectric layers incorporating a thermally shunted HBT developed at Wright Laboratories. Coplanar waveguides will be incorporated as the transmission medium. Extensive theoretical modeling and simulation will complement the experimental testing of the transmitter modules. Emphasis is placed on designing and implementing low loss vertical interconnects.

References:

[1] I.Toyoda & T. Tokumitsu, "Miniaturized Microwave Circuits on Multilayer MMICs," MWE '93 Microwave Workshop Digest, 335-38(1993).

[2] T.Tokumitsu, K.Nishikawa, K. Kamogawa, I. Toyoda & M. Aikawa," Three Dimensional MMIC Technology for Multifunction Integration and Possible Applications to Masterslice MMIC," IEEE MTT-S Digest, MMW (1996).

[3] I.Toyoda, T. Tokumitsu & M. Aikawa, "Highly Integrated Three-Dimensional MMIC Single-Chip Receiver and Transmitter," IEEE MTT-S Digest (1996).

[4] M.J.Tsai, C.Chen, T.S.Horng & N. Alexopolus, " Multiple arbitrary Shape Via Hole and Air Bride Transitions in Multilayered Structures," III MTT-S Digest, 707-10 (9916).

[5[K.Atsuki & K.Li, "Characteristics and Analysis Methods of Transmission Lines for Multilayer Substrates," MWE '93, Microwave Workshop Digest, 323-26(1993).

[6] H. Mandai, T.Tsuru & M. Kato, "Characteristic of Ceramic Multilayer Substrates and applications for RF Circuits," MWE 93 Microwave Workshop Digest, 327-30(1993).

[7] H.Yabuki & S.Maeda, "Characteristics of Multi-layer Soft Substrates and their applications to RF Circuit Modules," MWE '93 Microwave Workshop Digest, 331-34(1993).

[8] T. Krems, W. Haydl, H. Massler & J. Rudiger, "Millimeter Wave Performance of Chip Interconnections Using Wire Bonding and Flip Chip," IEEE MTT-S Digest (1996).

[9] P.C. Hsu & C.Nguyen, "New Multilayer Planar Transmission Lines for Microwave and Millimeter Wave Integrate Circuits," IEEE Trans. MTT-43, 1809-13(1995).

[10] Giudong Guo, "Active Phased Array Antenna Systems Using Ring Resonator Oscillators," M.S. Thesis, ECECS Dept. University of Cincinnati (June 1995).

[11] K. Kamogawa, T. Tokumitsu & M.Aikawa, "A Novel Microstrip Antenna Using Alumina-ceramic/Polyimide Multilayer Dielectric Substrate," IEEE MTT-S Digest (1096).

[12] P.M.Zavrocky, T.Earles, N.L.Pakrovsky, J.A.Gree & B. Burns, "Fabrication of Vertical Sidewalls by Anisotropic Etching of Silicon (100) Wafers," J.Electrochem. Soc., Vol. 141, 3182-88(1994).

[13] J.M.Kim, W.N.Carr, R.J.Zeto & L. Poli, "Reactive Ion Etching Techniques for Silicon Sidewall Angle Control in Micromachining,", J. Elctrochem. Soc., 1700-05(1992).

[14] R.Dettmer, T.Jenkins, J.Barrette, C.Bozada, G.DeSalvo, J.Ebel, J.Gillespie, C.Havasy, C.Ito, C.Pettiford, T.Quach, J.Sewell, D.Via & R. Anholt, "Effect of Device layout on the Thermal Resistance of High Power Thermally-Shunted Heterojunction Bipolar Transistors,' IEEE MTT-S Digest (1996).

KINETIC STUDIES OF THE THERMAL DECOMPOSITION OF DEMNUM AND X-1P USING THE SYSTEM FOR THERMAL DIAGNOSTIC STUDIES (STDS)

Dennis R. Flentge
Professor
Department of Science & Mathematics

Cedarville College
P. O. Box 601
Cedarville, OH 45314-0601

Final Report for:
Summer Faculty Research Program
Aero Propulsion and Power Directorate
Wright Laboratory

Sponsored by:
Air Force Office of Scientific Research
Bolling Air Force Base, DC

and

Aero Propulsion and Power Directorate
Wright Laboratory

September 1996

KINETIC STUDIES OF THE THERMAL DECOMPOSITION OF DEMNUM AND X-1P USING THE SYSTEM FOR THERMAL DIAGNOSTIC STUDIES (STDS)

Dennis R. Flentge
Professor
Department of Science and Mathematics
Cedarville College

Abstract

The System for Thermal Diagnostic Studies (STDS) links a thermal reactor cell directly to a GC/MS for the examination of gas phase behavior of materials as a function of temperature, time, and atmosphere. Demnum, a perfluoropolyalkyl ether, has been studied as a high temperature lubricant while X-1P, a cyclotriphosphazene, has shown potential as a vapor phase lubricant. The decomposition of Demnum S-65 was studied in the temperature range of 300°C to 750°C and X-1P was studied between 300°C and 625°C. Rate constants for the decomposition were determined for each substance.

KINETIC STUDIES OF THE THERMAL DECOMPOSITION OF DEMNUM AND X-1P USING THE SYSTEM FOR THERMAL DIAGNOSTIC STUDIES (STDS)

Dennis R. Flentge

Introduction

As the demands for increased efficiency and greater power are made on turbine engines, the need for lubricants that function well at higher temperatures has grown. In addition to searching for liquids that are stable at high temperatures, scientists and engineers have been examining materials that work as vapor phase lubricants. Demnum, a perfluoropolyalkyl ether, has been studied as a high temperature liquid lubricant while the cyclotriphosphazene X-1P shows potential as a vapor phase lubricant (*1, 2*). A knowledge of the decomposition, reaction rate constants, and activation energies of these compounds should contribute to the understanding of the processes occurring at elevated temperatures.

Methodology

The System for Thermal Diagnostic Studies (STDS) was designed by Rubey of the University of Dayton Research Institute to study incineration of hazardous wastes (*3, 4*). Since the STDS provides control of temperature, reactive atmosphere, residence time of the reactant in the reaction vessel, pressure, and degree of mixing, it is also an excellent tool to study the kinetics of vapor phase lubricant samples (*5*).

The STDS contains four integrated components. First, there is a control console that regulates the temperature of the reactor cell and the flow of the reactor gas through it. The second component, a thermal reaction compartment, is a Hewlett-Packard model 5890A gas chromatograph modified so that it can house the quartz reactor cell and the high temperature furnace. An unmodified model 5890A gas chromatograph is the third component. The thermal reaction products and unreacted parent material are swept into this chamber and are deposited near the beginning of the chromatographic column. A Hewlett-Packard model 5970B mass spectrometer is the last component in the system. Materials separated by the gas chromatograph are analyzed by the spectrometer.

Temperature, residence time of the parent material in the reactor, and the atmosphere in the reactor were components of interest in this study. The injector leading to the reactor cell was kept at 225°C and the oven surrounding the reactor cell and furnace was at 300°C. The temperature of the reactor cell, controlled by the furnace, was set at values ranging from 300°C to 750°C. Helium was the reactor gas for Demnum S-65 while air was used for X-1P. Residence time was established by the flow rate of the reactor gas.

A 0.1 microliter sample of the neat liquid was injected into the reaction compartment and the reactor gas carried the vaporized sample into the reactor cell. The flow was maintained for ten (10) minutes to insure that the entire sample had time to be carried through the reactor and that all of the products and

unreacted parent material had been transported to the beginning of the gas chromatographic column. Then the reactor gas flow was reduced and the helium flow through the chromatographic column was increased. The column was flushed two minutes to carry all of the reactor gas through the gas chromatograph and past the detectors of the mass spectrometer. Then the program controlling the temperature increase of the gas chromatograph and the detection of particles in the mass spectrometer was started. The temperature was raised from 50°C to 300°C at a rate of 5°/minute and was held at 300°C for 15 minutes for the Demnum S-65 samples and for 10 minutes for the X-1P samples.

Reaction rates were followed by measuring the areas of peaks associated with fragments of the molecules under study or of their decomposition products. Parent molecules were not observed because their molar masses are above the range detected by the mass spectrometer (35-800 amu).

The mass spectrometer's sensitivity varied from day to day. A sample of the parent material injected into the reactor set at 300°C served as the standard for each day's data. All data collected on that day were adjusted using the ratio of the total peak area of the daily standard to the peak area of a sample measured at the beginning of the data collection for a substance.

The chromatographic column, which is connected directly to the mass spectrometer, draws gas into itself at a rate that is independent of the flow rate of the reactor gas. Samples of 1% dodecane dissolved in hexane were injected at

several different reactor gas flow rates. A plot of the log of the peak area versus flow rate gave a relationship used to correct the data for the effect of flow rate.

Demnum S-65, a perfluoropolyalkyl ether, is a blend of oligimers that has an average molecular weight of about 4500. Its formula is $F\text{-}(CF_2CF_2CF_2\text{-}O)_n\text{-}CF_2CF_3$. The average value of n is 26 but its value may range from less than 15 to more than 40. As a high temperature lubricant candidate, its thermal decomposition temperature and the products formed in the decomposition are important.

X-1P is also a blend of several molecules with the general formula

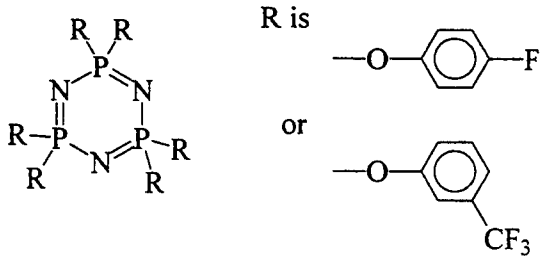

$N_3P_3R_mR'_{6-m}$, where m takes values from 0 to 6. R is the 4-fluorophenoxy group and R' is the 3-trifluoromethylphenoxy group. The most abundant molecule in the mixture has the molecular formula $N_3P_3R_2R'_4$. The mixture contains a set of molecules with formulas that have 100% R groups ($N_3P_3R_6$) to those with 100% R' groups ($N_3P_3R'_6$).

Results

Demnum S-65

Figure 1 shows the spectrum of Demnum S-65 passed through the reactor cell at 300°C. The complex spectrum is a consequence of the wide range of oligimers present in the mixture. The primary mass number that accounts for the spectrum corresponds to a C_3F_7 fragment which separates from the parent molecule. The total area associated with this peak was the basis for the evaluation of kinetic data.

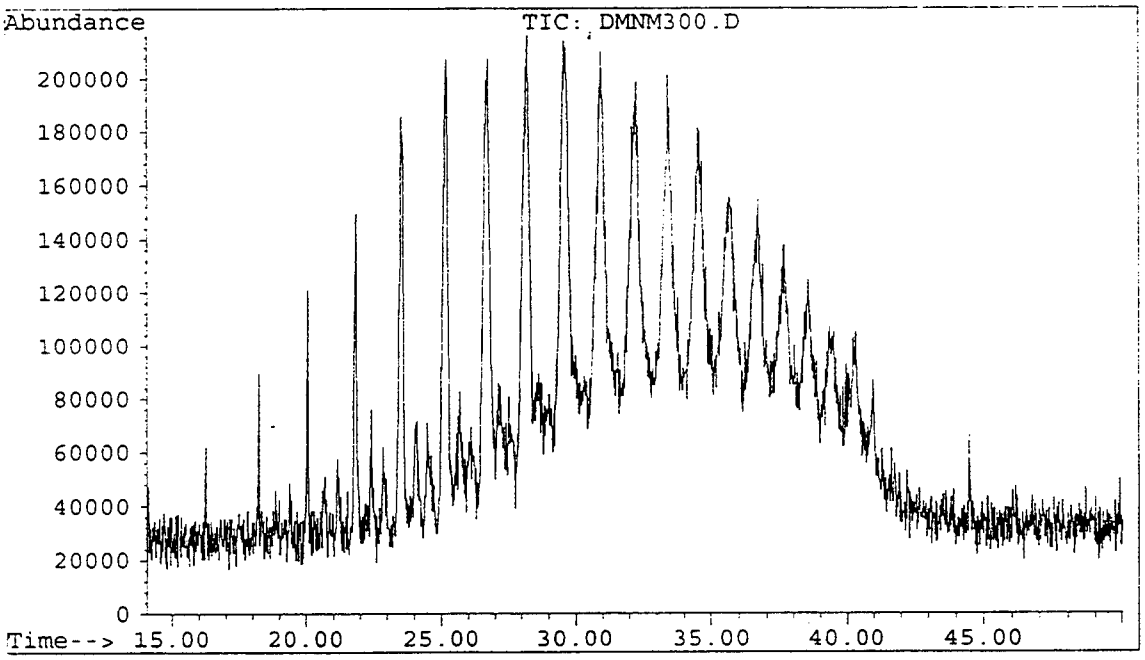

Figure 1

Figure 2 contains the spectrum of Demnum S-65 passed through the reactor cell at 750°C. The rate constant for the thermal decomposition reaction at

750°C was determined by plotting the total peak area versus residence time. Figure 3 shows a plot of the data that yields a rate constant of 1.59 s^{-1}. One goal of this project was to measure the activation energy for this reaction. However, a shift in the needs of the laboratory led to the kinetic study of X-1P.

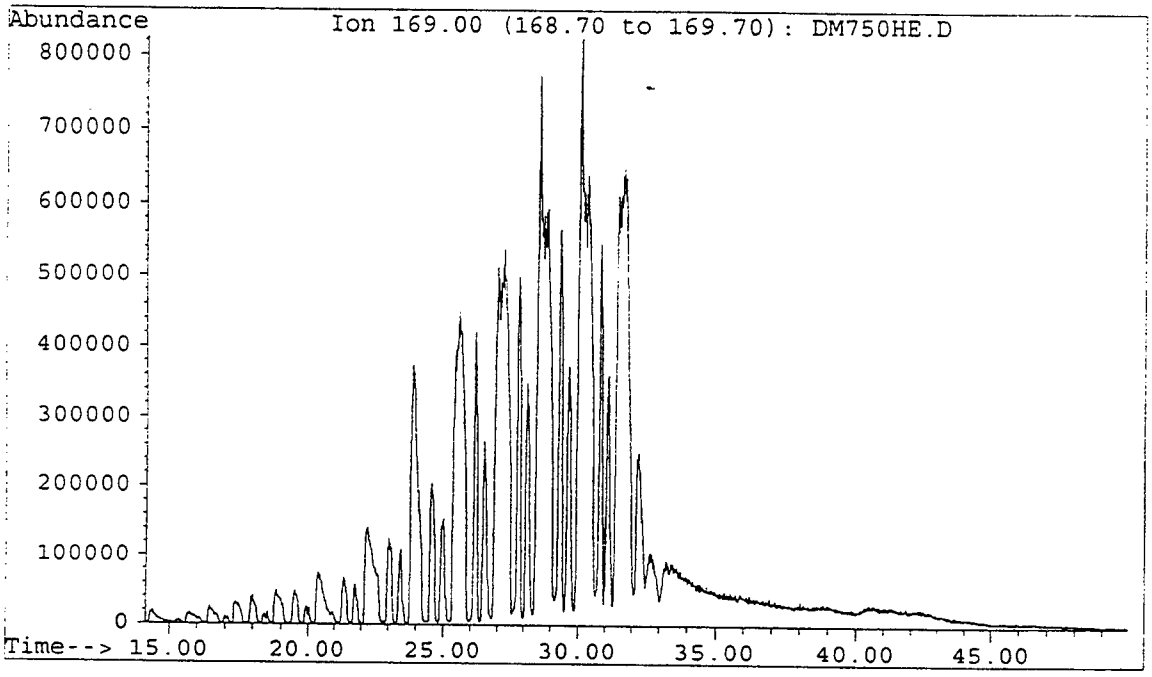

Figure 2

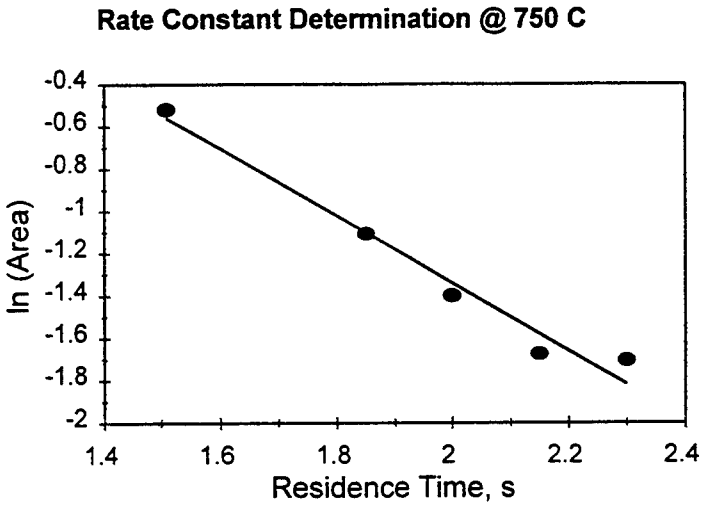

Figure 3

X-1P

Figure 4 shows the spectrum of X-1P passed through the reactor cell at 300°C. These peaks represent the contribution of 6 fragments from the X-1P molecule. Samples heated to higher temperatures showed the same spectral features. Figure 5 shows the plot of peak area versus temperature. The shape of the curve shows that a reaction is occurring at temperatures below 500°C.

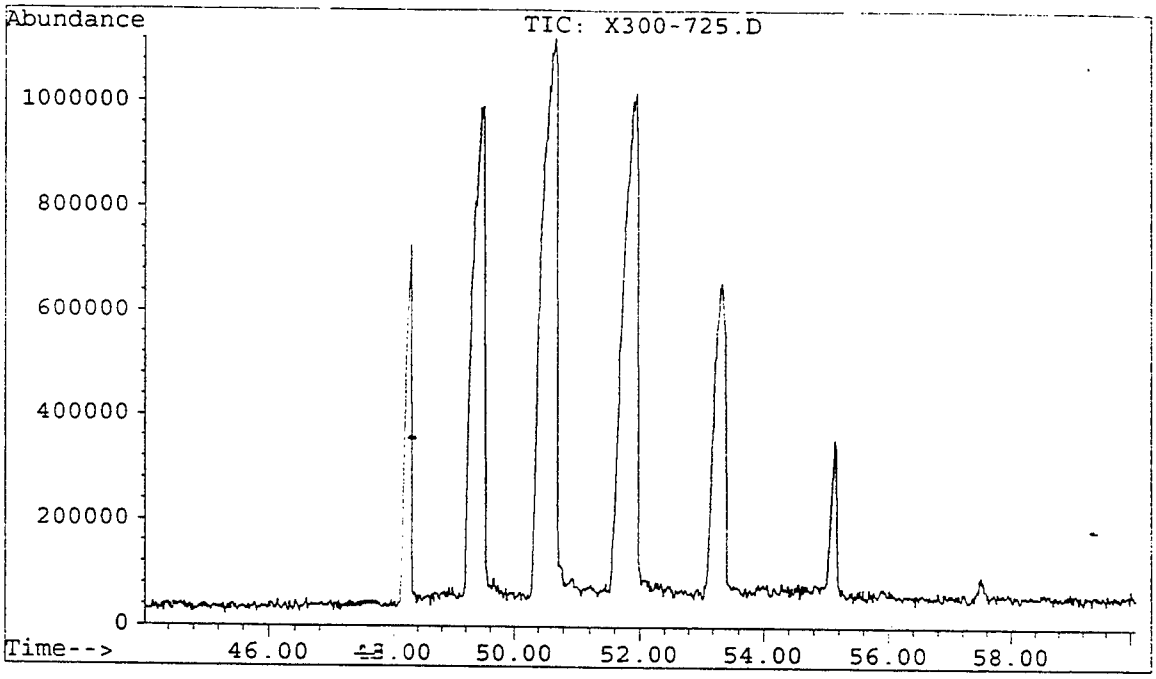

Figure 4

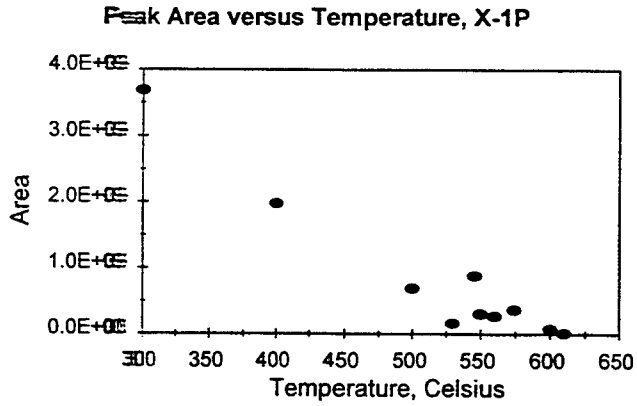

Figure 5

Rate constant studies were done at 560°C and 545°C. Figures 6 and 7 contain the data gathered in those studies. Examination of the plots shows a wide scatter in the data points. This is due primarily to the decline in the performance

of the mass spectrometer during August. Efforts made to compensate for this problem were unsuccessful.

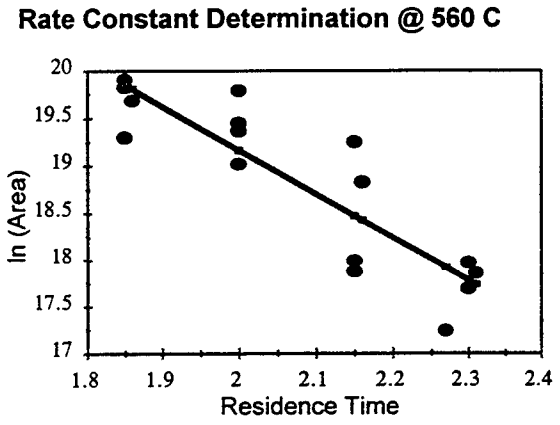

Figure 6

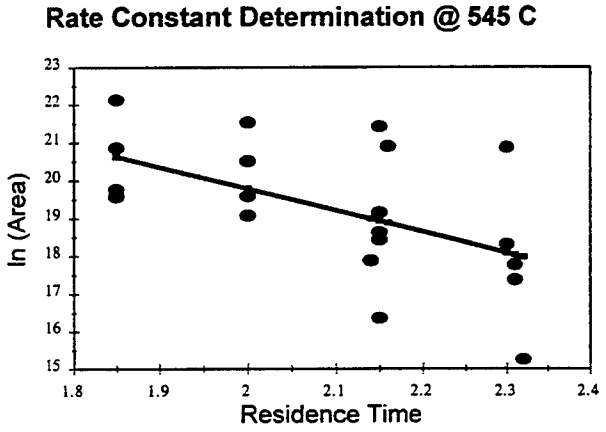

Figure 7

Conclusions and Recommendations

The STDS shows excellent potential as an instrument to examine the behavior of vapor phase lubricants. Results from the study of Demnum S-65 show that high quality kinetic data can be obtained from the system. In addition to the ability to separate and analyze products that can be trapped on a column at 50°C, it can also retain molecules of lower molar mass using a cryostatic trap. This allows one to examine the entire range of reaction products from the thermal decomposition of the lubricants.

The next step in this study is to measure rate constants for X-1P at temperatures below 500°C and determine the activation energy of the reaction. The cryostatic trap could be used to identify low molar mass products of the decomposition.

Additional kinetic studies on Demnum S-65 can be completed and activation energies calculated. Analysis of low molar mass components of the decomposition may identify corrosive products that cause rapid failure in systems using Demnum as a lubricant.

References

(*1*) Forster, Nelson H. and Trivedi, Hitesh K, "Rolling Contact Testing of Vapor Phase Lubricants: Part I--Material Evaluation," accepted for publication, **Tribology Transactions**.

(*2*) Forster, Nelson H. and Trivedi, Hitesh K, "Rolling Contact Testing of Vapor Phase Lubricants: Part II--System Performance Evaluation," accepted for publication, **Tribology Transactions**.

(*3*) Striebich, R. C. and Rubey, W. A., "A System for Thermal Diagnostic Studies," **American Laboratory**, January 1990.

(*4*) Rubey, Wayne A. and Grant, Richard A., "Design Aspects of a Modular Instrumentation System for Thermal Diagnostic Studies," **Rev. Sci. Instrum.**, 59(2), February 1988.

(*5*) Wright, Robert L., "The Gas Phase Decomposition and Trimethylolpropane Phosphate Neurotoxin Formation Potential of Tricresyl and t-Butylphenyl Phosphates," Technical Report WL-TR-96-2004, 1996.

NOVEL APPROACH FOR THE COMPRESSIVE STRENGTH IMPROVEMENT OF RIGID ROD POLYMERS

Himansu M. Gajiwala
Associate Professor
Department of Chemistry

Tuskegee University
Tuskegee, AL 36088.

Final Report for:
Summer Faculty Research Program
Wright Laboratory

Sponsored by:
Air Force Office of Scientific Research
Bolling Air Force Base, DC

and

Wright Laboratories

August 1996.

NOVEL APPROACH FOR THE COMPRESSIVE STRENGTH IMPROVEMENT OF RIGID ROD POLYMERS

Himansu M. Gajiwala
Associate Professor
Department of Chemistry
Tuskegee University

Abstract

Rigid rod polymers like PBZT, PBZO and PBZI are known for their excellent thermal stability, high modulus and high strength. However, one of the major drawback of these polymers is their low compressive strength. To overcome this problem a novel approach was taken and the new monomer was synthesized. This monomer was synthesized by reacting 4,4'-dibromo-2,2'-bis(4-methylbenzoxazolyl)biphenyl with 2-amino-p-cresol in PPSE, o-DCB mixture at an elevated temperature. The bromide functionality was subsequently replaced by cyano group and then hydrolysed to the carboxylic acid. Computer simulation on this monomer has indicated the non-planar geometry. The bulkiness and the thermal stability of the side group is indicative of the non planarity of the biphenyl rings in thermally treated polymers. This will result in 3-D cross-linked polymer of high compressive strength.

NOVEL APPROACH FOR THE COMPRESSIVE STRENGTH IMPROVEMENT OF RIGID ROD POLYMERS

Himansu M. Gajiwala

INTRODUCTION

The rigid-rod polybenzobisazole polymers that have received the greatest attention in the literature are poly([benzo(1,2-d:4,5d')bisthiazole-2,6-diyl]-1,4-phenylene) (PBZT), poly([benzo(1,2-d:5,4-d')bisoxazole-2,6-diyl]-1,4-phenylene) (PBZO) and poly([1,7-dihydrobenzo(1,2-d:4,5-d')bisimidazole-2,6-diyl]-1,4-phenylene) (PBZI) systems.

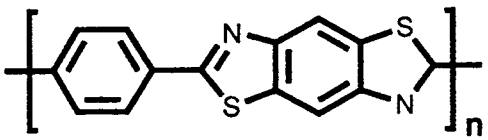

PBZT

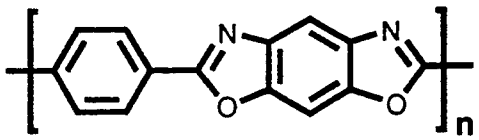

PBZO

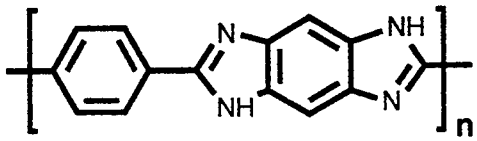

PBZI

All these polymers have been prepared by the polycondensation reactions in polyphosphoric acid. With the exception of PBZI, these polymers can be obtained as a lyotropic liquid crystalline solution. All these rigid rod polymers are soluble in strong acids like methane sulphonic acid (MSA), chlorosulphonic acid (CSA), sulfuric acid, etc. For all these polymers, as their glass transition temperature is higher than their decomposition temperature, they can be processed only from the solution. Processing of

these rigid rod polymer solutions from the liquid crystalline state produces very high modulus, high strength fibers and films. For PBZT and PBZO polymers, modulus values of 300GPa with tenacity values of 3.0GPa have been reported on wet-spun fibers after heat treatment. However, one of the major drawback of these polymers is their low compressive strength. For example, the synthetic rigid organic polymer like Kevlar 49 has the compressive strength of 365MPa whereas PBZT and PBZO have the compressive strengths of 270 and 200MPa respectively.

The low values of compressive strengths, in case of PBZT and PBZO polymers can be attributed to their structural features. Morphology studies of PBZT and PBZO fibers spun from liquid crystalline solutions have shown that fibers are the network of micro fibrils with no transverse coupling between the fibrils. This structural feature results in microfibrilar buckling when compressed, resulting into the low compressive strength. In the case of Kevlar, larger force is required to observe such buckling phenomena as fibrils are interconnected by weak hydrogen bonds. However, PAN based C-fibers show the highest compressive strength values because of cross-linking and/or interwining of the ribbon like chain structures. Based on this correlation, it can be generalized that if the fibers have the interconnected network than higher value of the compressive strength can be obtained.

Cross-linking is one of the approach that has been attempted in past to improve the compressive properties of PBZT and PBZO fibers. Cross-linking was achieved by synthesizing the monomers containing thermally labile methyl and/or cyclobutane rings. Copolymers were synthesized using these modified as well as the conventional monomers. Resulting copolymers were processed initially by the standard technique using the lyotropic liquid crystalline dope. The fibers/films thus obtained were then heat treated to decompose the thermally labile groups (methyl or cyclobutane ring) and to

generate highly reactive free radicals. These free radicals reacted with each other and generated a cross-linked system. When such cross-linked systems were tested for compressive strength, insignificant change in the compressive strength was observed. Morphology studies on these modified cross-linked copolymeric systems have revealed at least three reasons for the observed experimental findings:

1. Intramolecular cross-linking of the system in place of intermolecular cross linking:

This happens when the generated free radicals react intramolecularly instead of intermolecular reaction. For example, if 2,2'-dimethyl biphenyl moiety is used for the generation of the free radicals, then there is a chance that the non-planar dimethylbiphenyl moiety will become planar system as shown below when the free radicals are generated.

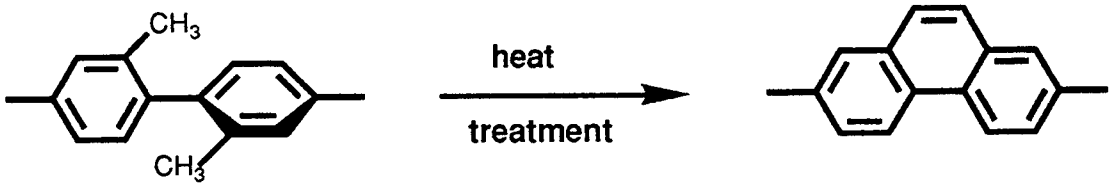

Non-planar **Planar**

If this type of reaction occurs than the system will not show intermolecular cross-linking and the resulting polymer will not exhibit improved compressive strength.

2. Two dimensional cross-linking instead of three dimensional cross-linking:

Sometimes the polymers containing non-planar monomeric systems containing the thermally labile groups, processed from the liquid crystalline state, react

intermolecularly when heated. However, thermodynamically, the resulting network is two dimensional rather than three dimensional. This also results in an insignificant change in the compressive strength of the polymer.

3. Intrafibrillar cross linking in place of interfibrillar cross linking:

Many times it has been observed that when polymers containing thermally labile groups are heat treated than the generated highly reactive free radicals react with the system that is in close proximity and results in the cross-linking within the fibrils. This happens when methyl groups are directly attached to the polymer backbone. In these cases, the distance of the free radical from the polymer backbone is not large enough to create the cross-linking between the fibrils. On the contrary, this type of system favors the intrafibrilar cross linking. Thus, once again, under the compressive loading, individual fibrils will take the load and will result in the buckling failure with insignificant improvement in the compressive failure load.

OBJECTIVE

The long term objective of the present research was to design new PBZT and PBZO type of the polymers having improved compressive strength. The **Reaction Schemes I and II** were designed to meet the above mentioned objective.

RATIONALE

The aromatic rings in the proposed biphenyl monomer are locked into one particular conformation due to the bulky benzoxazole pendant rings. Computer simulation results have indicated that the dihedral angle between the two aromatic rings of biphenyl is ~63° and the distance of the methyl groups on the pendant benzoxazole rings from the biphenyl backbone is 7.37°A. This indicates that the methyl groups are far away from the

polymer backbone. In addition, experimentally it has been found that the distance between two fibrils in case of conventional PBZT and PBZO is of the order of 4 °A. When methyl groups are directly attached to the PBZT or PBZO backbone, the methyl groups are at the distance of ~2°A from the backbone. This results in the intrafibrillar cross linking that does not improve the compressive strength significantly. In the proposed system, as the methyl groups are farther away from the backbone (7.37°A instead of ~2°A), this will help them to cross-link with the other methyl groups of the polymeric chains in the different fibril. This will help the interfibrillar cross-linking imparting better compressive strength to the resultant polymers. In addition, simulation results have indicated that the methyl groups are in two different planes and are in a somewhat locked conformation because of the bulkiness of the benzoxazole pendant group. This will result in three dimensional type of cross linking that in turn will further improve the compressive strength of the polymer.

EXPERIMENTAL

4,4'-dibromodiphenic acid (Daychem Inc.) was used after recrystallization water. 2- amino-p-cresol (Aldrich) was also used after recrystallization from water. Diphenic acid(Aldrich) and 2-aminophenol(Aldrich), 1,2-dichlorobenzene (O-DCB, anhydrous, Aldrich), Trimethylsilyl polyphosphate (PPSE, Fluka Chemicals) were used as received.

4,4' - dibromo-2,2' bis(4-methylbenzoxazolyl)biphenyl

To the 33mL mixture of PPSE:O-DCB (14mL:19mL), 2gms (5mmole) of 4,4'-dibromodiphenic acid and 1.23 gms (10 mmoles) of 2-amino-p-cresol were added. The solution temperature was raised to 140°C in one hour with continuous stirring under nitrogen atmosphere. The solution temperature was maintained at 140°C for the total of 16 hrs and then maintained at 160°C for an additional 20 hours. The solution was then

cooled to room temperature and added to 10% sodium bicarbonate solution. The organic layer is then extracted using ethyl acetate. Ethyl acetate was then roto evaporated and the product was precipitated as light yellow crystals by the addition of hexane. Required product was obtained in 10% yield.

Melting point: 166 - 168°C

IR: Absence of carbonyl and hydroxyl stretch.

^1H NMR in $CDCl_3$: 8.42ppm(d, J 2.04Hz), 7.63 ppm(d of d, J 8.19Hz and 2.1Hz), 7.35ppm (s), 7.18ppm (d, J 8.19Hz), 7.10ppm (d, J 8.28Hz), 7.02ppm (d of d, J 8.4Hz and 1.56Hz), 2.39ppm (s)

Mass spectrum: EIMS technique, 572, 574, 576

4,4' - dicyano-2,2' bis(4-methylbenzoxazolyl)biphenyl

A mixture of 4,4' - dibromo-2,2' bis(4-methylbenzoxazolyl)biphenyl (0.32gms), cuprous cyanide (0.3gms) and dry N-methyl-2-pyrrolidinone (3 ml) was heated under nitrogen for 22 hrs at 170°C. The reaction mixture was cooled to 60°C and poured into 100ml of 0.1%(w/v) sodium cyanide solution and stirred at 60°C for 1hr. The resulting precipitate was filtered and washed with water and dried to get 0.32gms of the required product.

IR: Showed presence of cyano group at 2139 cm^{-1}.

Mass spectrum: EIMS technique, 466, 334, 77

4,4' - dicarboxy-2,2' bis(4-methylbenzoxazolyl)biphenyl

A solution of 0.3gms of 4,4' - dibromo-2,2' bis(4-methylbenzoxazolyl)biphenyl, 2.5gms of 85% phosphoric acid and 0.99gms of phosphorous pentoxide was refluxed at 173°C for 24hrs. The solution was cooled to room temperature and precipitated in 450ml of distilled water. The precipitate thus obtained was filtered, washed with water and

dried. The product was dissolved in 10% potassium hydroxide and the solution was acidified to pH 2 using hydrochloric acid to get green color precipitate. The product was filtered, washed with water and dried.

IR: Absence of cyano group peak and the presence of peak at 1710cm^{-1} for the carbonyl group stretch along with hydroxyl group broad peak in the range of 2400-3500cm^{-1}.
Mass spectrum: EIMS technique, 504, 459, 372, 77

4,4'-biphenyldicarbonyl chloride

Solution mixture of 25gms of 4,4'-biphenyldicarboxylic acid, 150ml of thionyl chloride and four drops of dimethylformamide was refluxed for 24 hrs. Excess thionyl chloride was distilled off using 70 ml of toluene as the chaser solvent. Toluene was distilled till solution started forming the crystals. The solution was then cooled in ice and the clear toluene solution was decanted. The crystals were once again recrystallized using 200ml of fresh toluene. HPLC of the crystals indicated only one component as expected.

4,4'-dibenzoxazolebiphenyl (Model compound synthesis)

Solution of 4,4'-biphenyldicarbonyl chloride (1gm) and 2-aminophenol (0.7819 gms) in 83%polyphosphoric acid (12.4 gms) was swirled at 160°C under nitrogen atmosphere for 3 days. The solution was then precipitated on ice and filtered and washed with ~1000ml of hot water and finally with acetone and dried to get yellowish white granular material in 75% yield.
Melting point: (crude sample) 350 -365°C
IR: 1684cm^{-1}, 1605cm^{-1}, 1293cm^{-1},
Mass spectrum: EIMS technique - 388, 296

Polybenzoxazole from 4, 4'-biphenyldicarbonyl chloride (Model polymer synthesis)

Measured amounts of 4,4'biphenyldicarbonyl chloride (2gms) was mixed with diaminodithiophenol (1.7569gms) in 77% polyphosphoric acid (16.2264gms). The solution was slowly swirled under nitrogen purge at 60°C for 2 days. Additional amount of phosphorous pentoxide (5.7269 gms) was added to make 83% polyphosphoric acid. The solution temperature was then raised to 100°C and swirled under nitrogen overnight. Solution temperature was then raised to 197°C over a period of 2 days and maintained at that temperature for an additional 2 days. The solution was then cooled and precipitated on 700 ml of ice cold water. The precipitate was filtered, washed and dried to get 3.1 gms of the light green color product. The precipitate was further washed in soxhelt extractor for an additional two days to get 2.5 gms of the green color product.

Discussion

In order to synthesize 4,4' - dibromo-2,2' bis(4-methylbenzoxazolyl)biphenyl strong but neutral dehydrating agent PPSE was selected to prevent the possible intramolecular dehydration reaction. However, with this reaction, the yield of the required product was very low and to get very pure product column chromatography was essential. The NMR spectrum as well as IR and mass spectroscopy confirmed that the required product was obtained by this technique. To improve the yield, several experiments were carried out by varying several different reaction parameters. However, significant improvement in the yield was not observed. To overcome this, it was decided to use polyphosphoric acid as the dehydrating agent. When polyphosphoric acid was used, following reaction product was obtained in nearly quantitative yield.

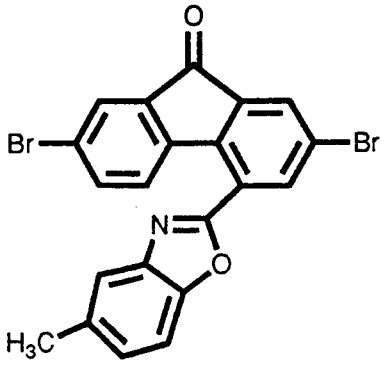

Structure of this yellowish green color crude product as well as the bright yellow colored NMP recrystallized product was confirmed by IR and Mass spectrum. Mass spectrum showed peaks at 467, 469 and 471 corresponding to M^+. IR shows a strong carbonyl group peak at 1722cm^{-1}. The recrystallized product had the melting point of 272 - 272.5°C. These results indicated that the required product can only be obtained by the use of PPSE.

The product obtained by the use of PPSE was then treated with cuprous cyanide to replace the bromine with cyano group. IR and mass spectroscopy confirmed the structure of the expected dicyano product. The dicyano product was then hydrolyzed using phosphoric acid. Once again the structure of the required product was confirmed by IR and mass spectroscopy.

In order to study the polymer made out of this novel system, it was essential to study the basic polymer system made out of 4.4'-biphenyl dicarboxylic acid. To judge the reactivity of this compound, it was decided to make the model compound using 4,4'-biphenyl dicarbonyl chloride and 2-aminophenol. The reaction was carried out as

indicated in the experimental section and the results indicated that the reaction is feasible. The structure of the product was confirmed by IR and Mass spectroscopy.

The basic polymeric system was tried using 4,4'-biphenyldicarbonyl chloride and diaminodithiophenol. The reaction product indicated that the reaction is feasible and further characterization study is needed to confirm the structure as well as the properties of the resultant polymer.

Thus, these reaction sequences indicated that the new type of dicarboxylic acid can be synthesized and it can be utilized for the synthesis of novel polybenzoxazole and polybenzthiazole that can exhibit better compressive strength.

Reaction Scheme 1: Monomer synthesis

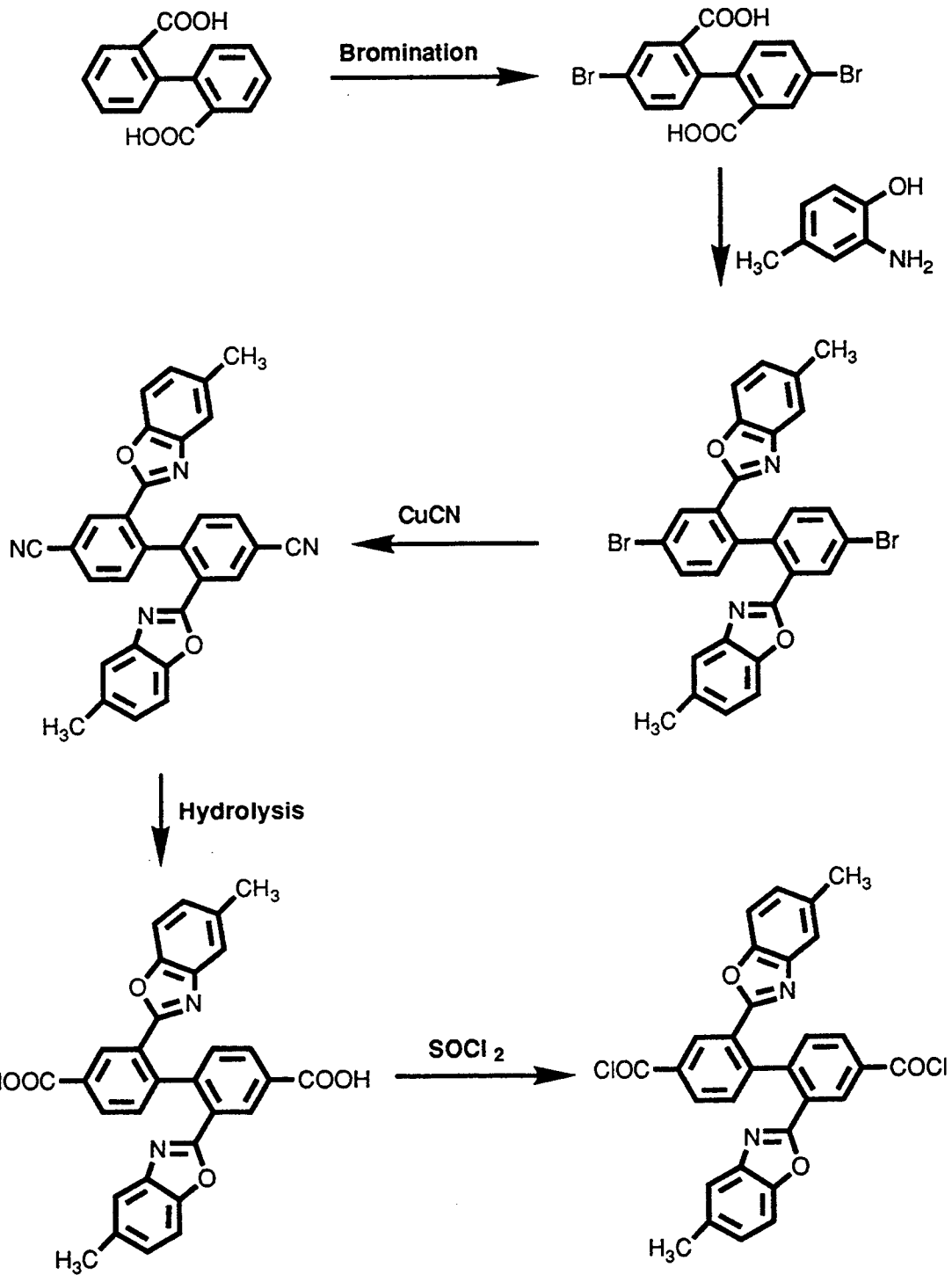

Reaction Scheme 2: Polymerization reactions

1.

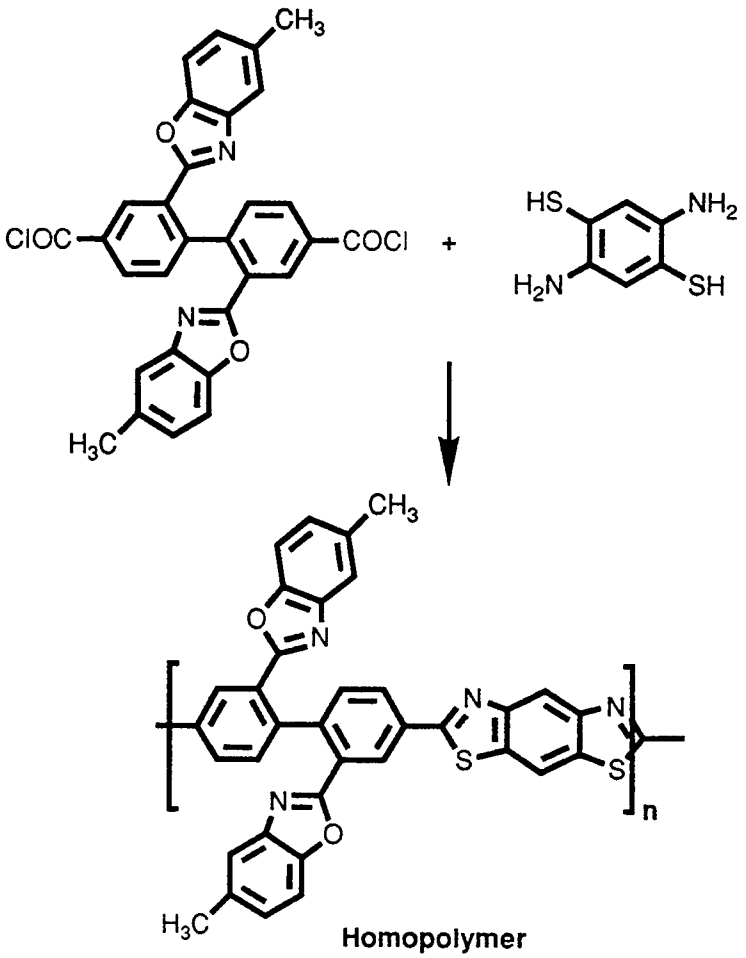

Homopolymer

2. Copolymer using terephthaloyl chloride as the third monomer.

3. Homo and Copolymer of benzoxazole type.

4. Homopolymers using 4,4'-biphenyl dicarboxylic acid.

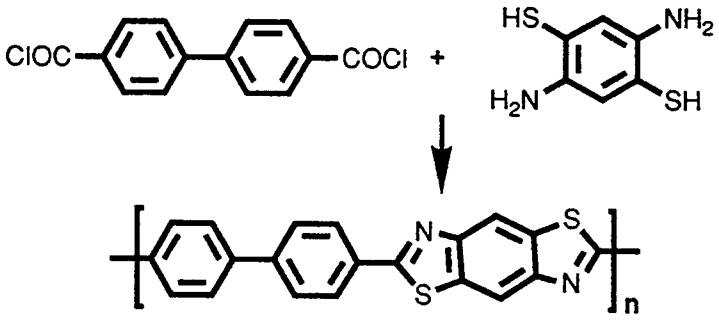

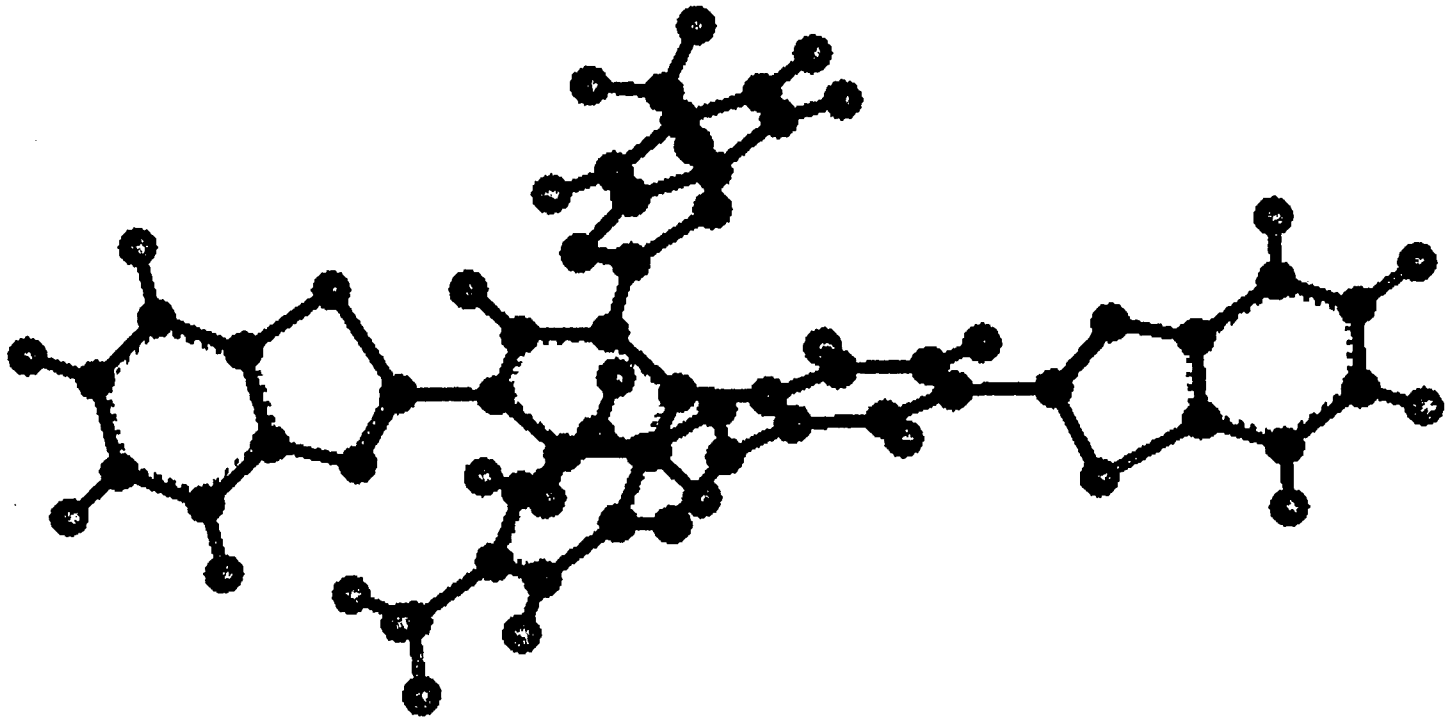

Figure 1: Computer simulation of the model compound showing non-planar biphenyl unit.

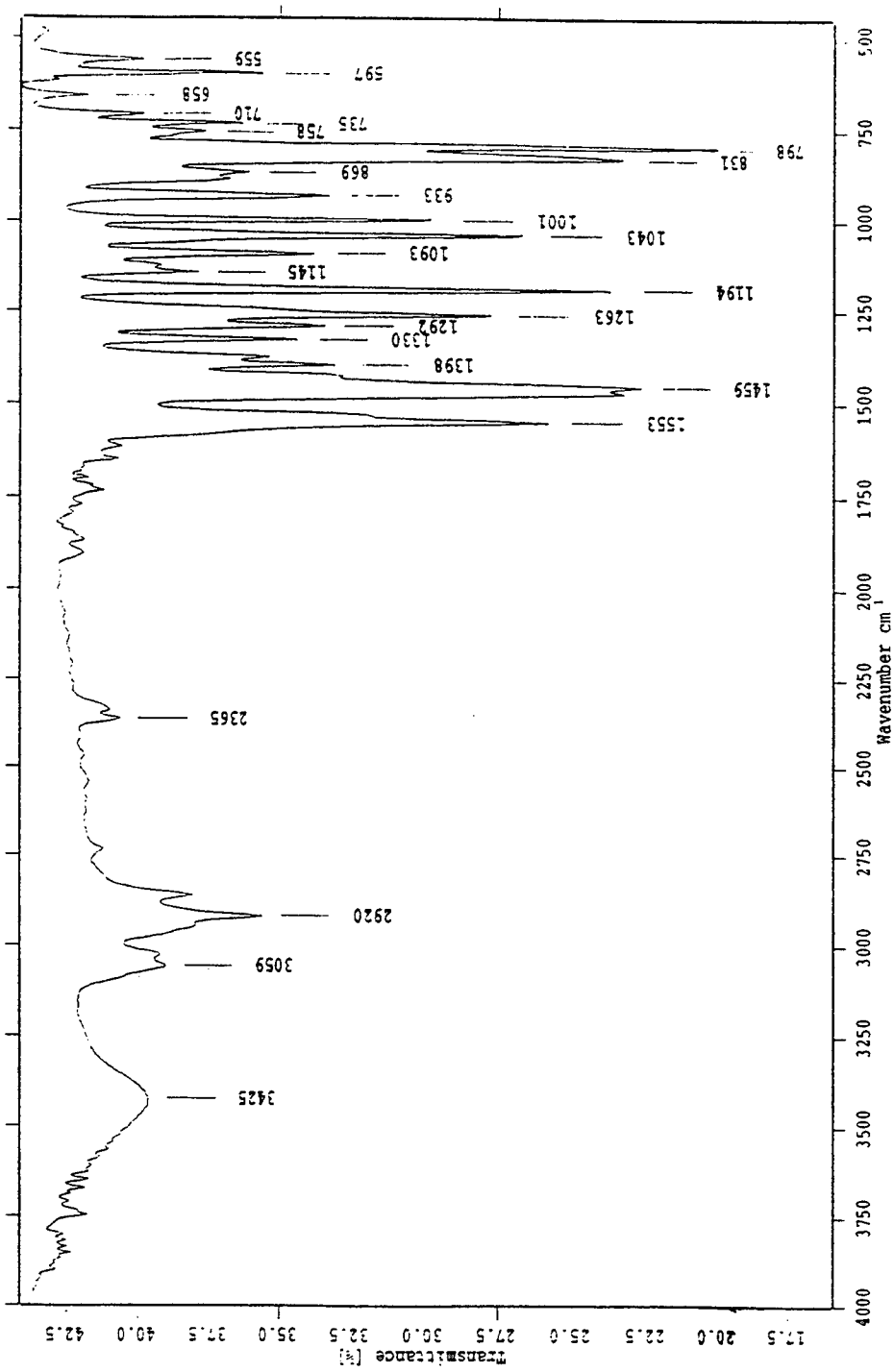

Figure 2: FTIR spectrum of 4,4'-dibromo-2,2'-bis(4-methylbenzoxazolyl)biphenyl

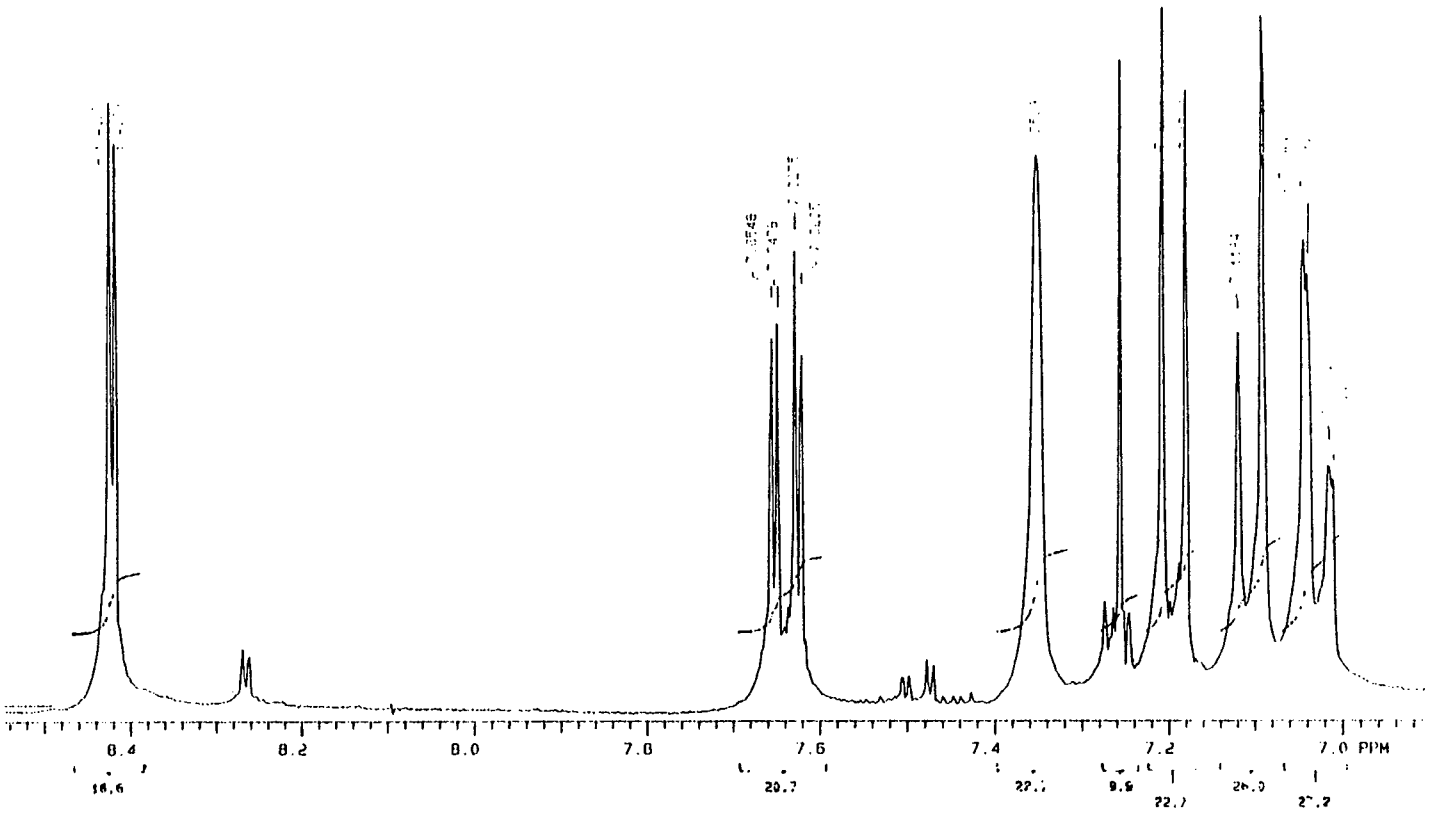

Figure 3: FTNMR spectrum of 4,4'-dibromo-2,2'-bis(4-methylbenzoxazolyl)biphenyl in DMSO-d6.

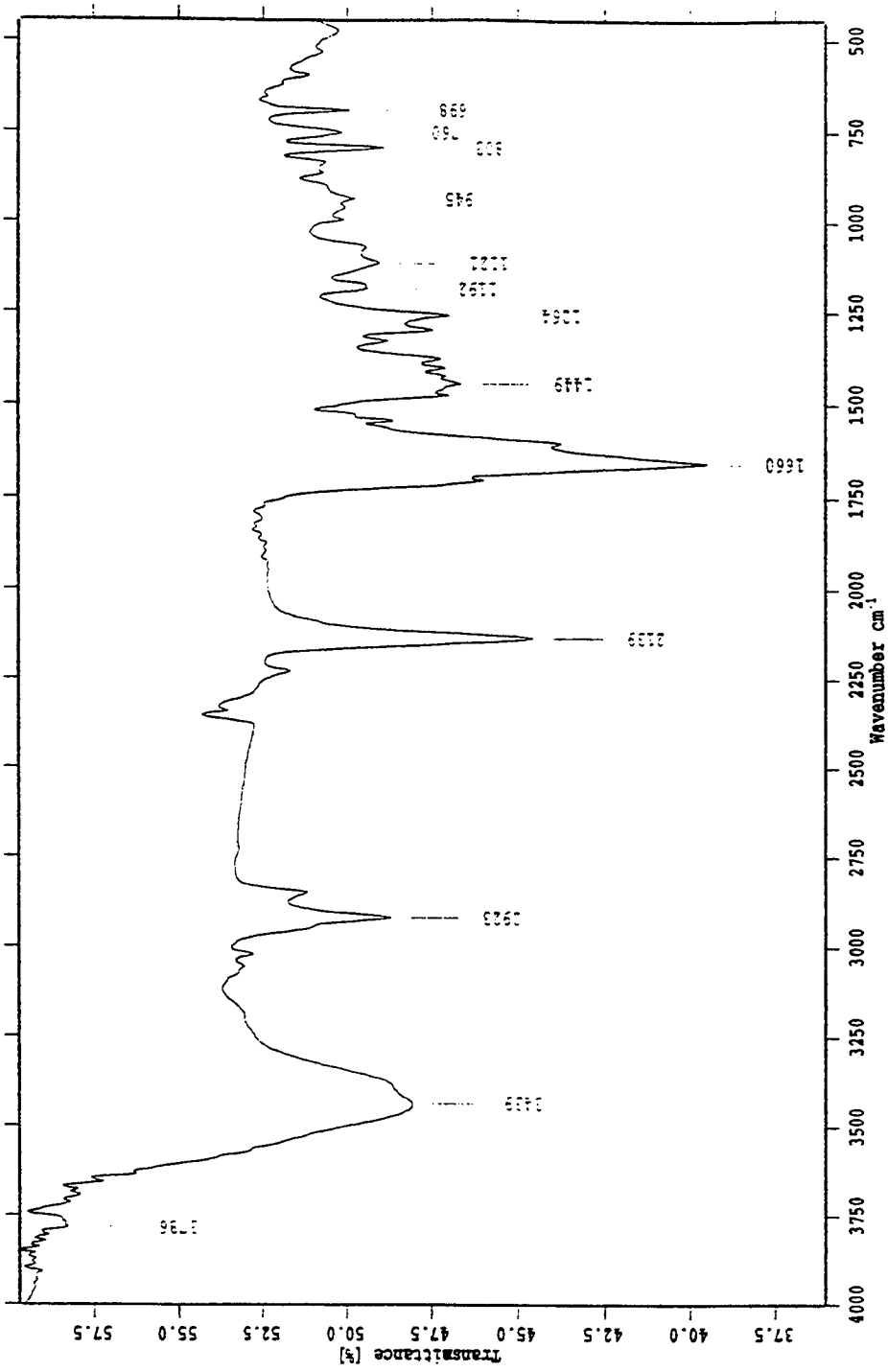

Figure 4: FTIR spectrum of the crude 4,4'-dicyano-2,2'-bis(4-methylbenzoxazolyl)biphenyl.

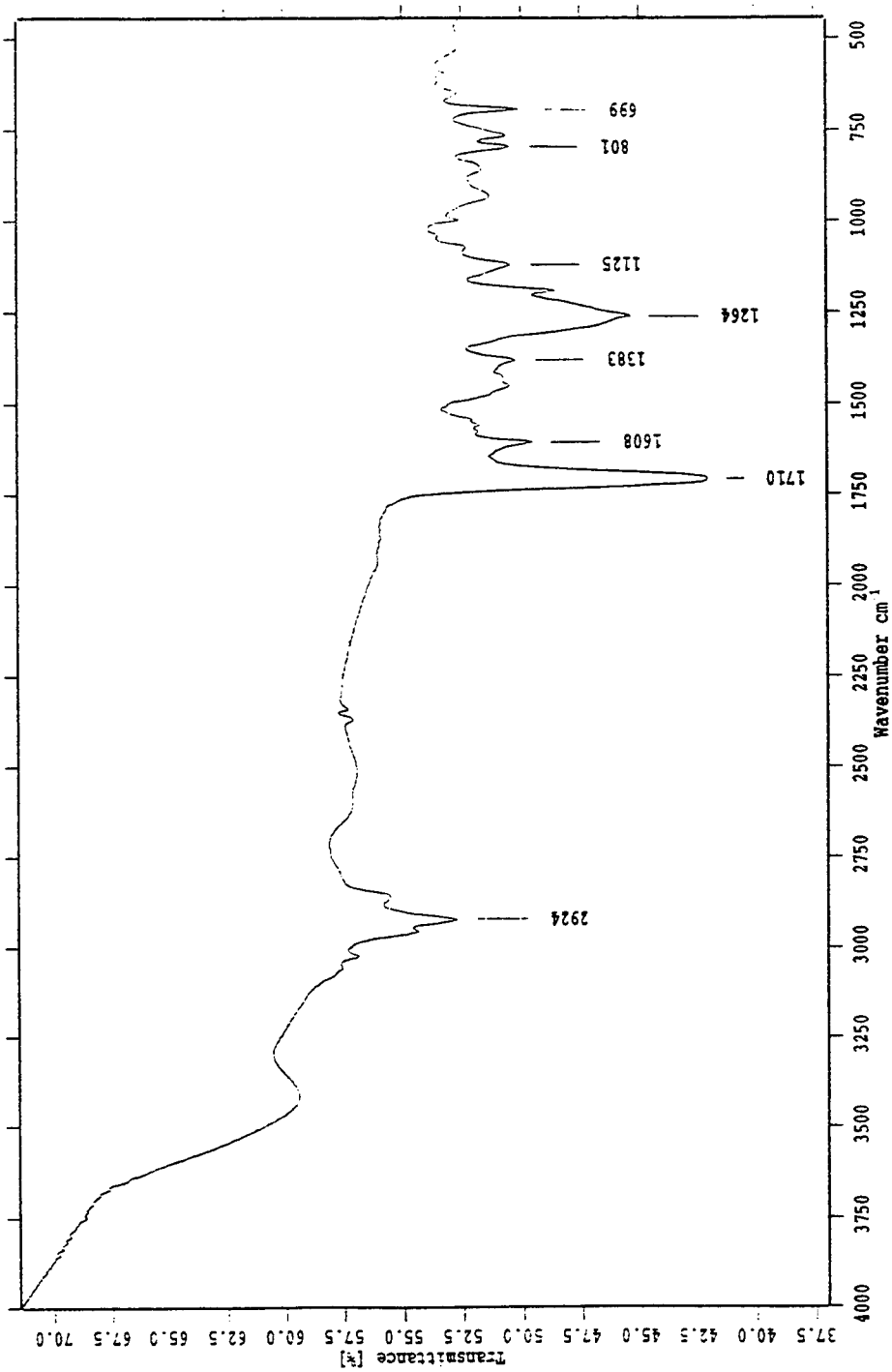

Figure 5: FTIR spectrum of the crude 4,4'-dicarboxy-2,2'-bis(4-methylbenzoxazolyl)biphenyl.

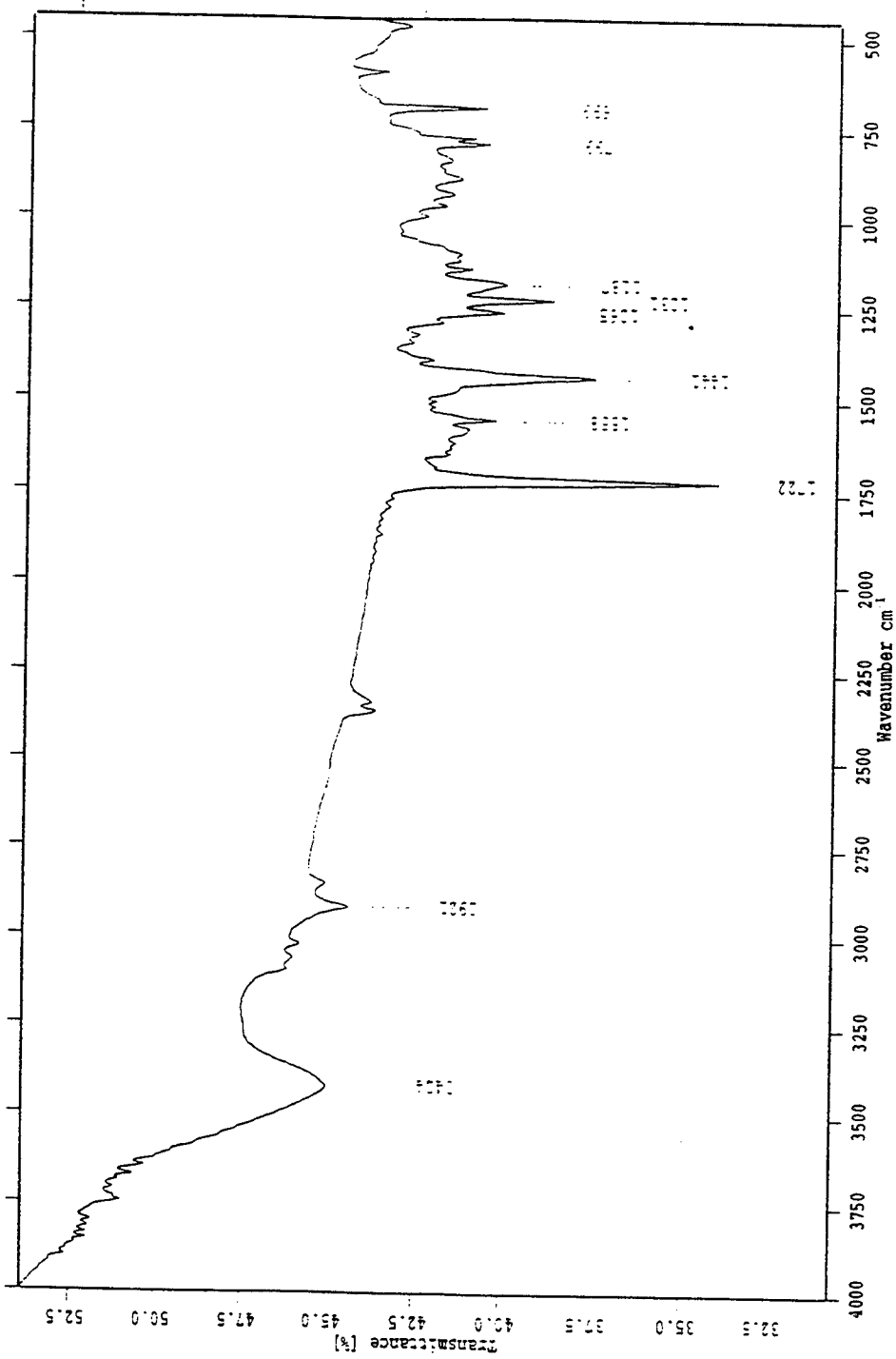

Figure 6: FTIR spectrum of the product obtained in polyphosphoric acid.

A FRAMEWORK FOR MANUFACTURING-ORIENTED, DESIGN-DIRECTED COST ESTIMATION

Allen G. Greenwood
Associate Professor
Department of Industrial Engineering

Mississippi State University
P. O. Box 9542
125 McCain Engineering Building
Mississippi State, MS 39762

Final Report for:
Summer Faculty Research Program
Wright Laboratory / Manufacturing Technology Directorate
Manufacturing and Engineering Systems Division

Sponsored by:
Air Force Office of Scientific Research
Bolling Air Force Base, DC

and

Wright Laboratory
Wright-Patterson Air Force Base, OH

September 1996

A FRAMEWORK FOR MANUFACTURING-ORIENTED, DESIGN-DIRECTED COST ESTIMATION

Allen G. Greenwood
Associate Professor
Department of Industrial Engineering
Mississippi State University

ABSTRACT

Defense system requirements have shifted from performance at all costs, to one of ensuring superiority, yet being affordable. As a result, affordability has become the primary focus of weapon system procurement. In order to develop affordable products, product design and manufacturing process design must be considered concurrently and early in the design phase. One approach to developing affordable systems is to combine the integrated product/process development (IPPD) process and virtual manufacturing (VM), or "manufacture in the computer." However, if product and process design issues are to be effectively considered, then cost, schedule, and risk assessment tools must be sensitive to changes in the product's physical design as well as to changes in the manufacturing system. Unfortunately, such tools are not available today. However, this deficiency provides an opportunity to totally rethink or "re-engineer/re-design" manufacturing cost estimating methodologies.

But, before "designing" and developing cost estimating methodologies that adequately address affordability issues, effectively support the IPPD process, relate product and process variables, operate in a virtual design environment, and model manufacturing and non-manufacturing indirect activities, the progression of modeling, analysis and costing -- from the individual features of the product being designed to its impact on the enterprise -- needs to be understood. This research provides a framework that defines the modeling and analysis progression from product features to an enterprise view of the production of the product. The framework provides the foundation for manufacturing-oriented, design-directed cost estimating (MODDCE).

A FRAMEWORK FOR MANUFACTURING-ORIENTED, DESIGN-DIRECTED COST ESTIMATION

Allen G. Greenwood

INTRODUCTION

> In the 21st Century, technologically superior Air Force weapons systems will be produced for half of the cost and fielded in half the time through a fully integrated commercial, military and organic industrial base. The existing fleet will be upgraded and/or modified to maintain its superiority with the same reductions in cost and time. ([1], p. i) The environment for today's cost estimator and analyst is certainly very challenging. Computerization, software, robots, composites, uncertainty, and integrated systems all challenge the applicability of our existing tools and techniques. (R. R. Crum, [2])

In most commercial and defense industries today, the focus is on affordability. Affordability is defined as the balance among requirements, costs, and budgets and considers both product performance and cost. A technology is considered affordable if it meets the customer's requirements, is within the customer's budget, and has the best value among available alternatives ([3], p. 2). This paper provides a framework for addressing both product and process cost issues, during the design phase. Before defining the framework, this section briefly provides the background, context, and motivation for this research, in terms of the current military design and manufacturing environment and state of the art in manufacturing cost estimating.

The Military Design and Manufacturing (and re-manufacturing) Environment

Any management system is affected by both a general environment and an operating environment. The general environment includes basic economic, social, political, and legal pressures that are brought to bear upon the firm or industry. More specifically, companies and industries must function in an operating environment that includes customers, suppliers, competition, government, technology (both internal and external) and the organization or management system itself. One of the primary characteristics of today's general business environment is change. The defense industry, like many others, is experiencing a period of rapid change. The change in the DoD's missions and needs is driven by a shifting and uncertain threat environment, e.g. collapse of the Soviet Union, strong downward fiscal pressures. As a result, affordability has become the primary focus of weapon system procurement. Defense system requirements have shifted from performance at all costs, to one of ensuring superiority, yet being affordable. DoD is adopting "a more balanced *cost of performance* view where weapon system life cycle cost is viewed as an *independent* variable, not simply fall-out as a *dependent* variable." [4]

The focus on affordability has led to widespread acquisition reform, utilization of integrated product teams (IPTs), application of an integrated product/process development (IPPD) process or

concurrent engineering, adoption of commercial practices in military production, military production on commercial lines, emphasis on sustainment (stretching the life cycle of weapon systems through modification and re-manufacture), etc. Few new major weapon system programs are expected in the foreseeable future and those programs that are developed will mostly be procured in low production volume and at a low production rate; in some cases, e.g. missiles, there will be low volume and a high product mix. Many weapon system components have no commercial counterpart and, due to the highly complex nature of the components and their low production volumes, many of the military's needs can not "compete" in the broader global market. Obviously, these current and future trends all present major challenges to the design and manufacture of superior yet affordable defense systems.

Affordability, a key metric in defense system acquisition and operation, considers both cost and performance and is obtained and maintained by (1) identifying and assessing cost drivers early in the life cycle, (2) considering process design and manufacturing operations early in the product life cycle, (3) effectively linking product and process design, especially in terms of cost, schedule, and risk, and (4) managing cost and risk over the system's entire life cycle. While affordability assessments need to address all phases of the product's life cycle, and the costs that will be incurred in those phases, i.e. life cycle cost, this project focuses only on the costs incurred in the production phase and the design and operation of manufacturing systems.

One vehicle for addressing affordability, and other issues, is through IPTs and the IPPD process. The IPTs must concurrently consider, either in person or over computer networks, product design and manufacturing process design in terms of product performance and cost tradeoffs. The largest payoffs result from effectively utilizing IPTs as early as possible in the design phase. The importance of early design decisions is widely recognized. It is often stated that roughly 70 percent of the total life cycle cost of the system is determined during conceptual design [5].

The relationships between the business and operating environment, the IPPD process, the concurrent consideration of product and process design, and the tradeoffs between cost and performance is represented graphically in Figure 1.

The cost/performance tradeoff graphic at the bottom of Figure 1, a variation on a concept put forth by Yoshimura [6], depicts the goal of design as seeking higher product performance and lower process cost; i.e., driving the design toward the "efficient frontier." The efficient frontier, the edge of the feasible region in Figure 1, contains the Pareto optimum design solutions -- those solutions where there exists no other feasible design solution that will yield an improvement in one objective without causing degradation in the other objective. Cost estimating methodologies are generally grouped into four categories [7]: (1) judgment - use of expert opinion of one or more qualified experts in the area to be estimated, (2) parametric -- mathematical expressions, often referred to as cost estimating relationships or CERs, that relate cost to independent cost driving variables, (3) analogy - use of actual costs from a similar existing or past programs with adjustments for complexity, technical or physical differences, to

derive a new system estimate, and (4) grass roots, also referred to as "engineering build up" or "detailed estimate" are performed at the functional level of the Work Breakdown Structure.

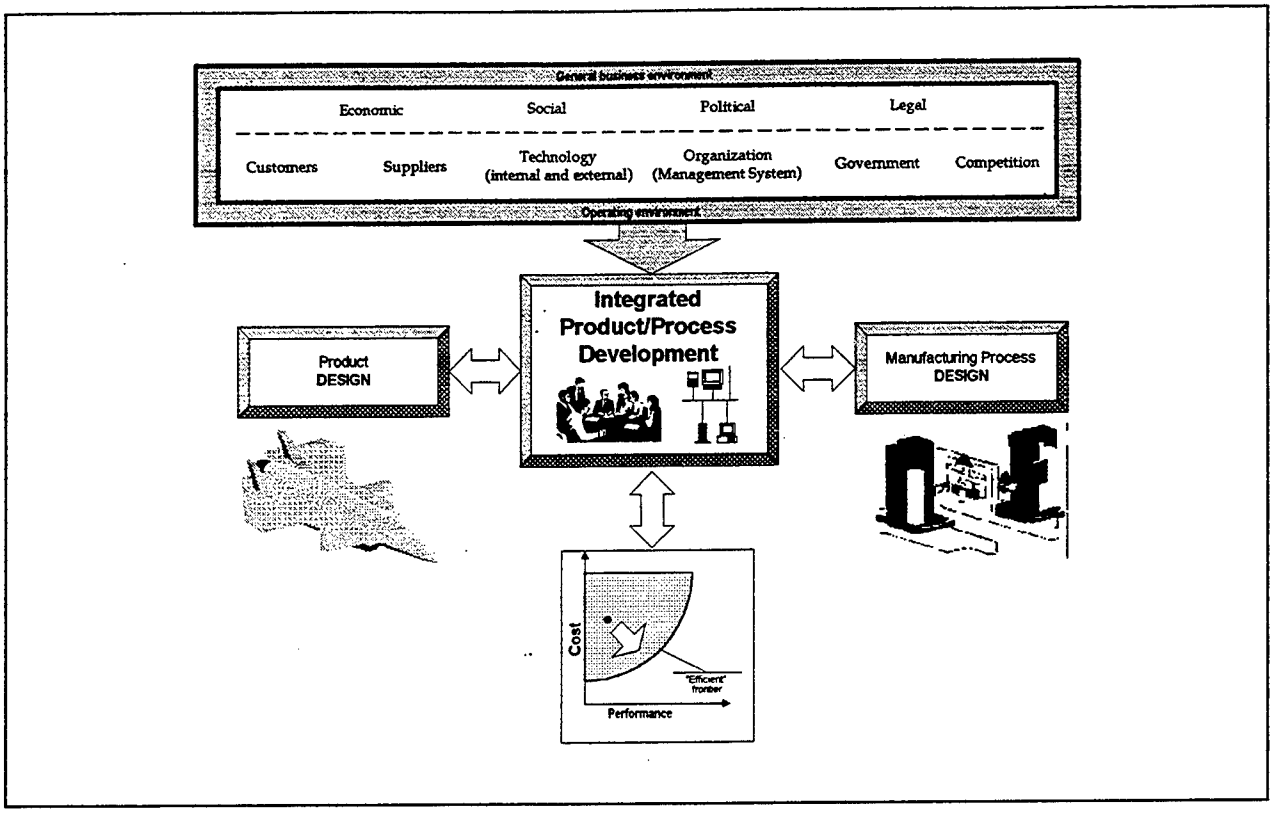

Figure 1: Affordability is the driving force in today's defense manufacturing environment.

One way to develop affordable products is through virtual manufacturing (VM), or "manufacture in the computer." VM is one of the key technologies which allows defense manufacturers to go beyond the assumptions driving the historic acquisition process because it provides four fundamental changes for defense manufacturing [8]: (1) VM can be used to prove the production scenarios, resulting in "pre-production hardened systems"; (2) VM can support the generation of more reliable estimates of production costs and schedule because the models are based on actual processes, not just parametrics; (3) modeling and simulation can significantly improve production flexibility, hence, reducing the fixed costs; and, (4) reliable predictions of costs, risk, and schedule can substantially improve the decision making process of acquisition managers.

In this new and evolving technology, fabrication and assembly of any product, including the associated manufacturing processes and all variables in the production environment from shop floor processes to enterprise transactions, are modeled and simulated in an integrated computer environment. VM accommodates the visualization of interacting production processes, process planning, scheduling, assembly planning, logistics from the line to the enterprise, and related impacting processes such as

accounting, purchasing, and management [9]. The move from solid models to virtual environment enables manufacturing and industrial engineers to design, test, and modify manufacturing processes without physical prototypes or production interruptions. It allows integrated product and process development (IPPD) in a virtual, 3-D world that is understood by all participants in the product and process design. ([10], pp. 35-36)

In order for IPTs to effectively consider product and process design issues, they need cost, schedule, and risk assessment tools that are sensitive to changes in the product's design, as well as to changes in the design of the manufacturing system. Unfortunately, such tools are not available today. A review by Thomas [11] of papers published in major journals in the past five years, resulted in the following conclusions: (1) research in manufacturing cost estimation has involved rather few people and as a result there are no broadly applicable mathematical models, (2) there is widespread dissatisfaction with the way overhead or indirect costs are handled, and (3) the lack of broadly applicable cost models leads to few efforts directed towards their integration into the CAD/IPPD systems.

Many cost models do not provide the capability to perform meaningful product/process trades and, in fact, may lead to an inefficient improvement focus. For example, many existing cost models are driven by parameters such as weight. As Dean [12] points out, "there are many perceptions of cost which people believe to be true and act upon, but which leads us in the wrong direction. ... The weight-based cost estimating relationship, as are many other common perceptions of cost, is quite misleading unless fully understood from a cost perspective and an engineering perspective." This is illustrated in Figure 2, using data from the Manufacturing 2005 Program ([13], [14]). In this case, if a design goal is to reduce manufacturing cost of the horizontal stabilizer and if CERs that are based on weight are used in the analysis, then the design focus would be on the stabilizer's skins. As seen in the table below, each skin comprises approximately one third of the weight of the structure and accounts for about one fifth of the cost. However, the ribs account for more than one third of the manufacturing cost but comprise less than ten percent of the weight.

Based on the research conducted during this project, the author adds the following issues to the list of concerns with the current state of manufacturing cost estimating in the IPPD process: (1) Cost model drivers need to be more closely related to the characteristics of manufacturing processes and operations. The process needs to be designed as much as the product; all too often the product is designed and then the process (manufacturing) must be designed to accommodate it or the product must be redesigned to accommodate the process. (2) Cost model drivers need to be more closely related to product features. (3) Manufacturing process design and resulting costs need to be considered earlier in the design of the product. (4) Product and process design must be sensitive to the existing or planned manufacturing state, especially in an agile environment; i.e. a design may change based on current factory utilization. Cost models need to capture the dynamics and stochastic nature of manufacturing. (5) The relationship between product/process costs and indirect costs need to be better defined and

understood. Indirect costs, both manufacturing and non-manufacturing, need to be "modeled" so that they can be addressed during design. (6) Legacy cost system data are often not tracked at the level of detail needed in design. (7) Legacy cost system data are often based on processes and methods that are no longer used.

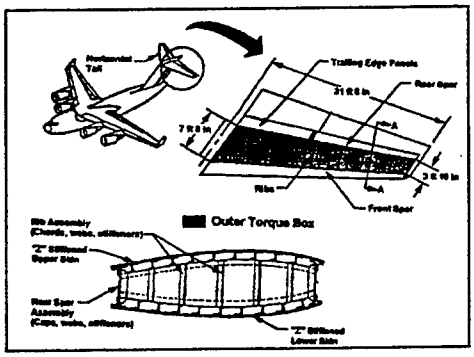

	Weight	Parts	Fasteners	Tools	Labor $	Material $	Manuf. Cost
Upper skin	32.2	12.9	19.7	11.0	15.7	22.1	21.1
Lower skin	33.7	13.6	23.5	9.9	13.8	34.5	20.7
Front spar	9.9	10.9	14.6	8.6	5.2	9.6	6.6
Read spar	9.7	4.6	8.6	7.0	7.2	8.9	7.7
Ribs	9.9	53.0	16.1	57.6	48.1	13.0	36.4
Box Assembly	1.8	5.1	7.6	5.7	9.2	0.0	6.1
Other	2.8	0.0	0.0	0.1	1.0	1.8	1.3

Source: Fondon, J. W., Jr., D. Rasmussen, et al. (1996). *Large Composite Structure – Commercial Military Integration (Military Products Using Best Commercial Practices) Phase I – Manufacturing 2005 Business Practices, Manufacturing Infrastructure, Process Technology Development, Volume II – Manufacturing 2005 Handbook.* Wright-Patterson Air Force Base, OH, Manufacturing Technology Directorate, Wright Laboratory, Air Force Materiel Command, p. ES-4, 36.

Figure 2: Many weight -driven cost models do not permit meaningful product/process trades.

Despite the shortcomings of past and current cost estimating methodologies and the lack of perceived value that they provide to the IPPD process, there are research efforts underway that are attempting to mitigate these problem; some of those efforts will be identified later in this report. It seems that if we can model and simulate the operation and behavior of a product and process, we certainly should be able to model and simulate a product/process's cost behavior. In fact, VM provides an opportunity to "re-engineer" costing methodologies. We need to freshly examine how costing *should* be done in a virtual environment, unencumbered by traditional accounting practices. New costing methodologies need to be *designed* to fit into tomorrow's environment.

But, before "designing" and developing cost estimating methodologies that adequately address affordability issues, effectively support the IPPD process and relate product and process variables, operate in a virtual design environment, and model manufacturing and non-manufacturing indirect activities, we need to understand the progression of modeling, analysis and costing from the individual features of the product being designed to its impact on the enterprise. The result of this research study is a framework that defines the modeling and analysis progression from product features to an enterprise view of the production of the product. The framework provides the foundation for manufacturing-oriented, design-directed cost estimation (MODDCE).

THE MODDCE FRAMEWORK

An overview of the manufacturing-oriented, design directed cost estimating (MODDCE) framework that was developed as part of this research study is provided in Figure 3. The framework is

composed of five levels that progress from a hierarchical decomposition of a product's features through three intermediate steps to an enterprise-level model that links product features with manufacturing and non-manufacturing entities throughout the enterprise. The highest or enterprise level provides the most comprehensive analysis capabilities for assessing the effect of changes in product and process design on the enterprise and the resulting effect of those changes on "total" cost. The progression to each level requires the completion of an activity. For example, in order to move from the hierarchical decomposition of a product's features to the corresponding manufacturing elements that create those features, requires an activity that maps or associates features with transformation elements. Each of the activities that link the five levels are described in the following sub-sections.

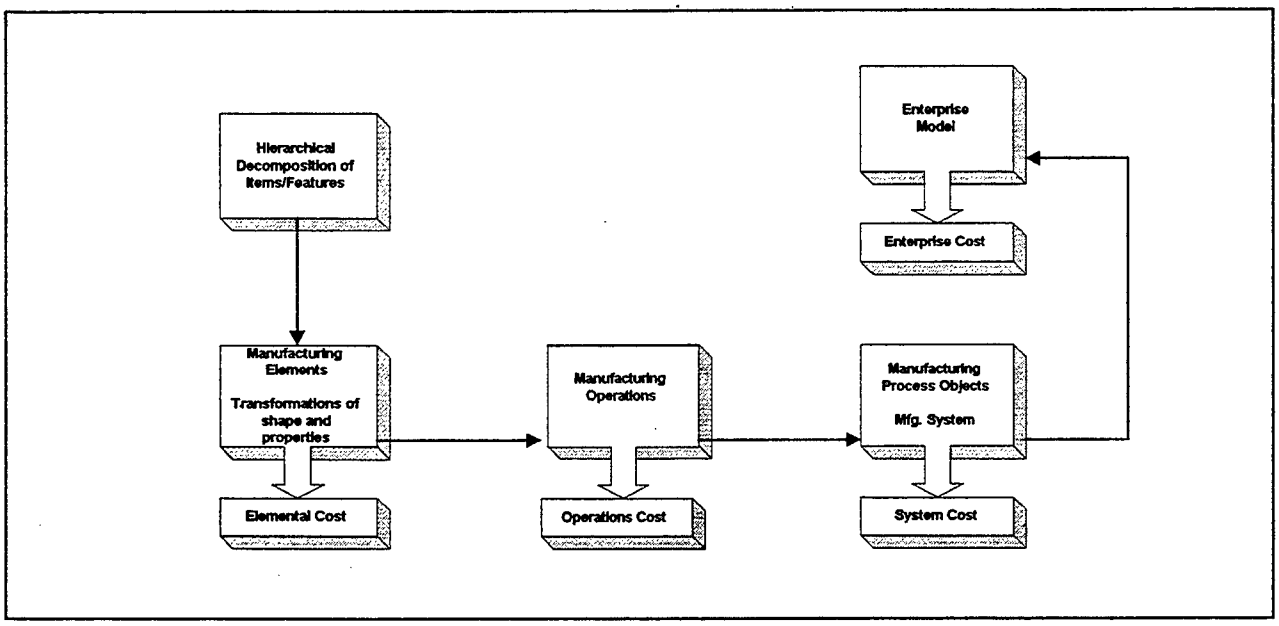

Figure 3: MODDCE framework provides the basis for "designing" and integrating costing methodologies that link product features to an enterprise view of the production of the product.

A preliminary and partial data model for implementing the MODDCE framework is provided in Figure 4. The data model is described in the framework subsections that are most closely related to each data model entity. As a matter of notation, lines with no double-headed arrows indicate a one-to-one relationships between entities, a double-headed arrow on one end represents a one-to-many relationship, and arrows on both ends represents a many-to-many relationship. For example, there is a many-to-many relationship between suppliers and items - an item may be obtained from multiple suppliers and a supplier may provide many items to the company. Also, there is an implied inheritance of information from entity to entity, as one moves from left to right in Figure 4; i.e., a manufacturing process object inherits all of the information about manufacturing operations, manufacturing elements, and product feature characteristics.

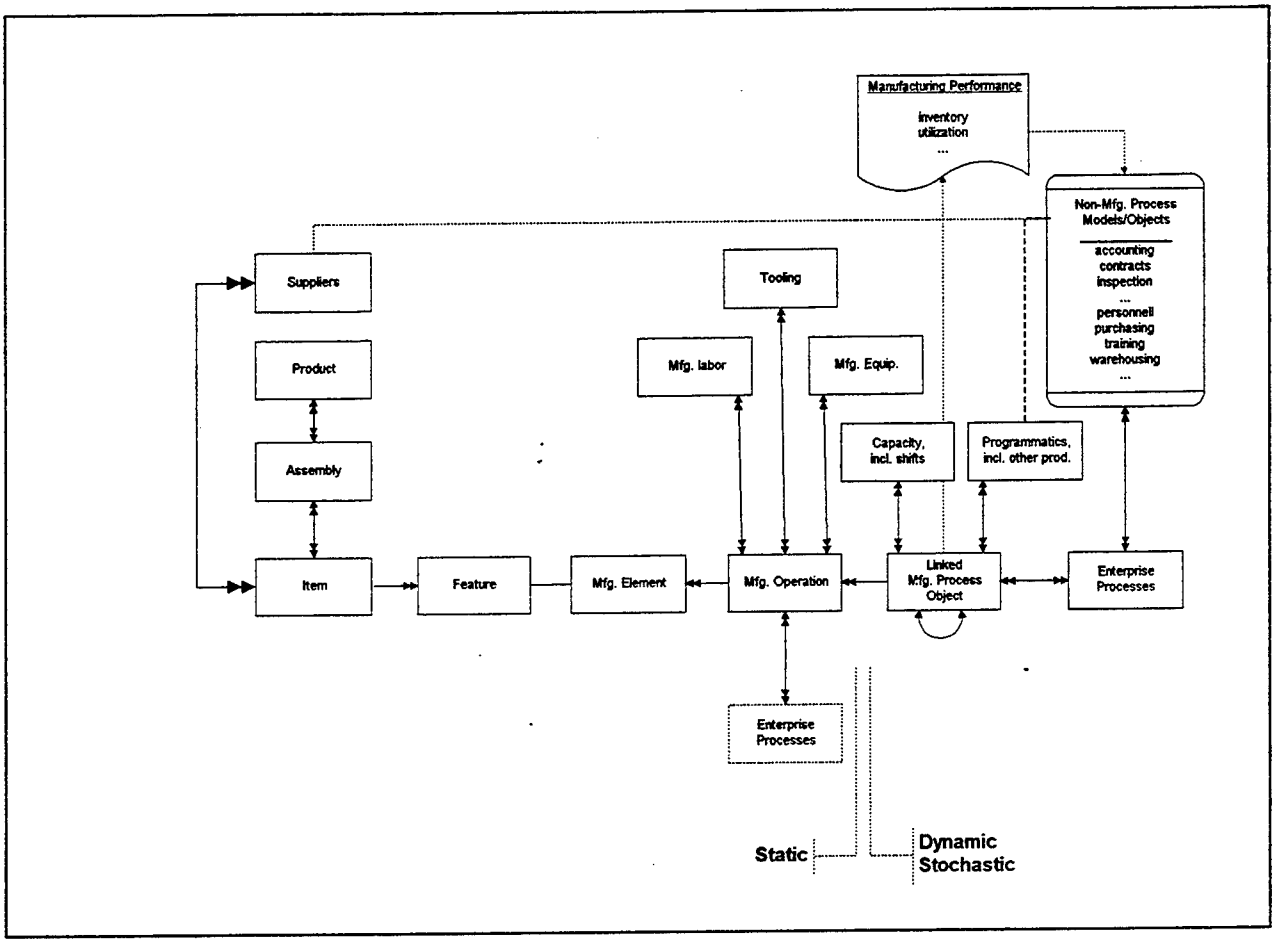

Figure 4: Preliminary and partial data model for the MODDCE framework.

Mapping product features to manufacturing elements

The process of mapping product features to manufacturing process elements is illustrated in Figure 5. A product is broken down into assemblies which are further broken down into *items*. This breakdown is represented in the data model in Figure 4 as a many-to-many relationship between products and assemblies and another many-to-many relationship between assemblies and items. Items are the lowest level of product definition that is addressed in the framework and are considered to be either fabricated or purchased. The example in Figure 5 shows an assembly named "widget" that is a part of a higher-order assembly and is composed of four items, two fabricated items (strap and slab) and two purchased items (block and fastener). Purchased items do not have features; their only characteristic is a part number. The part number links the item to a data base that includes such information as description, physical characteristics, supplier information, etc. Each fabricated item requires two types of information: basic data on the item -- such as part number, base material, size, etc. - and a list of features and a corresponding set of information on each feature. For example, in Figure 5,

the fabricated item "slab" has three features, two holes and one surface characteristic. Hole features would contain such information as diameter, depth, tolerance, location, etc. and surface features would contain such information as the face that is treated, purpose of treatment, material, etc.

Once all of the items have been defined and their features specified, a manufacturing *element* that creates the feature, either by transforming the shape of the item or altering its properties (non-shaping), is specified. There is a one-to-one relationship between a feature and an element. Elements are specified from a taxonomy of manufacturing processes, e.g. [15]. The element specification may be for a specific manufacturing process or for a more general process family. The choice of a manufacturing process is dictated by various considerations ([16], p. 1232): characteristics and properties of the workpiece material, shape, size, and thickness of the part, tolerances and surface finish requirements, functional requirements for the expected service life of the item, production volume and schedule, level of automation required to meet production volume and rate, costs involved in individual and combined aspects of the manufacturing operation. Numerous guidelines are available on the capabilities of various manufacturing processes for producing items from different materials, shape characteristics, tolerance and shape characteristics, etc. Some guidelines are incorporated into CAD software to provide real-time feedback to the designer. Cost guidelines are also available, usually on a relative basis. All too often these guidelines represent general trends and are not related to specific processes and product features. Few guidelines are available on the cost impact of production volume, rate, lead time, etc. These are factors that are becoming increasingly important to address during design especially when fewer new defense systems are being procured and there is a growing need to sustain and re-manufacture systems that are no longer being procured.

Using the Todd et al. taxonomy [15], a hole requires a shaping manufacturing process that could be either mass reducing or mass conserving. If a hole is created by mechanical mass reduction, further specification would require consideration of manufacturing processes that are chip-oriented (e.g. drilling) or shear-oriented (e.g. blanking). Alternatively, a hole could be created through a mass conservation process which may involve a consolidation process, such as casting, or a deformation process, such as forging. As shown in Figure 5, for the widget example, the hole features in the slab and straps are specified very generally; they are only identified as being mass reduction elements. On the other hand, the surface property of the slab in Figure 5 is specified more precisely as being a charge-transferred spray coating. Note that at this level of analysis, even if the methodology used to create the feature is precisely specified, such considerations as setup, simultaneous operations, resource availability, etc. are not considered.

Specification of manufacturing elements provide the first opportunity for cost assessment. However, in order to provide a cursory assessment of cost, a default manufacturing process would have to be associated with each element, e.g. the manufacturing process drilling could be the assumed process used to create a hole. Since each element is discrete and disjoint, it is more appropriate to begin

costing at the next level, the operations level. The transition to the operations level requires combining elements related to each feature into manufacturing operations; this activity is described in the following section.

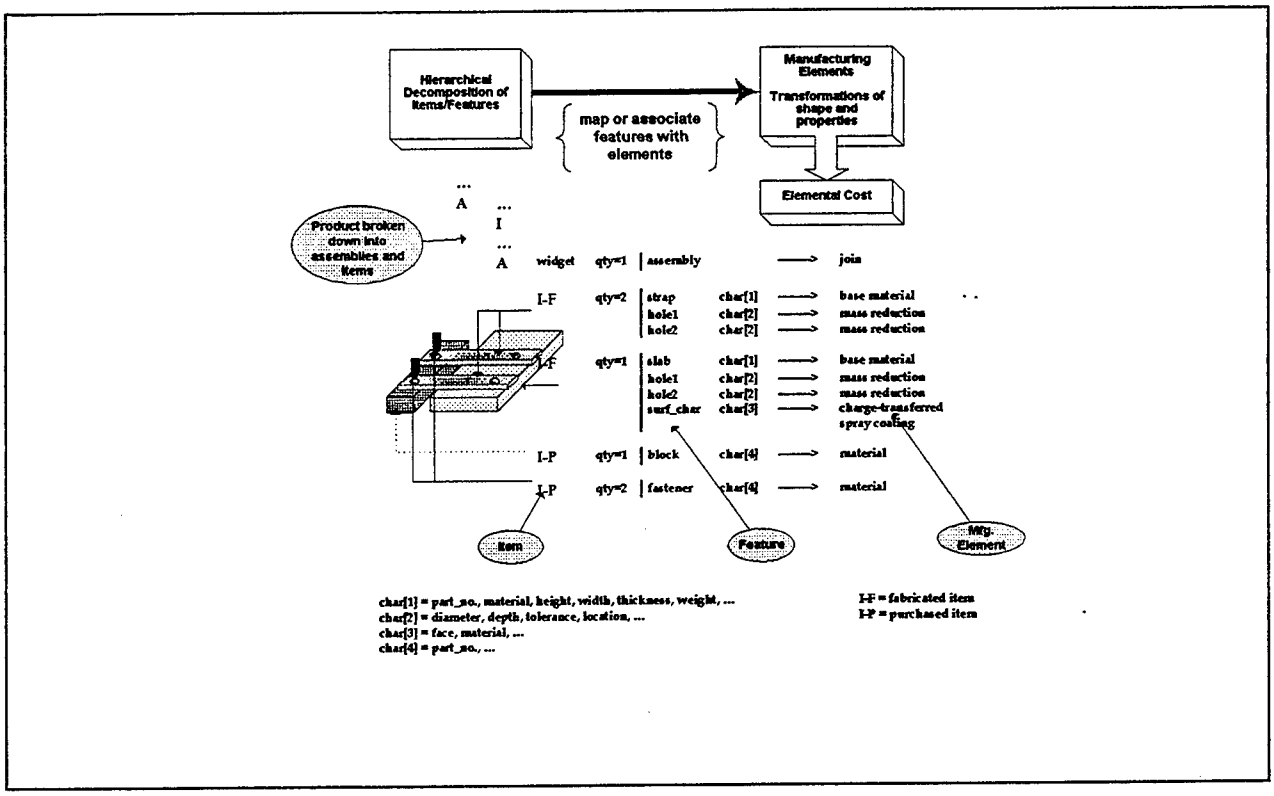

Figure 5: Mapping product features to manufacturing elements.

Combining manufacturing elements into operations

The second activity combines manufacturing elements for each feature, as described above, into manufacturing process *operations*. An illustration of this activity using the widget example is provided in Figure 6. The oval-shaped symbols in the figure represent manufacturing operations. As can be seen in Figure 6, the strap item is produced by stamping – the base material is cut to size and the two holes are formed in one step using the stamping process. Note that the creation of several feature elements have been combined in order to form the stamping operation and that the manufacturing process for creating the features has become more specifically defined, from the general mass reduction process family specified for the manufacturing elements to the particular process, stamping, specified as a process operation. It is at this level that specific equipment, labor skill requirements, and tooling are designated, as illustrated in the data model in Figure 4, where the manufacturing operations are linked to equipment, labor, and tooling data files. It is also at this level where precedence among elements and operations is defined. The dashed lines in Figure 6 indicate precedence; for example, for the slab item, the base material is cut first, then painted, and finally the holes are created through drilling.

Based on the research conducted during this study, this level of analysis is the current state of the art in cost estimating methodologies that directly link product features to process characteristics. Development of this capability is a part of two JSF/JAST projects. The Joint Strike Fighter (JSF) program, formerly the Joint Advanced Strike Fighter (JAST) program, is chartered to develop an affordable next-generation strike weapon system for the Navy, Marine Corps, Air Force, and our allies. Both projects - JMD, JAST Manufacturing Demonstration (prime contractor: Hughes Aircraft Company) and SAVE, Simulation Analysis Validation Environment (prime contractor: Lockheed Martin Tactical Aircraft Systems, LMTAS) - link feature-based CAD software (*Pro/E* and *CATIA*, respectively) to Cognition Corporation's *Cost Advantage* (CA) software system. CA is a design for manufacturing expert system that provides design guidance, manufacturing alternative analysis, producibility analysis, and predictive cost analysis. CA uses process models that are comprised of information and rules to estimate costs and advise engineers on the manufacturability of product designs. As part of this research program, the author met with engineers from Cognition Corporation and LMTAS [17] in order to better understand their development efforts.

However, in order to have a complete virtual manufacturing environment, the cost estimating capability must be extended beyond this process-level analysis to the system level and ultimately to the enterprise level. The following two sections describe these levels.

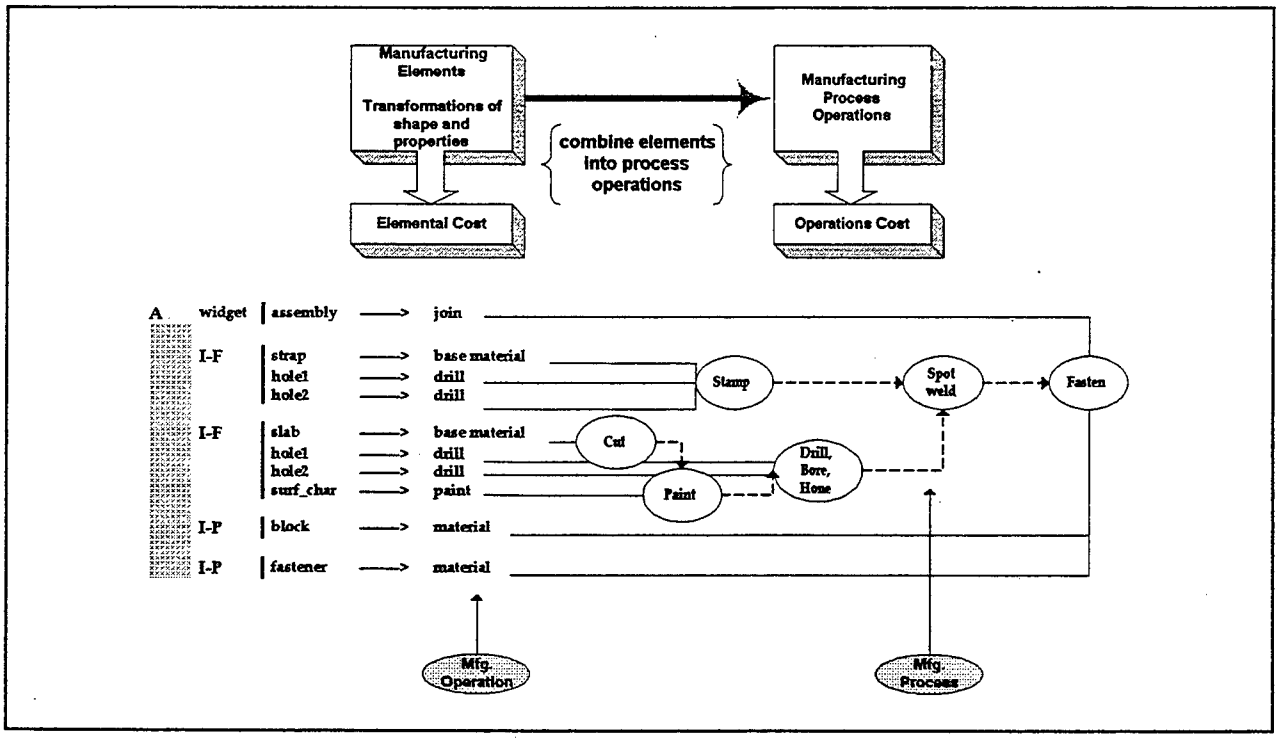

Figure 6: Combining elements into process operations.

Transforming process operations into manufacturing process objects

The third activity moves the modeling and analysis capability from the process level to the system level by transforming discrete process operations into system-level manufacturing process *objects*. It is at this level, and through the use of the objects, that manufacturing process operations are placed in the context of an actual production environment and the product is integrated into the fabric of a manufacturing environment. As a result, the objects become the basis for the design of production operations and facilities by considering such things as product movement, storage and handling issues, resource availability, interference with other products, grouping of elements into cells, etc. The combining of process operations into objects is analogous to implementing process plans into the production environment. The application of process objects is illustrated by the facility layout in the middle of Figure 7. In this case, continuing with the widget example, the strap item is created in the press area; the slab is created by slitting, is then painted, and fabrication is completed in the cell prior to assembly with the other items.

The symbols at the bottom of Figure 7 illustrate the differences between process operations and process objects. Process operations consider both the procedures (manufacturing steps) and the human and equipment resources that are required to perform the specific manufacturing activities. For example, the stamping process operation identifies the type of machine and operator that are needed to do the stamping, as well as the time required per item. As shown in the process object symbol in Figure 7, objects also consider procedures and resources but in addition they consider movement and storage of the product between and within objects, machine and operator capacities, programmatics, interaction with other products, and interaction among resources. Also, process operations are static; whereas, process objects are dynamic and stochastic - both of which are characteristics of most manufacturing systems. That is, process objects are time sensitive and have the ability to incorporate random events. Process objects obtain most of their power from imbedded methods, such as scheduling algorithms, simulation, etc.

It is only through manufacturing process objects and the interaction among objects that manufacturing performance, including costs, can be evaluated. The object provides output regarding both the expected value and distribution of such measures as completion times, throughput, operator and machine utilization, work-in-process inventory, space requirements, etc. System-level analysis provides a means to identify bottlenecks and other potential problems before the product is committed to production. It is only at this level that the impact of a product's characteristics on production process can be assessed and evaluated. This is especially important in an agile environment or for accommodating small batches of dissimilar products (e.g. items for the defense industry be produced on commercial lines). In fact, the design of the product may change based on the current state of the manufacturing facility, e.g. available resources, supplier constraints, etc.

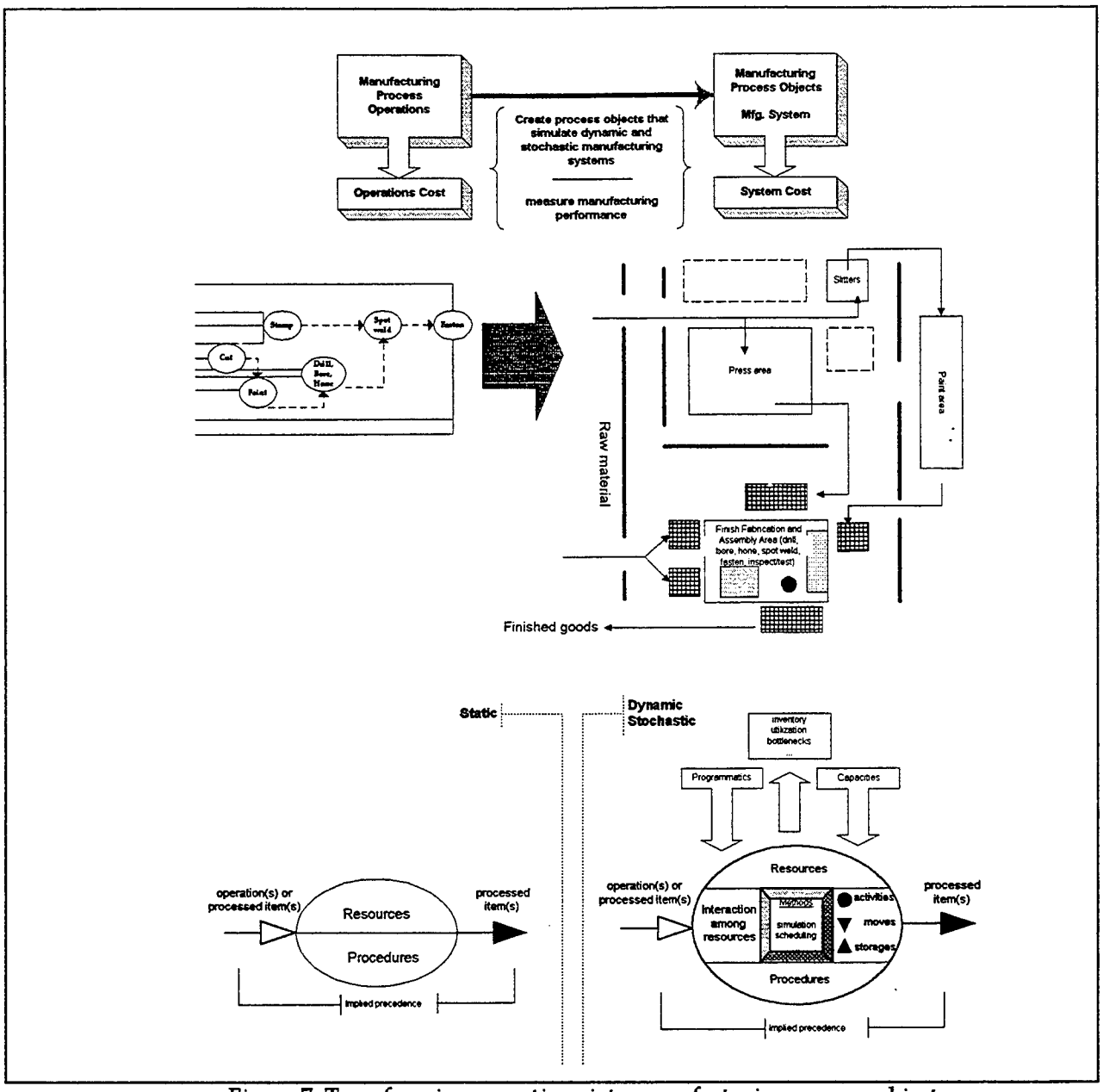

Figure 7: Transforming operations into manufacturing process objects.

The manufacturing process object is the next step beyond the current state of the art in the development of a virtual manufacturing environment that directly links product features to enterprise-level analyses. Therefore, a more detailed examination of the process object is provided in Figure 8. Arrivals to an object may be either individual items or batches, scheduled or random, and either originate external to the system being modeled or from another manufacturing process object. Process objects consider moves and storage to/from the object and within the object. In the example in Figure 8, an arrival requires a machine and an operator and may have to wait for either resource or for the appropriate tooling, additional materials, etc. The object typically includes rules for selecting resources

or for the resources to select products. Activity times, both machine and operator, are stochastic and sampled from probability distributions. Also, resources used by objects are not always available, due to scheduled or unscheduled maintenance, shift schedules, etc. Objects also include the modeling of the disposition of scrap and re-work. It is only through the dynamic and stochastic capabilities of the manufacturing process object that a system's performance can realistically be evaluated and virtual manufacturing can truly be achieved.

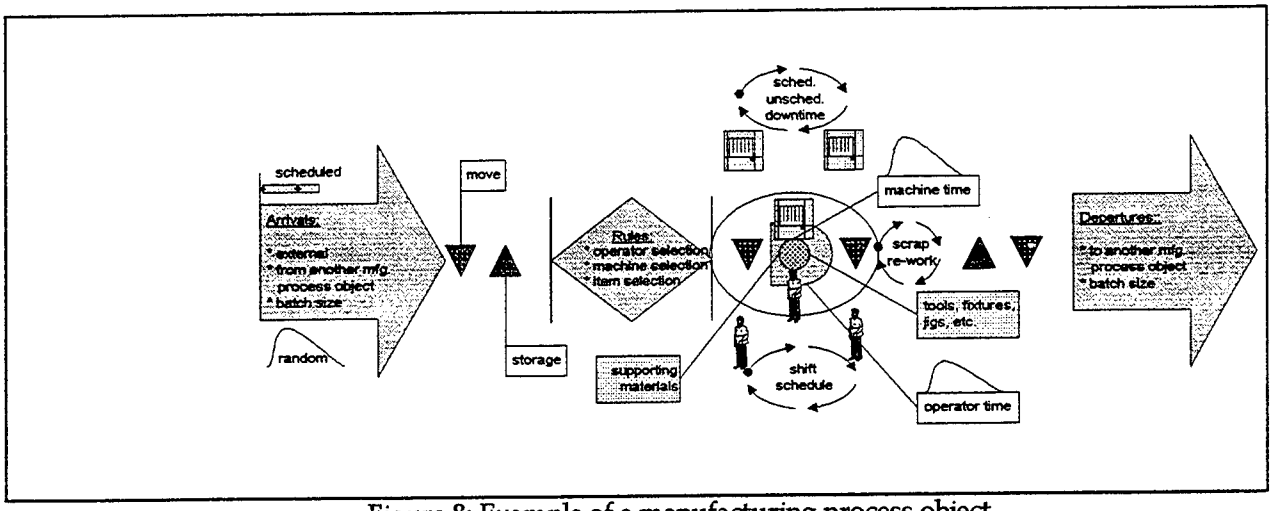

Figure 8: Example of a manufacturing process object.

Linking manufacturing process objects to enterprise processes

The highest level of cost analysis is at the enterprise level. Enterprise-level costing extends design sensitivity beyond direct manufacturing costs to include manufacturing and non-manufacturing indirect costs. The impact of changes in product/process design on indirect entities in the enterprise is assessed, and conversely, the impact of changes in indirect entities on manufacturing processes, and hence on the product, is also assessed. For example, specification of a new material during product design will not only affect operations in terms of the type of equipment used, labor skills, tooling, scrap rate, etc. but will also affect numerous indirect entities in the organization, including training, purchasing, warehousing, etc. Normally these effects are assumed to be captured in the application of very general overhead rates. However, enterprise-level costing permits a more realistic assessment of the impacts of product and process alternatives. In order to realize enterprise-level cost estimation, the firm's business processes must be identified, modeled, and linked to the appropriate manufacturing process object(s). This is illustrated in Figure 9 with the links between various functional entities in the organization. Also, as illustrated in Figure 9, enterprise is defined in its broadest context and includes all non-manufacturing entities in the company (administration, purchasing, etc.), as well as external entities such as customers and suppliers.

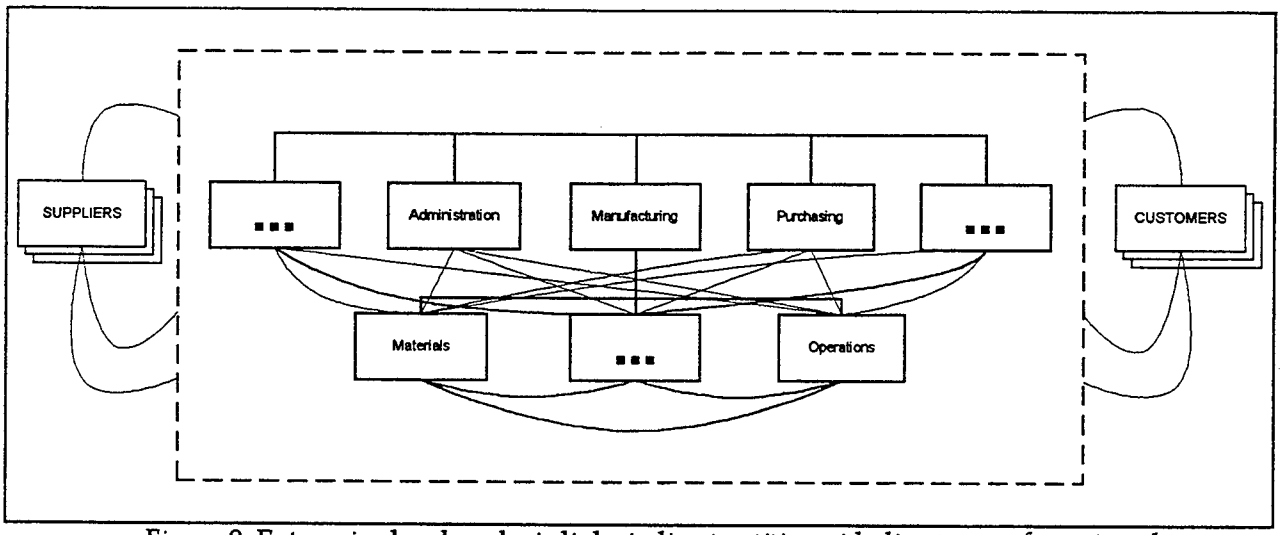

Figure 9: Enterprise-level analysis links indirect entities with direct manufacturing objects.

An example of a model of a business process is provided in Figure 10; the supplier management and procurement process was developed as part of the Manufacturing 2005 Program [13]. The process model illustrates the linkages between manufacturing and such entities as program management, engineering, quality assurance, the supplier, etc.

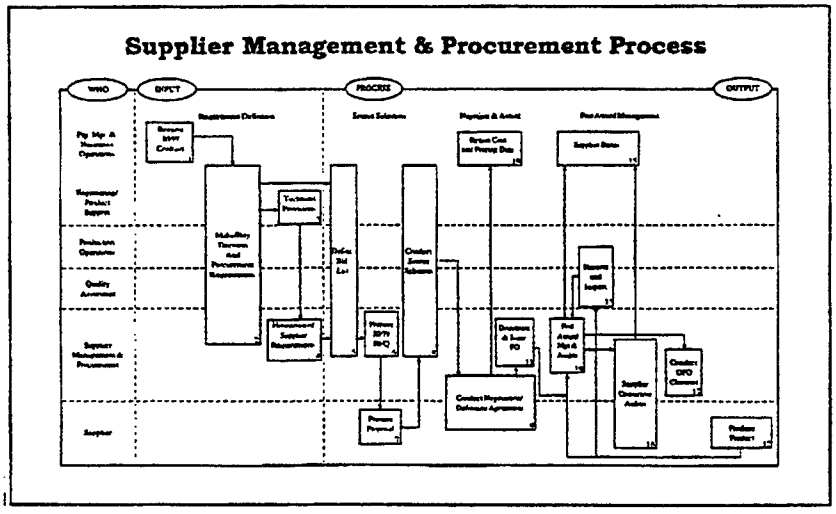

Source: Fondon, J. W., Jr., D. Rasmussen, et al. (1996). *Large Composite Structure – Commercial Military Integration (Military Products Using Best Commercial Practices) Phase I – Manufacturing 2005 Business Practices, Manufacturing Infrastructure, Process Technology Development, Volume II – Manufacturing 2005 Handbook.* Wright-Patterson Air Force Base, OH, Manufacturing Technology Directorate, Wright Laboratory, Air Force Materiel Command, p. B-16.

Figure 10: Example linkage between business and manufacturing processes.

As mentioned above, enterprise-level modeling and analysis results in a better understanding and a better definition of the behavior of overhead costs. Overhead costs are a significant component of total product cost. Raffi and Swamidass [18] report that in an average U.S. manufacturing firm, manufacturing overhead cost is about two and one half times the direct labor cost. Thomas [11] reports indirect costs to be 400 to 600 percent of direct costs in aerospace defense production. Despite the significance of overhead costs, little published research exists in this area. The MODDCE framework provides a foundation for modeling non-manufacturing processes and quantifying the effect of a process's behavior on overhead cost. New accounting methodologies, such as activity-based costing (ABC), will be required in order to model and link direct and indirect processes.

As part of this research project, the author visited the Northrop Grumman Commercial Aircraft Division (NG-CAD) in Dallas, TX in order to gain a better understanding of the costing and risk assessment methodologies used in the Manufacturing 20005 Program, Military Products using best Commercial/Military Practices (MP-C/MP) [19].

Development of an Application of the MODDCE Framework

This research project provides a framework for manufacturing-oriented, design-driven cost estimating. Subsequent research will develop an application to implement the framework. This section provides a brief and preliminary definition of the application.

As shown in Figure 11, a decision-support application that implements the MODDCE framework would include, at a minimum, the seamless integration of: relational and/or object-oriented database(s), a mechanical CAD package for product design (e.g. Cognition *Corporation's Mechanical Advantage,* Parametric Technology Corporation's *Pro/E*), process and cost modeling system(s) (e.g. Cognition Corporation's *Cost Advantage*), manufacturing process objects that would most likely be developed from manufacturing and/or object-oriented simulators (e.g. AESOP's *SIMPLE++*, ProModel Corporation's *ProModel*), and business modeling and simulation software (e.g. CACI's *SimProcess,* ProModel Corporation's *ProcessModel,* AdvanEdge Technologies Corporation's *OPTIMA!*). These components would be integrated using software such as Microsoft *Visual Basic* and/or Knowledge Base Engineering's *IKE* (*Integrated Knowledge Environment*). The application would be developed in a Microsoft Windows environment, most likely *Windows NT.*

Development of manufacturing process objects, development of the underlying database structure, modeling of business processes, integration of the technologies outlined above, and design of the user interface and decision-support environment would be required to effectively link product features and characteristics to manufacturing and enterprise-wide processes. The application would support the modeling of information flow as well as product and material flow. Costing methodologies, e.g. activity-based costing, need to be investigated in order to determine their applicability to this

environment and identify the best way to integrate the costing methodologies into the framework/application.

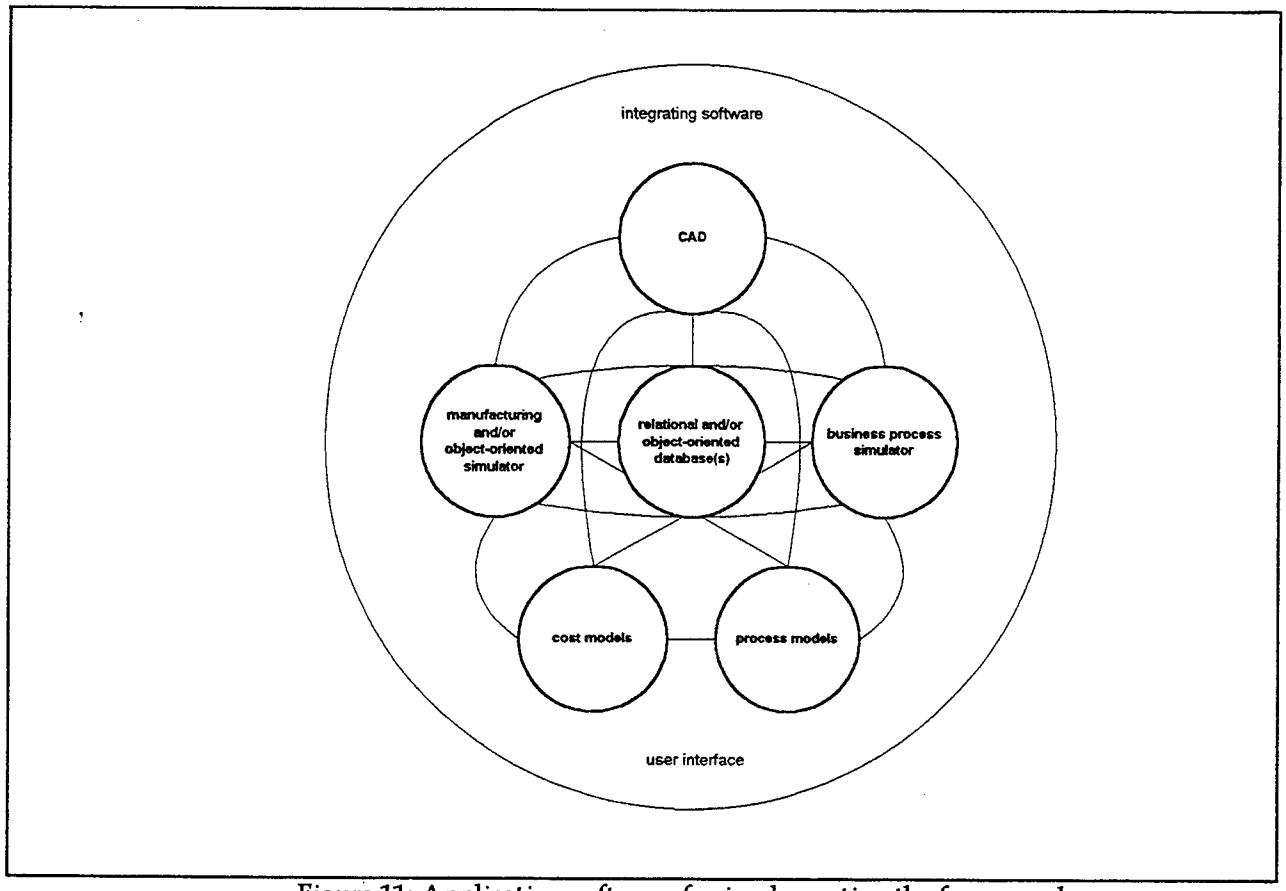

Figure 11: Application software for implementing the framework.

FUTURE RESEARCH ISSUES

As defined in the previous section, the next research activity is to begin the development of a prototypical application that demonstrates the proposed framework. This completed prototype will provide a laboratory for exploring a variety of issues related to cost estimating in an integrated product/process development environment and virtual design and manufacturing environments. Some of those issues include specification of the most appropriate costing methodologies for assessing both direct and indirect costs, the application of activity-based costing, application of machine learning, development of approaches for optimization of product/process design via simulation, etc.

Another area for further research, which would directly support the application development defined above, is the generalization and extension of the "innovative" costing work performed in support of the Manufacturing 2005, MP-C/MP (Military Products Using Best Commercial/Military Practices), Program ([13], [14]). One of the outcomes of the MP-C/MP Program is a detailed assessment

of the impact of numerous business practice, manufacturing infrastructure, and process technology improvement initiatives on product and process costs. The program clearly demonstrates that indirect cost categories can be linked to product and process characteristics. The MP-C/MP Program cost methodologies provide a basis for process modeling and linking manufacturing and non-manufacturing activities.

A third research project would involve the development of an industry "survey" or workshop that would determine and define the cost estimating needs for a virtual design environment. The project would solicit ideas on how cost estimating *should* be performed in such an environment.

CONCLUSIONS

Realization of the proposed framework would advance the state of the art of manufacturing cost estimating methodologies in the following ways: (1) Product design is directly linked to process design and manufacturing operations, thereby achieving "true" virtual manufacturing. Shop-floor and above-the-shop-floor assessments are performed in the computer before commitments are made to produce a product; e.g. potential bottlenecks can be identified and resolved before they occur. (2) Product and process design are directly linked to non-manufacturing activities in the enterprise, resulting in a more accurate and more meaningful assessment of indirect costs. (3) Product/process designs are assessed and "optimized" at the system level, rather than sub-optimized by functional area. (4) The framework is applicable throughout the product and process life cycles, thereby providing traceability of product design, manufacturing design, and cost. It also provides a growing knowledge base of past practices and lessons learned to be used in future designs. (5) The aforementioned knowledge base can be used not only for human learning, but as a basis for machine learning - a means to analyze and "optimize" the relationships between product features and the processes required to produce those features. (6) Product/process trades are made on "current" planned activities. This is especially important as the design cycle time shrinks -- current activities and plans for the facility may impact the selection of product/process design alternatives.

BIBLIOGRAPHY

1. Air Force Manufacturing Science & Technology Program. *FY96 Manufacturing Science and Technology Area Plan.* Wright-Patterson Air Force Base, OH: Headquarters, Air Force Material Command, Directorate of Science and Technology, August 1, 1995:

2. Kankey, R. and J. Robbins, eds. *Cost Analysis and Estimating: Shifting U.S. Priorities.* New York: Springer-Verlag, 1991.

3. Wright Laboratory Affordability Strategy Team. *Affordability in Science and Technology Development.* Wright-Patterson Air Force Base, OH: Wright Laboratory, June 9, 1993.

4. Kaminski, P.G. *The Defense Acquisition Challege: Technological Supremacy at an Affordable Cost.* JAST Industry Conference, 1995.

5. Dierolf, D.A. and K.J. Richter. *Computer-Aided Group Problem Solving for Unified Life Cycle Engineering (ULCE) Environment.* IDA Paper P-2149, Alexandria, VA: Institute for Defense Analyses, 1989.

6. Yoshimura, M. *Concurrent optimization of product design and manufacture,* in *Concurrent Engineering: Contemporary issues and modern design tools,* H.R. Parsaei, Editor. London: Chapman & Hall. 1993, pp. 159-183.

7. Modern Technologies Corporation. *Integrated Weapon Systems Management (IWSM) "How to" Manual for Manufacturing Cost Assessment (MCA).* Dayton, OH: Modern Technologies Corporation, 1995.

8. Lawrence Associates, Inc. *Virtual Manufacturing User Workshop.* Dayton, OH, 1994.

9. Lawrence Associates, Inc. *Virtual Manufacturing Technical Workshop.* Dayton, OH, 1994.

10. Noor, A.K. and S.R. Ellis. Engineering in a Virtual Environment. *Aerospace America,* July 1996, pp. 32-37.

11. Thomas, R. *Manufacturing Cost Estimation, Modeling and Control: A Review of the Literature.* Beavercreek, OH: Stratech, Inc., August 1994.

12. Dean, E. *Design for Competitive Advantage,* Internet, Hampton, VA: NASA Langley Research Center, 1996.

13. Fondon, J.W., Jr., Rasmussen, Dane *et al., Large Composite Structure -- Commercial Military Integration (Military Products Using Best Commercial Practices) Phase I -- Manufacturing 2005 Business Practices, Manufacturing Infrastructure, Process Technology Development, Volume II -- Manufacturing 2005 Handbook* Wright-Patterson Air Force Base, OH: Manufacturing Technology Directorate, Wright Laboratory, Air Force Materiel Command, 1996.

14. Riseley, M.K., T. Houpt, and S. Wheeler, *Large Composite Structure -- Commercial Military Integration (Military Products Using Best Commercial Practices) Phase I -- Manufacturing 2005 Business Practices, Manufacturing Infrastructure, Process Technology Development, Volume I -- Program Review.* Wright-Patterson Air Force Base, OH: Manufacturing Technology Directorate, Wright Laboratory, Air Force Materiel Command, 1996.

15. Todd, R.H. *et al, Manufacturing Process Reference Guide.* New York: Industrial Press Inc., 1994.

16. Kalpakjian, S. *Manufacturing Engineering and Technology.* Reading, MA: Addison-Wesley Publishing Company, 1992.

17. Greenwood, A.G., *Meeting on SAVE Program at LMTAS, 7/1/96.* Wright-Patterson Air Force Base, OH: Manufacturing Technology Directorate, Wright Laboratory.

18. Raffi, F. and P.M. Swamidass. Towards a Theory of Manufacturing Overhead Cost Behavior: A Conceptual and Empirical Analysis. *Journal of Operations Management,* October 1987 pp. 121-137.

19. Greenwood, A.G., *Meeting on Manufacturing 2005 Program at NG-CAD, 7/2/96.* Wright-Patterson Air Force Base, OH: Manufacturing Technology Directorate, Wright Laboratory.

AFFECTS OF INTERNATIONAL QUALITY STANDARDS ON BARE BASE WASTE DISPOSAL ALTERNATIVES

Rita A. Gregory
Assistant Professor
School of Civil and Environmental Engineering
Construction Engineering and Management

Georgia Institute of Technology
Atlanta, GA 30332-0355

Final Report for:
Summer Faculty Research Program
Wright Laboratory
Air Base Technology Branch
WL/ FIVC-OL

Sponsored by:
Air Force Office of Scientific Research
Bolling Air Force Base, DC

and

Wright Laboratory
Air Base Technology Branch
WL/FIVC-OL

September 1996

AFFECTS OF INTERNATIONAL QUALITY STANDARDS ON BARE BASE WASTE DISPOSAL ALTERNATIVES

Rita A. Gregory
Assistant Professor
School of Civil and Environmental Engineering
Construction Engineering and Management
Georgia Institute of Technology

Abstract

This research was sponsored by the Air Force Office of Scientific Research, Bolling AFB, DC and the Air Force Wright Laboratory Air Base Technology Branch (WL/FIVC-OL Tyndall AFB, FL) as part of the Summer Faculty Research Program. This research was designed to assist Wright Laboratory Air Base Technology Branch in identifying emerging technologies for the development of a versatile, air mobile, and environmentally safe waste processing system to support force deployment operations. In addition, a specific thrust of this researcher is to develop cost/benefit methodologies and to incorporate in the alternative development processes those aspects of engineering, socio-economic, and policy issues that could impact the cost effectiveness of alternative solutions. This final report discusses some of the issues that International Quality Standards could have on the design and cost effectiveness of Bare Base Waste Disposal Alternatives. Although these standards are still under development and there are not yet definitive policies (14, 15) on how the DoD will integrate these standards into their bare base deployments, a DoD wide Environmental Management Systems Committee has been formed. (14, 15) They will continue to evaluate the development of international standards to determine if they present an "opportunity for DoD to improve its environmental management," with a "primary motivation for (sic) regulatory relief and reduced costs." (14) This researcher believes these standards will require us to process waste more efficiently and environmentally sound, thereby provide solid ground to support technology innovation under development and proposed by Wright Laboratories.

AFFECTS OF INTERNATIONAL QUALITY STANDARDS ON BARE BASE WASTE DISPOSAL ALTERNATIVES

Rita A. Gregory

Introduction

This research was sponsored by the Air Force Office of Scientific Research, Bolling AFB, DC and the Air Force Wright Laboratory Air Base Technology Branch (WL/FIVC-OL Tyndall AFB, FL) as part of the Summer Faculty Research Program. This research was designed to assist Wright Laboratory Air Base Technology Branch in identifying emerging technologies for the development of a versatile, air mobile, and environmentally safe waste processing system to support force deployment operation. In addition, a specific thrust of this researcher is to develop cost/benefit methodologies and to incorporate in the alternative development processes those aspects of engineering, socio-economic, and policy issues that could impact the cost effectiveness of alternative solutions. This final report for the Summer Faculty Research Program discusses some of the issues that International Quality Standards--specifically ISO 9000, international standards for manufacturing and construction and ISO 14000, international standards for environmental management systems (1)--could have on the design and cost effectiveness of Bare Base Waste Disposal Alternatives. Although these standards are still under development and there are not yet definitive policies (14, 15) on how the DoD will integrate these standards into their bare base deployments, a DoD wide Environmental Management Systems Committee has been formed. (14, 15) Members of this committee believe "ISO 14000 will have greater impact on international trade than the ISO 9000" and "ISO 14000 will grow in importance over time." (14) They will continue to evaluate the development of international standards to determine if they present an "opportunity for DoD to improve its environmental management," with a "primary motivation for (sic) regulatory relief and reduced costs." (14)

The U.S. Army Corps of Engineers (COE) say the quality (management) system outlined under ISO 9002 is the standard most applicable to construction firms in the

private sector that support military construction. (16) The Louisville (KY) District is attempting registration under ISO 9000 and is tracking the development of ISO 14000. They say "Registration to the ISO 9000 standard demonstrates to our customers our commitment to quality and our ability to meet their specified requirements and to possibly exceed their service expectations. . . . ISO 9001 registration is a practical, commercial requirement for world-wide business organizations." (17) The ISO standards in the United States are known as ANSI/ASQC Q9000 series. (17)

International Standards are the way of the future for home bases and contingency deployments. This researcher believes these standards will require Air Force Bare Bases to process waste more efficiently and environmentally sound, thereby provide solid ground to support technology innovation under development and proposed by Wright Laboratories.

Background/Discussion of Problem

In the future, under the doctrine of "Global Reach...Global Power," the USAF is preparing to fight world wide from 1100-person Bare Bases consisting of only operating surfaces and a source of water. All other base infrastructure components must be rapidly brought via airlift. The USAF tasked Sverdrup Technology, Inc., TEAS Group with developing the "Bare Base Infrastructure Road Map," identifying deficiencies and defining promising technologies available in 1996 to 2015 for improving current austere base utility and facility equipment. Inadequate Waste Management Systems was one of the top ten deficiencies identified in this study. Several of the top priorities for immediate action recommended by the study were to quantify and characterize waste streams and investigate alternatives for waste disposal at Bare Bases. (2) The Office of Scientific Research sponsored research under the Summer Faculty Research Program was conducted with three major aspects: quantifying the waste stream, literature search on emerging technologies and commercial-off-the-shelf (COTS) for waste remediation, and identifying key policies or elements affecting the deployability and/or cost effectiveness of these technologies. Quantifying and characterizing the waste stream of an 1100-person deployed unit was not possible because there is no such exact team currently deployed.

The research team investigated several alternative sources for corollary data, such as the Silver Flag training site at Tyndall AFB, FL, the RED HORSE Squadron at Hurlbert AFB and their data from a recent Bosnia deployment, and the Logistics Civil Augmentation Program (LOGCAP) data form the Corps of Engineers at Winchester, VA. This data search is described by the Graduate Student Research Final Report, base page number 16. The technology matrix, with accompanying discussions and brain-storming on employment and deployment options, was provided under separate cover to the WL/FIVC project officer. The final aspect, policies and or elements affecting the deployability and/or cost effectiveness of the technologies, focused on the Global emphasis on international specification standards and developing laws that can restrict operating locations and limit equipment usage in deployed locations. This final report discusses this third aspect of this summer research.

Methodology

The methodology consisted of literature research on International Organization for Standardization (ISO), emerging laws or international policies, and company/industry experiences in accepting or adapting to the emerging trend for international standards. In addition, telephone interviews and/or discussions were held with various levels of the USAF and DoD policy makers and analysts (15) to ascertain an impact or strategy for incorporating these international standards in design or costing of alternative technologies. There was no final, published DoD or USAF policy available for reference.

Results

The International Organization for Standardization (ISO) is a worldwide federation, established in 1947, of 111 member countries represented mainly by industry and governmental standards groups. (1) Its mission "is to promote the development of standardization and related activities in the world with a view to facilitating the international exchange of goods and services, and to developing cooperation in the spheres of intellectual, scientific, technological, and economic activity. (ht.//www.iso.ch)" (1) The International Organization for Standardization (ISO) defines standards as

"documented agreements containing technical specifications or other precise criteria to be used consistently as rules, guidelines, or definitions of characteristics, to ensure that materials, products, processes, and services are fit for their purpose." These international agreements are, in turn, published as international standards or incorporated into national standards. (1) International concern on abuse of the environment is a rapidly growing trend.

Equally important in setting international standards is the European Union (EU). The EU population of 375 million is made up of Austria, Belgium, Denmark, Finland, France, Germany, Greece, Ireland, Italy, Luxembourg, the Netherlands, Portugal, Spain, Sweden, and the United Kingdom (U.K.). In addition to the EU, companies should anticipate international standards certification requirements from Norway, "seven nations in Eastern Europe, three Baltic nations, and two Mediterranean nations that are negotiating to enter the EU during the next ten years." (8) "This will increase the EU population to 500 million with an additional 400 million population in EU Associate Member States in North, West, and South Africa and the Caribbean." (8)

Bare Base deployment is inherently international, requires international or intercountry agreements (13), and will be affected by the movement on global sustainability, defined by the Brundtlandt Commission as "meeting the present human needs without compromising the ability for future generations to meet their own" (1). ISO 9000, international standards for manufacturing and construction and ISO 14000, international standards for environmental management systems (1) are receiving the most visibility. However, other movements such as the European Union Directive on Packaging and Packaging Waste (11), and the "1996 German Takeback Legislation" (1) and the German Topher Law (1) will have major impacts on deployment equipment and locations for Bare Bases. These and other emerging standards and/or legislation will be discussed relative to the impact on Bare Base deployments.

ISO 9000, the international standards for manufacturing and construction, is "something that's becoming necessary to do business around the world." (1) Many of the industries that provide equipment for DoD and companies that support through service contracts are actively seeking certification of compliance with ISO 9000. (12) "They

realize (sic) that compliance is (sic) voluntary...but ignoring these requirements could prove hazardous to their marketshare." (3) Defense Logistics Agency is examining how ISO 14000 (and presumably 9000) will work in its business environment, since 85% of their purchases are from small businesses. (14) Under current certification processes small businesses will be at a disadvantage. One reference noted for a small business, it took one year to achieve certification" (3). The Louisville District Corps of Engineers anticipates 12 to 18 months to achieve certification. (17) European Union (EU) is now legally requiring CE marking on all products sold, imported, or used in their countries. (5, 8) "CE is the French abbreviation for Conformite Europeene, which means European Conformity in English." (5) A mandatory examination and certification by a third party officially recognized by an EU Member State is required prior to affixing the CE mark. If a product is not marked as certified, it is considered an illegal product. Depending on the host nation law, it can be sent back, detained, confiscated, fined, or forced into compliance. In one case, it cost a company $48,000 to reengineer their product and resulted in six months delay to the customer. (9) Nonconformance penalties are set by each EU Member State and range from civil fines of $62,500 per infraction in Germany to $5,000 and three months in prison in the U.K. (5, 9) Potential of these fines must be included in the cost of doing business and the cost effectiveness of alternatives, but more importantly the potential of deploying forces being prohibited from entry to specific locations must be a major element in choosing waste disposal systems. Under the USAF doctrine of Global Reach-Global Power and Bare Base concepts, at no time can we allow a waste disposal system be the limiting element for deployable locations.

More specific standards, identified in the EU Declaration of Conformity, such as the EU Electromagnetic Compatibility Directive 89/336/EEC (6) and the EU Low Voltage Directive 73/23/EEC (7), may affect specific alternatives such as plasma torch technologies. In these directives "the manufacturer (of all parts and components) must take all measures necessary in order that the manufacturing process shall ensure compliance of the products with the technical documentation and the requirements of this directive." (7)

In addition to compliance, the EU requires all manufacturers to maintain a technical file that contains technical documentation to demonstrate the conformity of a product with the essential safety requirements of a directive or standard. (10) Under some directives the a manufacturer can "self-declare" conformance while other require third party certification. The Air Force Center for Environmental Excellence is considering seeking to become a third party certified for ISO 14000. The Air Force is not aware of any private companies in the U.S. that are currently qualified to be certifiers. (14)

Reducing the solid waste stream for Bare Base is inherently a better alternative to disposal. In characterizing the solid waste stream for Bare Base (refer to the Graduate Student Research Final Report, base page number 16 of this report), operational forces repeatedly identified packaging and shipping products as a major source of the waste stream. The EU Directive on Packaging and Packaging Waste 94/62/EC (modeled after the German packaging ordinance-VERPACKUNGSVERORDUNG) "covers all packaging and all packaging waste whether it is used or released at the industrial, commercial, office, shop, service, household, or any other level, regardless of the material used." (11) "Packaging means all products made of any materials of any nature to be used for the containment, protection, handling, delivery, and presentation of goods, from raw materials to processed goods, from the producer to the user or the consumer." (11) This directive established basic targets, quotas, and limitations, that are reviewed periodically for upgrade, for the member states and people operating in those states. EU operates on the "polluter pays" principle. "The polluter pays principle means that the responsibility for recycling and recovery falls upon the packager, not the end user." (11) Similarly the controversial "1996 German Takeback Legislation" requires the producer to "take back" its product after it has served its purpose--the end product after the customer no longer uses it. This law implies redesign of the full life-cycle of product development, plant lay-out, processes, usage, and disposal. These laws and directives will make obsolete the current Bare Base waste management alternative of using host nation landfills--thus supporting new technology alternatives that are more environmentally friendly.

Impact on Wright Laboratory Technology Thrusts for Bare Base Waste Processing

Air Force Civil Engineers directly support Global Reach-Global Power and mission readiness by providing the basing systems to protect, project, and support air and space systems and forces. (18) In the stated vision, the Air Force will maintain forward presence through contingency deployment and will provide engineering support to domestic defense and natural disasters. Operations will be conducted in host nations and/or at civilian airports. (18) Future projections anticipate up to 90% of Civil Engineering capabilities will be met with commercial off-the-shelf technologies. (18) Coordination/collaboration of research and development efforts is accomplished through teaming arrangements with industry, academia, other federal agencies and foreign governments. (18) These doctrine and issues underscore that International Standards will affect the processes of development and the products of development from Wright Laboratory.

The *Next Generation Bare Base Waste Processing System* (18) research and development project is an example of emerging technology that can fulfill both the fact and spirit of International Quality Standards. This project is studying the deployable bare base waste system for all potential waste streams with the goal of reducing waste volume, stabilizing pollutant and disease vectors, and recovering heat and decomposition gasses as alternative fuel sources. Plasma vitrification technology uses only 15% of air required of conventional incinerators and produces no harmful particulates, nor NOx/SOx emissions. Exhausted heat from plasma vitrification process can be recovered for electricity production or prime heat adsorbtion air conditioning. The payoff of this research will be improved mission readiness, enhanced environmental and health benefits, and reduced impact on the host nation landfill/site cleanup. (18)

Conclusions

The growing trend in international standards for environmental management and manufacturing/construction will be a driving factor in the selection of methods to dispose of Bare Base waste streams. Current methods, such as use of host nation land fills, will be

prohibited and/or will become excessively expensive to conform with international standard environmental requirements. International standards will have an impact on the cost effectiveness of alternatives of Bare Base waste disposal. More importantly, from an operational perspective, enforcement of international standards could limit which countries are willing to accept U.S. Bare Base forces, unless all our systems conform with their compliance requirements. These trends will become the ground work for technology innovation for systems that are more efficient and environmentally sound.

BIBLIOGRAPHY

1. Anonymous, "Standards of International Quality," Guest Lecturer Notes for Dr. Jerry Banks, ISYE 4897 course, Georgia Institute of Technology, Atlanta, GA, 1996.

2. Aeronautical Systems Center Directorate of Air Base Systems (ASC/VXO), "Bare Base Infrastructure Road Map," Eglin AFB, FL, Prepared by Sverdrup TEAS Group, 22 Mar 1996.

3. Banks, Dr. Jerry, ISYE 4897, "Standards of International Quality, Project Two: The Belt Corporation of America," Group 3: Yamada, Cardozo, Blanco, and Blitch, Georgia Institute of Technology, Atlanta, GA, 1996.

4. CISQ/SIS Fact Sheet EU-001-AIMD, "European Union Active Implantable Medical Devises Directive 90/385/EEC as Amended By 93/42/EEC and 93/68/EEC," Prepared by J.K. Kolka, Ph.D., J.D. and H. Grell-Lawe, Georgia Institute of Technology, Center for International Standards and Quality, Atlanta, GA, 1996.

5. CISQ/SIS Fact Sheet EU-002-CEM, "CE Marking," Prepared by J.K. Kolka, Ph.D., J.D. and H. Grell-Lawe, Georgia Institute of Technology, Center for International Standards and Quality, Atlanta, GA, 1996.

6. CISQ/SIS Fact Sheet EU-003-EMC, "European Union Electromagnetic Compatibility Directive 89/336/EEC as Amended By 92/31/EEC and 93/68/EEC," Prepared by J.K. Kolka, Ph.D., J.D. and H. Grell-Lawe, Georgia Institute of Technology, Center for International Standards and Quality, Atlanta, GA, 1996.

7. CISQ/SIS Fact Sheet EU-004-LOV, "European Union Low Voltage Directive 73/23/EEC As Amended BY 93/68/EEC," Prepared by J.K. Kolka, Ph.D., J.D. and H. Grell-Lawe, Georgia Institute of Technology, Center for International Standards and Quality, Atlanta, GA, 1996.

8. CISQ/SIS Fact Sheet EU-005-MACH, "European Union Machinery Directive 89/392/EEC As Amended By 91/368/EEC, 93/44/EEC, and 93/68/EEC," Prepared by J.K. Kolka, Ph.D., J.D. and H. Grell-Lawe, Georgia Institute of Technology, Center for International Standards and Quality, Atlanta, GA, 1996.

9. CISQ/SIS Fact Sheet EU-006-CEP, "Policing The European Union's CE Mark," Prepared by J.K. Kolka, Ph.D., J.D. and H. Grell-Lawe, Georgia Institute of Technology, Center for International Standards and Quality, Atlanta, GA, 1996.

10. CISQ/SIS Fact Sheet EU-007-TECH, "The European Union's Technical File Requirement," Prepared by J.K. Kolka, Ph.D., J.D. and H. Grell-Lawe, Georgia Institute of Technology, Center for International Standards and Quality, Atlanta, GA, 1996.

11. CISQ/SIS Fact Sheet EU-008-PACK, "European Union Directive on packaging and Packaging Waste 94/62/EC," Prepared by J.K. Kolka, Ph.D., J.D. and H. Grell-Lawe, Georgia Institute of Technology, Center for International Standards and Quality, Atlanta, GA, 1996.

12. Irving Professional Publishing, List of ISO 9000 Registered Companies, ISBN 0-7863-0777-3, Fairfax, VA 1996.

13. Jacobson, Timothy C., Waste Management, An American Corporate Success Story, Gateway Business Books, ISBN 0-89526-511-7, Washington, DC 1993

14. Office of the Under Secretary of Defense, Assistant Deputy Under Secretary of Defense, Memorandum: "Minutes of July 16, 1996 Environmental Management Systems Committee Meeting," Washington, DC, 16 Aug 1996.

15. Telephone interviews and/or points of contact:

a. Richard C. Armstrong, HQ COE Pulaski Building, Washington DC 202-761-8656.

b. Dr. John Austin, Deputy Under Secretary of Defense, Environmental Security, International Activities, 703- 695-3321 (DSN 225).

c. John Bravo-Prior AF/CE officer and State Department Contractor for international development.

d. Dr. Marcia Davies, Chief, HTRW Center of Expertise, Corps of Engineers, Omaha, NE, 402-697-2555.

e. Mr. Ed East, Chief, Engineering Management Branch, Engineering Division, Military Programs Directorate, HQ COE, Pulaski Building, Washington DC 202-761-1114.

f. Kathryn Elliott, Deputy Under Secretary of Defense, Environmental Security, International Activities, 703-614 3045 (DSN 224)

g. Col Pat Fink, Air Force Center for Environmental Excellence (AFCEE), Pollution Prevention Division, 210-536-3332 (DSN 240).

h. Mr. Tad McCall, Air Force Deputy Assistant Secretary (Environment, Safety and Occupational Health) (SAF/MIQ), 703-697-9297 (DSN 227).

i. Edmund Miller, Deputy Under Secretary of Defense, Environmental Security, Compliance Division, 703-604-5775 (DSN 664).

j. Carole Parker, Deputy Under Secretary of Defense, Environmental Security, Pollution Prevention Division, 703-604-5707 (DSN 664).

k. Andy Porth, Deputy Under Secretary of Defense, Environmental Security, Pollution Prevention Division, 703-604-1820 (DSN 664).

l. Maureen Sullivan, Deputy Under Secretary of Defense, Environmental Security, Compliance Division, 703-604-5807 (DSN 664).

m. Col Roy Salomon, Deputy Under Secretary of Defense, Environmental Security, Pollution Prevention Division, 703-604-1628 (DSN 664).

n. Col Bob Wallett, USAF Civil Engineer, Directorate of Environment, 703-697-3323 (DSN 227).

16. U.S. Army Corps of Engineers, Information Paper, Subj: ISO 9000, ISO 9001, ISO 9002, Washington DC, 27 Jun 1996.

17. U.S. Army Corps of Engineers, Brochure: "ISO 9000 Quality Standards, Questions and Answers," Louisville District, Louisville, KY, undated.

18. Wright Laboratory Air Base Technology, Strategic Development Plan FY96-25, Tyndall AFB, FL 32403-5323, 21 Aug 1996.

MISMATCH STRESSES, LAMELLAR MICROSTRUCTURE AND MECHANICAL PROPERTIES OF TiAl-ALLOYS

Michael Grinfeld
Research Professor of Mechanical and Aerospace Engineering
Department of Mechanical and Aerospace Engineering
Rutgers University Piscataway, NJ 08844

Final Report for:
Summer Faculty Research Program
Wright-Patterson Laboratories

Sponsored by:
Air Force Office of Scientific Research
Bolling AFB, Washington DC
and
Armstrong Laboratory

August 1996

MISMATCH STRESSES, LAMELLAR MICROSTRUCTURE AND MECHANICAL PROPERTIES OF TiAl-ALLOYS

Michael Grinfeld
Research Professor of Mechanical and Aerospace Engineering
Department of Mechanical and Aerospace Engineering, Rutgers University

Abstract

The elastic misfit stresses in TiAl alloys assume huge level of the order of the product of the elastic moduli times misfit deformations. The elastic energy associated with these stresses is enormously large also and it tries to relax via one of several possible mechanisms. Hence, there appears a driving force for the rearrangement of the material elements leading to the evolution accompanied by the creation of dislocations, migration of vacancies, development of interfacial corrugations, etc...

The goal of this research project is two-fold: i)to develop a theoretical approach which permits a self-consistence calculations of misfit stresses in TiAl lamellar multilayers and like structures, and ii)to develop a thermodynamic approach allowing one to study the possibility of stress relaxation by means of mass rearrangement in the vicinity of the interface between the lamellae. We assume that the rearrangement is accompanied by interfacial diffusion and migration of the vacancies. Since the full consideration of the coherent interface solid-solid includes lots of calculation and details we illustrate our results and approach by considering the much simpler but conceptually a very close problem of mass rearrangement in the vicinity of a stress-free interface.

MISMATCH STRESSES, LAMELLAR MICROSTRUCTURE AND MECHANICAL PROPERTIES OF TiAl-ALLOYS

Michael Grinfeld

1. Introduction

According to the publications of Dimiduk et al [3], Hazzledine et al [8] and others, the Ti-Al alloys improve almost all mechanical properties when they are in fully lamellar microstructural form. This is why this form of the microstructure attracts so much attention of the practitioners and researcher dealing with TiAl-alloys. Many fundamental features of this form of TiAl alloys remain unexplored and unclear. One of them is the magnitude of mismatched stresses in the lamellae, the mechanism of mismatch stresses relaxation and the influence of mismatch stresses on different mechanical properties. The source of these stresses is the lattice mismatch between the α- and γ-lamellae, and also between the γ-lamellae with different orientation. The crystallography and mismatch deformations in the TiAl-lamellae are explored pretty well nowadays by experimentalists, and it seems to be one of the urgent necessities to develop the theory allowing to calculate the mismatch stresses with the help of information relating to the crystallography and the mismatch strains. It is the central issue of this project to find the elastic misfit stresses in the TiAl-laminae. We have established rather simple compact formulae for the stresses within the lamellae (on certain distance from the external boundaries and the edges).

The misfit stresses are of the order of elastic moduli times misfit deformations. Since the misfit deformations have enormously high magnitude (as compared with the deformations in conventional macroscopic solids) the misfit stresses and corresponding elastic energy are both enormously large and they should be released via different mechanisms of stress relaxation including proliferation of misfit dislocations, migration of vacancies and dislocations, development of interfacial corrugations, etc... When working of this project we have developed i)some of our early results on the stress-driven rearrangement instabilities of the solid-solid interfaces to make them applicable to the Ti-Al lamellae and also ii)some of out results relating to the slow evolution of interfaces in pre-stressed solids. Though our developed approach do not face any conceptual obstacles for the applications to TiAl alloys we present here some preliminary results only on the both issues i)

and ii) because of the necessity of further routine calculations and analysis and because of volume limitations for this report.

2. Stresses in laminated elastic structure with misfit

2.1. The notion and geometry of misfit deformation

In this Section we give a simplified linear description of elastic heterogeneous systems with coherent interfaces and misfit strains (see Dimiduk et al [3], [4], Hazzledine et al [8], Kad et al [10] for the crystallographic description and physical motivation, and Grinfeld [6] for the more general situation and a more detailed description of the mechanics of heterogeneous solids with finite misfit deformations). Let us choose one of the unstressed configurations of the crystalline substance to be the reference basis for the lamellae elastic structure. In the reference configuration we choose some affine coordinate system x^i; the Latin indices run the values $1, 2, 3$; the summation convention over repeated indexes is implied in what follows. We remind the reader that each affine coordinate system has straight coordinate axes which are not necessarily perpendicular to each other (in particular, any Cartesian coordinate system is necessarily affine): in the following we specify the choice of a specific coordinate system which is the most convenient for the structure in question.

We denote by n^i the components of a unit vector which is perpendicular to the planes along which the lamellae match each other. The total displacement within L-th each of the lamellae $\underset{L}{U_i}\,(x^k)$ can be splitted into two parts

$$\underset{L}{U_i}\,(x^k) = \underset{L}{\Delta_{ij}}\,x^j + \underset{L}{u_i}\,(x^k) \tag{2.1}$$

where the first term $\underset{L}{\Delta_{ij}}\,x^j$ is associated with the misfit deformations whereas the second $\underset{L}{u_i}\,(x^k)$ is associated with the additional elastic deformations. We assume that the misfit strain $\underset{L}{\Delta_{ij}}$ itself does not generate any stresses in the sense that under this strain the isolated lamellae does not accumulate any elastic energy. The misfit strain, however, is the indirect source of huge elastic stresses within the laminated structure since the strains $\underset{L}{\Delta_{ij}}$ differ very significantly (as compared with conventional elastic deformations) within different lamellae. That difference in the misfit strain for different lamellae triggers paramount elastic strains $\partial_j\,\underset{L}{u_i}\,(x^k)$ and

stresses $\underset{L}{p^{ij}}$ because of the requirement of coherency across the interfaces between different lamellae. In what follows the coherency is implied as the continuity of the total displacement across the interfaces. Using the notation $[A]_K^{K+1}$ of the jump of the quantity A across the interface separating the lamellae numbered as $K+1$ and K we can present the coherency condition as follows:

$$[U_i]_K^{K+1} = \left[\Delta_{ij}x^j + u_i(x^k)\right]_K^{K+1} = 0 \tag{2.2}$$

If we choose the coordinate system in such a way that the coordinate planes $x^1 - x^2$ (i.e., the plane $x^3 = const$) coincide with the interfaces between the lamellae, the equation 2.2 appears to be equivalent to the following one:

$$\left[\Delta_{ij} + \partial_j u_i(x^k)\right]_K^{K+1} \delta_\alpha^i = 0 \tag{2.3}$$

Here and in what follows the Greek indices run the values $1, 2$ and the summation convention over repeated Greek indices is implied; the "shift" symbol δ_α^i is equal to 1 if $i = \alpha$ and it is equal to zero otherwise.

The equality of the forces across the coherent interface can be written as

$$\left[p^{ij}\right]_K^{K+1} n_j = 0 \tag{2.4}$$

The assumption of the linear elasticity gives the following formula:

$$\underset{L}{p^{ij}} = \underset{L}{c^{ijkl}}\, \partial_l \underset{L}{u_k} \tag{2.5}$$

where the elasticity tensors are symmetric with respect to the permutation of the indices $\underset{L}{c^{ijkl}} = \underset{L}{c^{jikl}} = \underset{L}{c^{klij}} = \ldots$ Combining 2.4, 2.5, we arrive at the following equations:

$$\left[c^{ijkl}\partial_l u_k\right]_K^{K+1} n_j = 0 \tag{2.6}$$

Within the bulk of each lamellae the following equilibrium equation should be satisfied:

$$\underset{L}{c^{ijkl}}\, \partial_k \partial_l \underset{L}{u_k} = 0 \tag{2.7}$$

The system of equations 2.3, 2.6, and 2.7 allows to find equilibrium displacement within each of the lamellae $\underset{L}{u_i}\ (x^k)$ provided the appropriate mechanical conditions at the external interface is specified.

The equilibrium displacements depend significantly on the "misfit" strains $\underset{L}{\Delta_{ij}}$ and the elasticity tensors $\underset{L}{c^{ijkl}}$. The following two experimental observations allow to simplify the system of equilibrium equation significantly:

i)the elasticities $\underset{L}{c^{ijkl}}$ are the same within each of the lamellae; in the following consideration we use for them the notation c^{ijkl},

ii)only the in-plane components $\underset{L}{\Delta_{\alpha\beta}}$ of the misfit strain $\underset{L}{\Delta_{ij}}$ deviate from zero; hence

$$\underset{L}{\Delta_{ij}} = \underset{L}{\Delta_{\alpha\beta}}\, \delta_i^\alpha \delta_j^\beta, \qquad \underset{L}{\Delta_{i\alpha}} = 0 \tag{2.8}$$

2.2. Some features of the stresses in laminated structures with misfit

The TiAl alloys often have a laminated structure with the laminae having the in-plane dimensions much greater as compared with their thickness. Because of this very feature some general conclusions regarding the equilibrium stress-strain fields can be made in advance (these conclusions can be made on the basis of both: the experiment and relevant asymptotic analysis of the elasticity equations). The equilibrium fields can be splitted into two parts: i)the uniform stress-strain fields on certain distance from the external boundary and the external edges comparable with the thicknesses of individual lamellae (in the following we name it the "internal" field), and ii)the edge distortions of the above "internal" field which appear to be very significant in the vicinity of the external interfaces (in the following we name it the "external" field). The conditions at the external interface cannot change the very fact of the uniform character of the "internal" field though they can change the specific parameters of the "internal" field; needless to say, that the conditions at the external surface play a crucial role in the formation of the "external" stress-strain field. Both - the "external" and the "internal" fields can play significant roles in different aspects of the behavior of the lamellae-like alloys.

2.3. Uniform misfit stresses of the "internal" field

2.3.1. General system of equations defining strain-stress field

The equilibrium "internal" uniform displacements within the plates $\underset{L}{u_i}\,(x^k)$ can be written as follows:

$$\underset{L}{u_i}\,(x^k) = \underset{L}{\kappa_{ij}}\, x^j \tag{2.9}$$

where is the unknown matrix of the equilibrium gradients. Inserting 2.9 in the equations 2.3 and 2.6 we get, respectively:

$$[\kappa_{ij}]_K^{K+1}\,\delta_\alpha^i = -\,[\Delta_{ij}]_K^{K+1}\,\delta_\alpha^i \tag{2.10}$$

$$\left[c^{ijkl}\kappa_{kl}\right]_K^{K+1} n_j = 0 \tag{2.11}$$

The system of algebraic equations 2.10-2.11 includes less equations, than the amount of the unknowns $\underset{L}{\kappa_{ij}}$. This system includes only the demands based on the mechanical equilibrium and coherency at the interfaces. To make the system self-sufficient certain additional physical ideas should be implemented. A deeper analysis shows that there are several "natural" extensions of the system 2.10-2.11. Here we shall discuss only two extensions which are of interest for TiAl multilayers. One of them concerns the "misfit" stresses in multilayers grown on a thick substrate, the other - the "misfit" stresses in the multilayer which are free from any external support. In the former case the substrate appears to be unstressed because of its thickness: we refer the misfit stresses in this case as the "on-substrate" misfit stresses. We counterpose these "on-substrate" misfit stresses to the "free" misfit stresses related to the latter case.

The case of the "free" misfit stresses is more difficult for the calculations and it will be studied first. For this very case and periodically repeated stocks of the lamellae the appropriate asymptotic analysis shows that for the following equation should be satisfied [17]:

$$\sum_{K=1}^{N} \underset{K}{H}\, \underset{K}{p}^{ij} = \sum_{K=1}^{N} \underset{K}{H}\, \underset{K}{c}^{ijkl} \underset{K}{\kappa_{kl}} = 0 \tag{2.12}$$

where $\underset{K}{H}$ is the thickness the K-th lamella within the period.

The $6(N-1)$ equations 2.10, $3(N-1)$ equations 2.11, and 9 2.12 form a closed system of equations with respect to $9N$ unknowns $\underset{K}{\kappa_{kl}}$. By using the equation 2.10 we can find $3N$ unknowns corresponding to the skew-symmetric (rotational) part of the gradients $\underset{K}{\kappa_{[kl]}}$. Calculation gives the following formulae:

$$\left[\kappa_{[ij]}\right]_K^{K+1} = \left[\Delta_{[\alpha\beta]}\right]_K^{K+1} \delta_i^\alpha \delta_j^\beta + 2\left[\kappa_{(k\alpha)}\right]_K^{K+1} n^k \delta_{[i}^\alpha n_{j]} \tag{2.13}$$

The equation 2.13 allows to calculate the equilibrium rotations $\underset{L_{[ij]}}{\kappa}$ within each individual lamellae provided the equilibrium deformations $\underset{L_{(k\alpha)}}{\kappa}$ have already

been determined from some other equations exhibited below. The equation 2.13 shows that i)the equilibrium rotation within the laminae are actually generated by the rotations in the misfit deformations and by the rotations associated with the deformations, and ii)the equilibrium displacements can be determined to within an arbitrary rotation of the sample as the whole.

For the $6N$ unknowns corresponding to the symmetric (deformation) part of the gradients $\underset{K}{\kappa_{(kl)}}$ we find the following $6N$ equations:

$$\left[\kappa_{(\alpha\beta)}\right]_K^{K+1} = -\left[\Delta_{(\alpha\beta)}\right]_K^{K+1} \tag{2.14}$$

$$\left[c^{ijkl}\kappa_{(kl)}\right]_K^{K+1} n_j = 0 \tag{2.15}$$

$$\sum_{K=1}^{N} \underset{K}{H}\, \underset{K}{c}^{ijkl} \underset{K}{\kappa_{(kl)}} = 0 \tag{2.16}$$

The equation 2.10 gives us, in particular

$$\underset{L}{\kappa_{(\alpha j)}}\, n^j = 0 \tag{2.17}$$

and, hence, the formula of the equilibrium rotation can be simplified to read

$$\left[\kappa_{[ij]}\right]_K^{K+1} = \left[\Delta_{[\alpha\beta]}\right]_K^{K+1} \delta_i^\alpha \delta_j^\beta \tag{2.18}$$

According to the equation 2.18 the equilibrium rotation is generated by the rotation in the misfit only, and not by the equilibrium deformations.

2.4. Misfit stresses in the "free" γ/γ plate-like periodic structure with isotropic moduli

In the case of the γ/γ lamellar structure the elastic moduli of the lamellae occur to be equal, and the master system 2.15-2.16 can be simplified significantly to read:

$$c^{ijkl}\left[\kappa_{(kl)}\right]_K^{K+1} n_j = 0 \tag{2.19}$$

$$\sum_{K=1}^{N} \underset{K}{H}\, \underset{K}{\kappa_{(kl)}} = 0 \tag{2.20}$$

Using the equations 2.14, 2.19, 2.20 we find the following formula of the equilibrium stresses $\underset{L}{p^{ij}}$ within the L-th lamella of the γ/γ laminated structure for the case of isotropic lamellae:

$$\underset{L}{p^{ij}} = \frac{\mu}{H}\sum_{K=1}^{N}\underset{K}{H}\left(\frac{2\nu}{1-\nu}\delta^{kl}\delta^{ij} + 2\delta^{ik}\delta^{jl} - \frac{2\nu}{1-\nu}\delta^{kl}n^i n^j\right)\left(\underset{K}{\Delta_{(kl)}} - \underset{L}{\Delta_{(kl)}}\right) \quad (2.21)$$

where μ is the shear modulus of the substance. Simple analysis shows that for the case under consideration the in-plane stresses $\underset{L}{p^{\alpha\beta}}$ only (α and β run the values 1 and 2) can assume non-zero values. For those very components the formula 2.21 can be simplified to read

$$\underset{L}{p^{\alpha\beta}} = \frac{\mu}{H}\sum_{K=1}^{N}\underset{K}{H}\left(\frac{2\nu}{1-\nu}\delta^{\alpha\beta}\,\delta^{\gamma\delta} + 2\delta^{\alpha\gamma}\delta^{\beta\delta}\right)\left(\underset{K}{\Delta_{(\gamma\delta)}} - \underset{L}{\Delta_{(\gamma\delta)}}\right) \quad (2.22)$$

2.5. Misfit stresses in the "free" α/γ - periodic structure (different elastic moduli)

2.5.1. α/γ - periodic structure (2-layers, isotropic elastic lamellae)

When considering the case of different elastic moduli we use the general system 2.14 - 2.16. First, we consider an analytical solution for the case of the isotropic elastic moduli and a periodic cell consisting of two lamellae: the one having the α-like structure and the other having the γ-like structure. A routine calculation gives the following result for the stresses within the lamellae:

$$\begin{aligned}
\underset{1}{p^{\alpha\beta}} &= R_p\,\frac{2\,\underset{1\,2\,2}{\mu\mu H}}{\underset{1\,1}{\mu H} + \underset{2\,2}{\mu H}}\left(\underset{2}{\Delta^{\gamma}_{\cdot\gamma}} - \underset{1}{\Delta^{\gamma}_{\cdot\gamma}}\right)\delta^{\alpha\beta} + \frac{2\,\underset{1\,2\,2}{\mu\mu H}}{\underset{1\,1}{\mu H} + \underset{2\,2}{\mu H}}\left(\underset{2}{\Delta^{(\alpha\beta)}} - \underset{1}{\Delta^{(\alpha\beta)}}\right) \quad (2.23)\\
\underset{2}{p^{\alpha\beta}} &= -R_p\,\frac{2\,\underset{1\,2\,1}{\mu\mu H}}{\underset{1\,1}{\mu H} + \underset{2\,2}{\mu H}}\left(\underset{2}{\Delta^{\gamma}_{\cdot\gamma}} - \underset{1}{\Delta^{\gamma}_{\cdot\gamma}}\right)\delta^{\alpha\beta} - \frac{2\,\underset{1\,2\,1}{\mu\mu H}}{\underset{1\,1}{\mu H} + \underset{2\,2}{\mu H}}\left(\underset{2}{\Delta^{(\alpha\beta)}} - \underset{1}{\Delta^{(\alpha\beta)}}\right)
\end{aligned}$$

where the constant R is defined as

$$R_p = \frac{\underset{1\,1}{\mu H}\left(1+3\,\underset{1}{C}\right)\underset{2}{C} + \underset{2\,2}{\mu H}\left(1+3\,\underset{2}{C}\right)\underset{1}{C}}{\underset{1\,1}{\mu H}\left(1+3\,\underset{1}{C}\right)\left(1+\underset{2}{C}\right) + \underset{2\,2}{\mu H}\left(1+3\,\underset{2}{C}\right)\left(1+\underset{1}{C}\right)}, \qquad \underset{K}{C} \equiv \frac{\underset{M}{\nu}}{1-2\,\underset{M}{\nu}} \quad (2.24)$$

The in-plane deformations within the lamellae $\underset{M}{\kappa}^{(\alpha\beta)}$ are equal to

$$\begin{aligned}
\underset{1}{\kappa}^{(\alpha\beta)} &= R_\kappa \left(\underset{2}{C} - \underset{1}{C}\right)\left(\Delta^{\gamma}_{2\,\cdot\gamma} - \Delta^{\gamma}_{1\,\cdot\gamma}\right)\delta^{\alpha\beta} + \frac{\underset{2\,2}{\mu H}}{\underset{1\,1}{\mu H} + \underset{2\,2}{\mu H}}\left(\Delta^{(\alpha\beta)}_{2} - \Delta^{(\alpha\beta)}_{1}\right) \qquad (2.25)\\
\underset{2}{\kappa}^{(\alpha\beta)} &= -R_\kappa \left(\underset{2}{C} - \underset{1}{C}\right)\left(\Delta^{\gamma}_{2\,\cdot\gamma} - \Delta^{\gamma}_{1\,\cdot\gamma}\right)\delta^{\alpha\beta} - \frac{\underset{1\,1}{\mu H}}{\underset{1\,1}{\mu H} + \underset{2\,2}{\mu H}}\left(\Delta^{(\alpha\beta)}_{2} - \Delta^{(\alpha\beta)}_{1}\right)
\end{aligned}$$

where

$$R_\kappa = \frac{\underset{1\,2\,1\,2}{\mu\mu HH}}{\underset{1\,1}{\mu H}\left(1+3\,\underset{1}{C}\right)\left(1+\underset{2}{C}\right) + \underset{2\,2}{\mu H}\left(1+3\,\underset{2}{C}\right)\left(1+\underset{1}{C}\right)} \qquad (2.26)$$

For the out-plane deformation components $\underset{M}{\kappa}^{(33)}$ we get the formulae

(2.27)

$$\begin{aligned}
\underset{1}{\kappa}^{(33)} &= -\frac{\left(1+3\,\underset{2}{C}\right)\underset{1\,2\,2}{C\mu H}}{\underset{1\,1}{\mu H}\left(1+3\,\underset{1}{C}\right)\left(1+\underset{2}{C}\right) + \underset{2\,2}{\mu H}\left(1+3\,\underset{2}{C}\right)\left(1+\underset{1}{C}\right)}\left(\Delta^{\gamma}_{2\,\cdot\gamma} - \Delta^{\gamma}_{1\,\cdot\gamma}\right)\\
\underset{2}{\kappa}^{(33)} &= \frac{\left(1+3\,\underset{1}{C}\right)\underset{2\,1\,1}{C\mu H}}{\underset{1\,1}{\mu H}\left(1+3\,\underset{1}{C}\right)\left(1+\underset{2}{C}\right) + \underset{2\,2}{\mu H}\left(1+3\,\underset{2}{C}\right)\left(1+\underset{1}{C}\right)}\left(\Delta^{\gamma}_{2\,\cdot\gamma} - \Delta^{\gamma}_{1\,\cdot\gamma}\right)
\end{aligned}$$

All other components of the deformation appear to be zero.

If the Poisson ratios of the phases are equal - $\underset{1}{\nu} = \underset{1}{\nu} = \nu$ - the formulae 2.24 - 2.27 allow some simplifications; in particular, we get the following formula of R in this case:

$$R_p = \frac{\nu}{1-\nu} \qquad (2.28)$$

If, in addition, the shear moduli are equal - $\underset{1}{\mu}=\underset{1}{\mu}=\mu$ - the formulae 2.23 of the stresses $\underset{M}{p}^{\alpha\beta}$ reads:

(2.29)

$$\begin{aligned}
\underset{1}{p}^{\alpha\beta} &= \frac{2\mu\,\underset{2}{H}}{\underset{1}{H} + \underset{2}{H}}\,\frac{\nu}{1-\nu}\left(\Delta^{\gamma}_{2\,\cdot\gamma} - \Delta^{\gamma}_{1\,\cdot\gamma}\right)\delta^{\alpha\beta} + \frac{2\mu\,\underset{2}{H}}{\underset{1}{H} + \underset{2}{H}}\left(\Delta^{(\alpha\beta)}_{2} - \Delta^{(\alpha\beta)}_{1}\right)\\
\underset{2}{p}^{\alpha\beta} &= -\frac{2\mu\,\underset{1}{H}}{\underset{1}{H} + \underset{2}{H}}\,\frac{\nu}{1-\nu}\left(\Delta^{\gamma}_{2\,\cdot\gamma} - \Delta^{\gamma}_{1\,\cdot\gamma}\right)\delta^{\alpha\beta} - \frac{2\mu\,\underset{1}{H}}{\underset{1}{H} + \underset{2}{H}}\left(\Delta^{(\alpha\beta)}_{2} - \Delta^{(\alpha\beta)}_{1}\right)
\end{aligned}$$

The formulae 2.29 appear to be in agreement with the formulae 2.23 as they should.

2.5.2. α/γ - periodic structure (N-layers, anisotropic elastic lamellae)

The analysis of this most general case is based on the system 2.14 - 2.16. It is convenient to introduce the following matrices:

$$\underset{L}{T}{}^{\alpha\beta}_{\pi\omega} = \sum_{K=1}^{K=N} \underset{K}{H}\, \underset{K}{c}{}^{\alpha\beta\gamma\delta}\, \underset{L\gamma\delta\pi\omega}{s}, \qquad \underset{L}{R}{}^{\alpha\beta} = \sum_{K=1}^{K=N} \underset{K}{H}\, \underset{K}{c}{}^{\alpha\beta\gamma\delta} \left(\underset{K\,(\gamma\delta)}{\Delta} - \underset{L\,(\gamma\delta)}{\Delta} \right) \tag{2.30}$$

where $\underset{L\gamma\delta\pi\omega}{s}$ are the "partial 1-2" part of the compliance tensor $\underset{Lijkl}{s}$; $\underset{L}{c}{}^{\alpha\beta\gamma\delta}$ is the inverse of $\underset{L\gamma\delta\pi\omega}{s}$, i.e., the tensor satisfying the relationship

$$\underset{L}{c}{}^{\alpha\beta\gamma\delta}\, \underset{L\gamma\delta\pi\omega}{s} = \delta^{\alpha}_{(\pi}\delta^{\beta}_{\omega)} \tag{2.31}$$

In terms of these "material" tensors the stress tensor within the L-th lamella $\underset{L}{p}{}^{\alpha\beta}$ can be calculated with the of the following linear system of equations:

$$\underset{L}{T}{}^{\alpha\beta}_{\pi\omega}\, \underset{L}{p}{}^{\pi\omega} = \underset{L}{R}{}^{\alpha\beta} \tag{2.32}$$

We remind the reader that in the equations 2.30 - 2.32 the indices run the values 1 and 2 only (not 3!).

The above program can be fulfilled explicitly in the case of isotropic lamellae. Corresponding calculations give the following formula of the stresses within the L-th lamella of the spatial period including N lamellae:

$$\underset{L}{p}{}^{\alpha\beta} = \sum_{M=1}^{N} \underset{M}{H} \left[\frac{2\,\underset{M}{\nu}\,\underset{M}{\mu}\,\underset{L}{T} - \left(1-\underset{M}{\nu}\right)\underset{L}{\mu}\,\underset{L}{F}}{\left(1-\underset{M}{\nu}\right) 2\,\underset{L}{T}\left(\underset{L}{T}+\underset{L}{F}\right)} \delta^{\alpha\beta}\delta_{\pi\omega} + \frac{\underset{M}{\mu}}{\underset{L}{T}} \delta^{\alpha}_{(\pi}\delta^{\beta}_{\omega)} \right] \left(\underset{M}{\Delta}{}^{(\pi\omega)} - \underset{L}{\Delta}{}^{(\pi\omega)} \right) \tag{2.33}$$

where $\underset{L}{T}$ and $\underset{L}{F}$ are defined as follows:

$$\underset{L}{T} = \frac{1}{2}\sum_{K=1}^{N} \underset{K}{H}\, \frac{\underset{K}{\mu}}{\underset{L}{\mu}}, \qquad \underset{L}{F} = \sum_{K=1}^{N} \underset{K}{H}\, \frac{\underset{K}{\mu}}{\underset{L}{\mu}} \frac{\underset{K}{\nu} - \underset{L}{\nu}}{\left(1-\underset{K}{\nu}\right)\left(1-\underset{L}{\nu}\right)} \tag{2.34}$$

2.6. Misfit stresses in the "on-substrate" periodic multilayers with different elastic moduli

The case of the "on-substrate" multilayer is of the primary interest in many applications, especially, those related to the deposition of thin films, though they are of a secondary interest in concerns the TiAl lamellar structure, and we pay much less attention to it in this report. In the "on-substrate" case the extremely thick substrate does not deform practically and it can be treated as if it is rigid. Because of this fact all the monolayers of the multilayer are "aware" of presence of the substrate only, and they "know" nothing about the existence of other monolayers. Therefore, we can rewrite the system 2.14, 2.15

$$\underset{M(\alpha\beta)}{\kappa} = - \underset{M}{\Delta}_{(\alpha\beta)} \tag{2.35}$$

$$\underset{M}{c}^{ijkl} \underset{M(kl)}{\kappa} n_j = - \underset{M}{c}^{ijkl} \underset{M(kl)}{\Delta} n_j \tag{2.36}$$

where if the "misfit" with respect to the lattice of the substrate $\underset{M(kl)}{\Delta}$. The system 2.35, 2.36 appears to be closed with respect to the unknown misfit deformations $\underset{M(kl)}{\kappa}$. It shows, in particular, that the stresses do not depend of the lamellae's thicknesses. In the case of isotropic lamellae we arrive at the following misfit deformations and stresses:

$$\underset{M(\alpha 3)}{\kappa} = 0, \qquad \underset{M(33)}{\kappa} = \frac{\nu_M}{1-\nu_M} \underset{M}{\Delta}^{\alpha}{}_{\alpha} \tag{2.37}$$

$$\underset{M(\alpha\beta)}{p} = -2\mu_M \left(\nu_M \underset{M}{\Delta}^{\gamma}{}_{\gamma} \delta_{\alpha\beta} + \Delta_{(\alpha\beta)} \right) \tag{2.38}$$

3. Role of vacancies in slow evolution of interfaces

The elastic misfit stresses in TiAl alloys assume huge level of the order of the product of the elastic moduli times misfit deformations. The elastic energy associated with these stresses is enormously large also. Hence, there appears a driving force for the rearrangement of the species leading to the evolution accompanied by the creation of dislocations, migration of vacancies, development of interfacial corrugations, etc... The goal of this Section is to develop a thermodynamic approach allowing one to study the possibility of stress relaxation by means of mass

rearrangement in the vicinity of the interface between the lamellae. We assume that the rearrangement is accompanied by interfacial diffusion and migration of the vacancies. Since the full consideration of the coherent interface solid-solid includes lots of calculation and details we illustrate our results and approach by considering the much simpler but conceptually a very close problem of mass rearrangement in the vicinity of a stress-free interface.

Mass transport through the bulk of solids is produced by the migration of vacancies whereas near surfaces the migration of vacancies is accompanied by surface diffusion, vaporization-sublimation, etc. (see, for instance, Christian [5]). The simplest and most robust features of the mechanism of surface diffusion has been studied by Mullins [15]. It is widely accepted that this mechanism dominates over migration of vacancies near traction-free surfaces. The situation can change dramatically at the nano-scale (see, for instance, Lee and Bennet [14]). At this level the very applicability of common thermodynamics seems questionable. Since at the nano-scale it is difficult to distinguish between the bulk and the surface part of the solid it seems natural, at least, to withdraw existing macro- and micro-scale "obvious" pre-assumptions and to explore the mechanism of interaction between surface diffusion and vacancy migration.

In this note three dissipation mechanisms are taken into account: i)dissip ation from the flow of vacancies at the surface, ii)dissipation from bulk diffusion of vacancies, iii)dissipation from surface diffusion. In addition to the bulk energy ϕ the Herring-like surface energy [9] is taken into account. We consider a slightly corrugated solid film of thickness H attached to a rigid substrate, see Figure. It is assumed that the vacancies can penetrate the bulk through the free interface Ξ of the film only. We denote the time by t, the spatial coordinates by x^k (the spatial - Latin - indices run 1,2,3, and summation over repeated indices is implied). $\chi(x^k,t)$ is the volume concentration of vacancies and $Q^i(x^k,t)$ is the vector of the volume flux of vacancies. We denote the surface coordinates of the free surfaces by ξ^β (the surface - Greek - indices run 1,2); $c(\xi^\beta,t)$ and $q^\alpha(\xi^\beta,t)$ are the normal velocity of the free surface and the surface flux of the species, respectively. Simple kinematics (Mullins, 1957 [15]; Christian, 1975 [5]; Grinfeld, 1994 [7]; Berdichevsky et al. 1996 [2]) leads to the following equations of mass conservation within the bulk

$$\frac{\partial \chi}{\partial t} = \frac{\partial Q^i}{\partial x^i} \tag{3.1}$$

and at the free surface

$$c(1-\chi) = Q^i n_i + \frac{\partial q^\alpha}{\partial \xi^\alpha} \tag{3.2}$$

where $n_i(\xi^\beta, t)$ is a unit normal to the surface. The first term on the right hand side of Eq. 3.2 describes the migration of the free surface from the flow of vacancies through the surface, while the second describes the migration of the surface from the surface diffusion.

In this "kinematic surrogate" of a complete thermodynamic theory we ignore the role of stresses and heat and suppose that the energy per unit volume ϕ is a function of the vacancy concentration χ, whereas the surface energy per unit area is a positive constant σ. The simplest "constitutive" equations of the volume and surface fluxes compatible with the requirement of energy dissipation read:

$$Q^i = D_b^{ij} \frac{\partial}{\partial x^j} \frac{\partial \phi}{\partial \chi} \tag{3.3}$$

$$q^\alpha = D^{\alpha\beta} \frac{\partial}{\partial \xi^\beta} \frac{\phi - \sigma\kappa}{1-\chi} \tag{3.4}$$

where D_b^{ij} and $D^{\alpha\beta}$ are the bulk and surface positive symmetric diffusion tensors, respectively; κ is a doubled mean curvature of the surface. The simplest equation to describe the flow of vacancies $Q^i n_i$ through the free surface compatible with the principle of energy dissipation reads

$$Q^i n_i = -D_I \frac{\phi + (1-\chi)\phi_\chi - \sigma\kappa}{1-\chi} \tag{3.5}$$

where D_I is a positive constant characterizing the resistance of the solid substance to penetrating of vacancies; $\phi_\chi = \partial\phi/\partial\chi$. For the sake of simplicity we assume that no vacancies flow through the film-substrate interface Σ:

$$Q^i n_i = 0 \tag{3.6}$$

The equations 3.1 - 3.6 form a closed self-consistent nonlinear system of the differential equations and boundary conditions for describing slow evolution of deformable elastic solids with vacancies.

We denote by χ° the equilibrium concentration of vacancies within the film when it has a plane free surface and is exposed to vacuum. Hence, according to Eq. 3.5, χ° satisfies the equation

$$\phi(\chi^\circ) + (1-\chi^\circ)\phi_\chi(\chi^\circ) = 0 \tag{3.7}$$

Let us assume now that the free surface Ξ is slightly corrugated. The evolution of this corrugation can be explored by linearizing the equations 3.1 - 3.7 in the vicinity of the uniform configuration with further consideration of the solutions of the form $\sim \exp(\eta t + ik_\alpha \xi^\alpha)$; here ξ^α are the Cartesian coordinates on the equilibrium plane surface, k_α is the in-plane wave-number of the corrugation, η is the growth-decay rate of the corrugations.

In the following we assume that the film is isotropic and contains a small concentration of vacancies $\chi^\circ \ll 1$. Hence, the diffusion tensors take on the form: $D_b^{ij} = D_b \delta^{ij}$, $D^{\alpha\beta} = D_s \delta^{\alpha\beta}$, where D_b and D_s are positive constants whereas δ^{ij} and $\delta^{\alpha\beta}$ are the spatial and surface Kronecker symbols. A routine computation results in the following dispersion equation for this case:

$$\left[D_b k \tanh\left(kH\sqrt{1 + \frac{\eta}{k^2 N D_b}} \right) + D_I \right] \left(\eta + D_s \sigma k^4 \right) + D_b D_I \sigma k^3 = 0 \qquad (3.8)$$

where $N = \partial^2 \phi(\chi^\circ)/\partial \chi^2$.

Eq. 3.8 shows that the real η are necessarily negative as they should be in the absence of destabilizing factors.

If $\eta/(k^2 N D_b) \ll 1$ we can derive from Eq. 3.8 the following dispersion relation:

$$\eta = -\sigma k^3 \frac{D_s D_b k^2 \tanh(kH) + D_I D_s k + D_b D_I}{D_b k \tanh(kH) + D_I} \qquad (3.9)$$

Eq. 3.9 shows clearly that the three dissipation mechanisms are not additive but interact with each other. It is quite instructive to extract from Eq. 3.9 Mullins' k^4-term by rewriting the equation in the form

$$\eta = -D_s \sigma k^4 \left(1 + \frac{1}{\frac{D_s k^2}{D_I} \tanh(kH) + \frac{D_s k}{D_b}} \right) \qquad (3.10)$$

The second terms in the brackets gives a correction to the "k^4-law" which might even dominate, depending on the magnitudes of the nondimensional numbers $D_s k^2/D_I$, $D_s k/D_b$, kH. First of all the assumption $\eta/(k^2 N D_b) \ll 1$ gives for the Mullins mode the following short wave-length limitation: $D_s \sigma k^2/N D_b \ll 1$. The correction term approaches zero at $D_s k^2/D_I \gg 1$ or $D_s k/D_b \gg 1$. For thin films the asymptote $kH \to 0$ is often of interest. In this limit Eq. 3.10 reads

$$\eta = -D_s \sigma k^4 \left(1 + \frac{D_b}{D_s k} \right) \qquad (3.11)$$

and for sufficiently long wave corrugations with $k^{-1} \geq D_s/D_b$ the correction term is comparable with the Mullins k^4-term. The k^3-term appears to dominate as $k \to 0$ and in this limit the rate η approaches $-D_b\sigma k^3$. The k^3 variation also holds for thick films in the case of "instantaneous kinetics" (very large values of D_I). We notice that the same dispersion equation $\eta \propto k^3$ is valid for the transport mechanism "vaporization-condensation" which is presumably more effective than the vacancy transport at macro- and micro-scale level but the situation could be opposite at the nano-scale level because the values of D_s, D_b, and D_I need not be the same as they are in macroscopic bodies.

It is well-known that stresses within the solid can destabilize flat interfaces when rearrangement of mass is allowed. Assuming that the film is isotropic and it is sufficiently thick we arrive the following generalization of Eq. 3.8:

$$\left(D_b k\sqrt{1+\frac{\eta}{k^2 N D_b}}+D_i\right)\eta + \left[\sqrt{1+\frac{\eta}{k^2 N D_b}}(D_k D_i + D_b D_s k^2)k^2 + D_i D_s k^3\right]\left[\sigma k - (1-\nu)\frac{T^2}{\mu}\right] = 0 \quad (3.12)$$

where ν is the Poisson ratio, T is the uniaxial stress. Eq. 3.12 can be presented in the following dimensionless form:

$$(\sqrt{1+R}+K_{ib})R + \left[\sqrt{1+R}(K_{ib}+K_{sb})+K_{ib}K_{sb}\right]\left[1-(1-\nu)\Phi\alpha\right]\tilde{\Upsilon} = 0 \quad (3.13)$$

where the dimensionless numbers R, K_{ib}, K_{sb}, $\Phi\alpha$, Υ are defined as follows:

$$R = \frac{\eta}{k^2 N D_b},\ K_{ib} = \frac{D_i}{D_b k},\ K_{sb} = \frac{D_s k}{D_b},\ \Phi\alpha = \frac{T^2}{\sigma\mu k},\ \Upsilon = \frac{\sigma k}{N} \quad (3.14)$$

At $R \ll 1$ we get the following nondimensional dispersion equation:

$$R = \frac{K_{ib}+K_{sb}+K_{ib}K_{sb}}{1+K_{ib}}\left[1-(1-\nu)\Phi\alpha\right]\Upsilon \quad (3.15)$$

which gives a consistent generalization of the dispersion equation of Asaro and Tiller (1972) [1], compatible also with the static stability criteria (see, for instance, Grinfeld, 1991 [6]; Nozières, 1991 [16]) though it differs from the criterion of Vasudev, Asaro and Tiller (1975) [18]exploring the same mechanism of rearrangement via the bulk diffusion in pre-stressed crystal. The possibility of stress driven "necking"of a rod caused by the migration of vacancies has been noticed by Larche and Cahn (1985) [12].

4. Conclusion

4.1. The main results of this project.

The elastic misfit stresses in TiAl alloys assume huge level of the order of the product of the elastic moduli times misfit deformations. The elastic energy associated with these stresses is enormously large also. Hence, there appears a driving force for the rearrangement of the material elements leading to the evolution accompanied by the creation of dislocations, migration of vacancies, development of interfacial corrugations, etc...

The goal of this research project was two-fold: i)to develop a theoretical approach which permits a self-consistence calculations of misfit stresses in TiAl lamellar multilayers and like structures, and ii)to develop a thermodynamic approach allowing one to study the possibility of stress relaxation by means of mass rearrangement in the vicinity of the interface between the lamellae.

We have developed a general scheme and establish several simple general formulae permitting to evaluate numerically and to analyze qualitatively misfit stresses in TiAl multilayers. On the basis of the model of coherent interfaces we arrive to the conclusion that one have to carefully distinguish between the "on-substrate" misfit stresses, on the one hand, and the "free-edge" misfit stresses, on the other case. The former case is more relevant for the stresses appearing at different processes of deposition: the misfit deformations and strains-in the "on-substrate" multilayers can be calculated with the help of the master system 2.35, 2.36 (for the general anisotropic case) and simple formulae 2.37, 2.38 for the case of isotropic monolayers. The "free-edge" misfit deformations and stresses can be calculated with the help of the master system of algebraic equations 2.14 - 2.16 for the arbitrary anisotropic lamellae with different moduli. Much more simple working formulae can be used in the case of isotropic lamellae:

i - 2.21, 2.22 for the case of equal elastic moduli (N-layer periodic multilayer in width),

ii - 2.23-2.29 for the case of different elastic moduli (2-layer period multilayer in width),

iii - 2.33, 2.34 for the case of different elastic moduli (N-layer periodic multilayer in width).

When studying possible mechanisms of stress relaxation we assumed that the rearrangement is accompanied by interfacial diffusion and migration of the vacan-

cies. Since the full consideration of the coherent interface solid-solid includes lots of calculation and details we illustrate our results and approach by considering the much simpler but conceptually a very close problem of mass rearrangement in the vicinity of a stress-free interface. Using one of the approaches of irreversible thermodynamics of solids we explored the slow evolution of corrugations at the free boundary of a crystalline substance. The central issues of this study are the roles and the interaction of the three dissipation mechanisms: i)the surface diffusion of the species, ii)the bulk diffusion of vacancies, and iii)the flow of vacancies within the solid from vacuum. For the flux of vacancies from vacuum we have postulated the constitutive equation 3.5 which can be easily justified on the basis of Onsager ideology (this means, basically, that the constitutive law for the flux should obey the linearity between the flux and corresponding driving force, and it has to provide the decay of the total accumulated energy). The new dissipative material constant D_I appearing in this modelling should be determined by quantitative measurement of different effects relating to the penetration of vacancies within the solid from vacuum (which is nothing else but rearrangement of the species accompanied by producing new vacancies in the vicinity of the free surface). One of the effects of this sort is the evolution of surface corrugations: the growth-decay rate of the corrugations depends, besides other parameters, on the value of D_I. We have derived a rather simple dispersion equation 3.8 of the growth rate of the surface corrugation η with the help of the master system of slow evolution (Eqs. 3.1 - 3.6) using the simplest model of the isotropic elastic solid with vacancies (Lifshitz, 1962 [13]). The equation 3.8 and its implications 3.9 - 3.11 allow one to find those corrugations for which the Mullins' k^4 - law gives acceptable approximation and those for which it does not. The equations 3.8 - 3.10 clearly show that the three above mentioned dissipative mechanism cannot be described as the linear superposition even for small disturbances (as they are treated usually in the existing literature).

As the side result of this study we have derived the dispersion equation 3.12 of the growth rate of surface corrugations in the pre-stressed crystal. Our dispersion equation appears to be consistent with the known thermodynamic criterion of the stress driven rearrangement instability as it should.

4.2. The most promising directions of future research

The result of this project demands further studies in what concerns both theory and experiment. The following directions of theoretical studies look the most

urgent and promising:

I Misfit stresses in the case of large misfit deformations (actually, only the "in-plane" misfit deformations can be supposed small geometrically - of the order of several % - in the first approximation; the shear deformations are actually extremely big of the order of hundred %%).

II Misfit stresses in the plate-like random structure

III The edge effects

- The edge effects in vicinity of free surface
- The edge effects in vicinity of intersection of two free surfaces
- The edge effects at the corners

IV The grain structure of the lamellae

- An isolated grain within a lamella
- An equilibrium shape of an isolated grain within a lamella
- Stability of an isolated grain within a lamella
- A periodic ensemble of the grains within the isolated lamella

V Effective elastic moduli of laminated elastic structures with large internal stresses

- Effective elastic moduli in the γ/γ - periodic structure (equal elastic moduli)
- Effective elastic moduli in the α/γ - periodic structure (different elastic moduli)

VI The non-elastic effects

- Relaxation of misfit stresses via the mechanism of the stress driven rearrangement instability at the coherent interfaces
- Relaxation of misfit stresses via proliferation of misfit dislocations
- Nucleation of misfit dislocations via the mechanism of the stress driven rearrangement instability

References

[1] Asaro R. J. and Tiller W.A., *Metall. Trans.* **3** (1972) 1789.

[2] Berdichevsky V.L., Hazzledine P.M. and Shoyhet B.I., (1996), submitted.

[3] Dimiduk D.M., Miracle Y.W. and Kim Y.W., *ISIJ Internat.* **31** (1991) 367.

[4] Dimiduk D.M. and Parthasarathy T.A., *Phil. Mag. Lett.* **71** (1995), 21.

[5] Christian J. W., Transformations in Metals and Alloys, (Pergamon Press), 1975.

[6] Grinfeld M.A., *Thermodynamic Methods in the Theory of Heterogeneous Systems*, (London: Longman) 1991.

[7] Grinfeld M.A., *Scanning Microscopy*, **8** (1994) 869.

[8] Hazzledine P.M., et al *MRS Symposium* **273** (1992) 81.

[9] Herring C., In *Structure and Properties of Solid Surfaces*, edited by R. Gomer and C.S. Smith (University of Chicago Press) 1953.

[10] Kad B.K. and Hazzledine P.M., *Phil. Mag. Lett.* **66** (1992), 133.

[11] Kassner K. and Misbah C., Europhys. Lett. **28** (1994) 245.

[12] Larché F.C. and Cahn J.W., *Acta Metall.* **33** (1985) 331.

[13] Lifshitz I.M, *Soviet Physics, ZETP* **17** (1962) 909.

[14] Lee M.Y. and Bennet P.A., *Phys. Rev. Lett.* **75** (1995) 4460.

[15] Mullins W.W., *J. Appl. Phys.* **28** (1957) 333.

[16] Nozières Ph., Lectures at Beg-Rohu Summer School (1989), in *Solids Far From Equilibrium*, edited by C. Godrèche, (Cambridge: Cambridge Univ. Press) 1991.

[17] Shoykhet B.A. Private communication.

[18] Vasudev P., Asaro R.J. and Tiller, A.W., *Acta Metall.* **23** (1975) 341.